Springer Series on Chemical Sensors and Biosensors 18
Series Editor: Gerald Urban

Peter Lieberzeit *Editor*

Piezoelectric Sensors

Springer

18
Springer Series on Chemical Sensors and Biosensors

Methods and Applications

Series Editor: Gerald Urban

Chemical sensors and biosensors are becoming more and more indispensable tools in life science, medicine, chemistry and biotechnology. The series covers exciting sensor-related aspects of chemistry, biochemistry, thin film and interface techniques, physics, including opto-electronics, measurement sciences and signal processing. The single volumes of the series focus on selected topics and will be edited by selected volume editors. The *Springer Series on Chemical Sensors and Biosensors* aims to publish state-of-the-art articles that can serve as invaluable tools for both practitioners and researchers active in this highly interdisciplinary field. The carefully edited collection of papers in each volume will give continuous inspiration for new research and will point to existing new trends and brand new applications.

Piezoelectric Sensors

Volume Editor:
Peter Lieberzeit

With contributions by

T. Aastrup · M. Almajdoub · G. Attia · Y. Chang · I. Chianella · X. Duan · I. Dufour · C. Durall · A. Feldner · N. Fourati · A. Ibrahim · J. A. Jackman · N. Jones · S. Khaoulani · P. Lieberzeit · T. Mirea · I. A. Nicholls · A. Nolting · W. Pang · E. Peiner · X. Sun · S. Suriyanarayanan · F. Thier · J. Völkle · D. Wallinder · Z. Wang · J. Xu · C. Zerrouki

Springer

Editor
Peter Lieberzeit
Department of Physical Chemistry
University of Vienna
Vienna, Austria

ISSN 1612-7617
Springer Series on Chemical Sensors and Biosensors
ISBN 978-3-031-53784-4 ISBN 978-3-031-53785-1 (eBook)
https://doi.org/10.1007/978-3-031-53785-1

This Springer imprint is published by the registered company Springer Nature Switzerland AG
The registered company address is: Gewerbestrasse 11, 6330 Cham, Switzerland

Series Editor

Gerald Urban
Institute for Microsystems Engineering
IMTEK - Laboratory for Sensors
Albert-Ludwigs-University
Freiburg, Baden-Württemberg
Germany

Preface

The present book succeeds the volume "Piezoelectric Sensors" published in 2007, without being its second edition in the strict sense of the word. Obviously, the field has strongly developed since then: the early 2000s still saw substantial fundamental work to better understand the physical and chemical processes governing the frequency responses observed on quartz crystal microbalances (QCMs), surface acoustic wave (SAW) resonators or Love wave resonators, among others. This especially comprised also improving the measuring approaches for making them better suited to operating in liquid phase. Such fundamental work is still necessary, but the focus nonetheless has shifted to other device types, especially FBARs, i.e. film bulk acoustic resonators, not least for making it possible to manufacture microsensors in integrated circuit systems. Furthermore, recording dissipation parameters in addition to frequency responses has gained increasing attention, not least for the occurrence of commercially available measuring systems based on such concepts. Finally, the last few decades have also seen non-piezoelectric mass-sensitive transducers emerging, such as microcantilever sensors. Hence, this book aims at giving readers an overview of current mass-sensitive measuring approaches, discussing both novel device types and application scenarios.

The book follows the same logic, as its predecessor: the first section comprises three chapters that discuss the fundamentals of three different mass-sensitive measuring strategies, namely the abovementioned FBAR, dissipative QCM (QCM-D), and microcantilevers. The reader may expect insights into the physics and measuring technique of those systems together with some application scenarios. The second, larger, section covers different application and functionalization scenarios that highlight the use of mass-sensitive devices to tackle analytical questions in chemistry and (molecular) biology. Though most of those chapters come from working groups in academia, there is also one from industry, which reflects the path of mass-sensitive measuring from "purely research" to commercial application.

I very much hope that the selection of chapters gives readers a fruitful insight into the area of mass-based chemo- and biosensing. Of course, it lacks some of the

fundamentals of long-existing devices. However, this volume in my opinion complements the one from 2007. It does not claim replacing it.

Finally, I want to express my deep gratitude to all the authors for the smooth, respectful, and very fruitful collaboration. I owe thanks to the series editor, Gerald Urban, who "nudged" me into facing this endeavour and then has shown great patience for any issues arising during the process. The same holds true for the publishing team at Springer, who were always at service, when needed. Last but not least, I am very grateful to my mentor, Professor Franz L. Dickert, who recently celebrated his 80th birthday: he introduced me into the world of mass-sensitive measuring, of which he has been a valued member ever since.

My hope is that readers enjoy reading the chapters as much as I did during the process.

Vienna, Austria Peter Lieberzeit
December 2023

Contents

Quartz Crystal Microbalance-Dissipation Technique for Tracking Dynamic Biomacromolecular Interactions

Joshua A. Jackman

Contents

Abstract The quartz crystal microbalance-dissipation (QCM-D) technique is a highly surface-sensitive technique for measuring biomacromolecular interactions that occur at solid–liquid interfaces. Key advantages of the acoustic-based QCM-D technique include its label-free format, fast measurement response, compatibility with various material interfaces, and high sensitivity to detect not only the amount and configuration of biomacromolecular adsorbates but also hydrodynamically coupled solvent near the sensor surface. This sensitivity is particularly important for detecting structural changes associated with dynamic biomacromolecular interactions relevant to biological systems. In this chapter, the main objective is to

J. A. Jackman (✉)
School of Chemical Engineering and Translational Nanobioscience Research Center, Sungkyunkwan University, Suwon, Republic of Korea
e-mail: jjackman@skku.edu

P. Lieberzeit (ed.), *Piezoelectric Sensors*, Springer Series on Chemical Sensors and Biosensors (2024) 18: 1–32, https://doi.org/10.1007/5346_2023_34,

Published online: 29 October 2023

introduce how the QCM-D technique is useful for medical and biotechnology applications related to tracking dynamic biomacromolecular interactions. The basic measurement principles of the QCM-D technique and popular modeling approaches are introduced before reviewing a selection of classical and recent application examples that involve lipid membranes, proteins, peptides, biosurfactants, and detergents. Two main classes of dynamic biomacromolecular interactions are covered as representative cases of different measurement scenarios, i.e., the structural transformation of (1) soft adsorbates into rigid adsorbates and (2) rigid adsorbates into soft adsorbates. Particular focus is placed on biomimetic lipid membrane platforms and on critically discussing the suitability of applying physics-based models to interpret QCM-D measurement data in specific biomacromolecular interaction cases. Alternative interpretation strategies based on empirical testing are also described in order to support biologically directed analyses. As presented in this chapter, ongoing progress in the field supports that the QCM-D technique has a bright future for studying complex biological phenomena at solid–liquid interfaces across a wide range of topics spanning fundamental and translational viewpoints.

Keywords Acoustic sensor, Adsorption, Biomacromolecules, Biosensor, Quartz crystal microbalance-dissipation (QCM-D)

1 Introduction

The quartz crystal microbalance-dissipation (QCM-D) technique is a widely used, label-free biosensing tool that is highly sensitive to the mass and conformational properties of biomacromolecular adsorbates at solid–liquid interfaces [1–3]. Compared to other label-free biosensing techniques, a key advantage of the QCM-D technique is its high sensitivity to adsorbed biomacromolecular mass and hydrodynamically coupled solvent whereas other options like refractive index-based optical biosensors are typically sensitive to adsorbed biomacromolecular mass only [4–6]. As such, the QCM-D technique is highly useful for distinguishing the structural configuration and conformational properties of different biomacromolecular assemblies such as adsorbed vesicle layers vs. supported lipid bilayers (SLBs) [7, 8]. While the QCM-D technique has demonstrated high versatility for a wide range of biological applications involving various types of biomacromolecules, arguably the most important contribution of QCM-D technology to advance understanding of biophysical phenomena has been in the area of studying complex structural transformations where adsorbates are converted from one form to another—cases which we consider within the class of dynamic biomacromolecular interactions [9–15]. Increasingly, such insights are helping to guide translational science applications like pharmaceutical drug development and sustainable chemicals discovery.

This chapter aims to critically introduce the QCM-D technique as a powerful tool to study complex structural transformations involving biomacromolecules, with a particular focus on transformations converting soft adsorbates into rigid ones and rigid adsorbates into soft ones. The basic measurement principles of the QCM-D technique, including experimental operation and data analysis options, are first covered before proceeding into more detailed case studies. In specific cases, detailed quantification of QCM-D responses is provided to illuminate application examples while the overall scope is to broadly highlight trends and practices in the usage of QCM-D technology for studying biological topics related to dynamic biomacromolecular interactions.

2 QCM-D Measurement Principles

The QCM-D technique is based on measuring the resonance frequency (Δf) shift and energy dissipation (ΔD) shift associated with an adsorbate on a sensor surface [16]. Typically, the QCM-D sensor chip consists of a piezoelectric, AT-cut quartz crystal that is placed between two electrodes and excited with an alternating current (AC) voltage that is applied across the electrodes, causing the sensor chip to oscillate in thickness shear mode at its fundamental resonance frequency and odd overtones thereof [17]. The frequency of oscillation is designated as f_n, where f is the frequency and n is the overtone number. QCM-D measurements are highly sensitive to the adsorbate mass (m) that includes both biomacromolecular mass and hydrodynamically coupled solvent [18]. When certain conditions are met, the Δf shift is proportional to Δm relative to the initial baseline (without adsorbate). In other words, the resonance frequency decreases proportionally to the added mass, which is a hallmark of conventional QCM measurements.

A key advantage of the QCM-D technique is the additional capability to simultaneously measure the dissipative properties of the adsorbate as well [19]. Periodically, the circuit driving the sensor chip's oscillation is opened in order to measure the energy dissipated per cycle [20]. The energy dissipation (D_n) is calculated from a ratio that takes into account the energy dissipated during a single oscillation after the voltage is removed and the total stored energy in the system. The ΔD shift is then calculated relative to the initial baseline (without adsorbate) and a large ΔD shift is associated with an adsorbate that quickly dissipates energy. In biomacromolecular measurements, a large ΔD shift typically corresponds to a soft adsorbate that exhibits viscoelastic character [21]. For example, a packed layer of adsorbed, intact lipid vesicles with hydrodynamically coupled solvent inside and in between the vesicles is considered a soft material (Fig. 1). On the other hand, a small ΔD shift is associated with an adsorbate that has low energy dissipation. It typically corresponds to a rigid adsorbate that exhibits non-viscoelastic character. For example, a supported lipid bilayer (SLB) coating on the sensor surface has a low fraction of hydrodynamically coupled solvent and is considered a rigid material.

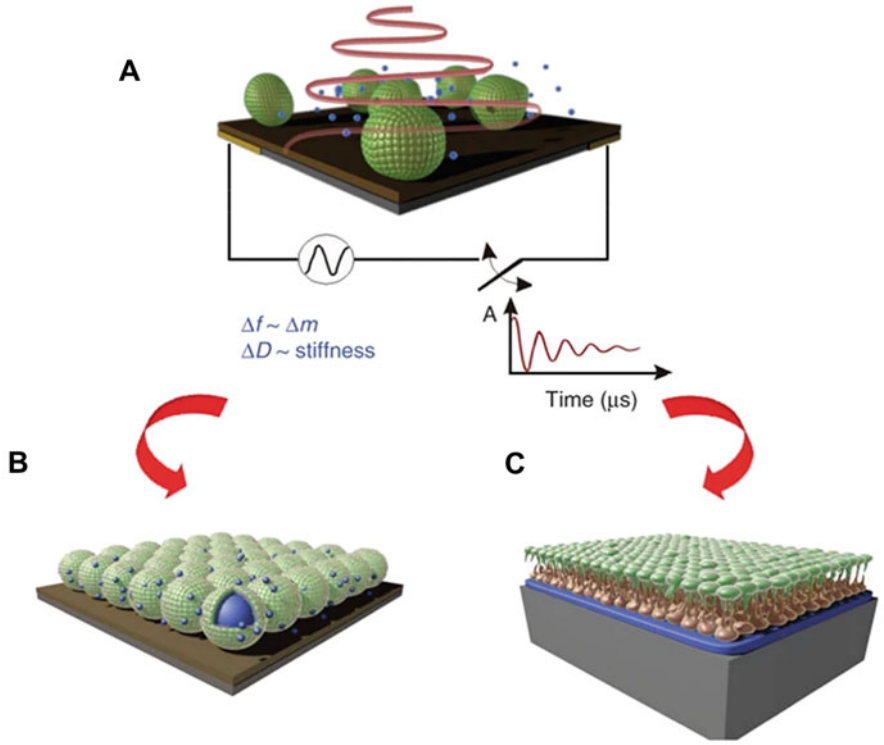

Fig. 1 QCM-D measurement approach for characterizing soft and rigid biomacromolecular adsorbates. (**a**) QCM-D sensing principle in which the resonance frequency of oscillation (f) of a quartz crystal sensor chip is sensitive to the amount and type of adsorbed biomacromolecular mass and hydrodynamically coupled solvent mass on the sensor surface. The frequency (Δf) shift is related to the amount of adsorbed mass while the energy dissipation (ΔD) shift is sensitive to the viscoelastic properties of the adsorbate, i.e., stiffness. Inset shows the oscillation decay when the circuit driving the oscillation is opened. A fast oscillation decay signifies greater energy dissipation while a slower decay indicates less energy dissipation. Representative schematics of (**b**) soft, viscoelastic films such as intact vesicle adlayers that contain a high fraction of hydrodynamically coupled solvent and (**c**) rigid, non-viscoelastic adlayers such as supported lipid bilayers that contain a low fraction of hydrodynamically coupled solvent. Adapted with permission from Ref. [23]. Copyright 2010 Springer Nature

Another important point about QCM-D experiments is that the measurements are usually conducted at different odd harmonics, including the fundamental resonance frequency and multiple odd overtones thereof. As such, time-resolved Δf and ΔD shifts are simultaneously collected at multiple frequencies and this feature is central to the high surface sensitivity of the QCM-D technique. The penetration depth of the acoustic wave at each harmonic is related to the wave frequency, whereby a shorter penetration depth (higher surface sensitivity) corresponds to a higher wave frequency [22]. For a typical QCM-D sensor chip with a fundamental resonance

frequency of 5 MHz, the penetration depth in aqueous solution is around ~240 nm whereas the penetration depth is only around ~69 nm at 65 MHz (13th overtone).

2.1 Experimental Operation

To study biomacromolecular interactions, QCM-D experiments are typically conducted in a flow-through microfluidic chamber and liquid exchange is regulated by a peristaltic pump. The first step involves properly mounting a clean QCM-D sensor chip in the measurement chamber and checking that the correct f and D values in air are obtained at different overtones [23]. Afterward, aqueous solution, such as the intended buffer for the planned experiments, is introduced into the measurement chamber and the f and D values in liquid are rechecked according to reference values [24]. The sensor surface immersed in the aqueous solution is considered the reference state, and the Δf and ΔD shifts at different overtones are recorded as a function of time until sufficiently stable baseline signals are achieved. Then, subsequent protocol steps such as adding the biomacromolecule(s) of interest or other reagents are conducted in equivalent solvent conditions so that any changes in the Δf and ΔD shifts are associated with adsorption processes, not changes in the bulk solution environment. After an adsorption event, a buffer washing step is usually performed to remove weakly attached molecules from more strongly attached ones. While the bulk solution may be temporarily exchanged to a different solvent in certain types of protocols (e.g., solvent-assisted lipid bilayer exchange for SLB formation [25]), it is critical that the final Δf and ΔD shifts corresponding to the adsorbate are reported relative to the initial f and D values in the equivalent bulk solution (without adsorbate) [26].

Operationally, the Δf and ΔD shifts are usually collected at multiple overtones and the presented data are reported in normalized form as $\Delta f_n/n$ and $\Delta D_n/n$ for comparison across different overtones. Of note, the data are usually collected every 1 s so the time resolution is suitable for tracking most types of biomacromolecular interactions with an ensemble-averaged readout. This normalized data presentation supports data interpretation and can guide selection of an appropriate model for data analysis. If the normalized Δf and ΔD shifts show overtone-independent responses, then the adsorbate is likely rigid and has low dissipative properties [23]. On the other hand, if the normalized Δf and ΔD shifts show overtone-dependent responses, then the adsorbate is probably soft and has high dissipative properties.

Of note, the choice of substrate coating on the QCM-D sensor chip is important to choose based on the intended experiment. Some of the most common options include gold, silicon oxide, and titanium oxide coatings. This surface specificity is widely discussed in the lipid adsorption literature as one major example. On gold and titanium oxide, zwitterionic lipid vesicles typically adsorb and do not rupture, resulting in the formation of a close-packed vesicle adlayer [27]. By contrast, on silicon oxide, zwitterionic lipid vesicles usually rupture to form an SLB coating [7].

2.2 Data Analysis

There are two main routes of QCM-D data analysis once the experimental data has been obtained. The first route is to directly analyze the obtained Δf and ΔD shifts in order to look for empirical trends. In some cases, the QCM-D measurement responses can be compared to typical values for similar systems reported in the literature. For example, it is well established that, for a 5-MHz QCM-D sensor chip, the typical Δf and ΔD shifts for a complete SLB on a silica-coated sensor surface are around -25 Hz and $\sim 0 \times 10^{-6}$, respectively, relative to buffer baseline values [23]. It is also possible to construct time-independent plots of the Δf vs. ΔD shifts in order to characterize the stages involved in adsorption processes along with the relative magnitude of changes in the adsorbate's mass and viscoelastic properties [28].

In order to further quantify molecular properties of the adsorbate such as film thickness or adsorbed mass, it is often helpful to convert the as-obtained Δf and ΔD shifts into more physically meaningful parameters. While various models have been developed for QCM-D data interpretation, it is necessary to carefully consider the biological system under consideration and to choose the appropriate model based on the film's dissipative properties. Also, different models have been derived based on various assumptions and the validity of those assumptions must be checked for the system under consideration.

For rigid films with low energy dissipation (oftentimes considered to be $\Delta D < \sim 1 \times 10^{-6}$; note that more formal definitions based on the $\Delta D/\Delta f$ ratio can also be considered), the Sauerbrey model is often applied for data analysis [29]. The key assumptions of the Sauerbrey model are that the adsorbate is laterally homogenous and has a uniform density. If these assumptions are valid and the adsorbate has low energy dissipation, then the Sauerbrey model can directly convert the Δf shift into the Δm shift based on a fixed proportionality constant that depends on the sensor chip's fundamental resonance frequency and related material properties. While the Sauerbrey model provides accurate mass quantification of rigid adsorbates such as self-assembled monolayers and SLBs, the Sauerbrey model underestimates the mass of soft adsorbates with viscoelastic properties due to viscous losses [30].

To analyze viscoelastic adsorbates with high energy dissipation, one of the most widely used approaches is the Voigt-Voinova model, in which case there are various assumptions about the system under consideration [31]. First, the sensor chip is assumed to be elastic and the adsorbate is treated as a single Voigt element (spring and dashpot represent the shear rigidity and viscosity, respectively). Second, the bulk solution (treated as a semi-infinite liquid) above the adsorbate is assumed to be Newtonian. Third, the adsorbate itself is assumed to have a uniform film thickness and density. Fourth, the viscosity of the adsorbate is assumed to be independent of the overtone frequency. Fifth, it is assumed there is no slip between the adsorbate and sensor surface. In effect, the adsorbate is considered to be a homogenous film with unknown viscosity, shear modulus, thickness, and density. By assuming a fixed adsorbate density (within a physically meaningful range), the time-resolved Δf and ΔD shift values collected at multiple overtones (usually, at least three) can be fit

according to the Voigt-Voinova model equations in order to extract the other unknown parameters, i.e., the film viscosity, shear modulus, and thickness [32]. While the Voigt-Voinova model assumes that the adsorbate is a uniform film, in practice, the modeling approach is often applied to adsorbates where the assumption is not fully valid, especially in cases of complex structural transformations as discussed in pertinent examples throughout this chapter. When interpreting parameters extracted from model fittings, it is important to judge the results both qualitatively and quantitatively based on the model applicability and to understand the scientific context in which the modeling is being performed.

In addition, for adsorption cases involving discrete nanoparticles (non-uniform films), other model-independent analysis methods have been reported to extract particle size and are discussed elsewhere [5, 33]. Another approach that utilizes a model derived from hydrodynamic simulations can also extract the size of non-deformed and deformed nanoparticles adsorbed on a sensor surface [34, 35]. Based on these different measurement scenarios, we first turn attention to cases involving the structural transformation of soft adsorbates into rigid ones.

3 Transformation of Soft Adsorbates into Rigid Adsorbates

From a QCM-D measurement perspective, one benefit of working with biomacromolecules is that they are inherently water-rich and exhibit soft, viscoelastic properties in many cases. Accordingly, there has been extensive interest in understanding how biomacromolecules adsorb onto sensor surfaces and in characterizing their dissipative properties, which can relate to different conformational states. These experimental efforts have supported the development and refinement of various QCM-D measurement strategies and modeling approaches. Perhaps one of the biggest advances in QCM-D data analysis has come from studying adsorbed biomacromolecular films that undergo structural transformations. In this section, we review selected application examples of soft viscoelastic adlayers that are transformed into rigid ones. The examples span pioneering work on protein crosslinking relevant to biological adhesion events to membrane–peptide interactions that are serving as the basis to develop next-generation medical therapies for infectious disease and cancer treatment.

3.1 Protein Crosslinking

Marine organisms such as barnacles and mussels can strongly attach to surfaces by using specialized adhesion proteins that adsorb tightly at solid–liquid interfaces and can undergo crosslinking to strengthen adhesive properties. One of the most interesting proteins in this class is the *Mytilus edulis* foot protein 1 (Mefp-1) and early work in the QCM-D field investigated how enzymatic and chemical crosslinking

approaches affected the mass and viscoelastic properties of Mefp-1 protein adsorbates on solid surfaces [36]. QCM-D measurements showed that the Mefp-1 protein formed soft, viscoelastic adlayers on hydrophobic methyl-terminated gold surfaces and rigid adlayers on hydrophilic silicon oxide surfaces. Interestingly, in the study, the Δm shift values were plotted from the Δf shift values by using the Sauerbrey equation while it was acknowledged that this procedure can introduce uncertainties. The approach was taken to compare the Δm shift values from QCM-D measurements with Δm shift values from complementary surface plasmon resonance (SPR) measurements, which are sensitive to adsorbed biomacromolecular mass only. Accordingly, the QCM-D-measured Δm and ΔD shift values for Mefp-1 protein adsorption on the hydrophobic surface were around 1,100 ng/cm^2 and ~13×10^{-6}, respectively. Conversely, the corresponding Δm and ΔD shift values for Mefp-1 protein adsorption on the hydrophilic surface were around 350 ng/cm^2 and ~2×10^{-6}, respectively. Interestingly, the subsequent addition of sodium periodate ($NaIO_4$), Cu^{2+} ions (in the form of $CuCl_2$), or the catechol oxidase enzyme to the viscoelastic protein film on the hydrophobic surface induced crosslinking and caused a marked reduction in the Δm and ΔD shift values, signifying loss of hydrodynamically coupled solvent mass and a corresponding increase in film rigidity. In addition to detecting protein crosslinking, the QCM-D measurements demonstrated high sensitivity to the crosslinking kinetics directly and to the degree of crosslinking indirectly.

Further investigation of Mefp-1 protein adsorption on the hydrophobic methyl-terminated gold surface was carried out by the QCM-D technique, with particular focus on the $NaIO_4$ treatment process [37] (Fig. 2). The authors critically examined the structural transformation process by using the Sauerbrey and Voigt-Voinova models and discovered that the latter approach could properly capture the film dynamics in terms of model fitting. It was observed that the initially viscoelastic protein adlayer had a water-rich thickness of ~20 nm and that crosslinking compressed the film to a much less hydrated state that had a thickness of ~5 nm. These results were compared to those obtained by SPR and ellipsometry and, while the three techniques were complementary, the findings also reinforced the utility of the QCM-D technique—and its high sensitivity to detecting hydrodynamically coupled solvent mass—for probing dynamic biomacromolecular interactions, especially structural transformations, at solid–liquid interfaces [38].

Interestingly, the same model system—Mefp-1 protein adsorption onto a hydrophobic methyl-terminated gold surface—has been additionally studied with the QCM-D technique in different environmental systems and it was discovered that subsequent addition of Mg^{2+} ions (in the form of $MgCl_2$) did not induce crosslinking (instead, a similar response was observed to that of a buffer washing control), whereas $NaIO_4$ treatment had the greatest crosslinking effect and the addition of Ca^{2+} ions (in the form of $CaCl_2$) had an intermediate effect [39]. These crosslinking effects not only provide interesting insights into the structural transformation of a soft adsorbate into a rigid one, but the corresponding conformational changes in the Mefp-1 protein have also been shown to be necessary to mediate binding to additional types of mussel adhesion proteins [40]. Aside from crosslinking effects, it has also been shown that Mefp-1 protein binds more greatly to silicon oxide and

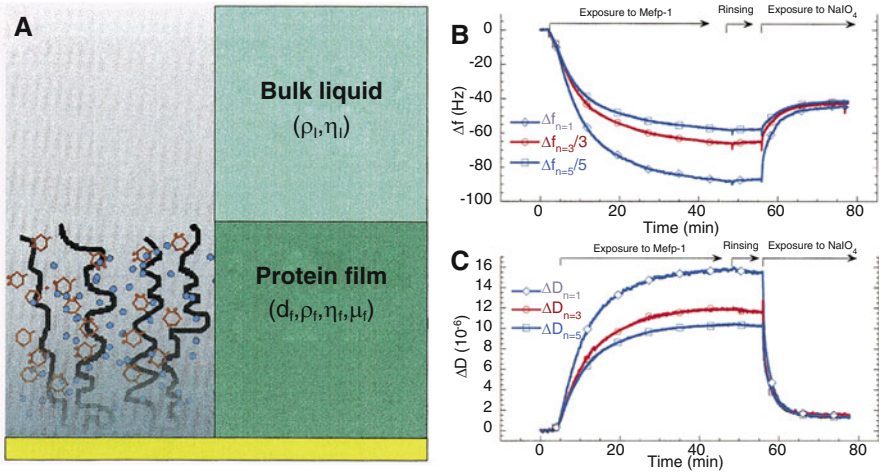

Fig. 2 QCM-D characterization of protein crosslinking and modeling approach. **(a)** Voigt-Voinova modeling parameters to analyze a viscoelastic protein film in between a bulk liquid and sensor surface. The bulk liquid is represented by density and viscosity and the protein film is represented by elastic modulus, viscosity, density, and thickness. QCM-D measurement traces for **(b)** resonance frequency (Δf) and **(c)** energy dissipation (ΔD) shift values due to Mefp-1 protein adsorption on a hydrophobic surface, followed by buffer washing and crosslinking step (due to $NaIO_4$ addition). Data are presented from the first, third, and fifth overtones. Adapted with permission from Ref. [37]. Copyright 2001 American Chemical Society

gold surfaces in the presence of palmitic acid, which is a 16-carbon long fatty acid [41].

In addition to the Mefp-1 protein, QCM-D measurements have been integral to determine that a phenolic polymer (PP) extracted from *Fucus serratus* seaweed can be crosslinked using a vanadium-dependent bromoperoxidase (BPO) enzyme [42]. Similar crosslinking phenomena have also been detected with QCM-D for ethyl(hydroxyethyl) cellulose (EHEC) and hydrophobically modified EHEC adsorbed at hydrophilic and hydrophobic surfaces, respectively, when divinyl sulfone (DVS) was added as a crosslinking agent [43]. From an applied perspective, it has also been possible to track the assembly and crosslinking of bovine serum albumin (BSA) protein adlayers on silicon oxide surfaces by glutaraldehyde treatment to prepare surface passivation coatings that have superior resistance to serum biofouling [44].

3.2 *Membrane–Peptide Interactions*

Antimicrobial peptides can disrupt the membranes surrounding pathogens such as bacteria, viruses, and fungi and are receiving growing attention as potential antibiotic replacements. While biological assays focus on the effect of peptide treatment

on pathogen infectivity and viability, biophysical assays provide direct insight into how peptides disrupt lipid membranes using model systems. In this regard, the QCM-D technique has proven useful in characterizing how antimicrobial peptides disrupt planar SLBs based on time-resolved Δf and ΔD shifts, especially with the ability to change the SLB composition to mimic human or microbial cell membranes, for example. Comparison of QCM-D fingerprints, i.e., time-independent plots of Δf and ΔD shifts, for different antimicrobial peptides has provided insight into the types of membrane-disruptive mechanisms involved, such as the carpet and barrel-stave models [45]. This differentiating ability is even greater when QCM-D experiments are done at multiple peptide concentrations in order to take into account concentration-dependent effects and thus consider the respective potency of different peptides as well [46]. While SLBs were widely used in early QCM-D studies on antimicrobial peptides, recent discussion has focused on how different types of softer, more viscoelastic model membrane platforms such as multilayers of lipid molecules and intact vesicle adlayers can provide distinct and highly sensitive fingerprinting signatures [47].

Among the different options, the intact vesicle adlayer has provided a high-sensitivity model membrane platform to detect morphological changes due to antimicrobial peptide treatment, especially in cases where membrane curvature can influence the membrane–peptide interactions. Oftentimes, the corresponding interaction kinetics upon peptide addition to the intact vesicle platform are complex and involve multiple steps in the Δf and ΔD shifts due to competing processes. In one intact vesicle platform study, the membrane-disruptive interactions of the antimicrobial peptide melittin were reported to follow the carpet mechanism and, while the soft vesicle adlayer was transformed into a more rigid film, the vesicle rupture process was incomplete and the treated adlayer was still highly dissipative ($\Delta D > 3 \times 10^{-6}$) [48]. This type of membrane-disruptive behavior with incomplete vesicle rupture has also been observed for the clinical stage LTX-315 anticancer peptide [49] and it is rare to find cases where the membrane–peptide interaction results in a complete structural transformation from a soft adsorbate to a rigid one.

In the course of studying the membrane association properties of an amphipathic, α-helical (AH) peptide derived from the hepatitis C virus (HCV) NS5A protein, it was discovered that the AH peptide could rupture an adlayer of intact lipid vesicles on a gold-coated QCM-D sensor chip [50]. When zwitterionic 1-palmitoyl-2-oleyl-*sn*-glycero-3-phosphocholine (POPC) lipid vesicles of ~59 nm diameter were added to the sensor surface, they adsorbed and remained intact without rupturing to form a close-packed adlayer corresponding to Δf and ΔD shifts values around -120 Hz and 8×10^{-6}, respectively, relative to the initial buffer baseline values. Interestingly, when the AH peptide was next added to the intact vesicle platform, the Δf and ΔD shift values further increased by around an additional -40 Hz and 14×10^{-6}, respectively, in a rapid and transient manner. The interaction kinetics indicated a large increase in the film's dissipative properties while the Δf and ΔD shifts then reverted back to final values around -25 Hz and 0.1×10^{-6}, respectively, during the interaction process. Remarkably, these final QCM-D responses corresponded to the expected values for a rigidly attached, complete SLB, which was further confirmed

by atomic force microscopy (AFM) imaging that detected a smooth surface and no presence of intact vesicles.

Successful SLB fabrication on gold by using the vesicle-rupturing AH peptide was an important advance because it was not previously possible; instead, zwitterionic lipid vesicles typically adsorbed and remained intact on gold and titanium oxide surfaces, unlike on silicon oxide surfaces where they typically rupture to form an SLB. As evidence of the general applicability of the AH peptide-mediated vesicle rupture process to form SLBs, similar QCM-D data detecting the vesicle-to-bilayer structural transformation was also obtained on titanium oxide-coated sensor chips. Further testing of a mutant AH peptide termed the NH peptide, in which three-point mutations were introduced to disrupt amphipathicity, was also performed and the QCM-D results showed negligible NH peptide interaction with the intact vesicle adlayer.

From a measurement perspective, the AH peptide-mediated structural transformation of a soft, intact vesicle adlayer into a rigid, supported lipid bilayer without chemical treatment (i.e., no covalent modification) provided a useful case study to analyze changes in the film's viscoelastic properties and suitability of different modeling approaches to interpret the measurement data [51] (Fig. 3). Prior to AH peptide addition, the intact vesicle adlayer exhibited high energy dissipation, which is considered non-Sauerbrey behavior and thus the Sauerbrey model underestimated the adsorbed mass. In other words, in the non-Sauerbrey regime, the Δf shift is not proportional to Δm, i.e., the adsorbed mass encompassing biomacromolecules and hydrodynamically coupled solvent. According to the Sauerbrey equation and assuming a uniform film density, the estimated vesicle adlayer thickness was overtone-dependent and in the range of 17–20 nm whereas the Voigt-Voinova model resulted in an estimated film thickness of 22 nm. On the other hand, the thickness properties of the resulting SLB, which exhibited low energy dissipation, were properly described by the Sauerbrey equation (~5 nm thickness) and agreed well with estimates by the Voigt-Voinova model. Another advantage of the Voigt-Voinova modeling approach is that information about the film's shear modulus and viscosity could be extracted; both parameters were observed to increase as a result of the structural transformation from a soft vesicle adlayer to a rigid SLB, which is physically consistent with the properties of the two film types.

The vesicle-to-bilayer structural transformation mediated by AH peptide treatment has provided a useful model system to study dynamic biomacromolecular interactions with the QCM-D technique and has also underscored the importance of lipid membrane platform design, especially since the AH peptide interacts differently with other types of supported phospholipid assemblies and does not cause rupture in those cases. For example, QCM-D measurements have shown that the AH peptide can bind to phospholipid-based and cell extract-derived SLBs, but the lipid adlayer coatings did not undergo a structural transformation in those cases [52]. Rather, the peptide could simply bind to planar SLB platforms and the attachment kinetics could be fit according to an exponential binding association model. Greater peptide binding to the cell extract-derived SLB platform was observed, suggesting that a molecular component not found in the model

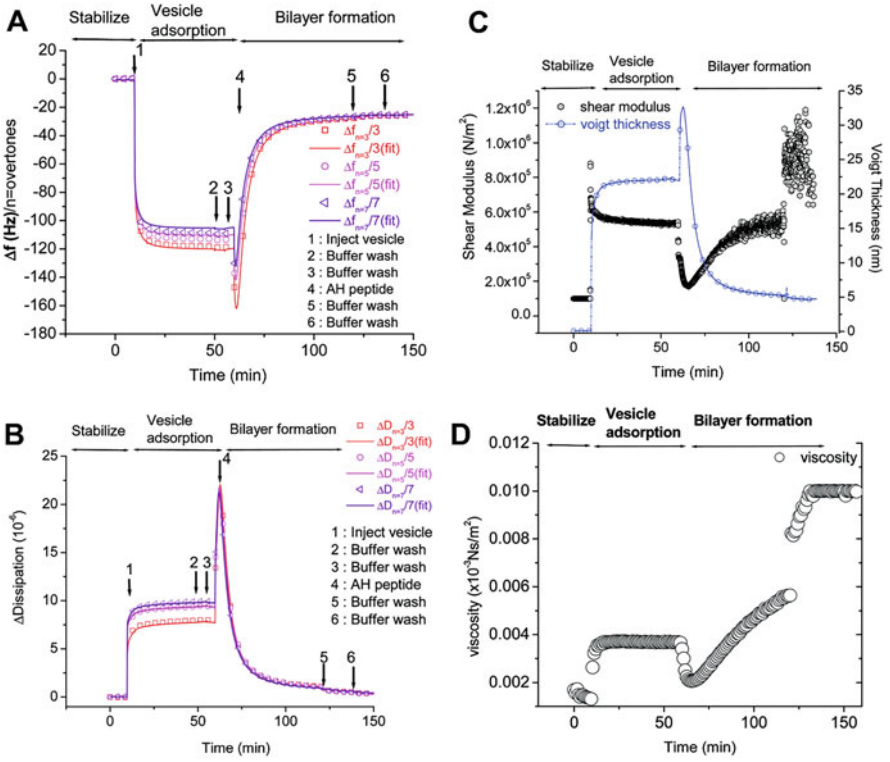

Fig. 3 Modeling AH peptide-mediated structural transformation of intact vesicle adlayer into supported lipid bilayer. Time-resolved changes in (**a**) resonance frequency (Δf) and (**b**) energy dissipation (ΔD) shift values due to intact vesicle adsorption, followed by AH peptide addition and subsequent supported lipid bilayer formation. The presented data are from the third, fifth, and seventh overtones along with the corresponding fits from Voigt-Voinova modeling. Time-resolved changes in effective (**c**) shear modulus and film thickness and (**d**) shear viscosity of the adsorbed film based on fitted data in panels (**a**) and (**b**). Adapted with permission from Ref. [51]. Copyright 2007 American Chemical Society

phospholipid-based SLB played an important role in enhancing membrane association. Further QCM-D investigation revealed that the AH peptide also contains a pair of lysine amino acids that can mediate specific binding to phosphatidylinositol 4,5-bisphosphate lipid, as demonstrated using non-rupturable, polymerized lipid vesicles that contained PI(4,5)P_2 or other phosphatidylinositol lipids as controls [53]. In the absence of PI(4,5)P_2 lipid, AH peptide binding to polymerized lipid vesicles was appreciably lower or negligible, demonstrating that lipid vesicles must have a certain degree of structural flexibility in order for the AH peptide to cause vesicle rupture. Also, with tethered lipid bilayer membranes that are only weakly coupled to the sensor surface, QCM-D measurements have demonstrated that the AH peptide can translocate across the lipid bilayer while preserving structural

integrity [54] (see also similar experimental evidence of AH peptide translocation in a giant unilamellar vesicle system [55]).

While the QCM-D technique is sensitive to the acoustic mass of the adsorbate (i.e., biomacromolecular mass and hydrodynamically coupled solvent mass), it is often advantageous to simultaneously perform other surface-sensitive measurements, especially by utilizing label-free optical sensing techniques that detect biomacromolecular mass only as briefly mentioned above. By coupling acoustic and optical sensing strategies with similar time resolutions in this manner, it becomes possible to temporally track changes in the hydration mass of adsorbates during complex biological phenomena. To better understand the mechanism of AH peptide-mediated vesicle rupture, a combined QCM-D and reflectometry setup has been reported to track the vesicle-to-bilayer structural transformation on a gold-coated QCM-D sensor chip [56]. This approach helped to determine that the large Δf and ΔD shifts associated with AH peptide binding to lipid vesicles were mainly due to vesicle swelling, i.e., an increase in hydration mass, rather than solely due to peptide binding. This finding supported that the vesicle–peptide interaction caused membrane morphological changes in the vesicle adlayer until a critical level of membrane destabilization was reached, triggering vesicle rupture and resulting SLB formation on the gold surface.

By performing simultaneous QCM-D and localized surface plasmon resonance (LSPR) measurements to track AH peptide-mediated vesicle rupture on a titanium oxide-coated QCM-D sensor chip, it has also been possible to unravel the relative time scales of SLB formation and excess lipid release into the bulk solvent on account of the LSPR technique's high sensitivity to changes in the local refractive index near the sensor surface (decay length of LSPR-enhanced electromagnetic field is on the order of 5–20 nm) [57]. Hence, the QCM-D technique is suitable for performing simultaneous measurements with different optical sensing techniques and careful selection of either matched or mismatched probing volumes between the acoustic and optical sensing techniques can be useful for unraveling dynamic biomacromolecular interactions.

From a fabrication perspective, the AH peptide has also proven useful as a vesicle-rupturing agent to form tethered lipid bilayers on mesoporous silica surfaces [58]. In that case, POPC lipid vesicles containing 2 mol% polymer-modified lipid tethers adsorbed onto an amine-modified surface, and then the AH peptide was introduced to trigger vesicle rupture and tethered lipid bilayer formation, as confirmed by QCM-D measurement responses. In addition, AH peptide addition has been used as a post-treatment step to improve the quality of incompletely formed SLBs in cases where vesicle rupture was incomplete and a fraction of intact vesicles had remained on the sensor surface [59].

3.3 Peptide Drug Development

While the vesicle-rupturing process induced by AH peptide enables useful fabrication possibilities, there is particularly high interest in understanding the structural transformation process in the context of biomedical applications. Membrane-enveloped biological nanoparticles like virus particles and cancer exosomes bear structural resemblance to synthetic lipid vesicles. Hence, investigating the vesicle rupture process and its dependence on various experimental factors such as peptide concentration and environmental conditions can help to develop membrane-targeting therapies that inhibit virus particles and exosomes [60, 61]. For example, the interaction kinetics, rupture efficiency, and magnitudes of the QCM-D responses can all provide insights to guide the development of membrane-targeting peptide therapeutics.

Toward this goal, it is important to develop standardized measurement platforms in order to compare measurement data across different experiments. The AH peptide-mediated vesicle rupture process has long been studied on various oxide surfaces but its dependance on the material properties of the solid support was an outstanding question. To address this question, the AH peptide-mediated vesicle rupture process was directly compared on different solid supports: gold, titanium oxide, and aluminum oxide [62]. While QCM-D measurements showed complete vesicle rupture on all three surfaces, the transient changes in vesicle adlayer properties during the structural transformation and corresponding interaction kinetics varied depending on the solid support. Appreciably larger maximum Δf and ΔD shifts occurred on gold and titanium oxide compared to aluminum oxide, whereas the overall structural transformation process was quicker on titanium oxide and aluminum oxide than on gold. It was suggested that the differences in the vesicle rupture process relate to variations in membrane curvature depending on the strength of the vesicle–substrate interaction, emphasizing the need to develop standardized measurement approaches for biophysical measurements.

Since the AH peptide can rupture small lipid vesicles, there has also been interest in exploring the effects of vesicle size on the rupture efficiency, i.e., the relative fraction of adsorbed vesicles that are ruptured. This line of research has been motivated by the basic structural similarity between lipid vesicles and membrane-enveloped virus particles, which led researchers to investigate whether the AH peptide might be able to also rupture enveloped virus particles. Using the QCM-D technique, it was discovered that the AH peptide can efficiently rupture vesicles up to 70 nm diameter whereas incomplete vesicle rupture or mainly peptide binding was observed to appreciably larger vesicles, especially those above ~150 nm diameter [63]. Importantly, the target size range of up to ~150 nm diameter also includes a wide range of medically important enveloped viruses and it was verified that the AH peptide disrupts membrane-enveloped hepatitis C virus (HCV) particles within the target size range but does not affect larger, membrane-enveloped vaccinia virus particles outside the target size range. It has been reported that this size selectivity arises from membrane curvature-dependent pore formation by the AH peptide [64],

which is a distinct type of selectivity from conventional antimicrobial peptides that mainly function by charge selectivity. Kinetic analysis of the QCM-D measurement response has further identified that AH peptide binding to small vesicles is cooperative but is noncooperative in the case of large vesicles [65]. Interestingly, unlike antimicrobial peptides, the AH peptide can efficiently rupture negatively charged, zwitterionic, and positively charged lipid vesicles while the magnitude of the structural transformation process was smaller for charged vesicles than zwitterionic vesicles [66].

While pore-mediated bacterial cell membrane disruption can cause antibacterial activity at even low pore densities due to loss of membrane-related biochemical gradients, the mechanisms by which pore formation in enveloped virus particles translates into antiviral activity are less well understood. To gain insight into the underlying biophysical processes, a detailed QCM-D and ellipsometry study was conducted to investigate AH peptide-mediated vesicle rupture across a wide range of peptide concentrations and cholesterol-containing membrane compositions [67]. Using the combined setup, it was possible to measure the bound peptide-to-lipid (P:L) ratio and it was determined that the bound P:L ratio required for membrane lysis is much larger than the P:L ratio corresponding to the onset of pore formation. This finding led to a new model of antiviral activity that described how membrane lysis of enveloped virus particles can occur once there is a critical density of peptide-induced pores in a highly curved membrane. In addition, a minimum bulk peptide concentration was needed for effective pore formation, otherwise, membrane lysis did not occur.

Based on the unique curvature-sensing mechanism of the AH peptide's membrane-disruptive activity, there have been efforts to develop a practically useful antiviral strategy, termed Lipid Envelope Antiviral Disruption (LEAD), to inhibit membrane-enveloped viruses in vivo. While the original AH peptide was composed of L-enantiomer amino acids (and is henceforth referred to as AH-L) that are susceptible to proteolytic degradation, a peptide redesign was reported to replace all L-enantiomer amino acids with D-enantiomer amino acids that are more resistant to proteolytic cleavage and the new peptide was called AH-D [68]. While the amino acid sequence of the AH-D peptide was preserved, this stereochemical switch increased the range of targeted vesicles up to ~300 nm diameter. Interestingly, QCM-D measurements showed that the AH-D peptide more quickly ruptured lipid vesicles and also caused greater dissipative changes in vesicle adlayer properties during the structural transformation process. In terms of antiviral drug evaluation, it should be emphasized that SLB formation is not biologically relevant while the vesicle rupture process itself, i.e., the structural transformation being tracked by QCM-D, provides insight into how and the extent to which peptide treatment may disrupt membrane-enveloped virus particles. Based on these biophysical results, the AH-D peptide was selected for further antiviral testing and was observed to therapeutically treat lethal Zika virus infection in a mouse model. The biological data supported that AH-D peptide treatment reduces the infectivity of Zika virus particles based on a direct virus-killing (virucidal) effect in line with the biophysical experiments.

In addition to antiviral applications, recent efforts have focused on repurposing the AH-D peptide to inhibit tumor-derived exosomes (T-EXOs) in vivo. T-EXOs are found in the slightly acidic tumor microenvironment (TME) and suppress immune cell function, limiting the efficacy of antibody-based cancer immunotherapies to treat cancer. Since membrane-enveloped virus particles and T-EXOs have similar lipid bilayer architectures, it was hypothesized that the AH-D peptide might be able to inhibit T-EXOs in vivo, which could lead to restored immune cell functions and better treatment outcomes together with antibody-based immunotherapies [69]. This therapeutic strategy can be considered as an extension of the LEAD strategy and is referred to as Lipid Envelope Exosome Disruption (LEED). Accordingly, QCM-D experiments showed that the AH-D peptide exhibited enhanced membrane disruption of lipid vesicles in TME-like pH conditions and this TME enhancement effect was attributed to more thermodynamically favorable membrane partitioning and greater peptide binding cooperativity. Interestingly, T-EXOs were attached to an antibody-functionalized SLB platform and additional QCM-D experiments showed that peptide-mediated T-EXO disruption was also enhanced under acidic pH conditions similar to those in the TME (Fig. 4). Based on these findings, the AH-D peptide was evaluated in anticancer tests and shown to decrease T-EXO levels in vivo, and was then applied in combination with an antibody-based immunotherapy to improve the treatment effect in a tumor-bearing mouse model.

4 Transformation of Rigid Adsorbates into Soft Adsorbates

In addition to tracking structural transformations of soft, viscoelastic adlayers into rigid adlayers, the QCM-D technique has proven useful for characterizing highly dissipative morphological changes that result from the interaction of biomacromolecules with rigid adlayers. Here, we focus attention on the interactions of antimicrobial lipids and other classes of single-chain amphiphiles with phospholipid membranes—a class of interactions relevant to antimicrobial-related membrane disruption as well as to a wider range of membrane perturbations such as membrane stiffening and fluidization. From a molecular perspective, single-chain lipid amphiphiles such as fatty acids and monoglycerides have distinct geometries compared to conventional, double-chain phospholipids. Hence, the insertion of a single-chain lipid amphiphile into a phospholipid bilayer induces local membrane strain arising from the variation in spontaneous curvatures of the different molecule types and can sometimes cause disruption of membrane-enveloped bacteria and viruses. In the case of a rigidly attached, two-dimensional supported lipid bilayer (SLB) that mimics the lipid bilayer architecture of biological membranes, the strain is mainly relieved by the SLB undergoing a three-dimensional membrane remodeling process, generating quasi-equilibrium structures such as protruding tubules and buds and the specific details depend on the physicochemical properties of the interacting single-chain lipid amphiphile and corresponding membrane strain profile.

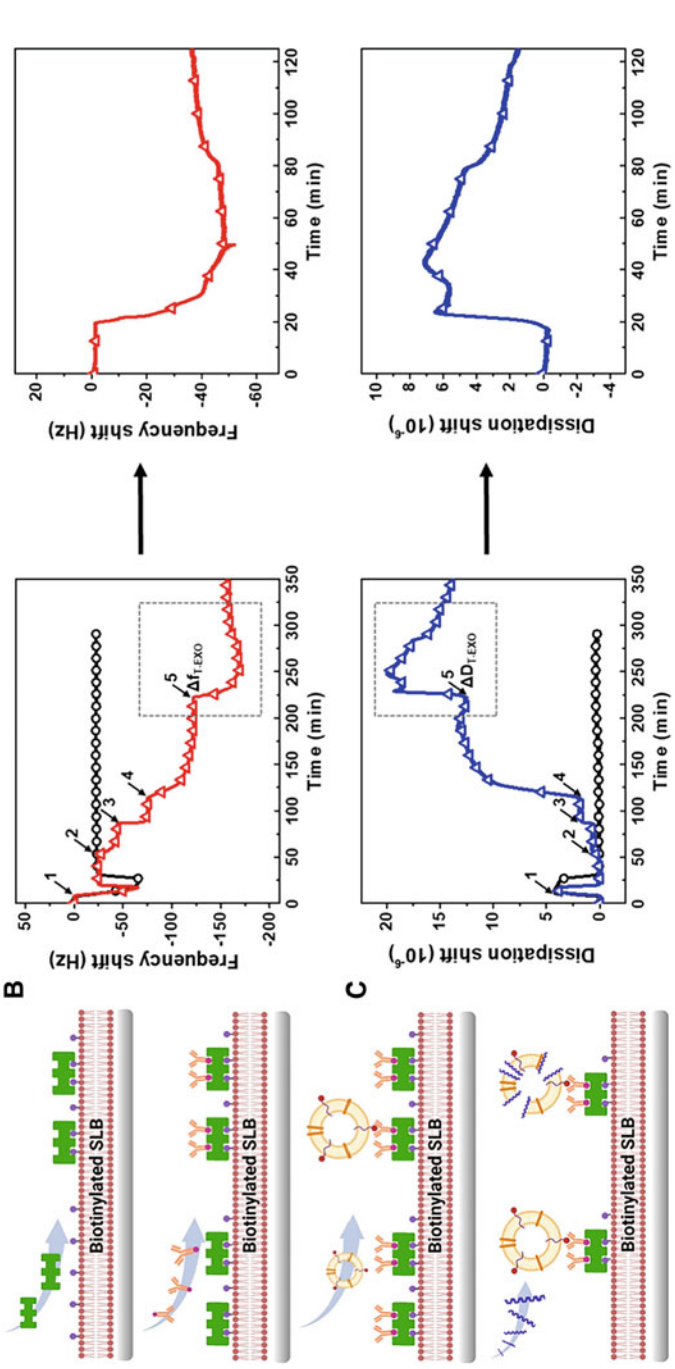

Fig. 4 QCM-D monitoring of tumor-derived exosome (T-EXO) disruption by AH-D peptide for LEED applications. (**a**) Schematic illustration of T-EXO attachment to a biotinylated supported lipid bilayer (SLB). After SLB fabrication, streptavidin protein was added followed by biotinylated PD-L1 antibody addition. Next, PD-L1-bearing T-EXOs were added and selectively attached to the SLB-tethered PD-L1 antibody. Time-resolved changes in (**b**) resonance frequency (Δf) and (**c**) energy dissipation (ΔD) shifts due to (1) bicelle addition to form a biotinylated SLB, (2) streptavidin protein addition, (3) biotinylated PD-L1 antibody addition, (4) T-EXO addition, and (5) AH-D peptide addition to induce T-EXO disruption. Dashed boxes correspond to peptide-mediated T-EXO disruption stage and data in that stage were normalized to focus on interaction kinetics (see right panels). Black lines in panels (**b**) and (**c**) correspond to negative control experiments in which case the SLB did not contain biotinylated lipids and hence streptavidin, biotinylated PD-L1 antibody, and T-EXOs did not adsorb in subsequent steps, which confirms selective attachment of T-EXOs in the main experiments as intended. Panels (**b**) and (**c**) are reprinted with permission from Ref. [69]. Copyright 2023 Springer Nature

4.1 Docosahexaenoic Acid: Prototypical Fatty Acid

The first reported example of detecting this type of biophysical phenomena with the QCM-D technique involved studying docosahexaenoic acid (DHA), which is a 22-carbon long polyunsaturated fatty acid that is known to interact with biological membranes [70]. In the QCM-D experiments, a zwitterionic POPC SLB was fabricated on a silica-coated sensor chip prior to adding different bulk DHA concentrations and monitoring time-resolved Δf and ΔD shifts that reflected changes in the acoustic mass and dissipative properties of the lipid adlayer, respectively. The initial fabrication of a rigid SLB was confirmed by Δf and ΔD shifts around -25 Hz and 0.1×10^{-6}, respectively, and the subsequent addition of 20 μM DHA to the POPC SLB platform had almost no effect on the QCM-D responses, which indicated negligible membrane interaction. In marked contrast, the addition of 100 or 200 μM DHA to the POPC SLB platform caused additional Δf shifts of -7 and -22 Hz, respectively, that demonstrated membrane interactions related to DHA binding. The corresponding ΔD shifts were around 1×10^{-6} and 6×10^{-6} and the approximately 10- and 60-fold increases in the lipid adlayer's dissipative properties pointed to a viscoelastic film, especially at the highest test concentration, with a large amount of hydrodynamically coupled solvent. Voigt-Voinova modeling was applied to analyze the adlayer properties throughout the interaction process. The modeled adlayer mass of the SLB platform by itself matched literature expectations and was in accordance with predictions from the Sauerbrey model whereas the modeled adlayer mass of the DHA-treated lipid adlayer after DHA addition was underestimated by the Sauerbrey model, as is typically observed with viscoelastic films. Interestingly, upon buffer washing, the QCM-D responses roughly returned to the typical ranges for an intact SLB, suggesting another transition in membrane morphology.

To directly characterize the membrane morphological changes, time-lapse fluorescence microscopy of a fluorescently labeled POPC SLB platform was performed and it was observed that 200 μM DHA addition triggered the formation of out-of-plane tubular protrusions and these lipid extensions could be removed by a buffer washing step. An important discovery was that the tubule protrusions were heterogenous in shape and density, which suggests that careful interpretation of modeling results must be made because a key assumption of both the Sauerbrey and Voigt-Voinova models—namely, a laterally homogenous adsorbate on the sensor surface—is not valid. To further interpret the measurement data, the authors analyzed time-independent plots of the Δf vs. ΔD shifts and noted that the nonlinear graph characteristics pointed to multiple interaction processes occurring simultaneously. From a chemical perspective, the concentration-dependent QCM-D results also supported that DHA micelles were the main species involved in inducing tubule formation because DHA was only active above its critical micelle concentration (~60 μM).

Using the QCM-D technique, follow-up work has further elucidated how membrane composition, including the presence of phosphatidylserine (PS) and

phosphatidylinositol (PI) lipids, affects DHA interactions with the SLB platform [71]. In the absence of Ca^{2+} ions, it was judged that DHA incorporation into PS- and PI-doped POPC SLBs was less than that into POPC SLBs while the inclusion of Ca^{2+} ions enabled similar DHA incorporation levels across the different membranes. It should be emphasized that the data interpretation implicitly treated the lipid adlayer as a uniform film in order to compare quantitative changes in effective film properties, however, it is likely that heterogenous tubule formation occurred in these cases as well. Another related QCM-D study also reported how inclusion of different fluorescent probes (at a relatively high 2 mol% fraction) affects DHA-POPC SLB interactions, highlighting the careful attention needed to compare interaction data across different measurement techniques [72].

4.2 Antimicrobial Lipid Evaluation

Aside from quantifying changes in the adsorbate film properties based on physics-based modeling, another promising approach has been to comparatively evaluate the membrane interactions of different types of antimicrobial lipids based on empirical evaluation of the QCM-D responses. Medium-chain saturated fatty acids and monoglycerides with 6–12 carbon long, hydrocarbon chains are among the most biologically potent antimicrobial lipids and, within this group, the 12-carbon long lauric acid (LA) and its monoglyceride derivative, glycerol monolaurate (GML), are considered to be the most biologically active. In the microbiology literature, it was long discussed how fatty acids and monoglycerides similarly disrupt phospholipid membranes, yet it was unclear why monoglycerides were typically more potent and the QCM-D technique has helped to address such questions.

To approach this topic, the interaction of LA and GML with 1,2-dioleoyl-*sn*-glycero-3-phosphocholine (DOPC) SLB platforms on silica-coated QCM-D sensor chips has been studied at different compound concentrations in order to identify concentration-dependent effects as well as the corresponding mechanisms of action [73] (Fig. 5). In the LA case, the compound was only active at and above 1,000 μM concentration in phosphate-buffered saline (pH 7.4) and 2,000 μM LA treatment caused the Δf shift to initially drop from −26 Hz (initial SLB value) to −42 Hz transiently before returning to around −31 Hz. The corresponding ΔD of the SLB platform increased transiently to 7×10^{-6} and then decreased modestly to 3×10^{-6}. In marked contrast, GML was mainly active at concentrations down to 125 μM—indicating greater potency, i.e., activity at a lower concentration—and retained a modest degree of activity down to around 16 μM. In this case, 500 μM GML treatment caused the Δf shift to initially drop from −26 Hz to −130 Hz in a monotonic fashion and the corresponding ΔD shift increased to ~70×10^{-6}. The magnitude of the QCM-D responses in the GML case are particularly remarkable, especially the changes in the film's dissipative properties that indicate large-scale membrane remodeling and are around an order-of-magnitude larger than what is typically seen with intact vesicle platforms. Time-lapse fluorescence microscopy

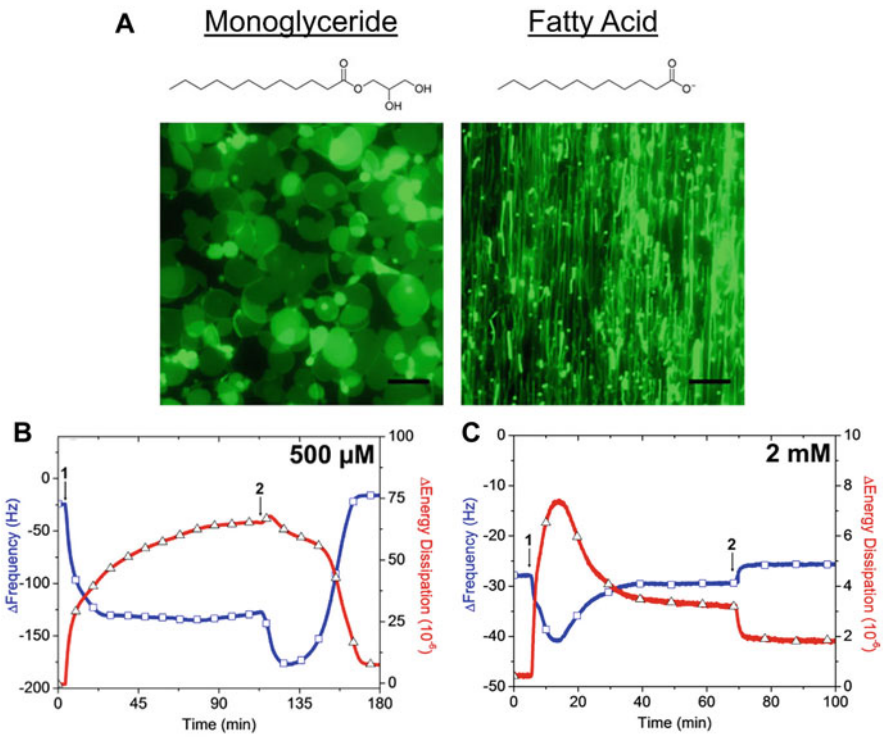

Fig. 5 Distinguishing membrane-disruptive effects of monoglycerides and fatty acids using supported lipid bilayer (SLB) platforms with the QCM-D technique. (**a**) Molecular structures of representative monoglycerides and fatty acids that cause membrane budding and tubule formation, respectively, according to time-lapse fluorescence microscopy experiments. Corresponding QCM-D data for membrane disruption of SLB platforms by (**b**) monoglycerides that cause membrane budding and (**c**) fatty acids that cause tubule formation under physiologically relevant pH conditions. Arrows 1 and 2 indicate compound addition to the SLB and a buffer washing step, respectively. Adapted with permission from Ref. [73]. Copyright 2015 American Chemical Society

imaging further confirmed that LA and GML caused membrane tubule and bud formation, respectively, and the concentration dependencies in the QCM-D experiments supported that both compounds were active only above their corresponding CMC values. Importantly, the study opened the door to assigning QCM-D measurement signatures based on the time-resolved patterns in the Δf and ΔD shifts to different types of membrane morphological changes without applying physics-based models to interpret the measurement data.

The ability to modify the lipid composition of the SLB on the QCM-D sensor surface has also proven advantageous for studying these membrane remodeling processes in greater detail. For example, cholesterol is often found in biological membranes and QCM-D testing has shown that cholesterol has unique effects on the membrane morphological changes caused by LA and GML [74]. In the LA case, a

higher fraction of cholesterol in the SLB led to more extensive tubule formation based on the QCM-D response magnitudes whereas cholesterol suppressed the membrane budding effects caused by GML. It has also been possible to study the effects of environmental pH on the membrane-disruptive properties of LA and GML [75]. While GML behaves similarly at pH 7.4 and 4.5, it was discovered that LA was more potent at pH 4.5—a condition relevant to skincare applications—due to protonation of its carboxylic acid headgroup, which resulted in a lower CMC, and also caused more extensive, budding-like membrane disruption.

At this juncture, it is valuable to comment on the high surface sensitivity of the QCM-D technique and the importance of the SLB platform design. While optical-based sensing techniques such as localized surface plasmon resonance (LSPR) are also sensitive to distinct patterns of membrane morphological changes caused by LA and GML, the detectable effects with those techniques are far more nuanced because LSPR is only sensitive to changes in the local refractive index arising from the amount and spatial proximity of adsorbed lipid molecules and is insensitive to changes in hydrodynamically coupled solvent [76]. By contrast, the QCM-D technique is highly sensitive to changes in hydrodynamically coupled solvent, which are likely the predominant cause of the large, measured Δf and ΔD shifts in these three-dimensional membrane remodeling processes. Additionally, while it is possible to detect antimicrobial lipid interactions with intact vesicle platforms using the QCM-D technique [77], the SLB platform is generally favorable because it provides a tool to clearly detect the structural transformation of a two-dimensional lipid adlayer into a three-dimensional lipid assembly.

The QCM-D measurement capabilities have also aided the biophysical characterization of a wide range of other antimicrobial lipids. In some biological studies, the 10-carbon long saturated fatty acid and monoglyceride pair, caprylic acid (CA) and monocaprin (MC), have been regarded as more biologically active than LA and GML, which made them attractive candidates to study using the SLB platform with the QCM-D technique [78]. It was discovered that the CA fatty acid caused tubule formation in a CMC-dependent manner that was similar to LA while the MC monoglyceride caused budding above its CMC but also caused tubule formation at concentrations as low as 4 times below its CMC. This dynamic interaction behavior could explain why MC is often used as a potent antiviral compound for inhibiting membrane-enveloped viruses. Further QCM-D investigation of 11-carbon fatty acids and monoglycerides showed similar trends in membrane-disruptive behavior [79], helping to establish structure–function relationship insights among medium chain, saturated fatty acids and monoglycerides. Recently, there has also been investigation of 18-carbon long, unsaturated fatty acids with 1, 2, or 3 degrees of unsaturation and membrane tubulation occurred in a CMC-dependent manner for all tested compounds [80]. Interestingly, the extent of membrane remodeling was greater for fatty acids with more degrees of unsaturation based on the QCM-D response magnitudes.

4.3 Mixture Optimization and Nano-Formulation Development

While studying the interactions of individual compounds with SLB platforms has helped to unravel molecular principles behind observed biophysical phenomena, there has also been interest in exploring how binary mixtures of different antimicrobial lipids cause membrane disruption. In one study, it was reported that mixtures of LA fatty acid and GML monoglyceride caused competing membrane morphological changes in DOPC SLB platforms resulting from simultaneous tubule and bud formation [81]. Whereas clear QCM-D measurement signatures are typically observed for tubule or bud formation, both activities occurring simultaneously resulted in complex, multi-step interaction kinetics and ultimately led to synergistic membrane disruption that exceeded the effects of LA or GML alone. On the other hand, mixtures of two monoglycerides, GML and MC, caused suppressed membrane budding compared to GML or MC alone based on the QCM-D response magnitudes [82]. These findings support that the QCM-D technique is useful for not only fundamental studies but also for optimizing the properties of antimicrobial lipid mixtures that self-assemble to form micelles as well as other types of nanostructured assemblies such as bicelles [83]. In addition, by studying membrane-disruptive interactions with the QCM-D technique, it has been possible to determine that a GML analogue with ether linkages instead of ester linkages, i.e., dodecylglycerol (DDG), exhibits greater membrane-disruptive activity than GML and subtle changes in chemical structure result in inducing elongated tubule formation instead of membrane budding [84].

4.4 Bacterial Quorum Sensing

The progress achieved in studying the membrane-disruptive interactions of antimicrobial lipids with the QCM-D technique has also led to interest in exploring other classes of biologically active amphiphiles. Among them, recent research has focused on *N*-acyl-l-homoserine lactones (AHLs), which are nonionic amphiphiles that function as signaling molecules for bacteria to communicate among individual cells. In the first study in this direction, the authors studied the interactions of the nonionic 3-oxo-C12-AHL—which possesses a saturated, 12-carbon long chain—with a DOPC SLB platform and observed that it caused microtubule formation and hemispherical cap (bud) formation in a concentration-dependent manner [85]. The anionic hydrolysis product, 3-oxo-C12-HS, was also studied by the QCM-D technique and exhibited similar types of membrane disruption, albeit with appreciably lower measurement responses. Molecular dynamics simulations were performed to rationalize the QCM-D data, demonstrating that there is a lower energy barrier for the nonionic 3-oxo-C12-AHL to translocate across the DOPC SLB leaflets and cause

greater membrane disruption whereas the anionic 3-oxo-C12-HS has a higher energy barrier.

Further testing has investigated how the membrane-disruptive interactions of 3-oxo-C12-AHL and 3-oxo-C12-HS depend on the membrane composition by doping DOPS SLBs with different amounts of cholesterol (Chol), 1,2-dioleoyl-*sn*-glycero-3-phosphoethanolamine (DOPE) or 1,2-dioleoyl-*sn*-glycero-3-phospho-l-serine (DOPS) [86]. The QCM-D measurements revealed marked changes in the type and extent of membrane remodeling processes for the mixed composition SLBs as compared to single-component DOPC SLBs, highlighting how membrane composition can affect dynamic transformations in terms of effects on amphiphile translocation, lipid packing, and phase separation among possible factors. Based on this measurement approach, various AHLs with different chain lengths and oxidation states (as indicated by the presence of a 3-oxo group) were tested and several trends were identified based on the QCM-D measurement results [87]. First, AHLs with a 3-oxo group generally demonstrated more extensive interactions with DOPC SLBs although there was no clear trend with respect to the chain length. The measured extent of membrane interaction also correlated with the type of membrane disruption; AHLs with a 3-oxo group tended to cause microtubule formation whereas AHLs lacking the 3-oxo group caused hemispherical cap (bud) formation.

4.5 Industrial Biosurfactant Testing

Recent industrial challenges involving the rise of antibiotic-resistant bacteria and the phaseout of certain detergents used to prevent microbial contamination in bioreactor-based manufacturing processes have motivated the search for environmentally friendly biosurfactants to inhibit membrane-enveloped pathogens such as bacteria and viruses. In addition to fatty acids and monoglycerides described above, other promising classes of nature-inspired biosurfactants have been explored and the QCM-D technique has proved central to validating their membrane-disruptive performance.

Recently, there have been extensive efforts to find biosurfactant replacements for the Triton X-100 (TX-100) detergent, which is widely used to inhibit membrane-enveloped pathogens potentially present in cell-based manufacturing and in the human blood supply, yet is being phased out due to environmental health concerns about a metabolic byproduct. Among potential candidates, Simulsol SL 11W (SL-11W) is a 11-carbon long, glycoside surfactant that was suggested to have similar antiviral properties to TX-100 [88]. This similarity in biological activities prompted a comparative evaluation of how TX-100 and SL-11W disrupt phospholipid membranes that are representative of viral envelopes. To address this question, the QCM-D technique was employed to investigate the concentration-dependent interactions of TX-100 and SL-11W with DOPC SLBs on silicon oxide-coated sensor chips [89]. Notably, it was first determined that TX-100 and SL-11W have distinct CMC values of 300 and 2,300 μM, respectively, which translated into

distinct potency ranges in terms of membrane-disruptive activity according to the QCM-D data. Indeed, both compounds caused membrane disruption in a CMC-dependent manner and TX-100 caused complete membrane solubilization. The initially fabricated DOPC SLBs had Δf and ΔD shifts around −25 Hz and 0.2×10^{-6}, respectively, while treatment with sufficiently high TX-100 concentrations (around ≥250 μM) caused final Δf and ΔD shifts around 0 Hz and $\sim 0 \times 10^{-6}$, respectively, relative to the buffer baseline values. These final values indicate that no lipid adlayer remained on the sensor surface, i.e., TX-100 caused irreversible membrane solubilization (Fig. 6). By contrast, sufficiently high SL-11W concentrations (around ≥2,000 μM) induced membrane budding-like morphological changes in a concentration-dependent manner and the effects were fully reversible upon buffer washing. Thus, the QCM-D approach showed that the two detergents, TX-100 and SL-11W, had distinct potencies and membrane disruption types while also enabling quantitative analysis of lipid bilayer removal levels based on the Δf shifts since final adlayers had low dissipative properties within the Sauerbrey regime.

The approach has been extended to other classes of industrial biosurfactants such as lactylates, which are also receiving attention as membrane-disruptive antimicrobials. Particular attention has been focused on sodium lauroyl lactylate (SLL), which has a 12-carbon long, saturated hydrocarbon chain, and its hydrolytic products, lauric acid (LA), and lactic acid (LacA) [90]. QCM-D experiments showed that SLL has an intermediate degree of membrane-disruptive activity that occurs in a CMC-dependent manner and lies between that of tubule-forming LA and complete solubilizers like TX-100 and sodium dodecyl sulfate (SDS). Indeed, SLL caused extensive membrane remodeling during the initial treatment step but solubilization only occurred upon a subsequent buffer washing step, whereas TX-100 and SDS caused complete membrane solubilization during the initial treatment step. Interestingly, a mixture of the SLL hydrolytic products, namely LA and LacA, caused more extensive transient membrane remodeling but no solubilization even after buffer washing. In addition, the membrane-disruptive properties of sodium caproyl lactylate, which has a 10-carbon long, saturated hydrocarbon chain and antifungal properties, have also been investigated using the QCM-D technique [91]. At sufficiently high concentration above its CMC, the compound demonstrated complete solubilization of a fungal membrane-mimicking SLB platform composed of 75 mol % POPC and 25 mol% 1-palmitoyl-2-oleoyl-*sn*-glycero-3-phospho-l-serine (POPS) and the active concentration range correlated with antifungal tests as well.

Aside from evaluating membrane-disruptive biosurfactants, there is also interest in developing surfactants that have more subtle membrane-modulating effects. For example, it was reported that a two-chain PEGylated mannosylerythritol lipid detergent could improve the efficiency of producing exosome-mimicking nanovesicles (ENVs) through a cell-based extrusion process [92]. Typically, it is difficult to extrude cells due to high membrane rigidity while pretreating the cells with this specific detergent softened cellular membranes to improve extrudability while not affecting cell viability. As a result, the detergent treatment resulted in a ~20-fold improvement in ENV production output and QCM-D experiments showed

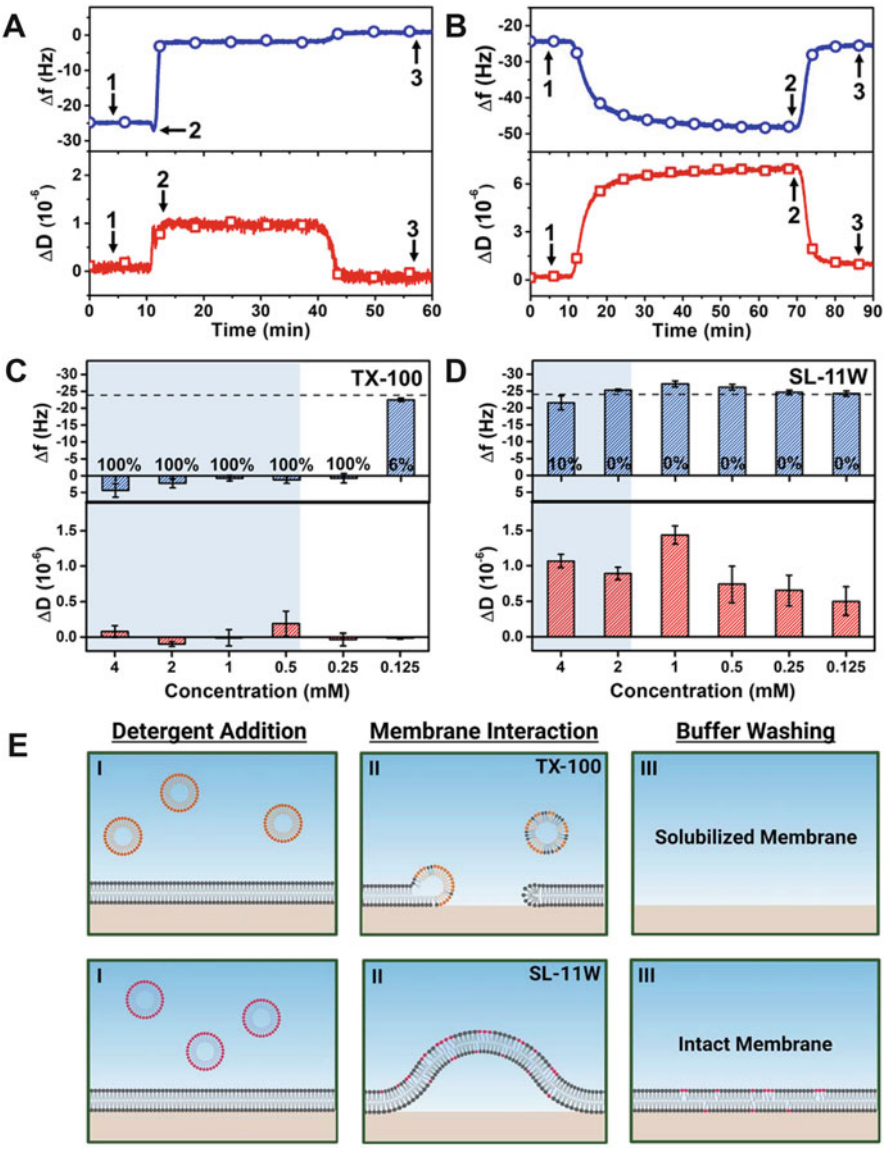

Fig. 6 QCM-D comparison of membrane-disruptive effects for Triton X-100 (TX-100) detergent and a replacement candidate (SL-11W). Representative QCM-D data for (**a**) TX-100 and (**b**) SL-11W disruption of supported lipid bilayer (SLB) platforms. Arrows 1, 2, and 3 denote measurement baselines, maximum responses, and final responses. Corresponding concentration-dependent data for final measurement responses due to (**c**) TX-100 and (**d**) SL-11W treatment effects indicate that TX-100 caused complete membrane solubilization above its critical micelle concentration (CMC) whereas SL-11W did not cause appreciable membrane solubilization either above or below its corresponding CMC value. (**e**) Schematic illustration of distinct membrane-disruptive effects of TX-100 and SL-11W detergents on SLB platforms. Adapted with permission from Ref. [89] under a CC BY 4.0 license

that the detergent caused membrane expansion/swelling of an SLB platform but did not cause membrane lysis. Interestingly, the membrane expansion/swelling persisted even after buffer washing, which suggests that the two-chain structure of the detergent enabled more stable membrane association than is typical with single-chain detergents.

5 Outlook

Over the past few decades, the QCM-D technique has evolved from serving as a highly sensitive mass balance in the nanogram scale range to becoming a versatile tool for studying dynamic biomacromolecular interactions. Central to this bioanalytical capability is the QCM-D technique's sensitivity to detect not only adsorbed biomacromolecular mass but also hydrodynamically coupled solvent. This capability distinguishes QCM-D from other popular, label-free biosensing techniques. Nevertheless, one challenge that has slowed down even wider spread usage and impact has been the difficulty in interpreting measurement data that is collected, especially for complex structural transformations. The specific challenge is twofold: (1) to make physical sense of the QCM-D Δf and ΔD shifts to describe molecular-level phenomena occurring at a solid-liquid interface; and (2) to be assured that the model used to interpret data is scientifically appropriate and to appreciate the strengths and limitations of applying the model in a given context. When physics-based models are applied to interpret QCM-D measurement data in appropriate systems, the biophysical knowledge and insights that are possible to obtain can be tremendous and progress is being made to increase accessibility of modeling options.

At the same time, as discussed in this chapter, some of the most exciting developments in utilizing the QCM-D technique for medical and biotechnology applications have involved model-free data interpretation. We foresee increasing usage in this direction, especially as QCM-D becomes a tool for not only fundamental understanding but also for bioanalytical comparison, especially in the applied biological sciences. Without fully unraveling the detailed changes in adsorbate properties during a structural transformation, there is still a wealth of information about interaction kinetics, potencies, and comparative mechanisms that can be obtained empirically from QCM-D measurements and can support translational-oriented research and development as well. As research trends move in this direction, we envision that exciting potential lies ahead for QCM-D technology at the interface of biophysics and translational nanobioscience.

Acknowledgments This work was supported by National Research Foundation of Korea (NRF) grants funded by the Korean government (MSIT) (Nos. 2020R1C1C1004385, 2021R1A4A1032782, and 2022K1A3A1A39085112) and by the Korea Drug Development Fund funded by the Ministry of Science and ICT, Ministry of Trade, Industry, and Energy, and Ministry of Health and Welfare (No. HN22C0624000022). In addition, this work was supported by the

International Research Development Program of the National Research Foundation of Korea (NRF) funded by the Ministry of Science and ICT (2020K1A3A1A39112724). This work was also partially supported by the SKKU Global Research Platform Research Fund, Sungkyunkwan University, 2023. Schematic illustration in Fig. 4a was created with BioRender.com under an academic lab subscription.

References

1. O'Sullivan CK, Guilbault GG (1999) Commercial quartz crystal microbalances – theory and applications. Biosens Bioelectron 14:663–670. https://doi.org/10.1016/S0956-5663(99)00040-8
2. Marx KA (2003) Quartz crystal microbalance: a useful tool for studying thin polymer films and complex biomolecular systems at the solution−surface interface. Biomacromolecules 4:1099–1120. https://doi.org/10.1021/bm020116i
3. Mujahid A, Afzal A, Dickert FL (2019) An overview of high frequency acoustic sensors – QCMs, SAWs and FBARs – chemical and biochemical applications. Sensors 19:4395. https://doi.org/10.3390/s19204395
4. Mashaghi A, Mashaghi S, Reviakine I et al (2014) Label-free characterization of biomembranes: from structure to dynamics. Chem Soc Rev 43:887–900. https://doi.org/10.1039/C3CS60243E
5. Reviakine I, Johannsmann D, Richter RP (2011) Hearing what you cannot see and visualizing what you hear: interpreting quartz crystal microbalance data from solvated interfaces. Anal Chem 83:8838–8848. https://doi.org/10.1021/ac201778h
6. Jackman JA, Ferhan AR, Cho N-J (2017) Nanoplasmonic sensors for biointerfacial science. Chem Soc Rev 46:3615–3660. https://doi.org/10.1039/C6CS00494F
7. Keller C, Kasemo B (1998) Surface specific kinetics of lipid vesicle adsorption measured with a quartz crystal microbalance. Biophys J 75:1397–1402. https://doi.org/10.1016/S0006-3495(98)74057-3
8. Keller C, Glasmästar K, Zhdanov V, Kasemo B (2000) Formation of supported membranes from vesicles. Phys Rev Lett 84:5443. https://doi.org/10.1103/PhysRevLett.84.5443
9. Höök F, Kasemo B (2006) The QCM-D technique for probing biomacromolecular recognition reactions. In: Janshoff A, Steinem C (eds) Piezoelectric sensors. Springer series on chemical sensors and biosensors, vol 5. Springer, Berlin. https://doi.org/10.1007/978-3-540-36568-6_12
10. Cooper MA, Singleton VT (2007) A survey of the 2001 to 2005 quartz crystal microbalance biosensor literature: applications of acoustic physics to the analysis of biomolecular interactions. J Mol Recognit 20:154–184. https://doi.org/10.1002/jmr.826
11. Dixon MC (2008) Quartz crystal microbalance with dissipation monitoring: enabling real-time characterization of biological materials and their interactions. J Biomol Tech 19:151
12. Becker B, Cooper MA (2011) A survey of the 2006–2009 quartz crystal microbalance biosensor literature. J Mol Recognit 24:754–787. https://doi.org/10.1002/jmr.1117
13. Speight RE, Cooper MA (2012) A survey of the 2010 quartz crystal microbalance literature. J Mol Recognit 25:451–473. https://doi.org/10.1002/jmr.2209
14. Cheng CI, Chang Y-P, Chu Y-H (2012) Biomolecular interactions and tools for their recognition: focus on the quartz crystal microbalance and its diverse surface chemistries and applications. Chem Soc Rev 41:1947–1971. https://doi.org/10.1039/C1CS15168A
15. Johannsmann D (2015) Gravimetric sensing. In: Johannsmann D (ed) The quartz crystal microbalance in soft matter research: fundamentals and modeling. Springer series on soft and biological matter, vol 5. Springer. https://doi.org/10.1007/978-3-319-07836-6

16. Rodahl R, Höök F, Fredriksson C et al (1997) Simultaneous frequency and dissipation factor QCM measurements of biomolecular adsorption and cell adhesion. Faraday Discuss 107:229–246. https://doi.org/10.1039/A703137H
17. Edvardsson M, Rodahl M, Kasemo B, Höök F (2005) A dual-frequency QCM-D setup operating at elevated oscillation amplitudes. Anal Chem 77:4918–4926. https://doi.org/10.1021/ac050116j
18. Rodahl M, Kasemo B (1996) On the measurement of thin liquid overlayers with the quartz-crystal microbalance. Sens Actuators A 54:448–456. https://doi.org/10.1016/S0924-4247(97)80002-7
19. Widom A, Krim J (1986) *Q* factors of quartz oscillator modes as a probe of submonolayer-film dynamics. Phys Rev B 34:1403. https://doi.org/10.1103/PhysRevB.34.1403
20. Rodahl M, Höök F, Krozer A et al (1995) Quartz crystal microbalance setup for frequency and *Q*-factor measurements in gaseous and liquid environments. Rev Sci Instrum 66:3924–3930. https://doi.org/10.1063/1.1145396
21. Easley AD, Ma T, Eneh CI et al (2022) A practical guide to quartz crystal microbalance with dissipation monitoring of thin polymer films. J Polym Sci 60:1090–1107. https://doi.org/10.1002/pol.20210324
22. Dunér G, Thormann E, Dėdinaitė A (2013) Quartz crystal microbalance with dissipation (QCM-D) studies of the viscoelastic response from a continuously growing grafted polyelectrolyte layer. J Colloid Interface Sci 408:229–234. https://doi.org/10.1016/j.jcis.2013.07.008
23. Cho N-J, Frank CW, Kasemo B, Höök F (2010) Quartz crystal microbalance with dissipation monitoring of supported lipid bilayers on various substrates. Nat Protoc 5:1096–1106. https://doi.org/10.1038/nprot.2010.65
24. Cho N-J, D'Amour JN, Stalgren J et al (2007) Quartz resonator signatures under Newtonian liquid loading for initial instrument check. J Colloid Interface Sci 315:248–254. https://doi.org/10.1016/j.jcis.2007.06.020
25. Ferhan AR, Yoon BK, Park S et al (2019) Solvent-assisted preparation of supported lipid bilayers. Nat Protoc 14:2091–2118. https://doi.org/10.1038/s41596-019-0174-2
26. Kanazawa KK, Gordon II JG (1985) The oscillation frequency of a quartz resonator in contact with liquid. Anal Chim Acta 175:99–105. https://doi.org/10.1016/S0003-2670(00)82721-X
27. Reviakine I, Rossetti FF, Morozov AN, Textor M (2005) Investigating the properties of supported vesicular layers on titanium dioxide by quartz crystal microbalance with dissipation measurements. J Chem Phys 122:204711. https://doi.org/10.1063/1.1908500
28. Reimhult E, Höök F, Kasemo B (2003) Intact vesicle adsorption and supported biomembrane formation from vesicles in solution: influence of surface chemistry, vesicle size, temperature, and osmotic pressure. Langmuir 19:1681–1691. https://doi.org/10.1021/la0263920
29. Sauerbrey G (1959) Verwendung von schwingquarzen zur wägung dünner schichten und zur mikrowägung. Z Phs 155:206–222. https://doi.org/10.1007/BF01337937
30. Voinova MV, Jonson M, Kasemo B (2002) 'Missing mass' effect in biosensor's QCM applications. Biosens Bioelectron 17:835–841. https://doi.org/10.1016/S0956-5663(02)00050-7
31. Voinova MV, Rodahl M, Jonson M, Kasemo B (1999) Viscoelastic acoustic response of layered polymer films at fluid-solid interfaces: continuum mechanics approach. Phys Scr 59:391. https://doi.org/10.1238/Physica.Regular.059a00391
32. Munro JC, Frank CW (2004) Polyacrylamide adsorption from aqueous solutions on gold and silver surfaces monitored by the quartz crystal microbalance. Macromolecules 37:925–938. https://doi.org/10.1021/ma030297w
33. Tellechea E, Johannsmann D, Steinmetz NF et al (2009) Model-independent analysis of QCM data on colloidal particle adsorption. Langmuir 25:5177–5184. https://doi.org/10.1021/la803912p
34. Gillissen JJ, Tabaei SR, Jackman JA, Cho N-J (2017) A model derived from hydrodynamic simulations for extracting the size of spherical particles from the quartz crystal microbalance. Analyst 142:3370–3379. https://doi.org/10.1039/C7AN00456G

35. Gillissen JJ, Jackman JA, Tabaei SR et al (2017) Quartz crystal microbalance model for quantitatively probing the deformation of adsorbed particles at low surface coverage. Anal Chem 89:11711–11718. https://doi.org/10.1021/acs.analchem.7b03179
36. Fant C, Sott K, Elwing H, Hook F (2000) Adsorption behavior and enzymatically or chemically induced cross-linking of a mussel adhesive protein. Biofouling 16:119–132. https://doi.org/10.1080/08927010009378437
37. Höök F, Kasemo B, Nylander T et al (2001) Variations in coupled water, viscoelastic properties, and film thickness of a Mefp-1 protein film during adsorption and cross-linking: a quartz crystal microbalance with dissipation monitoring, ellipsometry, and surface plasmon resonance study. Anal Chem 73:5796–5804. https://doi.org/10.1021/ac0106501
38. Berglin M, Hedlund J, Fant C, Elwing H (2005) Use of surface-sensitive methods for the study of adsorption and cross-linking of marine bioadhesives. J Adhes 81:805–822. https://doi.org/10.1080/00218460500189059
39. Hedlund J, Andersson M, Fant C et al (2009) Change of colloidal and surface properties of *Mytilus edulis* foot protein 1 in the presence of an oxidation ($NaIO_4$) or a complex-binding (Cu^{2+}) agent. Biomacromolecules 10:845–849. https://doi.org/10.1021/bm801325j
40. Fant C, Elwing H, Höök F (2002) The influence of cross-linking on protein−protein interactions in a marine adhesive: the case of two byssus plaque proteins from the blue mussel. Biomacromolecules 3:732–741. https://doi.org/10.1021/bm025506j
41. Xie L, Cao W, Sun C (2023) The study of fatty acid mediated Mefp-1 adsorption by quartz crystal microbalance with dissipation. J Adhes 99:1263–1281. https://doi.org/10.1080/00218464.2022.2099740
42. Berglin M, Delage L, Potin P et al (2004) Enzymatic cross-linking of a phenolic polymer extracted from the marine alga *Fucus serratus*. Biomacromolecules 5:2376–2383. https://doi.org/10.1021/bm0496864
43. Hedin J, Löfroth J-E, Nydén M (2007) Adsorption behavior and cross-linking of EHEC and HM-EHEC at hydrophilic and hydrophobic modified surfaces monitored by SPR and QCM-D. Langmuir 23:6148–6155. https://doi.org/10.1021/la063406j
44. Park JH, Sut TN, Jackman JA et al (2017) Controlling adsorption and passivation properties of bovine serum albumin on silica surfaces by ionic strength modulation and cross-linking. Phys Chem Chem Phys 19:8854–8865. https://doi.org/10.1039/C7CP01310H
45. McCubbin GA, Praporski S, Piantavigna S et al (2011) QCM-D fingerprinting of membrane-active peptides. Eur Biophys J 40:437–446. https://doi.org/10.1007/s00249-010-0652-5
46. Wang KF, Nagarajan R, Camesano TA (2015) Differentiating antimicrobial peptides interacting with lipid bilayer: molecular signatures derived from quartz crystal microbalance with dissipation monitoring. Biophys Chem 196:53–67. https://doi.org/10.1016/j.bpc.2014.09.003
47. Pandidan S, Mechler A (2020) Membrane morphology effects in quartz crystal microbalance characterization of antimicrobial peptide activity. Biophys Chem 262:106381. https://doi.org/10.1016/j.bpc.2020.106381
48. Lu N-Y, Yang K, Li J-L (2013) Vesicle deposition and subsequent membrane–melittin interactions on different substrates: a QCM-D experiment. Biochim Biophys Acta Biomembr 1828:1918–1925. https://doi.org/10.1016/j.bbamem.2013.04.013
49. Koo DJ, Sut TN, Tan SW et al (2022) Biophysical characterization of LTX-315 anticancer peptide interactions with model membrane platforms: effect of membrane surface charge. Int J Mol Sci 23:10558. https://doi.org/10.3390/ijms231810558
50. Cho N-J, Cho S-J, Cheong KH et al (2007) Employing an amphipathic viral peptide to create a lipid bilayer on Au and TiO_2. J Am Chem Soc 129:10050–10051. https://doi.org/10.1021/ja0701412
51. Cho N-J, Kanazawa KK, Glenn JS, Frank CW (2007) Employing two different quartz crystal microbalance models to study changes in viscoelastic behavior upon transformation of lipid vesicles to a bilayer on a gold surface. Anal Chem 79:7027–7035. https://doi.org/10.1021/ac0709504

52. Cho N-J, Cheong KH, Lee C et al (2007) Binding dynamics of hepatitis C virus' NS5A amphipathic peptide to cell and model membranes. J Virol 81:6682–6689. https://doi.org/10.1128/jvi.02783-06
53. Cho N-J, Lee C, Pang PS et al (2015) Phosphatidylinositol 4, 5-bisphosphate is an HCV NS5A ligand and mediates replication of the viral genome. Gastroenterology 148:616–625. https://doi.org/10.1053/j.gastro.2014.11.043
54. Park S, Avsar SY, Cornell B et al (2020) Probing the influence of tether density on tethered bilayer lipid membrane (tBLM)-peptide interactions. Appl Mater Today 18:100527. https://doi.org/10.1016/j.apmt.2019.100527
55. Hanson JM, Gettel DL, Tabaei SR et al (2016) Cholesterol-enriched domain formation induced by viral-encoded, membrane-active amphipathic peptide. Biophys J 110:176–187. https://doi.org/10.1016/j.bpj.2015.11.032
56. Cho N-J, Wang G, Edvardsson M et al (2009) Alpha-helical peptide-induced vesicle rupture revealing new insight into the vesicle fusion process as monitored *in situ* by quartz crystal microbalance-dissipation and reflectometry. Anal Chem 81:4752–4761. https://doi.org/10.1021/ac900242s
57. Ferhan AR, Jackman JA, Cho N-J (2016) Integration of quartz crystal microbalance-dissipation and reflection-mode localized surface plasmon resonance sensors for biomacromolecular interaction analysis. Anal Chem 88:12524–12531. https://doi.org/10.1021/acs.analchem.6b04303
58. Wallin M, Choi J-H, Kim SO et al (2015) Peptide-induced formation of a tethered lipid bilayer membrane on mesoporous silica. Eur Biophys J 44:27–36. https://doi.org/10.1007/s00249-014-0998-1
59. Kim MC, Gunnarsson A, Tabaei SR et al (2016) Supported lipid bilayer repair mediated by AH peptide. Phys Chem Chem Phys 18:3040–3047. https://doi.org/10.1039/C5CP06472D
60. Jackman JA, Cho N-J (2012) Model membrane platforms for biomedicine: case study on antiviral drug development. Biointerphases 7:18. https://doi.org/10.1007/s13758-011-0018-2
61. Yoon BK, Jeon W-Y, Sut TN et al (2020) Stopping membrane-enveloped viruses with nanotechnology strategies: toward antiviral drug development and pandemic preparedness. ACS Nano 15:125–148. https://doi.org/10.1021/acsnano.0c07489
62. Zan GH, Cho N-J (2014) Rupture of zwitterionic lipid vesicles by an amphipathic, α-helical peptide: indirect effects of sensor surface and implications for experimental analysis. Colloids Surf B Biointerfaces 121:340–346. https://doi.org/10.1016/j.colsurfb.2014.06.014
63. Cho N-J, Dvory-Sobol H, Xiong A et al (2009) Mechanism of an amphipathic α-helical peptide's antiviral activity involves size-dependent virus particle lysis. ACS Chem Biol 4:1061–1067. https://doi.org/10.1021/cb900149b
64. Tabaei SR, Rabe M, Zhdanov VP et al (2012) Single vesicle analysis reveals nanoscale membrane curvature selective pore formation in lipid membranes by an antiviral α-helical peptide. Nano Lett 12:5719–5725. https://doi.org/10.1021/nl3029637
65. Jackman JA, Zan GH, Zhdanov VP, Cho N-J (2013) Rupture of lipid vesicles by a broad-spectrum antiviral peptide: influence of vesicle size. J Phys Chem B 117:16117–16128. https://doi.org/10.1021/jp409716p
66. Zan GH, Jackman JA, Cho N-J (2014) AH peptide-mediated formation of charged planar lipid bilayers. J Phys Chem B 118:3616–3621. https://doi.org/10.1021/jp411648s
67. Jackman JA, Goh HZ, Zhdanov VP et al (2016) Deciphering how pore formation causes strain-induced membrane lysis of lipid vesicles. J Am Chem Soc 138:1406–1413. https://doi.org/10.1021/jacs.5b12491
68. Jackman JA, Costa VV, Park S et al (2018) Therapeutic treatment of Zika virus infection using a brain-penetrating antiviral peptide. Nat Mater 17:971–977. https://doi.org/10.1038/s41563-018-0194-2
69. Shin S, Ko H, Kim CH et al (2023) Curvature-sensing peptide inhibits tumour-derived exosomes for enhanced cancer immunotherapy. Nat Mater 22:656–665. https://doi.org/10.1038/s41563-023-01515-2

70. Thid D, Benkoski JJ, Svedhem S et al (2007) DHA-induced changes of supported lipid membrane morphology. Langmuir 23:5878–5881. https://doi.org/10.1021/la700523x
71. Flynn KR, Martin LL, Ackland ML, Torriero AA (2016) Real-time quartz crystal microbalance monitoring of free docosahexaenoic acid interactions with supported lipid bilayers. Langmuir 32:11717–11727. https://doi.org/10.1021/acs.langmuir.6b01984
72. Flynn KR, Sutti A, Martin LL et al (2018) Critical effects of polar fluorescent probes on the interaction of DHA with POPC supported lipid bilayers. Biochim Biophys Acta Biomembr 1860:1135–1142. https://doi.org/10.1016/j.bbamem.2018.01.013
73. Yoon BK, Jackman JA, Kim MC, Cho N-J (2015) Spectrum of membrane morphological responses to antibacterial fatty acids and related surfactants. Langmuir 31:10223–10232. https://doi.org/10.1021/acs.langmuir.5b02088
74. Kawakami LM, Yoon BK, Jackman JA et al (2017) Understanding how sterols regulate membrane remodeling in supported lipid bilayers. Langmuir 33:14756–14765. https://doi.org/10.1021/acs.langmuir.7b03236
75. Valle-González ER, Jackman JA, Yoon BK et al (2018) Characterizing how acidic pH conditions affect the membrane-disruptive activities of lauric acid and glycerol monolaurate. Langmuir 34:13745–13753. https://doi.org/10.1021/acs.langmuir.8b02536
76. Yoon BK, Park H, Zhdanov VP et al (2021) Real-time nanoplasmonic sensing of three-dimensional morphological changes in a supported lipid bilayer and antimicrobial testing applications. Biosens Bioelectron 174:112768. https://doi.org/10.1016/j.bios.2020.112768
77. Moon S, Yoon BK, Jackman JA (2022) Effect of membrane curvature nanoarchitectonics on membrane-disruptive interactions of antimicrobial lipids and surfactants. Langmuir 38:4606–4616. https://doi.org/10.1021/acs.langmuir.1c03384
78. Yoon BK, Jackman JA, Kim MC et al (2017) Correlating membrane morphological responses with micellar aggregation behavior of capric acid and monocaprin. Langmuir 33:2750–2759. https://doi.org/10.1021/acs.langmuir.6b03944
79. Yoon BK, Tan SW, Tan JYB et al (2022) Nanoarchitectonics-based model membrane platforms for probing membrane-disruptive interactions of odd-chain antimicrobial lipids. Nano Convergence 9:48. https://doi.org/10.1186/s40580-022-00339-1
80. Shin S, Tae H, Park S, Cho N-J (2023) Lipid membrane remodeling by the micellar aggregation of long-chain unsaturated fatty acids for sustainable antimicrobial strategies. Int J Mol Sci 24:9639. https://doi.org/10.3390/ijms24119639
81. Yoon BK, Park S, Ma GJ et al (2020) Competing interactions of fatty acids and monoglycerides trigger synergistic phospholipid membrane remodeling. J Phys Chem Lett 11:4951–4957. https://doi.org/10.1021/acs.jpclett.0c01138
82. Yoon BK, Park S, Jackman JA, Cho N-J (2020) Supported lipid bilayer platform for characterizing the optimization of mixed monoglyceride nano-micelles. Appl Mater Today 19:100598. https://doi.org/10.1016/j.apmt.2020.100598
83. Sut TN, Valle-González ER, Yoon BK et al (2021) Engineered lipid bicelle nanostructures for membrane-disruptive antibacterial applications. Appl Mater Today 22:100947. https://doi.org/10.1016/j.apmt.2021.100947
84. Yoon BK, Jackman JA, Park S et al (2019) Characterizing the membrane-disruptive behavior of dodecylglycerol using supported lipid bilayers. Langmuir 35:3568–3575. https://doi.org/10.1021/acs.langmuir.9b00244
85. Gahan CG, Patel SJ, Chen LM et al (2021) Bacterial quorum sensing signals promote large-scale remodeling of lipid membranes. Langmuir 37:9120–9136. https://doi.org/10.1021/acs.langmuir.1c01204
86. Gahan CG, Van Lehn RC, Blackwell HE, Lynn DM (2023) Interactions of bacterial quorum sensing signals with model lipid membranes: influence of membrane composition on membrane remodeling. Langmuir 39:295–307. https://doi.org/10.1021/acs.langmuir.2c02506
87. Gahan CG, Van Lehn RC, Blackwell HE, Lynn DM (2021) Interactions of bacterial quorum sensing signals with model lipid membranes: influence of acyl tail structure on multiscale response. Langmuir 37:12049–12058. https://doi.org/10.1021/acs.langmuir.1c01825

88. Luo W, Hickman D, Keykhosravani M et al (2020) Identification and characterization of a Triton X-100 replacement for virus inactivation. Biotechnol Prog 36:e3036. https://doi.org/10.1002/btpr.3036
89. Gooran N, Yoon BK, Jackman JA (2022) Supported lipid bilayer platform for characterizing the membrane-disruptive behaviors of Triton X-100 and potential detergent replacements. Int J Mol Sci 23:869. https://doi.org/10.3390/ijms23020869
90. Gooran N, Tan SW, Yoon BK, Jackman JA (2023) Unraveling membrane-disruptive properties of sodium lauroyl lactylate and its hydrolytic products: a QCM-D and EIS study. Int J Mol Sci 24:9283. https://doi.org/10.3390/ijms24119283
91. Stenbæk J, Löf D, Falkman P et al (2017) An alternative anionic bio-sustainable anti-fungal agent: investigation of its mode of action on the fungal cell membrane. J Colloid Interface Sci 497:242–248. https://doi.org/10.1016/j.jcis.2017.03.018
92. Kang JY, Yoon BK, Baek H et al (2022) Facile and scalable fabrication of exosome-mimicking nanovesicles through PEGylated lipid detergent-aided cell extrusion. Nanoscale 14:16581–16589. https://doi.org/10.1039/D2NR04272J

FBAR Devices: Fundamentals, Fabrication and Applications

Teona Mirea

Contents

Abstract Film Bulk Acoustic Resonators (FBARs), also known as Thin Film Bulk Acoustic Resonators (TFBARs), are one of the key players in the recent ongoing era of 5G technologies. We have hundreds of them in our pockets, as their principal application is exploited by the telecom industry in RF filters for smartphones. In addition to that, FBARs have boosted the performance limits of gravimetric sensors, providing resolutions in the pg and fg levels. Within the wide variety of electro-acoustic resonators technologies, which includes both Surface Acoustic Wave (SAW) and Bulk Acoustic Wave (BAW) based devices, FBARs withstand as the most capable candidates for high frequency operation, high power handling capabilities, small size, high performance, and IC compatibility. Although they are not new – they first appeared in the 1960s – their performance improvement and applications are continuously evolving. This chapter will guide the reader through the summarized story of FBARs. We will cover their fundamentals, manufacturing processes, their performance state of the art and their most relevant applications.

T. Mirea (✉)
Department of Electronic Engineering, CEMDATIC, Universidad Politécnica de Madrid, Madrid, Spain
e-mail: teona.mirea@upm.es

P. Lieberzeit (ed.), *Piezoelectric Sensors*, Springer Series on Chemical Sensors and Biosensors (2024) 18: 33–60, https://doi.org/10.1007/5346_2023_27,

Published online: 29 October 2023

Keywords FBAR applications, FBAR operation, Film bulk acoustic resonators, Piezoelectric materials, SMR fabrication, Solidly mounted resonator

Abbreviations

AlN	Aluminium nitride
AlScN	Aluminium scandium nitride
BAW	Bulk acoustic wave
FBAR	Film bulk acoustic resonator
FoM	Figure of merit
k_{eff}^2	Electromechanical coupling coefficient
$LiNbO_3$	Lithium niobate
PZT	Lead zirconate titanate
Q	Quality factor
QCM	Quartz crystal microbalance
SiO_2	Silicon dioxide
SMR	Solidly mounted resonator
TCF	Temperature coefficient of frequency
ZnO	Zinc oxide

1 Introduction and Background

Electroacoustic resonators are devices that exploit the piezoelectric effect to generate acoustic, or mechanical, waves and confine them inside a structure to create a resonant cavity. There exist two main kind of waves that can propagate in a material: longitudinal waves and shear waves. Their difference comes from their polarization. In longitudinal waves the particle displacement and the direction of wave propagation are parallel, while for shear waves these directions are perpendicular [1]. From a purer point of view, these types of waves should rather receive the name of quasi-longitudinal and quasi-shear, since in anisotropic materials pure longitudinal and pure shear waves do not exist [1–3]. These two main kinds of waves can be coupled together and generate different and complex acoustic modes. If the acoustic waves propagate along the surface of a material, they are called Surface Acoustic Waves (SAW). On the contrary, if they propagate through the bulk of a material, they are referred to as Bulk Acoustic Waves (BAW). Additional waves and acoustic modes can be considered a combination of both, e.g. Acoustic Plate Modes. SAW and BAW devices have been competing for years as the most adequate candidates for RF filters and other applications. The evolution of the microelectronic processes has allowed both types of devices to incorporate the thin film technology, which has boosted their performance and allowed the operation at higher frequencies.

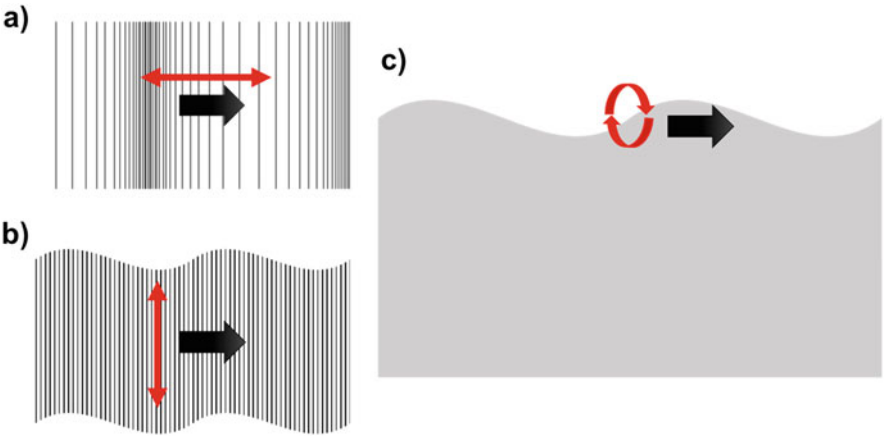

Fig. 1 Basic types of bulk acoustic waves: longitudinal (**a**) and shear (**b**). Example of surface acoustic wave (**c**). Black arrows show the propagation direction of the wave and red arrows the particle displacement

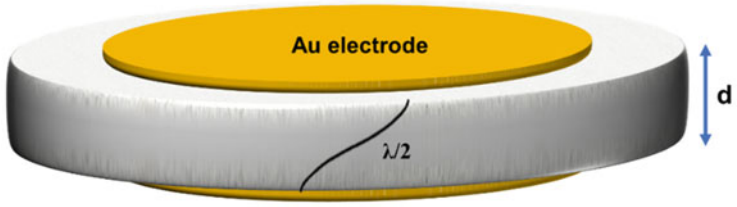

Fig. 2 Structure of a quartz crystal microbalance (QCM)

Nowadays, both technologies can be complementary, being BAW-based devices the most appropriate candidates for the highest frequency ranges (GHz) (Fig. 1).

FBARs are thin film devices based on BAW and exploiting thickness extensional modes. Their predecessor is the well-known Quartz Crystal Microbalance (QCM). QCMs and their applications are thoroughly treated in this book, but since FBARs follow the same working principle, it is worth revising their structure for a better understanding. A QCM has basically the structure of a capacitor, being composed of a quartz plate sandwiched between two electrodes (Fig. 2) on which we apply an electric potential difference. By doing so, we induce an electric field inside the quartz material. As quartz is a piezoelectric material – it can generate a mechanical deformation or strain when an electric field is applied and vice versa [4, 5] – acoustic waves are generated inside. These waves are reflected at the lower and upper electrode interfaces.

When the constructive interference condition is fulfilled, i.e. $d = N\frac{\lambda}{2}, \quad N \in \{1, 3, 5, 7 \ldots\}$, with λ being the acoustic wavelength and d the thickness of the plate, a resonance occurs with the following resonant frequency value:

$$f = \frac{v_w}{\lambda} = N\frac{v_w}{2d} \tag{1}$$

being v_w the acoustic wave velocity in the piezoelectric material.

From Eq. 1 we can extract that the operating frequency is mainly determined by the piezoelectric plate thickness. It is then evident that much thinner films were needed to achieve the market demands for higher operating frequencies. This is relevant not only in the telecom industry but also for high sensitivity sensors. Sauerbrey's equation, which relates the shifts in the resonant frequency Δf to mass attached to the surface of an electroacoustic resonator, suggests that the mass sensitivity is directly proportional to the operating frequency of the device [6]:

$$\Delta f = -\frac{2{f_0}^2\rho_s}{\sqrt{\rho_q \mu_q}} \tag{2}$$

where ρ_s is the density of the mass attached to the device, f_0 the operating frequency and ρ_q and μ_q the density and shear stiffness of the device substrate, in this case quartz.

Thin piezoelectric films appeared decades ago as a potential solution to increase operating frequencies. The first attempt consisted in the evaporation of a CdS thin film on a quartz crystal in 1967 [7]. During the subsequent years, the evolution of the microelectronic technologies allowed the fabrication of new and more advanced electroacoustic devices based on thin films. The first FBAR was fabricated using a thin piezoelectric ZnO film [8–10] and since then, different piezoelectric materials have been studied, being AlN one of the most employed ones [11, 12]. However, recent demands in the telecom industry have pushed the performance limits of FBAR and AlN has reached its limitations. New piezoelectric materials are being optimized and researched nowadays with the aim of substituting AlN in large-scale fabrication.

2 Fundamentals of Film Bulk Acoustic Resonators

2.1 FBAR Types

Compared to QCMs, FBARs employ piezoelectric films with thicknesses below the μm. Their most basic structure is a piezoelectric membrane sandwiched between two thin metallic electrodes and supported by a Si wafer (Fig. 3) [13]. One of the key points in FBAR design is the insulation strategy so the acoustic energy is kept within the resonant cavity (piezoelectric material) by preventing its coupling to the Si substrate. FBARs based on piezoelectric membranes are usually called suspended FBAR and can be achieved either by a deep-etching of the Si substrate (bulk micromachined), also referred to as membrane FBARs (Fig. 3a), or by etching an air-gap (surface micromachined), also referred to as air gap-FBARs. An alternative

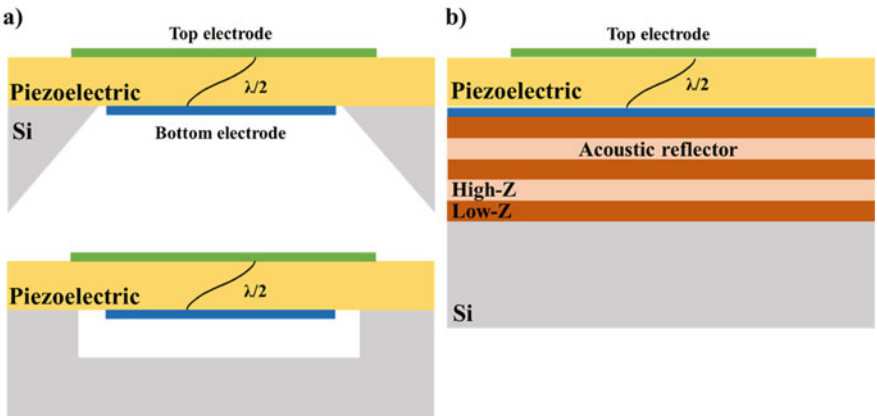

Fig. 3 FBAR structures: (**a**) Suspended in a membrane form (top) or using and air-gap (bottom); (**b**) Solidly Mounted Resonators (SMR)

and more rugged design are the Solidly Mounted Resonators (SMR) (Fig. 3b). Here, the isolation at the bottom electrode interface is achieved by depositing the piezoelectric/electrodes sandwich on an acoustic reflector made by alternating high and low acoustic impedance materials with a quarter wavelength ($\lambda/4$) thickness. This structure resembles an optical Bragg mirror and allows a reflection of 99.9% of the acoustic energy.

2.2 Operation Principles

From a physical point of view, we have described the operation of BAW resonators, in this case FBARs, as the generation of acoustic waves by means of a piezoelectric material and their confinement inside a resonant cavity due to reflections at the top and bottom interfaces. To understand the operation of these devices from an electrical point of view, different models were developed and are nowadays widely used for their simple simulation and design.

2.2.1 Butterworth–Van Dyke Model

The most basic electrical representation of an electromechanical resonator, including an FBAR, is the circuit described by Butterworth–Van Dyke (BVD) [14–16] shown in Fig. 4. This circuit represents the operation of the resonator by combining a motional branch (C_m, L_m and R_m), which describes the mechanical resonance, in parallel with an electrostatic branch (C_0 and R_0), which models the capacitance of the plate and the dielectric losses of the piezoelectric material, respectively. C_0 is a capacitor directly related to the dielectric permittivity of the piezoelectric material,

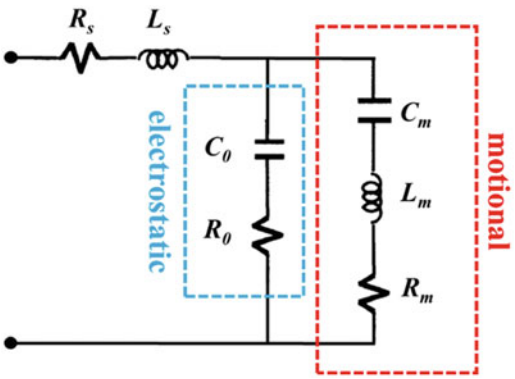

Fig. 4 BVD equivalent circuit of an electromechanical resonator with the corresponding motional and electrostatic branches

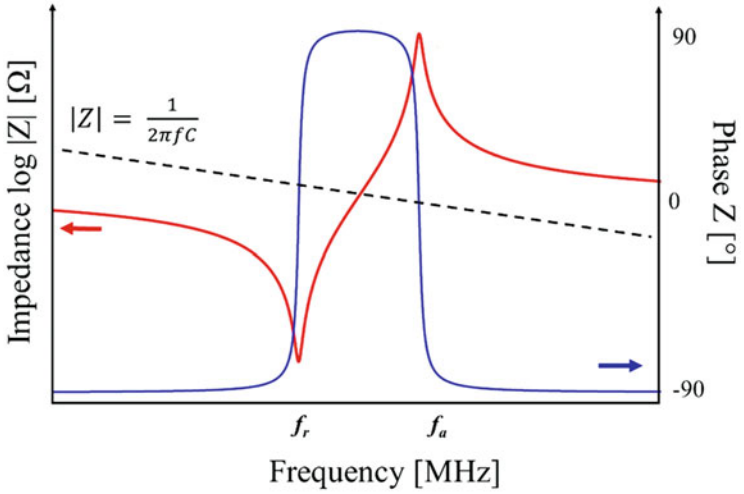

Fig. 5 Electrical impedance modulus and phase of the BVD equivalent circuit

its thickness and device area. R_0 is related to the dielectric losses of the piezoelectric material. The equivalent model also includes the electrical resistance of the electrodes (R_s) and the inductance formed by the electrode layout (L_s).

The electrical impedance (Z) of this equivalent circuit and its phase are plotted in Fig. 5. We can observe here two critical points: a minimum and a maximum of Z associated with a resonance and an antiresonance, respectively. The phase equals zero at both points as it shifts from −90° to 90° and vice versa. Far from these frequencies, Z represents a capacitor. At resonance, the reactance of the motional arm equals zero, passing almost all the current through this branch, limited only by R_s and R_m. We can see it as a series resonance or short circuit since Z tends to zero. This results in the following resonant frequency expression [17]:

$$f_r = \frac{1}{2\pi\sqrt{L_m C_m}} \tag{3}$$

At antiresonance, the reactance of the loop formed by the motional and electrostatic branch equals zero, hence the current flows within the loop formed by C_0 and the motional arm. Therefore, this parallel resonance can also be seen as an open circuit since Z tends to infinite. We can extract from this the following antiresonance frequency [17]:

$$f_a = \frac{1}{2\pi}\sqrt{\frac{C_m + C_0}{L_m C_m C_0}} \tag{4}$$

2.2.2 Mason's Model

Although the BVD-model provides a simple and fast electrical representation of the resonator behaviour, thin film-based devices cannot be fully described by this model solely. More complicated models can predict the 2D and 3D effects in FBARs, e.g. Finite Element Modelling [18, 19], however, a simple and accurate 1D model can predict the response of an FBAR promptly. The standard model in this case is based on Mason's design, which applies the transmission lines theory and reduces the response to 1D effects by considering the lateral dimensions infinite. More detailed descriptions can be found at [20]. Mason's model considers each film in the FBAR as a quadrupole. The advantage of this equivalency lies on the fact that these quadrupoles can be easily cascaded resembling the multilayer structure of an FBAR and is particularly useful for SMR, where several layers compose the acoustic reflector. This model allows a deeper understanding of the material properties influence on the FBAR operation. Through Mason's model we can also extract the electrical Z of the resonator and additionally understand and design the acoustic reflectors for SMRs. It is then worth to briefly describe Mason's model basics and the acoustic reflector theory.

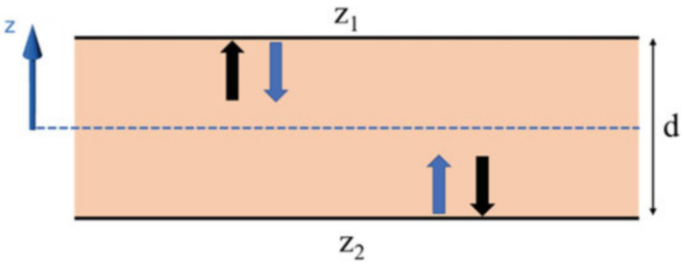

Fig. 6 Schematic of a non-piezoelectric slab of thickness d

We can start by considering a non-piezoelectric slab like in Fig. 6, where waves are reflected back and forward at the interfaces generating a mechanical wave with the following expression:

$$u(z) = \left(a\, e^{-\mathrm{j}kz} + b\, e^{jkz}\right) \tag{5}$$

where $k = \omega/v_w$ is the wavenumber, v_w is the propagation velocity of the wave, $\omega = 2\pi f$ is the angular frequency, and a and b the amplitudes of the incident and reflected waves, respectively.

Depending then on the type of wave we excite in the devices, the v_w will be different, being longitudinal waves faster than shear ones.

To calculate the mechanical force at the boundaries z_1 and z_2 we can derive the particle velocities v_1 and v_2 following:

$$v = \partial u/\partial t \tag{6}$$

and extract coefficients a and b:

$$j\omega a = \frac{v_1\, e^{jkz_2} - v_2\, e^{jkz_1}}{2j \sin kd} \tag{7}$$

$$j\omega b = \frac{v_2\, e^{-jkz_1} - v_1\, e^{-jkz_2}}{2j \sin kd} \tag{8}$$

Considering now the mechanical force as:

$$F = -A\, T$$

where A is the area over which we apply the force and T the stress. From Hooke's fundamental law [17] we know that $T = cS = c\,(\partial u/\partial z)$, where S is the strain in the film and c the stiffness constant, we can reach the following expression of force:

$$F = Ac\frac{\partial u}{\partial z} = jAck\left(a\, e^{-jkz} - b\, e^{jkz}\right) \tag{9}$$

By introducing the acoustic impedance (Z_a) definition:

$$Z_a = \frac{-T}{v} = \frac{-cS}{v} = \rho v_w = \frac{ck}{\omega} \tag{10}$$

We can combine all equations in the expression of the mechanical wave in the non-piezoelectric slab:

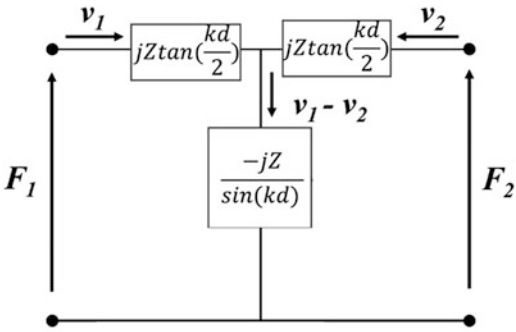

Fig. 7 Equivalent circuit representing Eqs. 11 and 12 as a transmission line network

$$F_1 = \frac{Z}{jsin(kd)}[v_1 - v_2] + jZ\tan\left(\frac{kd}{2}\right)v_1 \tag{11}$$

$$F_2 = \frac{Z}{jsin(kd)}[v_1 - v_2] - jZ\tan\left(\frac{kd}{2}\right)v_2 \tag{12}$$

These equations can be expressed in a matrix form and treated as a quadrupole, more specifically a T-impedance distributed network for a transmission line of length *kd* [21] (Fig. 7). For this equivalency we have considered the analogy between electrical voltage (V) and mechanical force (F), and between electrical current (I) and acoustic velocity (v). Therefore, we obtained an electrical circuit for a propagating wave in a non-piezoelectric slab. The matrix form expression allows total impedance calculations of multilayers by simply cascading the networks and multiplying the corresponding matrixes.

For the specific case of the piezoelectric material, the definition of the equivalent network must include the excitation of the slab by and AC signal and the property of the material, which transforms the mechanical energy to electrical and vice versa. Now the stress should be expressed as $T = c^E S - eE$, where E is the applied electric field, D the electric displacement and e the piezoelectric stress constant. From Maxwell's constitutive equation we also know that $D = \varepsilon E$, being ε the permittivity of the material. Additionally, the generated current can be expressed as $I = j\omega DA$ and the mechanical wave solution in the piezoelectric slab can be expressed by:

$$F_1 = \frac{Z}{jsin(kd)}[v_1 - v_2] + jZ\tan\left(\frac{kd}{2}\right)v_1 + \frac{e}{jw\varepsilon^S}I \tag{13}$$

$$F_2 = \frac{Z}{jsin(kd)}[v_1 - v_2] - jZtan\left(\frac{kd}{2}\right)v_2 + \frac{e}{jw\varepsilon^S}I \tag{14}$$

Since we are applying an electric signal to this slab, an additional I-V port must be added to the network. The voltage drop can be obtained by integrating the electric field between z_1 and z_2:

$$V = \frac{d\,I}{\varepsilon^S j\omega A} + \frac{e}{j\omega\varepsilon^S}(v_1 - v_2) \tag{15}$$

which leads to the following expression of the current:

$$I = j\omega C_0 + \frac{e}{\varepsilon^S} C_0 (v_1 - v_2) \tag{16}$$

being $C_0 = \varepsilon^S A/d$ the static capacitance of the dielectric plate. Figure 8 shows the equivalent network of an SMR, where the piezoelectric layer is cascaded with the top and bottom electrodes and all the layers in the acoustic reflector. The impedance of the device can be then extracted by considering the total mechanical loads at both acoustic ports of the piezoelectric layer, where materials properties have to be taken into account.

On the one hand, the electrical impedance of the device can be extracted from Mason's equivalent circuit as:

$$Z = \frac{1}{jwC_0 + \frac{1}{\frac{-1}{jwC_0} + n^2\left(-j\frac{Z_p}{\sin(kd)} + \frac{1}{\frac{1}{jZ_p\tan\left(kd\frac{kd}{2}\right)+Z_t} + \frac{1}{jZ_p\tan\left(\frac{kd}{2}\right)+Z_b}}\right)}} \tag{17}$$

where Z_t and Z_b represent the top and bottom acoustic impedance loads normalized by the piezoelectric acoustic impedance, Z_p. The transformer term is represented now by $n^2 = kd/(k_t^2 wC_0 Z_p)$. This total Z expression can be also reached by following the approach described by Lakin et al. for a composite resonator [22, 23].

On the other hand, for the reflector transmittance expression we need to consider the acoustic plan wave reflection coefficient Γ at the interfaces. That is, the reflection of acoustic waves at an interface between two materials with different acoustic impedances:

$$\Gamma = \frac{Z_l - Z_0}{Z_l + Z_0} \tag{18}$$

where Z_0 is the acoustic impedance for the incident wave at the interface and Z_l the acoustic impedance for the material adjacent to it. At each interface in the acoustic reflector, the plane waves are reflected and transmitted. This reflection must be as high as possible to prevent energy loss from the resonant cavity, that is, the transmittance (T_{dB}) must be as low as possible:

$$T_{dB} = 10\log_{10}\left(1 - |\Gamma|^2\right) \tag{19}$$

The total reflection of the stack should be ideally $|\Gamma| \approx 1$, therefore the input impedance of the reflector must be much smaller or much larger than that of the

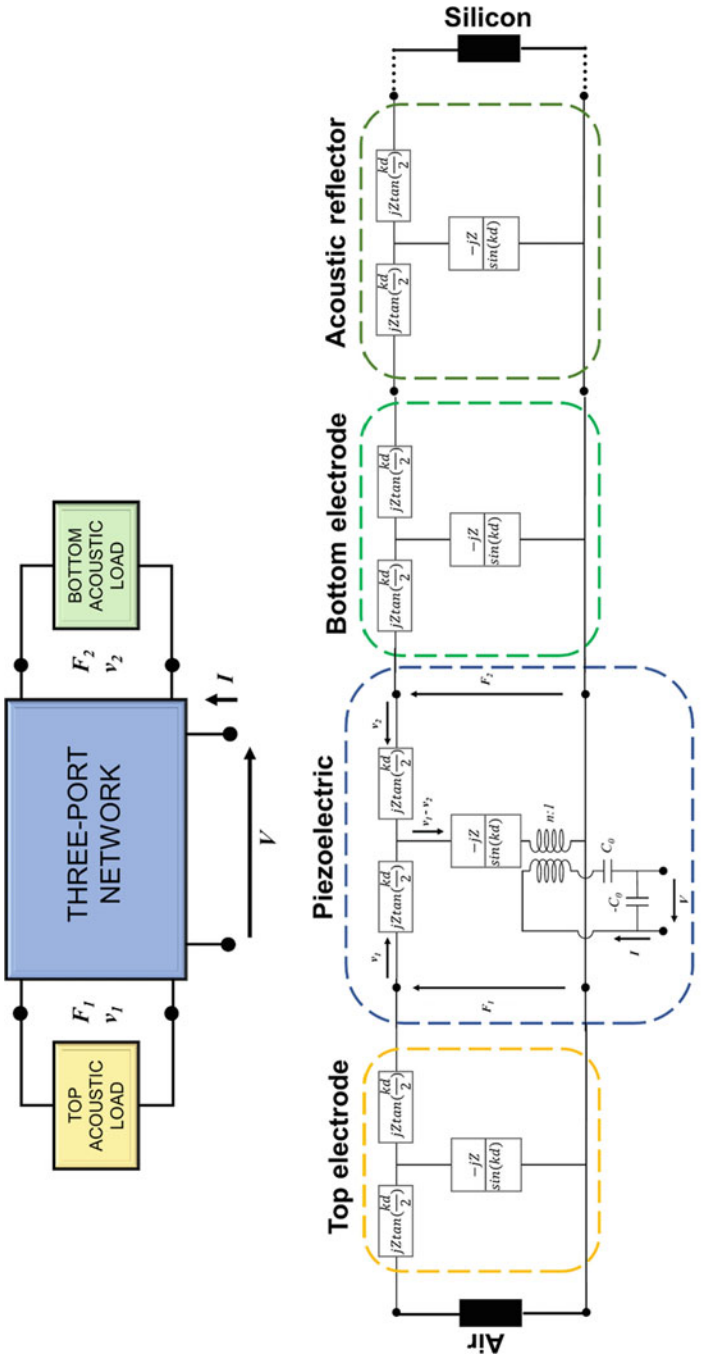

Fig. 8 Mason's model equivalent circuit for an SMR

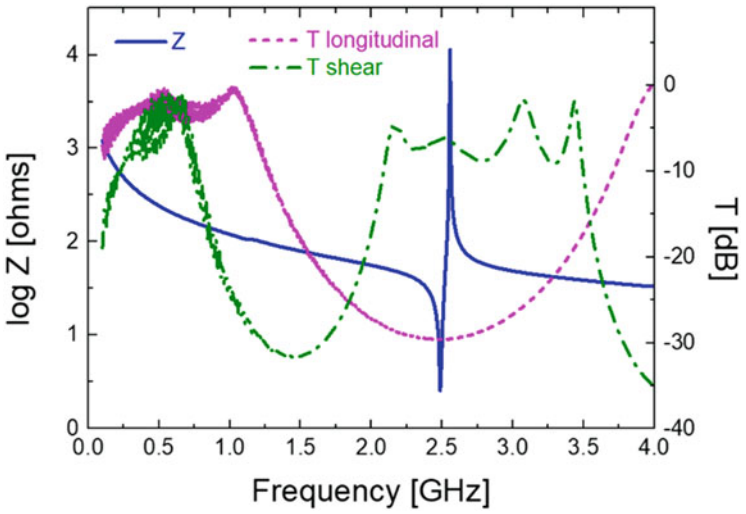

Fig. 9 Electrical impedance of an SMR designed for an optimal reflection of the longitudinal mode at 2.5 GHz

piezoelectric material. The total input impedance of the reflector stack (seen by the resonant cavity) can be calculated following the transmission line equation:

$$Z_{Rin} = Z_0 \left[\frac{Z_l + jZ_0 \tan\theta}{Z_0 + jZ_l \tan\theta} \right] \tag{20}$$

where θ is the total phase across the stack. As specified, the working principle of the acoustic reflector is based on the optical theory of Bragg reflectors. Each layer must be designed with a $\lambda/4$ thickness and alternating high and low impedance materials for an optimal reflection at a specific frequency and a specific type of wave. Figure 9 shows an example of the calculated electrical Z of an SMR together with the acoustic reflector transmission performance. Recall that two main types of waves can propagate: longitudinal and shear waves. For most FBAR applications, longitudinal waves are the ones excited, hence the acoustic mirror must be optimized to reflect longitudinal waves at the operating frequency (example from Fig. 9). Namely, the model includes longitudinal acoustic impedances based on the v_w of the longitudinal waves propagating in each material. However, as we know, pure modes do not exist in anisotropic materials, hence shear waves can be generated and both types of waves can be coupled. Optimization methods have been developed to improve acoustic reflectors by reflecting both longitudinal and shear waves at a specific frequency of operation [24]. The number of layers in the reflector is directly proportional to the reflection efficiency. These acoustic reflectors are usually designed with 5, 7, 9, 12 layers. A trade-off must be considered since the larger the number of layers, the better the reflection; however, the structural integrity of the

SMR can also be compromised due to mechanical stresses. The materials employed for acoustic reflectors will be discussed in the following sections.

2.3 Figures of Merit

For all applications of FBARs, and by extension of all electroacoustic resonators, there are two clear figures of merit (FoM) that the industry and researchers are always pursuing to improve: the effective electromechanical coupling coefficient (k_{eff}^2) and the quality factor (Q). Usually, both parameters are combined in a single FoM referred to as $k_{\text{eff}}^2 \times Q$.

On the one hand, k_{eff}^2 is an indicator of how efficiently the resonator transforms mechanical energy to electrical and vice versa. It has been defined employing different expressions [25]; however, the most accurate one follows the IEEE standard on piezoelectricity [26]:

$$k_{\text{eff}}^2 = \frac{\pi}{2}\frac{f_r}{f_a}\frac{1}{\tan\left(\frac{\pi}{2}\frac{f_r}{f_a}\right)} \tag{21}$$

being f_r and f_a the resonant and antiresonant frequencies. The larger the spacing between these two frequencies, the larger k_{eff}^2. It is worth specifying that k_{eff}^2 measures the efficiency of the whole devices, but there is an additional definition for the piezoelectric material electromechanical coupling coefficient (k^2), which measures the efficiency of the material alone. Therefore, a high k_{eff}^2 can only be achieved if the k^2 of the employed piezoelectric material is high. However, special attention must be paid to the device design, as it can lead to poor k_{eff}^2 if, for example, the acoustic isolation from the Si substrate in SMRs has not been optimized with a proper reflector design.

On the other hand, Q measures the ratio of the energy stored in the resonator to the energy lost or dissipated per cycle by damping processes [17]. One of the most accurate forms to extract this value uses the steepness of the phase curves at resonant or antiresonant frequencies [27, 28]:

$$Q_{r,a} = \frac{f_{r,a}}{2}\left(\frac{d\varphi(Z)}{df}\right)_{f_{r,a}} \tag{22}$$

To understand the loss mechanisms, we can also relate them to the BVD equivalent circuit, where the quality factors at resonance (Q_r) and antiresonance (Q_a) are related to the electrical components as follows:

$$Q_r \approx 2\pi f_r \frac{L_m}{R_S + R_m} \tag{23}$$

$$Q_a \approx 2\pi f_a \frac{L_m}{R_0 + R_m} \tag{24}$$

At resonance the quality factor is mainly affected by the series resistance R_S (Fig. 4), which is related to the electrode's materials, thicknesses, layout, and the electrical contact. At antiresonance the R_0 is the component that strongly influences the quality factor. This resistance is related to the losses in the piezoelectric material; hence, the material selection and its growth or deposition process play a key role.

A third parameter, not necessarily considered a formal FoM as the previous ones, but of important relevance for FBAR operation, is the Temperature Coefficient of Frequency (TCF). It defines how sensitive the device is to environmental temperature variations, which can strongly influence the device response by undesirable shifts in its resonant and antiresonant frequencies. It is defined as:

$$\mathrm{TCF} = \frac{\Delta f}{\Delta T f_0} \; 10^6 \left[\frac{\mathrm{ppm}}{^\circ\mathrm{C}}\right] \tag{25}$$

where Δf represents the variation in frequency due to a variation in temperature ΔT. The division by f_0 (the operating frequency of the device) is performed for normalization purposes. TCFs are usually given in ppm/°C or ppm/K. The aim in FBAR design and fabrication is to reduce this parameter as much as possible [29–32]. The techniques to achieve this are discussed in Sect. 3.2.

When applied to sensing applications, additional FoM have to be considered and will be discussed in Sect. 4.

3 Fabrication Processes

As introduced, the demands in the telecom industry have established the needs for miniaturization, high power handling capabilities, low cost and high operating frequencies, all without losing overall performance in FBARs. This has been translated to demands for thinner piezoelectric films and of higher quality, especially in terms of k_{eff}^2, as it is the main parameter defining the filters bandwidth. Thin piezoelectric films have been deposited using different methods like the chemical vapour deposition (CVD) or the physical vapour deposition (PVD) ones. Both methods include different techniques. One of the standard methods to achieve highly oriented and thin piezoelectric films is the reactive sputtering technique by either RF or pulsed DC. Advances in the sputtering technologies have allowed the control over the thickness, the crystal orientation, the stress and the composition of the films, hence over their piezoelectric quality. ZnO, AlN and AlScN have been successfully deposited by these means. Sputtering processes have also been a preferred choice for

the deposition of the metallic electrodes as well as for other films included in, for example, the SMR structures. Regarding the thin metallic electrodes, the typical materials are Al, Mo, W or more expensive ones like Pt or Ir. While the first ones are widely employed in large-scale fabrication, the last ones have proved to support the growth of higher quality piezoelectric films [33]. The roughness and conductivity of the metallic electrodes, especially of the bottom one, are also pivotal for the growth of a high-quality piezoelectric film and a high k_{eff}^2 device. The bottom electrode acts as a seed layer for the piezoelectric film growth; therefore, its surface roughness influences the preferred crystal orientation of this film [34, 35]. The stress and roughness of the metallic electrodes can be controlled by tuning the sputtering conditions, however that can be not enough. To improve even more the surface roughness of the metallic bottom electrode, chemical mechanical polishing (CMP) is employed. In SMR structures the CMP can be applied to the last reflector layer, which is usually SiO_2 [36]. In this same work, switching to e-beam evaporation methods to deposit Ir with a smoother surface has also shown an improvement on the AlN quality compared to sputtered Ir films.

Although pulsed DC reactive sputtering has been the undisputable method for the manufacturing of AlN and AlScN FBARs, the new imposed demands for thinner and higher quality piezoelectric films have switched the focus to other materials and deposition techniques. Alternative piezoelectric films like $LiNbO_3$ and $LiTaO_3$ have been deposited either by layer transfer methods or by CVD techniques [37, 38]. This section summarizes the research of different piezoelectric materials in FBARs and the fabrication process to manufacture the devices.

3.1 Evolution of Piezoelectric Materials

Piezoelectric materials like PZT and ZnO were the initial choices for FBAR fabrication [8, 39–42]; however, their increased losses and chemical and thermal instabilities placed AlN as the preferred industrial choice for decades. AlN offers high acoustic velocity, low acoustic losses at high frequencies and high thermal and chemical stability, which made it ideal for filters generations so far [11, 41, 43, 44]. AlN-based FBARs have achieved performances with k_{eff}^2 of 7% and Q factors as high as 2,000 [45] for operating frequencies of up to 2–3 GHz. Although this performance has been sufficient for decades, the telecom industry is now immersed in the 5G era, thus higher demands are required from acoustic resonators, particularly higher operating frequencies [46]. For these new frequency ranges, above 3 GHz, one of the problems faced by AlN is that it needs to be thinned below 0.8 μm thicknesses, which leads to decreased k_{eff}^2 and increased losses [47, 48]. Some works have developed thin high-quality AlN single crystals using Metal-Organic CVD techniques obtaining devices with k_{eff}^2 of 6.2% and Q factors of 2,136 [49]; however, this performance in terms of k_{eff}^2 is still not enough. Therefore, the FBAR industry has already evolved towards new generations of piezoelectric materials. One of them is AlScN [50], providing FBARs with k_{eff}^2 up to 16%

Table 1 Performances of FBARs fabricated using different piezoelectric materials and deposition methods

Material	Frequency [GHz]	TCF [ppm/K]	k_{eff}^2 [%]	Q	Deposition technique	Reference
PMnN-PZT	4	–	70	185	Sputtering (powder target)	[67]
AlN	2	−18	6.5–7	2000	Sputtering	[45, 68]
AlScN	3.5	–	16	1,070	Sputtering	[51]
$LiNbO_3$ (Y + 43°)	3.041	–	20.2	<100	Layer transfer	[59]
$LiNbO_3$ (Y + 163°)	4.78	−190	17.6	190	Layer transfer	[61]
$LiNbO_3$ (Y + 33°)	2.3	−60	21.4	255	Layer transfer	[60]

[51]. This material can be deposited by co-sputtering Al and Sc targets [52, 53], by building compound Al-Sc targets with small pellets of Sc [54] or by using alloyed AlSc targets with a specific Sc concentration [55]. A concentration of Sc close to 30% has provided, so far, the highest k_{eff}^2 [56]. Despite the improvement in k_{eff}^2, AlScN suffers from the presence of higher losses due to the Sc doping, which leads to poorer Q factors. To overcome the $k_{eff}^2 \times Q$ factors and push the technology to even higher frequency, the potential piezoelectric materials under study now are $LiNbO_3$ and $LiTaO_3$ [57–63]. These materials are not new, since their use as thick single crystals has been known for years, especially for SAW-based resonators [64]. FBARs based on $LiNbO_3$ have been fabricated earlier by direct bonding and wafer thinning [65], but the limitation of these processes did not allow operating frequencies higher than few hundred of MHz. Nonetheless, in recent years their thin film form has been widely researched and achieved by improved mechanical techniques. The most successful one has been, so far, the layer transfer, which combines ion implantation, wafer bonding and thermal splitting under a process known as Smart Cut™ [66]. With this method $LiNbO_3$ as thin as 300 nm has been obtained, providing FBARs operating at up to 8–9 GHz with k_{eff}^2 of 18.5% and Q factors of 160 [60]. Thicker films provided lower frequencies and higher k_{eff}^2. There is enormous interest in the industrialization of $LiNbO_3$ and $LiTaO_3$ deposition processes to obtain high-quality thin films; however, few are the studied PVD and CVD techniques that showed promising results, being one of them the Metal Organic-CVD method [38].

Compared to AlN, AlScN and $LiNbO_3$ may, from a first perspective, increase fabrication costs. However, the number of RF filters demanding higher operating frequencies for upcoming communication bands is rapidly increasing. As these materials are, so far, the most promising candidates to fulfil these requirements, the material cost can be covered by larger fabricated quantities. Table 1 shows a summary of the FBAR performances offered by the different piezoelectric materials used during the last decades, including the state of the art nowadays.

3.2 FBARs Structures and Their Fabrication Processes

As introduced, FBARs can be fabricated in three different structures [69]: membrane FBARs, air-gap FBARs and SMR. The first membrane FBARs appeared between the 1980s and 1990s as composite resonators [70, 71] and were based on ZnO deposited over a supporting Si membrane. Years later, advances in sputtering techniques allowed the deposition of piezoelectric materials of higher quality in terms of thermal and chemical stability and FBARs started using AlN, including supporting layers like, for example, Si_3N_4 [72]. A typical route of fabrication is shown in Fig. 10. To manufacture membrane FBARs, one of the most critical points after an optimized AlN deposition is the deep-etching of the Si substrate, which can be achieved by wet etching with, for example, a KOH etchant [73] or by Reactive Ion Etching (RIE), more particularly Deep-RIE [74].

During the same decade, air-gap FBARs were also introduced [75], with the main difference being the use of a surface micromachining technique instead of a bulk micromachining from the wafer backside. Here, a temporary support layer is used, usually SiO_2, which is removed by the under cutting etch to release the piezoelectric stack. An alternative method to build an air-gap underneath the piezoelectric sandwich is the so-called bridge type [76]. In this case the sacrificial layer and stress control methods are implemented to form the air-gap between the Si substrate and the bottom electrode (Fig. 11).

An additional step in the fabrication of suspended FBARs is usually taken to improve the TCF characteristics of the device, that is, to lower its sensitivity to environmental temperature variations. Although AlN has a low elastic coefficient of temperature compared to other piezoelectric materials, the effective TCF of the complete device can be lowered by adding a thin layer of SiO_2 to the structure (Fig. 12). SiO_2 is known to have a positive elastic coefficient of temperature, which

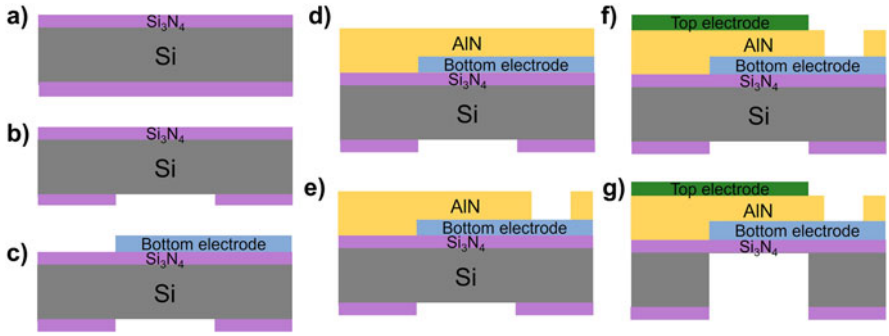

Fig. 10 Fabrication route of a membrane AlN-FBAR. (**a**) Growth of the sacrificial layer; (**b**) etching of the sacrificial layer on the backside of the Si wafer; (**c**) deposition of the bottom electrode; (**d**) growth of the piezoelectric AlN; (**e**) Via-hole through the AlN to access the bottom electrode; (**f**) deposition of the top electrode; (**g**) Deep-RIE of the Si wafer to release the membrane

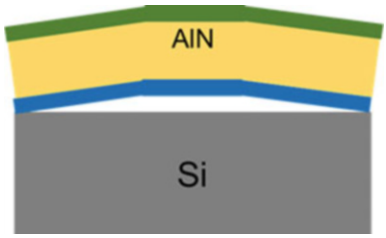

Fig. 11 Structure of a bridge type FBAR

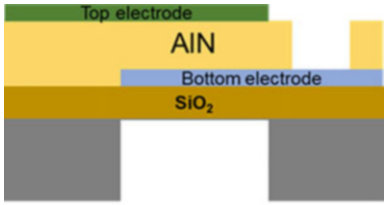

Fig. 12 Temperature compensated FBAR

compensates the negative one of AlN providing the FBAR with almost zero TCF [29, 30, 32].

Although SMRs were first presented in 1964 [77], their extended development also occurred during the 1990s [78, 79]. This structure appeared from the necessity of a more rugged stack by avoiding the piezoelectric membrane fragility. Despite that, the deposition of the piezoelectric material, and more particularly of the reflector layers, must be thoroughly optimized to preserve the mechanical integrity of the device. Compared to suspended FBARs, SMR also offer lower TCFs since SiO_2 is one of the preferred choices as low acoustic impedance material for the reflectors [80]. Figure 13 shows a fabrication process that does not require via-hole through the AlN to access the bottom electrode. This type of structure is based on a capacitive coupling, namely, the capacitor formed by the AlN and the electrodes becomes a short circuit at higher frequency due to the nature of the capacitors electric impedance. The devices are usually tested with a GS (Ground-Signal) or GSG (Ground-Signal-Ground) RF probe, being the active signal applied to the active area while the ground-signal is applied to the exterior metallic film (Fig. 13e). In this specific case the ground-signal is capacitively coupled to the bottom electrode at the high frequency operation of the SMR. Standard fabrication processes use via-holes through the AlN or the definition of AlN to a certain area without covering the bottom electrical contact (Fig. 14).

The thicknesses of the acoustic reflectors are deposited to fulfil the $\lambda/4$ rule of Bragg reflectors. This, of course, depends on the frequency of operation and the chosen materials for high and low acoustic impedance. However, specific strategies can additionally be employed to improve acoustic reflectors designs by reflecting both longitudinal and shear waves [24]. To achieve it, the acoustic reflectors must be deposited in an asymmetrical form, namely, the thicknesses of all high and low acoustic impedance materials will not be the same ($\lambda/4$).

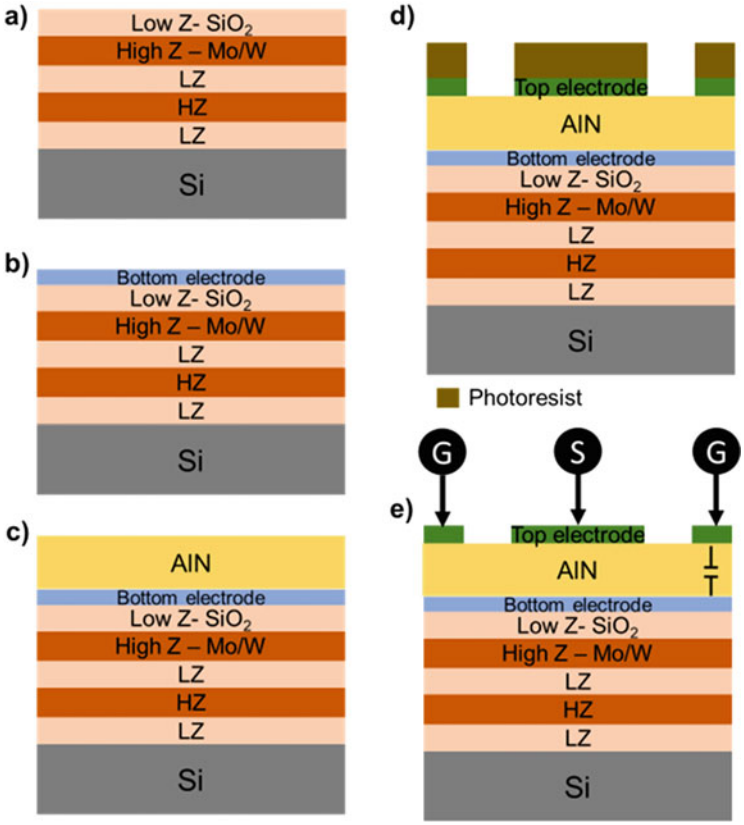

Fig. 13 Fabrication route of an SMR: (**a**) Alternate deposition of low and high acoustic impedance material to form the acoustic reflector; (**b**) deposition of the bottom electrode; (**c**) growth of the piezoelectric AlN; (**d**) deposition and definition of the top electrode; (**e**) GSG probing of the top electrode with access to the bottom electrode through capacitive coupling

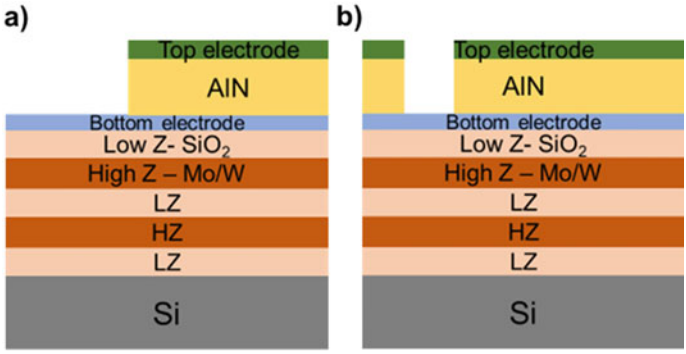

Fig. 14 SMR structures with direct access to the bottom electrode

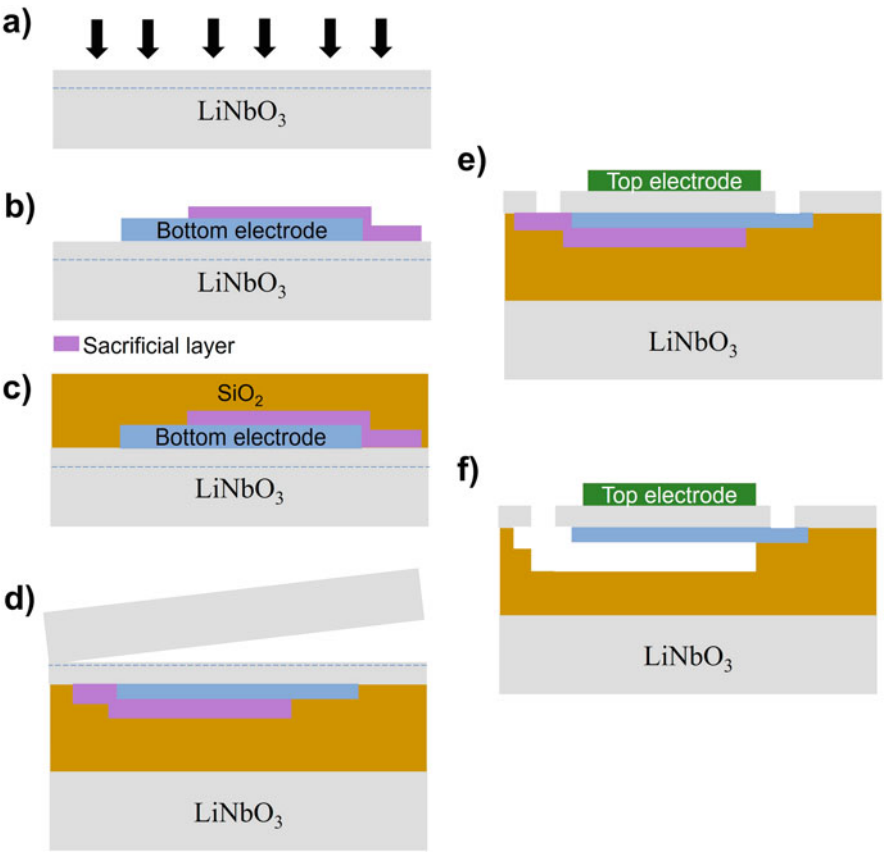

Fig. 15 Smart Cut™ process for layer transfer of $LiNbO_3$ thin films. (**a**) Ion implantation to generate a weak interface; (**b**) Deposition of bottom electrode and sacrificial layer; (**c**) SiO_2 deposition and planarization; (**d**) bonding onto host wafer with SiO_2; (**e**) Via-holes to access the bottom electrode and the sacrificial layer and top electrode deposition; (**f**) wet etching of sacrificial layer to leave a suspended FBAR

The recent focus on the benefits of $LiNbO_3$ piezoelectric materials has defined new ways of FBARs fabrication. As this material cannot be deposited by PVD methods with high quality yet, layer transfer methods have been optimized to a standard called Smart Cut™ [66] (Fig. 15).

From an industrial perspective, the large-scale fabrication of FBARs imply additional complications to the process. Besides the precise mechanical stress control during the deposition of the different thin films, particularly relevant for SMRs, some considerations need to be considered:

(i) The devices need to be singulated, which can be done by laser or stealth dicing.
(ii) Membrane FBARs do not allow stealth dicing due to the process aggressivity and the use of water cooling at high pressure. Membranes are too fragile.

(iii) If laser dicing is used, no metals can be present on the trenches where the laser passes. This includes additional masking steps to etch the metal at this spot.
(iv) SMRs can be singulated by both stealth and laser dicing. A standard practice is to define the reflector stack to a specific area in order to ease the dicing, particularly important for laser dicing. This adds more masking and etching steps to the process.

4 Applications

By now, the reader has already inferred from the previous sections that RF filters, particularly working in the GHz frequency ranges, are the main application of FBAR devices [81]. This application is not only the reason why the evolution of FBARs, including thin film deposition processes and micromachining methods, has been possible in such a short period of time, but is also the most mature and profitable one. AlN-based FBARs made possible the miniaturization, the performance improvement and lowered the cost of the increasingly imposed filters needed on our smartphones. Their manufacturing techniques allowed their integration with CMOS processes, which additionally reduced fabrication cost by integrating the readout electronics. However, other fields have also benefited from these performance improvements. The research in the sensing applications of FBARs started decades ago, but it has not been until the recent years that their full potential has been exploited.

4.1 Sensing Applications

From chemical to biological sensing, FBARs have boosted the mass resolution limits of their widely employed predecessors, QCMs, by reaching the pg or even fg levels. The basic operation principle of both, QCM and FBAR sensors, is based on their gravimetric ability. These devices respond to mass attached to their surface by varying their electrical behaviour [6]. This behaviour is observed in the shifts in their resonant or antiresonant frequencies, which are typically monitored by following the maximum of the admittance (Y) or impedance real parts, respectively. Figure 16 shows an example of a mass attachment event on an FBAR and the downward shift of its resonant frequency.

To monitor these shifts, FBARs can be integrated in oscillator topologies [82] or directly interrogated by network analysers [83]. In both cases, the device Q factors are relevant as it directly affects the mass resolution of the sensor. The sensitivity of an electroacoustic sensor can be defined in terms of the shifts in frequency Δf per mass variation Δm:

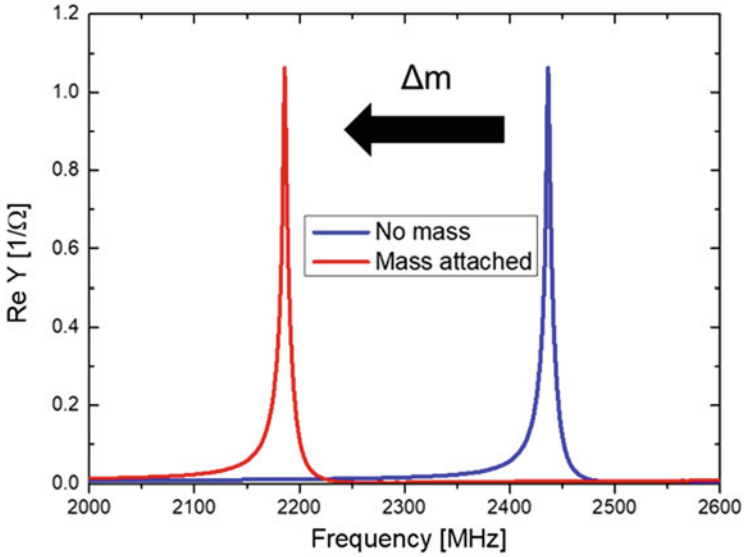

Fig. 16 Shift of the resonant frequency due to mass attachment Δm to the surface of an FBAR. The resonant frequency corresponds to the maximum of the admittance real part (Real Y)

$$S = \frac{\Delta f}{f_0} \frac{1}{\Delta m} \tag{26}$$

being f_0 the device resonant frequency, which is used for normalization purposes when comparing resonators operating at different frequencies. On the other hand, the limit of detection (LoD) of the sensor can be defined as the minimum detectable shift in frequency, again normalized by the resonant frequency for normalization:

$$\text{LOD} = \frac{\Delta f_{\min}}{f_0} \tag{27}$$

We can then define the resolution of the sensor as the minimum change in mass that can be detected by the resonant frequency:

$$R = \frac{\text{LOD}}{S} \tag{28}$$

The LoD is directly affected by the noise, which is also related to the Q factor of the devices. It is then clear that the performance of FBARs in terms of Q factors needs to be optimized if lower resolutions are pursued. This is also relevant from the readout electronics point of view.

By exploiting their gravimetric ability, FBARs have been thoroughly studied in gas [84–86] and particle sensing [87]. Their selectivity is mainly determined by the functionalization layer deposited on their surface. The proper operation in gaseous

environments can be performed by exciting the longitudinal mode. However, if operated in liquid environments, the longitudinal waves couple to the liquid in contact with the device surface and most of the energy is lost within this medium [6]. To prevent this, FBARs are operated in the shear mode by depositing the piezoelectric films with tilted gains [88–91]. By doing so, the energy dissipation in the liquid environment can be prevented and their application as biosensors can be exploited [92–95]. Since FBARs can be sensitive to other environmental variations, alternative applications have been also tested: viscosity sensors [96, 97] or humidity sensors [98].

Even if their application as sensors is less mature and not at such an industrial level as RF filters, during the last years different companies have emerged in this context to commercialize FBARs for environmental monitoring [99, 100] or specific bio-applications like the detection of SARS-CoV-2 [101].

References

1. Auld BA (1973) Acoustic fields and waves in solids. Wiley
2. Auld BA (1973) Acoustic fields and waves in solids, vol II. R.E. Krieger
3. Hashimoto K (2000) Surface acoustic wave devices in telecommunications. Springer
4. Mason WP (1981) Piezoelectricity, its history and applications. J Acoust Soc Am 70(6): 1561–1566. https://doi.org/10.1121/1.387221
5. Tichý J, Erhart J, Kittinger E, Přívratská J (2010) Fundamentals of piezoelectric sensorics. Principles of piezoelectricity. Springer, Berlin, pp 1–14. https://doi.org/10.1007/978-3-540-68427-5_1
6. Ballantine DS et al (1997) Acoustic wave sensors. Elsevier. https://doi.org/10.1016/B978-0-12-077460-9.50012-5
7. Sliker TR, Roberts DA (1967) A thin-film CdS-quartz composite resonator. J Appl Phys 38(5): 2350–2358. https://doi.org/10.1063/1.1709882
8. Lakin KM, Wang JS (1981) Acoustic bulk wave composite resonators. Appl Phys Lett 38(3): 125–127. https://doi.org/10.1063/1.92298
9. Grudkowski TW, Black JF, Reeder TM, Cullen DE, Wagner RA (1980) Fundamental-mode VHF/UHF minature acoustic resonators and filters on silicon. Appl Phys Lett 37(11):993–995. https://doi.org/10.1063/1.91745
10. Nakamura K, Sasaki H, Shimizu H (1981) ZnO/SiO2-diaphragm composite resonator on a silicon wafer. Electron Lett 17(14):507. https://doi.org/10.1049/el:19810355
11. Dubois M-A, Muralt P (1999) Properties of aluminum nitride thin films for piezoelectric transducers and microwave filter applications. Appl Phys Lett 74(20):3032. https://doi.org/10.1063/1.124055
12. Okano H, Tanaka N, Takahashi Y, Tanaka T, Shibata K, Nakano S (1994) Preparation of aluminum nitride thin films by reactive sputtering and their applications to GHz-band surface acoustic wave devices. Appl Phys Lett 64(2):166–168. https://doi.org/10.1063/1.111553
13. Lakin KM (2005) Thin film resonator technology. IEEE Trans Ultrason Ferroelectr Freq Control 52(5):707–716. https://doi.org/10.1109/TUFFC.2005.1503959
14. David J, Cheeke N (2002) Fundamentals and applications of ultrasonic waves. CRC Press LLC
15. Dye DW (1925) The piezo-electric quartz resonator and its equivalent electrical circuit. Proc Phys Soc Lond 38(1):399–458. https://doi.org/10.1088/1478-7814/38/1/344

16. Larson JD, Bradley PD, Wartenberg S, Ruby RC (n.d.) Modified Butterworth-Van Dyke circuit for FBAR resonators and automated measurement system. In: 2000 IEEE ultrasonics symposium. Proceedings. An international symposium. IEEE, pp 863–868. https://doi.org/10.1109/ULTSYM.2000.922679
17. Rosenbaum JF (1988) Bulk acoustic wave theory and devices. Artech House
18. Thalhammer R, Larson JD (2015) Finite element analysis of BAW devices: principles and perspectives. In: 2015 IEEE international ultrasonics symposium (IUS). IEEE, pp 1–10. https://doi.org/10.1109/ULTSYM.2015.0187
19. Makkonen T, Holappa A, Ellä J, Salomaa MM (2001) Finite element simulations of thin-film composite BAW resonators; Finite element simulations of thin-film composite BAW resonators. IEEE Trans Ultrason Ferroelectr Freq Control 48(5). https://doi.org/10.1109/58.949733
20. Mason WP (1977) Physical acoustics: principles and methods. Academic Press
21. Pozar DM (2001) Microwave and RF wireless systems. Wiley
22. Lakin KM (n.d.) Modeling of thin film resonators and filters. In: 1992 IEEE microwave symposium digest MTT-S. IEEE, pp 149–152. https://doi.org/10.1109/MWSYM.1992.187931
23. Lakin KM, Kline GR, McCarron KT (1993) High-Q microwave acoustic resonators and filters. IEEE Trans Microw Theory Tech 41(12):2139–2146. https://doi.org/10.1109/22.260698
24. Jose S, Jansman ABM, Hueting RJE, Schmitz J (2010) Optimized reflector stacks for solidly mounted bulk acoustic wave resonators. IEEE Trans Ultrason Ferroelectr Freq Control 57(12):2753–2763. https://doi.org/10.1109/TUFFC.2010.1749
25. Aigner R (2007) Bringing BAW technology into volume production: the ten commandments and the seven deadly sins. In: Third international symposium on acoustic wave devices for future mobile communication systems, Chiba, pp 85–93
26. IEEE Standard on Piezoelectricity (1987) IEEE Standard 176. https://doi.org/10.1109/IEEESTD.1988.79638
27. Feld DA, Parker R, Ruby R, Bradley P, Dong S (2008) After 60 years: a new formula for computing quality factor is warranted. Proc IEEE Ultrason Symp:431–436. https://doi.org/10.1109/ULTSYM.2008.0105
28. Ruby R, Parker R, Feld D (2008) Method of extracting unloaded Q applied across different resonator technologies. https://doi.org/10.1109/ULTSYM.2008.0446
29. Ivira B, Benech P, Fillit R, Ndagijimana F, Ancey P, Parat G (2008) Modeling for temperature compensation and temperature characterizations of BAW resonators at GHz frequencies. IEEE Trans Ultrason Ferroelectr Freq Control 55(2):421–430. https://doi.org/10.1109/TUFFC.2008.660
30. Lakin KM, McCarron KT, McDonald JF (n.d.) Temperature compensated bulk acoustic thin film resonators. In: 2000 IEEE ultrasonics symposium. Proceedings. An international symposium (Cat. No.00CH37121). IEEE, pp 855–858. https://doi.org/10.1109/ULTSYM.2000.922677
31. Allah MA, Kaitila J, Thalhammer R, Weber W, Schmitt-Landsiedel D (2009) Temperature compensated solidly mounted resonators with thin SiO2 layers. In: 2009 IEEE international ultrasonics symposium. IEEE, pp 859–862. https://doi.org/10.1109/ULTSYM.2009.5442034
32. Bjurström J, Wingqvist G, Yantchev V, Katardjiev I (2007) Temperature compensation of liquid FBAR sensors. J Micromech Microeng 17(3):651–658. https://doi.org/10.1088/0960-1317/17/3/030
33. Clement M, Olivares J, Iborra E, González-Castilla S, Rimmer N, Rastogi A (2009) AlN films sputtered on iridium electrodes for bulk acoustic wave resonators. Thin Solid Films 517(16):4673–4678. https://doi.org/10.1016/j.tsf.2009.02.139
34. Löbl HP et al (2001) Materials for bulk acoustic wave (BAW) resonators and filters. J Eur Ceram Soc 21(15):2633–2640. https://doi.org/10.1016/S0955-2219(01)00329-6
35. Lee S-H, Lee J-K, Yoon KH (2002) Growth of highly c-axis textured AlN films on Mo electrodes for film bulk acoustic wave resonators. J Vac Sci Technol A 21(1):1. https://doi.org/10.1116/1.1521961

36. Iborra E, Clement M, Capilla J, Olivares J, Felmetsger V (2012) Low-thickness high-quality aluminum nitride films for super high frequency solidly mounted resonators. Thin Solid Films 520(7):3060–3063. https://doi.org/10.1016/J.TSF.2011.11.007
37. Reinhardt A et al (2014) Acoustic filters based on thin single crystal LiNbO 3 films: status and prospects (Invited Paper). In: 2014 IEEE international ultrasonics symposium. https://doi.org/10.1109/ULTSYM.2014.0191
38. Bartasyte A, Margueron S, Baron T, Oliveri S, Boulet P (2017) Toward high-quality epitaxial LiNbO 3 and LiTaO 3 thin films for acoustic and optical applications. https://doi.org/10.1002/admi.201600998
39. Su Q-X, Kirby P, Komuro E, Imura M, Zhang Q, Whatmore R (2001) Thin-film bulk acoustic resonators and filters using ZnO and lead-zirconium-titanate thin films. IEEE Trans Microw Theory Tech 49(4):769. https://doi.org/10.1109/22.915462
40. Larson III JD, Gilbert SR, Xu B (2004) PZT material properties at UHF and microwave frequencies derived from FBAR measurements; PZT material properties at UHF and microwave frequencies derived from FBAR measurements. IEEE Ultrason Symp 1:2004. https://doi.org/10.1109/ULTSYM.2004.1417696
41. Ruby R, Bradley P, Larson Iii J, Oshmyansky Y, Figueredo D (2001) Ultra-miniature high-Q filters and duplexers using FBAR technology. In: 2001 IEEE international solid-state circuits conference. Digest of technical papers. ISSCC (Cat. No.01CH37177). https://doi.org/10.1109/ISSCC.2001.912569
42. Muralt P, Antifakos J, Cantoni M, Lanz R, Martin F, Ch PM (2005) Is there a better material for thin film BAW applications than AlN? IEEE Ultrason Symp 1:2005. https://doi.org/10.1109/ULTSYM.2005.1602858
43. Iborra E, Clement M, Olivares J, Sangrador J, Rimmer N, Rastogi A (2007) Aluminum nitride bulk acoustic wave devices with iridium bottom electrodes. In: IEEE ultrasonics symposium proceedings. https://doi.org/10.1109/ULTSYM.2007.160
44. Muralt P (2017) AlN thin film processing and basic properties. In: Piezoelectric MEMS resonators. Springer, Cham, pp 3–37. https://doi.org/10.1007/978-3-319-28688-4_1
45. Ruby R (2007) Review and comparison of bulk acoustic wave FBAR, SMR technology. In: 2007 IEEE ultrasonics symposium proceedings. IEEE, pp 1029–1040. https://doi.org/10.1109/ULTSYM.2007.262
46. Advanced BAW filter technology and its impact on 5G. https://www.rfglobalnet.com/doc/advanced-baw-filter-technology-and-its-impact-on-5g-0001
47. Martin F, Muralt P, Dubois M-A, Pezous A (2004) Thickness dependence of the properties of highly c-axis textured AlN thin films. J Vac Sci Technol A 22:361. https://doi.org/10.1116/1.1649343
48. Aigner MAR, Fattinger G, Tajic A, Volatier A, Dumont F, Stokes P (2015) The edge of tomorrow in BAW: innovate, ramp, repeat. In: Proceedings of international symposium on acoustic devices, Chiba, Japan, pp 7–12
49. Vetury R, Hodge MD, Shealy JB (2018) High power, wideband single crystal XBAW technology for sub-6 GHz micro RF filter applications. In: IEEE international ultrasonics symposium, IUS. IEEE Computer Society. https://doi.org/10.1109/ULTSYM.2018.8580045
50. Akiyama M, Kano K, Teshigahara A (2009) Influence of growth temperature and scandium concentration on piezoelectric response of scandium aluminum nitride alloy thin films. Appl Phys Lett 95:162107. https://doi.org/10.1063/1.3251072
51. Moe C et al (2020) Highly doped AlScN 3.5 GHz XBAW resonators with 16% k2eff for 5G RF filter applications. In: 2020 IEEE international Ultrasonics Symposium (IUS). IEEE, pp 1–4. https://doi.org/10.1109/IUS46767.2020.9251412
52. Akiyama M, Kamohara T, Kano K, Teshigahara A, Takeuchi Y, Kawahara N. Enhancement of piezoelectric response in scandium aluminum nitride alloy thin films prepared by dual reactive cosputtering. https://doi.org/10.1002/adma.200802611

53. Moreira M, Bjurström J, Katardjev I, Yantchev V (2011) Aluminum scandium nitride thin-film bulk acoustic resonators for wide band applications. Vacuum 86(1):23–26. https://doi.org/10.1016/J.VACUUM.2011.03.026
54. Clement M, Felmetsger V, Mirea T, Iborra E (2018) Reactive sputtering of AlScN thin Ulms with variable Sc content on 200 mm wafers. In: 2018 European frequency and time forum, EFTF 2018. Institute of Electrical and Electronics Engineers Inc, pp 13–16. https://doi.org/10.1109/EFTF.2018.8408987
55. Mertin S et al (2018) Piezoelectric and structural properties of c-axis textured aluminium scandium nitride thin films up to high scandium content. Surf Coat Technol 343:2–6. https://doi.org/10.1016/J.SURFCOAT.2018.01.046
56. Fichtner S, Reimer T, Chemnitz S, Lofink F, Wagner B (2015) Stress controlled pulsed direct current co-sputtered Al 1−x Sc x N as piezoelectric phase for micromechanical sensor applications. APL Mater 3:116102. https://doi.org/10.1063/1.4934756
57. Pijolat M et al (2010) LiNbO3 film bulk acoustic resonator. In: 2010 IEEE international frequency control symposium, FCS, pp 661–664. https://doi.org/10.1109/FREQ.2010.5556245
58. Astié V et al (2022) Towards stoichiometric LiNbO3 epitaxial thin films grown by DLI-MOCVD. Mar 2018, Accessed 20 Nov [Online]. https://hal.archives-ouvertes.fr/hal-02405067
59. Bai X et al (2020) The thin film bulk acoustic wave resonator based on single-crystalline Y-cut lithium niobate thin films. AIP Adv 10:75002. https://doi.org/10.1063/1.5143550
60. Reinhardt A et al (2021) Lithium niobate film bulk longitudinal wave resonator. In: 2021 joint conference of the European frequency and time forum and IEEE international frequency control symposium (EFTF/IFCS). https://doi.org/10.1109/EFTF/IFCS52194.2021.9604280
61. Bousquet M et al (2020) Lithium niobate film bulk acoustic wave resonator for sub-6 GHz filters; Lithium niobate film bulk acoustic wave resonator for sub-6 GHz filters. In: 2020 IEEE international ultrasonics symposium (IUS). https://doi.org/10.1109/IUS46767.2020.9251654
62. Osugi Y, Yoshino T, Suzuki K, Hirai T (2007) Single crystal FBAR with LiNbO3 and LiTaO3 piezoelectric substance layers. In: IEEE MTT-S international microwave symposium digest, pp 873–876. https://doi.org/10.1109/MWSYM.2007.380118
63. Bousquet M et al (2020) Potentialities of LiTaO3 for bulk acoustic wave filters; potentialities of LiTaO3 for bulk acoustic wave filters. In: 2020 IEEE international ultrasonics symposium (IUS). https://doi.org/10.1109/IUS46767.2020.9251463
64. Ruppel CCW (2017) Acoustic wave filter technology – a review. IEEE Trans Ultrason Ferroelectr Freq Control 64(9). https://doi.org/10.1109/TUFFC.2017.2690905
65. D. Gachon, G. Lengaigne, S. Benchabane, H. Majjad, S. Ballandras, and V. Laude, "High frequency bulk acoustic wave resonator using thinned monocrystalline lithium niobate; high frequency bulk acoustic wave resonator using thinned monocrystalline lithium niobate," 2006
66. Gorisse M et al (2019) High frequency LiNbO3 bulk wave resonator. In: 2019 joint conference of the IEEE international frequency control symposium and European frequency and time forum (EFTF/IFC). https://doi.org/10.1109/FCS.2019.8856017
67. Yamauchi N, Shirai T, Yoshihara T (2009) High coupling piezoelectric thin films of Pb(Zr,Ti)O3-based ternary perovskite compounds for GHz-range film bulk acoustic resonators. Appl Phys Lett 94:172903. https://doi.org/10.1063/1.3126060
68. Aigner R, Huynh N-H, Handtmann M, Marksteiner S (2005) Behavior of BAW devices at high power levels; behavior of BAW devices at high power levels. IEEE MTT-S Int Microwave Symp Digest 2005. https://doi.org/10.1109/MTT67880.2005.9387896
69. Lakin KM, Kline GR, Mccarron KT (1995) Development of miniature filters for wireless applications. IEEE Trans Microw Theory Tech 43(12):2933. https://doi.org/10.1109/22.475658
70. Lakin KM, Wanga JS (1980) UHF composite bulk wave resonators. https://doi.org/10.1109/ULTSYM.1980.197515

71. Vale C, Rosenbaum J, Horwitz S, Krishnasuamy S, Moore R (1990) FBAR filters at GHz frequencies. In: Forty-fourth annual symposium on frequencycontrol. https://doi.org/10.1109/FREQ.1990.177515
72. Ruby R, Merchant P (n.d.) Micromachined thin film bulk acoustic resonators. In: Proceedings of IEEE 48th annual symposium on frequency control. IEEE, pp 135–138. https://doi.org/10.1109/FREQ.1994.398344
73. Huang CL, Tay KW, Wu L (2005) Fabrication and performance analysis of film bulk acoustic wave resonators. Mater Lett 59(8–9):1012–1016. https://doi.org/10.1016/J.MATLET.2004.11.047
74. Laermer F, Franssila S, Sainiemi L, Kolari K (2015) Deep reactive ion etching. In: Handbook of silicon based MEMS materials and technologies2nd edn, pp 444–469. https://doi.org/10.1016/B978-0-323-29965-7.00021-X
75. Satoh H, Ebata Y, Suzuki H, Narahara C (1985) An air-gap type piezoelectric composite thin film resonator. https://doi.org/10.1109/FREQ.1985.200870
76. Taniguchi S, Yokoyama T, Iwaki M, Nishihara T, Ueda M, Satoh Y (2007) An air-gap type FBAR filter fabricated using a thin sacrificed layer on a flat substrate. Proc IEEE Ultrason Symp:600–603. https://doi.org/10.1109/ULTSYM.2007.156
77. Newell W (1964) Tuned integrated circuits – a state-of-the-art survey. Proc IEEE 52. https://doi.org/10.1109/PROC.1964.3453
78. Lawrence N, DworskyLuke CB (1993) Thin film resonator having stacked acoustic reflecting impedance matching layers and method
79. Dubois M-A, Muralt P, Matsumoto H, Plessky V (n.d.) Solidly mounted resonator based on aluminum nitride thin film. In: 1998 IEEE ultrasonics symposium. Proceedings. IEEE, pp 909–912. https://doi.org/10.1109/ULTSYM.1998.762291
80. Munir J, Mirea T, DeMiguel-Ramos M, Saeed MA, Bin Shaari A, Iborra E (2017) Effects of compensating the temperature coefficient of frequency with the acoustic reflector layers on the overall performance of solidly mounted resonators. Ultrasonics 74:153–160. https://doi.org/10.1016/j.ultras.2016.10.010
81. Lakin KM (2003) A review of thin-film resonator technology. IEEE Microw Mag 4(4):61–67. https://doi.org/10.1109/MMW.2003.1266067
82. Wang L, Lin A, Kim ES (2018) Miniature sensing system with FBAR-based oscillators and frequency shift detector. IEEE Sensors J 18(18):7633–7637. https://doi.org/10.1109/JSEN.2018.2858279
83. Mirea T, Chiodarelli N, Moreno M, Demiguel-Ramos M (2021) Portable network analyzers for full characterization of FBAR sensors: influence of readout parameters on sensor performance; portable network analyzers for full characterization of FBAR sensors: influence of readout parameters on sensor performance. In: 2021 joint conference of the European frequency and time forum and IEEE international frequency control symposium (EFTF/IFCS). https://doi.org/10.1109/EFTF/IFCS52194.2021.9604278
84. Johnston ML, Kymissis I, Shepard KL (2010) FBAR-CMOS oscillator array for mass-sensing applications. IEEE Sensors J 10(6):1042–1047. https://doi.org/10.1109/JSEN.2010.2042711
85. Gabl R et al (2003) Novel integrated FBAR sensors: a universal technology platform for bio- and gas-detection. In: Proceedings of IEEE sensors 2003 (IEEE Cat. No.03CH37498), vol 2, pp 1184–1188. https://doi.org/10.1109/ICSENS.2003.1279132
86. Tukkiniemi K, Rantala A, Nirschl M, Pitzer D, Huber T, Schreiter M (2009) Fully integrated FBAR sensor matrix for mass detection. Procedia Chem 1(1):1051–1054. https://doi.org/10.1016/J.PROCHE.2009.07.262
87. Thomas S, Villa-López FH, Theunis J, Peters J, Cole M, Gardner JW (2016) Particle sensor using solidly mounted resonators. IEEE Sens J 16(8):2282–2289. https://doi.org/10.1109/JSEN.2015.2512303
88. DeMiguel-Ramos M, Mirea T, Clement M, Olivares J, Sangrador J, Iborra E (2015) Optimized tilted c-axis AlN films for improved operation of shear mode resonators. Thin Solid Films 590:219–223. https://doi.org/10.1016/j.tsf.2015.08.010

89. Martin F et al (2006) Shear mode coupling and tilted grain growth of AlN thin films in BAW resonators. IEEE Trans Ultrason Ferroelectr Freq Control 53(7):1339–1343. https://doi.org/10.1109/TUFFC.2006.1665082
90. Rughoobur G et al (2015) Seed layer controlled deposition of ZnO films with a tilted c-axis for shear mode resonators. In: 2014 European frequency and time forum, EFTF 2014. https://doi.org/10.1109/EFTF.2014.7331491
91. Bjurström J, Wingqvist G, Katardjiev I (2017) Synthesis of textured thin piezoelectric AlN films with a nonzero c-axis mean tilt for the fabrication of shear mode resonators. IEEE Trans Ultrason Ferroelectr Freq Control 53(11):2095–2100. http://www.ncbi.nlm.nih.gov/pubmed/17091844
92. Katardjiev I, Yantchev V (2012) Recent developments in thin film electro-acoustic technology for biosensor applications. Vacuum 86(5):520–531. https://doi.org/10.1016/J.VACUUM.2011.10.012
93. Weber J et al (2006) Shear mode FBARs as highly sensitive liquid biosensors. https://doi.org/10.1016/j.sna.2006.01.005
94. Chen D et al (2017) Micro-electromechanical film bulk acoustic sensor for plasma and whole blood coagulation monitoring. Biosens Bioelectron 91:465–471. https://doi.org/10.1016/J.BIOS.2016.12.063
95. Zhang Y, Luo J, Flewitt AJ, Cai Z, Zhao X (2018) Film bulk acoustic resonators (FBARs) as biosensors: a review. Biosens Bioelectron 116:1–15. https://doi.org/10.1016/J.BIOS.2018.05.028
96. Manzaneque García T (2015) Density and viscosity sensors based on piezoelectric micro-resonators. Universidad de Castilla-la Mancha
97. Mirea T, Olivares J, Clement M, Iborra E (2019) Impact of FBAR design on its sensitivity as in-liquid gravimetric sensor. Sens Actuators A Phys 289. https://doi.org/10.1016/j.sna.2019.02.012
98. Liu J, Zhao Z, Fang Z, Liu Z, Zhu Y, Du L (2020) High-performance FBAR humidity sensor based on the PI film as the multifunctional layer. Sens Actuators B Chem 308. https://doi.org/10.1016/J.SNB.2020.127694
99. Lelantos. https://www.lelantostech.com/
100. Sorex Sensors. https://www.sorexsensors.com/
101. Qorvo Biotechnologies. https://www.qorvobiotech.com/#contact

Examples of Vibrating MEMS Sensing Physical Parameters for Chemical Gas Detection

Isabelle Dufour

Contents

Abstract This chapter presents advantages and drawbacks to achieve chemical detection without the use of sensitive coating by measuring physical properties of gas. Examples of such detections are presented using two kinds of vibrating MEMS: microcantilevers and capacitive micromachined ultrasonic transducers (CMUT). The main advantages of such sensors relying on their concept are their short response time, good reliability and no need for calibration during the sensor's life cycle. Their major drawback is that there is no selectivity if only one physical parameter measurement is done. To overcome this drawback, discrimination between different gas mixtures can be achieved by simultaneous measurements of multiple physical properties of the gas. This latter principle has been applied with either microcantilevers or CMUT with the simultaneous measurements of either viscosity and mass density or acoustic wave speed and attenuation of gas.

Keywords CMUT, Gas detection, Mass density, Microcantilever, Resonant MEMS, Sound absorption, Sound speed, Time of flight, Viscosity

I. Dufour (✉)
Laboratoire IMS, University of Bordeaux, Talence, France
e-mail: isabelle.dufour@ims-bordeaux.fr

P. Lieberzeit (ed.), *Piezoelectric Sensors*, Springer Series on Chemical Sensors and Biosensors (2024) 18: 61–78, https://doi.org/10.1007/5346_2023_28,

Published online: 19 October 2023

1 Context: General Principle

Chemical microsensors have not had the same industrial development as physical microsensors, such as accelerometers or gyroscopes, for example [1]. There are many reasons for this, including the facts that:

- the markets are niche markets specific to the species to be detected (*bottleneck a*),
- for each of the species to be detected, an appropriate sensitive layer must be developed or chosen (*bottleneck b*),
- chemical sensors are less reliable and have shorter life spans than physical sensors and they have greater drift (*bottleneck c*).

Classically, a chemical microsensor is composed of a transducer and a sensitive layer. The role of the sensitive coating is to interact with the targeted gas. This interaction causes changes in temperature, refractive index, electrical properties, mass or mechanical changes and the transducer transforms these changes into an electrical signal. The sensitive coatings are subjected to environmental effects including temperature, humidity and aging effects. Then, the long-term stability of the coatings and the resulting aging affect the reliability of the sensor more than the aging of the transducer itself.

An alternative method to detect and quantify chemical species is to use "physical sensors" which measure a physical property of the gas without need of chemical interaction with the sensor. Examples of physical properties of gas that can be measured are mass density, viscosity, thermal conductivity, and sound speed. These physical properties for major industrial gases are presented in Table 1, and some are very different from one gas to another. For example, hydrogen (H_2) has a sound speed 4 times greater than the one of air, its thermal conductivity is 7 times greater, its viscosity 2 times smaller, and its mass density 14 times smaller.

The detection of gas based on the measurement of gas physical properties does not need a sensitive layer. Then such sensors avoid having to choose or develop a new sensitive layer for each application depending on the species to be detected and the possible interferents [5] (*bottleneck b*). Moreover, such sensors become generic

Table 1 Physical properties of common industrial gases [2–4]

Gas	Mass density (kg/m^3) 1.015 bar, 15°C	Viscosity (μPa s) 1.015 bar, 0°C	Thermal conductivity ($mW\ m^{-1}\ K^{-1}$) 1.015 bar, 0°C	Sound speed ($m\ s^{-1}$) 1.015 bar, 20°C
CO_2	1.87	13.7	14.7	267
O_2	1.35	19.1	24.4	326
Air	1.22	17.2	24.4	343
N_2	1.18	16.6	24.0	349
CH_4	0.68	10.1	30.6	446
He	0.17	18.7	146.2	1,007
H_2	0.09	8.4	172.6	1,270

sensors and can address different niche markets without any long development process (*bottleneck a*). Finally, the absence of a sensitive coating, which is subjected to sorption or redox phenomena in classical chemical sensors, leads to a more reliable and reversible behavior (*bottleneck c*).

Examples of such physical sensors for gas detection are thermal conductivity sensors [6–8], mass density and viscosity sensors [9, 10], speed of sound sensors [11]. Commercialized devices also exist based on mass density [12] or thermal conductivity [13] measurements. Due to their physical principle, such sensors achieve good reliability and almost no drift. Their major drawback is that there is no selectivity nor discrimination because there is only one physical parameter measurement. Consequently, they are limited to determination of the concentration of a known binary mixture.

In this chapter, examples of physical sensors for gas detection using vibrating MEMS are presented. The presented results have been recently (2019–2022) realized in the IMS laboratory in collaboration with other French laboratories (GREMAN, LAAS, CRHEA). Moreover, it is shown how combining multiple physical properties measurement is possible to discriminate different gas mixtures and to determine the gas concentration. In Sect. 2, the vibrating MEMS are silicon microcantilevers, whereas in Sect. 3 they are silicon nitride capacitive micromachined ultrasonic transducers. Then, Sect. 4 presents how using such sensors (microcantilevers or CMUT) is possible to replace the selectivity, usually obtained with the use of a sensitive coating, by discrimination of different gas mixtures. Finally, Sect. 5 presents some potential applications of such sensors.

2 Detection Using Microcantilevers Without Sensitive Coating

The operational principle of an uncoated resonant microcantilever utilized as a chemical sensor relies on the influence exerted by the mass of the fluid displaced by the oscillating cantilever on its resonant frequency. Indeed, when the density of the surrounding fluid increases (decreases), the effective equivalent mass of the cantilever also increases (decreases), thus leading to a reduction (increase) in the resonant frequency. In the context of chemical detection in gaseous environments, variations in gas density can serve as an indicator of alterations in the concentration of specific chemical species within a gas mixture [14–16].

The outcomes presented herein were achieved using silicon microcantilevers featuring electromagnetic actuation and piezoresistive read-out (Fig. 1):

- The process of generating vibrations entails passing alternating current (AC) through the conductive wire situated along the cantilever's periphery. When a magnetic field aligned with the longitudinal axis of the beam is present, it generates an AC Lorenz force at the microcantilever's free end, subsequently inducing vibrations out of the plane.

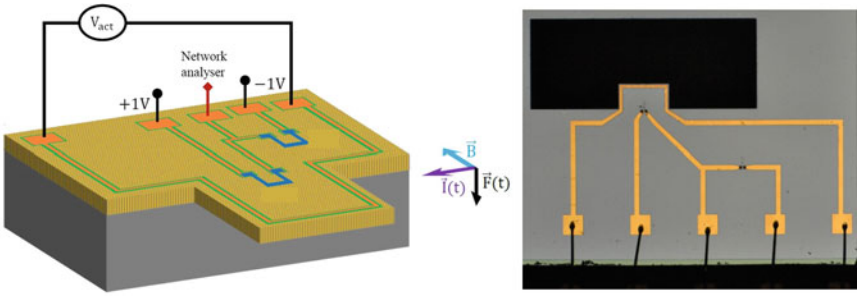

Fig. 1 Schematic representation and photo of the microcantilever with electromagnetic actuation and piezoresistive read-out

- To effectively capture these vibrations, the process incorporates the creation of two semiconductor strain gauges (boron-doped piezoresistors). They are organized in a semi-Wheatstone bridge setup: one gauge is positioned at the point of maximum strain (on the surface of the clamped-end of the microcantilever), while the second gauge is positioned on the rigid substrate.

To assess the impact of cantilever geometries (including rectangular, U-, and T-shaped microstructures) and dimensions, a series of microcantilevers were manufactured at LAAS (Toulouse, France) and subjected to testing at IMS (Bordeaux, France) [17]. The results demonstrated that for mass density measurement, uniform rectangular cantilevers exhibited superior performance compared to their T- and U-shaped counterparts. Additionally, the investigation revealed that broader and shorter beams manifested heightened sensitivity toward changes in mass density. The sensitivity of rectangular beams was found to follow a proportional relationship with b/L^2 (where b and L represent width and length, respectively), in accordance with the analytical model developed by IMS [14]. Interestingly, the thickness of the rectangular cantilevers didn't influence their sensitivity to mass density changes, despite its effect on the resonant frequency. Nevertheless, the noise on the resonant frequency is dependent on the microcantilever's thickness, underscoring the need for careful consideration when selecting the most suitable thickness for a given structural size (length and width). This consideration becomes especially relevant for optimizing the limit of detection.

Owing to the minor shifts in resonant frequency that require detection, novel characterization techniques have been developed to monitor these subtle frequency variations. The traditional approach to track changes in resonant frequency involves the identification of the resonant peak within the amplitude spectrum and tracking alterations in the associated frequency. However, the relative frequency variation for scenarios involving low hydrogen (H_2) concentration in nitrogen (N_2) is exceedingly small. For example, when utilizing a silicon microcantilever featuring dimensions of 1 mm length, 1 mm width, 10 μm thickness, and an approximate resonant frequency of 23 kHz, a concentration as low as 0.2% of H_2 in N_2 yields a resonant frequency shift of about 0.25 Hz (equivalent to a 10 ppm resonant frequency variation). As a

result, the conventional technique proves inadequate in capturing such minute frequency shifts accurately. Primarily, this is attributed to the challenge of accurately pinpointing the exact location of the resonant peak due to inherent measurement noise. Consequently, alternative characterization methods involving the analysis of gain and phase spectra have been experimented using measurement data [18]. Derived from the same dataset, the diverse methodologies used to extract resonant frequency yielded different signal-to-noise ratios, spanning from 1.2 for the conventional technique to 190 for the most effective strategy (which involved linearizing the phase around the resonant frequency). The results presented in this section predominantly rely on the application of phase linearization, often employing a silicon cantilever measuring 1 mm × 1 mm × 10 μm (with a resonant frequency of around 23 kHz and a quality factor of approximately 500 in atmospheric pressure).

To conduct gas detection, the microcantilever is positioned within a tightly sealed gas chamber, with a volume of 500 μl, and subjected to controlled gas flow conditions. Gas compositions containing binary mixtures featuring the desired elements (such as hydrogen, helium, carbon dioxide, or methane) and nitrogen are introduced into the chamber, employing gas bottles and a suite of mass-flow controllers (Brooks 5850S). Each binary mixture is systematically introduced at three distinct concentrations – namely, 5%, 4%, and 3% – for a time span of 400 s each. Between the introduction of each gas mixture, nitrogen is introduced for a 400 s interval, serving to assess potential drift and to underscore the sensor's reversibility. The resonant frequency shifts observed throughout this experiment are depicted in Fig. 2.

Based on the physical principles governing these sensors, the presence of gases lighter than nitrogen (such as H_2, He, and CH_4) results in an increase in the resonant frequency, while the presence of heavier gases (like CO_2) than nitrogen leads to a decrease in the resonant frequency. Furthermore, the trends match the full reversibility and quick response time (under 1 min). In our experiment, the primary factor influencing response time is the duration required for the flow feedback loop to stabilize concentration levels (a swifter control system could potentially achieve sub-1-min response times). Additionally, almost no drift is observed over the experiment's duration (a mere 0.15 Hz over 3 h without room temperature control). Of notable significance is the consistent shift in resonant frequency, surpassing 2 Hz for the tested concentrations (5%, 4%, and 3%) across all four gases (equivalent to 100 ppm of the resonant frequency). Moreover, the capability to measure even lower concentrations is facilitated by the minimal noise associated with measurements based on phase linearization (an exemplar of detecting 100 ppm of H_2 in N_2 is depicted in Fig. 3).

As proved with the measurements presented in Fig. 2, the resonant frequency measurement allows to discriminate if the gas becomes heavier or lighter but there is no selectivity between the different gas mixtures (He, H_2, and CH_4 can be confused with each other). Concerning this point, the measurement of another parameter (the quality factor) allows to discriminate between the different gas mixture (Sect. 4).

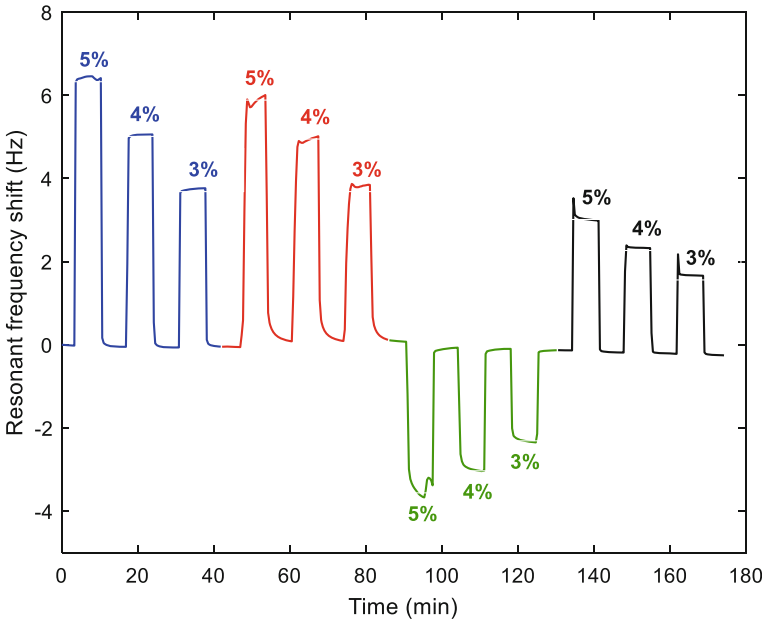

Fig. 2 Example of resonant frequency shifts measured with a 1 mm × 1 mm × 10 µm silicon cantilever with different concentrations (5%, 4%, 3%) of H_2 in N_2 (blue curve), He in N_2 (red curve), CO_2 in N_2 (green curve) and CH_4 in N_2 (black curve) with a gas flow of 100 ml/min at room temperature conditions (temperature ≈20°C, pressure ≈1 atm)

3 Detection Using CMUT Without Sensitive Coating

Another type of MEMS has been used to achieve chemical detection using gas physical properties measurement: silicon-based capacitive micromachined ultrasonic transducers (CMUT), which consist of small membranes that can be electrostatically actuated and the vibration can be measured with capacitive read-out.

The presented results have been achieved using silicon nitride CMUT microcantilevers fabricated at GREMAN (Tours, France) using the surface machining process described in [19]. Each CMUT sensor (8 mm × 0.8 mm) is composed of thousands of single CMUT in parallel (Fig. 4). Each membrane is a square (32 µm × 32 µm) of 450 nm thickness. The resonant frequency is around 8 MHz.

The same principle of gas detection as the one presented using microcantilever (Sect. 2) based on the spectrum measurement around resonant frequency has been used. In this case, the measurement is based on the measurement of the spectrum of the CMUT admittance. It has been proved that the more sensitive measurement is obtained with the measurement of the minimum of the admittance [20]. Examples of detection of H_2 or CO_2 in N_2 are presented in Fig. 5. Similar conclusions can be drawn from those in Sect. 2.

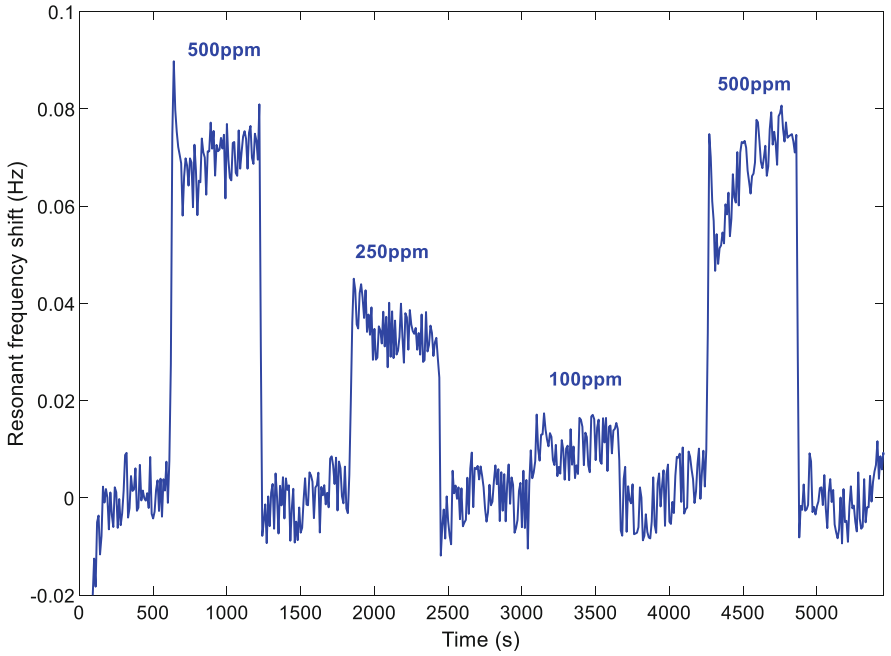

Fig. 3 Example of resonant frequency shifts measured with a 1 mm × 1 mm × 5 μm silicon cantilever with small concentrations (500 ppm, 250 ppm, and 100 ppm) of H_2 in N_2 with a gas flow of 100 ml/min at room temperature conditions (temperature ≈20°C, pressure ≈1 atm)

Besides, two other innovative uses of CMUT for the gas detection have also been demonstrated: the first one consists in measuring the propagation time between two CMUTs and the second one consists in measuring the attenuation of the acoustic wave between two CMUT [21–23].

The basic way to measure the time of flight between two CMUT consists in measuring the time that an ultrasound takes to propagate from a CMUT in emission mode to a CMUT in reception mode, both placed in front of each other. An ultrasonic pulse is sent through the gas mixture by a CMUT in emission mode. After traveling a distance of few millimeters, it is then received at the other end by another CMUT in reception mode (Fig. 6). Both the emission and the reception signals were acquired via a Picoscope2000 Series acquisition card and then analyzed through a basic peak detection algorithm.

Examples of detection of H_2 (sound velocity higher than the one of N_2) or CO_2 (sound velocity lower than the one of N_2) in N_2 are presented in Fig. 7. The measurements are in good agreement with analytical modeling [21]. As for the other measurements presented in this chapter, they are reversible, with almost no drift and response time below 1 min.

Although intuitive and effective, the measurement of the time of flight in the time domain presents some drawbacks. One of them being the need for a robust peak detection algorithm which usually is hard to integrate in a sensor and also required

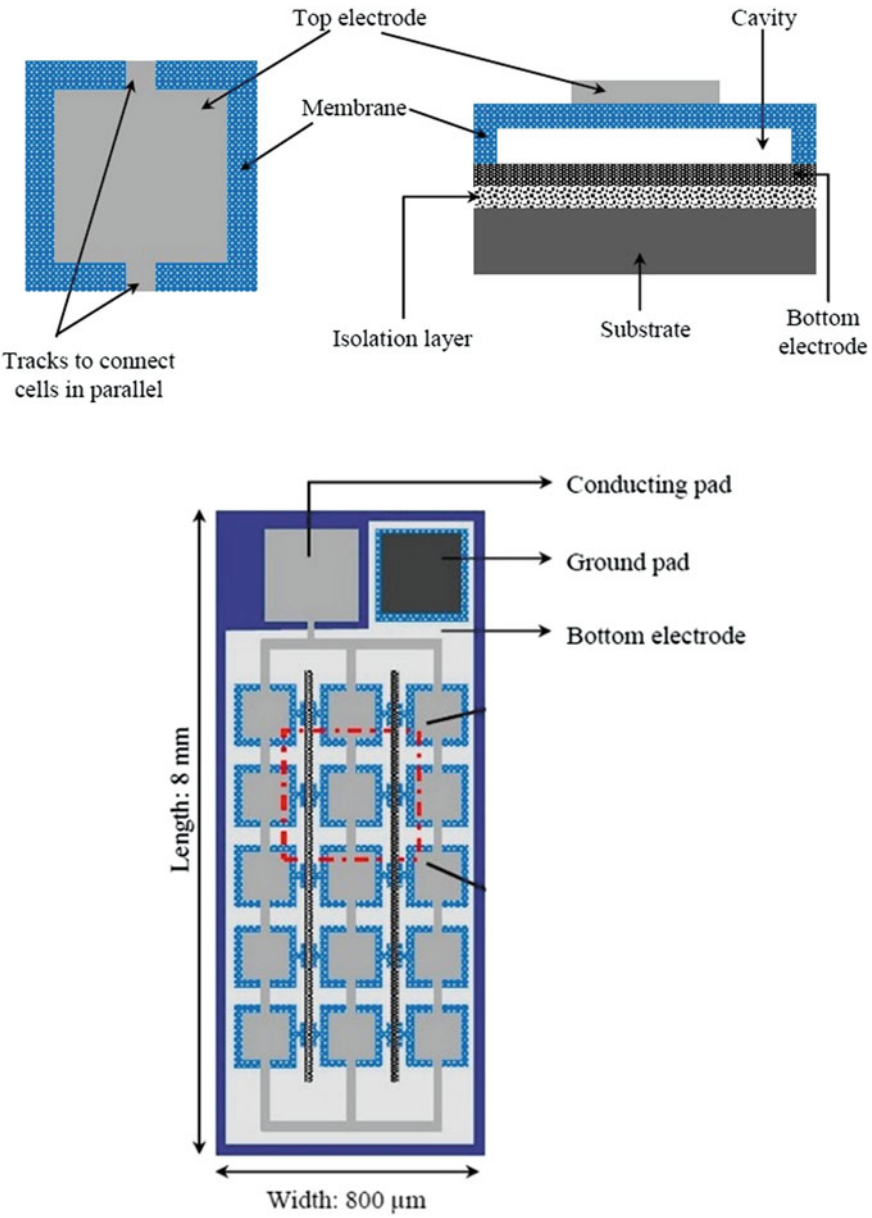

Fig. 4 Schematic representation of the CMUT membrane and CMUT chip

computational cost. Another issue is that a pulse generator is usually more expensive than a simple sine wave generator. An alternative method to measure the time of flight is to use the same setup (2 CMUT facing each other) but, instead of generating pulse, sinusoidal wave is emitted and received. In this case, the time of flight is the

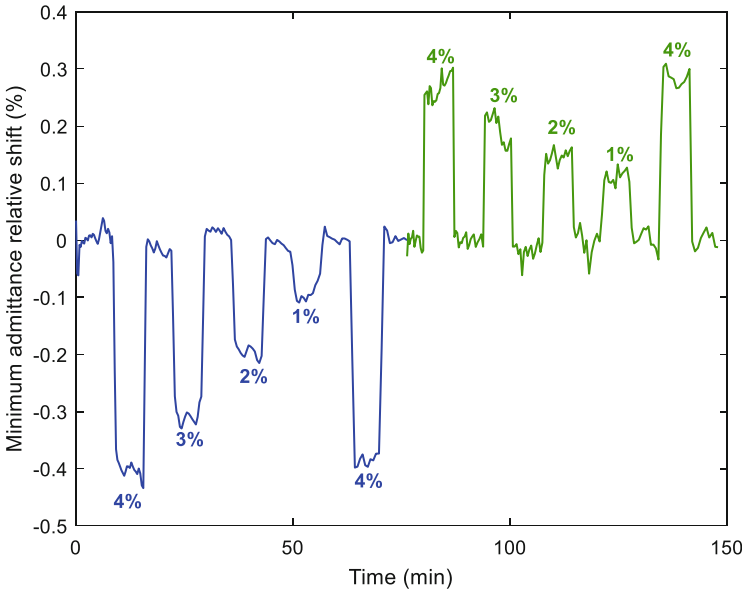

Fig. 5 Examples of gas detection using the measurement of the relative variation of the admittance of a silicon nitride CMUT composed of squared membranes (32 µm × 32 µm) on a 8 mm × 0.8 mm chip. The measurements have been made at different concentrations (4%, 3%, 2%, 1%) of H_2 in N_2 (blue curve) or CO_2 in N_2 (green curve) with a gas flow of 100 ml/min at room temperature conditions (temperature ≈20°C, pressure ≈1 atm)

slope of the phase between emitted and received signals as a function of the radial frequency. A data processing was set up in order to suppress the influence of the multiple echoes [24].

Examples of the same detection as those of Fig. 7 are presented in Fig. 8 with the time of flight measurement based on the spectrum of the phase. It can be easily seen that this method of measurement is less noisy.

Another physical property of the gas that can be measured with the same setup is the sound attenuation of the gas. Indeed, instead of measuring the delay that the acoustic wave takes to travel the cell, the amplitude of the sinusoidal signal amplitude can be measured: an increase in the gas attenuation decreases the amplitude of the signal. The advantage of the attenuation is that it is a frequency-dependent property and its dependence varies from one gas to another. For example, the attenuation at 4 MHz is much higher for H_2 than for CO_2 or CH_4. As shown in Fig. 9, an appropriate choice of the frequency measurement can achieve a kind of selectivity: MHz range is appropriate to detect hydrogen with small interference with other gases.

As the microcantilever-based measurements presented in Sect. 2, the CMUT-based measurements of this section are not selective: the time of flight measurement allows to discriminate if sound velocity of the gas increases or decreases and the attenuation measurement allows to achieve a partial selectivity by appropriate choice

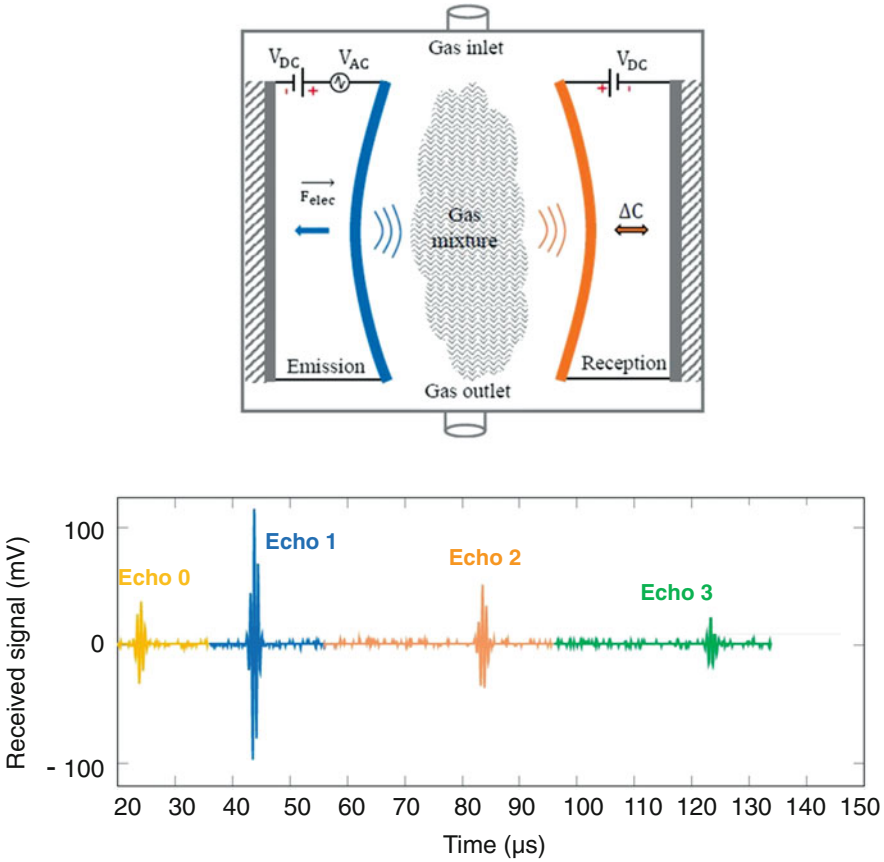

Fig. 6 Schematics illustrating the principle of a time of flight measurement for gas detection with 2 CMUT and example of measurements of echoes in nitrogen gas

of frequency. Combining time of flight measurement with attenuation measurement allows to discriminate between the different gas mixture (Sect. 4).

4 Discrimination of Gases with Multiple Physical Property Measurements

As presented in Sects. 2 and 3, resonant MEMS can be used to measure multiple physical properties of gas. One physical property measurement is not sufficient to achieve discrimination between different gases. Using the resonant MEMS spectrum, it is possible to measure simultaneously two gas physical properties and then to achieve discrimination between different gas mixtures and to measure their

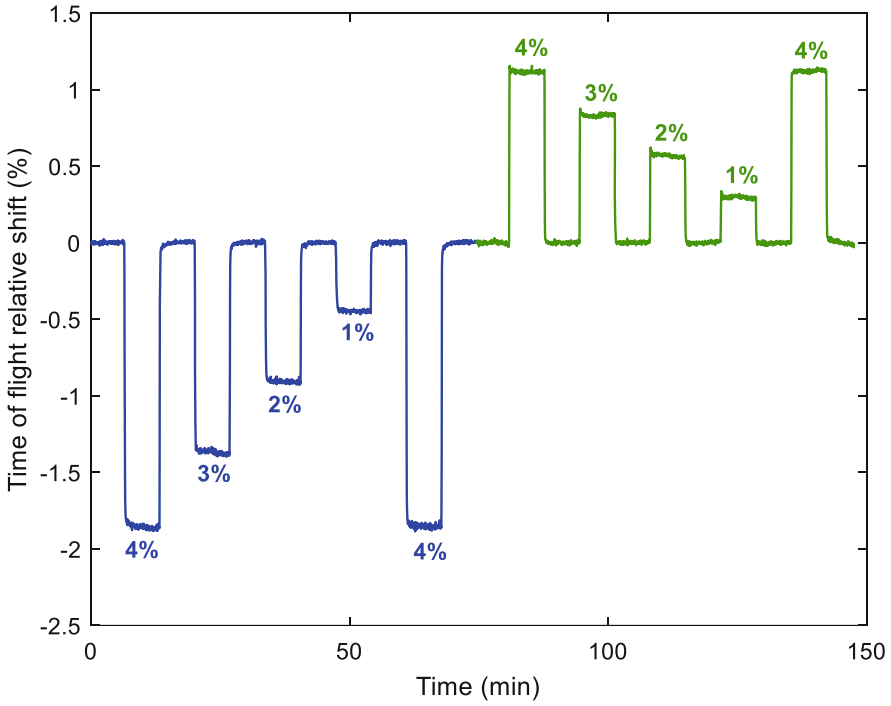

Fig. 7 Examples of gas detection using the time domain measurement of the relative shift of the time of flight between two CMUT. The CMUT are silicon nitride CMUT composed of squared membranes (32 μm × 32 μm) on a 8 mm × 0.8 mm chip. The measurements have been made at different concentrations (4%, 3%, 2%, 1%) of H_2 in N_2 (blue curve) or CO_2 in N_2 (green curve) with a gas flow of 100 ml/min at room temperature conditions (temperature ≈20°C, pressure ≈1 atm)

concentration. This will be shown in this section with both the microcantilevers and the CMUT of previous sections.

Using the spectrum measurement not far from the microcantilever resonant frequency, it is possible to measure both the resonant frequency and the quality factor of the microcantilever. Using a simple model [25] it is then possible to extract the relative variation of both the mass density and viscosity of the gas. In the plane (mass density, viscosity), the measurement points are not far from the one expected by theory (Fig. 10). Then, depending on where the point is in this plane the discrimination between different gas mixtures can easily be made and after that the mass density measurement, which is less noisy than the viscosity measurement, can be used to estimate the gas concentration.

On the same principle using the spectrum measurement of the signal of the receiver CMUT, it is possible to measure both the time of flight and the attenuation at each frequency (Figs. 8 and 9). As in the latter case (Fig. 10), depending on where the point is in the plane (attenuation, time of flight) the discrimination between

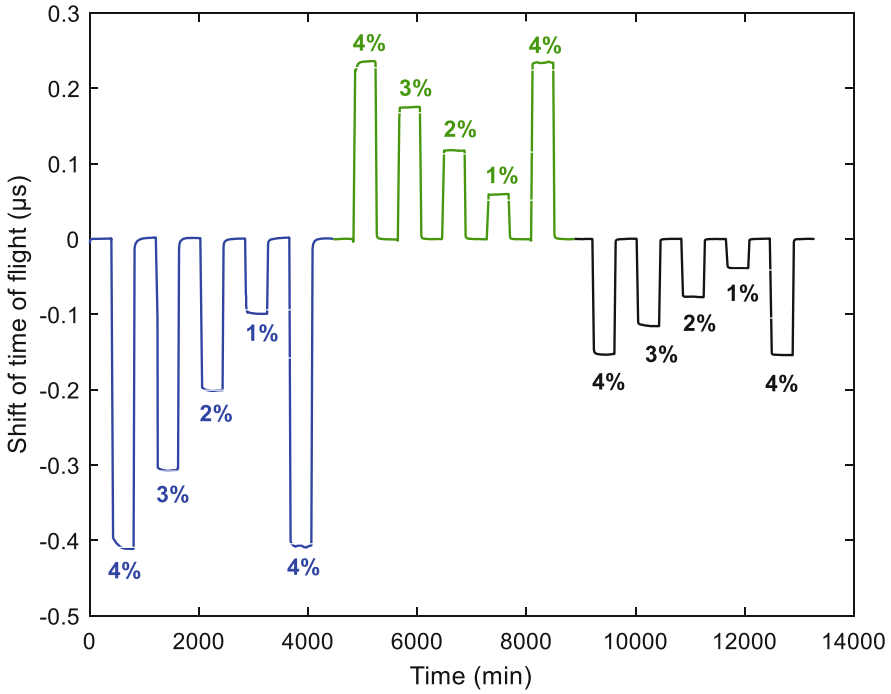

Fig. 8 Examples of gas detection using the frequency domain measurement of the shift of the time of flight between two CMUT. The CMUT are silicon nitride CMUT composed of squared membranes (32 µm × 32 µm) on an 8 mm × 1 mm chip. The measurements have been made at different concentrations (4%, 3%, 2%, 1%) of H_2 in N_2 (blue curve) or CO_2 in N_2 (green curve) or CH_4 in N_2 (black curve) with a gas flow of 100 ml/min at room temperature conditions (temperature ≈20°C, pressure ≈1 atm)

different gas mixtures can easily be made and the gas concentration can be deduced (Fig. 11).

5 Potential Applications

The presented sensors do not target a particular application, but, as the developed devices are generic, it is possible to use this kind of devices for different applications where quantitative determination of non-reactive gas compositions in gas mixtures requires particular attention. Such sensors could be of useful interest for a wide range of industries for the continuous monitoring of gases. Important markets include gas production, hydrocarbon fuel distribution, biogas production and distribution. Few possible applications are listed in more detail below:

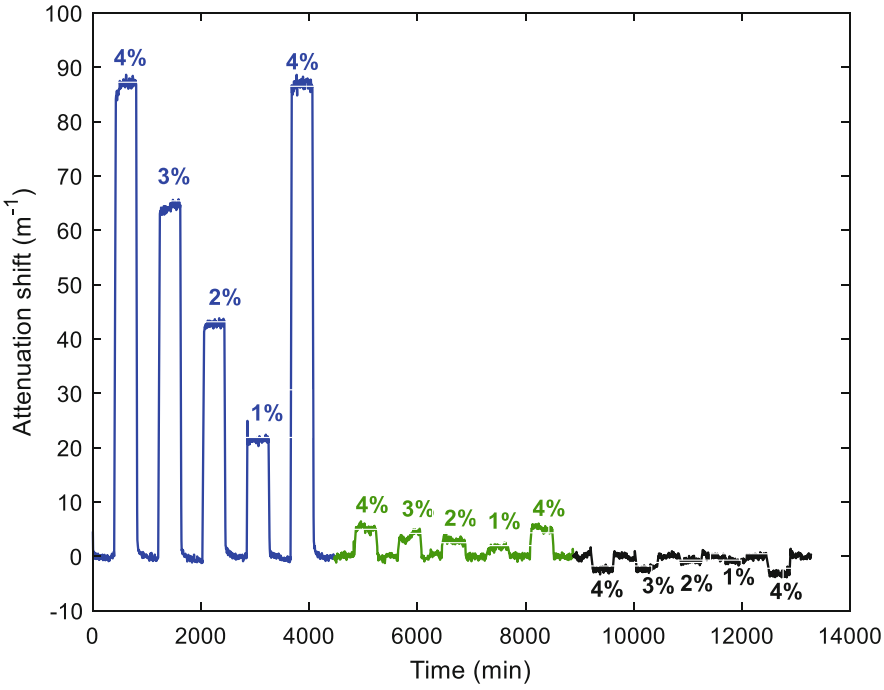

Fig. 9 Examples of gas detection using the frequency domain measurement of the attenuation shift between two CMUT at 4 MHz. The CMUT are silicon nitride CMUT composed of squared membranes (32 μm × 32 μm) on an 8 mm × 0.8 mm chip. The measurements have been made at different concentrations (4%, 3%, 2%, 1%) of H_2 in N_2 (blue curve) or CO_2 in N_2 (green curve) or CH_4 in N_2 (black curve) with a gas flow of 100 ml/min at room temperature conditions (temperature ≈20°C, pressure ≈1 atm)

- With the global population consistently on the rise, there is an exponential surge in the demand for diverse goods and services. This unfolding scenario of industrial expansion, coupled with the rapid growth of the populace, amplifies the need for energy, necessitating its provision through both traditional and renewable energy sources. Sustainable energy solutions have undoubtedly become the cornerstone of many contemporary scientific and technological advancements. Scientists are tirelessly seeking solutions that won't contribute to the prevailing carbon emissions. Within this context, it's noteworthy to highlight the widespread adoption of hydrogen-based energy generation as a means of securing clean energy. Hydrogen gas possesses an exceptional energy density. However, given the highly explosive nature of hydrogen-air mixtures within the 4–75% hydrogen concentration range, continuous monitoring of hydrogen concentration becomes paramount. This is especially crucial due to the potential risks associated with the production, storage, and transport of hydrogen gas. Consequently, vigilant monitoring of hydrogen gas concentration remains indispensable to avert potentially hazardous situations.

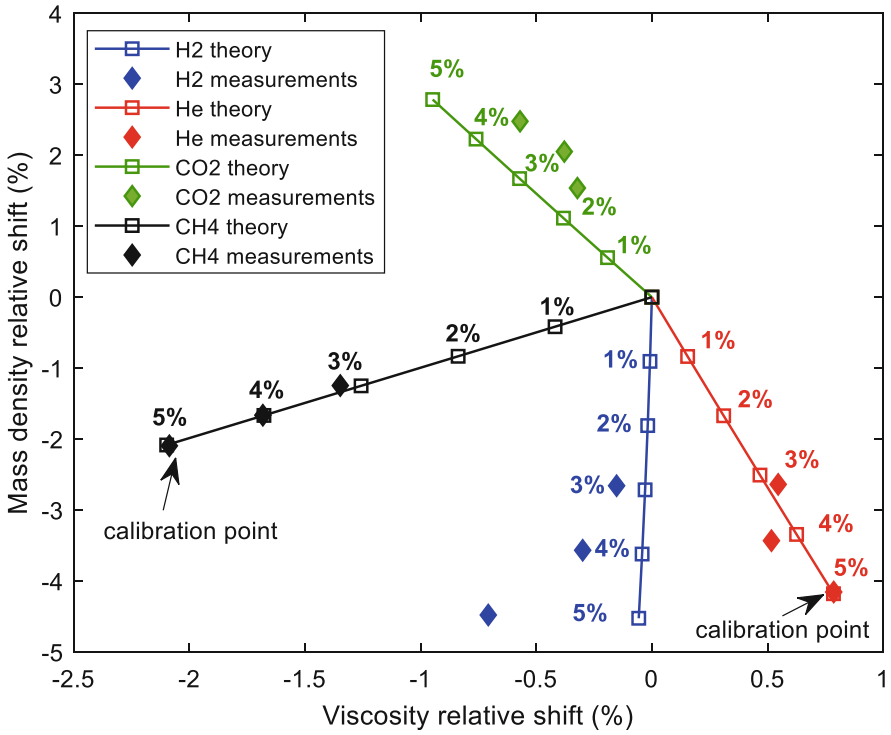

Fig. 10 Simultaneous measurements of both the mass density and the viscosity of the gas using the simultaneous measurement of both the resonant frequency and quality factor of a silicon cantilever (1 mm × 1 mm × 10 µm) with different concentrations (5%, 4%, 3%) of H_2 in N_2 (blue), He in N_2 (red), CO_2 in N_2 (green) and CH_4 in N_2 (black) with a gas flow of 100 ml/min at room temperature conditions (temperature ≈20°C, pressure ≈1 atm). The theoretical points are also reported

- The forthcoming French repository for radioactive waste is planned to encompass underground structures designed to house tens of thousands of cubic meters of high-level and intermediate-level long-lived radioactive waste, predominantly originating from French nuclear power plants. The CIGEO project aims to confine these waste products for an extended period, with the overarching objective of ensuring sustainable, secure, and reversible storage [26]. Central to the comprehensive monitoring strategy for geological disposal is the continuous observation and assessment of subsurface installations. The monitoring apparatus within such an environment must withstand the harsh conditions prevalent in a repository, particularly the radiation levels that could accelerate the deterioration of sensor materials. The adaptation of existing sensors or the creation of new ones becomes imperative to align with the technical demands of this application. This significance is especially pronounced in the domain of chemical sensors, where enhancing durability and minimizing maintenance requirements are paramount. In this context, the release of hydrogen is anticipated within the radioactive waste

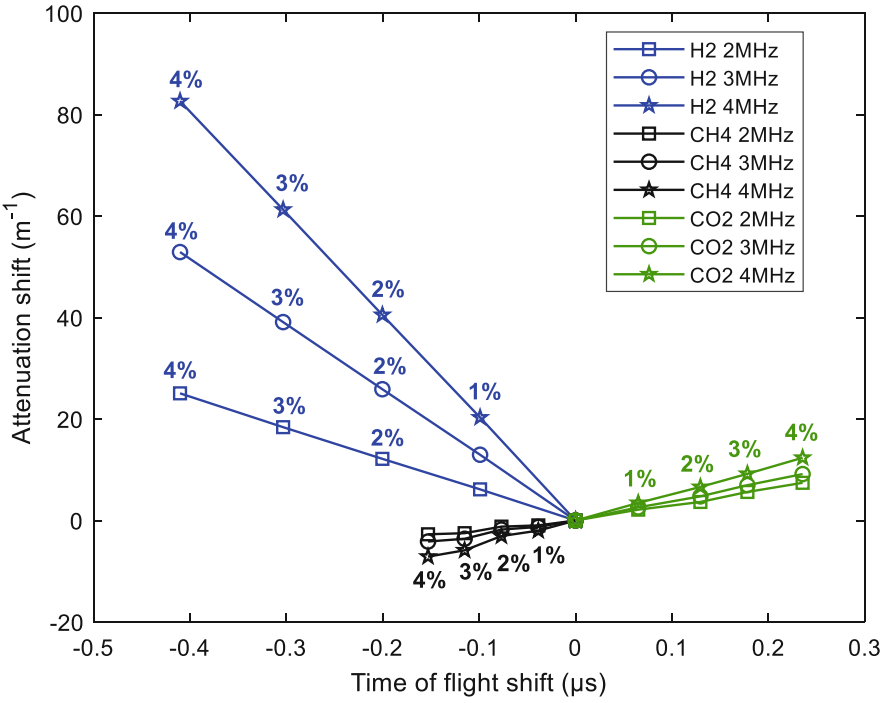

Fig. 11 Simultaneous measurements of both the time of flight and the sound attenuation of the gas using the simultaneous measurement of both amplitude and phase of the signal of the CMUT receiver with different concentrations (5%, 4%, 3%) of H_2 in N_2 (blue), He in N_2 (red), CO_2 in N_2 (green) and CH_4 in N_2 (black) with a gas flow of 100 ml/min at room temperature conditions (temperature ≈20°C, pressure ≈1 atm)

disposal facility, arising from both (i) the release of radioactive waste and (ii) the anoxic corrosion of metallic components. Consequently, as in the previous scenario, it becomes imperative to actively monitor the concentration of hydrogen gas within this radioactive repository, thereby averting any potential hazardous circumstances.

- Serving as a premium-grade industrial raw material, hydrogen finds extensive applications not only in industries such as nuclear, aerospace, and metallurgy, but also beyond. The molecular structure of hydrogen is incredibly compact, endowing it with exceptional permeability. Consequently, the minute gas molecules of H_2 are inclined to escape through even the most minuscule openings and fissures. As a result, the detection of hydrogen leakage emerges as a critical concern within a multitude of industrial domains.
- The same problem of leakage in small holes or permeable materials could happen with helium gas which is also composed of very small molecules. As described in [27] it is important to avoid exposing smartphones or smartwatches to helium, because the small gaseous molecules can bleed into the MEMS devices and stop

them from functioning. It is then important to control the concentration level of helium if helium is present not far.

- Since the liberation of the French gas market, the importance of fuel gases (i.e. natural gas) in industrial applications has increased significantly. Non-traditional sources result in a gas composition that can vary greatly. Sources of gas can be traditional dry gas from natural gas wells, wet shale gas, biogas and synthetic natural gas made from a blend of propane and air. Significant variation of gas composition and energy content (combustion potential) creates added complexities in the design of burner control systems. The percentage of non-combustible gas (CO_2 and N_2) in fuel gas can vary from 1 to 20% depending on the source. There is then a need to measure the gas composition of fuel gas.

Acknowledgment

The author wishes to warmly thank PhD students, post-docs, and colleagues without whom the results presented in this chapter could not have existed: Daniel Alquier, Johan Bertrand, Tayeb-Mohand Boudjiet, Dominique Certon, Luis Iglesias-Hernandez, Thierry Leïchlé, Maria Dolores Manrique-Juarez, Fabrice Mathieu, Laurent Mazenq, Jean-François Michaud, Liviu Nicu, Marc Portail, and Priyadarshini Shanmugam.

Financial Support This research was conducted thanks to the contest Programme d'Investissements d'Avenir of the French Government under the supervision of the French National Radioactive Waste Management Agency (ANDRA).

References

1. Gas and particle sensors-technology and market trends 2021 (Yole Développement)
2. encyclopedia.airliquide.com (2023, January)
3. www.engineeringtoolbox.com (2023, January)
4. Zuckerwar AJ (2002) Handbook of the speed of sound in real gases. Academic Press
5. Malik R, Tomer VK, Mishra YK, Lin L (2020) Functional gas sensing nanomaterials: a panoramic view. Appl Phys Rev 7:021301. https://doi.org/10.1063/1.5123479
6. Jones R, Gardner JW, DeLuca A, Longobardi G, Udrea F (2020) GaN-on-Si calorimetric thermal conductivity gas sensor, ECS meeting abstracts, MA2020-01, 2261. https://doi.org/10.1149/MA2020-01302261mtgabs)
7. Struk D, Shirkeb A, Mahdavifar A, Hesketh PJ, Stetter JR (2018) Investigating time-resolved response of micro thermal conductivity sensor under various modes of operation. Sens Actuators B 254:771–777. https://doi.org/10.1016/j.snb.2017.07.142
8. Berndt D, Muggli J, Wittwer F, Langer C, Heinrich S, Knittel T, Schreiner R (2020) MEMS-based thermal conductivity sensor for hydrogen gas detection in automotive applications. Sens Actuators A 305:111670. https://doi.org/10.1016/j.sna.2019.111670
9. Mehdaoui A, Huber C, Becker J, Schraner F, Villanueva LG. Design, simulation, fabrication and characterization of piezoelectric MEMS cantilever for gas density and viscosity sensors applications, SMSI 2021 conference – sensor and measurement science international. https://doi.org/10.5162/SMSI2021/A5.1
10. Badarlis A, Pfau A, Kalfas A (2015) Measurement and evaluation of the gas density and viscosity of pure gases and mixtures using micro-cantilever beam. Sensors 15(9). https://doi.org/10.3390/s150924318

11. Zipser L, Franke H, Bretschneider WD (2006) Acoustic sensors for analyzing binary gas mixtures. IEEE Sens J 6(3). https://doi.org/10.1109/JSEN.2006.874455
12. avenisense.com (2023, January)
13. www.neroxis.ch/oem-solutions (2023, January)
14. Tétin S, Caillard B, Ménil F, Debéda H, Lucat C, Pellet C, Dufour I (2010) Modeling and performance of uncoated microcantilever-based chemical sensors. Sens Actuators B 143:555–560. https://doi.org/10.1016/j.snb.2009.09.062
15. Kramer A, Paul TA (2013) High-precision density sensor for concentration monitoring of binary gas mixtures. Sens Actuators A 202:52–56. https://doi.org/10.1016/j.sna.2013.02.010
16. Sparks D, Smith R, Patel J, Najafi N (2011) A MEMS-based low pressure, light gas density and binary concentration sensor. Sens Actuators A 171:159–162. https://doi.org/10.1016/j.sna.2011.08.011
17. Boudjiet MT, Bertrand J, Mathieu F, Nicu L, Mazenq L, Leïchlé T, Heinrich SM, Pellet C, Dufour I (2015) Geometry optimization of uncoated silicon microcantilever-based gas density sensors. Sens Actuators B 208:600–607. https://doi.org/10.1016/j.snb.2014.11.067
18. Boudjiet MT, Bertrand J, Pellet C, Dufour I (2014) New characterization methods for monitoring small resonant frequency variation: experimental tests in the case of hydrogen detection with uncoated silicon microcantilever-based sensors. Sens Actuators B 199:269–276. https://doi.org/10.1016/j.snb.2014.03.098
19. Heller J, Boulme A, Alquier D, Ngo S, Certon D (2018) Performance evaluation of CMUT-based ultrasonic transformers for galvanic isolation. IEEE Trans Ultrason Ferroelectr Freq Cont 65:617–629. https://doi.org/10.1109/TUFFC.2018.2796303
20. Iglesias L, Shanmugam P, Michaud JF, Alquier D, Certon D, Dufour I (2020) Proof of concept and preliminary results of gas detection by measuring the admittance at the resonance and anti-resonance of an uncoated CMUT. Front Mech Eng 6. Article 14. https://doi.org/10.3389/fmech.2020.00014
21. Shanmugam P, Iglesias L, Michaud JF, Alquier D, Dufour I, Colin L, Certon D (2021) Broad bandwidth air-coupled micromachined ultrasonic transducers for gas sensing. Ultrasonics 114. Article 106410. https://doi.org/10.1016/j.ultras.2021.106410
22. Iglesias L, Shanmugam P, Michaud JF, Alquier D, Certon D, Dufour I. Cmut time of flight gas sensor by phase shift measurement, 18th international meeting on chemical sensors IMCS 2020, May 10–14th 2020. 3 p. https://doi.org/10.1149/MA2020-01312323mtgabs
23. Iglesias L, Shanmugam P, Michaud JF, Alquier D, Certon D, Dufour I (2021) Hydrogen selective gas sensor based on attenuation measurement of acoustic wave using uncoated CMUT. MEMS. January 25–29th 2021. 4 p. https://doi.org/10.1109/MEMS51782.2021.9375432
24. Iglesias L, Shanmugam P, Michaud JF, Alquier D, Certon D, Dufour I (2022) Gas discrimination by simultaneous sound velocity and attenuation measurements using uncoated capacitive micromachined ultrasonic transducers. Sci Rep. 12:744, 13 p. https://doi.org/10.1038/s41598-021-04689-4
25. Iglesias L. Boudjiet MT, Dufour I (2019) Discrimination and concentration measurement of different binary gas mixtures with a simple resonator through viscosity and mass density measurements Sens Actuators B 285:487–494. 10.1016/j.snb.2019.01.070 + corrigendum. https://doi.org/10.1016/j.snb.2020.129184
26. international.andra.fr/ (2023, January)
27. www.techspot.com/news/77195-apple-watches-iphone-can-temporarily-bricked-helium.html (2023, January)

QCM Strategies for Fundamental and Applied Measurements on Particles and Formulations

Iva Chianella

Contents

Abstract Quartz crystal microbalance (QCM) is a well-known analytical technique that enables sensitive and accurate measurement and characterization of materials adsorbed on a crystal's surface. QCM has been demonstrated to be highly reliable to measure and characterize the mass of deposited samples, in both gas and liquid phases. In addition, the technique offers real-time monitoring, as well as low operation costs. These features make QCM suitable for a wide range of applications, from mass sensing for biosensors to the study of biomolecules, nanoparticles, and functionalized surface interactions. Hence, QCM has been exploited for the optimization of nanoparticles, thin films, and drugs' formulations, for the development of their manufacturing process and as a versatile and easy-to-use tool for quality control. This chapter, therefore, firstly summarizes and critically reviews the latest fundamental and applied research studies on the implementations of QCM and QCM-D (QCM with dissipation factor) for the characterization of particles, films, and their interactions both with surfaces and the environment. Then research studies on the use of QCM in the pharmaceutical industry for the optimization of drugs'

I. Chianella (✉)
School of Aerospace, Transport and Manufacturing, Cranfield University, Cranfield, Bedfordshire, UK
e-mail: i.chianella.1998@cranfield.ac.uk

P. Lieberzeit (ed.), *Piezoelectric Sensors*, Springer Series on Chemical Sensors and Biosensors (2024) 18: 79–104, https://doi.org/10.1007/5346_2023_35,

Published online: 24 November 2023

formulations and for quality-control post manufacturing are also presented and discussed.

Keywords Drug formulations, Particle characterization, QCM, QCM-D, Quality control

1 Introduction

The quartz crystal microbalance (QCM) is a measurement technique that enables highly sensitive characterization of deposited samples both in gas and in liquid and has found wide applications in surface sciences and biotechnology [1–3]. QCM is a label-free and acoustic sensor, based on the piezoelectric effect discovered by the Curies in the late nineteenth century. Piezoelectricity states that the application of a voltage to materials with specific symmetry properties in their crystal lattice (piezoelectric) results in mechanical deformation (oscillation) [1]. If the frequency of the applied voltage matches the crystal's resonance frequency (or its multiples, which are called overtones), a wave is generated inside the crystal. Depending on the cut of the crystal, different kinds of oscillations may arise. AT-cut crystals, used in QCM, vibrate in a thickness-shear mode, where the wave of oscillation travels through the body of the crystal. This implies that the frequency of oscillation is affected by the crystal's thickness and by the presence of adsorbates on the crystal surface. In the most common measurement configurations, at each overtone, both the resonance frequency of oscillation, f, as well as the dissipation of the oscillation (D) can be measured. As the overtone number increases, the penetration depth (δ) of the oscillation wave from the crystal into the adsorbed layer and into the bulk fluid decreases and the specific value can be calculated. For example, in aqueous solutions, for a 5 MHz resonating AT-cut quartz crystal, δ is 240–250 nm at the fundamental resonant frequency, f_0, and it is 68 nm at the 13^{th} overtone [2]. Changes to f and D signals (Δf and ΔD) may occur due to adsorption, desorption, physical changes (e.g., swelling or shrinking), and structural reconfiguration events occurring on the quartz crystal surface [3, 4]. Both for QCM and especially for QCM-D, several models have been proposed to establish a relationship between the frequency and the dissipation changes and either the mass of the material adsorbed or the adsorbate viscoelastic properties, especially when measurements are done in the presence of fluids. Among the several models that have been proposed, the Sauerbrey model (Eq. 1) [5], which envisages direct proportionality between the Δf and the mass adsorbed on the sensor is the most common, for measurements done in gas phase and when the adsorbed material is flat, rigid, and firmly attached to the quartz crystal.

$$\Delta m = -\left(\frac{C}{n}\right)\Delta f \tag{1}$$

where Δm is the mass adsorbed on the crystal surface, C is the sensitivity constant, n is overtone, and Δf is the change in the sensor frequency.

Several models have been proposed to relate the change in frequency and the phenomenon taking place on the crystal surface in the presence of a rigid and firmly attached adsorbate, when this is exposed to liquids. One of the earliest models (dating from the late 1940) is expressed in Eq. 2.

$$\Delta f_n = -\frac{f_n}{2}\Delta D_n = -\frac{1}{C}\sqrt{\frac{n\eta_l\rho_l}{2\omega_F}} \tag{2}$$

where n is overtone, η_l and ρ_l are the liquid viscosity and density, respectively, and ω_F is the angular fundamental resonance frequency.

Equation 2 is typically attributed to Kanazawa and Gordon [6]; it states that the decrease in frequency and the increase in dissipation are both proportional to the square root of the product of the liquid's viscosity and density. Since QCM is sensitive to the properties of the bulk liquid, a reference measurement in the same liquid is often necessary for separating bulk liquid contribution from the film properties. Other viscoelastic models (e.g., Voigt or Kelvin-Voigt models, Eq. 3) [5, 7] have been proposed for when the material is not rigidly adsorbed on the crystal, but consists of a soft layer.

$$D \approx \frac{E_{\text{dissipated}}}{E_{\text{store}}} \tag{3}$$

In these models, frequency and dissipation are functions of the deposited material's thickness (d_m), its density (ρ_m), its viscosity (η_m), and its shear modulus (μ_m), as well as the density (ρ_l) and viscosity (η_l) of the bulk contacting liquid (or gas) [2].

Such models allow to relate the Δf and ΔD signals to specific characteristic of the material adsorbed (e.g., hydrodynamic diameter of nanoparticles), as well as understanding phenomena such as swelling, fouling, sorption, and ion exchange [2]. Such features have seen the use of QCM and particularly QCM-D, for a variety of applications from the optimization of drugs' formulations [8, 9] and the development of their manufacturing systems [10], to the use of QCM as a tool for quality control during or post drugs' production [11]. Therefore, this chapter firstly will critically review the most recent fundamental studies on the use of QCM or QCM-D to characterize nanomaterial (e.g., nanoparticles), nanofilms, and biomolecules attached on piezoelectric crystals. Then applications of QCM and QCM-D for drug development and quality control in the pharmaceutical industry will also be reviewed and discussed.

2 QCM and QCM-D as a Tool for the Characterization of Nanomaterials

The information on nanomaterials (e.g., biomolecules, metal nanoparticles, bacteria, viruses, etc.), their adsorption kinetics, and their adhesives' contact strength to a particular surface are essential in many scientific fields including analytical sciences, medicine, biology, and catalysis. Therefore, several research groups have focused on how QCM and especially QCM-D signals can be exploited to extract important information of the nanomaterials adsorbed on the crystal surface. In many studies, QCM and QCM-D signals (Δf and ΔD) have been analyzed using several numerical and simulation tools to establish relationships between the signal shifts and the characteristic of the adsorbate. For example, for measurements done in liquid, the Δf recorded is not only proportional to the mass of the adsorbed layer, but also to the characteristics of the hydrodynamically coupled fluid. The relationship between the QCM signal and the characteristic of the adsorbed layer depends on whether this is homogenous or heterogenous. For homogenous and rigid layers, the Sauerbrey or the Kanazawa and Gordon models (Eqs. 1 and 2, respectively), where there is a proportionality between the sensor frequency (f) and the mass of the adsorbate, can be applied for measurements done in gas and in liquids [1, 6].

Heterogenous layers (i.e., a layer of discrete particles) are more difficult to simulate. Several models have been proposed; one of the most common, the Voigt or the Kelvin-Voigt viscoelastic models relates the measured dissipation factor (D), shown in (Eq. 3), with changes on the deposited material and the environment (air/liquid). The relationship between the material adsorbed and the environment can become very complex. For example, in a dense layer of particles, the QCM signal does not only depend on the mass of the nanomaterial and on the hydrodynamic interaction of the particles with the surrounding liquid, but also on the hydrodynamic interactions among the particles themselves (e.g., the sensing of the disturbances generated in the fluid by neighboring particles), making the system difficult to simulate and described numerically. The particle-particle hydrodynamic interactions disappear for sparsely packed layers simplifying the system drastically. Therefore, Gillissen and colleagues have simulated numerically the hydrodynamic behavior of a sparse layer of spherical nanoparticles rigidly attached to the QCM sensor [12]. The simulation enabled the generation of a model, which from the QCM-D signal, permitted the evaluation of the nanoparticles' size in the range of $\delta/a < 3$, where δ is the sensor's penetration depth and a is the particle's radius. The model allowed them to estimate the size of globular proteins, viruses, colloids, and spherical vesicles, with therefore applications to a wide range of bioparticles. In another work, the group used the model to quantitatively measure the deformation of adsorbed particles (a layer of fluid-like and gel-like liposomes of 34 nm radius) at low surface coverage [13]. Similarly, Adamczyk and co-workers [14] have developed a theoretical model that enabled them to interpret the adsorption kinetics of nano- and micro-size particles on rough surfaces from the Δf and ΔD signals. The model accounted not only for rigidly attached nanoparticles, but also for lightly

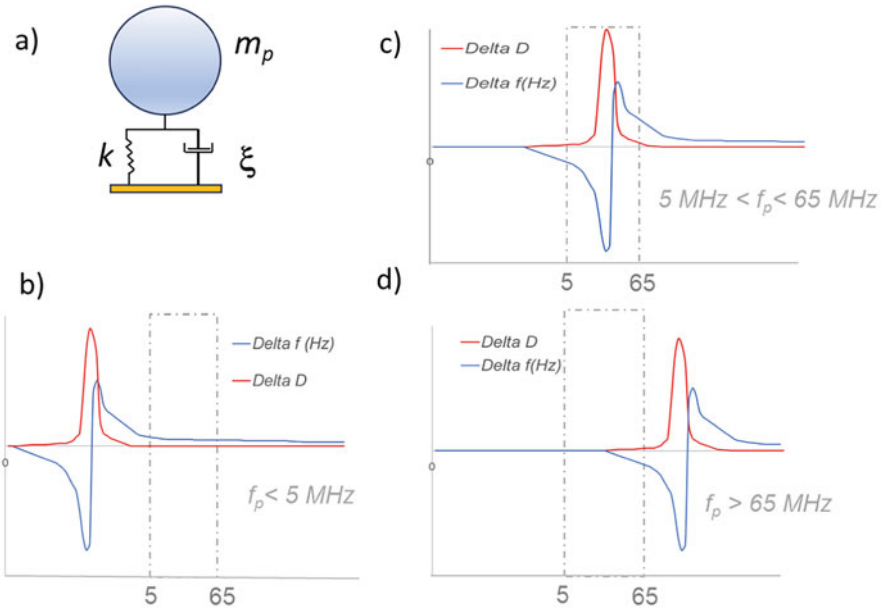

Fig. 1 Schematic diagram of the coupled resonator model. (**a**) Particle with mass, mp adhering to a sensor surface through a viscoelastic bond comprised of a spring with a spring constant (k), and with a drag coefficient (ξ), yielding a particle resonance frequency fp. (**b**), (**c**), and (**d**) Theoretical shifts in the sensor resonance frequency (Δfs) and dissipation changes (ΔD) for particles adhering with different adhesive bond stiffnesses to a QCM-D sensor. Particle resonance frequency fp increases with the adhesive bond stiffness, and the frequency of zero-crossing (fs = fp) can only be observed within what is referred to as "the window of observable QCM-D frequencies", indicated by the dashed rectangles. Illustration adapted from [15]

adsorbed materials. In addition, it evidenced the importance of the roughness and the homogeneity of the QCM sensors surface on the adhesion strength of both micro- and nanoparticles. In many cases, for example on medical implants, the adhesion of biomolecules such as osteoblast cells needs to be promoted to achieve a successful implant integration. In other cases, for example to reduce the spread of viruses and bacteria, metal/glass/plastic surfaces are modified to minimize the adhesion of the biomolecules. Therefore, the model showed the potential to estimate the attachment of different size nanoparticles to various surfaces or surface treatments, enabling to find conditions either to promote or prevent attachment.

Similarly, Van der Western and colleagues [15] have used a window-equipped QCM-D for the high-throughput analysis to estimate the averaged viscoelasticity of the bond between colloids and several surfaces by measuring simultaneously up to 10^6 colloidal particles. The group assumed that when colloidal particles are sparsely adsorbed on a sensor surface, they act as individual, coupled resonators, whose schematic representation is presented in Fig. 1a. Such individual resonators will impact the resonance frequency shift (Δf) measured, as well as the dissipation energy (ΔD). The development of the coupled resonator model has greatly widened

the applications of QCM-D, which were previously confined to molecular mass adsorption. The group also indicated that whereas bond viscoelasticity of individual particles of the same kind often shows large variations, QCM-D identifies a well-defined zero-value in sensor resonance frequency shift (Δfs), when particle and sensor resonance frequencies match (fs equals to fp), Fig. 1b. These zero crossing frequencies are only observed when the adhering particles oscillate at frequencies within the window of the sensor fundamental resonance frequency and its overtones, which for a 5 MHz QCM, ranges from 5 MHz to 65 MHz (see dashed rectangles in Fig. 1b). The asymptotic shift from a negative to a positive Δf takes place when fp equals fs and is accompanied by a maximum in ΔD. This coupled-resonator model was finally able to explain the positive Δf signals often reported in literature following the adsorption of materials on the crystal surface.

Using the coupled resonator model, the group was able to relate the Δf and ΔD to the bond viscoelasticity using the Kelvin-Voight equation as reported below in Eq. 4.

$$\Delta f + \frac{i\Delta D f_s}{2} = \frac{f_F m_p}{\pi Z_q} \times N_p \left[\frac{\omega_s\left(\omega_p^2 - \gamma^2\right) - \omega_s \omega_p^4}{\left(\omega_s^2 - \omega_p^2\right)^2 + \omega_s^2 \gamma^2} + i \frac{\omega_s^4 \gamma}{\left(\omega_s^2 - \omega_p^2\right)^2 + \omega_s^2 \gamma^2} \right] \quad (4)$$

where Δf (Hz) is the shift in QCM-D resonance frequency, ΔD is the change in dissipation, f_F is the fundamental resonance frequency of the sensor (5 MHz), f_s is the QCM-D sensor surface resonance frequency, m_p is the particle mass (kg), ω_s is the sensor resonance angular frequency ($\omega_s = 2\,\pi\,f_s$), ω_p is the particle resonance angular frequency ($\omega_p = 2\,\pi\,f_p$), Z_q is the acoustic impedance of an AT-cut quartz crystal (8.8×10^6 kg m^{-2} s^{-1}), N_p is the number of adhering particles per unit sensor area (m^2), and γ equals ξ/m_p with ξ being the drag coefficient, indicative of the viscous component of the bond [16].

Using the developed model, the group analyzed QCM-D data to calculate the elasticity (the spring constant) and viscosity (the drag coefficient) of biotic (*S. Salivarius* HB7) and abiotic (silica particles with 0.5 μm radius) particles adhering to different sensor surfaces (e.g., silica crystal, biotinylated crystal surface, hydrophobic Au, hydrophobic and hydrophilic self-assembled monolayers). Knowledge of the elasticity and viscosity of the bond through which colloidal particles adhere to a surface can help to understand better the mechanisms of particle adhesion. This would aid the development of new strategies to detach or prevent the attachment of several harmful particles such as viruses and bacteria.

In another example, where QCM was used to study colloidal particles, the device was utilized to monitor the evaporation of colloidal suspensions of alumina nanoparticles on a sensor surface [17]. Both the concentration of the colloidal suspension and the size of the particles were varied for the study. The group was able to record QCM data that enabled them to distinguish the several stages of evaporation. Furthermore, they developed a mathematical model allowing to perform a quantitative analysis. They concluded that for diluted solution the frequency

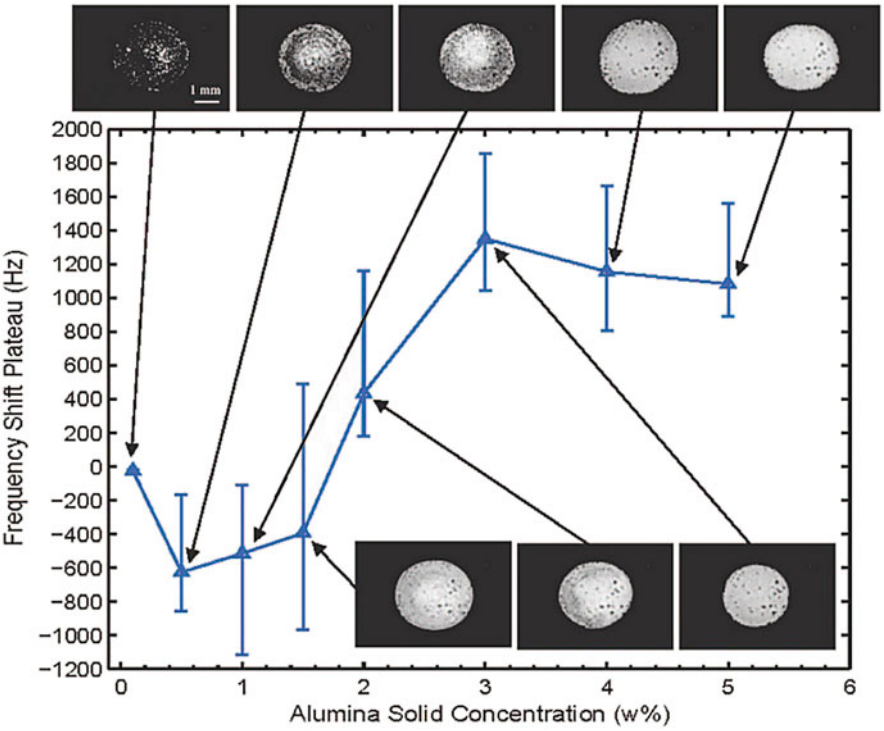

Fig. 2 Frequency shift during complete drying of 1 μm alumina colloid suspension droplets with varying solid concentration. Representative microscope images taken after the water was evaporated show the residual alumina topography at each concentration. Reproduced with permission from [17]

shifts were indeed representative of the mass of particles adsorbed on the crystal, but in the presence of concentrated solutions the bond stiffness of the resulting layers and interparticle interactions were the dominating factors for the frequency shifts. These were then made accountable for the positive frequency shifts seen at complete evaporation (Fig. 2). They concluded that the signals observed with smaller particles were mainly due to bond stiffness generated by Van der Waals interactions, while for bigger particles, a capillary or sandcastle effect was considered responsible for the signals, highlighting the importance of relating the frequency shift to the appropriate phenomenon.

When studying the adsorption and binding kinetics of materials on an oscillating sensor surface, care needs to be taken about the oscillating amplitude used. In 2005 Höök's group studied the effect of the sensor shear amplitude (from 1 to 10 V) on the adsorption of several types of material: (i) lipid vesicles to a SiO_2 surface; (ii) streptavidin to a biotin-modified substrate; (iii) neutroavidin- (or single stranded DNA) polystyrene bead (200 nm) to a biotin (or DNA) modified surface [18, 19]. The results show that the most used amplitude (1 V) does not affect the

binding of any of the nanomaterials tested (with Mw between 10 kDa and 200 kDa). However, an effect of the oscillation amplitude was found on the binding of polystyrene nanoparticles (>200 kDa); particularly, it was observed that particle's saturation binding decreased with increments of the oscillation amplitude. To explain this effect, Höök and colleagues considered that the oscillation amplitude has its maximum in the center of the crystal and decays to zero at the crystal's edges. Hence, they explained the effect by proposing a critical oscillation amplitude, Ac, above which there is no binding, but below which the binding is not influenced. The group also stated that for a specific Ac value, there is a critical radius, rc, within which the binding is completely suppressed, but beyond which the binding is not influenced. If the oscillation amplitude is high enough the particle binding can be totally disrupted. Experimentally, for both types of polystyrene immobilization mechanisms studied (via DNA hybridization or biotin-avidin binding) no effect in the saturation binding was observed with oscillation amplitude up to ~5 nm, but a significant decrease was seen for oscillation above ~10 nm. The similarity of the behavior for the different immobilization mechanisms implies that the effect was due to the size of the nanoparticles rather than to the substrate-nanoparticles bond strength and numbers. Therefore, the effect of the shear sensor amplitude on the crystal's adsorption needs to be considered when using QCM when measuring particles larger than 100–200 nm.

3 QCM and QCM-D as a Tool for the Characterization of Polymeric Films

Thin, porous films are used in numerous scientific fields and for a wide variety of applications, from energy storage [20] to sensing [21, 22]. In the last two decades, QCM and especially QCM-D have been used for the characterization of such films. The technique has been utilized as a tool to follow the formation of films [23–26] as well as to study the performance of the resulting viscoelastic layers in different environments [5, 27].

Thin polymeric films can be considered soft coatings, which remain rigidly attached to a crystal surface and are characterized by reduced values of their bulk complex shear moduli. Quantification of the complex shear modulus can be carried out using the changes in frequency and dissipation factor over multiple overtones measured experimentally and fitted using suitable viscoelastic models [28]. Such viscoelastic coatings are characterized by both frequency and dissipation factor changes dependent on the overtone order, n. The mass change occurring in viscoelastic films cannot be estimated by the Sauerbrey's equation (Eq. 1), but this becomes an input parameter in more complex equations. Such equations have a high number of viscoelastic parameters that are influenced by the nature of the coating and the liquid in contact with it. Therefore, by following the changes in

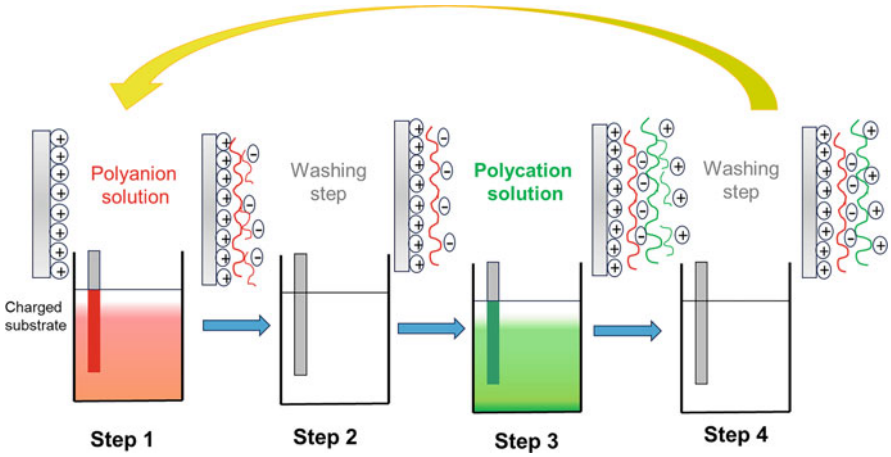

Fig. 3 Diagram of the LBL film-deposition process, based on the alternating exposure of a charged substrate to solutions of positively and negatively charged polyelectrolytes. A rinsing step (usually in water) is included between the two previously described adsorption processes, to remove excess as well as to prevent cross-contamination of the polyelectrolyte solutions. Illustration adapted from [35]

frequency and dissipation factors many phenomena occurring in the viscoelastic layers can be explained and monitored.

One of the most common methods to create thin polymeric films on a surface is the layer-by-layer (LbL) deposition. With these techniques, layers of polyelectrolytes with opposite charges can be deposited efficiently to obtain layers used for a variety of applications including drug delivery [29–31], sensing [32], and energy (e.g., for organic solar cells [33, 34]). A schematic representation of the LbL deposition process starting from a positively charged surface is depicted in Fig. 3.

QCM and especially QCM-D has been used extensively to characterize and understand the behavior of such films when subjected to different conditions and environments.

Lutkenhaus and colleagues [25] stated that to exploit LbL layers properly, characterizing their thermal properties and estimating the layers' glass transition temperatures (Tg) are critical, as the performance of the films would depend strongly on whether they are rubbery or glassy. In addition, the films' Tg values and the presence of several Tgs can be correlated to the films' composition and internal structure. Therefore, the group have used QCM-D to follow the formation of poly (allylamine hydrochloride)/poly(acrylic acid) (PAH/PAA) assembled at different pH values (pH 3.5, 5.0, and 9.0) [25] and the formation of poly (diallyldimethylammonium chloride)/poly(styrene sulphonate) (PDADMA/PSS) assembled from solution with varied anionic concentrations (i.e., 0.25–1.25 M NaCl) [26]. The thermal properties of the resulting LbL layers (70–300 nm) were then evaluated by estimating the Tg values using a thermally controlled QCM-D. They compared the results with those examined by modulated differential scanning

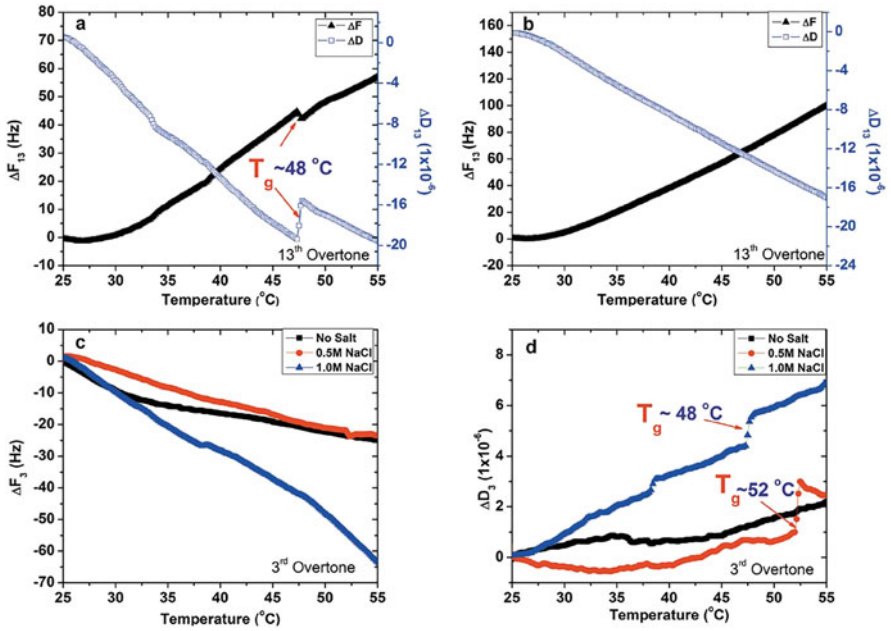

Fig. 4 Temperature dependence of ΔF and ΔD for the 13th overtone of (**a**) a LbL film assembled from 1.0 M NaCl and (**b**) a bare crystal in 1.0 M NaCl. Temperature dependence of corrected ΔF (**c**) and ΔD (**d**) for PEI/(PDADMA/PSS)7 LbL films assembled from 0, 0.5, and 1.0 M NaCl. Reproduced with permission from [26]

calorimetry (DSC) of the same LbL produced in "bulk" (1–1.5 μm). In both studies, QCM-D signals agreed with the DSC and seemed suitable to characterize thermal properties and enable estimating Tg values and how these were affected by film formation and composition. Figure 4 shows an example of one of the results obtained. Specifically, while Fig. 4a depicts the ΔF and the ΔD (13^{th} overtones) raw signals recorded while increasing temperature for a PEI/$(PDADMA/PSS)_7$ LbL film assembled from 1.0 M NaCl, Fig. 3b shows the same two QCM-D signals obtained for a bare crystal also immersed in 1.0 M NaCl. As the viscosity and density of the solution in contact with the crystal is affected by the temperature, so is the signal of a bare electrode. Therefore, for easier identification of the LbL film Tg, the changes in frequency and dissipation of the bare crystal were subtracted from the frequency and dissipation changes of the LbL assemblies, resulting in Fig. 3c, d, where the Tg values for films prepared in different concentration of NaCl can be clearly seen, especially in the ΔD plots.

It is well known that solutions with different electrolytes, ionic strengths, and concentrations have a strong influence on the formation of LbL layers [35–38], but their effect of the films post-formation is less explored. Nevertheless, it has already been proposed that specific electrolytes with different ionic strength can have several effects such as shrinking and swelling on the LbL layers post-formation

[39]. QCM-D has been demonstrated to be an efficient tool to study and investigate the effect of several electrolytes and their strength on the LbL films. For example, again the Lutkenhaus group exposed LbL films of PDADMA/PSS, prepared using 0.5 M NaCl, to several electrolytes such as NaCl, KCl, NaBr, and KBr [23]; the last one has been reported to have a strong effect on the swelling of the LbL layers [40]. The same films in free-standing forms were also analyzed for comparison by ^{1}H NMR and neutron activation analysis. The QCM-D results showed that salts containing Br^{-} had a more pronounced swelling effect on the films than salts containing Cl^{-}. In addition, using the QCM-D, the group was able to follow in detail how various concentration ranges of KBr affected the PDADMA/PSS differently. This allowed them to hypothesize not only the forces behind the changes (i.e., electrostatic repulsion), but were able to observe salt annealing at the highest electrolyte concentration tested.

LbL films made of biocompatible electrolytes such as chitosan, alginate, hyaluronic acid, dextran, heparin, etc., have been explored for regenerative medicine, tissue engineering, and drug delivery thanks to their ease of preparation and the ability to tune their physical properties, such as size, composition, porosity, surface functionalization, and colloidal stability [41]. Borge and colleagues [42] have explored hybrid supramolecular multi-layered biomaterials, comprising high-molecular-weight biopolymers (i.e., alginate) and oppositely charged low-molecular-weight peptide amphiphiles (PAs), through LbL assembly. The process of LbL formation was followed by QCM-D, which was able to reveal that alginate and PAs could be successfully combined to achieve stable supramolecular systems that are promising for biomedical applications. Similarly, Sergeeva and co-workers [43] used QCM-D to study the formation of several LbL films made of charged natural and synthetic polyelectrolytes. The QCM-D signals observed during LbL deposition were analyzed qualitatively to estimate the viscoelastic properties of the films and their interactions with serum components. The group also investigated how the composition of the LbL films was able to influence cells adhesion (fibroblasts) and proliferation, permitting to select the best multilayers for cell cultures. The results underlined that cell adhesion is a highly complex process governed by several surface's features including: (i) functionality, (ii) morphology, (iii) affinity for serum components, and (iv) changes in surface properties generated by adsorbing biomolecules. Of the many LbL-films tested, the group observed that poly (4-styrenesulfonate)/poly(allyl amine) multilayers were best suited for attachment of fibroblast cultures.

QCM-D has also been used to characterize drug attachment and release to and from LbL films in the presence of several stimuli, allowing to tune the LbL composition until the desired kinetics was achieved. Aykut and colleagues [44] have used QCM-D to study the drug loading/release of LbL films made of PDADMA/PSS and PDADMA/PAA. The composition of the films as well as the pH and ionic strength were changed to achieve maximum drug loading and the desired release kinetics [44]. Figure 5 shows the QCM-D signal of the loading and desorption at different pHs (pH 6.3, pH 2.0, and pH 11) of the drug IBF-Na on the LbL film $(PDADMA_{5.5}/PSS_{5.5})_{10}$. In Fig. 5, the film was exposed to the drug in step

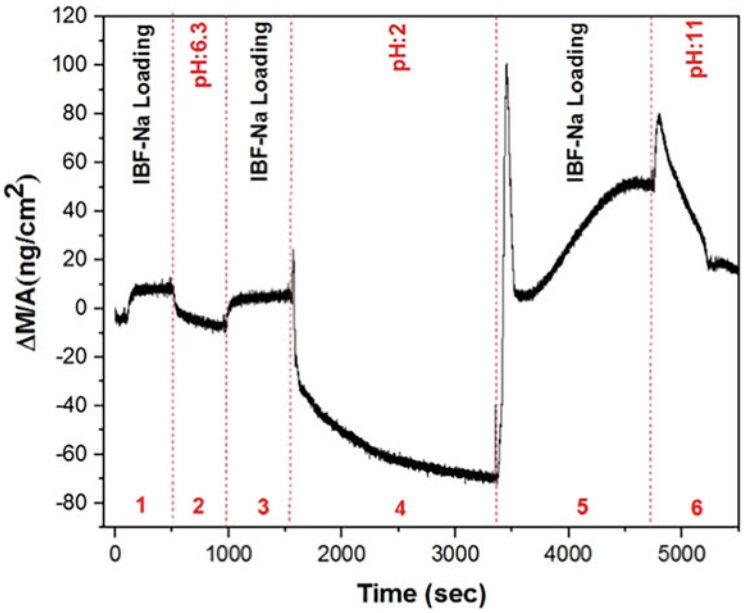

Fig. 5 An example of QCM-D graph for IBF-Na loading/desorption to/from $(PDADMA_{5.5}/PSS_{5.5})_{10.}$ (ΔM/A is the change of mass per unit area). Reproduced with permission from [44]

1 and an increase in signal, confirming attachment of IBF-Na to the LbL film, was obtained. In step 2, a pure water wash (pH 6.3) was applied to remove the loaded drug, demonstrated by the decrease in signal. In step 3, IBF-Na was loaded again, and a smaller increase than in step 1 was observed, with the difference corresponding to 7 ng/cm^2. This indicates that the water wash in step 2, in addition to removing the drug, might have removed loosely bound polyelectrolytes from the LbL film. In step 4, a solution with pH 2 was passed on the IBF-Na-loaded LbL film, and the sharp decrease in signal showed that this solution was able to desorb not only the entire amount of drug, but also 11% of the LbL film. The subsequent loading step (5) showed a much higher adsorption of drug as compared to step 1 and 2, revealing morphological/structural changes in the LbL layer generated by the exposure to the strongly acidic solution in step 4. In step 6, a solution with pH 11 was used to trigger the release, but only 27.5% of the drug was desorbed, while 72.5% remained attached, most likely through electrostatic and hydrophobic interactions present between IBF-Na and the LbL film in basic conditions. The group followed the drug attachment and release also by analyzing the solutions by UV-Vis spectroscopy. Both analytical techniques gave consistent results demonstrating that the QCM-D is a powerful tool to study and characterize materials for drug delivery.

Lipid nanoparticles (LNPs) are another promising type of nanomaterial for drug delivery, in particular for intracellular delivery, as their cellular uptake can be modulated by changing their composition. Usually, one optimizes the composition to achieve the desired uptake and performance by a combination of time-consuming

in vitro and in vivo studies. QCM-D has shown to be a quick tool to study the interactions between several LNPs and serum proteins permitting to identify those with the best chance to have high uptake by the cells. In this way, only the most promising LPN candidates would be selected to progress to in vitro and in vivo studies saving time and resources [9]. Sebastiani and co-workers used two approaches to screen for the best LPN candidates. In the first approach, QCM crystals were functionalized with antibodies against a target protein fundamental for maximum cells uptake, enabling to identify which LNPs possessed such protein in their corona. In the second approach the crystals were functionalized with LNPs via polyethylene glycol to study the interactions of the lipid nanoparticles with serum proteins. These two experimental approaches enabled the group to predict the composition of LNPs protein corona and therefore to estimate the nanoparticles chance to approach and cross the cell membranes.

4 QCM and QCM-D to Study Molecule-Surface Interactions and Molecule-Molecule Interactions

In the last 10–15 years QCM and QCM-D have demonstrated to be powerful tools to study interactions among biomolecules and/or chemicals as well as interactions between biomolecules (or chemicals) and surfaces.

The chemistry used to immobilize receptors on sensor surfaces as well as to reduce non-specific interactions caused by the complex composition of clinical and environmental samples is paramount for the development of specific and selective diagnostic devices. Among the several chemicals available, polyethylene glycol (PEG) is one of the most promising for both immobilizing a receptor and minimizing the binding of non-targeted chemicals contained in a sample. Du and co-workers [45] used QCM-D to study the combination of a long-chain PEG (PEG_{24}) and a short-chain PEG (PEG_4) for sensing applications. While PEG_{24} was used to achieve optimal immobilization of the antibodies for binding with the antigen, PEG_4 was used to fill the unoccupied sensor's surface providing an anti-fouling layer capable to minimize binding of other proteins and chemicals present in complex biological fluids such as plasma. The use of QCM-D allowed to visualize how changing the ratios between the two PEGs on the sensor surface influenced the behavior of the resulting sensors in terms of both sensitivity and specificity permitting to identify the ratio leading to the best performance.

The use of QCM-D to optimize surface chemistries has been used not only to develop biosensors, but also in the field of tissue engineering and regenerative medicine. For these, surfaces are usually covered with a layer of functional proteins and growth factors. Many chemistries have been developed to covalently attach proteins and other biomolecules to surfaces in a chemo- and regioselective fashion. For example, peptide or imine bonds can be formed upon reaction of N-hydroxysuccinimide or aldehyde functionalities (attached to the sensor surface),

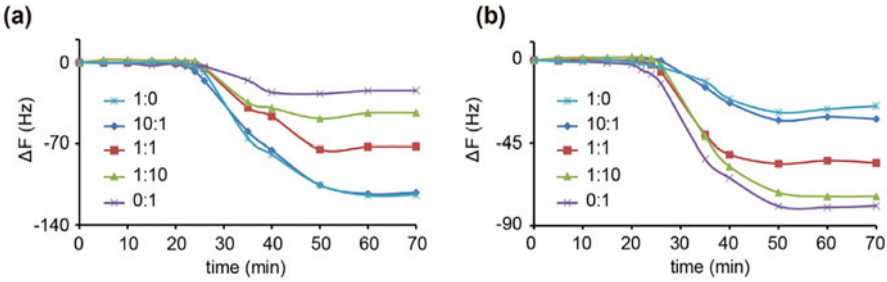

Fig. 6 QCM dynamic analysis of the binding affinity to specific antibodies: (**a**) anti-BMP-2 and (**b**) anti-fibronectin. Modified surfaces containing a previously adsorbed BMP-2 and fibronectin mixture with combinations of various ratios, including 1:0, 10:1, 1:1, 1:10, and 0:1, were used as the surfaces for binding affinity characterization. Reproduced with permission from [48]

with the carboxylic groups present in proteins. An alternative approach to immobilize proteins and growth factors on a surface is using supramolecular chemistry, enabling mild and reversible protein attachment [46]. Goor and co-workers [47] have used QCM-D as well as fluorescence spectroscopy to monitor the binding of proteins to a combination of a hydrogen bonding motif, 2-ureido-4-pyrimidinon (UPy), with a Cucurbit[8]uril (Q8)-based macrocyclic host–guest assembly. Whereas UPy was directly attached on the crystal surface, Q8 and the protein solution were incubated with the crystal in subsequent steps. In agreement with fluorescence spectroscopy, QCM-D data displayed successful ternary complex formation on the crystal surface, with a small mass increase observed upon incubation of Q8 and a large mass increase observed after subsequent incubation of the protein. Following a washing step, a decrease on the mass adsorbed was observed, which demonstrated the reversible nature of the supramolecular host–guest system. In contrast to fluorescence spectroscopy, QCM-D was able to reveal the presence of nonspecific binding of Q8 to the sensor surface, highlighting the need of additional surface-blocking steps. This demonstrated the advantage of using QCM over fluorescence spectroscopy to optimize the surface chemistry for tissue engineering.

To obtain a more in-depth understanding of protein-surface interactions, QCM-D together with protein assay tests were used to study the controlled and competing surface adsorption of several functional proteins. This enabled to have a model of a multifunctional platform, useful for guiding biological activities [48]. For the study, a hydrophobic chemical (polychloro-para-xylylene) was first attached on the sensor surface. Then, the adsorption of morphogenetic protein 2 (BMP-2) and fibronectin both individually and in combination was characterized by QCM-D. When the two proteins were adsorbed together, several ratios were tested and the proteins' actual distribution in the resulting layers were characterized by QCM-D using anti-BMP-2 and anti-fibronectin antibody. Specific binding of the antibody to its corresponding protein enabled to estimate the amount of each protein attached on the surface when different ratios were used in the immobilization solution (Fig. 6). Then, the multifaceted and synergistic biological activities of the adsorbed BMP-2 and fibronectin

were examined by culturing porcine adipose stem cells (pADSCs) on the modified sensors' surfaces. Finally, protein assays were then carried out at several time intervals (e.g., 24 and 72 h) on the resulting cell cultures to evaluate the osteogenesis activity of BMP-2 and the cell proliferation activity of fibronectin (two biological activities highly desired when growing new tissues). The results confirmed that there was indeed a synergic effect of the two proteins as a high degree of both osteogenesis and proliferation activity on the cell cultures was observed on sensors' surfaces containing both BMP-2 and fibronectin. On the other hand, cells grown on surfaces with only one protein immobilized evidenced either a high degree of osteogenesis or proliferation and a very low degree of the other activity. The study also evidenced how the two biological activities could be modulated by controlling the adsorption conditions (proteins ratios) utilized at the immobilization step, which could be followed and characterized by the QCM-D data.

In another example, QCM-D was used to monitor the production and to characterize supported lipid bilayers (SLB): a mimic of the lipid bilayer that constitutes the backbone of cell membranes. Thanks to its amphiphilic properties, the lipid bilayer acts as a protective layer isolating the inside of the cells from the external environment and thus regulates what enters and exits the cells. SBL are a widely accepted model to mimic cell membranes and, therefore, to study many critical biomacromolecular interactions. In fact, SLBs are extremely versatile as they can be functionalized with different functional groups mimicking those found in cell membranes; furthermore, they can incorporate membrane-associated proteins (transmembrane and peripheral). QCM-D has proven to be a powerful tool to study the formation of SLBs as well as their real-time dynamic interactions with biomolecules [49–52]. For instance, the technique was used to monitor the generation of SLB by surface-mediated vesicle fusion on several different hydrophilic surfaces such as oxides of silicon, gold, and titanium (all rich in hydroxyl groups) [49]. Figure 7a illustrates an example of the QCM signals (Δf in blue and ΔD in red) recorded during the formation of the SLB. In the study, an amphipathic α-helical (AH) peptide was used to form the SLB, as it can interact strongly with lipid vesicles absorbed on hydrophilic surfaces, causing their rapture [53]. Figure 7a clearly shows the addition, at around 10 min of the AH-peptide and its swelling effect on the absorbed intact vesicle, demonstrated by a sharp decrease of the Δf signal and a mirrored sharp increase of the ΔD signal. The vesicle's rupture due to the AH-peptide is then evidenced at around 60 min by the dramatic change in f and D signals, after which the increasing Δf and decreasing ΔD signals are due to the difference in thickness and viscoelastic properties (calculated using both the Sauerbrey and Voigt models) of the resulting SBL layer as compared with the intact vesicle. Figure 7b shows a schematic representation of the structural transformation from an adsorbed, intact vesicle to a SBL. QCM-D was used to assess the viscoelastic properties of the layers during formation under several different conditions and to record in real time the interactions of the resulting layers with the environment. The same group, for example, studied the adsorption of three proteins (C3, C3b, and properdin) on SLB with either positive or negative charges and were able to observe how the

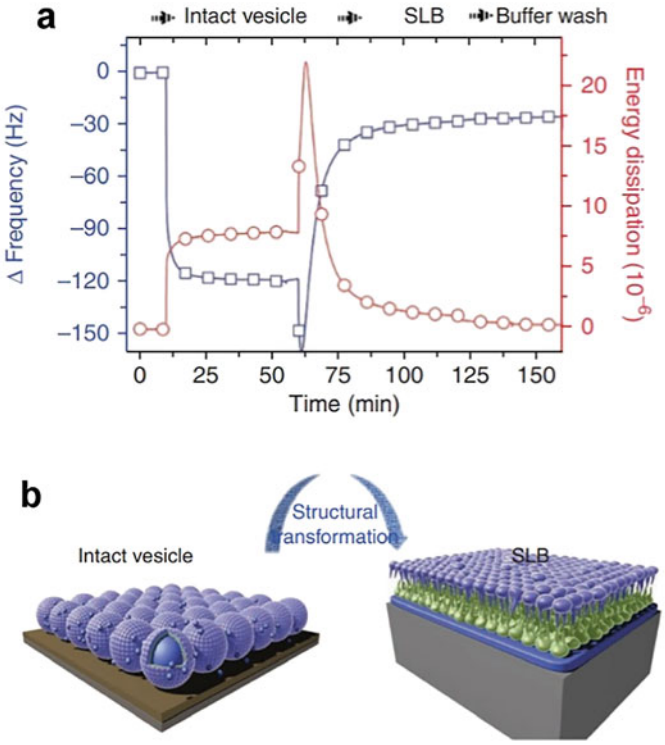

Fig. 7 (**a**) QCM-D signal recorded during SLB formation: a layer of intact vesicle is formed first and this is ruptured following the addition of a specific short chain peptide (AH) leading to SLB formation; (**b**) a schematic representation of the AH peptide-mediated structural transformation from adsorbed, intact vesicle to a SLB. Reproduced with permission from [49]

uptake in the SLB was dependent on both the charges and protein concentrations [52].

It is paramount to understand the interactions between materials, proteins, and cells for developing biomaterials suitable for a wide variety of medical applications such as orthopedic implants, implantable devices, and tissue engineering. QCM-D has shown to be able to provide an insight into such interactions, becoming a useful characterization tool when developing new materials. Kushiro and co-workers [54] aimed to study the effects of chemical functional groups on the attachment of proteins and cells onto orthopedic implants. For that purpose, they used QCM-D to evaluate the binding of fibronectin followed by fibroblasts L929 to surfaces comprising of different self-assembled monolayers (SAMs) and specifically COOH-SAM, NH_2-SAM, CH_3-SAM, OH-SAM. Using QCM-D, they were able not only to gain information on the viscoelastic properties of the surface-adsorbed fibronectin, but they could visualize the different patterns of ΔF and ΔD observed on the various SAM surfaces during L929 cell adhesion. Following further analyses and

comparison, they suggested that the ΔF and ΔD patterns were unique signatures of protein adsorption and cell adhesion behaviors, which could be modulated by the various chemical functional groups introduced on the surfaces using the different SAM. This demonstrated that QCM-D has the potential of becoming a rapid in vitro platform for the dynamic evaluation of protein and cell behaviors on novel biomaterials. A similar study was conducted by Kao and colleagues, who, after generating either positively or negatively charged SAMs, used QCM-D to follow the attachment of NIH3T3 mouse embryonic fibroblasts. The group was able to see a strong effect of charge and therefore of the surface potential of the SAM, not only on the number of cells attached, but also on the way the cells were immobilizing on the surfaces. In fact, whereas a positive surface potential generated an evenly spread and soft cell monolayer, a negative surface potential, in contrast, led to a triple rigid layer of cells, resembling an extracellular matrix [55].

QCM-D has proven a powerful tool to study cells attachment and physical properties of the resulting layer [56]. Tymchenko and colleagues [57] demonstrated that ΔD could not only yield information on the attachment of fibroblasts (NIH3T3) to the crystal surface, but also assess in real time the reversible changes in the viscoelastic properties of the surface-attached cells, induced by the cytoskeleton-perturbing drug cytochalasin D. This demonstrates how QCM-D can be utilized to screen in vitro a selection of drugs and to observe their effect on specific cell lines.

Small amounts of reactive oxygen species (ROS), such as H_2O_2, are necessary to activate the body's cellular defense response (oxidative eustress). In contrast, high levels of ROS lead to cellular damage (oxidative distress). The over-exposition of cells to oxidizing agents, such as H_2O_2, may lead to changes in cellular redox potential and morphology, which in turn affects the cells' viscoelastic properties. Oxidative stress of cells is usually evaluated by immunological methods such as ELISA and Western Blot. However, these techniques, although informative, are end point and hence unable to follow the morphological changes of the cells in real time. Therefore, Shoaib and Trabrizian [58] explored whether QCM-D could be used to evaluate the degree of oxidative stress on the morphology of cells' monolayers. Specifically, they have used a pre-osteoblast murine cell line (MC3T3) and studied the effect of various concentrations of H_2O_2 on the cells' viscoelastic by following changes of the QCM-D response (ΔD). The QCM-D data showed that when the cells were exposed to level of H_2O_2 below 25 μM, the morphology changes of the monolayer were reversible (confirmed also by SEM, AFM, and fluorescence microscopy). On the other hand, when the levels of H_2O_2 were between 50 μM and 10 mM the viscoelastic/morphology changes of the cell monolayers were irreversible, presenting a shrinkage of the cytoskeleton with a decrease in cell density, which was also supported by viability assays. This demonstrated that QCM-D allows to estimate with ease the viscoelastic properties of cells and can be used to investigate cell recovery from oxidative stress, enabling to distinguish between oxidative eustress and distress. The technique could also potentially be used to screen for antioxidants able to reduce cells' oxidative distress without suppressing oxidative eustress.

5 QCM and QCM-D for Drug Development and Quality Control

As described in the sections above, QCM and QCM-D can be used to understand the interactions between a functionalized crystal surface and particles (or biomolecules or chemicals), which is extremely useful for many different applications. The sensitivity and the ease of use of QCM have let researchers to explore the technique as a tool to either screen new drugs or to aid the quality control of existing drugs in the pharmaceutical industry.

In the last 10–15 years, recombinant antibodies have become a powerful therapeutic option for clinicians to treat a variety of conditions either cancer-related (particularly blood cancer) or non-cancer-related (autoimmune disease, infectious disease, ophthalmic, dermatologic and respiratory disorders) [59]. Every year since 2014, between 6 and 12 new therapeutic antibodies (Ab) have been granted first approval in the USA and in Europe [60]. Therapeutic Ab is usually administered intravenously, but researchers are currently investigating alternative routes of administration that are less invasive allowing patients to self-medicate and become more compliant with treatments. Injecting the respective Ab subcutaneously is one of the modes of administration currently considered. This route requires using small injection volumes, in the order of 1–1.5 mL. In turn, this means that antibody concentrations in the injection dose need to be much higher (150–200 mg mL^{-1}) as compared to intravenous injections [61]. Antibody solutions containing such high concentrations deteriorate by aggregation or precipitation. Therefore, one needs to add excipients to stabilize the Ab solution. Screening and selecting the excipient, complying best with pharmaceutical formulations in vitro, is challenging as solutions with high protein concentrations tend to be highly viscous. Therefore, most common analytical techniques, such as static or dynamic light scattering require to dilute the solutions to obtain meaningful results [62]. On the contrary, Hartl and colleagues [63] have demonstrated that QCM-D can be used as a high-frequency rheology tool to study the changes of highly concentrated solutions of monoclonal Ab in the presence of excipients. For the analysis, the crystal surface, resonating at 5 MHz, was firstly passivated with poly-L-lysine-graft-poly(ethylene glycol) to reduce the adsorption of the proteins on the surface. Then, they measured changes in frequency and dissipation at several overtones. As the solutions display viscoelastic behavior, both Δf and the ΔD (or $\Delta\Gamma$, where Γ is the shift at half-bandwidth, with $\Delta D = 2\Gamma/f$) were then fitted into a Maxwell model allowing to obtain information on the shear modulus at relaxation time, τ, and the shear modulus at the inverse relaxation time, G^* (at the "cross-over frequency" $\omega_c = 1/\tau$, where ω is frequency) of the highly concentrated protein solution in contact with the crystal. This enabled the group to understand the effect of the two chosen excipients (histidine and citrate) on the Ab solution and therefore to select the most suitable.

The presence of sub-visible (2–100 μm) protein particles (protein aggregates) and non-protein particles (silicone or air bubbles) is another important parameter that needs monitoring in pre-filled, silicone-coated syringes containing therapeutic

proteins. Formation of such particles indicates the deterioration of the liquid contained in the syringe. Therefore, suitable stabilizers need to be identified and added to prolong the shelf-life of the liquid contained in the syringe. Currently, there are not many analytical techniques that permit one to identify suitable stabilizers that are capable to alter or delay the formation of protein and non-protein particles. Zheng and colleagues [8] proposed the use of micro-flow imaging (MFI), a microscopy-based dynamic imaging system, that allows for evaluating particle sizes and their shapes in the micro-range. The group used MFI to study the effect of an anionic surfactant polysorbate (PS-80) on the formation of such micro-range particles. They observed that the presence of PS-80 under stirring strongly delays particle formation. To better understand the surfactant's effect at the nano-level, the group exploited the "nano" sensitivity of QCM-D. For the study, gold crystals were first coated with silicon oil. These were then equilibrated in a buffer without surfactant and exposed to solutions of therapeutic proteins with and without PS-80, while recording both Δf and ΔD. The Voigt viscoelastic model was applied for the data analysis based on the positive changes seen in dissipation. The modeling involved fitting-simulated frequency changes to the experimental profiles until obtaining a satisfactory fit. The QCM results indicate that PS-80 most likely interacts with the hydrophobic parts of the proteins thus minimizing aggregation. The QCM data also further demonstrated that PS-80 most likely was able to block the leakage of silicone from syringe walls into solution thus reducing the formation of silicone particles and prolonging the shelf-life of the drug.

Regarding the use of QCM in the pharmaceutical industry, a few studies reported in the literature have highlighted the use of QCM to characterize metered-dose inhalers (MDI), which are commonly used to deliver drugs directly to the bronchi and lungs when treating respiratory disorders and chronic conditions, such as asthma. MDI contains a therapeutically active ingredient (drug) together with excipients (e.g., lactose, surfactant, etc.), dissolved or suspended in a propellant in a compact pressurized aerosol dispenser. Particle size is one of the most important factors influencing deposition of the active MDI drugs in the lungs. The size distribution of pharmaceutical aerosols is commonly measured by the Andersen Mark II cascade impactor (a flow system to deliver the inhaler for the analysis). It determines particle sizes based on inertial separation, followed by UV/high-performance liquid chromatography (HPLC) analysis of the deposited particles [64–66]. Although efficient, the technique is time consuming and expensive. Therefore, one study [67] has investigated whether a QCM impactor that includes the crystal in the impactor could be used to assess particle sizes in MDI in real time, providing a fast and cheap analysis. Five MDI formulations were studied: three contained high amounts of surfactant, one with a high drug loading, and one with an additional excipient (menthol). Similarly to Andersen impactor, cut-offs in a range of sizes were used in the QCM impactor to enable only specific particles size reaching the crystal for their mass quantitation. The particle distributions in the inhalers, obtained by QCM, were then compared with those achieved measuring the same samples with the Andersen impactor. The results showed that for most measurements the two techniques agreed, demonstrating that QCM have the potential to

replace the more expensive and time-consuming analytical device to estimate MDI particles distribution.

In our group, we have also investigated the use of QCM to characterize MDI as well as multi-dose powder inhalers (MDPI). The latter are a similar type of inhaler, which contains and dispenses the therapeutic drug as dry powder rather than as an aerosol. As mentioned above, inertial separation methods [66] as well as laser diffraction analysis are used to determine the particle size of MDI [68]. Similarly, isothermal microcalorimetry, X-ray diffraction, and scanning electron microscopy have been used to determine powder morphology and electrostatic charges in MDPI [69]. However, to date, no analytical tools exist to monitor the quality of materials in both MDI and MDPI during and after manufacturing. Therefore, we explored whether QCM could be used to both optimize the composition during the inhalers' development and for post-manufacturing quality control [11]. In one case, QCM was used to explore particle-surface and particle-particle macroscale interactions within components typically found in MDPI. For this purpose, some MDPI components (polyvinyl chloride (PVC) and poly acetate) were immobilized on the crystals and others were injected as powder in a gas stream. Figure 8a shows a typical result obtained by exposing a PVC-coated crystal to several injection of the drug fluticasone propionate (FP) powder in an air stream. The results show that although QCM data did not allow to quantify binding among the different components, it was indeed useful to provide qualitative information on the interactions among the several MDPI components, hence, enabling a facile screening of excipients to optimize formulations capable of avoiding drugs' aggregation and/or coagulation.

In the same study, we also explored whether QCM could be useful as an in-line analytical tool for quality control of MDI post manufacturing [11]. For this, a pressurized system was designed and fabricated, which allowed for dispensing the inhalers in a fluoroalkane (HFA) stream (mimicking the manufacturing set up) and with the QCM crystal sitting in-line (Fig. 9).

Then a selection of different FP MDI pedigrees (slightly different formulations) was tested using the QCM pressurized system, while recording the frequency. An example of the results, depicted in Fig. 8b, shows that QCM was indeed able to distinguish MDI with slightly different formulations, proving that it could be used as an in-line analytical instrument for quality control of MDI during or post manufacturing.

6 Conclusions

The ability of QCM to characterize chemicals, biomolecules, and particles both at the "nano" and "macro" level has made the corresponding techniques a powerful tool not only in diagnostics, but for characterizing materials in several scientific fields, from the medical to the energy sectors. The variety of studies reviewed by this chapter, where QCM has been used to characterize materials (e.g., nanoparticles and thin films) or to understand inter-particles, inter-molecules, and surface-molecule

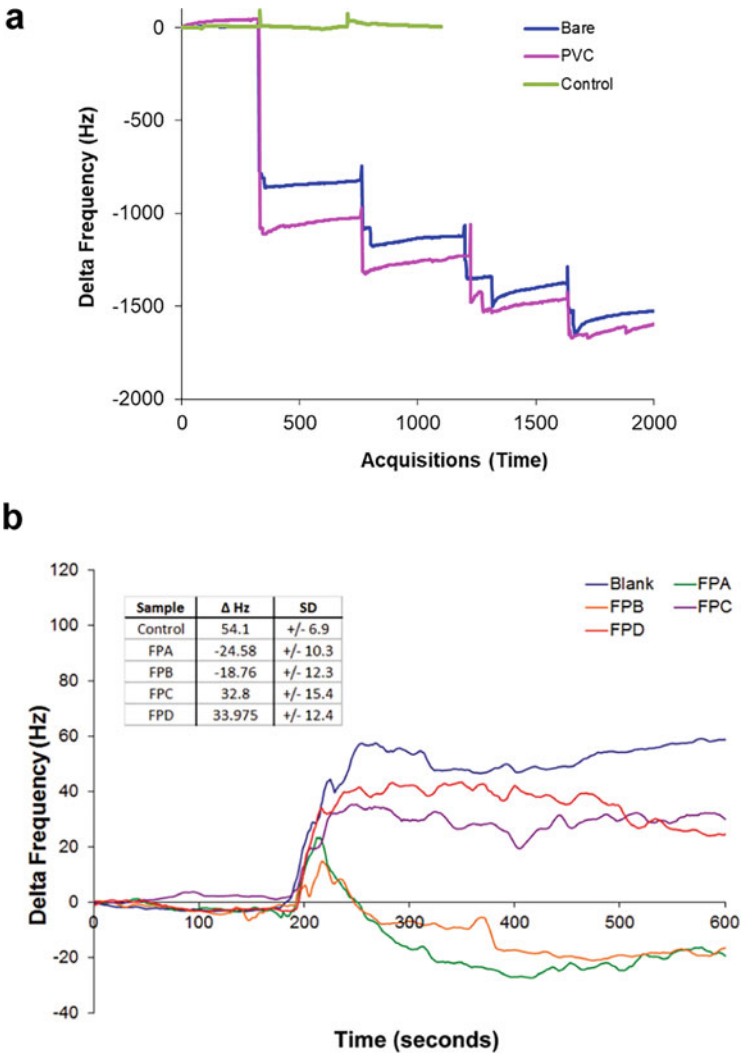

Fig. 8 (**a**) QCM response in gas phase to injections of FP powder using a bare (blue) and PVC modified (pink) surfaces; (**b**) average response of QCM versus unknown FP pedigrees in HFA, and the corresponding control [11]. Reproduced from [11] with permission from the Royal Society of Chemistry

interactions has demonstrated the versatility of the techniques. Nevertheless, whereas it is straightforward to record changes in frequency and dissipation when using QCM, many different mathematical models, whose detailed description was beyond the scope of this chapter, have been presented for the interpretation of the data. This highlights the importance of deeply understanding the physical phenomenon or the material under investigation, before the QCM signals can be used

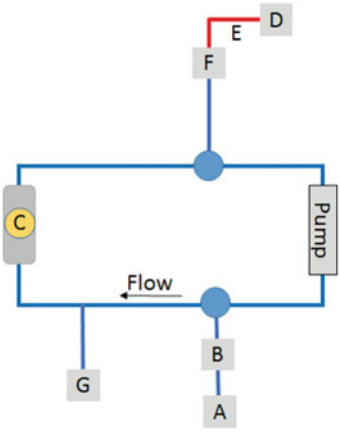

Fig. 9 Schematic of pressurized gas experimental setup. (**A**) Injector port. (**B**) Valve. (**C**) QCM pressure cell. (**D**) Release valve. (**E**) Buffer loop. (**F**) Valve. (**G**) Pressure gauge. Reproduced from permission from [11]

accurately to quantify features or to understand interactions. Despite this, with more mathematical models for QCM data interpretation becoming wildly accepted, the opportunity to manufacture low-cost devices and the ability of the technique to acquire real-time data make QCM a powerful tool in many analytical applications including quality control for in-line manufacturing processes in several industries.

References

1. Reviakine I, Johannsmann D, Richter RP (2011) Hearing what you cannot see and visualizing what you hear: interpreting quartz crystal microbalance data from solvated interfaces. Anal Chem 83. https://doi.org/10.1021/ac201778h
2. Easley AD, Ma T, Eneh CI, Yun J, Thakur RM, Lutkenhaus JL (2022) A practical guide to quartz crystal microbalance with dissipation monitoring of thin polymer films. J Polym Sci 60
3. Rodahl M, Höök F, Krozer A, Brzezinski P, Kasemo B (1995) Quartz crystal microbalance setup for frequency and Q-factor measurements in gaseous and liquid environments. Rev Sci Instrum 66. https://doi.org/10.1063/1.1145396
4. Rodahl M, Höök F, Fredriksson C, Keller CA, Krozer A, Brzezinski P, Voinova M, Kasemo B (1997) Simultaneous frequency and dissipation factor QCM measurements of biomolecular adsorption and cell adhesion. Faraday Discuss 107. https://doi.org/10.1039/a703137h
5. Shpigel N, Sigalov S, Malchik F, Levi MD, Girshevitz O, Khalfin RL, Aurbach D (2019) Quantification of porosity in extensively nanoporous thin films in contact with gases and liquids. Nat Commun 10. https://doi.org/10.1038/s41467-019-12277-4
6. Kanazawa KK, Gordon JG (1985) Frequency of a quartz microbalance in contact with liquid. Anal Chem 57. https://doi.org/10.1021/ac00285a062
7. Dunér G, Thormann E, Dedinaite A (2013) Quartz crystal microbalance with dissipation (QCM-D) studies of the viscoelastic response from a continuously growing grafted polyelectrolyte layer. J Colloid Interface Sci 408. https://doi.org/10.1016/j.jcis.2013.07.008
8. Zheng S, Puri A, Li J, Jaiswal A, Adams M (2017) Particle characterization for a protein drug product stored in pre-filled syringes using micro-flow imaging, archimedes, and quartz crystal microbalance with dissipation. AAPS J 19. https://doi.org/10.1208/s12248-016-9983-1

9. Sebastiani F, Yanez Arteta M, Lindfors L, Cárdenas M (2022) Screening of the binding affinity of serum proteins to lipid nanoparticles in a cell free environment. J Colloid Interface Sci 610. https://doi.org/10.1016/j.jcis.2021.11.117
10. Migoń D, Wasilewski T, Suchy D (2020) Application of QCM in peptide and protein-based drug product development. Molecules 25
11. Turner NW, Bloxham M, Piletsky SA, Whitcombe MJ, Chianella I (2017) The use of a quartz crystal microbalance as an analytical tool to monitor particle/surface and particle/particle interactions under dry ambient and pressurized conditions: a study using common inhaler components. Analyst 142. https://doi.org/10.1039/c6an01572g
12. Gillissen JJJ, Tabaei SR, Jackman JA, Cho NJ (2017) A model derived from hydrodynamic simulations for extracting the size of spherical particles from the quartz crystal microbalance. Analyst 142. https://doi.org/10.1039/c7an00456g
13. Gillissen JJJ, Jackman JA, Tabaei SR, Yoon BK, Cho NJ (2017) Quartz crystal microbalance model for quantitatively probing the deformation of adsorbed particles at low surface coverage. Anal Chem 89. https://doi.org/10.1021/acs.analchem.7b03179
14. Adamczyk Z, Sadowska M, Żeliszewska P (2020) Applicability of QCM-D for quantitative measurements of nano- and microparticle deposition kinetics: theoretical modeling and experiments. Anal Chem 92. https://doi.org/10.1021/acs.analchem.0c03115
15. van der Westen R, van der Mei HC, De Raedt H, Olsson ALJ, Busscher HJ, Sharma PK (2016) Quantification of the viscoelasticity of the bond of biotic and abiotic particles adhering to solid-liquid interfaces using a window-equipped quartz crystal microbalance with dissipation. Colloids Surf B Biointerfaces 148. https://doi.org/10.1016/j.colsurfb.2016.08.062
16. Van Der Westen R, Sharma PK, De Raedt H, Vermue I, Van Der Mei HC, Busscher HJ (2017) Elastic and viscous bond components in the adhesion of colloidal particles and fibrillated streptococci to QCM-D crystal surfaces with different hydrophobicities using kelvin-Voigt and Maxwell models. Phys Chem Chem Phys 19. https://doi.org/10.1039/c7cp04676f
17. Zhuang H, Lu P, Lim SP, Lee HP (2008) Study of the evaporation of colloidal suspension droplets with the quartz crystal microbalance. Langmuir 24. https://doi.org/10.1021/la800661g
18. Edvardsson M, Rodahl M, Kasemo B, Höök F (2005) A dual-frequency QCM-D setup operating at elevated oscillation amplitudes. Anal Chem 77. https://doi.org/10.1021/ac050116j
19. Edvardsson M, Rodahl M, Höök F (2006) Investigation of binding event perturbations caused by elevated QCM-D oscillation amplitude. Analyst 131. https://doi.org/10.1039/b601800a
20. Borenstein A, Hanna O, Attias R, Luski S, Brousse T, Aurbach D (2017) Carbon-based composite materials for supercapacitor electrodes. A review. J Mater Chem A Mater:5
21. Romero Guerra M, Chianella I, Piletska EV, Karim K, Turner APF, Piletsky SA (2009) Development of a piezoelectric sensor for the detection of methamphetamine. Analyst 134. https://doi.org/10.1039/b819351g
22. D'Aurelio R, Tothill IE, Salbini M, Calò F, Mazzotta E, Malitesta C, Chianella I (2021) A comparison of EIS and QCM NanoMIP-based sensors for morphine. Nanomaterials 11. https://doi.org/10.3390/nano11123360
23. O'Neal JT, Dai EY, Zhang Y, Clark KB, Wilcox KG, George IM, Ramasamy NE, Enriquez D, Batys P, Sammalkorpi M et al (2018) QCM-D investigation of swelling behavior of layer-by-layer thin films upon exposure to monovalent ions. Langmuir 34. https://doi.org/10.1021/acs.langmuir.7b02836
24. Antonio JLS, Martins VL, Córdoba de Torresi SI, Torresi RM (2019) QCM-D study of electrochemical synthesis of 3D polypyrrole thin films for negative electrodes in supercapacitors. Electrochim Acta 324. https://doi.org/10.1016/j.electacta.2019.134887
25. Vidyasagar A, Sung C, Losensky K, Lutkenhaus JL (2012) PH-dependent thermal transitions in hydrated layer-by-layer assemblies containing weak polyelectrolytes. Macromolecules 45. https://doi.org/10.1021/ma3020454
26. Vidyasagar A, Sung C, Gamble R, Lutkenhaus JL (2012) Thermal transitions in dry and hydrated layer-by-layer assemblies exhibiting linear and exponential growth. ACS Nano 6. https://doi.org/10.1021/nn301526b

27. Levi MD, Shpigel N, Sigalov S, Dargel V, Daikhin L, Aurbach D (2017) In situ porous structure characterization of electrodes for energy storage and conversion by EQCM-D: a review. Electrochim Acta 232. https://doi.org/10.1016/j.electacta.2017.02.149
28. Voinova MV, Rodahl M, Jonson M, Kasemo B (1999) Viscoelastic acoustic response of layered polymer films at fluid-solid interfaces: continuum mechanics approach. Phys Scr 59. https://doi.org/10.1238/physica.regular.059a00391
29. Alkekhia D, Hammond PT, Shukla A (2020) Layer-by-layer biomaterials for drug delivery. Annu Rev Biomed Eng 22
30. Ariga K, Lvov YM, Kawakami K, Ji Q, Hill JP (2011) Layer-by-layer self-assembled shells for drug delivery. Adv Drug Deliv Rev 63
31. Zhang X, Liang T, Ma Q (2021) Layer-by-layer assembled nano-drug delivery systems for cancer treatment. Drug Deliv 28. https://doi.org/10.1080/10717544.2021.1905748
32. Erkmen C, Selcuk O, Unal DN, Kurbanoglu S, Uslu B (2022) Layer-by-layer modification strategies for electrochemical detection of biomarkers. Biosens Bioelectron X 12. https://doi.org/10.1016/j.biosx.2022.100270
33. Wang Y, Zhan X (2016) Layer-by-layer processed organic solar cells. Adv Energy Mater 6. https://doi.org/10.1002/aenm.201600414
34. Sun R, Guo J, Sun C, Wang T, Luo Z, Zhang Z, Jiao X, Tang W, Yang C, Li Y et al (2019) A universal layer-by-layer solution-processing approach for efficient non-fullerene organic solar cells. Energ Environ Sci 12. https://doi.org/10.1039/c8ee02560f
35. Dubas ST, Schlenoff JB (2001) Polyelectrolyte multilayers containing a weak polyacid: construction and deconstruction. Macromolecules 34. https://doi.org/10.1021/ma001720t
36. Gui Z, Du B, Qian J, An Q, Zhao Q (2011) Construction and deconstruction of multilayer films containing polycarboxybetaine: effect of PH and ionic strength. J Colloid Interface Sci 353. https://doi.org/10.1016/j.jcis.2010.09.026
37. Schoeler B, Kumaraswamy G, Caruso F (2002) Investigation of the influence of polyelectrolyte charge density on the growth of multilayer thin films prepared by the layer-by-layer technique. Macromolecules 35. https://doi.org/10.1021/ma011349p
38. Okutan M, Deligöz H (2019) Effect of external salt addition on the structural, morphological and electrochemical properties of flexible PEDOT:PSS based LbL multilayered films. Colloids Surf A Physicochem Eng Asp 580. https://doi.org/10.1016/j.colsurfa.2019.123695
39. Ghostine RA, Jisr RM, Lehaf A, Schlenoff JB (2013) Roughness and salt annealing in a polyelectrolyte multilayer. Langmuir 29. https://doi.org/10.1021/la401632x
40. Salomäki M, Kankare J (2008) Specific anion effect in swelling of polyelectrolyte multilayers. Macromolecules 41. https://doi.org/10.1021/ma800315j
41. Kurapati R, Groth TW, Raichur AM (2019) Recent developments in layer-by-layer technique for drug delivery applications. ACS Appl Bio Mater 2. https://doi.org/10.1021/acsabm.9b00703
42. Borges J, Sousa MP, Cinar G, Caridade SG, Guler MO, Mano JF (2017) Nanoengineering hybrid supramolecular multilayered biomaterials using polysaccharides and self-assembling peptide amphiphiles. Adv Funct Mater:27. https://doi.org/10.1002/adfm.201605122
43. Sergeeva YN, Huang T, Felix O, Jung L, Tropel P, Viville S, Decher G (2016) What is really driving cell–surface interactions? Layer-by-layer assembled films may help to answer questions concerning cell attachment and response to biomaterials. Biointerphases 11. https://doi.org/10.1116/1.4943046
44. Yılmaz Aykut D, Yolaçan Ö, Deligöz H (2020) PH stimuli drug loading/release platforms from LbL single/blend films: QCM-D and in-vitro studies. Colloids Surf A Physicochem Eng Asp 602. https://doi.org/10.1016/j.colsurfa.2020.125113
45. Du Y, Jin J, Jiang W (2018) A study of polyethylene glycol backfilling for enhancing target recognition using QCM-D and DPI. J Mater Chem B 6. https://doi.org/10.1039/C8TB01526K
46. Wasserberg D, Cabanas-Danés J, Subramaniam V, Huskens J, Jonkheijm P (2018) Orthogonal supramolecular protein assembly on patterned bifunctional surfaces. Chem Commun 54. https://doi.org/10.1039/c7cc09808a

47. Goor OJGM, Bosmans RPG, Brunsveld L, Dankers PYW (2017) Cucurbituril-mediated immobilization of fluorescent proteins on supramolecular biomaterials. J Polym Sci A Polym Chem 55. https://doi.org/10.1002/pola.28743
48. Guan ZY, Huang CW, Huang MC, Wu CY, Liu HY, Ding ST, Chen HY (2017) Controlling multi-function of biomaterials interfaces based on multiple and competing adsorption of functional proteins. Colloids Surf B Biointerfaces 149. https://doi.org/10.1016/j.colsurfb.2016.10.005
49. Cho NJ, Frank CW, Kasemo B, Höök F (2010) Quartz crystal microbalance with dissipation monitoring of supported lipid bilayers on various substrates. Nat Protoc 5. https://doi.org/10.1038/nprot.2010.65
50. Cho N-J, Cheong KH, Lee C, Frank CW, Glenn JS (2007) Binding dynamics of hepatitis C virus' NS5A amphipathic peptide to cell and model membranes. J Virol 81. https://doi.org/10.1128/jvi.02783-06
51. Yorulmaz S, Jackman JA, Hunziker W, Cho NJ (2015) Supported lipid bilayer platform to test inhibitors of the membrane attack complex: insights into biomacromolecular assembly and regulation. Biomacromolecules 16. https://doi.org/10.1021/acs.biomac.5b01060
52. Yorulmaz S, Jackman JA, Hunziker W, Cho NJ (2016) Influence of membrane surface charge on adsorption of complement proteins onto supported lipid bilayers. Colloids Surf B Biointerfaces 148. https://doi.org/10.1016/j.colsurfb.2016.08.036
53. Anderson TH, Min Y, Weirich KL, Zeng H, Fygenson D, Israelachvili JN (2009) Formation of supported bilayers on silica substrates. Langmuir 25. https://doi.org/10.1021/la900181c
54. Kushiro K, Lee CH, Takai M (2016) Simultaneous characterization of protein-material and cell-protein interactions using dynamic QCM-D analysis on SAM surfaces. Biomater Sci 4. https://doi.org/10.1039/c5bm00613a
55. Kao WL, Chang HY, Lin KY, Lee YW, Shyue JJ (2017) Effect of surface potential on the adhesion behavior of NIH3T3 cells revealed by quartz crystal microbalance with dissipation monitoring (QCM-D). J Phys Chem C 121. https://doi.org/10.1021/acs.jpcc.6b11217
56. Saitakis M, Gizeli E (2012) Acoustic sensors as a biophysical tool for probing cell attachment and cell/surface interactions. Cell Mol Life Sci 69
57. Tymchenko N, Nileba E, Voinova MV, Gold J, Kasemo B, Svedhem S (2012) Reversible changes in cell morphology due to cytoskeletal rearrangements measured in real-time by QCM-D. Biointerphases 7. https://doi.org/10.1007/s13758-012-0043-9
58. Shoaib S, Tabrizian M (2019) A QCM-D sensing strategy for investigating the real-time effects of oxidative stress on the viscoelastic properties of pre-osteoblast cells. Sens Actuators B Chem 293. https://doi.org/10.1016/j.snb.2019.04.154
59. Leavy O (2010) Therapeutic antibodies: past, present and future. Nat Rev Immunol:10
60. Al Ojaimi Y, Blin T, Lamamy J, Gracia M, Pitiot A, Denevault-Sabourin C, Joubert N, Pouget JP, Gouilleux-Gruart V, Heuzé-Vourc'h, N. et al (2022) Therapeutic antibodies – natural and pathological barriers and strategies to overcome them. Pharmacol Ther:233
61. Garidel P, Kuhn AB, Schäfer LV, Karow-Zwick AR, Blech M (2017) High-concentration protein formulations: how high is high? Eur J Pharm Biopharm 119. https://doi.org/10.1016/j.ejpb.2017.06.029
62. Muschol M, Rosenberger F (1995) Interactions in undersaturated and supersaturated lysozyme solutions: static and dynamic light scattering results. J Chem Phys 103. https://doi.org/10.1063/1.469891
63. Hartl J, Peschel A, Johannsmann D, Garidel P (2017) Characterizing protein-protein-interaction in high-concentration monoclonal antibody systems with the quartz crystal microbalance. Phys Chem Chem Phys 19. https://doi.org/10.1039/c7cp05711c
64. Stein SW (1999) Size distribution measurements of metered dose inhalers using Andersen mark II Cascade impactors. Int J Pharm 186. https://doi.org/10.1016/S0378-5173(99)00136-2
65. Bonam M, Christopher D, Cipolla D, Donovan B, Goodwin D, Holmes S, Lyapustina S, Mitchell J, Nichols S, Pettersson G et al (2008) Minimizing variability of Cascade impaction measurements in inhalers and nebulizers. AAPS PharmSciTech 9

66. Holzner PM, Müller BW (1995) Particle size determination of metered dose inhalers with inertial separation methods: apparatus A and B (BP), four stage Impinger and Andersen mark II Cascade impactor. Int J Pharm 116. https://doi.org/10.1016/0378-5173(94)00263-5
67. Tzou TZ (1999) Aerodynamic particle size of metered-dose inhalers determined by the quartz crystal microbalance and the Andersen Cascade impactor. Int J Pharm 186. https://doi.org/10.1016/S0378-5173(99)00139-8
68. Jones SA, Martin GP, Brown MB (2005) High-pressure aerosol suspensions – a novel laser diffraction particle sizing system for hydrofluoroalkane pressurised metered dose inhalers. Int J Pharm 302. https://doi.org/10.1016/j.ijpharm.2005.07.001
69. Murtomaa M, Strengell S, Laine E, Bailey A (2003) Measurement of electrostatic charge of an aerosol using a grid-probe. J Electrostat 58. https://doi.org/10.1016/S0304-3886(03)00048-2

Robust QCM-Based Sensing and Assay Formats in Commercialized Systems

Claudia Durall, Daniel Wallinder, Ahmed Ibrahim, Andreas Nolting, Mahmoud Almajdoub, Nicholas Jones, Subramanian Suriyanarayanan, Ian A. Nicholls, and Teodor Aastrup

Contents

Abstract Attana's Quartz Crystal Microbalance (QCM) analytical instruments have been developed to study in vitro biological interactions, mimicking the in vivo conditions. Attana's superior technology for kinetic interaction studies allows to perform different assays, including biochemical, crude, sera, cell, and

C. Durall, D. Wallinder, A. Ibrahim, A. Nolting, M. Almajdoub, and T. Aastrup (✉)
Attana AB, Stockholm, Sweden
e-mail: claudia.durall@attana.com; daniel.wallinder@attana.com; ahmed.ibrahim@attana.com; andreas.nolting@attana.com; mahmoud.almajdoub@attana.com; teodor.aastrup@attana.com

N. Jones
Withers and Rogers LLP, London, UK
e-mail: njones@withersrogers.com

S. Suriyanarayanan and I. A. Nicholls
Department of Chemistry and Biomedical Sciences, Linnaeus University, Kalmar, Sweden
e-mail: subramanian.suriyanarayanan@lnu.se; ian.nicholls@lnu.se

P. Lieberzeit (ed.), *Piezoelectric Sensors*, Springer Series on Chemical Sensors and Biosensors (2024) 18: 105–142, https://doi.org/10.1007/5346_2023_29,

Published online: 7 November 2023

tissue-based, in vitro diagnostic and material chemistry assays, in real time and label free. With the focus to validate, select, and optimize drug candidates prior to clinical trials, Attana has helped pharmaceutical companies to increase their efficiency and profitability. In addition, the Attana instruments and services have been used in many other applications and research as described in this chapter.

Keywords Biochemical assays, Cell-based assays, Drug discovery, In vitro diagnostics, Kinetics, Material science, Tissue-based assays

1 Introduction

Attana was founded in 2002 with the intention of building a high precision QCM technology and therefore characterize molecular interactions exactly as they occur in the human body, basically with the principle of predicting in vivo results through in vitro assays. Since then, a proprietary label-free biosensor instrument for biochemical, crude, sera, whole blood, cell and tissue-based assays as well as the Attana Virus Analytics (AVA™) platform – a proprietary in vitro diagnostics (IVD) tool was developed. The proprietary products and services have been developed for life science industries like Big Pharma, biotech companies, and academic institutions as well as diagnostic tools for research.

The Attana's Quartz Crystal Microbalance (QCM) technology is optimized for real-time analysis and shown to be very versatile and can determine specificity, kinetics, and affinity, among other binding characteristics of biomolecules and macrostructures varying species such as purified proteins, DNA, particles like nanoparticles or virus-like particles, viruses, fixed or non-fixed cells (including suspension or adherent cells) and tissues [1–6]. In addition, crude extracts, sera, or even whole blood can be used in the system as the technology is not based on optical measurements. Attana offers a wide range of services (selling/renting instruments (including preventive maintenance), contract research, development of assays, and more.

It is known that the process from drug discovery to regulatory review and approval is long and expensive (estimated cost 2 billion USD) (Fig. 1a) and only one out of 10 candidates entering clinical trials is approved. The QCM technology, with exceptional accuracy, can measure and analyze the efficacy of drug candidates and the potential side effects – prior to starting clinical trials (Fig. 1b). The results from Attana have shown a 100% success rate in clinical trials, saving 50% of the clinical trial cost (average per costumer) as well as increasing the probability of success from phase I to approval by 4.4x. In addition, the QCM instruments have been widely used in academic and research institutes and biopharma companies, and for many applications as it is discussed in Sect. 3.

The process of screening and validating drugs involves the initial assessment where candidates are studied as well as the potential success is ranked (Fig. 2a). In

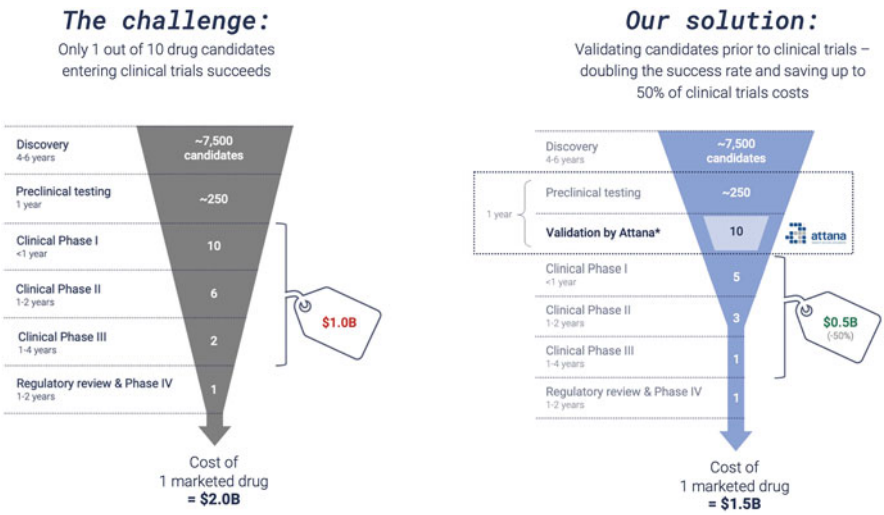

Fig. 1 Pipeline and cost from drug discovery to approval. (**a**) Traditional process where only one out of 10 drug candidates entering clinical trials succeeds, (**b**) Process where the drug candidates have been validated by Attana prior to clinical trials. The success rate is doubled, saving up to 50% of clinical costs

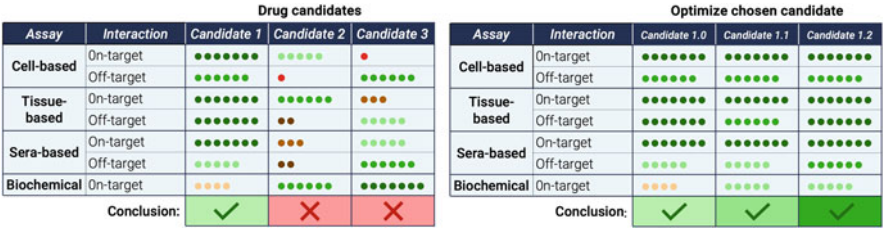

Fig. 2 Example of how Attana ranks drug candidates. (**a**) Example of validation and selection candidates for clinical trials, (**b**) Example of optimization of a selected candidate

some cases, modification of the drug is not needed but, in some others, optimization is recommended (Fig. 2b).

So far, 103 candidates for Pharmaceutical Drug Development prior to entering in clinical trials were analyzed by the Attana technology. 67 of the candidates were not approved by our assays showing either poor safety or efficacy. This was proven, since one candidate entered the clinical trials and failed in phase II (Fig. 3). The other 36 candidates were approved and validated by QCM instruments and analysis. However, 24 of 36 did not have financing for clinical studies while the other 12 candidates entered clinical trials. All candidates are still in the clinical trial pipeline showing the high success of the Attana's experiments and analysis. (Please

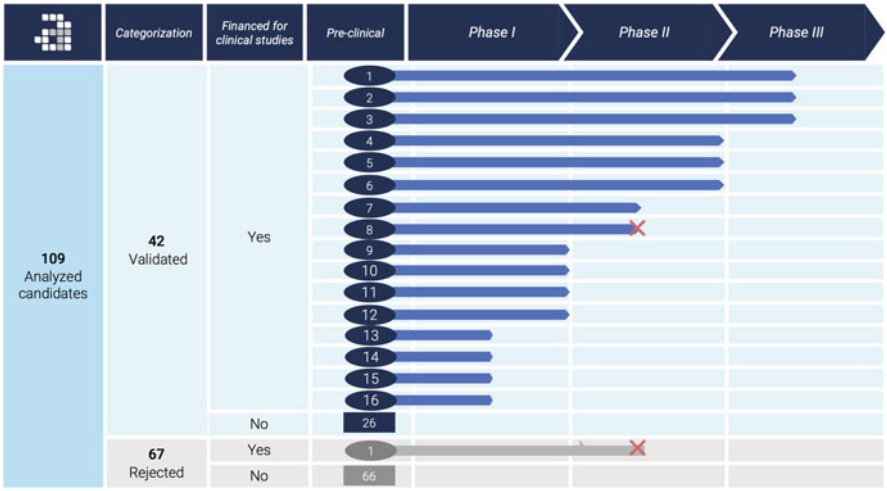

Fig. 3 Attana's track record in 2023 where 100+ analyzed candidates has so far shown the Attana's QCM technology has a high accuracy in determining which candidates will succeed in clinical trials as well as improving clinical trials success rates and increasing productivity

note that candidate 7 was interrupted of clinical trials because a competitor released a similar drug (Fig. 3).

Since the advent of COVID-19, our company has focused on developing an IVD tool and further showed their reliability and versatility. As a result, Attana launched the Attana Virus Analytics (AVA™) platform which is a genetic tool for diagnostics. In addition, the AVA™ SARS-CoV-2 IgG Immunoassay was CE certified and registered under the Swedish Medical Products Agency's Regulation (LVFS 2001: 7) on in vitro diagnostic medical devices as a General IVDD (for professional use).

2 QCM Technology

The Attana QCM biosensor instruments is a superior technology for high quality kinetic interaction studies. The advantages of the fully automated instrument include (i) dual-channel (one for experiments, one for referencing) (ii) continuous flow, (iii) flow rate control, (iv) temperature control, (v) automated injections, (vi) real-time monitoring of data acquisition, (vii) label-free technology, and (viii) effective intra- and inter-referencing and data analysis (Fig. 4).

Fig. 4 The Attana A250 instrument. Numbers indicate the different hardware components where 1 corresponds to the Attana measuring unit, 2 – C-fast robot, 3 – Solvent tray, 4 – Cooling unit with the analyte plates, and 5 – Wash tray

2.1 Instrument

To meet the requirement of sensitivity, reproducibility, and robustness, the instrument must fulfill demands on the fluidic system, temperature control, electronic circuit (oscillator and measurement system), and sample handling. For optimization of the system, one must often consider requirements which contradict each other. For example, to minimize sample consumption, narrow dimensions of the fluidic system are preferable, but on the other hand it increases the risk for clogging and system failure.

2.1.1 Temperature Control

The temperature sensitivity of quartz crystals varies greatly with the crystallographic cut. AT cut is usually preferred for QCM applications due to its relatively flat temperature-frequency curve around room temperature. However, the actual value depends also on factors such as frequency, size, mounting technique, oscillator electronics and loading of the crystal. For QCM applications in liquid the temperature sensitivity will be higher compared to gaseous applications due to the viscous loading of the surface. Any temperature variation will also change the density and viscosity of the liquid and influence the frequency.

To achieve sub-Hertz resolution a temperature stability of around 0.01°C is usually required for liquid applications. If a continuous liquid flow is used care must be taken so the liquid is temperature stabilized before it arrives to the sensor

cell. When a reference channel is used, it is also of importance to minimize any temperature variation between the channels.

The properties of the electronic components of the oscillator and the frequency measurements will also be affected by the temperature. Therefore, the oscillator circuit should also be temperature stabilized. For frequency measurement, an oven control oscillator gives sufficient stability.

2.1.2 Fluidic System

To deliver the sample to the sensor cell a continuous flow system is convenient where the sample is incorporated to the flow as plug before the sample reaches the sensor cell. To avoid dispersion of the sample the fluidic volume between the sample introduction and sensor cell should be as small as possible. On the other hand, narrow fluidics increase the risk for clogging and the time for sample introduction must long enough to be sufficient to equalize the temperature to the sensor cell temperature.

To drive the flow one or more pumps are needed. Since the crystal is sensitive to pressure variations, the pump chosen should have low flow variations to avoid noise and the flow rate should be relatively insensitive to back pressure to deliver a precise flow over time.

The pulse variations from the pump can be handled by increasing the compliance in the system (for instance, by using soft tubing or reservoir), this will cause some time delay for the flow to stabilize after a flow-change or when injecting a sample with considerably higher or lower viscosity than the buffer.

Since air bubbles on the sensor surface will disturb the measurements, care must be taken to degassing the buffer and avoid the introduction of air when injecting sample. An in-line continuous degassing system is preferable since the uptake of air to a degassed buffer is relatively fast.

The sensor cell design is the most sensitive part of the fluidic system. For demanding applications, like kinetic measurements of biological systems, one should avoid mass transport limitations and limit dispersion of the sample. Therefore, a large sensor cell must be avoided. With a small cross-section of the cell a high flow velocity can be achieved with moderate flow rate, which gives the advantage to consume less sample (which can be expensive) alternatively allows longer contact times. Besides requirements on the size of the sensor cell, it is important that the cell sealing and contacts do not clamp the crystal too much which will severely decrease the Q-value and increase the temperature sensitivity. Attana has addressed these issues with a disposable single use sensor chip which can easily be inserted to the instrument and dock to the fluidic system.

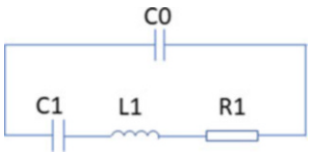

Fig. 5 Crystal equivalent circuit

2.1.3 Crystal/Oscillator

The frequency of crystal vibration is mainly determined by cut, size, and shape of the crystal. Attana uses AT-cut crystals which vibrate in thickness shear mode (BAW) at 10 MHz fundamental frequency which has shown to give high sensitivity and low noise for kinetic measurements of a wide range of biological systems.

With a circular crystal/sensor area the risk for unwanted vibrational modes is reduced together with high Q-value and low temperature dependence.

To drive the vibration of the crystal an electronic oscillator circuit is needed. Two major types of oscillator circuit can be used for thickness shear mode, either working at near the series resonance or at the parallel resonance. For QCM applications, the series resonance is mainly used, because it reduces the influence of parasitic capacitances, better control of the frequency phase, and easier drive of heavily loaded crystals. The circuit can work with constant amplitude or current or alternatively let the current and amplitude vary freely. For frequency stability it is preferred to work with constant amplitude or current.

The crystal properties can be described with the equivalent electric circuit in Fig. 5, where the L1 is related to the displaced mass, C1 is related to the stored energy during oscillation, R1 is the energy dissipation, C0 is the mainly due static capacitance between the electrodes. L1, C1, and R1 are commonly referred to as the motional branch as it defines the electromechanical characteristics of the resonator. More complicated models are used for describing the properties when working in liquid, but in general, the impedance of the motional branch will increase. In case the impedance of the motional branch is considerably higher than the impedance due to the static capacitance (for instance, when loading the crystal with high viscous liquids), oscillation is not possible unless the C0 compensation can be performed with the oscillator circuit.

For best performance the C0 compensation should be calibrated for each individual oscillator, since parasitic capacitance can vary slightly between each individual circuits.

2.1.4 Sample Handling

In order to get valid and reproducible results when working with sensitive samples such as proteins, virus, cells, etc., special care must be taken with samples. An automated sample handling system avoids differences in handling between operators, operator mistakes, and so on. Also, time-consuming and monotonous work is

avoided. Possibility to store the sample in controlled temperature before the actual measurement is needed for time-consuming measurements and with samples sensitive to temperature.

2.2 Consumables

Given that a suitable measurement unit is in place, the consumables will determine the actual application and information output. Selection of the optimal combination of sensors, reagents, and operating buffers is a critical feature for assay performance. It is also of high importance to understand the intended use of the experimental information. E.g., if the consumables are used for scientific research or for commercial drug development, it will put various degrees of requirements of automation, reproducibility, and traceability.

For QCM-based sensors there are two main different paths to choose. Quartz crystal assembled by the instrument operator or premade sensor chips. Quartz crystals for operator assembly are mainly applicable in the academic field where a high degree of assays freedom is desirable, e.g. performing different surface coatings for developing functional surface. Preassembled sensor chips are preferable for industrial applications or academic research focusing on, e.g., biological studies where influence of operator needs to be eliminated and reproducibility and traceability are of major concern.

Here, we will focus on the requirements of preassembled sensor chips for Life Science and diagnostics. Generally preassembled sensor chips have a functionalized surface to enable that a desired biological interaction occur on the sensor surface and therefore the ligand is immobilized or captured. That interaction is transduced into a measurable signal and consequently analyzed. The most common sensor chips that Attana produces are: (i) low non-specific binding (LNB), (ii) low non-specific binding for cell cultivation (LNB-CC) sensor chips (Note: that LNB and LNB-CC are based on a carboxyl surface), (iii) polystyrene sensor chip, and (iv) the cell optimized polystyrene (COP-1) sensor chip (v) other sensor chips with different chemistries are also available.

2.2.1 Covalent Ligand Immobilization

To obtain a functionalized surface, immobilization chemistry is applied. A frequently used method is to amine coupling a ligand, but other methods such as aldehyde coupling and thiol coupling are also possible. In short, amine coupling uses primary amine groups on the ligand after activation of the surface, whereas aldehyde coupling uses the reaction between oxidated carbohydrates in the ligand and carbohydrazide groups or hydrazine on the surface. Thiol coupling utilizes the thiol-disulfide exchange between thiol groups and active disulfides added either to the ligand or to the surface.

2.2.2 Tag-Based Immobilization

If the ligand has a tag, e.g. from purification steps, it can be used for immobilization. Frequently used tags are biotin, histidine, and glutathione S-transferase. One advantage with tag-immobilization is that the orientation of the immobilization is controlled to where the tag is located. In many cases, that generates a more similar orientation of the immobilized ligand compared to, e.g., amine coupling.

2.2.3 Capturing Approach

Capture assays have some major advantages. They are relatively generic minimizing assay development time since regeneration conditions are usually for the capturing antibody. It is also suitable for unstable ligands sensitive for regeneration since no regeneration of the ligand-analyte is necessary. As with the tag-based immobilization a good control of immobilization orientation is obtained.

Antibody capturing assays can be used for several applications (Fig. 6), such as hybridoma supernatant off-rate screening. Capturing approach can also be combined with tags, where, e.g., an anti-His antibody can be used for capturing His-tag molecules. However, there are certain drawbacks with capturing antibodies. The capturing antibody should preferably have a significant slower off-rate than the ligand-analyte off-rate. From a practical point of view, this usually means that a second assay is necessary for slow off-rates where detailed kinetics is important.

2.2.4 Physisorption Surfaces

The most traditional sensor surface is based on adsorption/physisorption. Adsorption is the process whereby atoms or molecules gather on a surface by means of physical

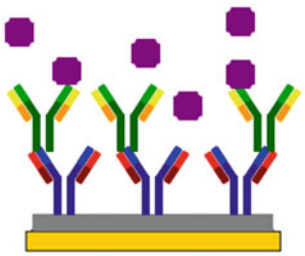

Fig. 6 Depicts a capture assay where a capture molecule (blue/red) is immobilized on a surface. The selected ligand (green/yellow) is captured on the capture molecule. All the ligand molecules will face the same direction, which creates a uniform surface. The analyte (purple) is subsequently injected and the binding and dissociation constants between the ligand and the analyte can be measured. Regeneration strips the surface down to the capture molecule (blue/red) and the cycle can be repeated

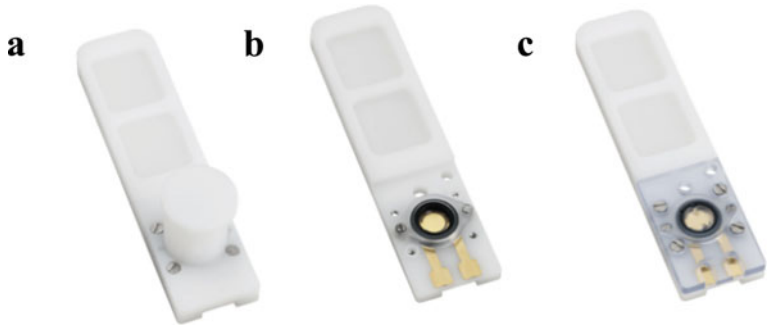

Fig. 7 COP-1 sensor chip. (**a**) Cell chip with cultivation lid, (**b**) without lid for microscopic evaluation and (**c**) with measurement lid

or chemical attraction. The properties of this process are determined by the properties of the molecules, the buffer, and the surface material. For instance, in QCM applications, the binding of a molecule with a polystyrene surface will consist of van der Waals forces (induced dipole–dipole bonds and hydrogen bonds). A more hydrophobic surface gives more induced dipole bonds and less hydrogen bonds. The Attana Polystyrene Sensor surface is used for analysis of proteins or other molecules after immobilization to the surface through adsorption. Unlike conventional studies on polystyrene surfaces in, for instance, ELISA, the Attana instrument provides the possibility to regenerate the surface and expose it to various analyte concentrations with the purpose of determining kinetics and affinity constants. Attana's polystyrene surface is hydrophobic, which ensures stable adsorption of hydrophobic molecules to the surface. The procedure uses ex situ immobilization of the molecule, that is, the immobilization is done in the sensor chip outside of the instrument, and therefore the immobilization level cannot be monitored. Adsorption on a polystyrene surface may be beneficial when other types of binding obscure the sites of interest, as would be the case with e.g. an amine group bound to a carboxyl surface, where the amine site is the site of interest. Many different types of molecules can be adsorbed to the polystyrene surface, such as proteins, peptides, lipids, lipoproteins, and glycolipids.

The Attana COP-1 sensor chip is a polystyrene surface optimized to enable cell growth (Fig. 7). The optimization of polystyrene improves hydrophilicity and wettability as the treatment interacts with the polystyrene, generating a variety of oxygen-containing functionalities, such as C-O, C=O, or COOH at the polymer surface. Wettability has been shown to be an important attribute for cell attachment and downstream cell performance. The wettability of the COP-1 sensor surface is in accordance with the requirement for standard tissue culture surfaces. Functional testing of the COP-1 sensor surfaces can be performed by evaluating attachment and cell growth (Fig. 8), together with interaction analysis.

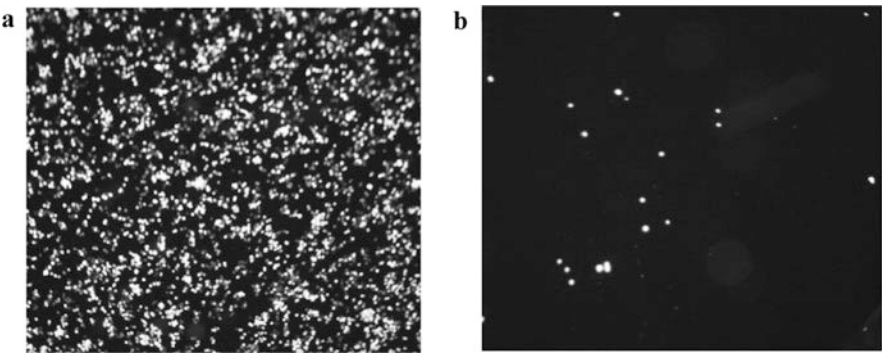

Fig. 8 MDA-MB-468 cells grown 24 h on COP-1, stained with DAPI and visualized under the microscope (**a**) and standard polystyrene surface (**b**)

2.3 Software

Operation of the Attana Cell™ 200/250 system is controlled by Attaché which is the gateway to all Attana software: Attester Software, C-Fast Software, and Evaluation Software. The Attester Software enables real-time monitoring of interactions and data collection. In addition, it controls and monitors the flow rate, the temperature, the degasser, and frequency readouts. It also allows doing manual injections if desired. The C-Fast Software is used for control and programming of the C-Fast for automated experiments. In this case, the C-Fast list is set (flow rate, temperature, volume injected, dissociation time, etc.) and the experiments are performed automatically by the robot (Moduvision technologies) leading to reduce significantly the "hands-on" time. The Evaluation Software is the data handling software used for analysis of experimental data. The evaluation software allows you to subtract blanks, reference (if used), and perform the kinetic analysis as well as off-rate and steady-state equilibrium analysis (Langmuir and Scatchard plotting) and even simulate data.

In addition, in 2022 the Attana Virus Analytics Reporter software was launched. The software allows to analyze the patient data and give the immune profile with detailed information about the quantity of non-specific and specific immune response, the quality of the immune response and the quantification on Immunoglobulin G toward an antigen.

2.4 Intellectual Property (IP)

2.4.1 The Importance of Intellectual Property Protection in the Commercial Environment

In a competitive commercial field, it is important not to neglect intellectual property (IP) protection – both that which may be obtained for your own products and

methods and that which may exist in the hands of your competitors. IP can be a powerful commercial tool, and hence can add significantly to a company's valuation. Equally, an awareness of competitor IP is essential, since infringement of IP can lead to serious consequences, even where at the time of infringement the IP was not known to you.

2.4.2 Use of Intellectual Property Protection for Biosensor Products and Methods

The major types of IP protection – patents, designs, and trademarks – can all be obtained in the biosensor field. When discussing IP protection, it is important to remember that such protection is only likely to have commercial value if the market places a value on what is protected. A granted patent related to a product that the market does not want, and hence one which no competitor would ever seek to make is probably valueless.

In the biosensor field, patents are the most common, and typically most important, form of IP protection and will be dealt with in further detail below. Briefly put, design protection (registered and unregistered) is a lower-cost, readily obtainable form of protection relating to the appearance of products. It can be useful, but for a competitor to infringe a design, its product must typically have a highly similar appearance to that which is covered by the design protection. Trademark protection is primarily aimed at the protection of brands (e.g., company name, product names, logos, etc.) and is intended to prevent others from taking advantage of the reputation of the right-holder by offering products or services connected with names, logos, etc., which are identical or similar to those which are protected.

The patents system is complex. As with the other forms of IP mentioned above, patents are also territorial in nature. Accordingly, despite international harmonization of certain aspects of patent law over the years, multiple different legal systems typically need to be navigated. Plenty of information is freely available regarding major patent offices and the legal frameworks and procedures under which they operate (see, for example, the websites of the European Patent Office (EPO) (https://www.epo.org/), United States Patent and Trademark Office (USPTO) (https://www.uspto.gov/patents), and the World Intellectual Property Organization, which administers the Patent Cooperation Treaty (PCT) system (https://www.wipo.int/pct/en/). However, most companies engage a Patent Attorney to advise them and help them through the various processes, and indeed in many territories the use of a locally qualified Patent Attorney is a legal requirement.

Patents can be obtained for products (apparatus, consumables, sensor chips, etc.), methods (analytical protocols, immobilization methods, methods of enhancing sensitivity, etc.) and, in many territories, uses (that is, new ways of using known products or materials). An important advantage of patent protection for products is that it provides an absolute monopoly, by which it is meant that for a patent to be

infringed, it is merely required that a third-party product falls within the scope of the patent; it is irrelevant whether the third party was aware of the patent at the time the infringing act was carried out. A related advantage of patents lies in the way the scope of protection is assessed. Patents contain one or more claims, which define the protective scope in technical (physical and/or chemical) terms. The claims will aim to define the "inventive concept," rather than being limited to the precise embodiment of that concept which the inventor has produced. As such, infringement may occur when a third party makes a product which merely includes all the technical features required by the patent claim, even if the third-party product looks different, has additional technical features and even if it is an improvement on the patented product.

In order to obtain a patent, most major patent offices require that the claimed invention is novel and possesses an inventive step over existing, publicly available knowledge (the "prior art"). (Industrial applicability is a third criterion in most patent laws, but this is a low hurdle which can generally be ignored in most biosensor-related developments.) Novelty means that the claimed invention is not disclosed as a whole in a single public disclosure made before the effective filing date of the patent application. An inventive step requires (in simplified terms) that the claimed invention would not have been obvious to the skilled person (or team) in the relevant technical field, compared to the prior art as a whole, taking into account the skilled person's "common general knowledge."

There are many freely available online resources which enable searching for prior art. Such a search is often a useful step to take at an early stage in an R&D program, since it can provide an initial indication of what has been done before, who else has been working in the field, and what scope of protection is likely to be available for the product or process being developed. The European Patent Office's "Espacenet" website (https://worldwide.espacenet.com/) is well established, and Google Patents is also popular (https://patents.google.com/). There are also plenty of search companies who offer prior art searches as their core business, and these are typically provided quickly and at relatively low cost.

Assuming that a granted patent can be obtained, it can be used to prevent competitor companies from developing products or methods which fall within the claims of the patent. Fundamentally, this allows the patent holder to operate in the market with reduced competition, and hence greater control over the pricing of its products or methods which fall within the patent. It can also be used for revenue generation, where a competitor is permitted under a license to supply their product or method in accordance with agreed terms, in return for a royalty. In certain countries (e.g., the UK), tax breaks are also available in relation to profits generated by products which fall under a granted patent (https://www.gov.uk/guidance/corporation-tax-the-patent-box). Obtaining granted patents can be a slow process, but many major patent offices have facilities for achieving accelerated examination and grant.

A portfolio approach to patent protection can be particularly powerful for a company. It may be appropriate to obtain a patent related to a new biosensor apparatus, but competition from third parties may be hindered to a greater extent if

subsequent patents can also be obtained for consumables (e.g., sensor chips, sample preparation kits), methods of using the apparatus, and downstream improvements to the apparatus. Not only does such a portfolio make it harder for a competitor to "work-around" the patent protection, but it also lengthens the effective term of protection. Since patents are limited in duration (in most territories) to 20 years from the filing date, the portfolio approach potentially allows protection for improvements, consumables, etc. to outlast that of the biosensor apparatus itself.

Freedom-to-Operate

Having an awareness of third-party patents is also crucial in the biosensor field. Significant money can be wasted in developing a product or method, if that product or method falls within the claims of a third-party patent and hence cannot be made or offered for sale without a license. It is important to note that obtaining a patent for your own product or method does not prevent you from infringing a third-party patent having claims broad enough to cover your product or method. A consideration of "freedom-to-operate" is thus an important part of a company's R&D strategy.

The existence of a relevant third-party patent does not necessarily mean an R&D program must be halted. The major patent offices can (and frequently do) grant patents which are not valid, for example because the patent office examination did not uncover a key item of prior art. When confronted with a third-party patent, the key initial steps to take are therefore to check whether the patent is granted and in force, and then to assess whether the patent is valid. The first of these steps might sound obvious, but it is not uncommon for companies to panic when they find a pending, third-party patent application having broad claims which cover relevant technology; such claims may be narrowed during examination, or patents in relevant territories may never actually be granted, for example because the claimed subject-matter is not novel and/or inventive or simply because the third party decides to abandon the application. Most major patent offices provide free online search tools for determining the status of patents and applications (for example, the EPO's online register (https://register.epo.org/advancedSearch) and the USPTO's Patent Center (https://patentcenter.uspto.gov/). The second step is more complicated, but typically involves having a search performed for prior art which may put into doubt the novelty and/or inventive step of the claimed subject-matter. Ultimately, only valid patents can be infringed, and most patent disputes will involve a counterclaim of invalidity from the party alleged to infringe. A coherent invalidity case will often mean that no formal (i.e., court or patent office) proceedings arise, with the parties settling the matter (with or without a license being granted).

The patents system can seem daunting, but with the help of a good Patent Attorney and with the recognition that patents are a commercial tool and not an end in themselves, they can be powerful and valuable assets for any company in this field.

3 Applications

Attana's QCM biosensors are used to determine kinetics and affinity, among other binding characteristics of biomolecules of varying species such as proteins [1], viruses [2], and virus-like particles [3], fixed and non-fixed cells [4, 5], and recently on cancer tissues [6].

The purpose of this section is to provide information on several aspects that need to be considered before starting the experiments and during optimization of the assays, different applications and analysis as well as relevant assays and examples where the Attana's QCM was used.

3.1 Kinetics

The simple model of kinetic binding describes how molecule A reversely binds molecule B to form complex AB:

$$\mathrm{A} + \mathrm{B} \underset{kd}{\overset{ka}{\rightleftarrows}} \mathrm{AB} \tag{1}$$

where A is analyte, B is immobilized ligand, and AB is surface bound complex, k_a is the association rate constant (two molecules bind to each other), k_d dissociation rate constant (two molecules break the interaction). The interaction strength – the affinity (k_D) – can be derived from equilibrium steady state (when the two molecules bind to each other is at the same rate as the two molecules break the bond) or calculated directly from the kinetic rate constants. The affinity is $K_\mathrm{A} = 1/K_\mathrm{D} = k_a/k_d$ where K_A is the association equilibrium constant and K_D the dissociation equilibrium constant.

When using the Attana QCM instruments, proteins, cells, or tissues are immobilized/captured on the sensor surface. In the instrument the frequency is continuously registered (Fig. 9a) and due to the advanced fluidics, the baseline stabilization time is low. When the signal is stable (2 Hz/10 min), the analyte (e.g., antibody) can be injected over the sensor surface and the binding event is registered as a change in frequency over time (Fig. 9b). During this phase the association rate (also called on-rate) constant can be calculated. When the injection is over, the running buffer is passing over the sensor chip, and the bond between the analyte and ligand breaks leading to a change in frequency over the time. In this phase the dissociation rate (also called off-rate) constant can be calculated (Fig. 9c). The result is highly specific real-time kinetic interaction data with a dramatically reduced background signal. Other binding parameters such as affinity or maximum binding can then be determined.

When the association rate is fast, the reaction can become limited by diffusion of analyte to the sensor surface and the mass transport limited model should be used. Mass transport limitation can also be observed if the coverage of ligand on the

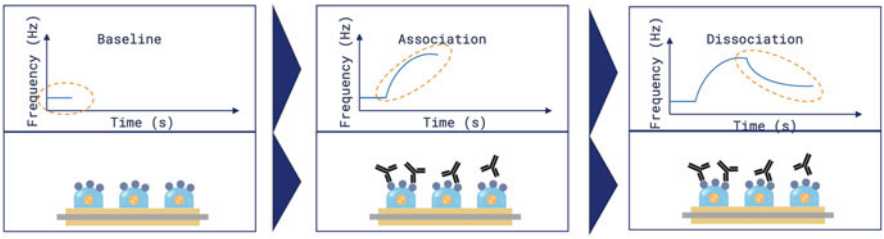

Fig. 9 Example of an experimental readout. The frequency must be stable (2 Hz/10 min) after the protein, cell or tissue has been immobilized/captured before starting the injections (**a**). The injection of the analyte binds to the receptor changing the mass on the biosensor and therefore the frequency–the association rate constant is calculated (**b**). The injection of the analyte stops and the bond between the analyte and receptor breaks changing the mass on the biosensor and therefore the frequency–the dissociation rate constant is calculated (**c**)

surface is too dense. The mass transport limited model includes an extra term, k_t, which describes the diffusion of analyte from the bulk to and away from the surface:

$$\mathrm{A_{bulk}} \underset{kt}{\overset{kt}{\rightleftarrows}} \mathrm{A_{surface}} + \mathrm{B} \underset{kd}{\overset{ka}{\rightleftarrows}} \mathrm{AB} \tag{2}$$

To assess if the binding is mass transport limited, different flow rates using an intermediate concentration of the analyte can be used. If the system is mass transport limited, reduce the surface density and/or use a higher flow rate. For a non-limited system, the association rate is not dependent on the flow rate.

3.1.1 Maximum Binding Capacity (Bmax)

Ideally, experiments should be performed until the ligand is saturated (all receptors are interacting with the analyte and therefore a higher concentration of analyte will not result in a higher frequency response). If the signal is saturated, the number of receptors can be calculated as (Eqs. 3–6):

$$1\,\mathrm{Hz} \sim 0.7\,\mathrm{ng} \tag{3}$$

$$\mathrm{B\,max}\ 0.7 = \mathrm{A\,ng} \tag{4}$$

$$\frac{\mathrm{A} \cdot 10^{-9}\ \frac{\mathrm{g}}{\mathrm{mol}}}{\mathrm{MW}} = \mathrm{Bmol} \tag{5}$$

$$\frac{\mathrm{Bmol} \cdot N_\mathrm{A}}{\text{number of cells}} = \text{receptors/cell} \tag{6}$$

where Bmax is the maximum binding capacity calculated by the Attana Evaluation software, MW is the molecular weight of the analyte (in grams), and $\mathrm{N_A}$ is the Avogadro constant ($6.02 \times 10^{23}\ \mathrm{mol^{-1}}$).

3.1.2 Affinity

Many are focused on affinity of an interaction (K_D) but it is very important to study and understand the kinetics. Different binding reactions can show the same affinity ($K_D = kd/ka$) but the association and dissociation phase and therefore the specificity can be very different. In order to have an accurate affinity, the steady state of a reaction should be reached; however, sometimes it is not experimentally possible. It is very important to consider the association and dissociation phases and not only focus on affinity, especially during drug discovery, screening, and validation studies.

3.1.3 One-to-One and One-to-Two Models

When the interaction mechanism involves a monovalent analyte and only one binding site on the ligand, only one curve phase can be observed during the association and dissociation phase (one to one model). This is common when biochemical assays are performed with monovalent and purified samples. However, when multivalent molecules or more biologically relevant samples (cells, tissues, serum, etc.) are used, the interaction can show a multivalent pattern patent and usually a one-to-two model can be applied. In this case, there are several scenarios where the most important ones are the following: (i) One monovalent analyte interacts to the specific receptor but also interacts weakly with a non-specific receptor, (ii) The analyte interacts with cell membrane components, (iii) The analyte interacts with sera/blood components (when sera or blood is used), (iv) A multivalent analyte interacts to the receptor but also interacts with two or more receptors causing avidity. Attana has developed an analysis tool to study the dissociation phase and therefore estimate if the binding has a one-to-one or a one-to-two model.

3.2 Analyte Characteristics

3.2.1 Off-Rate Interactions

The possibility to screen interactions based on the *kd*/off-rate alone has several advantages when, e.g., selecting the antibody clones that produce antibodies with the slowest off-rate already in hybridoma supernatants. The sample does not need to be purified, the concentration can be unknown, and it is fast [7].

3.2.2 Off-Target Interactions

When drug candidates are discovered or modified/optimized, they are intended to bind and have an effect on target molecule or cell. However, even when high specificity is shown, off-target interactions can occur leading to have adverse effects

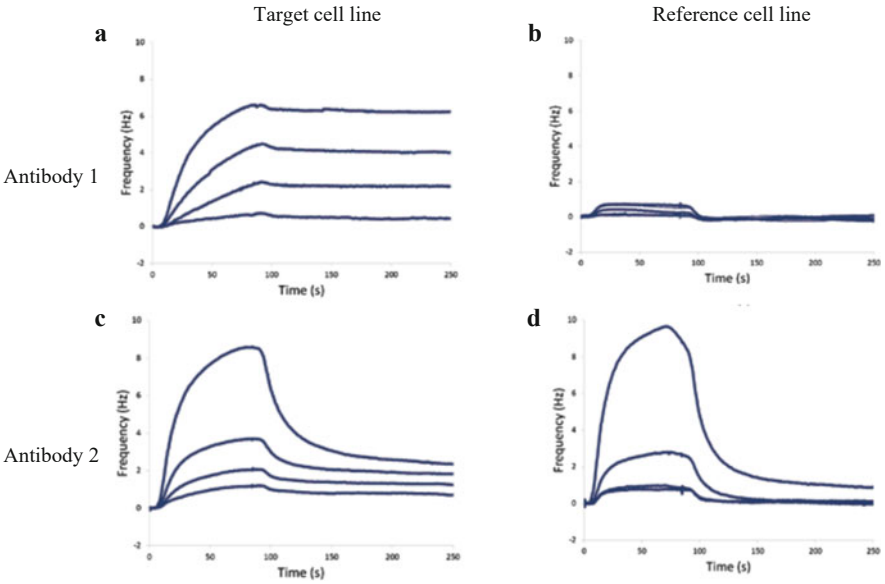

Fig. 10 Kinetic binding of two antibodies on the target and reference line. Antibody 1 binds specifically to the target cell line (**a**) but not to the reference cell line (**b**) showing to be a good candidate for clinical trials. Antibody 2 binds to both target (**c**) and reference (**d**) cell lines showing off-target interactions and leading to the conclusion that this drug needs to be optimized or will fail in clinical trials. (Source [8])

and therefore fail in clinical trials. Studying off-target interactions using cells or sera provides an added value (since it is more biologically relevant) to the analysis and validation of a drug candidate compared to purified receptors in buffer. The Attana instruments have helped different biopharma companies to study the off-target interactions with cells (Fig. 10) and when drugs are diluted in sera.

3.2.3 Epitope Binning

In the selection process for identification of optimal monoclonal antibodies for immunoassay development (targeting the same epitope), analyses are typically performed using different methods such as determination of dose-response curves (for all possible antibody–antigen combinations) and epitope binning (also called epitope mapping). The Attana's QCM instruments allow to study the epitope binning by immobilizing an antigen on the biosensor surface and injecting the antibody candidates and analyze if a "competition" for the antigen occurs [9, 10].

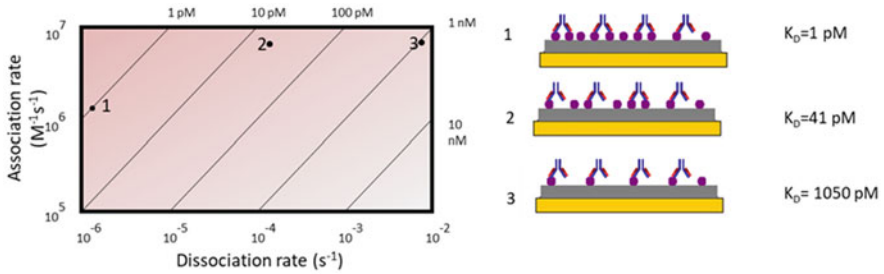

Fig. 11 Plot of the antibody binding coefficients of an interaction where the surface density is ranging from high to low. 1 corresponds to high density, 2 – medium density, 3 – low density

3.2.4 Avidity

The biochemical assay format is particularly suited for the investigation of avidity, the combined strength of several bond interactions, as opposed to affinity which describes the strength of a single bond interaction. Under such conditions where an avidity effect occurs, the attraction between the interaction partners is stronger than would have been expected when simply adding together the affinities of the participating bonds. An example of such conditions is when a molecule has several binding sites.

Practically this means that if, e.g., an antibody with its two binding sites is used as the analyte and the antigen is immobilized on the surface, different surface densities have to be tested to make sure that the results generated are free from avidity effects. At high surface density two antigens are close enough to have one antibody bind them simultaneously and avidity occurs, resulting in a falsely slow dissociation. As the surface density is titrated down, the dissociation rate will increase and finally stabilize when no more avidity occurs (Fig. 11), [11].

3.2.5 Enthalpy/Entropy

When using QCM, it is also possible to indirectly calculate the thermodynamics parameters of a binding reaction. In this case, different temperatures need to be tested in order to get the kinetic parameters without irreversibly denaturing the analyte and/or ligand. The obtained affinities can be used to calculate the Gibbs energy (Gibbs free energy equation) as well as the entropy and enthalpy (Van't Hoff equation) [12, 13].

3.2.6 Active Concentration

When studying proteins, it is essential to be able to measure active concentrations with great accuracy and specificity. Current standard methods do not capture the

active concentration or isomer influence and require time-consuming procedures. The Attana's QCM instruments allow to study the active concentrations in a fast and automatic manner, and it has helped several biopharma companies to perform quality control testing batch-to-batch differences and to probe protein stability. First, the association phase slope is plotted against concentration to calculate a standard curve. Then, unknown samples are then injected, their slopes calculated, and their active concentrations determined.

3.2.7 Degree of Aggregation

Protein aggregation is a phenomenon that occurs when proteins that are mis-folded interact and aggregate. It is known that drug-protein aggregation leads to immune-mediated adverse effects and therefore the degree of aggregation is an important aspect to investigate. The Attana's QCM instruments allow studying the degree of aggregation in a simple and automated manner. For instance, an antibody is immobilized on the biosensor surface and the protein to be studied is injected every 10 min (same concentration). If an increase in the signal is observed over time, more mass is interacting with the antibody and therefore aggregation is occurring (Fig. 12).

3.2.8 Influence of Buffer

Kinetic interactions have shown different kinetic profiles when different buffers or media are used (Fig. 13). This reflects that in vitro results are often unrealistic since only buffers are used. For drug validation, Attana always recommend mimicking the human body fluids and therefore use sera or other mock fluids, as components may interfere on the analyte binding and therefore the kinetics.

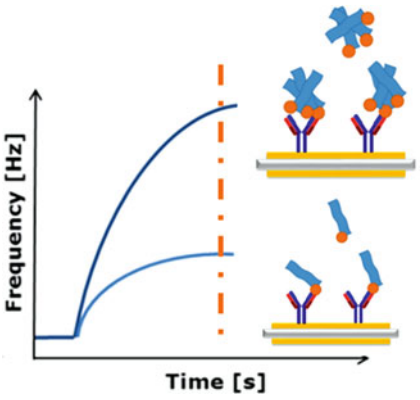

Fig. 12 Example of an experiment for aggregation scouting. If injections of the same concentration of analyte increase over the time, there is indication of aggregation

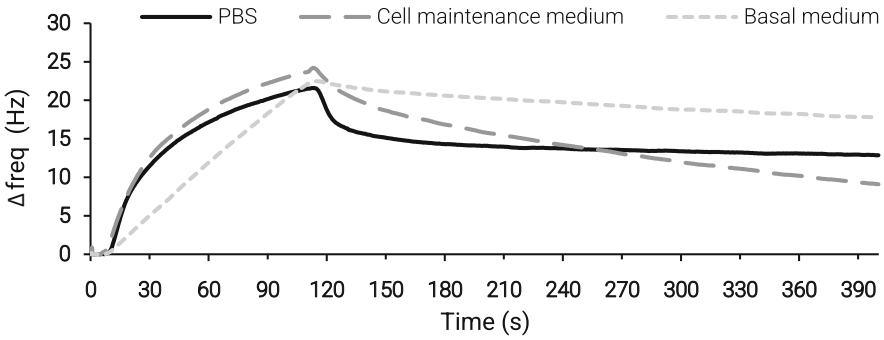

Fig. 13 Example of influence of buffer on the binding of the analyte to the ligand. Different kinetic profiles can be observed when different buffers/media are used

3.3 Experimental Preparation and Flow

This section gives a guideline of the experimental flow and aspects to consider as well as optimization steps before starting experiments.

1. Plan your experiment, assay (biochemical, cell or tissue-based) and select the appropriate chip, reagents, buffers, etc.
2. Immobilize or capture one of the interacting molecules, cells or tissues to be studied (referred to as the ligand). In general, determination of kinetic rate constants is best performed on a surface with as low density of the immobilized ligand as possible while maintaining reproducible analyte binding. A high surface density is used when maximum sensitivity is needed.
3. Choosing the reference. The reference surface must be as similar as possible to the active surface. In biochemical assays, often, a so-called mock ligand is immobilized on the reference surface. Ideally, the mock ligand should be identical to the ligand on the active surface but modified in way so that it does not bind the analyte. If such mock ligand is not available a list of alternatives is presented in Fig. 14a. Ideally, in cell-based experiments, identical cells expressing the target of interest modified in its binding site should be used, but such cells are not always readily available, and a non-exhaustive list of alternatives is presented in Fig. 14b.

4. After docking the sensor chips with immobilized/captured ligands in the Attana instrument, the sensor chips need time to equilibrate to the new conditions in the flow cell. The stabilization time differs between different types of traditional surfaces, due to differences in wettability. This is especially important when using the polystyrene sensor surface, which is very hydrophobic. Also, in comparison with traditional surfaces, cell and tissue surfaces are heavy and complex, leading to a longer stabilization time.

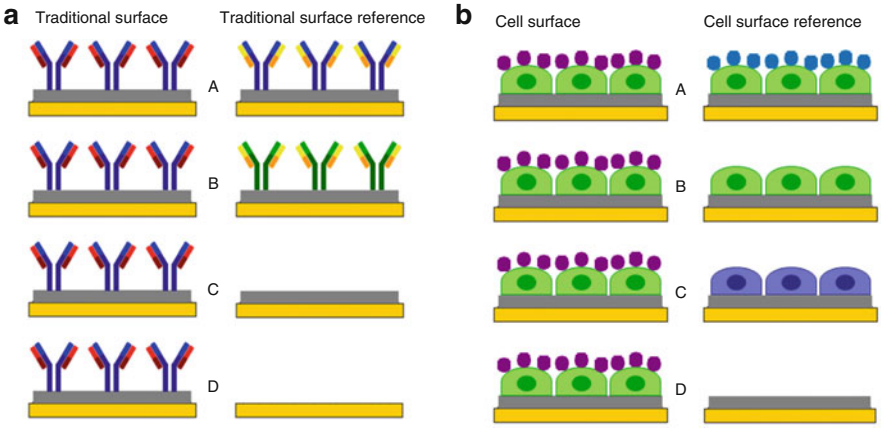

Fig. 14 Examples of different types of experimental setup for referencing. (**a**) Example of different references (the right column) and their corresponding analyte of interest to the left. A: Mock ligand, B: Similar type of biomolecule, C: Activated/deactivated surface, D: Non-treated surface for biochemical assays, (**b**) Example of different references (the right column) and their corresponding analyte of interest to the left. A: Mock surface, B and C: Similar surface, D: No cells

5. Test for binding between the ligand and the interacting molecule in solution (referred to as the analyte). If the K_D is known, a concentration of 50% of the K_D is an appropriate starting point. If the K_D is not known an appropriate concentration, where the binding reaction is close to or reaches equilibrium, must be found empirically by performing a single cycle kinetics (also known as kinetic titration – see point 7). The flow rate suitable for an experiment plays an important role when testing binding since it consequently leads to the contact time between the ligand and the analyte.
6. Determine appropriate running buffer and regeneration conditions for the molecules to be studied. All buffers must be prepared with high quality water and filtered before use. The regeneration solution should be able to break the interaction between the ligand and the analyte without affecting the surface binding capacity. The most common solutions are: 10 mM glycine pH 1–3, NaCl, 1 M, 20 mM NaOH pH 12, 100 mM HCl pH 1 and more. However, there are cases where regeneration cannot be achieved and therefore, we recommend using single cycle kinetics.
7. It is highly recommended to do multicycle kinetics where experiments are performed in replicates – at least three different concentrations (optimal five) and three injections/concentration. The analyte injections must be performed by starting from the lowest to the highest concentration (one cycle) and repeating the cycle three times. The recommended experimental flow is starting with a blank injection, followed by the analyte injection and finalizing with regeneration. Please note that it is important to match the composition of the blank and analyte solution. Unfortunately, the regeneration scouting is sometimes challenging, and time consuming and single cycle kinetics is required. Single cycle

kinetics consists of injecting sequential increasing concentrations of analyte until the ligand is saturated. Then a long dissociation time is required. Even though single cycle kinetics is a fast assay, the fitted model and kinetic parameters are not as accurate as multicycle kinetics.

3.4 Assays

In the following section several selected examples for biochemical, cell-based, tissue-based and the AVA™ Immunoassay are presented.

3.4.1 Biochemical-Based Assays

Biochemical applications with the Attana's QCM biosensor are used in a variety of fields including nanoparticle characterization [14, 15], development of in vitro diagnostics [16, 17], vaccine development [3, 18–20], and characterization of therapeutic antibodies [21–23].

For instance, Palladini et al. [3] use a novel virus-like particle (VLP)-based vaccine platform and show that directional, high-density display of human HER2 on the surface of VLPs allows induction of therapeutically potent anti-HER2 autoantibody responses. The Attana instrument was used to proof the ability of the HER2-VLP vaccine to induce high-affinity anti-HER2 IgG response by studying the interaction of total IgG from HER2-VLP immunized mice with recombinant HER2. The HER2-VLP vaccine shows prominent anti-cancer response, with potential as a new cost-effective modality for prevention and treatment of HER2-positive cancer.

The same approach was use by Fougeroux et al. [19] for development of a novel SARS-CoV-2 vaccine which utilizes Capsid-like particles (CLP) decorated with the SARS-CoV-2 receptor-binding domain. QCM experiments demonstrate that both soluble recombinant RBD and RBD displayed on CLPs bind the ACE2 receptor with nanomolar affinity (Fig. 15). In mice, the RBD-CLP vaccines induce higher levels of serum anti-spike antibodies than the soluble RBD vaccines with strong virus neutralization activity.

The Kontermann research group [22] has developed a novel tetravalent, bispecific single-chain diabody-Fc fusion protein targeting EGFR and HER3 (also known as ErbB3) that integrates the antigen-binding sites of a humanized version of cetuximab as well as a recently developed anti-HER3 antibody, IgG 3-43. In binding experiments with the Attana QCM sensors it could be demonstrated that this bispecific antibody combines the binding properties of the parental antibodies. This was also observed in biochemical and in vitro two-dimensional and three-dimensional cell culture assays.

Targeting canonical Wnt receptors such as LRP5/6 holds great promise for treatment of cancer. Fenderico et al. [23] have identified single-domain antibody fragments (VHH) that strongly inhibit Wnt3/3a-induced β-catenin-mediated

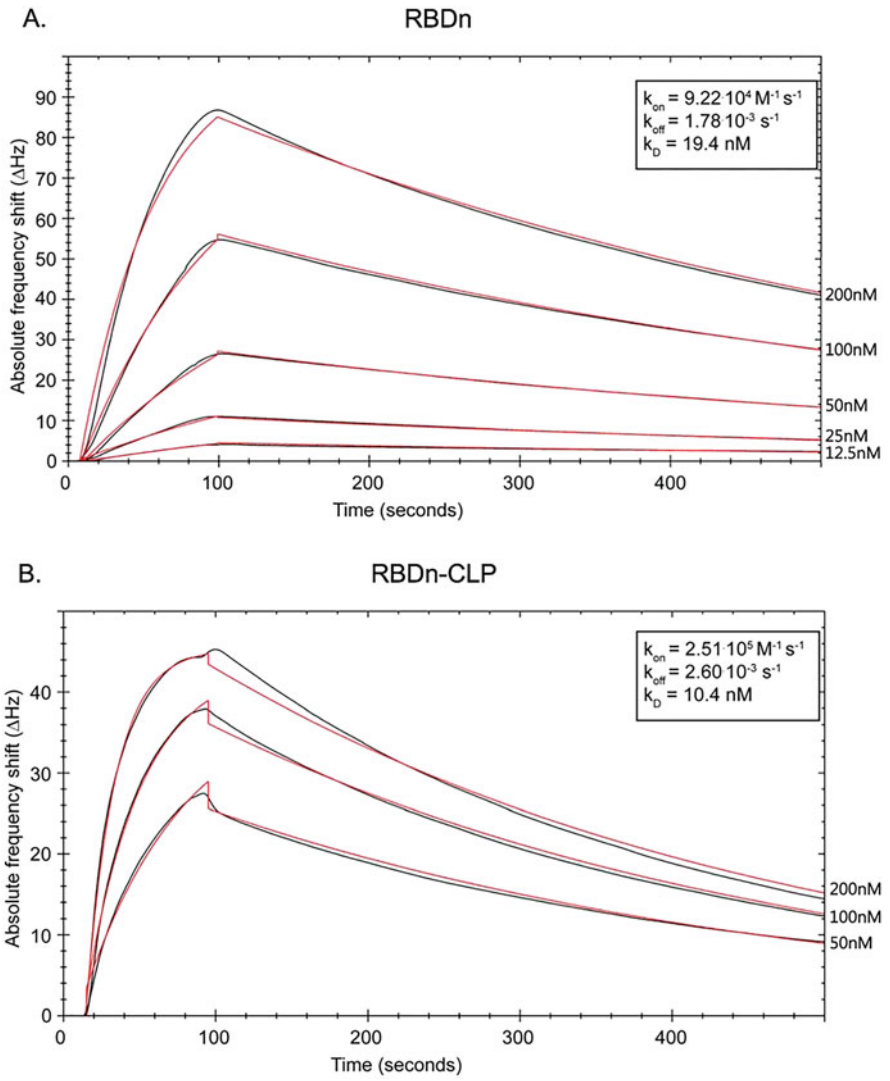

Fig. 15 (**a**) Binding of RBDn to immobilized hACE2. (**b**) Binding of ExpreS2 produced ACE2 to immobilized RBDn-CLP. Real-time binding sensorgrams (black curves) are fitted using a 1:1 simple binding model (red curve). (Source [19])

transcription in cells, while leaving Wnt1 responses unaffected. Characterization of LRP6 binding kinetics using QCM revealed that the tested VHHs displayed nanomolar range binding affinities for LRP6-P3E3P4E4, characterized by relatively fast association rates and mid-range dissociation rates (Fig. 16).

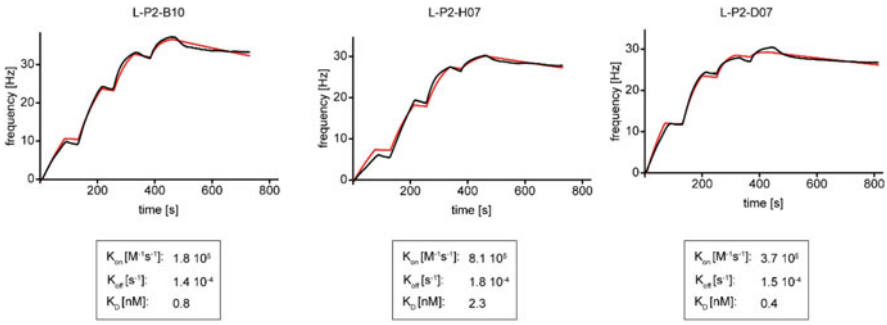

Fig. 16 Sensorgrams showing binding between anti-LRP6 VHH and immobilized LRP6P3E3P4E4 measured in Hertz as a function of time by a single cycle kinetic assay using increasing concentrations of VHH ranging from 30 pM to 250 pM. The black lines represent data and the red lines represent fitted curves. (Source [23])

Crude Samples or Serum

When working with crude samples, such as supernatants, lysates or serum, in many cases a preceding purification step is necessary before interaction constants can be determined in kinetic interaction experiments. This is time-consuming, labor-intensive and results in loss of yield.

Attana's proprietary low non-specific binding (LNB) surfaces extend the possibilities for screening in crude samples, such as supernatants, serums, and lysates, without the need for using capture setups. The method can be used for clone selection, vaccine screening, biomarker discovery, biomanufacturing, and performance studies in biologically relevant environments.

Examples for crude sample applications are label-free, direct methods to screen antibodies in hybridoma supernatants and scaffold proteins in bacterial lysates, using the dual-channel Attana 200 system and LNB surfaces. In both experiments antigen was immobilized on the surface and 96 *E. coli* lysates and 25 Hybridoma supernatants were screened on an automated Attana 200 system (Attana A200). The dissociation of the bound antibodies (hybridoma supernatants) or scaffold proteins (*E. coli* lysates) was sampled for at least 5 min. Buffer injections and reference surfaces were used for referencing. By using this method, dissociation rate constants (k_d) could be easily obtained for all 221 samples. Samples were then ranked according to their respective dissociation rate constants from the antigen.

Recently, Gu et al. [17] developed an assay using Attana's QCM technology where neutralizing antibodies in serum were studied. 168 patient serum samples pre-vaccination, 3 weeks, three and 6 months after the first vaccine dose were used demonstrating the reduction of neutralizing antibodies after 6 months of the vaccine dose.

3.4.2 Cell-Based Assays

Kinetic studies using suspension cells (mammalian, bacterial, etc.) and adherent cells (fixed and non-fixed) have been performed with the Attana Cell A200 and A250 instrument using different assays.

Suspension Cells

The LNB Carboxyl surface is part of the Attana (low non-specific binding for cell cultivation) LNB-CC chip that allows capture of cells on the sensor surface and measurements of interactions. Cells of interest are captured to the exposed surface by a capturing molecule of choice such as lectins: The ligand is covalently coupled to the surface using amine coupling. The cell density at the sensor surface must be optimized to obtain better results and fully covered surfaces must be avoided. After capture, cells can be fixed with an appropriate method.

For instance, Kalograiaki et al. [24] studied the carbohydrate membrane structures of bacteria using lectins. Concanavalin was immobilized on LNB-CC surfaces and four different strains of *Haemophilus influenzae* were captured on the biosensor surface. The results showed different kinetic constants leading to the discovery of new insights of bacterial typing.

Bode et al. [25] discovered that Dectin-1 (expressed in dendritic cells) plays a crucial role binding to annexins exposed on apoptotic cells. Concanavalin was immobilized on LNB-CC and two transfected (expressing and knockout of Dectin-1) Mono Mac 6 cell lines were captured. Annexin coated vesicles and depleted zymosan (activates Dectin-1) were used as analytes. The result showed binding of annexin to Dectin-1 expressing cells (with an affinity of nanomolar range) and also that the annexins and the activation of Dectin-1 do not share the same receptor.

A recent study [26] used fixed and non-fixed, undifferentiated, and differentiated human histiocytic lymphoma U937 cells to study the binding effect of histidine-rich glycoprotein and stanniocalcin 2 proteins. A lectin was immobilized on LNB-CC surfaces and 2×10^5 differentiated or undifferentiated cells were captured. The results showed that histidine-rich glycoprotein binds with more affinity to differentiated cells (Fig. 17) and induces phagocytosis, and that both proteins bind to each other as well as showing higher affinity when the cells are differentiated.

Adherent Cells

The COP-1 surface is part of the Attana COP-1 Cell Sensor chip that allows growth of cells directly on the sensor surface and measurements of interactions. Cells of interest are directly cultivated on the COP-1 surface: Cells are seeded in the cultivation chip, placed at appropriate environmental conditions, and allowed to adhere and grow on the sensor surface. Growth time depends on cell line and target of interest and must be optimized. After cultivation, cells can be fixed with an appropriate method.

For instance, Elmlund et al. [27] studied the interaction of a therapeutic antibody with human ovarian adenocarcinoma epithelial cancer cells (SKOV3) on COP-1

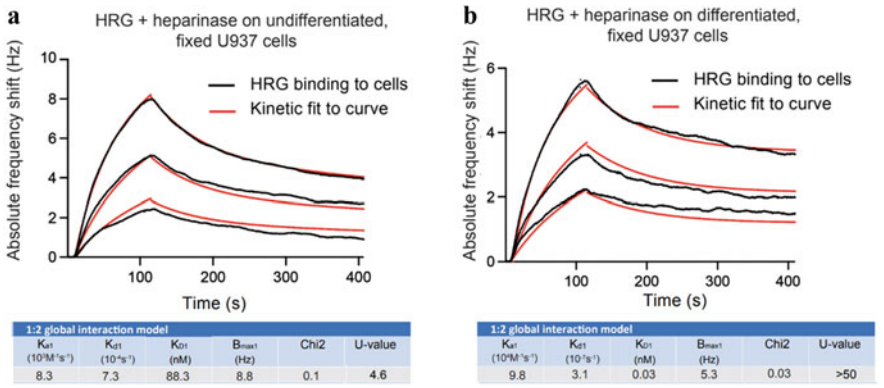

1:2 global interaction model

K_{d1} ($10^3 M^{-1}s^{-1}$)	K_{d1} ($10^{-3}s^{-1}$)	K_{D1} (nM)	B_{max1} (Hz)	Chi2	U-value
8.3	7.3	88.3	8.8	0.1	4.6

1:2 global interaction model

K_{d1} ($10^3 M^{-1}s^{-1}$)	K_{d1} ($10^{-3}s^{-1}$)	K_{D1} (nM)	B_{max1} (Hz)	Chi2	U-value
9.8	3.1	0.03	5.3	0.03	>50

Fig. 17 Binding of histidine-rich glycoprotein on undifferentiated (**a**) and differentiated (**b**) U937 cells. (Source [26])

surfaces. This study demonstrated that QCM is relevant for detailed binding kinetic information of drugs in a more natural environment than purified receptors.

Salanti et al. [28] deeply studied the binding of rVAR2 with colorectal adenocarcinoma cells using COP-1 surfaces and QCM, with an affinity of 13 nM. This study also demonstrated the importance of studying target and off-target interactions since VAR2 was fused with compounds that inhibit cancer growth and only targeted cancer cells.

Peiris et al. [4] studied the importance of glycosylation of cancer cells and its interference during abnormal cell proliferation. In this case, the human breast cell line SKBR-3 was grown on COP-1 surfaces and the binding of an antibody (Herceptin) (Fig. 18) and the lectin concanavalin (Con A) was studied when cells were intact or deglycosylated. It was demonstrated that Herceptin has more access to the binding site when cells were deglycosylated (Fig. 18).

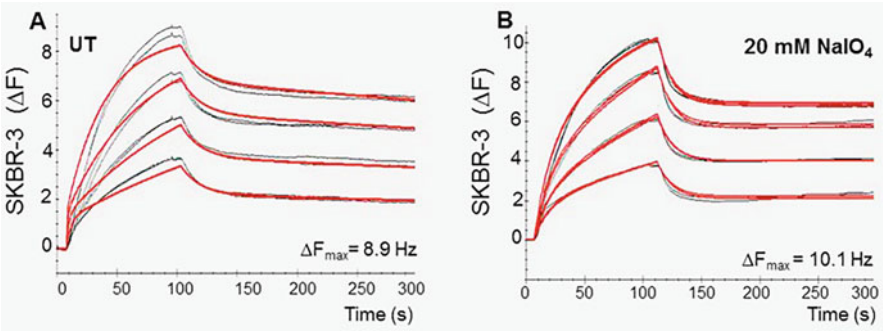

Fig. 18 Herceptin binding interaction with SKBR-3 cells before (**a**) and after (**b**) deglycosylation. (Source [4])

Jennbacken et al. [29] investigated paracrine factors that induce cardiac regeneration when heart failure occurs. The human cardiac progenitor cells and human primary cardiac fibroblasts were immobilized on the COP-1 surfaces and FGF9 and FGF16 were injected. The data suggested that these two paracrine factors bind to different receptors.

3.4.3 Tissues

Immunohistochemistry (IHC) is an essential method used to determine the localization and distribution of antigens of interest in tissues. IHC requires several laborious steps from tissue deparaffinization to antigen retrieval, long incubation with antibodies and finally staining with an appropriate dye and imaging with fluorescent or inverted microscope. It also requires that the used antibodies should be labeled with fluorochromes [30] or enzymes [31].

As mentioned above, QCM technology is a label-free biosensor and real-time platform, which detects and measures the strength of molecular interactions between the analytes with targets in tissues without need for long incubation with primary antibodies as well as no need for tagged antibodies and no staining step, which in the end save time and reduce the running costs.

Formalin-fixed paraffin embedded tissues were studied using Attana QCM biosensors for expression and molecular interaction of recombinant malaria protein (rVAR2) to the placental-like chondroitin sulfate (pl-CS) receptors in breast and prostate cancer tissues and in human primary placental tissues [6]. It was found that the QCM technology confirms that rVAR2 protein did not interact with normal tonsil tissues but interact specifically only with placental tissues and cancer tissues (Fig. 19). The data showed that the placental-like chondroitin receptors are highly expressed in cancer tissues and the has high affinity toward the targeting analyte with K_D values in nanomolar range. With the Attana's QCM biosensors in-situ interactions between the analytes and ligands can be determined, which add another dimension for the histopathological study; not only determination of the expression and distribution pattern of targets but also measure kinetics and affinity of the interaction, which give more quantitative information for cancer diagnostics, drug development, and patient stratification.

In a recent pilot study performed in our research lab (under supervision of Professor Miriam Dweck), Attana's QCM technology was utilized to investigate the interaction of various lectin proteins with different breast and colon cancer tissues. The 2.5 μM thickness of breast cancer tissues was immobilized on specialized Attana QCM COP-1 surfaces then subjected to various injections of different concentrations of plant lectins such as Concanavalin A (CON A), Peanut Agglutinin (PNA), Dolichos Biflorus Agglutinin (DBA), and Ricinus Communis Agglutinin (RCA). The study showed changes in interaction response between lectins and tissue receptors (glycocalyx) and were directly proportional to the concentration of the lectin and to the stained tissue section when viewed under light microscopy using conventional immunohistochemistry. However, more informative readouts were

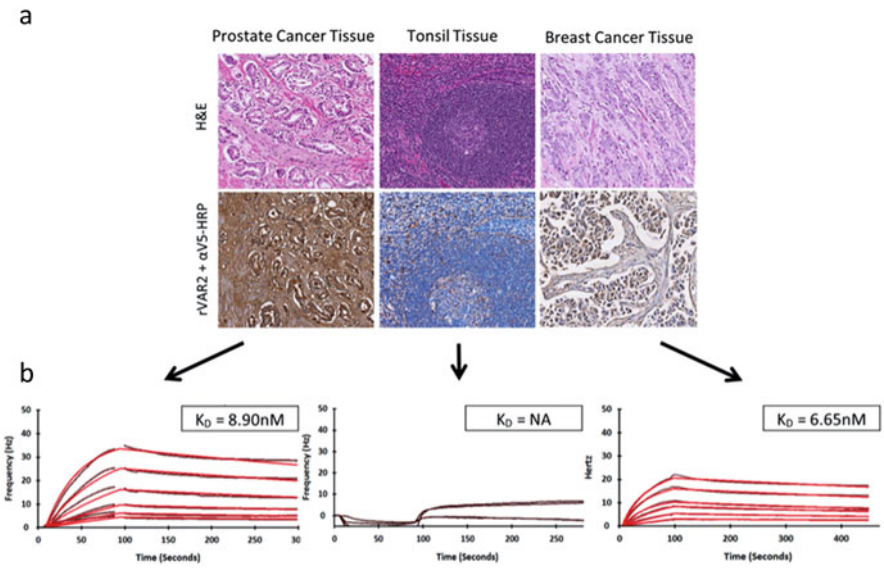

Fig. 19 The molecular interaction between rVar2 and pl-CS receptors in tissues. (**a**) Immunohistochemistry staining of rVAR2 in prostate cancer, normal tonsil tissues, and breast cancer tissues, (**b**) kinetic experiment of the matched tissues on Attana COP-1 surfaces for binding analysis of different dilution of rVAR2 protein. The curve fitting was done with Trace Drawer software. Black curves represent original data, red curves represent fitted data. The dissociation equilibrium constants (KD) are listed. (Source [6])

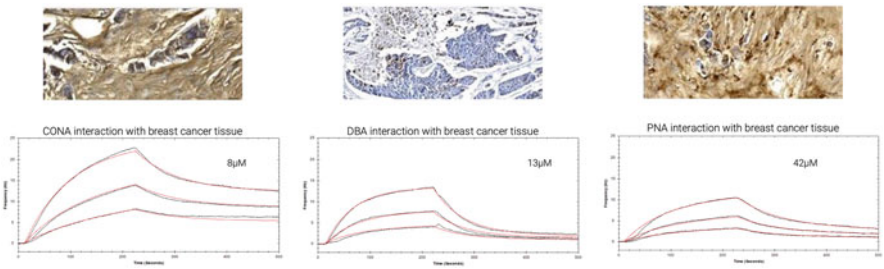

Fig. 20 Lectins differentially interact with the breast cancer tissue. (**a**) Immunohistochemistry staining of CONA, DBA, and PNA lectins in breast cancer tissue, (**b**) kinetic experiment of the matched tissues on Attana COP-1 surfaces for binding analysis of different dilution of lectins. The curve fitting was done with Trace Drawer software. Black curves represent original data, red curves represent fitted data. The date is extracted from the collaborative work with University of Westminster

concluded from kinetic experiments using Attana QCM platform. The interaction between lectins and breast cancer tissues was in micromolar range as shown in Fig. 20.

3.4.4 In Vitro Diagnostics: Attana Virus Analytics (AVA™)

There is a constant need in the medical field to have the necessary equipment to help diagnose and thus facilitate the process of detection and treatment of diseases. The most commonly used is the IVD [32]. IVD covers a wide spectrum of laboratory analyses, for example, not exclusively, diagnoses, monitoring, and providing information about diseases progression, as well as predicting treatment response [32, 33]. In addition, IVD contributes to disease risk assessment and provides the powerful tools for infection or disease management [34]. IVD samples collected from the human body consist of tissue, blood, urine, saliva, and other body fluids [35]. With the COVID-19 pandemic caused by SARS-CoV-2 virus, there was an urgent need for reliable, sensitive, robust, and fast technology which can process the test samples collected from the infected person or recovered from COVID-19.

Since the advent of COVID-19, Attana has focused on developing a diagnostic tool, the Attana Virus Analytics (AVA™) which uses the Attana's QCM biosensor for the detection and measurement of antibody-antigen binding in a real-time, label-free, and flow-based. Specifically, the AVA™ SARS-CoV-2 IgG Immunoassay is CE certified and registered under the Swedish Medical Products Agency's Regulation (LVFS 2001:7) on in vitro diagnostic medical devices as a General IVDD (for professional use). In this case, the different antigens (receptor-binding domain (RBD) from the different SARS-CoV-2 variants are immobilized on LNB biosensor surfaces. Serum samples from patients are injected over the surface followed by the injection of different anti-immunoglobulin isotypes (Fig. 21).

The unique and novel IVD assay that Attana has developed has several advantages over the standard assays: (i) reduced time for sample preparation, (ii) no incubation time, (iii) more data acquisition (continuous readout – no end point assay), and (iv) easy to operate avoiding highly skilled operator. In addition, since more information is acquired during the assay, it leads to a detailed patient's immunity profile. The immune profile includes the quantification of the total non-specific immune response, the specific immune response, the quality of the

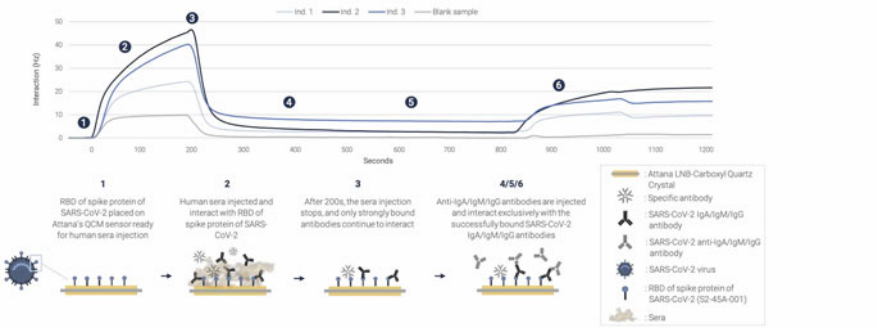

Fig. 21 Scheme and examples of the AVA™ SARS-CoV-2 IgG Immunoassay

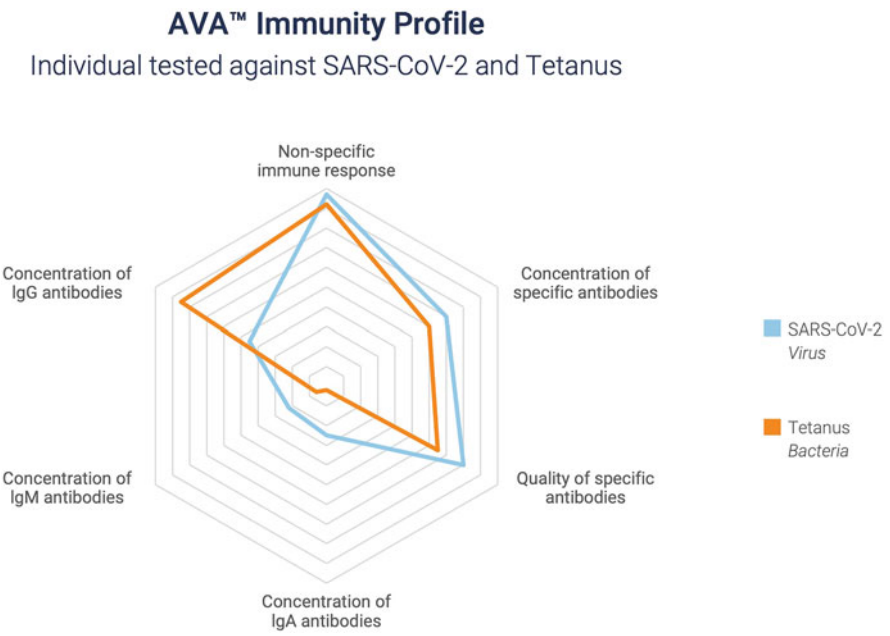

Fig. 22 Example of the AVA™ immune profile for SARS-CoV-2 (blue) and Tetanus (orange)

antibodies, and the quantity of different Immunoglobulins IgA, IgM, and IgG (Fig. 22).

The Attana's R&D is currently working to expand Attana's AVA™ diagnostic platform by including additional assays and exploring the potential for a point-of-care device based on whole blood samples.

3.5 Material Science

In addition to biological assays, the Attana's QCM technology has been used extensively for material science research. The gold electrode-coated quartz crystal resonator surface provides a versatile platform for chemical elaboration in order to enhance sensor performance. Through the judicious selection of surface chemical functionality and structural morphological features, sensor performance can be improved by increasing numbers of recognition sites, improvement of analyte mass transfer properties and enhancing selectivity through suppression of non-specific binding [36–38] (Fig. 23).

The mainstay for resonator surface modification has long been the use of the sulfur-gold bond for the preparation of self-assembled monolayers (SAMs) using thiols [39–43]. SAMs can provide ready access to surfaces with a wide range of

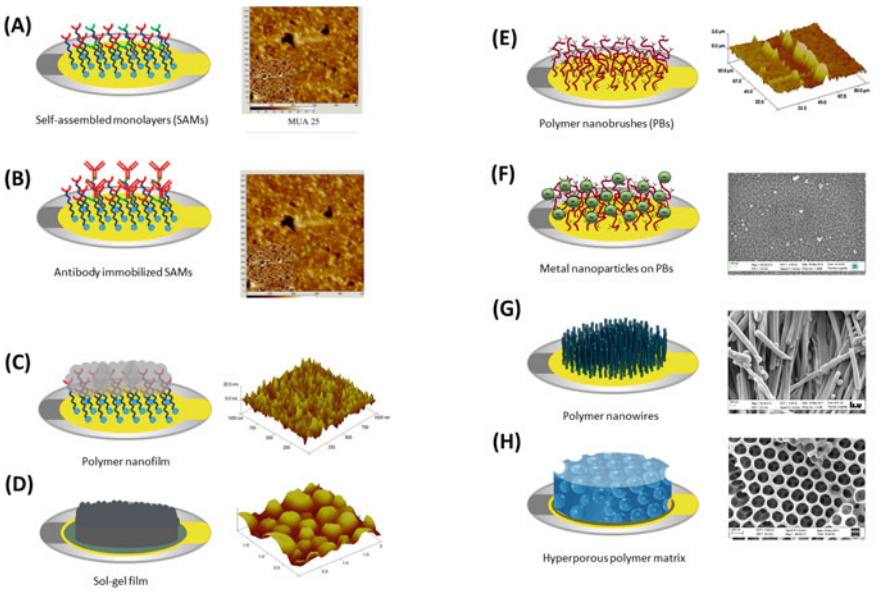

Fig. 23 Strategies of adaption of resonator surfaces with materials: (**a**) self-assembled monolayers, (**b**) biomolecule (antibody)-functionalized-self-assembled monolayers [74], (**c**) polymer nanofilms [50], (**d**) sol-gel (SiO_2) [75], (**e**) polymer nanobrushes [60], (**f**) metal nanoparticle (Pd)-decorated polymer nanobrushes [76], (**g**) polymer nanowires [67], (**h**) hyperporous polymer networks [64]

chemical functionalities, charged, neutral hydrophilic or hydrophobic, and can be used for further chemical functionalization or for the physisorption or covalent immobilization of materials. The use of mixtures of thiols provides access to mixed self-assembled monolayers (mSAMs), where variation in the concentration of surface functionalities can be achieved, thus allowing for control over the density of immobilized structures, and over the surface hydrophobicity and charge (Fig. X-A and B) [44, 45]. Spin-coating and covalent immobilization of polymers to SAMs or mSAMs have been extensively used to develop sensor surfaces with thin film coatings with specific functionalities for use in subsequent derivatization [46–50] (Fig. X-C), as used in the case of the carboxyl functionalized Attana LNB-CC Cell sensor chip [15, 51].

Silicon dioxide-coated gold electrode-coated quartz crystal resonator surfaces provide an alternative platform for surface decoration [52, 53] as they allow the use of sol–gel chemistry to access the wide array of functionalities available with polysiloxanes and organosilicas [54–56] (Fig. X-D). Some recent examples using this type of QCM sensor chip include using them for molecularly imprinted polymer-metal organic framework composites for detection of tyramine [57] and the molecular imprinting of azobenzene carboxylic acid on a TiO2 ultrathin film using a surface sol-gel process [58, 59].

Polymer brushes immobilized on resonator surfaces have been used to enhance sensor sensitivity through increasing the number of sites for analyte binding, by

virtue of the increased material surface areas and improved analyte mass transfer due to their flexible nature [60] (Fig. X-E). Generally, the polymer brushes are prepared either by immobilization of preformed polymer chains or by formation of polymer chains from the sensor surface [61]. Examples include the development of dextran-derivatized surfaces and a series of poly(2-hydroxacrylates) for evaluating antifouling properties [62, 63]. Finally, polyethylenimine (PEI) polymer brushes [49], which are comprised of a 1:2:1 ratio of primary, secondary, and tertiary amines, have been used for the immobilization of palladium nanoparticles on sensor chips as a platform for the Suzuki reaction in a QCM instrument (Fig. 23).

More recently, strategies for enhancing sensor performance have been explored for engineering long-range three-dimensional structural features into synthetic polymer and biopolymer-based materials coating resonator surfaces. Synthetic polymers have been prepared by either electrochemical or thermally or photochemically initiated free radical polymerization on resonator surfaces using sacrificial templates. The types of sacrificial material include monodisperse polystyrene beads [64–66], anodized alumina (AA) membranes [64, 67, 68], and micelles [67, 69, 70]. In the case of monodisperse polystyrene beads, highly regular interconnected hyperporous polymers are obtained (Fig. X-H), while nanowire- and fibril-coated surfaces are obtained when using AA membranes (Fig. X-G) or micelles as sacrificial templates, respectively. QCM sensor surface materials with hierarchical structuring have been obtained in combination with these strategies using molecular imprinting technology [71–73]. QCM sensors for biotin and its derivatives [66, 68], and small drug molecules, e.g., aspirin [67] and bupivacaine, up to 100-fold sensitivity enhancements could be obtained relative to control materials [69, 70]. Recently, the possibility of using plant-derived biomacromolecules, the maize protein zein, milk protein casein and crab shell derived chitin were to construct hierarchically structured materials that significantly enhanced sensor response using the above techniques [65] (Fig. 23).

In summary, the significant recent developments achieved through material-based strategies for enhancing QCM sensor surface performance pave the way for further identifying additional material compositions and architectures that can enhance sensor performance.

4 Conclusions

Attana has developed biosensors for analysis of biomolecular interactions and can be used to determine specificity, kinetics, and affinity, amongst other binding characteristics of biomolecules and macrostructures of varying species such as proteins, cells, tissues, and more. With the focus on (i) power (versatile biosensor measuring in real-time, label-free, providing high quality data and resulting in-depth analyses of molecular interactions in a wide variety of applications) and (ii) simplicity (the Attana's instruments are developed with the end-user in mind: plug-and-play operation, rapid start-up, intuitive assay setup and pre-programmed methods and

templates are just a few of the system features, resulting in saving time and maximizing productivity in your research), the Attana's instruments have been employed at universities, leading life science and biopharma companies worldwide, working in a wide variety of research fields.

References

1. Wu CX, Li X, Song S et al (2017) QCM biosensor based on polydopamine surface for real-time analysis of the binding kinetics of protein-protein interactions. Polym J 9(10):482
2. Brien JD, Sukupolvi-Petty S, Williams KL et al (2013) Protection by immunoglobulin dual-affinity retargeting antibodies against dengue virus. J Virol 87(13):7747–7753
3. Palladini A, Thrane S, Janitzek CM et al (2018) Virus-like particle display of HER2 induces potent anti-cancers responses. Onco Targets Ther 7(3)
4. Peiris D, Spector AF, Lomax-Browne H et al (2017) Cellular glycosylation affects Herceptin binding and sensitivity of breast cancer cells to doxorubicin and growth factors. Sci Rep 7: 43006
5. Xueming Li X, Song S, Shuai O et al (2015) Real-time and label-free analysis of binding thermodynamics of carbohydrate-protein interactions on unfixed cancer cell surfaces using a QCM biosensor. Sci Rep 5:14066
6. Clausen TM, Ayres M, Zarni H et al (2016) Real-time and label free determination of ligand binding-kinetics to primary cancer tissue specimens; a novel tool for the assessment of biomarker targeting. Sens Bio-Sen Res 9:23–30
7. Pandey S (2010) Hybridoma technology for production of monoclonal antibodies. Int J Pharm Sci Rev Res 1(2):88–94
8. Altun S, Aastrup T (2017) Off-target testing assays. Biotechnology J:56–57
9. Zettlitz KA, Seitter J, Müller D et al (2010) Humanization of a mouse monoclonal antibody directed against a cell surface-exposed epitope of membrane-associated heat shock protein 70 (Hsp70). Mol Biotechnol 46(3):265–278
10. Grellier B, Le Pogam F, Vitorino M et al (2014) 3D modeling and characterization of the human CD115 monoclonal antibody H27K15 epitope and design of a chimeric CD115 target. MAbs 6(2):533–546
11. Richter F, Zettlitz KA, Seifert O et al (2019) Monovalent TNF receptor 1-selective antibody with improved affinity and neutralizing activity. MAbs 11(1):166–177
12. Multia E, Sirén H, Andersson K et al (2017) Thermodynamic and kinetic approaches for evaluation of monoclonal antibody – lipoprotein interactions. Anal Biochem 518:25–34
13. Mouline Z, Mahon E, Gomez E et al (2014) Entropy-driven lectin-recognition of multivalent glycovesicles. Chem Commun 50(6):731–733
14. Gianneli M, Polo E, Lopez H et al (2018) Label-free in-flow detection of receptor recognition motifs on the biomolecular corona of nanoparticles. Nanoscale 10(12):5474–5481
15. Mahajan R, Suriyanarayanan S, Olsson GD et al (2022) Oxytocin-selective nanogel antibody mimics. Int J Mol Sci 23(5):2534
16. Vrhovac L, Šelemetjev S, Vatić S et al (2021) Novel approach to the measurement of antithyroglobulin antibodies in human serum – application of the quartz crystal microbalance sensors. Talanta 223(Pt 2):121588
17. Gu Y, Shunmuganathan B, Qian X et al (2022) Defining factors that influence vaccine-induced, cross-variant neutralizing antibodies for SARS-CoV-2 in Asians. medRxiv
18. Nilsson OB, Adedoyin J, Rhyner C et al (2011) In vitro evolution of allergy vaccine candidates, with maintained structure, but reduced B cell and T cell activation capacity. PloS One 6(9): e24558

19. Fougeroux C, Goksøyr L, Idorn M et al (2021) Capsid-like particles decorated with the SARS-CoV-2 receptor-binding domain elicit strong virus neutralization activity. Nat Commun 12(1): 324
20. Van Oosten L, Altenburg JJ, Fougeroux C et al (2021) Two-component nanoparticle vaccine displaying glycosylated spike S1 domain induces neutralizing antibody response against SARS-CoV-2 variants. MBio 12(5):e0181321
21. Curtin F, Perron H, Kromminga A et al (2015) Preclinical and early clinical development of GNbAC1, a humanized IgG4 monoclonal antibody targeting endogenous retroviral MSRV-Env protein. MAbs 7(1):265–275
22. Rau A, Lieb WS, Seifert O et al (2020) Inhibition of tumor cell growth and cancer stem cell expansion by a bispecific antibody targeting EGFR and HER3. Mol Cancer Ther 19(7): 1474–1485
23. Fenderico N, Van Scherpenzeel RC, Goldflam M et al (2019) Anti-LRP5/6 VHHs promote differentiation of Wnt-hypersensitive intestinal stem cells. Nat Commun 10(1):365
24. Kalograiaki I, Euba B, Fernández-Alonso M et al (2018) Differential recognition of Haemophilus influenzae whole bacterial cells and isolated lipooligosaccharides by galactose-specific lectins. Sci Rep 8:16292
25. Bode K, Bujupi F, Link C et al (2019) Dectin-1 binding to annexins on apoptotic cells induces peripheral immune tolerance via NADPH oxidase-2. Cell Rep 29(13):4435–4446
26. Persson T, Kaito H, Durall C et al (2022) Quartz crystal microbalance measurement of histidine-rich glycoprotein and stanniocalcin-2 binding to each other and to. Inflammatory Cells 11:2684
27. Elmlund L, Käck C, Aastrup T et al (2015) Study of the interaction of Trastuzumab and SKOV3 epithelial cancer cells using a quartz crystal microbalance. Sensors 15:5884–5894
28. Salanti A, Clausen TM, Agerbæk MØ et al (2015) Targeting human cancer by a glycosaminoglycan binding malaria protein. Cancer Cell 28(4):500–514
29. Jennbacken K, Wågberg F, Karlsson U et al (2019) Phenotypic screen with the human Secretome identifies FGF16 as inducing proliferation of iPSC-derived cardiac progenitor cells. Int J Mol Sci 20:6037
30. de Boer E, Warram JM, Tucker MD et al (2015) In vivo fluorescence immunohistochemistry: localization of fluorescently labeled Cetuximab in squamous cell carcinomas. Sci Rep 5:10169
31. Mason DY, Sammons R (1978) Alkaline phosphatase and peroxidase for double immunoenzymatic labelling of cellular constituents. J Clin Pathol 31(5):454–460
32. Rohr UP, Binder C, Dieterle T (2016) The value of in vitro diagnostic testing in medical practice: a status report. PloS One 11(3):e0149856
33. Raman G, Avendano E, Chen M (2013) Update on emerging genetic tests currently available for clinical use in common cancers, in technology assessment report. Agency for Healthcare Research and Quality, Rockville
34. Billings PR (2006) Three barriers to innovative diagnostics. Nat Biotechnol 24:917–918
35. Zhang J, Lan T, Lu Y (2020) Translating in vitro diagnostics from centralized laboratories to point-of-care locations using commercially-available handheld meters. Trends Anal Chem 124: 115782
36. Lucklum R, Behling C, Hauptmann P (2000) Signal amplification with multilayer arrangements on chemical quartz-crystal-resonator sensors. IEEE Trans Ultrason Ferroelectr Freq Control 47(5):1246–1252
37. Emir Diltemiz S, Keçili R, Ersöz A et al (2017) Molecular imprinting Technology in Quartz Crystal Microbalance (QCM) sensors. Sensors 17:454
38. Jia MF, Zhang Z, Li JH et al (2018) Molecular imprinting technology for microorganism analysis. Trac-Trends Anal Chem 106:190–201
39. Pandey LM (2020) Surface engineering of personal protective equipments (PPEs) to prevent the contagious infections of SARS-CoV-2. Expert Rev Proteomics 17:425–432
40. Kim YT, McCarley RL, Bard AJ (1993) Observation of n-octadecanethiol multilayer formation from solution onto gold. Kangmuir 9(8):1941–1944

41. Naumann R, Schiller SM, Giess F et al (2003) Tethered lipid bilayers on ultraflat gold surfaces. Langmuir 19:5435–5443
42. Tanahashi M, Matsuda T (1997) Surface functional group dependence on apatite formation on self-assembled monolayers in a simulated body fluid. J Biomed Mater Res 34:305–315
43. Zhang Y, Luo SZ, Tang YJ et al (2006) Carbohydrate-protein interactions by "clicked" carbohydrate self-assembled monolayers. Anal Chem 78:2001–2008
44. Love JC, Estroff LA, Kriebel JK et al (2005) Self-assembled monolayers of thiolates on metals as a form of nanotechnology. Chem Rev 105:1103–1170
45. Huang E, Satjapipat M, Han SB et al (2001) Surface structure and coverage of an oligonucleotide probe tethered onto a gold substrate and its hybridization efficiency for a polynucleotide target. Langmuir 17:1215–1224
46. Lee BS, Chi YS, Lee KB et al (2007) Functionalization of poly(oligo(ethylene glycol)methacrylate) films on gold and Si/SiO2 for immobilization of proteins and cells: SPR and QCM studies. Biomacromolecules 8:3922–3929
47. Muller M, Yan XP, Lee SW et al (2005) Lubrication properties of a brushlike copolymer as a function of the amount of solvent absorbed within the brush. Macromolecules 38:5706–5713
48. Pena-Pereira F, Duarte RMBO, Duarte AC (2012) Immobilization strategies and analytical applications for metallic and metal-oxide nanomaterials on surfaces. TrAC 40:90–105
49. Suriyanarayanan S, Lee HH, Liedberg B et al (2013) Protein-resistant hyperbranched polyethyleneimine brush surfaces. J Colloid Interface Sci 396:307–315
50. Elmlund L, Suriyanarayanan S, Wiklander JG et al (2014) Biotin selective polymer nano-films. J Nanobiotechnol 12:8
51. Wu C, Li X, Song S et al (2017) QCM biosensor based on polydopamine surface for real-time analysis of the binding kinetics of protein-protein interactions. Polymers 9(10):482
52. Liu GM, Zhang GZ (2005) Collapse and swelling of thermally sensitive poly (N-isopropylacrylamide) brushes monitored with a quartz crystal microbalance. J Phys Chem B 109:743–747
53. Albet-Torres N, O'Mahony J, Charlton C et al (2007) Mode of heavy meromyosin adsorption and motor function correlated with surface hydrophobicity and charge. Langmuir 23:11147–11156
54. Brinker CJ, Scherer GW (1990) Hydrolysis and condensation II: silicates. In: Brinker CJ (ed) Sol-gel science. Academic Press, San Diego, pp 96–233
55. Ferey G (2008) Hybrid porous solids: past, present, future. Chem Soc Rev 37:191–214
56. Shea KJ, Moreau J, Loy DA et al (2004) Molecular-engineering nanostructured hybrid organic-inorganic materials. In: Gomez-Romero P, Sanchez C (eds) Functional hybrid materials. Wiley-VCH, Weinheim, pp 50–85
57. Yao CX, Zhao N, Liu JM et al (2020) Ultra-stable UiO-66 involved molecularly imprinted polymers for specific and sensitive determination of tyramine based on quartz crystal microbalance technology. Polymers 12:281
58. Ichinose I, Senzu H, Kunitake T (1996) Stepwise adsorption of metal alkoxides on hydrolyzed surfaces: a surface sol-gel process. Chem Lett 25(10):831–832
59. Lee SW, Ichinose I, Kunitake T (1998) Molecular imprinting of azobenzene carboxylic acid on a TiO2 ultrathin film by the surface sol-gel process. Langmuir 14:2857–2863
60. Matsuguchi M, Takaoka K, Kai H (2015) HCl gas adsorption/desorption properties of poly (N-isopropylacrylamide) brushes grafted onto quartz resonator for gas-sensing applications. Sens Actuators B Chem 208:106–111
61. Sartore L, Barbaglio M, Borgese L et al (2011) Polymer-grafted QCM chemical sensor and application to heavy metal ions real time detection. Sens Actuators B Chem 155:538–544
62. Dubois J, Gaudreault C, Vermette P (2009) Biofouling of dextran-derivative layers investigated by quartz crystal microbalance. Colloids Surf B Biointerfaces 71:293–299
63. Yoshikawa C, Qiu J, Huang CF et al (2015) Non-biofouling property of well-defined concentrated polymer brushes. Colloids Surf B Biointerfaces 127:213–220

64. Nilsson SME, Suriyanarayanan S, Kathiravan S et al (2019) Enantioselective hyperporous molecularly imprinted thin film polymers. RSC Adv 9:33653–33656
65. Suriyanarayanan S, Nicholls IA (2021) Making nanostructured materials from maize, milk and malacostraca. Sci Rep 11:24420
66. Suriyanarayanan S, Petrone L, Ederth T et al (2013) Biotinyl moiety-selective polymer films with highly ordered macropores. Commun Chem 49:5274–5276
67. Suriyanarayanan S, Mandal S, Ramanujam K et al (2017) Electrochemically synthesized molecularly imprinted polythiophene nanostructures as recognition elements for an aspirin-chemosensor. Sen Actuators B Chem 253:428–436
68. Mandal S, Suriyanarayanan S, Nicholls IA et al (2018) Selective sensing of the biotinyl moiety using molecularly imprinted polyaniline nanowires. J Electrochem Soc 165:B669
69. Ndizeye N, Suriyanarayanan S, Nicholls IA (2018) Hierarchical polymeric architectures through molecular imprinting in liquid crystalline environments. Eur Polym J 106:223–231
70. Suriyanarayanan S, Nawaz H, Ndizeye N et al (2014) Hierarchical thin film architectures for enhanced sensor performance: liquid crystal-mediated electrochemical synthesis of nanostructured imprinted polymer films for the selective recognition of bupivacaine. Biosensors 4:90–110
71. Haupt K, Mosbach K (2000) Molecularly imprinted polymers and their use in biomimetic sensors. Chem Rev 100:2495–2504
72. Wackerlig J, Lieberzeit PA (2015) Molecularly imprinted polymer nanoparticles in chemical sensing – synthesis, characterisation and application. Sen Actuators B Chem 207:144–157
73. Eersels K, Lieberzeit P, Wagner PA (2016) Review on synthetic receptors for bioparticle detection created by surface-imprinting techniques – from principles to applications. ACS Sensors 1:1171–1187
74. Briand E, Gu C, Boujday S (2007) Functionalisation of gold surfaces with thiolate SAMs: topography/bioactivity relationship – a combined FT-RAIRS, AFM and QCM investigation. Surf Sci 601:3850–3855
75. Mujahid A, Lieberzeit PA, Dickert FL (2010) Chemical sensors based on molecularly imprinted sol-gel materials. Materials 3:2196–2217
76. Anaspure P, Suriyanarayanan S, Nicholls IA (2021) Palladium nanoparticles immobilized on polyethylenimine-derivatized gold surfaces for catalysis of Suzuki reactions: development and application in a lab-on-a-chip context. RSC Adv 11:35161–35164

Biological, Bio-Derived, and Biomimetic Receptors in Mass-Sensitive Sensing

Adriana Feldner, Julia Völkle, Felix Thier, and Peter Lieberzeit

Contents

A. Feldner, J. Völkle, F. Thier, and P. Lieberzeit (✉)
University of Vienna, Faculty for Chemistry, Department of Physical Chemistry, Vienna, Austria
e-mail: adriana.katharina.feldner@univie.ac.at; Julia.Voelkle@univie.ac.at; Felix.Thier@univie.ac.at; Peter.Lieberzeit@univie.ac.at

P. Lieberzeit (ed.), *Piezoelectric Sensors*, Springer Series on Chemical Sensors and Biosensors (2024) 18: 143–224, https://doi.org/10.1007/5346_2023_30,

Published online: 7 November 2023

Abstract A range of biological recognition materials have been implemented in sensing leading to biosensors based on, e.g., antibodies and enzymes. Aside from these, a wide variety of biomimetic approaches have been published, not least in the context of mass-sensitive sensing. These range from receptors derived directly from nature, such as peptides or (olfactory) proteins, to fully artificial systems, such as molecularly imprinted polymers. This chapter introduces a wide range of such man-made receptor strategies in the context of mass-sensitive sensing. It also covers the most promising application areas identified in the literature, namely diagnostics, environmental monitoring, food safety, and public security. A larger part of the chapter covers molecularly imprinted polymers (MIP) and their role in mass-sensitive sensing, because those have turned out to be the most widespread type of biomimetic recognition species in this context.

Keywords Aptamers, Artificial receptors, Bio-inspired receptors, Biomimetic recognition, Molecularly imprinted polymers

1 Introduction

1.1 Mass-Sensitive Devices

Acoustic sensors are widely used for biomimetic sensing. Compared to other transducers, they have one main advantage, which is label-free detection. Acoustic devices are mass-sensitive, which means that the sensor reacts to the mass of the analyte deposited on the sensor surface. In fact, every analyte has a mass, which makes it the most universal physical property to address and distinguishes it, e.g., from optical and electrochemical properties. If a suitable receptor is available, mass-sensitive devices hence can detect a wide range of different analytes in both gaseous and liquid media. Eliminating the labeling step also makes them cost- and time-efficient [1].

1.1.1 Piezoelectric Effect

Most acoustic devices have one thing in common: their working principle relies on the piezoelectric effect, which was discovered in 1880 by Jacques and Pierre Curie. The brothers found that crystals lacking an inversion center generate voltage when being deformed by external force. The opposite effect, i.e., the so-called inverse piezoelectric effect, occurs when applying voltage deforms the material. Several piezoelectric materials are available for sensing purposes, of which quartz is the most popular one, because it is abundant and cheap [2]. Other examples include Rochelle salt, lithium niobate and tantalate, gallium arsenide, and gallium orthophosphate, among others [1].

Applying alternating voltage to piezoelectric devices induces mechanical oscillation, whose exact type depends on both the material and the cutting angle [2]. One can classify the resulting acoustic devices according to the type of wave propagation, namely bulk acoustic waves and surface acoustic waves. Bulk acoustic waves travel through the material, while surface acoustic waves propagate along the surface. When the analyte binds to the sensor surface, this changes some wave parameters, such as resonance frequency or acoustic wave velocity [3].

In 1959, Günther Sauerbrey discovered that the change in frequency is proportional to the mass adsorbed on the surface of a piezoelectric device [4]. This relationship stated in Eq. 1 allows us to use acoustic resonators for developing mass-sensitive sensors.

The Sauerbrey Equation [4]

$$\Delta f = -\frac{2f_0^2}{A\sqrt{\rho\mu}}\Delta m \tag{1}$$

Δf frequency change, f_0 fundamental frequency, A active area, ρ density of the piezoelectric material, and μ shear modulus.

The Sauerbrey equation assumes rigid, (indefinitely) thin films attached to the electrode and the absence of mechanical interactions with the medium. Therefore, it is only valid in the gas phase. In liquids one needs to consider further parameters such as viscosity and density of the surrounding medium. Kanazawa and Gordon developed Eq. 2 that describes the change in oscillation frequency in liquids [5].

The equation by Kanazawa and Gordon [5]

$$\Delta f = -f_0^{3/2}\left(\eta_L\rho_L/\pi\mu_Q\rho_Q\right)^{1/2} \tag{2}$$

Δf frequency change, f_0 fundamental frequency of the dry crystal, η_L elastic modulus of the liquid, ρ_L density of the liquid, η_Q elastic modulus of quartz, and ρ_Q density of quartz.

1.1.2 Bulk Acoustic Devices

Quartz Crystal Microbalance: QCM

The quartz crystal microbalance (QCM) as a matter of fact is the best-known example for a bulk acoustic device and even of piezoelectric sensors in general. Its advantages include straightforward design, easy availability, and low cost because quartz is abundant on earth. Furthermore, it is possible to operate QCMs in both gaseous and liquid phases. The device consists of a thin AT-cut quartz plate comprising metal electrodes on both sides. Figure 1 shows a schematic of such a device. When applying alternating voltage to the electrodes, the quartz starts to

Fig. 1 Schematic of a QCM sensor

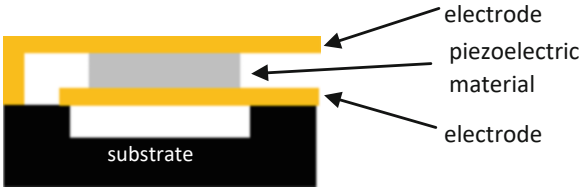

Fig. 2 Schematic of an FBAR sensor

oscillate in thickness shear mode. Typical resonance frequencies of QCMs are in the range 2–20 MHz. Higher resonance frequencies lead to higher sensitivity. Therefore, thinner quartz substrates lead to higher resonance frequencies. Hence, there is a limit to increasing sensitivity of QCMs: very thin quartz plates are too fragile to be mechanically stable and can easily break during handling and measurements [3].

The QCM is also sensitive to changes in viscosity or density of the surrounding medium. What seems a disadvantage at first sight is actually useful for measuring: the corresponding technique is called quartz crystal microbalance with dissipation monitoring (QCM-D). It allows for determining both the mass and viscoelastic properties of an adsorbed layer in situ [6].

Next to viscoelasticity, changes in temperature also heavily affect the frequency behavior of QCM sensors in liquid phase, and, to a much lesser extent, also in gas phase. To obtain reliable signals in non-thermostated measurement setups, one can use sensors comprising an additional reference electrode on the same quartz substrate. With this dual electrode setup, signals that originate from variations in non-specific, ambient conditions such as temperature or viscosity can be compensated for by subtracting the reference from the measurement signal [7].

Film Bulk Acoustic Wave Resonator: FBAR

The (thin)-film bulk acoustic wave resonator (FBAR) is a lesser known member of the family of BAW devices. In many ways, FBARs are similar to QCMs. They differ from one another mainly in size, thickness, and substrate material. Figure 2 depicts a typical FBAR device. FBARs are fabricated from very thin piezoelectric substrates sandwiched between two electrodes. Instead of quartz, they usually consist of zinc oxide (ZnO) or aluminum nitride (AlN) thin films, among others. Those materials have high acoustic velocities and low acoustic loss. Together with the reduced thickness this leads to higher resonance frequencies than in QCMs. Typical FBAR frequencies range from sub-GHz to 10 GHz. This means that FBARs reach higher sensitivities than QCMs. FBARs can be operated in gaseous and liquid phase since the damping of the acoustic waves of these devices is low [8].

1.1.3 Surface Acoustic Devices

Surface Acoustic Wave Resonator: SAW

SAW devices contain interdigitated metal electrodes on the surfaces of piezoelectric substrates. Applying alternating voltage to these electrodes generates an acoustic wave that propagates over the surface in a way first described by Lord Rayleigh [9]. Such a wave is confined to the surface and travels perpendicular to the electrodes. In the case of resonators, reflectors on the sensor surface reflect the waves back (whereas delay lines lack these reflectors). SAW devices can comprise either one set of interdigitated electrodes (single port SAW) or two sets.

Figure 3 shows a SAW sensor with two sets of interdigitated electrodes. In such two-port devices, one of the electrodes acts as the signal input, and the other one as the output. The acoustic waves travel from the input to the output. It is possible to deposit a recognition layer in the area between the two electrode structures. Interaction of the analyte with this layer leads to changes in wave propagation and thus affects the signal that reaches the output electrode. The design of the SAW device directly influences the properties of the surface acoustic wave. The width of the interdigitated electrodes, for instance, determines the fundamental frequency. Surface acoustic wave (SAW) devices reach higher resonance frequencies compared to QCM. Typical frequencies are in the range of several hundred MHz to GHz. This makes SAW devices extremely sensitive. Other advantages of the transducer include fast responses, ruggedness, and small size [1].

SAW devices are highly suitable for detecting gaseous analytes. Their main drawback is the fact that liquids damp the longitudinal phase of the waves due to their high viscosity. This leads to a loss of acoustic energy, as it is partly transferred to the liquid. However, there are ways to solve this problem. By adjusting the cutting angle of the piezoelectric material, one can generate so-called shear horizontal wave surface acoustic wave resonators (SH-SAW), sometimes also referred to as shear transverse wave resonators (STW). They are useful for SAW measurements in liquids since the design minimizes energy loss due to damping. Additionally, the high dielectric constant of some liquids is another reason for limited application of SAW devices. Quartz, which is the most common substrate for SAW sensor

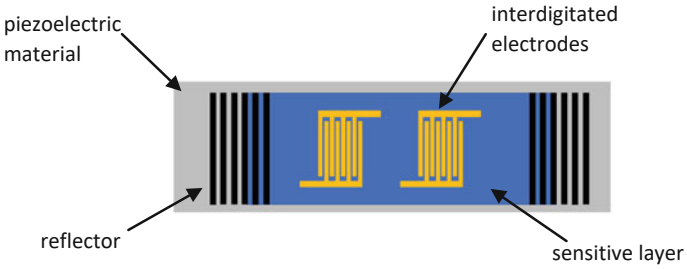

Fig. 3 Two-port SAW device

fabrication, has a relatively low dielectric constant, which leads to poor electro-acoustic coupling. This problem can be solved by using materials with a higher dielectric constant, such as $LiTaO_3$. Finally, sensor design is another factor: the substrates of Lamb wave devices have a confined thickness in the micrometer range [1]. Love wave resonators are SH-SAW resonators comprising a thin guiding layer on the sensor surface. The waves traveling through the waveguide layer are called Love waves. The interfacial layer also protects the sensor surface from highly conductive solvents and chemicals in the liquid. Waveguide layers usually consist of dielectric materials, such as silicon dioxide, silicon nitride, or polymers [10].

SAW-RFID-Tags

SAW-based radio-frequency identification (RFID) is a system used for rapid and automatic tracking and detection using a tag and a reader. A transmitter sends a radio pulse which is received by interdigital transducers (IDTs) of a SAW device. There it is processed into acoustic waves. The waves go through reflectors and produce an acoustic wave signature. The acoustic waves are sent back to the IDTs. There they are converted back to radio signals. RFID devices contain a single IDE port and a unique reflector pattern. One can coat them with chemical recognition layers to obtain wireless remote sensor systems [1].

Microcantilever Sensors

Microcantilevers are usually known from atomic force microscopy (AFM). However, it is possible to fabricate sensors from free-standing oscillating cantilevers consisting of piezoelectric materials. The resulting devices react to mass deposition with frequency changes similar to QCM. Figure 4 shows an example of such a microcantilever sensor. They can also be used in liquid phase. However, the immersion depth of the transducer strongly influences the frequency response [11].

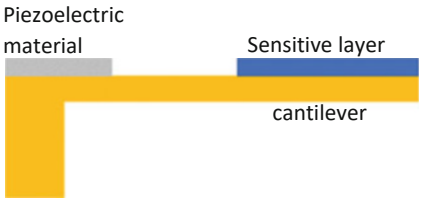

Fig. 4 Microcantilever sensor

2 Receptor Strategies for Mass-Sensitive Detection

Per se, mass-sensitive devices are of course not selective: any mass deposited on their surfaces leads to corresponding frequency effects. It is, therefore, the task of chemistry and materials' sciences to generate or implement selectivity through depositing suitable recognition layers on the respective device surface. The following section will briefly touch on biological recognition material followed by introducing the current range of state-of-the-art biomimetic receptors.

2.1 Biological and Bio-Derived Receptors

2.1.1 Enzymes

The glucose sensor for blood sugar monitoring is the most well-known and widespread enzyme-based biosensor. It usually utilizes glucose oxidase or glucose-1-dehydrogenase. The enzymatic reaction produces hydrogen peroxide which diffuses to the electrode. There, it is re-oxidized and thus generates the signal. The electron flow is proportional to glucose concentration and can be measured electrochemically [12]. Even though enzymes are not the most popular material for sensing layers on mass-sensitive sensors, there are indeed a few studies on this topic. The main challenge lies in enzyme immobilization on the electrodes in a way that they retain their stability and activity. Often, this takes place via self-assembled monolayers (SAMs) of suitable linkers: for example, Nihira et al. immobilized dextransucrase on QCM electrodes via amine coupling using α-amino-ω-carboxyl poly(ethylene glycol)$_{44}$ as a spacer and 3,3′-dithiodipropionic acid [13]. Diltemitz et al. coated QCM electrodes with acetylcholinesterase immobilized in poly(styrene-maleic anhydride) nanofibers. Often those approaches are used to study the kinetics of enzymatic reactions [14].

2.1.2 Antibodies

Antibodies or immunoglobulins are Y-shaped proteins that recognize and bind to foreign species, such as bacteria or viruses in the body in a highly specific manner. Using QCM sensors based on natural antibodies to detect viruses in a rapid, sensitive, and specific manner is especially interesting, because viruses are hardly accessible for rapid analysis. The type of antibody used and its orientation on the sensor surface directly impact device performance. So far, antibody-QCM sensors are not an established standard technique for viral diagnostics. Nevertheless, a considerable number of systems for virus detection via antibody-modified QCM have been published. Examples of those include a QCM immunosensor using magnetic nanobeads and polyclonal anti-H5 antibodies to detect the avian influenza

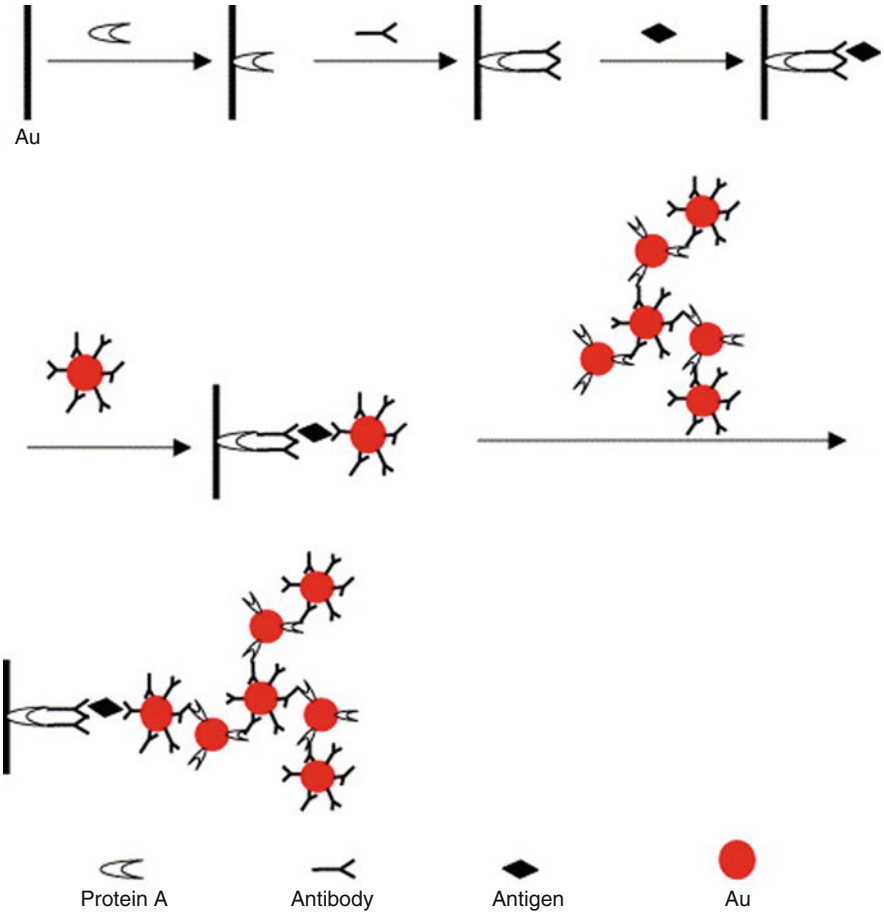

Fig. 5 Dendritic amplification of the antigen–antibody recognition using antibody-functionalized Au nanoparticles followed by the dendritic complex of protein-functionalized Au nanoparticles and antibody-functionalized Au nanoparticles. Reprinted with permission from [16], © Elsevier

virus (AIV) H5N1 in agricultural, food, environmental, and clinical samples. The magnetic nanobeads in this case serve to amplify the signal caused by the binding reaction [15].

Dendritic amplification is another way of signal amplification; Fig. 5 depicts the process: [16] for this purpose, Chu et al. immobilized goat anti-human immunoglobulin G (IgG) to bind human IgG. They achieved primary amplification by adding antibody-functionalized nanoparticles and secondary dendritic amplification by immunocomplex formation between protein A- and antibody-functionalized nanoparticles.

Another approach targeted the maize chlorotic mottle virus: here, the antibody was immobilized on QCM electrodes via a monolayer of 3-mercaptopropanoic acid

and 11-mercaptoundecanoic acid. This sensor was then developed further to detect other highly virulent species, such as the Ebola virus [17]. Further examples include detection of H3N2 canine influenza virus and canine parvovirus [18].

2.1.3 Olfactory Receptor Proteins

Though antibodies are of course a widespread – and rather common – choice as receptors, also other proteins have been successfully applied in piezoelectric sensing. For instance, olfactory receptor proteins are becoming increasingly popular in gas sensing: the olfactory receptor (OR 1) superfamily comprises a repertoire of about 1,000 different G protein-coupled receptors. In nature, they transform chemical information into electrical signals that the brain decodes and experiences as smells.

Early experiments immobilized crude fractionated ORPs from olfactory epithelium taken from bullfrogs on QCMs. These respond reversibly to several odorants. Later a receptor from *Caenorhabditis elegans* (ODR-10) expressed in *E. coli* was coated onto QCMs which then responded selectively to diacetyl, the natural ligand of this receptor [19].

Ko et al. expressed olfactory receptors on the surfaces of cultured cells and immobilized them on QCMs for detecting binding of odorant molecules to the olfactory receptors. They produced a stable cell line of HEK-293 cells, immobilized the cells on the sensors, and demonstrated a clear response to octyl aldehyde [20].

Another approach utilized olfactory cells rather than only proteins as a functional layer on SAW sensors. Sf9 cells form a monolayer on the surface of $LiTaO_3$ SAW devices. Furthermore, the cells are able to grow on these devices over extended periods of time [21].

2.1.4 Peptides

Protein-based recognition hence leads to appreciable sensing properties. However, protein molecules are difficult to purify from natural sources and often very tedious to synthesize. For these reasons, the design of artificial receptors is one of the main goals of sensor biotechnology. Short peptides represent an opportunity for that purpose: first, a large variety of different molecules are available by combining the 21 natural amino acids. Second, fast screening techniques of peptide libraries are available. Third, automated synthesis is possible. Thus, it is possible to prepare relatively large amounts of highly purified peptides at comparably low cost compared to, e.g., monoclonal antibodies. Furthermore, it is relatively easy to modify and model peptides to further enhance binding.

There are several ways to obtain peptides for sensing:

1. Designed synthetic peptides: These are artificial peptides based on known interactions between amino acids and targets. The goal is not to build highly organized binding sites, but peptide motifs to allow for intermolecular self-organization over the sensor surface.
2. Short peptides from random phage display: Here, the peptides are selected randomly from large, commercially available phage display libraries.
3. Peptide receptors for ligand sensing: The known sequence of a natural receptor is reduced to a stable, synthesizable size. Alternatively, binding sites can be created on a designed peptide scaffold.
4. Ligands for receptor sensing: Short peptides serve as elements to detect a defined receptor. Examples for this are antimicrobial and cell-penetrating peptides to sense bacterial cells or antigenic peptide sequences for antibody sensing [22].

Peptide-based mass-sensitive sensors have been reported for a variety of analytes including whole cells, proteins, small organic molecules, and ions.

For instance, it is also possible to replace the above-mentioned entire olfactory receptors by peptides simulating their respective binding sites. One can deposit those on the surfaces of QCM electrodes to form a sensitive layer. For example, the peptide LEKKKKDC-NH2 derived from an aldehyde binding site in the HarmOBP7 protein was synthesized and used as a sensing material in a biosensor leading to reproducible sensor responses for acetaldehyde [23].

Another approach reports a polypeptide sensor based on an olfactory receptor to detect acetic acid at low concentrations and at room temperature. The sensor exhibited repeatable response to acetic acid and reproducibility among multiple sensors. Figure 6 shows the sensor fabrication and measurement [24].

Peptide-based strategies are not only useful for detecting single analytes, but also for sensor arrays. An example for this is simultaneous detection and identification of various classes of volatile organic compounds by a QCM-based array comprising six sensors coated with synthetic polypeptides together with conducting polymers. The sensor module selectively and sensitively detects and discriminates analytes such as acetic acid, butyric acid, ammonia, dimethyl amine, benzene, chlorobenzene, and their mixtures via characterized profiles [25].

Of course, peptide-based sensing is not restricted to the gas phase: for instance, a peptide immobilized as a stable and highly packed SAM was reported to detect vancomycin. It is formed in the presence of a designed spacer, containing several poly(ethylene glycol) units that modulate polarity [26].

When designing artificial recognition sequences, molecular modeling of the actual interaction center usually decreases the overall synthesis time, because candidate receptors can be selected in silico: detection of the mussel heat shock protein HSP70 in crude extracts of the mussel mantle by artificial heptapeptides on QCM is an example for this approach. After finding optimal amino acid sequences to interact with the hapten of HSP70, the researchers immobilized them on QCM and compared the sensor results obtained with those of HSP70-specific antibodies. Both methods result in similar selectivity and sensitivity [27].

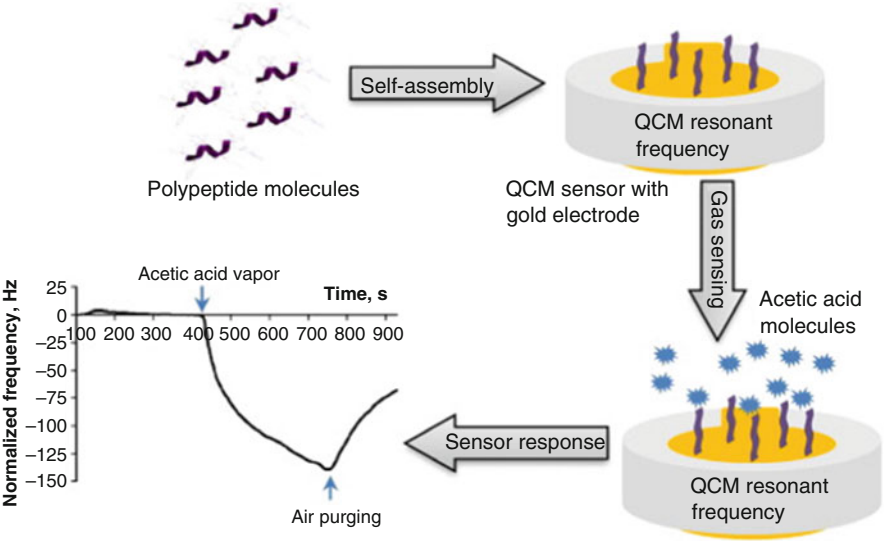

Fig. 6 Schematics showing the QCM sensor development process. Reprinted with permission from [24], © Elsevier

2.1.5 DNA

One of the most important challenges in utilizing DNA as the selective receptor layers in QCM-based sensors is immobilizing it on the surfaces of QCM electrodes. This requires modifying Au electrodes with thiols that form a self-assembled monolayer. In other approaches, DNA is first attached to biotin followed by immobilizing the complex on an avidin or streptavidin layer on the QCM electrodes. Although these techniques are both well established and efficiently work in biosensors, this additional fabrication step is tedious and requires additional reagents. Nevertheless, the resulting sensors are usually highly selective and sensitive, offsetting the larger synthesis effort. Once the device is ready to use, it is able to recognize different viruses selectively and to quantify them via hybridization of their genomic sequence with the DNA probe [17]. A few examples for DNA-QCM sensors include the detection of hepatitis B virus (HepBV) [28], hepatitis C virus (HepCV) [29], human papilloma virus (HPV) [30], and dengue virus [31].

2.1.6 Aptamers

Aptamers are short-to-medium sequences of single-stranded nucleic acids (DNA or RNA), typically in the range of 20–90 nucleotides. They are relatively easy to adapt to a variety of analytes, to which they bind in a manner that is analogous to

antibodies. Target species among others comprise ions or small molecules, a wide range of proteins, and even entire cells.

Aptamers are produced by systematic evolution of ligands by exponential enrichment (SELEX). This process takes only a few weeks, which is relatively fast compared to the time needed to produce monoclonal antibodies. Aptamers are also much more stable than antibodies and withstand harsher conditions. Utilizing aptamers with QCMs as transducers makes sense: they are relatively small; hence there are no problems related to swelling, which usually decreases the electronic quality of QCM signals. Despite these advantages, only relatively few QCM aptasensors have been reported for viruses. Nonetheless, there are some promising results, mainly for sensing AIV H5N1 and HIV-1, which indicate the potential of aptamer-QCM viral diagnostic systems [17].

Wang et al. applied a slightly different approach: Instead of using streptavidin–biotin complexation, they bound the aptamer directly to a thiol monolayer via an NHS linker. Furthermore, they increased the active surface area by nanostructuring to detect AIV H5N1 [32].

Brockman et al. established a method to amplify the signal generated by a QCM aptasensor for AIV H5N1. They first immobilized streptavidin directly to the QCM surface and then bound biotinylated aptamers to it to detect the viruses. Finally, the QCM aptasensor signal was amplified by adding aptamer-coated magnetic nanobeads. Nanobead amplification of the sensor signal was effective at low AIV H5N1 concentrations [33].

Recently, a slightly more complex approach was developed and utilized by Wang et al., who incorporated the aptamers for AIV detection into a hydrogel. The hydrogel approach has certain advantages: for example, it helps enhancing the measuring effect and protecting the aptamer against degradation [34].

Piezoelectric aptasensors for small molecules often require signal amplification, since low-molecular-weight species, especially at small concentrations, do not cause detectable frequency shifts. Usually, nanoparticles are used to enhance the effect. For example, Tian et al. used gold nanoparticles for their aptasensor for okadaic acid [35]. Yuan et al. developed a sandwich strategy to enable the detection of trace amounts of arsenite via a QCM aptasensor. First they prepared a self-assembled monolayer (SAM) of mercaptoethylamine to which the arsenite can bind. Then they added gold nanoparticles modified with arsenite aptamer. The modified particles bind to the analyte via the aptamer and form a sandwich. Arsenite first binds to the SAM on the gold surface of the QCM and then the nanoparticles attach to them. Figure 7 shows the process. Nanoparticle binding increases the sensor signal in a way that allows for detecting trace concentrations of arsenite [36].

Neves et al. use a very different strategy for their acoustic wave sensing platform with anti-cocaine MN4 DNA aptamer. They immobilized the biomolecule in an adlayer of S-(11-tri-chlorosilyl-undecanyl)-benzenethiosulfonate (BTS). Unlike other variants only the tertiary structure of this aptamer changes during target binding. Repeated regenerability of the sensor platform was demonstrated. They postulated that analyte loading leads to conformational changes of the aptamer upon binding. The sensor in this work is one of the few examples of a bulk acoustic wave

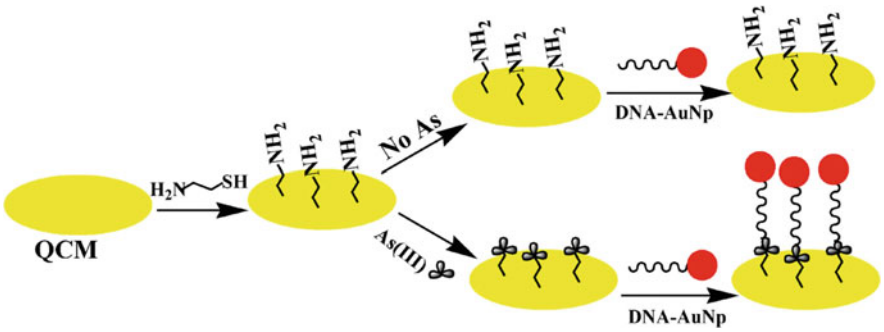

Fig. 7 Scheme of the piezoelectric biosensor for arsenite detection. Reprinted with permission from [36], © Springer

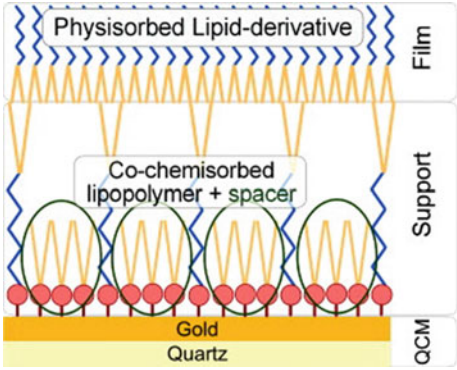

Fig. 8 Representation of the reported fabrication method. The spacer lipids (circled) separate the lipopolymer macromolecules (blue). Reprinted with permission from [38], © Elsevier

aptasensor that is able to directly detect the binding interaction between an aptamer and a small molecule without a signal amplification step [37].

2.1.7 Self-Assembled Monolayers (SAM)

Self-assembled monolayers are not only useful tools for immobilizing other receptors on (mass-sensitive) devices but also serve as recognition layers in their own right: for instance, Wysinski and Nakamoto presented an approach using lipopolymers, materials composed of lipid and polymeric moieties, linked covalently within one macromolecule (see Fig. 8). Distearoyl lipids grafted with poly(ethylene glycol) of various chain lengths were directly immobilized on QCM sensors. The pegylated lipids discriminated various odorants according to their functional groups. Spacer lipids adsorbed between the lipopolymers. Further layers of lipopolymers can adsorb on top of the mixed SAMs. The resulting sensors exhibit higher sensitivity to the analytes compared to sensors without spacer. Additionally, they were better at discriminating the odorants from one another [38].

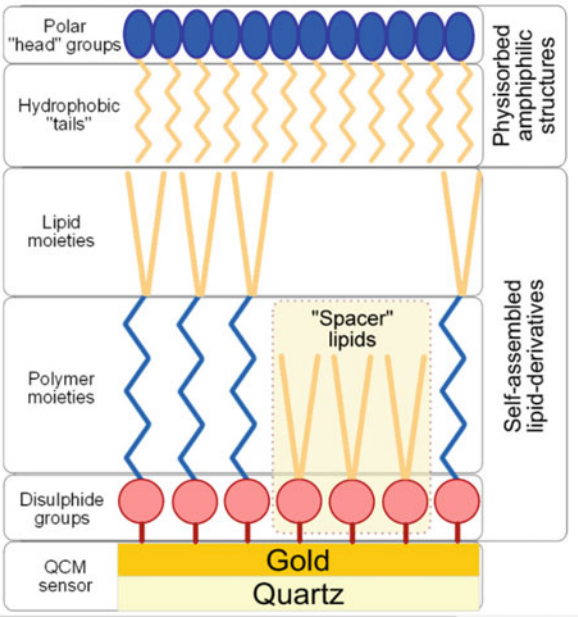

Fig. 9 Schematic of the fabrication of QCM odor sensors using lipid derivatives. Reprinted with permission from [39], © John Wiley & Sons

A different study utilized the same concept with two types of lipopolymers terminated with either ether or disulfide groups, resulting in mixed lipopolymer SAMs. To further modify it, the authors adsorbed amphiphilic species on top of the SAM. Figure 9 shows a schematic of the layer structure. The approach allowed for fabricating QCMs with very good sensitivity toward odorants with the physisorbed material increasing the ability to discriminate between different analytes [39].

Using mixed SAMs allows for fine-tuning the affinity and selectivity of the receptor layer by adjusting the chain length, functional groups, and ratio of the different SAM components. Lieberzeit et al. for example were able to selectively detect xylene in concentrations as low as 10 ppm using SAWs coated with mixed SAMs of trimethylchloro- and 7-octenyldimethylchlorosilane. The different chain lengths of the two silanes result in molecular cavities within the monolayer that serve as adsorption sites for the analyte. By computational simulation, the ratio of octenyl and trimethyl molecules was optimized to yield binding sites tailored toward the size and chemical functionality of the analyte [40].

The SAM approach is also inherently useful for immobilizing a ligand to detect a larger protein: for example, N-acetylglucosamine (GlcNAc) binds to wheat germ agglutinin (WGA) lectin. GlcNAc was linked to p-nitrophenol for immobilization followed by reducing the nitro group and binding it to cysteine. This is necessary because the respective binding pocket in WGA is not located on the outer surface of the quaternary structure, but somewhat within the molecule. QCM measurements revealed that the sensor reaches maximum sensitivity toward the analyte when 5,000 parts cysteine per one part ligand are present in the SAM: this ratio allows for forming a protein monolayer on the ligands without steric hindrance. The same

systems could be transferred to different strains of influenza A virus (H5N3, H5N1, H1N3) since GlcNAc is part of the oligosaccharide ligand responsible for the first binding step [41].

2.2 *Inorganic Receptors*

Developing sensor layers that mimic the highly selective recognition capabilities of biological receptors is both intriguing and demanding. A large body of research focuses on applying recognition units directly inspired by molecular structures found in nature – as the previous section also illustrates. However, they often face similar challenges as their natural counterparts: most importantly, limitations regarding long-term stability at non-physiological conditions. Therefore, it is of huge scientific and practical interest to synthesize novel artificial materials that are more stable against physical and chemical impact. The main challenge in developing such recognition layers lies in achieving sufficient selectivity.

2.2.1 Two-Dimensional Atomic Crystals

Two-dimensional (2D) atomic crystals hold great promise in biomimetic sensing. Sparked by the first isolation of graphene in 2004 [42], a wide range of such ultra-thin inorganic materials have been synthesized and investigated for sensing applications. Typically, they comprise a 2D layered structure that is only one or several atomic layers thin, but relatively large in terms of lateral dimensions, namely up to several millimeters. Within the layers, atoms are covalently interconnected, while individual nanosheets are stacked via weaker van der Waals interactions [43, 44]. Next to their exceptionally high conductivity, mechanical strength, and flexibility, 2D materials exhibit remarkably high specific surface areas, providing ample space for potential analyte adsorption sites in sensor applications. Most prominent in piezoelectric detection are the graphene derivatives graphene oxide (GO) and its reduced form (rGO). Recently, research efforts also focused on other graphene-like 2D structures such as transition metal dichalcogenides (TMDs) and MXenes [45–48].

Pristine graphene offers little room for selective recognition. Each sheet consists of a monolayer of sp^2-hybridized carbon atoms arranged in a tightly packed honeycomb. Most notably, aromatic structures can adsorb via π–π stacking. But due to the strong and unselective nature of this interaction, it is primarily used to immobilize biomolecules onto graphene layers, rather than directly for sensing purposes [49]. Some inherent selectivity regarding different volatile organic compounds can be attributed to the presence of defects within the material that provide adsorption sites. However, one can achieve only limited selectivity, which in addition is difficult to adjust [50, 51]. The hydrophobic nature of the material poses further challenges, making it poorly dispersible in water and most organic solvents. Hence, there are

very few applications using pristine graphene as selective layers for piezoelectric sensors [52, 53].

GO- and rGO on the other hand consist of a mixture of sp^2- and sp^3-hybridized carbon atoms that can bear epoxide and hydroxyl groups at the surface, as well as carboxyl groups at the edges, making them readily dispersible in water and polar solvents [52]. The oxygen functional groups also provide more selective interaction sites for molecular recognition and further derivatization of the sensing layers. For instance, formaldehyde concentrations as low as 1.7 ppm could be detected by GO-coated QCM. As the signal recovered quickly and almost completely after flushing with air, the sensor response can be attributed to hydrogen bonding between the GO functional groups and the analyte [54]. Similar findings have been reported by Yao et al., who observed excellent humidity sensing properties of GO-coated QCMs in the range of 6.4–93.5% relative humidity. Again, the sensing mechanism can be explained by analyte adsorption via H-bonding at lower RH. For higher RH (>54.3%), interlayer expansion stress of the GO films due to swelling also influences the frequency response. This swelling behavior leads to large frequency shifts, but is also linked to a decline of the quality factor (Q-factor), due to energy dissipation by the increased motional resistance of the sensing layer [55] This problem can be addressed by taking advantage of the oxygen functionalities for further fine-tuning the sensing materials' properties. For example, conjugating the carboxylic acid groups at the edges of GO flakes with ethanolamine leads to a much faster response and recovery when exposed to humid air and an overall improvement of the Q-factor at higher RH, with no obvious decrease to up to 75% RH [56].

While there are many examples of highly sensitive GO-based piezoelectric devices for detecting small analytes in the gas phase, implementing graphene derivatives as selective layers on a wider scale still faces substantial obstacles. The highly reactive nature of the oxygenated groups leads to broad cross-sensitivities, thus posing a major challenge when it comes to implementing GO-based sensors in complex environments [52]. Chemical derivatization is one way to introduce more selective interaction centers. However, this is no trivial task: multiple reactions may occur simultaneously during functionalization, resulting in inhomogeneous GO layers lacking a well-defined chemical structure [53].

Transition metal dichalcogenides (TMDs) are a group of 2D materials that has been heavily researched since the early 2010s regarding their use in biomimetic detection [44]. One TMD nanosheet consists of three covalently bound atomic layers, namely a transition metal layer (M: element of group 4–10) sandwiched between two chalcogen layers (X: S, Se, or Te). Most prominent in sensing are molybdenum disulfide (MoS_2) and tungsten disulfide (WS_2) because it is possible to obtain them by mechanical exfoliation from relatively abundant, naturally occurring layered minerals. To date more than 40 TMDs have been reported and investigated [57]. Next to their elemental diversity, TMDs also exhibit a range of different structural configurations that heavily influence the material properties. Depending on stacking order and coordination of the metal atom, they occur in various polymorphic forms, depicted in Fig. 10: 1T (tetragonal), 2H (hexagonal), and 3R (rhombohedral) [47, 59]. This inherent chemical and structural variability is very

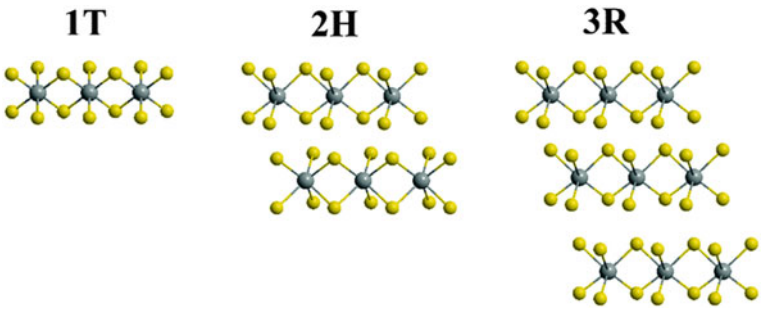

Fig. 10 Stacking order of the most common TMD polytypes: 1T, 2H, and 3R. Gray spheres: transition metal atoms, yellow spheres: chalcogen atoms [58]

appealing in terms of sensing applications, as it offers room for fine-tuning sensitivity and selectivity toward one specific analyte.

For instance, Alev et al. reported WS_2 thin film-coated QCMs with high selectivity toward the nerve agent simulant dimethyl methylphosphonate (DMMP) when compared to the response toward various other hazardous gases, including acetone, toluene, xylene, isopropanol, hydrogen cyanide, hydrogen sulfide, 2-chloroethyl sulfide, and ammonia. They explained this exceptionally high affinity by the polar nature of the P=O and -OCH_3 functional groups in DMMP, strongly adsorbing on the surface-active sites of WS_2. They were also able to further tune material sensitivity by adjusting the base pressure in the magnetron sputtering chamber when depositing the WS_2 thin films. Sensing layers produced at lower pressures contained a larger number of sulfur vacancies that acted as active sites to incorporate oxygen and selectively bind DMMPs, yielding a calculated LOD of 5 ppb in dry air. This suggests that controlled adjustment of surface defects leads to strong changes in material affinity [60].

Wang et al. reported similar findings regarding the sensing performance of MoS_2-coated resonant microcantilevers. They compared the frequency responses of both 1T and 2H Mo_2S phases toward formaldehyde, CO, CO_2, H_2S, SO_2, NO, NO_2, and NH_3. While both sensor layers showed the largest response toward HCHO, this effect was comparably small for the 1T polymorph. The 2H phase on the other hand was almost 10-times more sensitive toward HCHO compared to the other analytes. Supported by density functional theory (DFT) calculations of the binding energies, this strong difference in sensitivity can be explained by the higher surface defect concentration in 2H-MoS_2 due to lattice instabilities. The defects and vacancies can form O-H and Mo-O bonds with formaldehyde, providing a large number of selective adsorption sites [61].

Aside from manipulating defect sites and morphology, doping with other elements also appears a promising method for adjusting the sensing behavior of TMDs. For instance, Sanyal et al. conducted an *in silico* study investigating the binding energies of Ag-, Au-, Pd-, and Ti-decorated VSe_2 toward the toxin nitrobenzene. Their findings suggest a strong influence of the dopant on binding interactions and

recovery time, with Pd-doped VSe_2 being the most promising system for nitrobenzene detection [62].

While the large chemical and structural variability of TMDs offers plenty of choices for selectivity engineering, it also introduces the need for rational design and machine-learning assisted assessment of sensing layers, because a conventional "trial-and-error" approach is unrealistic given the vast number of material and analyte combinations [43]. Furthermore, in order to broadly implement TMDs in chemical sensors one needs to tackle their strong response to ambient humidity, as well as the tendency of some TMD layers, most prominently WS_2, to oxidize at room temperature and ambient conditions, resulting in a drastically altered sensor performance over time [44].

MXenes are an emerging family of two-dimensional multilayered nanostructures first synthesized in 2011 [63] with the general formula $M_{n+1}X_nT_x$ ($n = 1,2,3$). Each nanosheet consists of one X layer (X = carbon or nitrogen) sandwiched between two M layers, with M being an early transition metal such as Ti, V, Sc, and Cr. T refers to the surface functional groups, namely -OH, -O, and -F. Additionally, MXenes consisting of ordered double transition metals, formulated as $M'_2M''C_2$ and $M'_2M''_2C_3$, were predicted and synthesized in 2015 [64].

Given their rich chemical variability, MXenes are promising candidates for developing specifically tailored, highly selective sensing layers. Next to the variety in transition metals, the surface functional groups offer room for selective interaction and further chemical modification [65]. Moreover, it is possible to adjust the distance between individual nanosheets by intercalating organic molecules or metal cations, which may drastically increase the number of available binding sites [66]. Yet, few applications using MXenes as sensing layers for piezoelectric devices have been published to date. Most notably, Li et al. investigated the response of one of the most established MXenes, $Ti_3C_3T_x$ (T = F, OH) toward ambient humidity, as well as its selectivity toward other VOCs using a 10 MHz QCM. They observed excellent humidity sensing properties with a sensitivity of 12.8 Hz per percent RH, good repeatability, and long-term stability. Moreover, the material was highly selective toward RH changes, with much smaller responses toward ethanol, acetone, formaldehyde, benzene, ammonia, NO_2, CH_4, SO_2, and HF. Investigations of the sensing mechanism using DFT calculations revealed that the surface F adsorption sites play an important role and enhance the humidity sensing properties [67].

One reason for the rather slow progress in developing MXene-based sensing layers might be the relatively laborious synthesis procedure. In contrast to graphene derivatives and TMDs, one cannot obtain MXenes by simple mechanical exfoliation of naturally occurring compounds. Typically, they require a multi-step synthesis process that includes HF etching of the MAX precursors (A = element of group 13 or 14) to yield the MX-layered bulk material. The subsequent exfoliation step requires large organic intercalants to weaken interlayer interactions in MX materials, which increases the risk of introducing contaminations. As each synthesis step heavily influences product quality and surface properties, it is necessary to control and optimize the process precisely to obtain reproducible results [65].

2.2.2 Crystalline Porous Materials

As mentioned in the previous section, the large surface-to-volume ratio of 2D nanomaterials is a key characteristic when it comes to developing biomimetic receptor layers. With specific surface areas ranging from 1,000 to 10,000 m^2/g [68], crystalline porous materials offer even larger potential to adsorb analytes, making them highly appealing candidates for developing highly sensitive piezoelectric devices. Next to the naturally occurring mineral zeolite, extensive research efforts have been focused on applying highly tailored metal-organic frameworks.

Metal organic frameworks (MOFs) are a class of crystalline porous materials composed of metal nodes (metal ions or clusters) interconnected by organic linkers via strong coordination bonds. Usually, transition metal ions serve as coordination centers, providing a large variability in coordination number, geometry, and oxidation state. Usually, multivalent organic molecules, most commonly with N- or O-donor atoms (e.g., carboxylates or amines), are the ligands [69, 70]. The large variety of structural components gives rise to a seemingly unlimited number of combinations available as highly specific sensor materials.

Given that MOFs are available through bottom-up synthesis, it is possible to define key properties such as porosity, morphology, rigidity, crystallographic phase, and size, as well as chemical functionalities during synthesis. For example, Uehara et al. were able to adjust the size of $[Cu_3(btc)_2]_n$ nanocrystals by controlling crystallization speed. Subsequent assessment of the mass uptake of methanol and hexane vapors using a gold-coated QCM substrate revealed much faster sensor responses for the smallest nanocrystals of around 100 nm size, illustrating that sorption kinetics and therefore sensor performance strongly depend on crystal size [71].

Chirality is another key property that one can control during synthesis and that strongly influences adsorption behavior of the material. For example, Liu et al. reported the growth of enantiopure $[\{Zn_2(cam)_2(dabco)\}_n]$ MOFs on self-assembled monolayer (SAM) substrates (Fig. 11, left). Sensing layers were grown in situ on QCM electrodes modified with either COOH- or pyridyl-terminated SAMs. These functional groups control nucleation of crystal growth, resulting in either (+) or (−) orientation of the chiral camphorate (cam) ligand. Adsorption measurements of either R- or S-2,5-hexanediol revealed 1.5 times higher affinity of the (+)-1-MOF toward the R-enantiomer and vice versa (Fig. 11, right) [72].

The well-defined, tunable pore size of MOFs is also useful to exclude analytes above a certain size from entering the sensing layer. For instance, Paschke et al. compared the responses of SAW resonators coated with two different MFU-4-type MOFs ($Zn_5Cl_4(BBTA)_3$, $BBTA^{2-}$ = *1H,5H*-benzo(1,2-d:4,5-d′)bistriazolate). The short, rigid $BBTA^{2-}$ linker of MFU-4 was extended by two additional six-membered rings to yield the MFU-4*l* framework. The resulting difference in pore diameter (MFU-4: 2.5 Å, MFU-4*l*: 9.1 Å) strongly influenced selectivity of the two materials: while MFU-4 was useful to detect CO_2 concentrations as low as

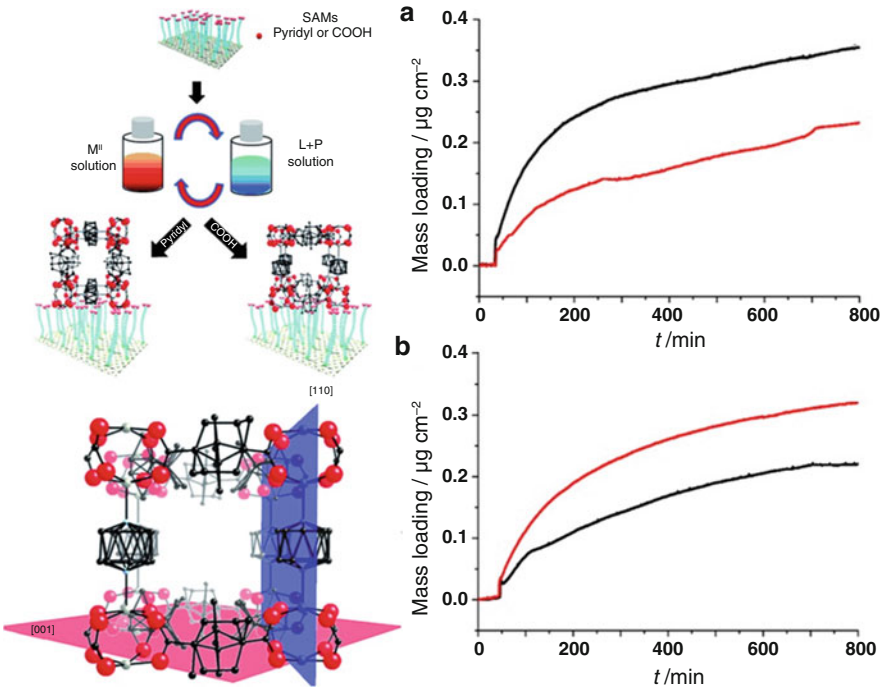

Fig. 11 Left – op: Two principal growth directions and of [{Zn2(cam)2(dabco)}n]; bottom: schematic illustrations of oriented growth in the (001) orientation on pyridyl-terminated (PPMT) and the (110) orientation on COOH-terminated (MHDA) SAMs on gold substrates. Right: QCM profiles of specific mass uptake of each enantiomer from the gas phase: a) R-HDO (black) and S-HDO (red) over (+)-1 (20 cycles) and b) R-HDO (black) and S-HDO (red) over (−)-1 (20 cycles). The difference in the absolute adsorption values for the two samples may arise from a slight difference in the total amount of SURMOF deposited on the QCM substrate surface. Reprinted with permission from [72] © John Wiley and Sons

1 ppm, even 100% CH_4 did not lead to signals. On the other hand, the larger structure of MFU-4*l* showed strong response toward both gases [73].

Next to structural properties, selectivity is closely related to the nature of metal center and ligand. Haighighi et al. for instance investigated the selectivity toward various VOCs of a QCM coated with MIL-101(Cr), an MOF composed of Cr metal centers and terephthalic acid ligands. In addition to appreciable sensitivity, repeatability, reversibility, and long-term stability, the sensor layers showed high selectivity to pyridine. Its signal was 3–24 times higher compared to alcohols, ketones, halomethanes, alkanes, and heterocyclic aliphatic compounds, most likely due to π–π interactions between pyridine and the aromatic linker moieties [74]. One can further tune affinity by chemical functionalization of metal center or linker. For example, the sensitivity and selectivity of MIL-101 (Cr) toward HF vapors drastically increase when replacing the terephthalic acid ligand by its amino-

functionalized analogue (2-aminoterephthalic acid), thereby introducing highly specific hydrogen bond interactions toward HF [75].

The large variety of functional components and tunable structural characteristics makes MOFs highly promising sensing materials in piezoelectric detection. However, there are challenges when it comes to their widespread implementation in real-life applications. As illustrated, the MOF structure is crucial in terms of sensor performance. Given the complexity of the system, however, this final structure often is difficult to predict and requires precise control over a multitude of parameters, such as pH, ionic strength, and concentration of organic matter. In addition, MOFs often comprise expensive ligands, which makes large-scale manufacturing a major challenge. While in terms of sensor performance, some very impressive results have been reported, the stability of MOFs, especially at humid conditions, needs improving. Another obstacle is the limited number of analytes: to date, it is difficult to achieve pore sizes above 2 nm [68, 69].

2.2.3 Composite Sensor Materials

Biomimetic receptor layer research has yielded a plethora of highly tailored materials. While sometimes impressive in terms of sensor performance, many face distinct obstacles, such as broad cross-selectivity and limited stability at ambient conditions. Composite sensor layers comprising two or more functional components can, when designed correctly, mitigate such shortcomings, often yielding sensor performances surpassing those of the individual base materials.

For instance, Qi and coworkers developed an exceptionally stable QCM-based humidity sensor using a blend of graphene quantum dots (GQDs) and the naturally occurring, highly hydrophilic polysaccharide chitosan (CS). While CS offers ample and rather selective binding sites for water molecules, its low mechanical stability results in an overall poor and rapidly declining Q-factor. In contrast, GQD-CS composites improve the sensor performance drastically, yielding fast response and recovery times, low humidity hysteresis, and good long-term stability [76].

While desirable for some applications, high humidity responsiveness often poses a major problem when it comes to applying sensors in real-life environments. To reduce the influence of ambient humidity on the aldehyde detection performance of a QCM sensor, Chen et al. used a blend of amino-functionalized graphene oxide flakes and TEOS-functionalized, hydrophobic silica nanoparticles. While the amino functional groups on the GO surface provided selective H-bonding sites for the analyte, the hydrophobic component of the composite minimized the influence of water vapors, resulting in unaltered sensor characteristics until up to 80% RH [77].

Besides improved mechanical and/or chemical stability and reduced cross-reactivity, nanocomposite-based receptor layers have also shown enhanced sensitivities, owing to better distribution of the recognition units and increased specific surface area. For example, Zhou et al. blended WS_2 with multi-walled carbon nanotubes (MWCNTs). This reduces agglomeration of the WS_2 nanosheets, providing a higher number of accessible binding sites. Moreover, the mesoporous

composite structure leads to increased specific surface area, resulting in sensitivity around 1.5 times higher than that of pure WS_2 and twice as high as the value measured for the MWCNTs-coated sensor [78].

Similarly, Wang et al. fabricated a SAW-based formaldehyde sensor using the zeolitic imidazolate framework ZIF-8, blended with the polyethyleneimine (PEI) and bacterial cellulose (BC). Here, PEI provides selective interaction sites via its amine groups, while the porous BC network structure significantly increases the available surface area. As both materials strongly adsorb water, ZIF-8 is used to increase surface hydrophobicity, reducing the sensor drift to less than 5% in a RH range from 10 to 93%. Moreover, ZIF-8 even further increases the specific surface area due to increasing surface roughness. It provides additional analyte adsorption sites via its Zn^{2+} metal center, enhancing sensitivity further to concentrations as low as 100 ppb [79].

Overall, a rational design of nanocomposites has proven a highly promising way to overcome some of the shortcomings and obstacles biomimetic sensor layers have faced so far. On the flip side, this introduces another level of complexity. Most often, nanocomposite fabrication requires extensive trial and error and introduces additional steps and challenges in terms of reproducibility into the manufacturing process [52].

3 Molecular Imprinting

Molecularly imprinted polymers (MIP) have proven highly useful, robust, selective receptor layers in sensing. In general, MIP synthesis relies on a templating approach: polymer networks containing specific binding sites result from polymerizing functional and crosslinking monomers in the presence of a target molecule, also termed template. Removing the template then yields cavities that match analytes' shape, size, and chemical functionality [80]. One can synthesize MIPs as films and micro- or nanoparticles. While MIP particles offer larger surface-to-volume ratio and, hence, often high sensitivity and reduced non-specific interactions [81, 82], they require additional immobilization onto the respective transducer. Thin-film MIPs, on the other hand, can be applied on the transducer surface in a straightforward way by, for example, spin-coating or roll-to-roll imprinting. The possibility of growing a film directly on the transducer surface, e.g., via electropolymerization, is another important feature coming with thin films.

The following sections discuss different MIP synthesis pathways, highlighting the advantages and disadvantages of each approach.

3.1 Radical Polymerization

Radical polymerization is the most widespread and straightforward way to synthesize polymers. Here, monomers and crosslinker are mixed with a radical initiator/starter. Exciting the initiator by temperature or light generates radicals that attack polymerizable groups eventually leading to chain propagation. Basically, radical polymerization can be divided into two approaches: free-radical polymerization (FRP) and controlled/"living" radical polymerization (CRP). FRP dominates classical MIP synthesis, because it is straightforward and can be adapted to various reaction conditions. However, the controllable reaction parameters of CRP introduce new possibilities in designing MIP-based receptors [83]. In detail, the two approaches work as follows:

3.2 Free-Radical Polymerization

Free-radical polymerization brings together monomers, crosslinkers, initiators, and, optionally, solvents. Classic FRP undergoes the three main steps of radical initiation, chain propagation, and chain termination. There are two initiators widely used in FRP: azobisisobutyronitrile (AIBN) and benzoyl peroxide (BPO). Figure 12 summarizes FRP of styrene and divinylbenzene initiated by AIBN.

Free initiator radicals generally attack acryloyl or vinyl groups of monomers. This leads to intermediate radicals. In return, chain propagation results in diverse polymer chains with high molecular mass until termination (i.e., recombination of two chain

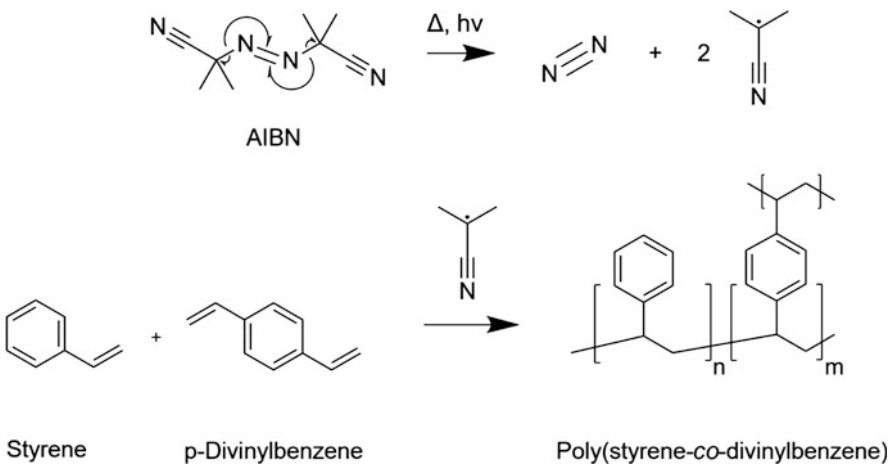

Fig. 12 Homolytic cleavage of the radical initiator AIBN leads to the generation of free radicals, which can attack vinyl groups (i.e., vinyl groups of styrene and divinylbenzene)

radicals to form a stable molecule and disproportionation with the transfer of a hydrogen atom to form two stable molecules) [84].

FRP has been used widely to synthesize MIPs for small molecules (via bulk imprinting) [85–87], large (bio)macromolecules, and cells (via surface imprinting) [88–90].

Despite offering straightforward and uncomplicated synthesis, FRP remains with some drawbacks: one cannot control polymer chain lengths and architectures; affinity distribution of binding sites, porosity, and (inner) morphology are heterogeneous. In some cases, the number of imprinted sites is low [83, 88]. Still, FRP accounts for the largest number of MIPs and, in general, for about 50% of all commercially synthesized polymers [91]. The reasons are straightforward synthesis and advantages in terms of reagent purity and possibility to upscale the process.

3.3 Controlled Radical Polymerization

One way to overcome (at least to some extent) the above-stated issues with FRP is to use controlled or "living" radical polymerization (CRP). This strategy introduces the possibility to control both polymer chain growth and termination steps [84]. With this, it is possible to improve structural homogeneity and crosslinking densities. Additionally, it allows for controlling the thickness of a grafted polymer film through immobilizing the initiator on the respective surface [88, 92].

There are different CRP approaches. The most popular ones were established in the 1990s: atom transfer radical polymerization (ATRP) and reversible addition-fragmentation chain-transfer (RAFT). ATRP developed from atom transfer radical addition (ATRA). ATRA can be regarded as a modified Kharasch addition reaction and allows for synthesizing 1:1 adducts of alkyl halides and alkenes catalyzed by transition metal complexes [91]. Fig. 13 shows a reaction scheme of ATRP. Contrary to ATRA, halide back-transfer in ATRP is reversible, allowing for multiple additions. A redox process controls those conditions. Transferring the halogen atom from the halide (R-X) via homolytic cleavage results in oxidation of the transition metal complex (Mt^{n+1}) and the formation of a free-radical species ($R^{\cdot}$). The radical species can then propagate between monomers (M) until halide back-transfer from the metal complex stops the chain reaction, leaving the system in its dormant state (Mt^{n}). Hence, one achieves constant equilibrium between the growing chain and the dormant form [81]. Thus, this technique allows for controlling polymer chain growth. ATRP, however, comes with the disadvantage of being limited to only a

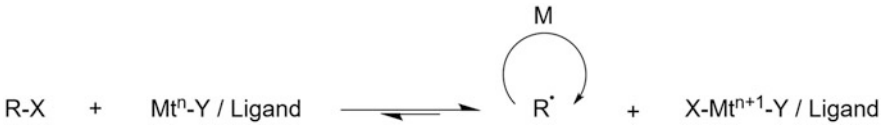

Fig. 13 Schematic of the ATRP process

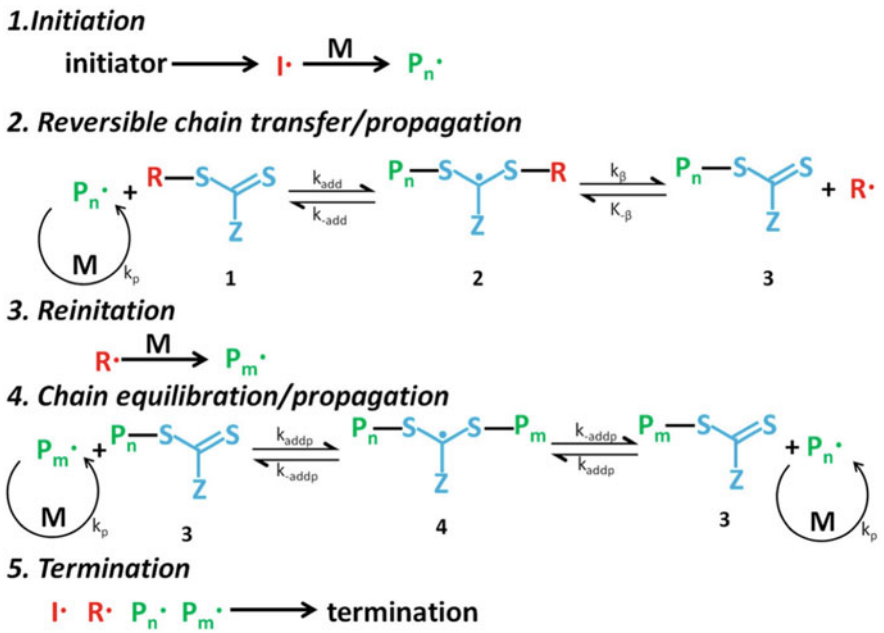

Fig. 14 Schematic overview of the RAFT polymerization process [99]

distinct set of monomers. Acidic monomers, e.g., methacrylic acid and acrylic acid, can be problematic since they tend to interfere with common catalysts [93]. Nonetheless, several MIPs synthesized via ATRP and derived techniques were published. Small molecule templates include histamine [94] and cortisol [95]; larger entities comprise α-fetoprotein [96] and ribonuclease A [97].

The second important technique is RAFT, which is regarded as the most suitable CRP technique for MIP synthesis [83]. Originally developed in 1998 [98], RAFT has the advantage of being applicable to a wide range of monomers while still providing control over the polymerization. Figure 14 shows a sketch of the RAFT process. The radical $I^{\cdot}$ from the initiator reacts with monomers M, yielding a propagating radical $P_n^{\cdot}$ (step 1). $P_n^{\cdot}$ then forms an intermediate radical (2) by reacting with the RAFT agent (1), leading to generation of a dormant chain (3) and a new radical $R^{\cdot}$ (step 2). The new radical then reacts with a monomer in a re-initiation process (step 3) to form a new propagating radical $P_m^{\cdot}$. An equilibrium forms between the dormant species (3) and the active propagating radicals. Thus, all polymer chains have an equal probability to grow (step 4). Although minimized, the termination reaction undergoes the same principle as in standard radical polymerization (step 5).

The RAFT setup is identical to conventional FRP, with the only difference that one adds a RAFT agent instead of a conventional chain transfer agent (if needed) [100]. This allows for rapid transfer of propagating polymer chains in a degenerative way. This chain transfer function is the core piece of the reaction, as it constantly

competes with propagation and thereby reduces the possibility of (early) chain termination [83]. Naturally, this leads to controllability of the polymerization process. The RAFT agent is designed in such a way that it is the more attractive reaction partner for radicals than other polymerizable groups. Therefore, it slows down polymerization by reducing the number of propagation events. The RAFT agent generally consists of a thiocarbonylthio group (S=C-S) with modifiable side groups (e.g., dithioesters, dithiocarbamates, trithiocarbonates, and xanthanes). The choice of suitable RAFT agents depends on the monomers used [99]. An additional advantage of RAFT is that it allows for using the same initiators as in FRP (e.g., AIBN or BPO).

Examples of MIPs designed with RAFT include the analytes ibuprofen [101] and 17β-estradiol [102]. To the best of our knowledge, there are currently no surface-imprinted polymer films for larger (bio)species using RAFT.

3.4 Polyaddition

Polyurethanes are the most widely used polyaddition products in MIP synthesis. Even though less frequent, polyurethanes have found their way into chemical sensing, as well: some of the pioneers of surface imprinting, the group of Dickert, used polyurethanes for their MIPs. This polymer class results from polyaddition of di- or polyisocyanates and polyhydroxy monomers [84], usually to form thin MIP films. Those films were successfully applied to detect small molecules in the form of volatile compounds and aromatic hydrocarbons, as well as bacteria, yeast, and red blood cells [84].

3.5 Electropolymerization

Electropolymerization is a very elegant strategy to generate thin-film MIPs in situ directly on the respective transducer. The basic process comprises formation of an electrically conducting polymer layer at an electrode surface in the presence of the template analyte. The reaction usually takes place using a conventional three-electrode setup, consisting of a working electrode (to be coated with the polymer), a reference electrode (usually Ag/AgCl or, in some cases, saturated calomel), and a counter-electrode (typically platinum or nickel). The three-electrode setup is placed into a solution containing monomers, a solvent, and a supporting electrolyte. Naturally, the choice of these three components is crucial for the outcome, as they determine the morphology of the respective polymer film [103]. Electropolymerization can proceed voltammetrically, potentiostatically, and galvanostatically, with voltammetry being the most popular technique. Relying on cyclic voltammetry, it is possible to control polymer film thickness via adjusting the voltage range. Additionally, it is possible to tune polymer oxidation, as well as polymerization rate at the electrode surface, usually through the sweep rate

[103]. Electropolymerization has proven especially useful for biospecies: it does not require an initiator, meaning that it does not require heat or UV light to start polymerization. Second, most electropolymerization reactions take place in water or buffer, which is of course the most suitable medium for biospecies [104]. For MIP synthesis, one can directly mix the template analytes with the respective set of monomers. In the case of large biomolecules or even cells, one can immobilize them on the electrode surface [105]. Typical monomers for electrochemical MIP synthesis include pyrrole, o-phenylenediamine, aniline, phenol, carbazole, and, more recently, scopoletin [103, 106]. Analytes of interest range from small molecules, such as pharmaceuticals (e.g., paracetamol [107] and erythromycin [108]), to enzymes (e.g., cytochrome P450 [109]), proteins (e.g., human chorionic gonadotropin protein [110]), viruses (e.g., SARS-CoV-2 [111]), and cells (e.g., bacteria [112–114]). Most electrochemically synthesized MIPs are thin films.

3.6 Imprinting Strategies

In the case of MIPs, one needs to consider the different imprinting strategies. Basically, it is possible to distinguish bulk and surface imprinting. Figure 15 sketches the two techniques. In bulk imprinting, the template is embedded in the polymer bulk. This leads to a vast number of binding sites, but also brings the challenge of template extraction: diffusion governs both removing the analyte and rebinding it. Thus, this approach is most frequently used for small molecules. MIPs

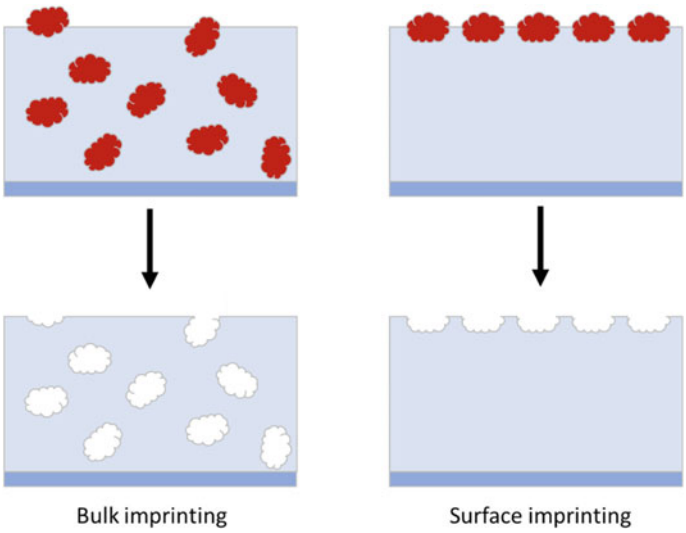

Fig. 15 Bulk-imprinted polymers possess a larger number of binding sites while surface-imprinted polymers have easier accessibility of cavities

for larger entities, ranging from biomolecules (e.g., peptides or proteins) to entire cells, usually result from surface imprinting. This generates cavities only on the polymer surface, leading to a lower number of binding sites. However, it results in faster binding kinetics, easier surface characterization and analysis, and the possibility to tailor the imprints directly to the desired needs.

3.7 Bulk Imprinting

Bulk-imprinted polymers bind the analyte in their whole bulk. Most bulk MIPs are particles, thin films, or monoliths. In all cases, the monomers are directly mixed with the respective template and suitable solvents. Compared to surface imprinting, bulk imprinting typically requires higher crosslinking and template-to-monomer ratios. Therefore, it is best suited for small molecules as the template for this diffusion-controlled approach [84]. Overall, bulk imprinting achieves the maximum possible number of binding sites. The templates fulfill two functions: first, they govern selectivity by shaping the respective recognition sites in terms of chemical and steric properties. Second, they may also generate diffusion routes within the polymer matrix, leading to accessible binding sites in the first place. To generate measurable signals, the analyte needs to occupy a relatively large number of binding sites.

In their latest review, Cowen and Cheffena [85] describe the process of "porogen imprinting" and its emerging role in gas sensing with bulk-imprinted MIPs. In this approach, the template analyte is used as the solvent itself: one would consider this using huge excess amount of template. Contrary to the classic approach of "template imprinting," however, porogen imprinting does not necessarily lead to increased sensitivity or selectivity [85]. Therefore, it seems that there is an optimal template-to-monomer ratio to fully utilize the potential of binding site generation.

In one of their studies, Afzal et al. [115] used both approaches (porogen and template imprinting, respectively). The authors prepared MIPs for ethyl acetate by imprinting polyurethane (PU) using porogen imprinting, and, vice versa, methacrylic acid-*co*-ethylene glycol dimethacrylate (McE) – MIPs for formaldehyde using template imprinting. While in the first approach no other solvent than the analyte itself (i.e., ethyl acetate) came into play, the latter MIP relied on bubbling formaldehyde through THF containing the monomer mixture. Even though the two imprinting mechanisms are different, the outcome is similar: Spin-coating the MIP layers onto a 10 MHz QCM resonator resulted in a sensing system that could selectively detect low amounts (5–25 ppm) of ethyl acetate and formaldehyde vapors (Fig. 16).

Naturally, bulk imprinting is not limited for sensing analytes in the gas phase. Several sensors using MIPs fabricated via bulk imprinting measure in the liquid phase [116, 117].

Wang et al. proposed a different approach of using bulk-imprinted MIP monoliths to detect gossypol [118], a toxic compound found in the seeds of cotton plants. In

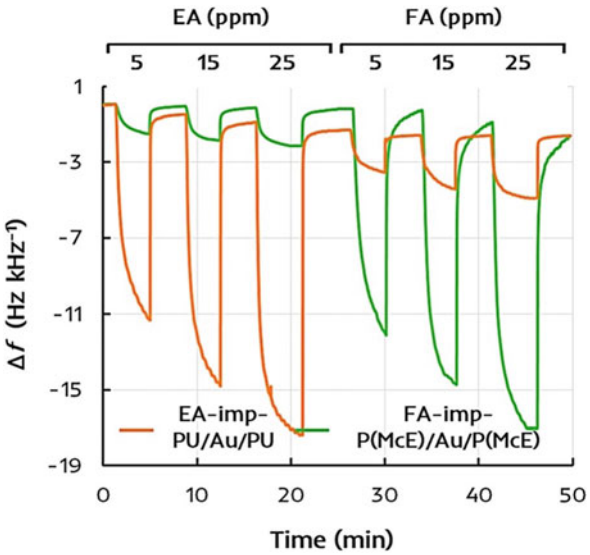

Fig. 16 Normalized sensor responses of a 10 MHz QCM resonator coated with porogen-imprinted PU and template-imprinted McE to detect low amounts of ethyl acetate and formaldehyde vapors, respectively. Sensitive layers were produced by coating the QCM electrodes with an initial imprinted polymer layer, gold nanoparticles (Au), and a final imprinted polymer layer (EA-imp-PU/Au/PU and FA-imp-P(McE)/Au/P(McE)). Frequency shifts were normalized to 1 kHz (i.e., 40 nm) of layer thickness. Reprinted with permission from [115], © Elsevier

their bulk polymerization procedure, they relied on the functional monomers dimethylaminoethyl methacrylate and ethylene glycol dimethacrylate. The resulting MIPs revealed an adsorption capacity of 564 mg g^{-1} gossypol. Additionally, Wang et al. prepared MIPs for the same analyte using surface layer imprinting and a sol-gel process. Compared to those two approaches, the bulk-imprinted MIP showed the highest adsorption capacity, but exhibited slower adsorption kinetics. Hence, bulk imprinting is favorable for binding larger quantities of gossypol, while surface imprinting and the sol-gel method lead to more rapid adsorption kinetics.

However, the latter approach also highlights the potential of using surface imprinting for small molecules to achieve rapid binding kinetics. As an example, Park et al. manufactured surface-imprinted MIP thin films to detect caffeine with QCM sensor response times of 20 min for the initial rapid rebinding process and 40 min until the equilibrium state was reached [119]. Surface imprinting, however, still is the method of choice for larger analytes, though not being limited to them.

3.8 Surface Imprinting

As the name already implies, surface imprinting generates cavities only on polymer surfaces. In contrast to diffusion-controlled rebinding in bulk imprinted MIPs, binding kinetics govern selective recognition (i.e., rebinding) of surface imprints. The imprinted materials can take the form of thin films [120] or particles [121], as well as composites [122]. Binding kinetics are faster compared to bulk MIPs, which goes hand in hand with short response and recovery times. It is fairly easy to remove the analyte from the polymer surface: it detaches faster compared to an analyte buried in the bulk of a polymer matrix. In theory, this improves reversibility of the resulting receptors. Nonetheless, also surface imprints contain both geometrical and chemical information of the respective analyte. There are numerous publications in the literature using surface imprinting, ranging from detecting small molecules and biomacromolecules to proteins and even whole cells or microorganisms [123–126]. Compared to the bulk approach, surface imprinting, however, comes with one major drawback: reduced sensitivity. The limited number of recognition sites naturally allows for fewer bound analytes. One must take that into account when designing novel artificial receptor layers, especially when the target analyte is small. Imprinting of larger entities, e.g., proteins, remains challenging: size, structural complexity, and stability toward environmental changes (e.g., pH and temperature) are an issue for the bulk approach. Thus, one can conclude: the larger the analyte, the more favorable is surface imprinting. One of the first approaches of modern surface imprinting indeed relied on large analytes: Alexander and Vulfson in 1997 [127] were the first to report the use of whole cells, i.e., bacteria, as a lithographic mask to imprint polymer surfaces. In their study, they prepared micron-sized imprints of *Listeria monocytogenes* and *Staphylococcus aureus* using self-assembly. Starting with a two-phase system consisting of hydrophilic amine monomers and diacid chloride in a dispersed organic phase, the template bacteria assembled at the phase boundaries between organic and aqueous phases. There, the reactants formed a polyamide layer embedding the bacteria around the microcapsules. To obtain solid polymer beads, a diacrylate monomer was polymerized in the core of the microcapsules. The authors removed bacteria by acid hydrolysis, leaving behind surface imprints in the dimensions of the respective cells. Figure 17 shows the surfaces of the imprinted polymer beads. However, this ground-breaking study did not yet assess rebinding.

Ye et al. later applied similar concepts to synthesize surface-imprinted polymer beads for bacterial recognition [128], namely Pickering emulsions relying on bacteria cells as the stabilizer. First described in 1907 [129], Pickering emulsions represent the process of forming an emulsion between water and oil phases using solid particles instead of surfactants as the stabilizing agents [130]. Ye and coworkers relied on a first self-assembly step of negatively charged bacteria (i.e., *Escherichia coli* and *Micrococcus luteus*) to a positively charged vinyl-containing pre-polymer (i.e., *N*-acrylchitosan). This bacteria–pre-polymer assembly served as the particle stabilizer for the Pickering emulsion in water. The oil phase consisted of

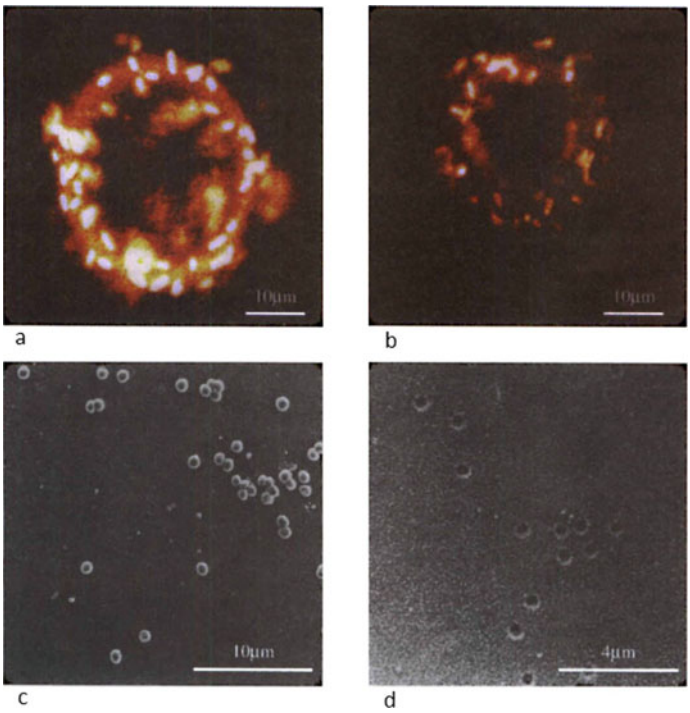

Fig. 17 Confocal laser scanning microscopy (CLSM) images of (**a**) ethidium bromide-stained *Listeria monocytogenes* cells attached to a polyamide microcapsule and (**b**) stained *Listeria monocytogenes* imprints. SEM images of (**c**) *S. aureus* cells partly embedded in the polymer surface after polymerization of the core and (**d**) imprints of *S. aureus* cells after cell removal from the polymer surface. Reprinted with permission from [127], © John Wiley & Sons

crosslinking, hydrophobic monomers and a radical initiator. FRP was then used to form polymer beads with the covalently attached pre-polymer–bacteria assembly. The bacteria were then removed, leaving behind surface imprints on the beads (Fig. 18).

The authors used the surface-imprinted beads to conduct rebinding experiments by incubating them with respective bacteria. The uptake of *E. coli* was more pronounced with the *E. coli*-imprinted beads compared to the uptake of *M. luteus*. Vice versa, the same was valid for *M. luteus* uptake with *M. luteus*-imprinted beads (Fig. 19).

Dickert et al. published fundamental work on integrating surface-imprinted polymer thin films with (piezoelectric) sensor platforms in 2001 [131]. Microcontact, or "stamp," imprinting served to generate yeast imprints on a polyurethane surface. Stamp imprinting commonly refers to the process of immobilizing the respective template compound on a solid substrate and pressing it into the pre-polymer mixture spin-coated on the surface of the transducer (i.e., 10 MHz QCM resonators). After adequate template extraction, cavities are formed on the film surface, resembling the

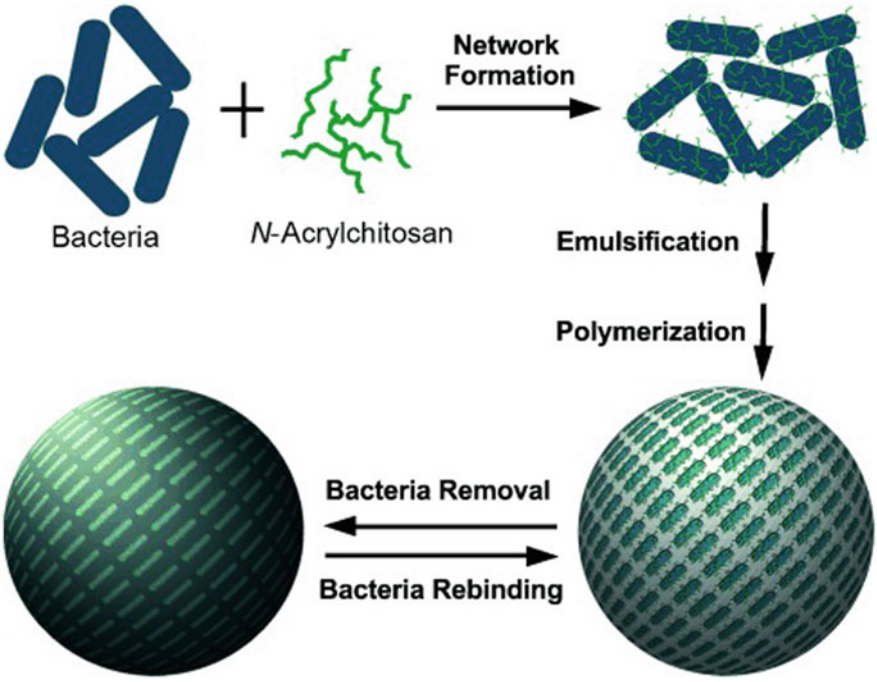

Fig. 18 Schematic overview of the process of bacteria assembling with the monomer N-acrylchitosan, followed by Pickering emulsion polymerization to form stable bacteria beads which can be used for rebinding. Reprinted with permission from [128], © John Wiley & Sons

dimensions of the respective template compound immobilized on the stamp (Fig. 20).

In their work, Dickert and co-authors achieved detection limits of 10^4 cells/mL and high selectivity toward the imprinted *Saccharomyces cerevisiae*. In the following years, researchers of the same group extended the stamping technique to a broad range of analytes, ranging from (lipo)proteins [132–134] to whole-cell approaches comprising viruses [132], bacteria [135, 136], and pollen [137], as well as human red blood cells [138].

Commonly, the stamping technique now serves as a surface imprinting tool for numerous applications. The Wagner group at KU Leuven used PDMS stamps to imprint polymer layers serving as receptors in the heat transfer method (HTM). The basic principle of the HTM is that binding of analytes to surface imprints decreases the heat transfer rate from a heated aluminum chip to the respective buffer [139]. This decrease in heat transfer rate can be measured. The group was successful in detecting various whole-cell analytes with this approach, e.g., macrophages and cancer cells [139], as well as bacteria [140]. Another approach uses surface-imprinted polymers to detect yeast with impedance spectroscopy as the readout system at a low detection limit of 30 cells/mL [141].

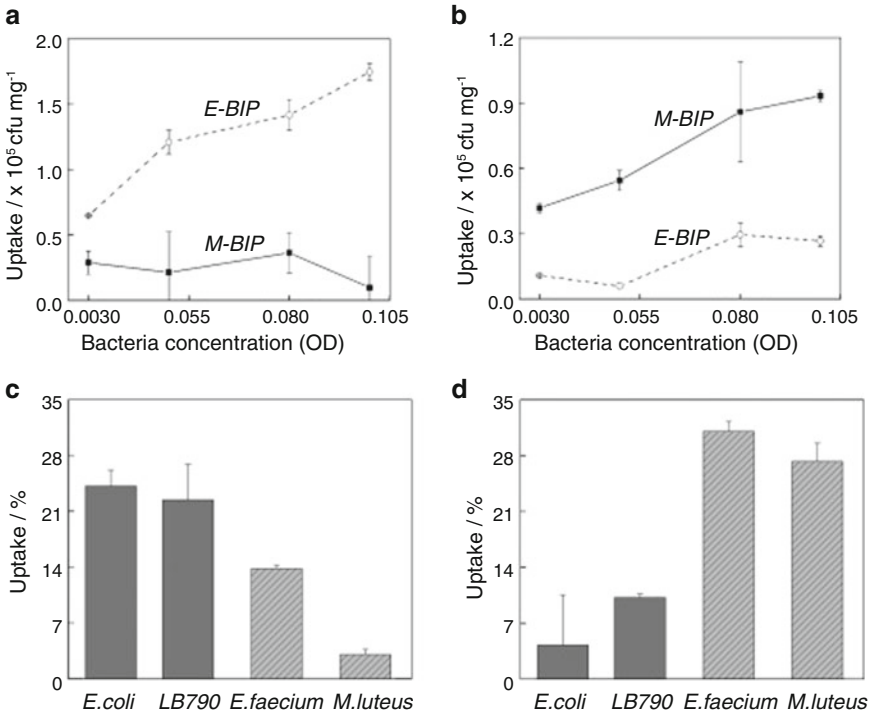

Fig. 19 (**a**, **b**) *E. coli* (**a**) and *M. luteus* (**b**) uptake with *E. coli*- and *M. luteus*-imprinted polymer beads (E-BIP and M-BIP), respectively, at different concentrations. (**c**, **d**) Uptake of different bacteria cells at the same concentration (optical density at 600 nm = 0.05) with E-BIP (**c**) and M-BIP (**d**) beads. Reprinted with permission from [128], © John Wiley & Sons

For proteins, He et al. [90] summarized the advantages and disadvantages of different imprinting techniques in their latest review (Table 1). In addition to bulk and surface imprinting, they also describe the process of epitope imprinting, which is a subclass of surface imprinting: here, one generates imprints of a specific epitope on the polymer surface. The approach takes the concept of an "artificial antibody" quite literally: antibodies detect their antigens by interacting with a distinct molecular domain on the amino acid chain, the epitope. The same applies to the emerging surface-imprinted polymers, which result from using a short peptide as the template. As the peptide represents an epitope of the whole protein, the receptor layers are useful to recognize the entire protein [124].

The term "epitope approach" first appeared in the work of Rachkov and Minoura in 2001 [142] and has since then emerged in numerous imprinting approaches of proteins or larger peptides. In their initial work, Rachkov and Minoura chose the C-terminal chain (YPLG) of the nonapeptide oxytocin as the template. Their epitope MIPs successfully captured the epitope, as well as the whole peptide. Since those pioneering experiments, researchers used the approach to synthesize imprinted polymers for a vast number of proteins. The advantages of this approach compared

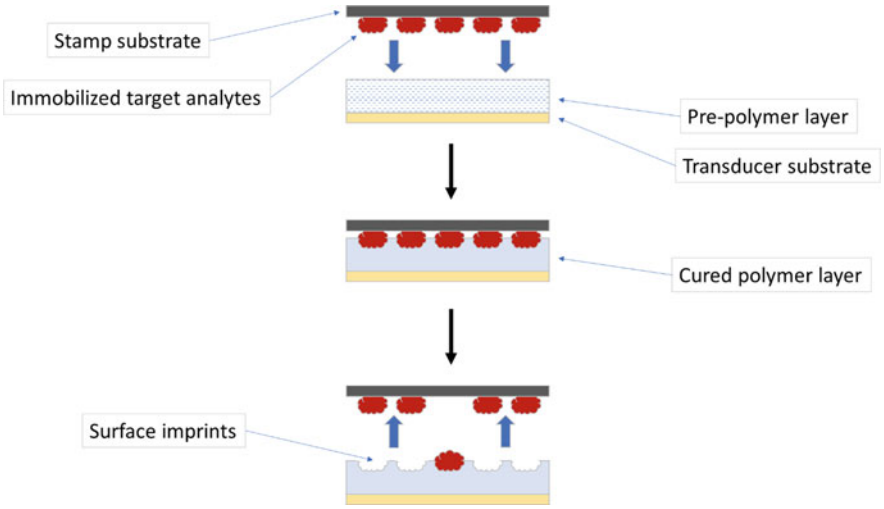

Fig. 20 Microcontact, or "stamp", imprinting generates cavities only on the polymer surface via pressing the immobilized target analyte on a stamp substrate into the pre-polymer layer coated onto the transducer surface. Stamp removal and analyte extraction leads to the generation of cavities

to imprinting the protein as a whole are logical: a protein possesses numerous functionalities that can serve as potential binding sites when imprinted wholly. Thus, epitope imprinting decreases the amount of non-specific binding, as the receptor layer can only recognize a single, distinct peptide sequence. Additionally, using smaller and less complex templates makes it easier to immobilize and remove them. This goes hand in hand with template stability: environmental changes do not affect immobilized peptides to the same extent as entire proteins: those may lose their natural conformation upon, e.g., pH changes and the use of solvents [90]. Epitope imprinting is an emerging field with target proteins covering a broad range of molecular weights [143–145]. Of course, the approach requires both the amino acid sequence of the peptide chain to be known and sufficient knowledge of protein conformation.

Last but not least, another emerging field gained interest in the past decade: so-called post-imprinting modification (PIM). Especially the work of Takeuchi and his group delivered substantial insight on the fact that one can modify the imprinted cavity after synthesizing the MIP to achieve better binding/recognition characteristics and to fine-tune the detection process [146]. This approach requires functional monomers that one can modify after removing the template (Fig. 21). With this, it is possible to introduce novel possibilities into MIPs. For example, one can modify the cavity with a fluorescent dye that will be cleaved off the functional monomers upon analyte binding, serving as a reporter molecule to indicate successful binding. The inherent sensitivity of fluorescence allows for achieving low detection limits: for α-fetoprotein (AFP) it is 1 ng/mL, which is 20 times lower than the LOD of SPR; it therefore reaches the range of commercially available ELISA kits [96].

Table 1 Imprinting approaches for proteins. Reprinted with permission from [90], © The Royal Society of Chemistry

Synthesis methods for PIPs	Merits	Drawbacks
Bulk imprinting	1. The most straightforward method	1. Long binding equilibrium time caused by limited diffusibility
	2. High-density imprinting sites	2. Non-specific adsorption for homologous peptides
		3. Limited imprinting efficiency derived from the conformational changes and solubility of proteins
		4. Binding sites will be destroyed by the mechanical crushing and grinding processes
Surface imprinting	1. Quick binding kinetics derived from the favorable accessibility of proteins in and out of the imprinted sites	1. Limited binding capacity due to the relatively low amount of template proteins for imprinting
	2. Multiple advanced functionalities by using various nanomaterials as substrates	
Epitope imprinting	1. The epitope peptides with simple structures could facilitate the immobilization and removal of templates	1. Ineffective when the amino acid sequence of protein is unknown
	2. Also, decrease the non-specific binding sites	2. Suffer from limited accessibility to imprinted sites in the rebinding process
	3. Epitope peptides were more stable, more available, and cost-effective	
Boronate affinity-based molecular imprinting	1. The reversible boronate affinity could facilitate the immobilization and removal of glycosylation templates	1. Mostly used for glycoprotein imprinting
	2. Enhanced specificity for glycoprotein	
Solid-phase synthesis	1. Automated operation and short production time	1. Heterogeneous recognition sites from the variation of protein orientation
	2. High purity of nanoMIPs with high affinity	2. Low amount of templates immobilized on the solid support
	3. Templates were reusable	
	4. More homogeneous binding sites and high specific affinity	
	5. High stability and good solubility of nanoMIPs	
	6. Advanced functionalities by introducing functional nanomaterials	
Post-imprinting modification	1. Post-modification of the imprinted cavity	1. Rational design of complex functional monomers

(continued)

Table 1 (continued)

Synthesis methods for PIPs	Merits	Drawbacks
	2. Introduce more functionalities by various chemical derivatization	2. A tedious chemical synthesis procedure
		3. The effect of chemical modifications on the rebinding process is unknown

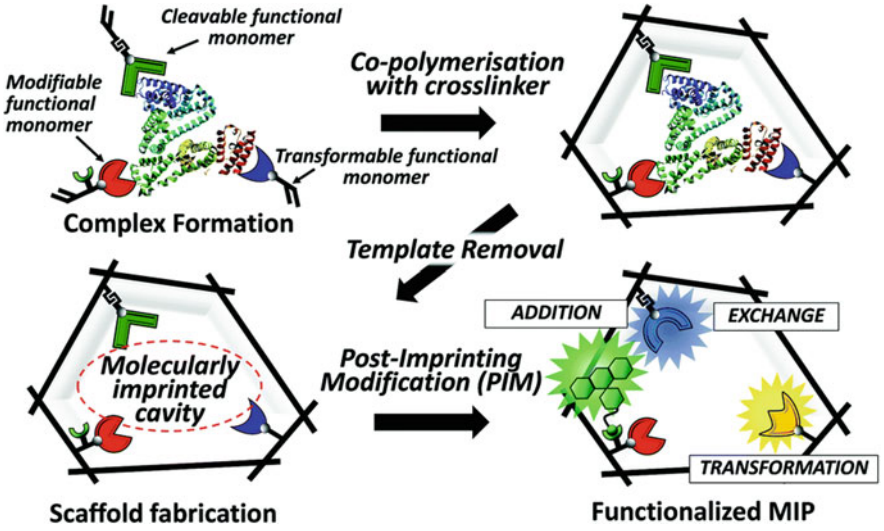

Fig. 21 Scheme of molecular imprinting and the several possibilities for post-imprinting modifications. Reprinted with permission from [146], © The Royal Society of Chemistry

3.9 MIP Nanoparticles

While there is enormous research output in implementing biomimetic selective receptors based on macroscale imprinted polymers, there are still only a few real-world applications. One can relate this lack of widespread commercial application to several technological limitations of traditional imprinting protocols. Generally, synthesis and sensor design may be quite complex and difficult to standardize, rendering it unsuitable for large-scale industrial production [147, 148]. Moreover, affinity of the cavities is directly linked to varying template orientation and location during polymerization, resulting in heterogeneous binding sites that hamper quantitative detection and lead to high non-specific adsorption [80].

Therefore, substantial research efforts focused toward developing imprinted polymers on the nanoscale, as they offer a high surface-to-volume ratio, potentially providing a large number of easily accessible binding sites, faster binding kinetics, and fewer residual template captured inside the polymer network. First endeavors

toward that goal focused on bulk polymerization of MIP monoliths, followed by elaborate grinding, crushing, milling, and sieving to obtain the nanosized material. Next to the rather time-consuming nature of this multi-step procedure, up to 50% of the initial polymer mass is lost during processing. Moreover, it results in irregular particle shapes and highly variable sizes [149]. For this reason, recent efforts focused on direct bottom-up synthesis of nanosized imprinted polymer particles (nanoMIPs). Among the techniques leading to MIP nanobeads, precipitation polymerization, emulsion polymerization, core-shell MIPs, and solid-phase synthesis are the most frequently used ones [80].

3.10 Emulsion Polymerization

Emulsion polymerization is a well-established method to synthesize spherical polymer particles of diameters down to the low nanometer range. Generally, one disperses the template together with monomers and crosslinker – all of which are lipophilic – in an aqueous solution containing a surfactant. Then, stirring leads to monomer droplets. Polymerization is started by adding a water-soluble initiator or applying heat. In traditional emulsion polymerization, particles mainly form within monomer-swollen surfactant micelles or via precipitation of growing oligomers in the continuous phase. As illustrated in Fig. 22 (a), the polymerization rate depends on monomer transport from the micron-sized monomer droplets through the aqueous phase. This limits the choice of monomers and reduces overall polymerization speed. To circumvent this, monomer droplets of diameters below 500 nm can be formed by applying higher shear forces, e.g., by ultrasonication, the use of co-stabilizers (typically a highly water-insoluble molecule, for example lauryl methacrylate), or large amounts of surfactant. In those mini- or micro-emulsions, particles nucleate directly inside the monomer droplets, yielding highly reproducible nanoparticles with very narrow size distributions and high molecular weight [151, 152].

The main drawback is that all emulsion polymerization approaches suffer from the presence of surfactants and co-stabilizer during polymerization. For one, they can disrupt formation of template-specific cavities at the forming MIP particle surface and, in the case of biomolecule imprinting, cause protein denaturation. Moreover, surfactants are usually hard to remove from the final product, requiring time-consuming washing steps and sometimes harsh conditions that may alter the binding sites within the polymer. In some cases, it is possible to address this issue in a rather elegant manner by modifying the templates in a way that they function as a surfactant on their own. For instance, Zeng et al. produced nanoMIPs with affinities comparable to those of natural antibodies by coupling a hydrophilic peptide template with fatty acid chains. Polymerization took place in a water-in-oil emulsion, with the hydrophilic region of the modified template oriented toward the monomer droplet [153]. *Pickering emulsion polymerization* offers another possibility to arrange the template in a more oriented manner at the particles surface. Here, solid particles instead of a surfactant stabilize the droplet. By either conjugating the template to the

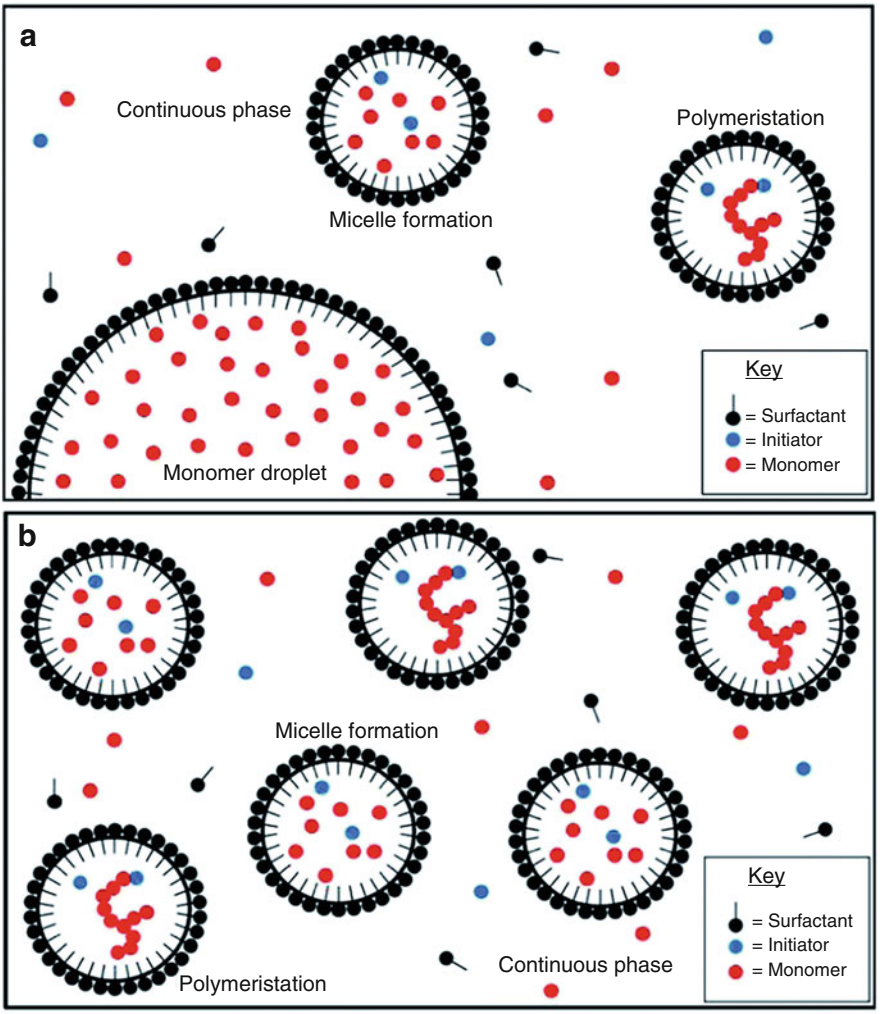

Fig. 22 The mechanisms of emulsion polymerization (**a**) and micro-emulsion polymerization (**b**) [150]

solid particle surfaces or, in some cases, using microorganisms such as bacteria both as template and as emulsifier, it is possible to synthesize nanoMIPs with well-accessible binding sites and high affinity constants [80, 84, 154–156].

3.11 Precipitation Polymerization

Precipitation polymerization takes place in highly diluted, homogeneous mixtures of functional monomers, crosslinker, and template. As shown in Fig. 23, nuclei form through oligomer aggregation and keep growing, capturing radicals from the polymerization mixture via residual vinyl groups at their surfaces. At some point, the particles precipitate and form a stable colloidal solution. This happens either enthalpically, i.e., when the polymer chain exceeds its solubility, or entropically, by expulsion of the solvent from the polymer network due to high crosslinking density [80, 149, 157]. The choice of solvent or solvent mixture with respect to the solubility parameter of the monomers and resulting polymer therefore is crucial when it comes to adjusting the size of the synthesized particles. Additionally, key properties including porosity are also largely governed by the solvent environment. The type and amount of crosslinker also heavily influence particle size. Finally, the overall monomer concentration and agitation speed also need careful adjusting to prevent aggregation or coagulation of the particles, thus decreasing polydispersity of the final product [158–161]. Nanoparticles synthesized by precipitation polymerization typically are well-defined spheres with narrow size distributions [162, 163]. Furthermore, they require no stabilizer or surfactant, making this method very appealing for imprinting applications: those components otherwise would interfere with template–monomer interactions or alter the nanoMIPs' surface chemistry [92]. Templates successfully used to synthesize imprinted nanoparticles based

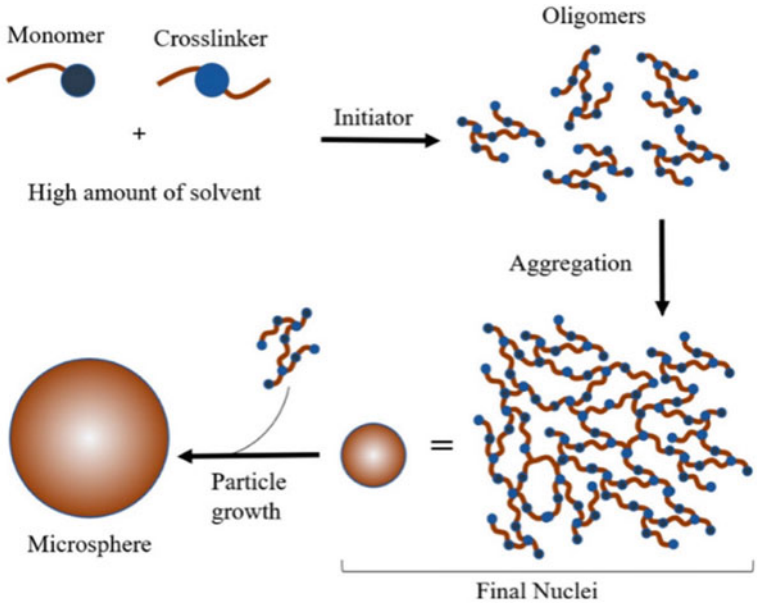

Fig. 23 The mechanism of precipitation polymerization [156]

on precipitation polymerization range from small organic compounds such as vanillin, nicotine, glucose, and propranolol [161, 164–166] to peptide sequences [166, 167] and whole proteins [167].

Nonetheless, there are several drawbacks to this method. For one, it requires very dilute solutions, as monomer concentrations above 2–5 w/v% may cause coagulation, aggregation, or macrogelation of the polymer product. This significantly reduces the polymerization rate and raises the need for large quantities of organic solvents, as well as increased amounts of template. The low concentration of functional components may also negatively affect the monomer–template affinity complex by shifting the equilibrium to the uncomplexed state, hampering the formation of selective cavities on the particle surface [80, 156, 168].

3.12 Core-Shell Polymerization

Core-shell approaches aim at coating prefabricated core nanoparticles with thin imprinted polymer layers. This approach allows for synthesizing a large variety of functional nanoMIPs. By coating, for example, metal particles, one can achieve signal enhancement in various optical and gravimetric detection methods due to the increased (optical) density of the recognition units. Further examples include core-shell MIPs containing magnetic nanoparticles as well as quantum dots for fluorescence imaging [156, 161–176]. Several synthetic methods are applied to generate MIP layers on top of nanosized solid supports. Precipitation and emulsion polymerization that utilize the core material as seed particles are common; they come with the advantages and challenges mentioned in the previous sections. More sophisticated approaches employ surface grafting, yielding highly controllable layer thicknesses. Here, functional components such as monomers, initiator, or RAFT agents are immobilized on the core particle before polymerization takes place. Similarly, conjugating the template molecule onto the NP surface, followed by controlled MIP thin-film grafting and template removal, is highly promising when it comes to imprinting larger analytes. However, the low thickness of MIPs in core-shell approaches may eventually complicate imprinting of bulky proteins. Additionally, approaches relying on surface grafting often include many steps and chemicals. This complicates the overall synthesis procedure [80, 84, 154, 168, 177].

3.13 Solid Phase Synthesis

Solid-phase synthesis is one of the latest, highly promising approaches, yielding nanoMIPs with affinities comparable to those of natural antibodies. Developed over the past decade by the groups of S. Piletsky and K. Haupt, it involves covalent immobilization of the template onto a solid support, most commonly glass beads or silica gel. After polymerization in the presence of the immobilized template, a

two-step purification procedure ensures separation of non-specific binding polymer material from high-affinity nanoMIPs (Fig. 24). By choosing the correct elution conditions, one can wash off unreacted monomers and low-affinity components, while the high-affinity fraction remains attached to the solid phase, owing to their strong interaction with the analyte. Those highly specific non-covalent interactions are broken in the second washing step, which for example includes higher temperature or a different solvent mixture. Thus, one obtains very pure fractions of high-affinity particles.

By choosing the appropriate immobilization strategy, this method allows for precisely controlling the orientation of the template during polymerization, yielding highly reproducible, narrowly distributed affinity constants. Next to their high affinity and selectivity, such nanoMIPs also generally contain one cavity per particle, resembling the binding behavior of monoclonal antibodies. This allows for developing MIP-based quantitative assay formats and implementing nanoMIPs as antibody analogues in well-established bioassays, such as the enzyme-linked immunosorbent assay (ELISA) [178, 179]. As the template molecules remain attached to the solid phase after affinity separation, the resulting product is template-free, avoiding corruption of assay results by template bleeding. Moreover, one can often reuse the template-functionalized solid phase for further synthesis cycles. This is especially appealing when it comes to the imprinting of expensive analytes. Overall, solid-phase synthesis represents a simple procedure to reproducibly obtain high-quality nanoMIPs also in automated systems. However, it comes with some drawbacks: most notably, high-affinity particle yields are quite low, as the major fraction of initial monomer mass is discarded during the first washing step. Another obstacle can arise during template immobilization. While one can often draw on well-established bioconjugation protocols, great care must be taken when immobilizing very small analytes. Choosing a functional group for conjugation can significantly impact on the quality and type of interaction sites in the final MIP. For larger biomolecules, the main challenge lies in immobilizing the template in a single, well-defined orientation, which may require advanced synthesis procedures. Here, the most promising approach in terms of protein recognition is so-called epitope imprinting, which was introduced in the previous section on surface imprinting strategies. A key advantage here is the use of tailor-made epitope sections that allows for incorporation of a sequence designated for conjugation [148, 169, 180].

3.14 Surface Characterization of MIPs

Surface-imprinted polymers (SIPs) provide a robust alternative to antibodies. Characterizing their surfaces in a suitable manner allows for facilitating reproducible synthesis, investigating template removal, and analyte rebinding. When considering surface characterization, microscopy immediately comes to mind. It is straightforward to visualize large analytes, e.g., bacteria and human cells, via light microscopy. It will fail, however, when analyte/imprint size lies below the Abbe limit. In that

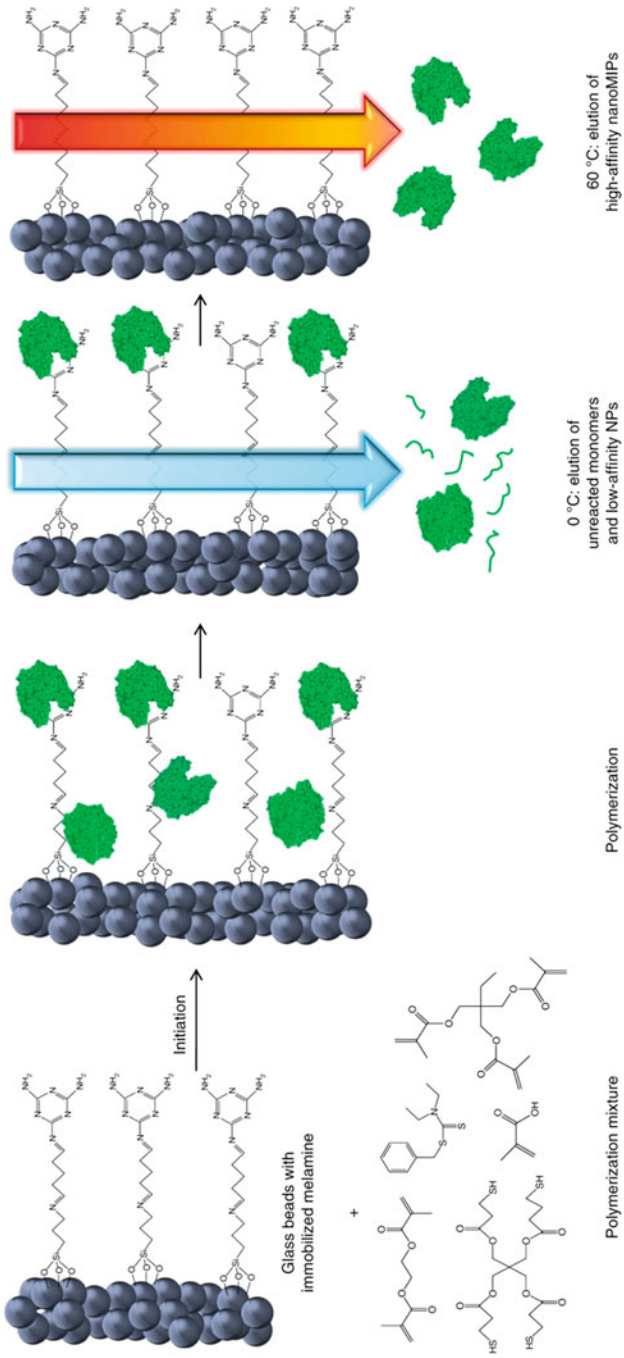

Fig. 24 Schematic representation of the solid-phase synthesis and separation of melamine-imprinted nanoMIPs. Reprinted with permission from [148], © Nature Protocols

case, one must rely on other methods that allow for higher resolution. Additionally, light microscopy has the drawback of not revealing information on sample height (z-axis). Atomic force microscopy (AFM) makes it possible to overcome both the limitations in resolution and z-information. It allows for mapping surfaces on the nanoscale. Furthermore, one can operate it in distinct modes tailored to the nature of the sample and the desired results. However, they all rely on the same principle: a sharp probe attached to an elastic cantilever scans across the sample surface. A laser beam is focused directly on the cantilever; thus, cantilever deflection (depending on surface morphology) changes the light path of the laser, which one can detect through multisegment photodiodes (usually four segments: two vertical and horizontal each). In principle, it is possible to achieve atomic resolution [181]. More advanced AFM techniques, e.g., Peak Force Quantitative Nanomechanics (PF-QNM), allow for obtaining additional information: for instance, Werner et al. recently used it to tackle bacteria imprints on the nanoscale [155]. In their work, they characterized the imprinted surface of *Escherichia coli*-imprinted polymer thin films and imprinted polymer microbeads. Naturally, both approaches led to rod-shaped imprints resembling the dimensions of the *E. coli* cells. Nonetheless, the authors found distinct differences in the generated cavities. Stamp imprinting yielded the desired cavities, additionally showing imprinted patterns of the nanosized substructures on the bacteria cell wall. This was not the case in the imprints originating from the Pickering emulsion: surfaces showed increased roughness, governed by globular structures influencing the adhesion characteristics. Those globular structures, most likely originating from lipopolysaccharides, were remainders of the imprinted bacteria cells in the emulsion approach. This work highlights the importance of surface characterization in molecular imprinting: even though the same set of monomers and the same template analyte were used, the resulting imprints showed distinct differences.

Two other studies by Bräuer et al. use Raman microscopy accompanied by AFM and PF-QNM to analyze bacteria-imprinted surfaces [182, 183]. This work shows that it is possible to characterize the surfaces of bacteria-imprinted thin films with confocal Raman microscopy in a way to obtain insights into MIP selectivity. Most publications using Raman spectroscopy on/with MIPs rely on surface-enhanced Raman spectroscopy (SERS) [184]. Chemometric tools helped in establishing a model that is not only useful for differentiating between imprint and polymer matrix, but also between two different bacteria species (i.e., *E. coli* and *Bacillus cereus*) with 95% accuracy [182]. The follow-up study demonstrated that it is possible to differentiate the imprints resulting from the two bacteria species in an acrylate-based polymer matrix, again highlighting differences in surface chemistry between cavities originating from different bacteria types [183].

Besides AFM and Raman microscopy, characterizing SIP morphologies traditionally relies on high-resolution electron microscopy techniques, such as scanning electron microscopy (SEM) and transmission electron microscopy (TEM) [185].

Additionally, fine structural analysis has been reported using X-ray photoelectron spectroscopy (XPS) [185]. In XPS, a surface is irradiated with X-rays leading to the release of photoelectrons. The energy of these photoelectrons correlates to a distinct

element. Since this method is element-specific, it is mostly used for characterizing MIPs for small molecules (e.g., caffeine [119], adenine [186], and sulfadimethoxine [187]). Thereby, it is possible to visualize successful imprinting, removal of the template, or analyte rebinding.

A much simpler technique is using static contact angle measurements (SCA). Here, a liquid drop (i.e., water or an organic solvent) is placed on the surface and left to spread. One then determines the contact angle. This may sound simple, but gives insights into hydrophilicity/hydrophobicity of sample surfaces. Imprinting, for example, may shift surface hydrophilicity. Thus, comparing the contact angles of MIP and NIP layers may allow for assessing imprinting success, as used by Pernites et al. [188]. The same holds true for measuring contact angles before and after template removal, respectively [185]. Finally, MIPs need to be adapted to the respective sample matrix: Song et al., for example, used contact angle measurements to determine hydrophilicity of their imprinted polymer microspheres for glutathione in aqueous media [189].

Finally, laser diffraction analysis (LDA) and dynamic light scattering (DLS) serve for obtaining information regarding diameters of MIP particles. While the first technique is typically used for larger MIP beads, DLS has proven useful in the nanometer range [81, 190]. Surface areas and porosities of imprinted polymer films or particles can be determined using nitrogen gas adsorption and mercury intrusion porosimetry. To obtain chemical information about the MIP, nuclear magnetic resonance (NMR) or infrared (IR) spectroscopy can be used, accompanying the previously mentioned Raman spectroscopy [84].

4 Applications

4.1 Medical Applications

Implementing piezoelectric sensors in medical diagnostics is of great scientific and practical interest, as they offer a range of benefits over more traditional approaches: for one, piezoelectric devices are energy-efficient and straightforward to miniaturize. They circumvent the need for highly skilled staff and extensive laboratory equipment, which most state-of-the-art methods require, e.g., liquid and gas chromatography, mass spectrometry, and polymerase chain reaction (PCR). This reduces diagnosis cost and time and helps moving health care toward being more affordable, decentralized point-of-care type. Moreover, biomimetic receptors tend to be more stable than traditional recognition units (e.g., antibodies, enzymes, and cells), thus requiring neither cold storage and cold-chain logistics nor time-consuming culturing procedures.

Low-molecular-weight analytes are very attractive targets, especially for biomimetic-based point-of-care devices, not least because they are difficult to detect with immunosensors. Antibody production toward small molecules requires prior

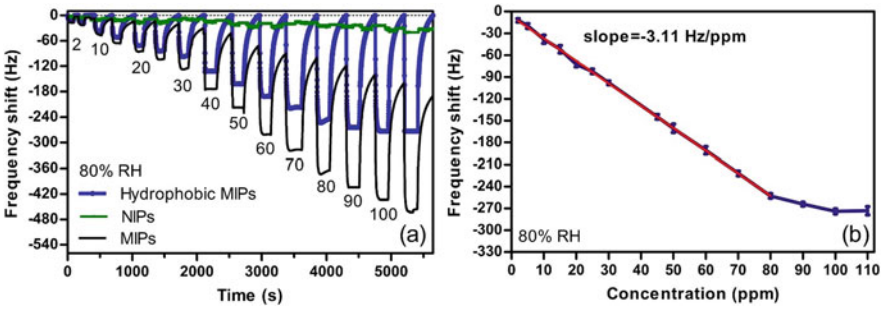

Fig. 25 Responses of NIPs, MIPs, and hydrophobic MIPs composite-based QCM gas sensor toward different concentrations of hexanal with 80% RH. Reprinted with permission from [194], © Elsevier

conjugation to a macromolecular scaffold, often resulting in antibodies that bind to the conjugated carrier protein, rather than the analyte itself.

Detecting disease biomarkers is one of the most important applications requiring recognition of small molecules in complex environments. Early diagnosis of severe diseases can significantly improve chances of recovery, which raises the need for low-cost, decentralized assay systems, facilitating regular and widespread screening for such early warning indicators. For instance, it is possible to detect some cancer biomarkers, e.g., metabolically derived aldehydes, directly in patients' breath. A main challenge here lies in the low limits of detection required for such diagnostic tools.

Owing to their large surface-to-volume ratio, nanostructured sensing layers are highly suitable for gravimetric detection of small volatile organic compounds (VOCs), as their large surface area drastically increases sensitivity. Using for instance multi-walled carbon nanotubes, mesoporous SiO_2 nanoparticles, and composites of graphene and TiO_2 nanoparticles, LODs in the low- to sub-ppm region have been reported [191–193].

Next to the high sensitivity required, the humid conditions pose a major challenge when it comes to developing breath sensors. A very promising approach to address this obstacle is to use composites containing MIPs for selective recognition and hydrophobic silica particles to minimize the influence of ambient humidity. Chen et al. presented such a system based on hexanal-imprinted methacrylic acid (MAA), cross-linked with ethylene glycol dimethacrylate (EGDMA). Compared to the pure MIP layers, this significantly reduced sensor drift, thus allowing for reliable detection of hexanal from 14.1 to 27.3 ppm at 80% relative humidity (Fig. 25). With a correlation factor of 98%, the results measured with the composite sensor were in good agreement with concentrations determined by solid-phase micro-extraction-gas chromatography mass spectrometry (SPME-GCMS) [194].

Besides humidity, the presence of numerous other VOCs in the human breath needs considering. An approach to tackle detection in such complex mixtures is the use of sensor arrays combined with principal component analysis (PCA) for analyte

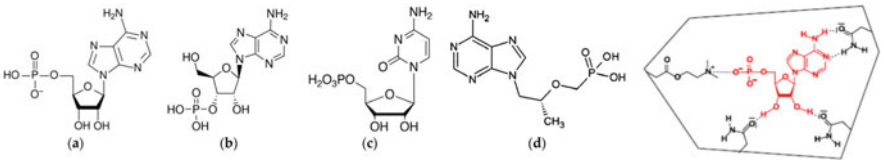

Fig. 26 Left: Nucleotides used for rebinding: (**a**) adenosine-5′-monophosphate (AMP); (**b**) adenosine-3′-monophosphate (3’-AMP); (**c**) cytidine-5′-monophosphate (5’-CMP); (**d**) 2-phosphono methoxypropyl adenine (PMPA). Right: Binding sites in AMP-MIP [196]

discrimination. To that end, Liu et al. evaluated 13 different sol-gel MIPs (MISGs) using hexanoic, nonanoic, and benzoic acid as pseudo-templates for the breath biomarkers hexanal, nonanal, and benzaldehyde. The final sensor array consisted of five optimized MISGs and was able to detect and correctly recognize the three different aldehydes at low concentrations [195].

Piezoelectric devices with biomimetic recognition units also represent a promising tool for biomarker detection in liquid phase. Dejous et al. developed a shear horizontal acoustic wave sensor coated with an acrylamide-based imprinted polymer to detect the cancer biomarker adenosine-5′-monophosphate (AMP). They tested selectivity compared to structurally related biomolecules adenosine-3′--monophosphate (3’-AMP), cytidine-5′-monophosphate (5’-CMP), and 2-phosphono methoxy propyl adenine (PMPA), which are shown in Fig. 26. The response toward AMP was three times higher compared to PMPA, while almost no signal was observed for the other two analytes. The moderate cross-sensitivity to PMPA can be explained by its flexible structure, facilitating the formation of hydrogen bonds inside the cavity via its phosphate group and heterocycle. The other two competitors are more rigid and differ in polarity and location of OH group (3’-AMP) or nucleobase (5’-CMP), resulting in a lack of specific interactions toward the polymer’s binding sites (Fig. 26, right) [196].

It is feasible to selectively detect even larger, structurally more complex biomarkers such as bilirubin (M_w = 584 g/mol), an indicator for liver malfunction, using bulk imprinting of fairly simple polymer systems. Cicek et al. modified QCM sensors with imprinted poly(HEMA-co-EGDMA). They reported an LOD of 0.9 µg/mL and an LOQ of 0.45 µg/mL. Selectivity factors range from 2.19 to 5.92 when compared to the response toward biliverdin, cholesterol, and estradiol. Moreover, first promising results were reported on the use of the sensor system in human plasma and artificial urine [197].

Protein detection is another important application for biomimetic sensing layers when it comes to developing cost- and time-efficient diagnostic devices. Here, aptamers are a very popular choice, owing to their relatively fast synthesis and a wide range of potential targets. For instance, the disease biomarker thrombin could be detected down to the low nanomolar range using aptamer-functionalized QCMs [198]. Similar results were reported by Zhang and coworkers, who were also able to obtain excellent selectivity, with a negligible response of the sensor toward IgG and IgE at 10-fold concentration [199].

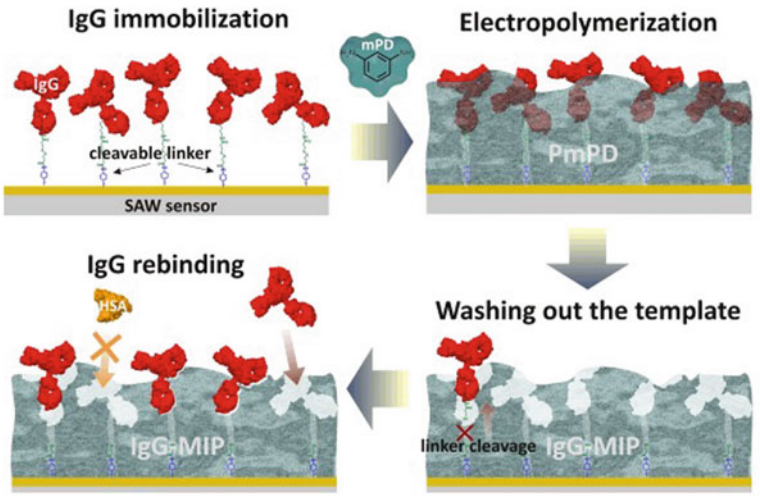

Fig. 27 Schematic representation of the electropolymerization-based synthesis procedure for IgG-MIP sensing layers integrated into a SAW chip. Reprinted with permissions from [200], © Elsevier

Since protein detection of real-life samples usually takes place in complex environments, using tailored imprinted polymers is a highly promising route to improve selectivity. As mentioned earlier, biomacromolecule imprinting is very challenging, especially regarding binding site accessibility and variations in three-dimensional protein conformation during imprinting. This has been addressed by introducing more elaborate imprinting protocols, such as microcontact imprinting, synthesis of nanoscale MIPs, and imprinting epitopes rather than entire proteins.

For instance, Tretjakov et al. presented a very elegant way to fix analyte orientation during polymerization and thus ensure formation of accessible imprints on the polymer surface: the analyte immunoglobulin G (IgG) was immobilized on a SAW chip surface via a cleavable linker, as illustrated in Fig. 27. MIP layers formed by electrodeposition of poly(*m*-phenylenediamine). MIP thickness was monitored and controlled precisely during electropolymerization, thus ensuring that the analyte could be easily removed by linker cleavage, leaving behind well-defined, accessible imprints at the polymer surface. Layer height optimization led to a maximized imprinting factor of 4.0. The approach made it possible to detect IgG concentrations as low as 0.4 nM, with the response toward immunoglobulin A and human serum albumin (HSA) being four and ten times lower, respectively [200].

Stamp imprinting is another way to generate protein-specific cavities at the MIP surface and ensure complete template removal. This method has been employed by Chunta et al. to detect oxidized-low-density lipoprotein (oxLDL), which is an indicator for increased arthrosclerosis and coronary artery disease risk. The template was immobilized on solid glass substrates which were then placed onto the pre-polymerized MIP mixture, comprising the functional monomer MAA and

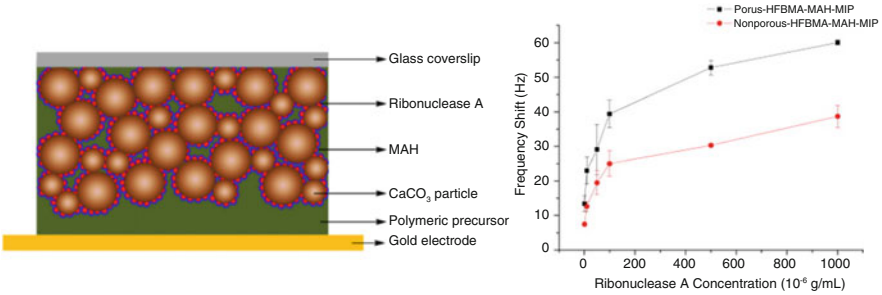

Fig. 28 Left: Schematic for the structure of macroporous protein surface-imprinted film coated on a QCM electrode. Right: Frequency shifts of the porous and non-porous HFBMA-MAH-MIPs upon exposure to increasing concentrations of ribonuclease A solutions. Error bars indicate the standard deviation in triplicated experiments. Reprinted with permission from [202], © Elsevier

N-vinylpyrrolidone (NVP). The resulting sensor layers displayed low cross-reactivity toward high-density lipoprotein (HDL), low-density lipoprotein (LDL), very-low-density lipoprotein (VLDL), and human serum albumin (HSA). The analyte could be detected in clinically relevant concentrations (86–5,600 μg/dL) as confirmed by commercial ELISA test kits (correlation coefficient: $R = 0.98$). Moreover, measurements in serum revealed a recovery rate of 92–107%, making this sensor system highly promising for real-life implementation [201].

Liu et al. [202] successfully varied protein surface imprinting: as Fig. 28 shows, they prepared glass stamps functionalized with calcium carbonate nanoparticles impregnated with the analyte, ribonuclease A. Then, MIP layers were formed by photopolymerization of 2,2,3,4,4,4-hexafluorobutyl methacrylate (HFBMA) and the crosslinker trimethylolpropane trimethacrylate (TRIM). Additionally, N-methacryloyl-histidine (MAH) was used as functional monomer to improve the polymers' hydrophilicity. After polymerization, the $CaCO_3$ particles were completely dissolved with 2% hydrochloric acid, followed by template removal with aqueous sodium chloride solution. This process yields a highly porous polymer layer with very large specific surface area and template binding sites located at the interface. Owing to the much higher number of available and well-accessible binding sites, strong signal enhancement could be observed for porous MIP films compared to non-porous reference layers. Moreover, introducing fluorinated functional groups using HFBMA as functional monomer significantly reduced non-specific binding, increasing the selectivity factor compared to lysozyme up to four times [202].

One can also obtain large, highly selective surface areas for protein detection by synthesizing nanostructured MIPs. For instance, Sener et al. prepared lysozyme-imprinted MIP nanoparticles of around 50 nm diameter by mini-emulsion polymerization. Using a simple drop-coating protocol, functionalized QCM sensors were obtained and assessed in both aqueous solution and egg white. MIPs were highly selective when compared to the response toward albumin. In aqueous solution, the

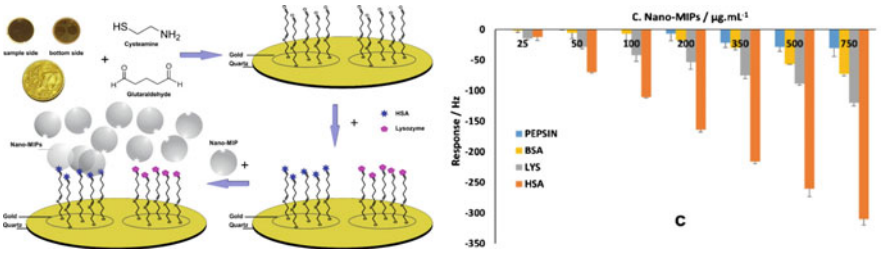

Fig. 29 Left: Sensor setup for competitive assay. Right: QCM results of HSA-, BSA-, pepsin-, and lysozyme-modified electrodes exposed to HAS-imprinted nanoMIPs [82]

LOD was calculated to 1.2 ng/mL, while in the complex matrix of chicken egg white, lysozyme concentrations as low as 460 ng/mL could be detected [203].

MIP nanoparticles can not only be employed for sensor surface functionalization but also as antibody analogues in direct and competitive assays. In a study by Sudjarwo et al., nanoMIPs with high affinities toward HSA were obtained by solid-phase synthesis. For selectivity assessment, they were then injected onto a two-channel QCM chip, functionalized with the template and a different protein on the second channel. As shown in Fig. 29, this resulted in selectivity factors ranging from 1.2 (BSA) to 4.1 (pepsin). For the competitive assay, HSA and nanoMIP solutions were mixed prior to injection onto a template-modified sensor chip, yielding LOD values of 5.3 µg/mL (80 nM) and an LOQ of 16.2 µg/mL (244 nM). Furthermore, assessment of the assay in artificial urine revealed highly satisfactory recovery rates, ranging from 101.6 to 106.5% [82].

Epitope imprinting is a further, increasingly popular approach toward detecting complex biomacromolecules. Here, only short peptide sequences located at the analyte surface are used as the template, mitigating challenges such as conformational changes during imprinting and incomplete removal of bulky analytes after imprinting. Ma et al. made use of this approach, reporting impressive results for imprinting a sequence of 9 amino acids of HSA. The functional monomer zinc acrylate was polymerized in the presence of the short-chain peptide and spin-coated onto a QCM sensor. As shown in Fig. 30, the sensor system showed exceptionally high response toward HSA, with an LOD of 0.026 µg/mL. Moreover, selectivity against lysozyme, transferrin, and horseradish peroxidase turned out promising. At recovery rates of 99.3% and 103.0% of 0.15 and 0.2 µg/mL HSA in diluted human serum, this sensor system is highly suited for measurements in real-life samples [204].

Viruses are among the most investigated targets for MIP-based sensor devices. To date, detecting and identifying viruses mostly requires time- and resource-consuming PCR analysis or immunoassays like the ELISA. Here, surface-imprinted MIPs that can selectively distinguish between viruses of different size, shape, and chemical functionality offer a fast and inexpensive alternative.

MIP thin-film-coated QCMs have been utilized for a large variety of viruses. Wangchareansak et al. focused on the detection and differentiation of the influenza A

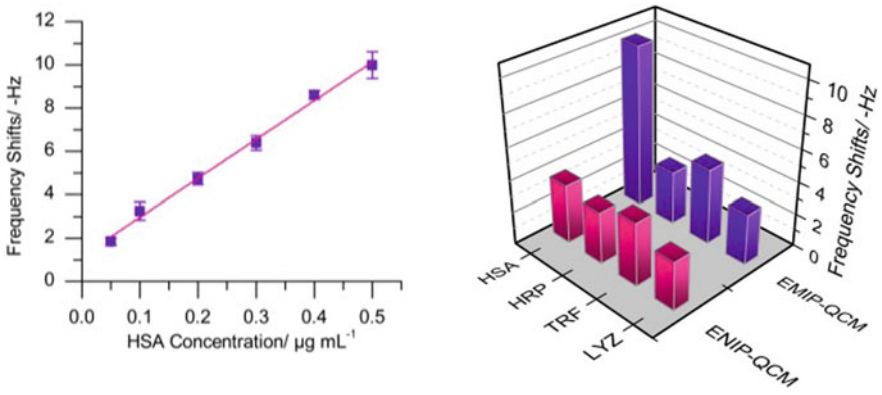

Fig. 30 Left: Sensor characteristic of the EMIP-QCM sensor. Right: Frequency shifts of EMIP-QCM and ENIP-QCM sensors toward different proteins. Reprinted with permission from [204], © Elsevier

virus. They employed stamp imprinting of five different virus strains (H5N1, H5N3, H1N1, H1N3, H6N1) to obtain surface-imprinted acrylamide-based polymers. Each MIP displayed the largest response toward the subtype it was imprinted with. Their results suggest that it is possible to conduct PCA-based virus fingerprinting using a small subset of MIPs [205]. In a later publication, they employed a similar imprinting protocol to develop an evaluation method for antiviral agents. Often, binding of inhibitor molecules is accompanied by conformational changes in the virus structure. These alterations affect the virus probes' affinity toward the highly selective polymer cavities. Such an assay system therefore would allow for high-throughput screening of possible therapeutic agents [206].

Stamp imprinting was also successfully employed for the selective detection of the human rhinovirus (HRV). Using a polymer system composed of bisphenol A, phloroglucinol, and hexamethylene diisocyanate, Hayden et al. were able to measure HRV-1a concentrations as low as 150 ng/mL. Moreover, the MIP layers were selective when compared to HRV-16, suggesting a chemical recognition process, as both virus serotypes have the same shape and dimensions [132]. Similarly, Jenik et al. produced PU-based MIP layers imprinted with three different HRV serotypes. The MIP layers successfully distinguished the different HRV types and showed only little response to the foot-and-mouth disease virus (FMDV) [207] (Fig. 31).

The already mentioned epitope imprinting method is also highly attractive when it comes to synthesizing MIPs that selectively recognize viruses. Next to better control over template orientation during imprinting, it also makes MIP production for highly dangerous analytes possible without the need for strict safety protocols, which would be required when working with the whole virus.

Tai et al. for instance used a 15 amino acid sequence from the dengue virus nonstructural protein (NS1). Template immobilization onto a gold QCM surface took place via self-assembly, followed by photopolymerization of the acrylamide-based MIP thin film. The sensor displayed high affinity toward the 15-mer peptide

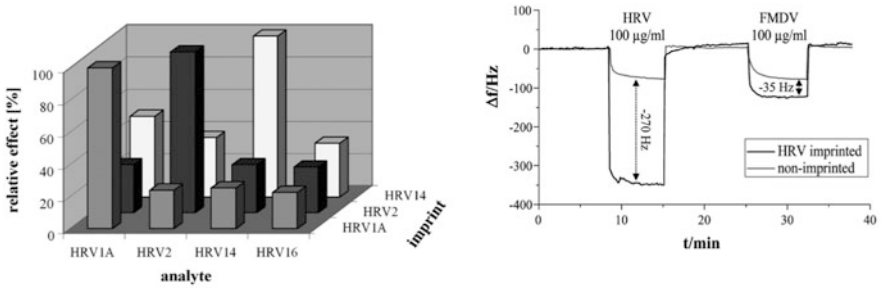

Fig. 31 Left: Summarized comparison of the obtained effects with the generated sensors toward various HRV serotypes. Right: Comparison of the frequency response of the 10 MHz QCM, coated with polyurethane and imprinted with HRV toward suspensions of HRV and FMDV, respectively. Reprinted with permission from [207], © American Chemical Society

sequence, as well as the purified NS1 protein. In contrast, almost no response was measured toward the nonapeptide oxytocin [208]. Similarly, Buensuceso et al. chose a slightly shorter NS1 peptide sequence containing 11 amino acids. Electropolymerization of the functional monomer (2,2′:5′,2″-terthiophene)-3′-acetic acid on an E-QCM surface was followed by template removal via potential washing. The QCMs response was evaluated not only with regard to the imprinted epitope but also toward the entire NS1 protein. With a linear range from 0.2 to 10 µg/mL and an LOD of 0.056 µg/mL for the whole protein, this sensor is highly suitable for assessing elevated NS1 levels in serum, with reported levels ranging from 100 to 600 ng/mL [209].

Also, Lu et al. successfully utilized epitope imprinting to detect human immunodeficiency virus type 1 (HIV-1). They coated QCM sensors with polydopamine thin films, imprinted with a 35-amino acid long sequence from the HIV-1 glycoprotein gp41. With this sensor system, the template peptide could be detected in concentrations as low as 3.17 nm. Moreover, LODs for gp41 (2 ng/mL) were comparable to those of ELISA systems. Selectivity assessment was done with bovine serum albumin (BSA), a 30-mer control peptide, and two peptides containing either 2 or 11 mutated amino acids compared to the template. While the 2 M peptide could not be distinguished from the template molecule, significantly lower responses were measured for the 11 M peptide, BSA, and the control peptide. The recovery rates of 86.5–94.1% in human urine samples underpin the high potential of this sensor system for real-life applications [210].

4.2 Environmental Applications

4.2.1 Volatile Organic Compounds (VOCs)

Monitoring the levels of volatile organic compounds (VOC) is important, especially when they are potentially harmful to nature and human health and introduced into the environment. Mass-sensitive devices have proven useful to tackle this issue when combined with biomimetic recognition:

For instance, Matsuguchi et al. reported a QCM sensor with MIP particles in a PMMA matrix. They prepared MIPs in either toluene or p-xylene as solvents. The resulting sensors tended to be selective to the solvent in which the polymer had been prepared. The response of the sensor toward toluene or p-xylene vapor was reversible. However, the response time was slow: the MIP particles were embedded into a matrix protein, which renders binding sites less accessible [211].

Similarly, Dickert et al. reported toluene-imprinted polystyrene layers with an almost sevenfold selectivity toward the template compared to the same concentration of xylene. Moreover, they were able to synthesize *o*-xylene-imprinted polystyrene layers to distinguish between different isomers: while exposure to *o*-xylene resulted in a strong response of the QCM sensor, the *p*- and *m*-isomers resulted in only small (*p*) to negligible (*m*) signals [212].

Arrays consisting of several sensors are a good way to increase selectivity and analysis speed by monitoring several analytes simultaneously. Each of them is coated with a material that shows a certain amount of selectivity to a specific analyte or a group of analytes, respectively. Hence, they allow for detecting several different analytes simultaneously.

For instance, Dickert et al. developed a QCM array comprising five different imprinted materials targeting aliphatic alcohols, ethyl acetate, and limonene, respectively. The sixth QCM electrode comprised an affinity material to monitor humidity. Measurements in a commercial composter allowed for following the underlying degradation processes: in the beginning, the concentration of alcohols decreases in the headspace, followed by an increase in ethyl acetate concentration. Later the concentrations of alcohols increase again followed by detecting limonene toward the end of the process. Sensor responses followed the pattern observed by gas chromatography combined with mass spectrometry (GC-MS) [213]. A related study by Lu et al. describes a sensor module consisting of six QCMs coated with synthetic polypeptides together with conducting polymers. They used it to detect and identify individual VOCs and mixtures, respectively, simultaneously. The system is both sufficiently sensitive and selective to detect and discriminate species via odor profiles obtained by exposing the array to defined amounts of the individual analytes and applying principal component analysis to the datasets [25].

A similar approach by Lubert et al. consists of surface acoustic wave (SAW) resonator-based electronic noses comprising pre-concentrators. When installed at chemical storage, the sensors proved suitable for detecting the source of organic

contamination in the air. The main objective of this work was to design an alarm system that can locate the origin of leaking organic vapors [214].

Iglesias and his colleagues developed a hybrid system composed of a quartz crystal tuning fork array coated with a polyurethane-based MIP for selective recognition and separation in short chromatographic columns. It combines sensitivity and selectivity of the sensors with a fast, miniaturized separation method. The system successfully and selectively recognized and separated the structurally very similar analytes benzene, toluene, ethylbenzene, and xylenes in gasoline vapors [215].

Polycyclic aromatic hydrocarbons (PAH) are products of incomplete combustion and potent carcinogens. Stanley et al. used the formation of π–π sandwich complexes of their aromatic rings and immobilized anthracene carbonic acid in an aliphatic monolayer on QCM. They achieved detection limits of 2 ppb [216]. Lieberzeit et al. developed a similar system based on polyurethane MIPs on QCM. By imprinting PAH mixtures of naphthalene and pyrene they could increase selectivity and sensitivity. With this improvement they increased the layer uptake by one order of magnitude. A corresponding non-imprinted reference was used to subtract unspecific binding events [217].

Torad et al. prepared several types of nanoporous carbons (NPCs) by in situ carbothermal treatment of zeolitic imidazolate frameworks (ZIFs) in different inert atmospheres that turned out to be suitable for discriminating different vaporized aromatic compounds. Carbothermal treatment with H_2 gas and the existence of Co in the material led to the formation of carbon nanotube (CNT)-containing NPCs which increased sensitivity and selectivity toward toxic volatile aromatic hydrocarbons over the aliphatic analogues. These results suggest that the CNTs on the framework surface are responsible for this behavior [218].

Synthesizing MOF films at ambient conditions is a major challenge. This is particularly the case for pillared-layer MOF films due to their anisotropic structures. Kim et al. demonstrated a protocol to achieve dense and continuous pillared-layer MOF thin films via aluminum-doped zinc oxide as a template and hydroxyl double salt (HDS) intermediates at room temperature. They successfully transferred the material to a QCM sensor to detect CO_2 even at moderate humidity levels [219].

Devkota et al. reported a zeolitic imidazolate framework-8 (ZIF-8) MOF on a SAW reflective delay line for sensitive detection of carbon dioxide (CO_2) and methane (CH_4) at ambient conditions. In particular, they showed that a four times higher sensitivity was achieved by using a 860 MHz SAW reflective delay line instead of a 430 MHz with the same material, which, by the way, is the factor one would theoretically expect [220].

Wong et al. fabricated a nanocomposite film consisting of hybrid TiO_2–SnO_2/multi-walled carbon nanotube (MWCNT)-doped copper-benzenetricarboxylate (Cu-BTC). With this sensor they could detect trace amounts of ammonia at ambient conditions. Hybrid TiO_2–SnO_2/MWCNT doping prevents the framework from decomposing in the presence of humidity and ammonia [221].

However, sometimes even very straightforward inorganic matrices serve as sensing materials. For instance, when detecting mercury vapors, Sabri et al. report a composite monolayer comprising monodisperse polystyrene nanospheres as well

as gold and silver nanostructures deposited on QCM that proved useful for sensing of Hg^0 vapor in the presence of interfering gas species [222].

4.2.2 Metal Ions

Heavy metal ions of course represent a key analyte in environmental applications. However, mass-sensitive devices play only a limited role when detecting them, not least because electrochemical sensing offers excellent tools for that purpose. Nonetheless, there are some examples of mass-sensitive detection in that regard. For example, Sun et al. developed a QCM sensor based on CdTe nanospheres modified with thioglycolic acid (TGA; see Fig. 32) to detect heavy metal ions in aqueous solution. The ions adsorb at the TGA. The CdTe nanospheres amplify the mass signals six times compared to TGA only [223].

Hg(II) ions are among the most toxic species in the environment. To address them, Li et al. synthesized a bipyridine-containing hydrazone-linked covalent organic framework (COF). They prepared a COF-based QCM sensor growing the COF in situ on amino-modified QCM. Figure 33 summarizes the working principle. The resulting sensor was useful to detect Hg(II) ions in aqueous solution with good selectivity and relatively low detection limit linked to the specific coordination interaction between the Hg(II) ions and N,N′-chelating sites in the pore walls of the COF. This can be seen in Fig. 34 [224].

Tokuyama et al. presented a novel zirconia synthetic polymeric hydrogel loaded with nanoparticles for detecting arsenic in an aqueous solution. They prepared the composite hydrogel by polymerizing an aqueous solution containing N, N-dimethylacrylamide as the monomer, a crosslinker, an initiator, and zirconia

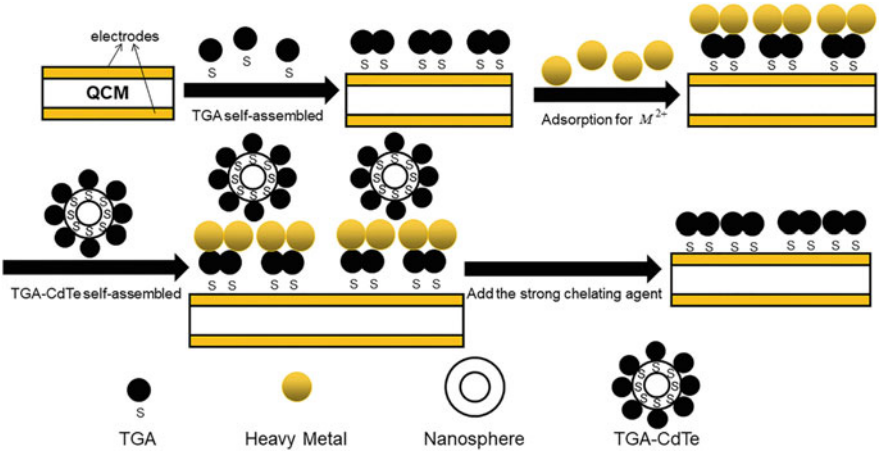

Fig. 32 The experimental procedure of the TGA–CdTe QCM sensor. Reprinted with permission from [223], © Springer

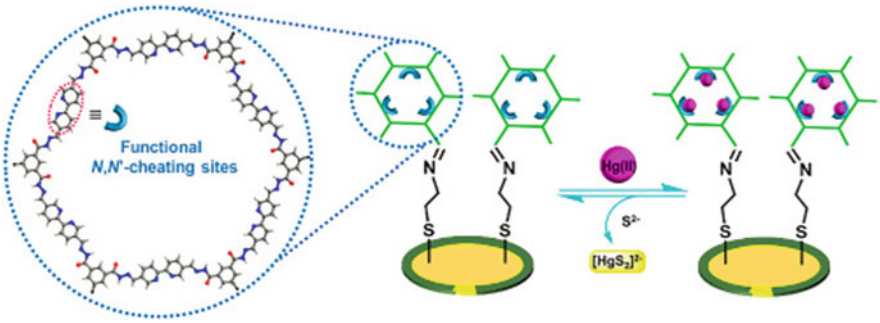

Fig. 33 Working principle of the Hg(II) sensor. Reprinted with permission from [224], © Elsevier

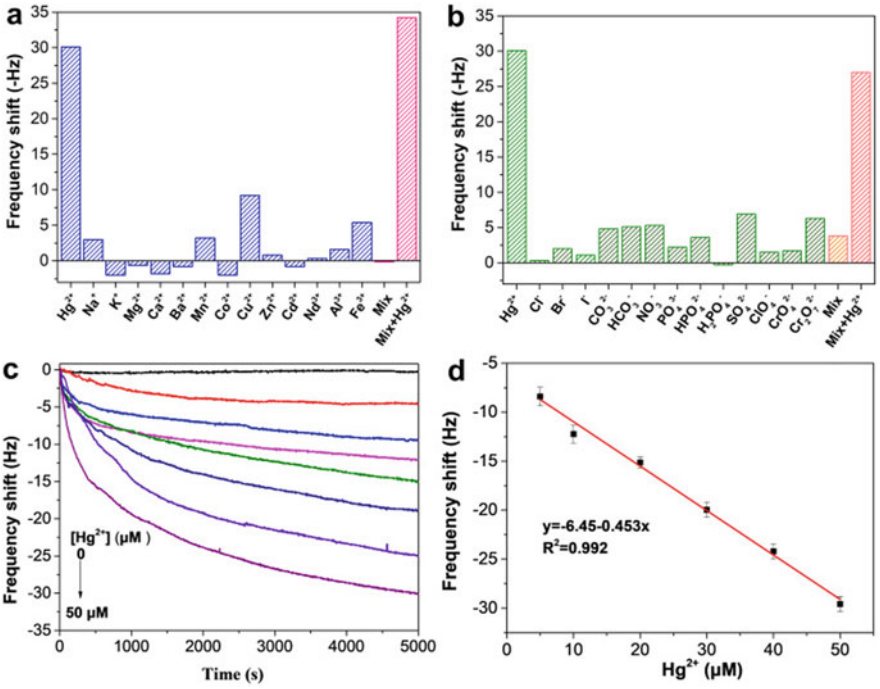

Fig. 34 Frequency changes of the QCM sensor in response to (**a**) various metal ions and (**b**) various anions in water. (**c**) Real-time frequency response of the sensor to Hg^{2+} with increasing concentration. (**d**) The linear relationship between the frequency shift and the concentration of Hg^{2+}. Reprinted with permission from [224], © Elsevier

nanoparticles. The hydrogel selectively adsorbed As(III) and As(V), which leads to appreciable QCM sensor responses even in the presence of other ions, such as Na(I), Mg(II), and Ca(II) [225].

4.2.3 Pesticides/Herbicides/Insecticides

The use of glyphosate as an herbicide leads to substantial controversy. In this context, Mazouzet al. designed biomimetic polymer layers to detect glyphosate in a selective manner. They coated surface acoustic wave (SAW) sensors with polypyrrole MIPs leading to detection limits in the order of 1 pM [226].

Chlorpyrifos is one of the most frequently used broad-spectrum organophosphate insecticides. Kadirsoy et al. prepared a molecularly imprinted QCM sensor on delaminated sulfur-doped MXene for chlorpyrifos. MXenes are two-dimensional materials consisting of early transition metal carbides or carbonitrides. This study used it for its large specific active area. The resulting sensor was tested in orange juice samples; it achieved high recovery demonstrating that it can detect chlorpyrifos in real samples [227].

Gao et al. developed QCM sensors coated with MIP films for the detection of the organophosphorus pesticide profenofos in water. They prepared a sensor system by using entrapment and in situ self-assembly approaches. Of those, in situ self-assembly leads to the best results with respect to affinity and selectivity in real samples [228].

Addressing a different pesticide class, Prasad et al. developed a sensor that analyzes organo-chlorinated pesticide residues in real samples. They prepared dual-template-imprinted biomimetic dendritic nanofibers for dichlorodiphenyltrichloroethane and hexachlorobenzene. First, they immobilized 2,5-thiophene dicarbonyl dichloride molecules on the surface of QCM gold electrodes; then, they covalently attached dendron molecules. This was followed by free-radical polymerization with a crosslinker in the presence of both target analytes. This process led to the formation of self-assembled molecularly imprinted dendrimer nanofibers attached to the gold surface [229].

QCM sensors based on MIPs for paraoxon recognition have been developed by Özkütük et al. They used chitosan-Cd(II) modified with thiourea and epichlorohydrin as the functional monomer and crosslinker, respectively [230]. In another work, the same group used N-(2-aminoethyl)-3-aminopropyltrimethoxysilane–Cu(II) as a new metal-chelating monomer cross-linked with tetraethoxysilane [231].

For detecting chlorotriazines, Yaqub et al. performed in situ MIP synthesis directly on gold electrodes of QCM sensors. The resulting biomimetic sensor shows reversible and selective sensor responses for chlorotriazine moieties with minor structural differences. Selectivity toward atrazine is up to 9 times higher than its metabolites and structural analogues. Furthermore, they prepared imprinted nanoparticles. The particles showed no saturation effects in contrast to the bulk material in the concentration range observed [232].

4.2.4 Bacteria

Detecting biological species in environmental samples is indeed very interesting, because, for instance, the presence of some coliform bacteria or viruses can indicate contamination with wastewater. To tackle this, Latif et al. used surface-imprinted polyurethane MIP as QCM sensor coating able to detect the analyte selectively in mixtures of interfering compounds. They utilized a double molecular imprinting approach comprising of using the bacteria MIP as templates for a second stamp imprinting step. By this, it is possible to transfer the geometry and functionality of bacteria onto synthetic polymer, i.e., to generate "plastic copies" of the cells. This strategy allows for synthesizing multiple sensor coatings with similar sensitivity and selectivity. Figure 35 shows some AFM images of the respective imprints [233].

In another publication, the authors present *Escherichia coli*-imprinted polymers to detect the bacteria with QCM sensors and compared the sensor results of atomic force microscopy measurements to correlate sensor responses to the surface occupancy in AFM. To test selectivity, they also prepared imprints for *Bacillus subtilis* spores. In this way, it was possible to differentiate spores of different Bacillus species and selectively detect them through the MIP-based sensors [135]. Imprinting with *B. cereus* led to similar results [234].

In contrast, Lian et al. presented non-MIP approach: [235] they prepared an aptamer/graphene piezoelectric sensor to detect *Staphylococcus aureus* using a specific *S. aureus* aptamer as a recognition element on the sensor. They first bound graphene to the interdigital gold electrodes via 4-mercaptobenzene-

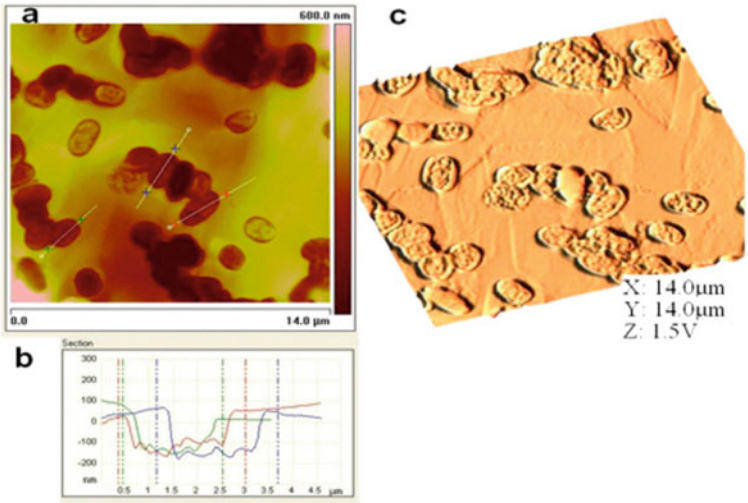

Fig. 35 Polyurethane layer with *E. coli* cavities, imprinted with a synthetic bacteria stamp (replica of *E. coli* W) made of silicon. (**a**) Two-dimensional presentation of the surface with AFM-contact mode; (**b**) depth profile of the indicated cavities in figure (**a**); (**c**) three-dimensional presentation of the polymer section from figure (**a**) [233]

diazonium tetrafluoroborate salt. Then they immobilized the *S. aureus* aptamers onto the graphene via π–π stacking of DNA bases, which has become a fairly standard way for that purpose. When *S. aureus* is present in the sample, the DNA bases interact with the aptamer. Thereby the aptamer detaches, which results in a mass-sensitive signal.

4.2.5 Antibiotics, Drugs, and Hormones

Even though antibiotics have revolutionized medicine by making many infections treatable, their overuse is a concern in health management. Monitoring antibiotics levels in the environment is highly desirable but challenging. In terms of mass-sensitive sensing, Shaheen et al. developed a heterostructured hybrid material consisting of two-dimensional bismuth nanosheets augmented by molecularly imprinted networks as can be seen in Fig. 36. When applied in QCM sensors, they achieved high selectivity of chloramphenicol over its interfering and structural analogues, such as clindamycin, thiamphenicol, and florfenicol. The prepared composite interface offers the advantage of selective binding and excellent sensitivity

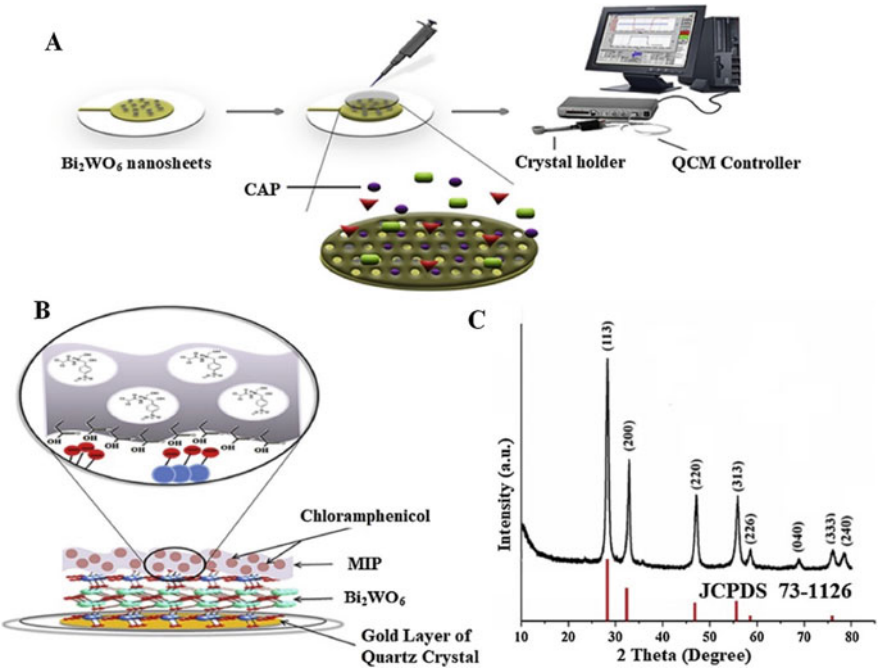

Fig. 36 (**a**) Schematic diagram illustrating the design of the mass-sensitive detection of chloramphenicol; (**b**) proposed mechanism for chloramphenicol, MIP, and Bi_2WO_6 nanosheets interactions; (**c**) structural characterization by the XRD profile of Bi_2WO_6 nanosheet. Reprinted with permission from [236], © Elsevier

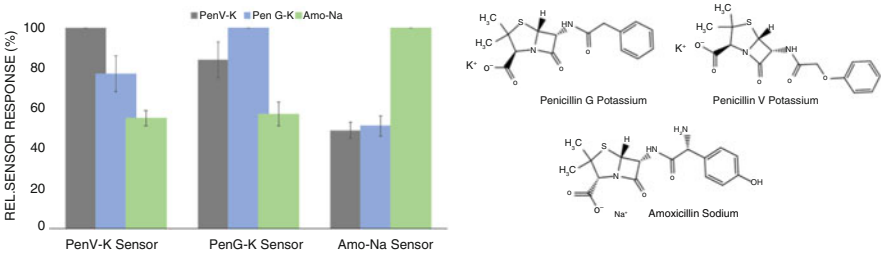

Fig. 37 Left: Relative sensor responses for PenV-K, PenG-K, and Amo-Na sensors toward the target penicillin at c = 2.50 mM. Right: Chemical structures of target penicillin compounds [238]

due to special heterostructured morphology, in addition to benefits in terms of ruggedness and online monitoring [236].

In a different approach, Ayankojo and coworkers employed electropolymerization to detect amoxycillin. They took advantage of the fact that electrodeposition allows for precise control of polymer film growth. When they optimized the layer height of meta-phenylenediamine-based MIPs, it turned out that the imprinting factor strongly depends on film thickness, with polymer layers around 25 nm yielding the maximum value of 3.05. Besides a very low LOD of 0.2 nM, selectivity studies toward two other commonly administered antibiotics, doxycycline and sulfamethizole, showed good discrimination between the different antibiotics classes [237].

Selectivity of MIP thin films is not limited to different antibiotic types: even structurally similar molecules from the same antibiotic class can be distinguished from each other. For example, MIP thin films composed of MAA cross-linked with EGDMA were imprinted with penicillin V potassium salt (PenV-K), penicillin G potassium salt (PenG-K), or amoxycillin sodium salt (Amo-Na). All analytes share a beta-lactam ring as a core motif and PenV and PenG differ from each other by only one oxygen atom. Nonetheless, MIP responses showed up to 50% relative selectivity toward the analyte they were imprinted with and LODs in the sub-nanomolar range [238] (Fig. 37).

While the reported selectivities and sensitivities obtained from MIP-based piezoelectric devices are impressive, it is imperative to assess their functionality in real-life samples. In that context, Bereli et al. developed a QCM sensor coated with amoxicillin-imprinted poly(hydroxyethyl methacrylate-methacrylic acid) and evaluated the sensors' performance not only in aqueous solution but also in chicken egg white as a representative for complex biological matrices. They reported a very low LOD of 0.0023 ng/mL and a linear range from 0.1 to 10.0 ng/mL in aqueous solution. Moreover, recovery of 2.0 and 4.0 ng/mL analyte in the chicken egg samples ranged from 96.00 to 99.00%, which is highly promising for developing future applications in real-life samples [239].

Of course, antibiotics are not the only class of drugs that are interesting from the sensing point of view. For instance, Eslami et al. demonstrated how it is possible to fine-tune polypyrrole-based MIPs in an elegant way toward maximum sensitivity

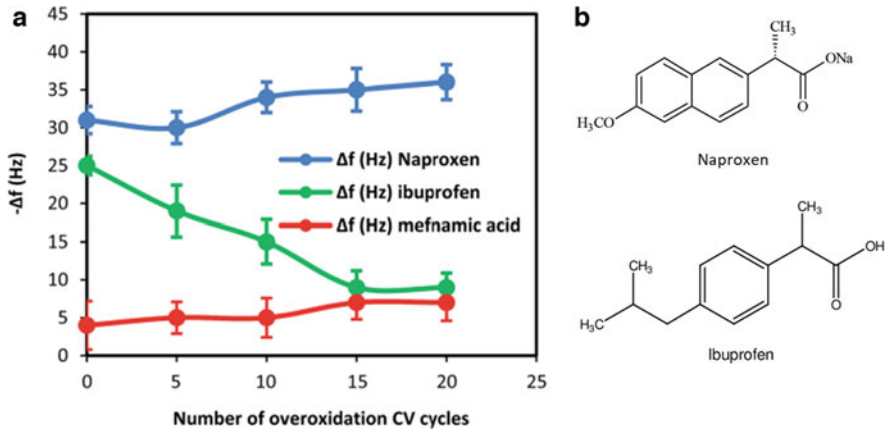

Fig. 38 The response of sensor with different degree of overoxidation by different overoxidation CV cycles for the same concentrations of aqueous solution of analyte (NAP) 5 mM and interfering molecules with similar structure (ibuprofen 10 mM and mefenamic acid 10 μM) (**a**) and (**b**) the molecular structures of naproxen and ibuprofen. Reprinted with permission from [240], © Elsevier

and selectivity for the nonsteroidal anti-inflammatory analgesic naproxen (NAP). MIP films were deposited directly onto a QCM electrode by electropolymerization, which allows for easy and complete template removal by overoxidation. Moreover, higher selectivity compared to the smaller, anionic molecule ibuprofen was observed with an increasing number of oxidation cycles, as shown in Fig. 38. This can be related to the loss of positively charged sites within the polymer backbone, limiting the uptake to more bulky anionic analytes with delocalized negative charge. This made it possible to detect NAP concentrations as low as 0.1 μmol/L, with improved selectivity to previously reported sensors [240].

Latif et al. used a bulk imprinting approach to detect estradiols, which are endocrine-disrupting chemicals (EDCs). They fabricated a highly sensitive, selective, and robust QCM sensor for real-time monitoring of 17β-estradiol, one of the most potent EDCs, in water samples. Molecularly imprinted polyurethane served as a sensing layer. Optimization of porogen and crosslinker content in the polymer led to improved sensitivity, selectivity, and response time of the sensor [233].

4.3 Food Safety

The increasing world population ultimately leads to an increasing demand for food. Of course, this needs to be safe to consume. However, several incidents in the past have shown that this is not always the case. In 2008, for example, the Chinese milk scandal became public: Food producers added melamine – a bulk chemical – to their dairy products to increase nitrogen content, which then pretended higher protein content of the products. However, melamine can cause serious kidney damage in

infants. When the scandal became public, already 250,000 children were affected, of which 52,000 were hospitalized. The death of six babies was directly related to contaminated dairy products [241]. Such incidents make it clear that safety monitoring of food products becomes increasingly important. Piezoelectric sensors with biomimetic receptor layers found their way into food analysis and food safety testing. Target analytes range from chemical (e.g., pesticides and pharmaceuticals) to biological (e.g., bacterial and fungal). The melamine scandal stated above led Zeilinger et al. to develop a mass-sensitive sensing system based on QCMs with MIP thin films as receptor layers [242]. They reported an LOD of 8 μM when melamine was dissolved in water. When measured in a real-life matrix, i.e., milk, it was impossible to reproduce the low LOD due to adduct formation between melamine and milk proteins. The sensor performed best in whey: this matrix contains a relatively small amount of protein. Nonetheless, it is still possible to measure higher melamine concentrations in real-life dairy products.

Small molecules contaminating food are the main focus of biomimetic sensor and receptor layer development. The larger part of work published so far relies on using molecularly imprinted polymers [87]. Pesticides are interesting targets for such approaches. In 2019, Cakir and coworkers created MIP nanofilms on QCM and SPR chips to detect 2,4-dichlorophenoxyacetic acid (2,4-D) in apple juice [243]. 2,4-D is a widely used herbicide and classified as a possible carcinogen to humans by the IARC [244]. Their sensors achieved a detection limit of 20.17 ng/L for the QCM transducer and 24.57 ng/L for the SPR approach. Those values are below the LODs of current state-of-the-art sensors used to detect 2,4-D. Additionally, the sensors showed good reusability: they could be used in five consecutive cycles over a time period of 5 weeks. The MIPs were tested for selectivity toward the target compound by exposing them to structurally similar compounds, namely 2,4,6-trichlorobenzoic acid and 2,4-dichlorophenol. The results showed that the binding of 2,4-D is favored compared to the structurally similar compounds and only low cross-selectivity was noted.

Several other studies exist using similar MIP-QCM setups to detect pesticides in food samples. Dayal et al. created a hydrophilic molecularly imprinted polymer based on poly(vinylidene difluoride) to detect the insecticide trichlorfon [245]. The researchers achieved an LOD of 15.77 ppb, and the sensor showed good recoveries (92.7–98.1%) when applied in spiked lettuce samples. Fang et al. published a study applying the MIP-QCM setup to detect metolcarb, another insecticide frequently used in agricultural production [246]. With their imprinted poly(methacrylic acid-*co*-ethylene glycol dimethacrylate), the group established an LOD of 2.309 μg/L with a low response time of 12 min. Measurements in real-life food matrices (namely apple juice, pear, and cabbage) showed satisfactory recoveries (85.3–95.5%).

Fungi pose another interesting target for the application of piezoelectric sensors with biomimetic receptor layers. More specifically, mycotoxins originating from fungal contaminations can be detected. They are secondary metabolites of the fungal species, which can give rise to significant risks for humans and animals. Especially the toxins produced by *Aspergillus*, *Penicillium*, and *Fusarium* species pose a threat to food safety and are therefore the most important targets for analysis [247]. Most

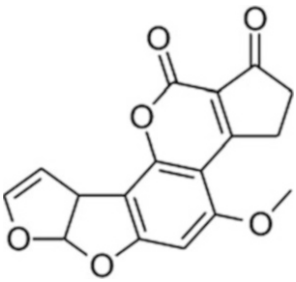

Fig. 39 Structure of aflatoxin B1 (AFB1), the target analyte used in the study of Gu and coworkers [250]

piezoelectric sensors utilizing biomimetic recognition elements for mycotoxins rely on QCM transducers and MIPs [248–250]. For example, Gu and co-workers developed a QCM sensor to determine aflatoxin B1. The sensor is based on a composite comprising a gold nanoparticle-doped MIP layer and a covalent organic framework [250]. Aflatoxin B1 (AFB1, Fig. 39) is one of the most dangerous mycotoxins produced by *Aspergillus parasiticus* and *Aspergillus flavus*, typically infesting wheat and maize plants. Several MIP-based approaches were developed aiming at detecting AFB1 [251]. The approach of Gu et al. achieves detection limits as low as 2.8 pg/mL with a wide linear range from 0.05 to 75 ng/mL. When applied to real-life samples, i.e., spiked samples of peanut, pistachio, rice, and wheat, the authors achieved good recovery rates (87.0–101.7%). In their study, they applied a covalent organic framework (COF) co-polymerized with gold nanoparticles (AuNPs) to yield an additional substrate layer, which could be anchored directly at the QCM gold electrode (Fig. 40a). COFs helped to increase the specific surface layer, leading to a larger number of MIP recognition sites. Naturally, this increased sensitivity. O-aminothiophenol-functionalized AuNPs (o-ATP@AuNPs) were used as a functional monomer to be electropolymerized in the presence of the template compound (AFB1) on the COF-AuNP framework (Fig. 40b). In addition to the low LOD of the device, the authors could achieve high selectivity for AFB1: sensor responses of six different mycotoxins were significantly lower. Adding the COF-AuNP layer led to an approx. twofold signal increase compared to the same system lacking this matrix. NIP reference layers only showed low, concentration-independent signals due to the lack of specific recognition sites. Results are summarized in Fig. 41.

Of course, antibiotics are notable examples of small molecules important in food analysis (e.g., penicillin [252]), as well as additives in feed products (e.g., ractopamine [253]).

Food contamination by microorganisms represents another interesting sensing approach. Several research groups developed biosensing applications for foodborne viruses (e.g., norovirus, hepatitis A and B, and rotavirus [254–256]). However, the main emphasis in this context, i.e., the use of biomimetic receptor layers coupled with piezoelectric sensing devices, lies on bacteria. Those can serve as an indicator of food hygiene, as well as the source of the outbreak of foodborne diseases (e.g., *Escherichia coli* and *Salmonella*). *E. coli* not only serves as a fecal indicator for, e.g., water contamination [257], but can also lead to severe food poisoning with

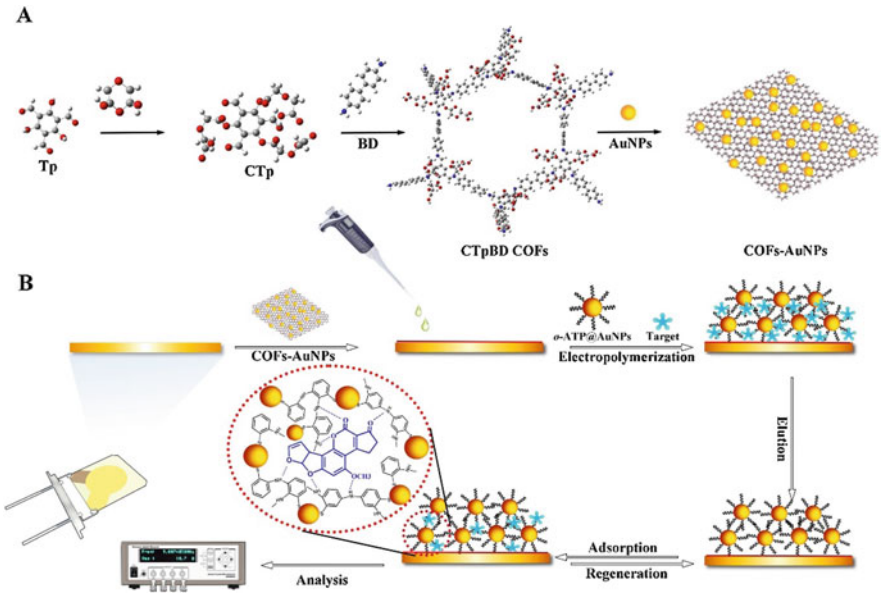

Fig. 40 (**a**) Synthesis of a covalent organic framework (COF) and polymerization with gold nanoparticles (AuNPs) to yield a highly structured, porous network (COFs-AuNPs). (**b**) Application of the COFs-AuNPs network as an additional substrate layer directly on the QCM transducer. Subsequent electropolymerization of o-ATP@AuNPs with the target analyte AFB1 leads to the generation of a highly selective MIP layer, which can be used to detect AFB1. Reprinted with permission from [250], © Elsevier

sometimes fatal consequences [258]. Therefore, monitoring *E. coli* is a crucial task for food safety. Spagnolo et al. recently developed an ultra-high-frequency electromagnetic piezoelectric acoustic sensor device (EMPAS) with a biomimetic aptamer receptor layer to detect *E. coli* in milk [259]. The sensing system could achieve LODs of 35 CFU/mL in PBS and 8 CFU/mL in cow's milk. In milk samples, it resulted in an LOQ of 34 CFU/mL. Bacterial safety limits in milk in different countries are not necessarily the same but usually lie in the region of thousands per mL. Thus, the established LODs are well below the safety regulations. In their work, the authors additionally coated the EMPAS crystal with the anti-fouling linker 3-(3-(trichlorosilylpropyloxy) propanoyl chloride (MEG-Cl), which they developed in their previous work [260]. This dramatically reduces non-specific binding, as it prevents bacteria cells from adhering to the bare piezoelectric crystal surface.

Several approaches exist using molecularly imprinted polymers to detect *E. coli* in food samples [125, 140, 251, 261]. Among piezoelectric devices, most of the transducer-MIP combinations rely on QCMs with surface-imprinted receptor layers [262, 263]. Yilmaz et al. [263], for example, developed a QCM-based sensor with a microcontact ("stamp")-imprinted polymer layer. A set of acrylates (i.e., 2-hydroxyethyl methacrylate and ethylene glycol dimethacrylate) together with N-methacryloyl l-histidine methylester (MAH) were chosen as functional and

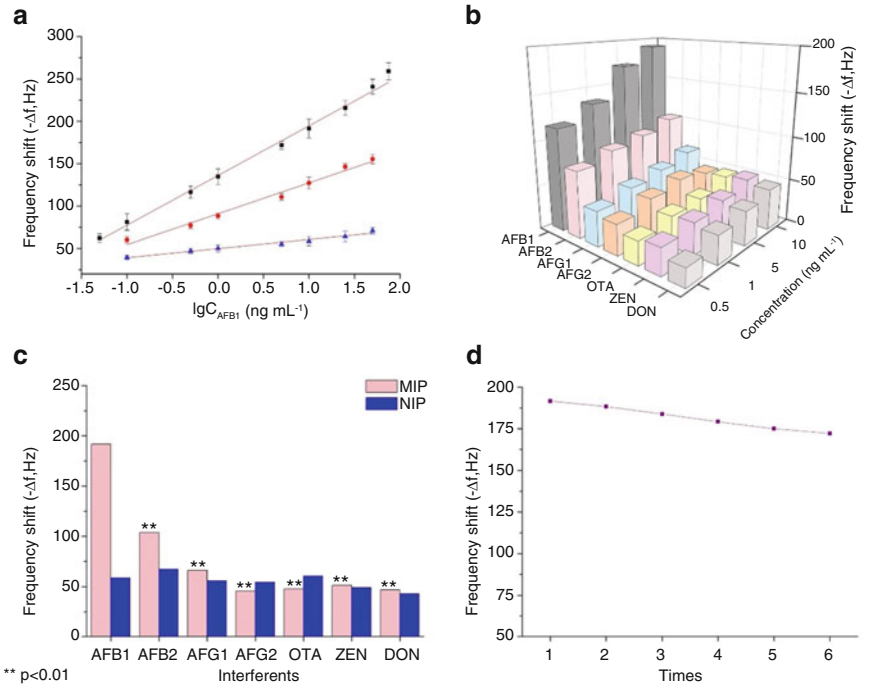

Fig. 41 (**a**) Calibration curves for sensing setup using a MIP-COFs-AuNP layer (black), a MIP layer without the COF network as an additional substrate (red) and a NIP-COFs-AuNP layer (blue). Results show that sensitivity and frequency shifts are highly increased when using the COF-AuNP adlayer. Additionally, NIP layers respond with lower signals, indicating the success of imprinting. (**b**) Selectivity studies of the sensing system toward AFB1 and six interfering mycotoxins with structural similarity. (**c**) Frequency shifts of MIP layer and NIP layer for 10 ng/mL AFB1 and interferants. (**d**) Stability and reusability of the sensing system for 15 days. Reprinted with permission from [250], © Elsevier

crosslinking monomers. MAH is a polymerizable form of histidine, giving the receptor layer additional "protein-like" characteristics. Imprinted thin films were created using the stamping method with covalently immobilized *E. coli* cells on glass slides. The resulting sensor achieved an LOD of 3.72×10^5 CFU/mL in aqueous solution. Even though this value lies far above the LODs claimed by groups using aptamers on QCMs [259, 264], it has the advantage of being robust and stable toward environmental changes as a consequence of the MIP layer. Yilmaz et al. also could apply their *E. coli* sensor in apple juice, a real-life matrix.

Other examples for the detection of bacteria in food samples using biomimetic receptor materials and piezoelectric transducers include *Salmonella* in milk samples, *Campylobacter jejuni* in poultry, and *Mycobacterium tuberculosis* and *Staphylococcus aureus* in buffer samples [265].

4.4 Public Security: Explosives and Illicit Drugs

Biomimetic receptor layers on piezoelectric sensing substrates have found their way into public health and security as well. Here, one can distinguish between two big categories: drugs and explosives. Detecting explosive materials is an important task in everyday life, especially at places with increased traffic (e.g., public transport hubs). Naturally, this process needs to be fast and silent. Several research groups published studies relying on molecularly imprinted polymers to detect explosives [266]. Nitroaromatics and nitroamines are the most prominent group of explosives (e.g., 2,4,6-trinitrotoluene (TNT), 2,4,6-trinitrophenol (TNP), and 1,3,5-trinitroperhydro-1,3,5-triazine (RDX)). Due to their aromatic properties, most published research relies on optical or electrochemical sensing. However, a few studies exist that use a piezoelectric transducer. An early paper by Tomita et al. [267] on the detection of mononitrotoluene (MNTs) vapor in 1979 described the use of piezoelectric quartz crystals coated with a layer of Carbowax 1000 (polyethylene glycol). They could detect MNT vapor in the ppb to ppm range at a response time of only 10 s. Even though no serious interferences were observed from most other organic or inorganic vapors, high concentrations of perfumes and organic solvents caused non-specific signals or even dissolved the coating. Of course, a lot has changed since that early study, especially in terms of selectivity toward the respective explosive compound and stability of the receptor layers: for instance, a study by Bunte and co-authors [268] demonstrates the development of MIP layers on QCMs to selectively detect TNT vapors. With that, molecular imprinting found its way into explosives' detection. Huynh and coworkers [269] created a sensing system based on simultaneous chronoamperometry (CA) and piezoelectric microgravimetry (PM) detection of nitroaromatic compounds using MIPs. The imprinted polymer was based on thiophenes and synthesized directly on the transducers via electropolymerization. Measuring with PM in the liquid phase, the group could achieve LODs of 0.02 mM for TNP, 0.07 mM for TNT, 0.15 mM for TNB, and 0.76 mM for DNT in 0.2 M NaCl solutions of water/ACN (1:1, v:v). Those values were lower than the LODs achieved with CA. Selectivities toward the respective compounds were higher for PM, with selectivity factors ranging from 4.8 (for TNP) to 2.7 (for TNB). Figure 42 shows the structures of the detected explosives, highlighting their structural similarity.

Illegal drugs of abuse pose a serious threat to human health and public safety. In their 2022 world drug report, investigators and researchers of the United Nations

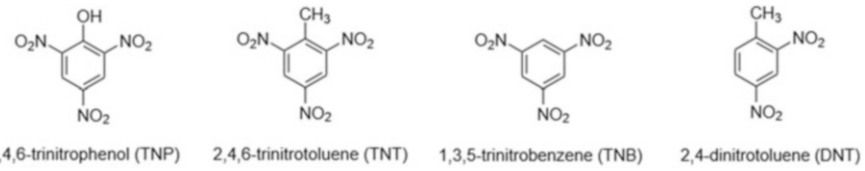

Fig. 42 Detected explosives in the study [269] show distinct structural similarity

Office on Drugs and Crime (UNODC) state that illicit drug abuse is still on the rise [270]. Counteractions need to be taken by societies and countries to tackle that increasing problem. A crucial step here is of course the detection of illegal substances of abuse. Thompson and coworkers [37] developed a piezoelectric aptasensor to detect cocaine. According to UNODC, cocaine production and distribution has significantly increased in 2022 [270]. In their work, Thompson's group applied the electromagnetic piezoelectric acoustic sensor (EMPAS), a device developed by the group [271], to establish an ultra-high-frequency acoustic wave aptasensor. They used 20 MHz AT-cut quartz disks and functionalized them with a S-(11-tri-chlorosilyl-undecanyl)-benzenethiosulfonate (BTS) adlayer. To selectively entrap cocaine, the cocaine-binding DNA aptamer, MN4, was immobilized on the BTS adlayer. Other than the QCM, the EMPAS uses an external electromagnetic field to excite the quartz resonator to resonance. There, the quartz disk is placed with a minimal gap (approx. 30 μm) above a coil-capacitor circuit in a flow cell. The coil generates secondary electric fields which propagate through space and excite the quartz disk to resonance. This technique allows the user to measure at much higher frequencies (i.e., 860 MHz; 43rd harmonic) compared to the conventional QCM, and, thus, to achieve increased analytical sensitivity. This allowed the group to reach a very low LOD of 0.9 μM when measuring cocaine samples in PBS buffer. Saturation was found to be at around 100 μM. Adding urea allowed for releasing the analyte from the aptamer without destroying it, making repeated analyses possible. In a follow-up study, researchers of the same group exchanged the aptamer MN4 with the structure-switching cocaine aptamer MN6 [272]. This allowed them to achieve an LOD of 0.3 μM. They explained this increased analytical performance by the ability of the EMPAS system to detect the structural rearrangement of the MN6 aptamer upon cocaine binding.

Several sensing systems for the detection of illicit drugs using MIP layers as receptor elements have been reported [273]. Similar to explosives' detection, most of them rely on optical or electrochemical transducing strategies. However, few studies with piezoelectric transducers exist. For example, Guerra et al. developed a piezoelectric sensing system for detecting methamphetamine based on MIPs [274]. They used in situ polymerization to synthesize the bulk-imprinted MIP directly on the QCM gold surface. The MIP consisted of itaconic acid and hydroxyethyl methacrylate monomers cross-linked with ethylene glycol dimethacrylate. With their approach, Guerra and coworkers could measure methamphetamine in a concentration range of 1–40 μg/mL and postulated a detection limit of 1 μg/mL.

5 Conclusion and Outlook

Whereas the number of mass-sensitive transducer types has been comparably low, vastly differing receptor strategies are in the literature. Most of those make use of self-organization in one way or another: either they interact with a specific target analyte (class) in an optimized manner or synthesis includes self-organization steps –

usually directed by a template – at some point. Despite being researched for at least two to three decades by now, they still receive very substantial attention in both academia and applied research. Nonetheless, a second focus of research increasingly gathers attention: the body of literature aiming at actually integrating biomimetic sensing tools into production processes of devices slowly but steadily increases. For mass-sensitive sensing, this means increasing focus on device techniques that are compatible with lithographic production of integrated sensor systems, such as FBARs. From the measuring side of things, commercialized chemosensors of course still strongly rely on electrochemical or electrical transduction, because those require only straightforward measuring techniques. However, many mass-sensitive devices yield frequency as the output signal, which is also straightforward to measure and integrate into data processing strategies. Hence, biomimetics have been proving their potential in research and continue doing so. Thoroughly assessing sensing layer's long-term stability and developing viable strategies to compensate for variations in ambient conditions are key steps toward implementing biomimetic mass-sensitive devices in real-life applications.

The next few decades will see if they deliver on their promise on a commercial basis: that, of course, depends not only on technology but also market needs and viabilities of the devices designed.

References

1. Mujahid A, Dickert FL (2017) Surface acousticwave (SAW) for chemical sensing applications of recognition layers. Sensors 17:1–26. https://doi.org/10.3390/s17122716
2. Uludağ Y, Piletsky SA, Turner APF, Cooper MA (2007) Piezoelectric sensors based on molecular imprinted polymers for detection of low molecular mass analytes. FEBS J 274: 5471–5480. https://doi.org/10.1111/j.1742-4658.2007.06079.x
3. Mujahid A, Afzal A, Dickert FL (2019) An overview of high frequency acoustic – QCMs, SAWs and FBARs – chemical and biochemical applications. Sensors 19:4395
4. Sauerbrey G (1959) Verwendung von Schwingquarzen zur Wägung dünner Schichten und zur Mikrowägung. Z Phys 155:206–222. https://doi.org/10.1007/BF01337937
5. Keiji Kanazawa K, Gordon JG (1985) The oscillation frequency of a quartz resonator in contact with liquid. Anal Chim Acta 175:99–105. https://doi.org/10.1016/S0003-2670(00)82721-X
6. Chen Q, Xu S, Liu Q et al (2016) QCM-D study of nanoparticle interactions. Adv Colloid Interface Sci 233:94–114
7. Lieberzeit PA, Glanznig G, Jenik M et al (2005) Soft lithography in chemical sensing – analytes from molecules to cells. Sensors 5:509–518. https://doi.org/10.3390/s5120509
8. Zhang Y, Luo J, Flewitt AJ et al (2018) Film bulk acoustic resonators (FBARs) as biosensors: a review. Biosens Bioelectron 116:1–15. https://doi.org/10.1016/j.bios.2018.05.028
9. Rayleigh L (1885) On waves propagated along the plane surface of an elastic solid. Proc Lond Math Soc s1–17:4–11. https://doi.org/10.1112/plms/s1-17.1.4
10. Voiculescu I, Nordin AN (2012) Acoustic wave based MEMS devices, development and applications. In: Islam N (ed) Microelectromechanical systems and devices. InTech
11. Lieberzeit PA, Dickert FL (2008) Rapid bioanalysis with chemical sensors: novel strategies for devices and artificial recognition membranes. Anal Bioanal Chem 391:1629–1639. https://doi.org/10.1007/s00216-008-1909-z

12. Yoo EH, Lee SY (2010) Glucose biosensors: an overview of use in clinical practice. Sensors 10:4558–4576. https://doi.org/10.3390/s100504558
13. Nihira T, Mori T, Asakura M, Okahata Y (2011) Kinetic studies of dextransucrase enzyme reactions on a substrate- or enzyme-immobilized 27 MHz quartz crystal microbalance. Langmuir 27:2107–2111. https://doi.org/10.1021/la104550m
14. Yağmuroğlu O, Diltemiz SE (2020) Development of QCM based biosensor for the selective and sensitive detection of paraoxon. Anal Biochem 591. https://doi.org/10.1016/j.ab.2019.113572
15. Li D, Wang J, Wang R et al (2011) A nanobeads amplified QCM immunosensor for the detection of avian influenza virus H5N1. Biosens Bioelectron 26:4146–4154. https://doi.org/10.1016/j.bios.2011.04.010
16. Chu X, Zhao ZL, Shen GL, Yu RQ (2006) Quartz crystal microbalance immunoassay with dendritic amplification using colloidal gold immunocomplex. Sens Actuators B 114:696–704. https://doi.org/10.1016/j.snb.2005.06.014
17. Afzal A, Mujahid A, Schirhagl R et al (2017) Gravimetric viral diagnostics: QCM based biosensors for early detection of viruses. Chemosensors 5:1–25. https://doi.org/10.3390/chemosensors5010007
18. Kim YK, Lim SI, Cho YY et al (2014) Detection of H3N2 canine influenza virus using a quartz crystal microbalance. J Virol Methods 208:16–20. https://doi.org/10.1016/j.jviromet.2014.07.022
19. Persaud KC (2012) Biomimetic olfactory sensors. IEEE Sens J 12:3108–3112. https://doi.org/10.1109/JSEN.2012.2214118
20. Chen KS, Chen SC, Lin HR et al (2007) A novel technique to immobilize DNA on surface of a quartz crystal microbalance by plasma treatment and graft polymerization. Mater Sci Eng C 27:716–724. https://doi.org/10.1016/j.msec.2006.07.004
21. Jordan MD, Challiss RAJ (2011) Expression of insect olfactory receptors for biosensing on SAW sensors. Procedia Comput Sci 7:281–282. https://doi.org/10.1016/j.procs.2011.09.044
22. Pavan S, Berti F (2012) Short peptides as biosensor transducers. Anal Bioanal Chem 402:3055–3070. https://doi.org/10.1007/s00216-011-5589-8
23. Wasilewski T, Szulczyński B, Kamysz W et al (2018) Evaluation of three peptide immobilization techniques on a qcm surface related to acetaldehyde responses in the gas phase. Sensors 18:1–15. https://doi.org/10.3390/s18113942
24. Panigrahi S, Sankaran S, Mallik S et al (2012) Olfactory receptor-based polypeptide sensor for acetic acid VOC detection. Mater Sci Eng C 32:1307–1313. https://doi.org/10.1016/j.msec.2011.11.003
25. Lu HH, Rao YK, Wu TZ, Tzeng YM (2009) Direct characterization and quantification of volatile organic compounds by piezoelectric module chips sensor. Sens Actuators B 137:741–746. https://doi.org/10.1016/j.snb.2009.01.060
26. Tseng MC, Chang YP, Chu YH (2007) Quantitative measurements of vancomycin binding to self-assembled peptide monolayers on chips by quartz crystal microbalance. Anal Biochem 371:1–9. https://doi.org/10.1016/j.ab.2007.08.035
27. Hussain M, Wackerlig J, Lieberzeit PA (2013) Biomimetic strategies for sensing biological species. Biosensors 3:89–107. https://doi.org/10.3390/bios3010089
28. Giamblanco N, Conoci S, Russo D, Marletta G (2015) Single-step label-free hepatitis B virus detection by a piezoelectric biosensor. RSC Adv 5:38152–38158. https://doi.org/10.1039/c5ra03467a
29. Skládal P, Dos Santos RC, Yamanaka H, Da Costa PI (2004) Piezoelectric biosensors for real-time monitoring of hybridization and detection of hepatitis C virus. J Virol Methods 117:145–151. https://doi.org/10.1016/j.jviromet.2004.01.005
30. Dell'Atti D, Zavaglia M, Tombelli S et al (2007) Development of combined DNA-based piezoelectric biosensors for the simultaneous detection and genotyping of high risk human papilloma virus strains. Clin Chim Acta 383:140–146. https://doi.org/10.1016/j.cca.2007.05.009

31. Chen SH, Chuang YC, Lu YC et al (2009) A method of layer-by-layer gold nanoparticle hybridization in a quartz crystal microbalance DNA sensing system used to detect dengue virus. Nanotechnology 20. https://doi.org/10.1088/0957-4484/20/21/215501
32. Wang R, Wang L, Callaway ZT et al (2017) A nanowell-based QCM aptasensor for rapid and sensitive detection of avian influenza virus. Sens Actuators B 240:934–940. https://doi.org/10.1016/j.snb.2016.09.067
33. Brockman L, Wang R, Lum J, Li Y (2013) QCM Aptasensor for rapid and specific detection of avian influenza virus. Open J Appl Biosens 02:97–103. https://doi.org/10.4236/ojab.2013.24013
34. Xu L, Wang R, Kelso LC et al (2016) A target-responsive and size-dependent hydrogel aptasensor embedded with QD fluorescent reporters for rapid detection of avian influenza virus H5N1. Sens Actuators B 234:98–108. https://doi.org/10.1016/j.snb.2016.04.156
35. Tian Y, Zhu P, Chen Y et al (2021) Piezoelectric aptasensor with gold nanoparticle amplification for the label-free detection of okadaic acid. Sens Actuators B 346:130446. https://doi.org/10.1016/j.snb.2021.130446
36. Yuan M, Zhang Q, Song Z et al (2019) Piezoelectric arsenite aptasensor based on the use of a self-assembled mercaptoethylamine monolayer and gold nanoparticles. Microchim Acta 186. https://doi.org/10.1007/s00604-019-3373-1
37. Neves MAD, Blaszykowski C, Bokhari S, Thompson M (2015) Ultra-high frequency piezoelectric aptasensor for the label-free detection of cocaine. Biosens Bioelectron 72:383–392. https://doi.org/10.1016/j.bios.2015.05.038
38. Wyszynski B, Somboon P, Nakamoto T (2008) Mixed self-assembled lipopolymers with spacer lipids enhancing sensitivity of lipid-derivative QCMs for odor sensors. Sens Actuators B 134:72–78. https://doi.org/10.1016/j.snb.2008.04.015
39. Wyszynski B, Nakamoto T (2009) Linking biological and artificial olfaction: biomimetic quartz crystal microbalance odor sensors. IEEJ Trans Electr Electron Eng 4:334–338. https://doi.org/10.1002/tee.20414
40. Lieberzeit P, Greibl W, Jenik M et al (2007) Cavities generated by self-organised monolayers as sensitive coatings for surface acoustic wave resonators. Anal Bioanal Chem 387:561–566. https://doi.org/10.1007/s00216-006-0978-0
41. Wangchareansak T, Sangma C, Ngernmeesri P et al (2013) Self-assembled glucosamine monolayers as biomimetic receptors for detecting WGA lectin and influenza virus with a quartz crystal microbalance. Anal Bioanal Chem 405:6471–6478. https://doi.org/10.1007/s00216-013-7057-0
42. Novoselov KS, Geim AK, Morozov SV et al (2004) Electric field in atomically thin carbon films. Science 306:666–669. https://doi.org/10.1126/SCIENCE.1102896/SUPPL_FILE/NOVOSELOV.SOM.PDF
43. Bai Y, Sun L, Yu Q et al (2022) Biomolecule capturing and sensing on 2D transition metal dichalcogenide canvas. Nano Res Energy. https://doi.org/10.26599/nre.2023.9120043
44. Donarelli M, Ottaviano L (2018) 2d materials for gas sensing applications: a review on graphene oxide, mos2, ws2 and phosphorene. Sensors 18. https://doi.org/10.3390/s18113638
45. Cao J, Chen Q, Wang X et al (2021) Review article recent development of gas sensing platforms based on 2D atomic crystals. https://doi.org/10.34133/2021/9863038
46. Wang B, Gu Y, Chen L et al (2022) Gas sensing devices based on two-dimensional materials: a review. Nanotechnology 33. https://doi.org/10.1088/1361-6528/ac5df5
47. Sulleiro MV, Dominguez-Alfaro A, Alegret N et al (2022) 2D materials towards sensing technology: from fundamentals to applications. Sens Bio-Sensing Res 38. https://doi.org/10.1016/j.sbsr.2022.100540
48. Chang C, Chen W, Chen Y et al (2021) Recent progress on two-dimensional materials. Acta Phys Chim Sin 37:1–151. https://doi.org/10.3866/PKU.WHXB202108017
49. Li D, Zhang W, Yu X et al (2016) When biomolecules meet graphene: from molecular level interactions to material design and applications. Nanoscale 8:19491–19509

50. Van Quang V, Hung VN, Tuan LA et al (2014) Graphene-coated quartz crystal microbalance for detection of volatile organic compounds at room temperature. Thin Solid Films 568:6–12. https://doi.org/10.1016/j.tsf.2014.07.036
51. Lv C, Hu C, Luo J et al (2019) Recent advances in graphene-based humidity sensors. Nanomaterials 9
52. Fauzi F, Rianjanu A, Santoso I, Triyana K (2021) Gas and humidity sensing with quartz crystal microbalance (QCM) coated with graphene-based materials – a mini review. Sensors Actuators A Phys 330:112837
53. Guo S, Garaj S, Bianco A, Ménard-Moyon C (2022) Controlling covalent chemistry on graphene oxide. Nat Rev Phys 4:247–262
54. Yang M, He J (2016) Graphene oxide as quartz crystal microbalance sensing layers for detection of formaldehyde. Sens Actuators B 228:486–490. https://doi.org/10.1016/j.snb.2016.01.046
55. Yao Y, Chen X, Guo H, Wu Z (2011) Graphene oxide thin film coated quartz crystal microbalance for humidity detection. Appl Surf Sci 257:7778–7782. https://doi.org/10.1016/j.apsusc.2011.04.028
56. Ho CY, Wu YS (2020) Diamine decorated graphene oxide film on quartz crystal microbalance for humidity-sensing analysis. Appl Surf Sci 510. https://doi.org/10.1016/j.apsusc.2020.145257
57. Zhang X, Teng SY, Loy ACM et al (2020) Transition metal dichalcogenides for the application of pollution reduction: a review. Nanomaterials 10:1012. https://doi.org/10.3390/NANO10061012
58. Coogan Á, Gun'Ko YK (2021) Solution-based "bottom-up" synthesis of group VI transition metal dichalcogenides and their applications. Mater Adv 2:146–164. https://doi.org/10.1039/d0ma00697a
59. Filipovic L, Selberherr S (2021) Gas sensing with two-dimensional materials beyond graphene. IEEE. https://doi.org/10.1109/MIEL52794.2021.9569088
60. Alev O, Özdemir O, Goldenberg E et al (2022) WS2 thin film based quartz crystal microbalance gas sensor for dimethyl methylphosphonate detection at room temperature. Thin Solid Films 745:2–9. https://doi.org/10.1016/j.tsf.2022.139097
61. Wang D, Guo J, Wang Z et al (2022) Two-dimensional MoS 2 for resonant-gravimetric detection of ppb-level formaldehyde. Cite This Anal Chem 2022:18050–18058. https://doi.org/10.1021/acs.analchem.2c04532
62. Sanyal G, Lakshmy S, Vaidyanathan A et al (2022) Detection of nitrobenzene in pristine and metal decorated 2D dichalcogenide VSe2: perspectives from density functional theory. Surf Interfaces 29. https://doi.org/10.1016/j.surfin.2022.101816
63. Naguib M, Kurtoglu M, Presser V et al (2011) Two-dimensional nanocrystals produced by exfoliation of Ti 3AlC 2. Adv Mater 23:4248–4253. https://doi.org/10.1002/adma.201102306
64. Anasori B, Xie Y, Beidaghi M et al (2015) Two-dimensional, ordered, double transition metals carbides (MXenes). ACS Nano 9:9507–9516. https://doi.org/10.1021/acsnano.5b03591
65. Hajian S, Maddipatla D, Narakathu BB, Atashbar MZ (2022) MXene-based flexible sensors: a review. Front Sens 3:32. https://doi.org/10.3389/fsens.2022.1006749
66. Li Q, Li Y, Zeng W (2021) Preparation and application of 2D MXene-based gas sensors: a review. https://doi.org/10.3390/chemosensors9080225
67. Li R, Fan Y, Ma Z et al (2021) Controllable preparation of ultrathin MXene nanosheets and their excellent QCM humidity sensing properties enhanced by fluoride doping. Microchim Acta 188:1–11. https://doi.org/10.1007/s00604-021-04723-2
68. Li J, Wang X, Zhao G et al (2018) Metal-organic framework-based materials: superior adsorbents for the capture of toxic and radioactive metal ions. Chem Soc Rev 47:2322–2356
69. Gargiulo V, Alfè M, Giordano L, Lettieri S (2022) Materials for chemical sensing: a comprehensive review on the recent advances and outlook using ionic liquids, metal–organic frameworks (MOFs), and MOF-based composites. Chemosensors 10

70. Schneemann A, Henke S, Schwedler I, Fischer RA (2014) Targeted manipulation of metal-organic frameworks to direct sorption properties. ChemPhysChem 15:823–839
71. Uehara H, Diring S, Furukawa S et al (2011) Porous coordination polymer hybrid device with quartz oscillator: effect of crystal size on sorption kinetics. J Am Chem Soc 133:11932–11935. https://doi.org/10.1021/ja205082p
72. Liu B, Shekhah O, Arslan HK et al (2012) Metal-organic frameworks enantiopure metal-organic framework thin films: oriented SURMOF growth and enantioselective adsorption. Angew Chem Int Ed 51:807–810. https://doi.org/10.1002/anie.201104240
73. Paschke B, Wixforth A, Denysenko D, Volkmer D (2017) Fast surface acoustic wave-based sensors to investigate the kinetics of gas uptake in ultra-microporous frameworks. ACS Sens 2: 740–747. https://doi.org/10.1021/acssensors.7b00014
74. Haghighi E, Zeinali S (2019) Nanoporous MIL-101(Cr) as a sensing layer coated on a quartz crystal microbalance (QCM) nanosensor to detect volatile organic compounds (VOCs). RSC Adv 9:24460–24470. https://doi.org/10.1039/c9ra04152d
75. Wu M, Ma Z, Fan Y et al (2022) Materials design, sensing performance and mechanism of anhydrous hydrogen fluoride gas sensor based on amino-functionalized MIL-101(Cr) for new energy vehicles. Coatings 12. https://doi.org/10.3390/coatings12020260
76. Qi P, Zhang T, Shao J et al (2019) A QCM humidity sensor constructed by graphene quantum dots and chitosan composites. Sens Actuators A Phys 287:93–101. https://doi.org/10.1016/j.sna.2019.01.009
77. Chen W, Wang Z, Gu S et al (2020) Hydrophobic amino-functionalized graphene oxide nanocomposite for aldehydes detection in fish fillets. Sens Actuators B 306. https://doi.org/10.1016/j.snb.2019.127579
78. Zhou Q, Zhu L, Zheng C, Wang J (2021) Nanoporous functionalized WS2/MWCNTs nanocomposite for trimethylamine detection based on quartz crystal microbalance gas sensor. ACS Appl Mater Interfaces 13:41339–41350. https://doi.org/10.1021/acsami.1c12213
79. Wang JL, Shang JH, Guo YJ et al (2021) Hydrophobic metal organic framework for enhancing performance of acoustic wave formaldehyde sensor based on polyethyleneimine and bacterial cellulose nanofilms. J Mater Sci Mater Electron 32:18551–18564. https://doi.org/10.1007/s10854-021-06241-6
80. Refaat D, Aggour MG, Farghali AA et al (2019) Strategies for molecular imprinting and the evolution of MIP nanoparticles as plastic antibodies – synthesis and applications. Int J Mol Sci 20. https://doi.org/10.3390/ijms20246304
81. Altintas Z, Abdin MJ, Tothill AM et al (2016) Ultrasensitive detection of endotoxins using computationally designed nanoMIPs. Anal Chim Acta 935:239–248. https://doi.org/10.1016/j.aca.2016.06.013
82. Sudjarwo WAA, Dobler MT, Lieberzeit PA (2022) QCM-based assay designs for human serum albumin. Anal Bioanal Chem 414:731–741. https://doi.org/10.1007/s00216-021-03771-0
83. Beyazit S, Tse Sum Bui B, Haupt K, Gonzato C (2016) Molecularly imprinted polymer nanomaterials and nanocomposites by controlled/living radical polymerization. Prog Polym Sci 62:1–21. https://doi.org/10.1016/j.progpolymsci.2016.04.001
84. Wackerlig J, Lieberzeit PA (2016) Polymers, molecularly imprinted. Ullmann's Encycl Ind Chem:1–20. https://doi.org/10.1002/14356007.q21_q01
85. Cowen T, Cheffena M (2022) Template imprinting versus porogen imprinting of small molecules: a review of molecularly imprinted polymers in gas sensing. Int J Mol Sci 23. https://doi.org/10.3390/ijms23179642
86. Kadhem AJ, Gentile GJ, de Cortalezzi MMF (2021) Molecularly imprinted polymers (Mips) in sensors for environmental and biomedical applications: a review
87. Arreguin-Campos R, Jiménez-Monroy KL, Diliën H et al (2021) Imprinted polymers as synthetic receptors in sensors for food safety. Biosensors 11. https://doi.org/10.3390/BIOS11020046

88. Unger C, Lieberzeit PA (2021) Molecularly imprinted thin film surfaces in sensing: chances and challenges. React Funct Polym 161:104855. https://doi.org/10.1016/j.reactfunctpolym.2021.104855
89. Cui F, Zhou Z, Zhou HS (2020) Molecularly imprinted polymers and surface imprinted polymers based electrochemical biosensor for infectious diseases. Sensors 20. https://doi.org/10.3390/s20040996
90. He Y, Lin Z (2022) Recent advances in protein-imprinted polymers: synthesis, applications and challenges. J Mater Chem B 10:6571–6589. https://doi.org/10.1039/d2tb00273f
91. Braunecker WA, Matyjaszewski K (2007) Controlled/living radical polymerization: features, developments, and perspectives. Prog Polym Sci 32:93–146. https://doi.org/10.1016/j.progpolymsci.2006.11.002
92. Orowitz TE, Sombo PPAAA, Rahayu D, Hasanah AN (2020) Microsphere polymers in molecular imprinting: current and future perspectives. Molecules 25. https://doi.org/10.3390/molecules25143256
93. Matyjaszewski K, Xia J (2001) Atom transfer radical polymerization. Chem Rev 101:2921–2990. https://doi.org/10.1002/9783527809080.cataz01278
94. Ramakers G, Wackers G, Trouillet V et al (2019) Laser-grafted molecularly imprinted polymers for the detection of histamine from organocatalyzed atom transfer radical polymerization. Macromolecules 52:2304–2313. https://doi.org/10.1021/acs.macromol.8b02339
95. Suda N, Sunayama H, Kitayama Y et al (2017) Oriented, molecularly imprinted cavities with dual binding sites for highly sensitive and selective recognition of cortisol. R Soc Open Sci 4. https://doi.org/10.1098/rsos.170300
96. Horikawa R, Sunayama H, Kitayama Y et al (2016) A programmable signaling molecular recognition nanocavity prepared by molecular imprinting and post-imprinting modifications. Angew Chem Int Ed 55:13023–13027. https://doi.org/10.1002/anie.201605992
97. Sasaki S, Ooya T, Kitayama Y, Takeuchi T (2015) Molecularly imprinted protein recognition thin films constructed by controlled/living radical polymerization. J Biosci Bioeng 119:200–205. https://doi.org/10.1016/j.jbiosc.2014.06.019
98. Chiefari J, Chong YK, Ercole F et al (1998) Living free-radical polymerization by reversible addition – fragmentation chain transfer: the RAFT process. Macromolecules 31:5559–5562. https://doi.org/10.1021/ma9804951
99. Tian X, Ding J, Zhang B et al (2018) Recent advances in RAFT polymerization: novel initiation mechanisms and optoelectronic applications. Polymers (Basel) 10. https://doi.org/10.3390/polym10030318
100. Barner-Kowollik C, Perrier S (2008) The future of reversible addition fragmentation chain transfer polymerization. J Polym Sci Part A Polym Chem 46:5715–5723. https://doi.org/10.1002/pola
101. Yildirim E, Caykara T (2018) Ibuprofen-imprinted ultrathin poly[N-(2-hydroxypropyl) methacrylamide] films. J Appl Polym Sci 135:1–7. https://doi.org/10.1002/app.45707
102. Wang Y, Jiao SQ, Chen XL, Wei TX (2017) An efficient grafting technique for producing molecularly imprinted film: via reversible addition-fragmentation chain transfer polymerization. Anal Methods 9:5356–5364. https://doi.org/10.1039/c7ay01623a
103. Crapnell RD, Hudson A, Foster CW et al (2019) Recent advances in electrosynthesized molecularly imprinted polymer sensing platforms for bioanalyte detection. Sensors 19. https://doi.org/10.3390/s19051204
104. Erdössy J, Horváth V, Yarman A et al (2016) Electrosynthesized molecularly imprinted polymers for protein recognition. Trends Anal Chem 79:179–190. https://doi.org/10.1016/j.trac.2015.12.018
105. Peng L, Yarman A, Jetzschmann KJ et al (2016) Molecularly imprinted electropolymer for a hexameric heme protein with direct electron transfer and peroxide electrocatalysis. Sensors 16. https://doi.org/10.3390/s16030272

106. Dechtrirat D, Gajovic-Eichelmann N, Bier FF, Scheller FW (2014) Hybrid material for protein sensing based on electrosynthesized MIP on a mannose terminated self-assembled monolayer. Adv Funct Mater 24:2233–2239. https://doi.org/10.1002/adfm.201303148
107. Peng Y, Wu Z, Liu Z (2014) An electrochemical sensor for paracetamol based on an electropolymerized molecularly imprinted o-phenylenediamine film on a multi-walled carbon nanotube modified glassy carbon electrode. Anal Methods 6:5673–5681. https://doi.org/10.1039/c4ay00753k
108. Ayankojo AG, Reut J, Ciocan V et al (2020) Molecularly imprinted polymer-based sensor for electrochemical detection of erythromycin. Talanta 209:120502. https://doi.org/10.1016/j.talanta.2019.120502
109. Jetzschmann KJ, Tank S, Jágerszki G et al (2019) Bio-electrosynthesis of vectorially imprinted polymer nanofilms for cytochrome P450cam. ChemElectroChem:1818–1823. https://doi.org/10.1002/celc.201801851
110. Dabrowski M, Zimińska A, Kalecki J et al (2019) Facile fabrication of surface-imprinted macroporous films for chemosensing of human chorionic gonadotropin hormone. ACS Appl Mater Interfaces 11:9265–9276. https://doi.org/10.1021/acsami.8b17951
111. El Sharif HF, Dennison SR, Tully M et al (2022) Evaluation of electropolymerized molecularly imprinted polymers (E-MIPs) on disposable electrodes for detection of SARS-CoV-2 in saliva. Anal Chim Acta 1206:339777. https://doi.org/10.1016/j.aca.2022.339777
112. Tokonami S, Nakadoi Y, Takahashi M et al (2013) Label-free and selective bacteria detection using a film with transferred bacterial configuration. Anal Chem 85:4925–4929. https://doi.org/10.1021/ac3034618
113. Chen S, Chen X, Zhang L et al (2017) Electrochemiluminescence detection of Escherichia coli O157:H7 based on a novel polydopamine surface imprinted polymer biosensor. ACS Appl Mater Interfaces 9:5430–5436. https://doi.org/10.1021/acsami.6b12455
114. Ait Lahcen A, Arduini F, Lista F, Amine A (2018) Label-free electrochemical sensor based on spore-imprinted polymer for Bacillus cereus spore detection. Sens Actuators B 276:114–120. https://doi.org/10.1016/j.snb.2018.08.031
115. Afzal A, Feroz S, Iqbal N et al (2016) A collaborative effect of imprinted polymers and Au nanoparticles on bioanalogous detection of organic vapors. Sens Actuators B 231:431–439. https://doi.org/10.1016/j.snb.2016.03.050
116. Chen L, Wang X, Lu W et al (2016) Molecular imprinting: perspectives and applications. Chem Soc Rev 45:2137–2211. https://doi.org/10.1039/c6cs00061d
117. Belbruno JJ (2019) Molecularly imprinted polymers. Chem Rev 119:94–119. https://doi.org/10.1021/acs.chemrev.8b00171
118. Wang L, Zhi K, Zhang Y et al (2019) Molecularly imprinted polymers for gossypol via sol-gel, bulk, and surface layer imprinting – a comparative study. Polymers (Basel) 11. https://doi.org/10.3390/polym11040602
119. Park JY (2016) Effect of lithographically designed structures on the caffeine sensing properties of surface imprinted films. Analyst 141:5709–5713. https://doi.org/10.1039/c6an01665k
120. Yongabi D, Khorshid M, Losada-Pérez P et al (2018) Cell detection by surface imprinted polymers SIPs: a study to unravel the recognition mechanisms. Sens Actuators B 255:907–917. https://doi.org/10.1016/j.snb.2017.08.122
121. Ding X, Heiden PA (2014) Recent developments in molecularly imprinted nanoparticles by surface imprinting techniques. Macromol Mater Eng 299:268–282. https://doi.org/10.1002/mame.201300160
122. Bompart M, De Wilde Y, Haupt K (2010) Chemical nanosensors based on composite molecularly imprinted polymer particles and surface-enhanced Raman scattering. Adv Mater 22:2343–2348. https://doi.org/10.1002/adma.200904442
123. Turner NW, Jeans CW, Brain KR et al (2006) From 3D to 2D: a review of the molecular imprinting of proteins. Biotechnol Prog 22:1474–1489. https://doi.org/10.1002/bp060122g

124. Mujahid A, Iqbal N, Afzal A (2013) Bioimprinting strategies: from soft lithography to biomimetic sensors and beyond. Biotechnol Adv 31:1435–1447. https://doi.org/10.1016/j.biotechadv.2013.06.008
125. Eersels K, Lieberzeit P, Wagner P (2016) A review on synthetic receptors for bioparticle detection created by surface-imprinting techniques – from principles to applications. ACS Sensors 1:1171–1187. https://doi.org/10.1021/acssensors.6b00572
126. Dong C, Shi H, Han Y et al (2021) Molecularly imprinted polymers by the surface imprinting technique. Eur Polym J 145:110231. https://doi.org/10.1016/j.eurpolymj.2020.110231
127. Alexander C, Vulfson EN (1997) Spatially functionalized polymer surfaces produced via cell-mediated lithography. Adv Mater 9:751–755. https://doi.org/10.1002/adma.19970090916
128. Shen X, Svensson Bonde J, Kamra T et al (2014) Bacterial imprinting at Pickering emulsion interfaces. Angew Chem Int Ed 53:10687–10690. https://doi.org/10.1002/anie.201406049
129. Pickering SU (1907) Emulsions. J Chem Soc Trans:2001–2021
130. Dupont H, Maingret V, Schmitt V, Héroguez V (2021) New insights into the formulation and polymerization of Pickering emulsions stabilized by natural organic particles. Macromolecules 54:4945–4970. https://doi.org/10.1021/acs.macromol.1c00225
131. Hayden O, Dickert FL (2001) Selective microorganism detection with cell surface imprinted polymers. Adv Mater 13:1480–1483. https://doi.org/10.1002/1521-4095(200110)13:19<1480::AID-ADMA1480>3.0.CO;2-V
132. Hayden O, Lieberzeit PA, Blaas D, Dickert FL (2006) Artificial antibodies for bioanalyte detection – sensing viruses and proteins. Adv Funct Mater 16:1269–1278. https://doi.org/10.1002/ADFM.200500626
133. Chunta S, Suedee R, Lieberzeit PA (2016) Low-density lipoprotein sensor based on molecularly imprinted polymer. Anal Chem 88:1419–1425. https://doi.org/10.1021/acs.analchem.5b04091
134. Chunta S, Boonsriwong W, Wattanasin P et al (2021) Direct assessment of very-low-density lipoprotein by mass sensitive sensor with molecularly imprinted polymers. Talanta 221:121549. https://doi.org/10.1016/j.talanta.2020.121549
135. Latif U, Can S, Sussitz HF, Dickert FL (2020) Molecular imprinted based quartz crystal microbalance sensors for bacteria and spores. Chemosensors 8:1–11. https://doi.org/10.3390/CHEMOSENSORS8030064
136. Hayden O, Bindeus R, Dickert FL (2003) Combining atomic force microscope and quartz crystal microbalance studies for cell detection. Meas Sci Technol 14:1876–1881. https://doi.org/10.1088/0957-0233/14/11/004
137. Jenik M, Seifner A, Lieberzeit P, Dickert FL (2009) Pollen-imprinted polyurethanes for QCM allergen sensors. Anal Bioanal Chem 394:523–528. https://doi.org/10.1007/s00216-009-2718-8
138. Hayden O, Mann KJ, Krassnig S, Dickert FL (2006) Biomimetic ABO blood-group typing. Angew Chem Int Ed 45:2626–2629. https://doi.org/10.1002/anie.200502857
139. Eersels K, Van Grinsven B, Ethirajan A et al (2013) Selective identification of macrophages and cancer cells based on thermal transport through surface-imprinted polymer layers. ACS Appl Mater Interfaces 5:7258–7267. https://doi.org/10.1021/am401605d
140. Cornelis P, Givanoudi S, Yongabi D et al (2019) Sensitive and specific detection of E. coli using biomimetic receptors in combination with a modified heat-transfer method. Biosens Bioelectron 136:97–105. https://doi.org/10.1016/j.bios.2019.04.026
141. Stilman W, Yongabi D, Bakhshi Sichani S et al (2021) Detection of yeast strains by combining surface-imprinted polymers with impedance-based readout. Sens Actuators B 340:129917. https://doi.org/10.1016/j.snb.2021.129917
142. Rachkov A, Minoura N (2001) Towards molecularly imprinted polymers selective to peptides and proteins. The epitope approach. Biochim Biophys Acta Protein Struct Mol Enzymol 1544:255–266. https://doi.org/10.1016/S0167-4838(00)00226-0

143. Khumsap T, Corpuz A, Nguyen LT (2021) Epitope-imprinted polymers: applications in protein recognition and separation. RSC Adv 11:11403–11414. https://doi.org/10.1039/d0ra10742e
144. Teixeira SPB, Reis RL, Peppas NA et al (2021) Epitope-imprinted polymers: design principles of synthetic binding partners for natural biomacromolecules. Sci Adv 7. https://doi.org/10.1126/sciadv.abi9884
145. Dietl S, Sobek H, Mizaikoff B (2021) Epitope-imprinted polymers for biomacromolecules: recent strategies, future challenges and selected applications. Trends Anal Chem 143:116414. https://doi.org/10.1016/j.trac.2021.116414
146. Takeuchi T, Sunayama H (2018) Beyond natural antibodies-a new generation of synthetic antibodies created by post-imprinting modification of molecularly imprinted polymers. Chem Commun 54:6243–6251. https://doi.org/10.1039/c8cc02923g
147. Moczko E, Poma A, Guerreiro A et al (2013) Surface-modified multifunctional MIP nanoparticles. Nanoscale 5:3733–3741. https://doi.org/10.1039/c3nr00354j
148. Canfarotta F, Poma A, Guerreiro A, Piletsky S (2016) Solid-phase synthesis of molecularly imprinted nanoparticles. Nat Protoc 11:443–455. https://doi.org/10.1038/nprot.2016.030
149. Renkecz T, Horvath V (2017) Preparation of molecularly imprinted microspheres by precipitation polymerization. Methods Mol Biol 1575:341–352. https://doi.org/10.1007/978-1-4939-6857-2_21
150. Bonham JA, Faers MA, Van Duijneveldt JS (2014) Non-aqueous microgel particles: synthesis, properties and applications. Soft Matter 10:9384–9398. https://doi.org/10.1039/c4sm01834f
151. Lovell PA, Schork FJ (2020) Fundamentals of emulsion polymerization. Biomacromolecules 21:4396–4441. https://doi.org/10.1021/acs.biomac.0c00769
152. Asua JM (2002) Miniemulsion polymerization. Prog Polym Sci 27:1283–1346. https://doi.org/10.1016/S0079-6700(02)00010-2
153. Zeng Z, Hoshino Y, Rodriguez A et al (2010) Synthetic polymer nanoparticles with antibody-like affinity for a hydrophilic peptide. ACS Nano 4:199–204. https://doi.org/10.1021/nn901256s
154. Wackerlig J, Schirhagl R (2016) Applications of molecularly imprinted polymer nanoparticles and their advances toward industrial use: a review. Anal Chem 88:250–261. https://doi.org/10.1021/acs.analchem.5b03804
155. Werner M, Glück MS, Bräuer B et al (2022) Investigations on sub-structures within cavities of surface imprinted polymers using AFM and PF-QNM†. Soft Matter 18:2245–2251. https://doi.org/10.1039/d2sm00137c
156. Orowitz TE, Sombo PPAAA, Rahayu D, Hasanah AN (2020) Microsphere polymers in molecular imprinting: current and future perspectives. Molecules 25
157. Zhang R, Gao R, Gou Q et al (2022) Precipitation polymerization: a powerful tool for preparation of uniform polymer particles. Polymers (Basel) 14. https://doi.org/10.3390/polym14091851
158. Shim SE, Yang S, Jin MJ et al (2004) Effect of the polymerization parameters on the morphology and spherical particle size of poly(styrene-co-divinylbenzene) prepared by precipitation polymerization. Colloid Polym Sci 283:41–48. https://doi.org/10.1007/s00396-004-1086-3
159. Jiang M, Shi Y, Zhang RL et al (2009) Selective molecularly imprinted stationary phases for bisphenol A analysis prepared by modified precipitation polymerization. J Sep Sci 32:3265A–3273A. https://doi.org/10.1002/jssc.200900207
160. Medina-Castillo AL (2020) Thermodynamic principles of precipitation polymerization and role of fractal nanostructures in the particle size control. Macromolecules 53:5687–5700. https://doi.org/10.1021/acs.macromol.0c00973
161. Rostamizadeh K, Abdollahi H, Parsajoo C (2013) Synthesis, optimization, and characterization of molecularly imprinted nanoparticles. Int Nano Lett 3. https://doi.org/10.1186/2228-5326-3-20

162. Bai F, Yang X, Huang W (2004) Synthesis of narrow or monodisperse poly(divinylbenzene) microspheres by distillation-precipitation polymerization. Macromolecules 37:9746–9752. https://doi.org/10.1021/ma048566l
163. Ye L, Cormack PAG, Mosbach K (1999) Molecularly imprinted monodisperse microspheres for competitive radioassay. Anal Commun 36:35–38. https://doi.org/10.1039/A809014I
164. Su L, Guo X, Han S (2014) Preparation and evaluation of vanillin molecularly imprinted polymer microspheres by reversible addition-fragmentation chain transfer precipitation polymerization. Anal Methods 6:2512–2517. https://doi.org/10.1039/c3ay41892h
165. Sambe H, Hoshina K, Moaddel R et al (2006) Uniformly-sized, molecularly imprinted polymers for nicotine by precipitation polymerization. J Chromatogr A 1134:88–94. https://doi.org/10.1016/j.chroma.2006.08.073
166. Xu J, Haupt K, Tse Sum Bui B (2017) Core-shell molecularly imprinted polymer nanoparticles as synthetic antibodies in a Sandwich fluoroimmunoassay for trypsin determination in human serum. ACS Appl Mater Interfaces 9:24476–24483. https://doi.org/10.1021/acsami.7b05844
167. Capriotti A, Piovesana S, Zenezini Chiozzi R et al (2020) Does the protein corona take over the selectivity of molecularly imprinted nanoparticles? The biological challenges to recognition. J Proteomics 219:103736. https://doi.org/10.1016/j.jprot.2020.103736
168. Poma A, Turner APF, Piletsky SA (2010) Advances in the manufacture of MIP nanoparticles. Trends Biotechnol 28:629–637. https://doi.org/10.1016/j.tibtech.2010.08.006
169. Cenci L, Tatti R, Tognato R et al (2018) Synthesis and characterization of peptide-imprinted nanogels of controllable size and affinity. Eur Polym J 109:453–459. https://doi.org/10.1016/j.eurpolymj.2018.08.031
170. Özkan A, Atar N, Yola ML (2019) Enhanced surface plasmon resonance (SPR) signals based on immobilization of core-shell nanoparticles incorporated boron nitride nanosheets: development of molecularly imprinted SPR nanosensor for anticancer drug, etoposide. Biosens Bioelectron 130:293–298. https://doi.org/10.1016/j.bios.2019.01.053
171. Lin CI, Joseph AK, Chang CK, Der LY (2004) Synthesis and photoluminescence study of molecularly imprinted polymers appended onto CdSe/ZnS core-shells. Biosens Bioelectron 20:127–131. https://doi.org/10.1016/j.bios.2003.10.017
172. Shahar T, Sicron T, Mandler D (2017) Nanosphere molecularly imprinted polymers doped with gold nanoparticles for high selectivity molecular sensors. Nano Res 10:1056–1063. https://doi.org/10.1007/s12274-016-1366-5
173. Zhao C, Jia G, Lu W, Gong Q (2017) A piezoelectric magnetic molecularly imprinted surface sensor for the detection of Sudan I. J Alloys Compd 710:711–716. https://doi.org/10.1016/j.jallcom.2017.03.316
174. Munawar H, Safaryan AHM, De Girolamo A et al (2019) Determination of Fumonisin B1 in maize using molecularly imprinted polymer nanoparticles-based assay. Food Chem 298:125044. https://doi.org/10.1016/j.foodchem.2019.125044
175. Orbay S, Kocaturk O, Sanyal R, Sanyal A (2022) Molecularly imprinted polymer-coated inorganic nanoparticles: fabrication and biomedical applications. Micromachines 13:1–23. https://doi.org/10.3390/mi13091464
176. Bhogal S, Kaur K, Malik AK et al (2020) Core-shell structured molecularly imprinted materials for sensing applications. Trends Anal Chem 133:116043. https://doi.org/10.1016/j.trac.2020.116043
177. Dabrowski M, Lach P, Cieplak M, Kutner W (2018) Nanostructured molecularly imprinted polymers for protein chemosensing. Biosens Bioelectron 102:17–26. https://doi.org/10.1016/j.bios.2017.10.045
178. Garcia Y, Smolinska-Kempisty K, Pereira E et al (2017) Development of competitive 'pseudo'-ELISA assay for measurement of cocaine and its metabolites using molecularly imprinted polymer nanoparticles. Anal Methods 9:4592–4598. https://doi.org/10.1039/c7ay01523b

179. Cáceres C, Canfarotta F, Chianella I et al (2016) Does size matter? Study of performance of pseudo-ELISAs based on molecularly imprinted polymer nanoparticles prepared for analytes of different sizes. Analyst 141:1405–1412. https://doi.org/10.1039/c5an02018b
180. Haupt K, Medina Rangel PX, Bui BTS (2020) Molecularly imprinted polymers: antibody mimics for bioimaging and therapy. Chem Rev 120:9554–9582. https://doi.org/10.1021/acs.chemrev.0c00428
181. Giessibl FJ (2005) AFM's path to atomic resolution. Mater Today 8:32–41. https://doi.org/10.1016/S1369-7021(05)00844-8
182. Bräuer B, Thier F, Bittermann M et al (2022) Raman studies on surface-imprinted polymers to distinguish the polymer surface, imprints, and different bacteria. ACS Appl Bio Mater 5:160–171. https://doi.org/10.1021/acsabm.1c01020
183. Bräuer B, Werner M, Baurecht D, Lieberzeit PA (2022) Raman and scanning probe microscopy for differentiating surface imprints of E. coli and B. cereus. J Mater Chem:B6758–B6767. https://doi.org/10.1039/d2tb00283c
184. Ma J, Yan M, Feng G et al (2021) An overview on molecular imprinted polymers combined with surface-enhanced Raman spectroscopy chemical sensors toward analytical applications. Talanta 225:122031. https://doi.org/10.1016/j.talanta.2020.122031
185. De Middeleer G, Dubruel P, De Saeger S (2016) Characterization of MIP and MIP functionalized surfaces: current state-of-the-art. Trends Anal Chem 76:71–85. https://doi.org/10.1016/j.trac.2015.11.007
186. Pietrzyk A, Suriyanarayanan S, Kutner W et al (2010) Molecularly imprinted polymer (MIP) based piezoelectric microgravimetry chemosensor for selective determination of adenine. Biosens Bioelectron 25:2522–2529. https://doi.org/10.1016/j.bios.2010.04.015
187. Turco A, Corvaglia S, Mazzotta E (2015) Electrochemical sensor for sulfadimethoxine based on molecularly imprinted polypyrrole: study of imprinting parameters. Biosens Bioelectron 63:240–247. https://doi.org/10.1016/j.bios.2014.07.045
188. Pernites RB, Ponnapati RR, Advincula RC (2010) Surface plasmon resonance (SPR) detection of theophylline via electropolymerized molecularly imprinted polythiophenes. Macromolecules 43:9724–9735. https://doi.org/10.1021/ma101868y
189. Song R, Hu X, Guan P et al (2016) Surface modification of imprinted polymer microspheres with ultrathin hydrophilic shells to improve selective recognition of glutathione in aqueous media. Mater Sci Eng C 60:1–6. https://doi.org/10.1016/j.msec.2015.11.018
190. Smolinska-Kempisty K, Guerreiro A, Canfarotta F et al (2016) A comparison of the performance of molecularly imprinted polymer nanoparticles for small molecule targets and antibodies in the ELISA format. Sci Rep 6:1–7. https://doi.org/10.1038/srep37638
191. Cai J, Yan Y, Wang W et al (2021) Detection of formic acid and acetic acid gases by a QCM sensor coated with an acidified multi-walled carbon nanotube membrane. https://doi-org.uaccess.univie.ac.at. https://doi.org/10.1080/09593330.2021.1983025
192. Ogimoto Y, Selyanchyn R, Takahara N et al (2015) Detection of ammonia in human breath using quartz crystal microbalance sensors with functionalized mesoporous SiO 2 nanoparticle films. Sens Actuators B 215:428–436. https://doi.org/10.1016/j.snb.2015.03.103
193. Jayawardena S, Siriwardena HD, Rajapakse RMG et al (2019) Fabrication of a quartz crystal microbalance sensor based on graphene oxide/TiO 2 composite for the detection of chemical vapors at room temperature. https://doi.org/10.1016/j.apsusc.2019.06.280
194. Chen W, Wang Z, Gu S, Wang J (2019) Detection of hexanal in humid circumstances using hydrophobic molecularly imprinted polymers composite. Sens Actuators B 291:141–147. https://doi.org/10.1016/j.snb.2019.04.065
195. Liu C, Wyszynski B, Yatabe R et al (2017) Molecularly imprinted sol-gel-based QCM sensor arrays for the detection and recognition of volatile aldehydes. Sensors 17:1–15. https://doi.org/10.3390/s17020382
196. Dejous C, Hallil H, Raimbault V et al (2016) Love acousticwave-based devices and molecularly-imprinted polymers as versatile sensors for electronic nose or tongue for cancer monitoring. Sensors 16:1–16. https://doi.org/10.3390/s16060915

197. Çiçek Ç, Yilmaz F, Özgür E et al (2016) Molecularly imprinted quartz crystal microbalance sensor (QCM) for bilirubin detection. Chemosensors 4. https://doi.org/10.3390/chemosensors4040021
198. Hianik T, Ostatná V, Zajacová Z et al (2004) Detection of aptamer-protein interactions using QCM and electrochemical indicator methods. https://doi.org/10.1016/j.bmcl.2004.10.083
199. Zhang Z, Liu S, Shi Y et al (2014) Label-free aptamer biosensor for thrombin detection on a nanocomposite of graphene and plasma polymerized allylamine. J Mater Chem B 2:1530–1538. https://doi.org/10.1039/c3tb21464h
200. Tretjakov A, Syritski V, Reut J et al (2016) Molecularly imprinted polymer film interfaced with surface acoustic wave technology as a sensing platform for label-free protein detection. Anal Chim Acta 902:182–188. https://doi.org/10.1016/j.aca.2015.11.004
201. Chunta S, Suedee R, Boonsriwong W, Lieberzeit PA (2020) Biomimetic sensors targeting oxidized-low-density lipoprotein with molecularly imprinted polymers. Anal Chim Acta 1116: 27–35. https://doi.org/10.1016/j.aca.2020.04.017
202. Liu S, Zhou D, Guo T (2013) Construction of a novel macroporous imprinted biosensor based on quartz crystal microbalance for ribonuclease A detection. Biosens Bioelectron 42:80–86. https://doi.org/10.1016/j.bios.2012.11.002
203. Sener G, Ozgur E, Yilmaz E et al (2010) Quartz crystal microbalance based nanosensor for lysozyme detection with lysozyme imprinted nanoparticles. Biosens Bioelectron 26:815–821. https://doi.org/10.1016/j.bios.2010.06.003
204. Ma XT, He XW, Li WY, Zhang YK (2017) Epitope molecularly imprinted polymer coated quartz crystal microbalance sensor for the determination of human serum albumin. Sens Actuators B 246:879–886. https://doi.org/10.1016/j.snb.2017.02.137
205. Wangchareansak T, Thitithanyanont A, Chuakheaw D et al (2013) Influenza A virus molecularly imprinted polymers and their application in virus sub-type classification. J Mater Chem B 1:2190–2197. https://doi.org/10.1039/c3tb00027c
206. Wangchareansak T, Thitithanyanont A, Chuakheaw D et al (2014) A novel approach to identify molecular binding to the influenza virus H5N1: screening using molecularly imprinted polymers (MIPs). MedChemComm 5:617–621. https://doi.org/10.1039/c3md00272a
207. Jenik M, Schirhagl R, Schirk C et al (2009) Sensing picornaviruses using molecular imprinting techniques on a quartz crystal microbalance. Anal Chem 81:5320–5326. https://doi.org/10.1021/ac8019569
208. Tai D-F, Lin C-Y, Wu T-Z, Chen L-K (2005) Recognition of dengue virus protein using epitope-mediated molecularly imprinted film. Anal Chem. https://doi.org/10.1021/ac0504060
209. Buensuceso CE, Tiu BDB, Lee LP et al (2022) Electropolymerized-molecularly imprinted polymers (E-MIPS) as sensing elements for the detection of dengue infection. Anal Bioanal Chem 414:1347–1357. https://doi.org/10.1007/s00216-021-03757-y
210. Lu C-H, Zhang Y, Tang S-F et al (2012) Sensing HIV related protein using epitope imprinted hydrophilic polymer coated quartz crystal microbalance. Biosens Bioelectron 31:439–444. https://doi.org/10.1016/j.bios.2011.11.008
211. Matsuguchi M, Uno T (2006) Molecular imprinting strategy for solvent molecules and its application for QCM-based VOC vapor sensing. Sens Actuators B 113:94–99. https://doi.org/10.1016/j.snb.2005.02.028
212. Dickert FL, Lieberzeit P, Miarecka SG et al (2004) Synthetic receptors for chemical sensors – subnano- and micrometre patterning by imprinting techniques. Biosens Bioelectron 20:1040–1044. https://doi.org/10.1016/j.bios.2004.07.011
213. Dickert FL, Lieberzeit PA, Achatz P et al (2004) QCM array for on-line-monitoring of composting procedures. Analyst 129:432–437. https://doi.org/10.1039/b315356h
214. Lieberzeit PA, Dickert FL (2007) Sensor technology and its application in environmental analysis. Anal Bioanal Chem 387:237–247. https://doi.org/10.1007/s00216-006-0926-z
215. Iglesias RA, Tsow F, Wang R et al (2009) Hybrid separation and detection device for analysis of benzene, toluene, ethylbenzene, and xylenes in complex samples. Anal Chem 81:8930–8935. https://doi.org/10.1021/ac9015769

216. Stanley S, Percival CJ, Auer M et al (2003) Detection of polycyclic aromatic hydrocarbons using quartz crystal microbalances. Anal Chem 75:1573–1577. https://doi.org/10.1021/ac0257546
217. Lieberzeit PA, Halikias K, Afzal A, Dickert FL (2008) Polymers imprinted with PAH mixtures-comparing fluorescence and QCM sensors. Anal Bioanal Chem 392:1405–1410. https://doi.org/10.1007/s00216-008-2413-1
218. Torad NL, Kim J, Kim M et al (2021) Nanoarchitectured porous carbons derived from ZIFs toward highly sensitive and selective QCM sensor for hazardous aromatic vapors. J Hazard Mater 405:304–3894. https://doi.org/10.1016/j.jhazmat.2020.124248
219. Kim K-J, Ellis JE, Howard BH, Ohodnicki PR (2021) Centimeter-scale pillared-layer metal–organic framework thin films mediated by hydroxy double salt intermediates for CO 2 sensor applications. Cite This ACS Appl Mater Interfaces 13. https://doi.org/10.1021/acsami.0c19621
220. Devkota J, Greve DW, Hong T et al (2020) An 860 MHz wireless surface acoustic wave sensor with a metal-organic framework sensing layer for CO2 and CH4. IEEE Sens J 20:9740–9747. https://doi.org/10.1109/JSEN.2020.2990997
221. Wong D, Abuzalat O, Mostafa S et al (2020) Intense pulsed light-based synthesis of hybrid TiO 2-SnO 2 /MWCNT doped Cu-BTC for room temperature ammonia sensing †. J Mater Chem C 8:7567. https://doi.org/10.1039/d0tc00762e
222. Sabri YM, Kandjani AE, Ippolito SJ, Bhargava SK (2015) Nanosphere monolayer on a transducer for enhanced detection of gaseous heavy metal. https://doi.org/10.1021/am507069z
223. Sun P, Chen Y, Yan M, Tang T (2020) Enhancement of QCM detection for heavy metal ions based on TGA modified CdTe nanospheres. 30:525–531. https://doi.org/10.1007/s10904-019-01212-1
224. Li DM, Li SQ, Huang JY et al (2021) A recyclable bipyridine-containing covalent organic framework-based QCM sensor for detection of Hg(II) ion in aqueous solution. J Solid State Chem 302. https://doi.org/10.1016/j.jssc.2021.122421
225. Tokuyama H, Kitamura E, Seida Y (2019) Development of zirconia nanoparticle-loaded hydrogel for arsenic adsorption and sensing. https://doi.org/10.1016/j.reactfunctpolym.2019.104427
226. Mazouz Z, Rahali S, Fourati N et al (2017) Highly selective polypyrrole MIP-based gravimetric and electrochemical sensors for picomolar detection of glyphosate. Sensors 17:1–15. https://doi.org/10.3390/s17112586
227. Kadirsoy S, Atar N, Yola ML (2020) Molecularly imprinted QCM sensor based on delaminated MXene for chlorpyrifos detection and QCM sensor validation. New J Chem 44:6524–6532. https://doi.org/10.1039/d0nj00951b
228. Gao N, Dong J, Liu M et al (2012) Development of molecularly imprinted polymer films used for detection of profenofos based on a quartz crystal microbalance sensor. Analyst 137:1252–1258. https://doi.org/10.1039/c2an16120f
229. Prasad BB, Jauhari D (2015) A dual-template biomimetic molecularly imprinted dendrimer-based piezoelectric sensor for ultratrace analysis of organochlorine pesticides. Sens Actuators B 207:542–551. https://doi.org/10.1016/j.snb.2014.10.115
230. Özkütük EB, Diltemiz SE, Özalp E et al (2013) Paraoxon imprinted biopolymer based QCM sensor. Mater Chem Phys 139:107–112. https://doi.org/10.1016/j.matchemphys.2012.12.068
231. Özkütük EB, Diltemiz SE, Özalp E et al (2013) Silan based paraoxon memories onto QCM electrodes. J Ind Eng Chem 19:1788–1792. https://doi.org/10.1016/j.jiec.2013.02.021
232. Yaqub S, Latif U, Dickert FL (2011) Plastic antibodies as chemical sensor material for atrazine detection. Sens Actuators B 160:227–233. https://doi.org/10.1016/j.snb.2011.07.039
233. Latif U, Qian J, Can S, Dickert FL (2014) Biomimetic receptors for bioanalyte detection by quartz crystal microbalances – from molecules to cells. Sensors 14:23419–23438. https://doi.org/10.3390/s141223419
234. Spieker E, Lieberzeit PA (2016) Molecular imprinting studies for developing QCM-sensors for bacillus cereus. Procedia Eng 168:561–564. https://doi.org/10.1016/j.proeng.2016.11.525

235. Lian Y, He F, Wang H, Tong F (2015) A new aptamer/graphene interdigitated gold electrode piezoelectric sensor for rapid and specific detection of Staphylococcus aureus. Biosens Bioelectron 65:314–319. https://doi.org/10.1016/j.bios.2014.10.017
236. Shaheen A, Taj A, Liberzeit PA et al (2020) Design of heterostructured hybrids comprising ultrathin 2D bismuth tungstate nanosheets reinforced by chloramphenicol imprinted polymers used as biomimetic interfaces for mass-sensitive detection. Colloids Surf B Biointerfaces 188: 110775. https://doi.org/10.1016/j.colsurfb.2020.110775
237. Ayankojo AG, Reut J, Boroznjak R et al (2018) Molecularly imprinted poly(meta-phenylenediamine) based QCM sensor for detecting amoxicillin. Sens Actuators B 258: 766–774. https://doi.org/10.1016/j.snb.2017.11.194
238. Haghdoust S, Arshad U, Mujahid A et al (2021) Development of a MIP-based QCM sensor for selective detection of penicillins in aqueous media. Chemosensors 9. https://doi.org/10.3390/chemosensors9120362
239. Bereli N, Çimen D, Hüseynli S, Denizli A (2020) Detection of amoxicillin residues in egg extract with a molecularly imprinted polymer on gold microchip using surface plasmon resonance and quartz crystal microbalance methods. J Food Sci 85:4152–4160. https://doi.org/10.1111/1750-3841.15529
240. Eslami MR, Alizadeh N (2016) Nanostructured conducting molecularly imprinted polypyrrole based quartz crystal microbalance sensor for naproxen determination and its electrochemical impedance study. RSC Adv 6:9387–9395. https://doi.org/10.1039/c5ra21489k
241. Pei X, Tandon A, Alldrick A et al (2011) The China melamine milk scandal and its implications for food safety regulation. Food Policy 36:412–420. https://doi.org/10.1016/j.foodpol.2011.03.008
242. Zeilinger M, Sussitz H, Cuypers W et al (2019) Mass-sensitive sensing of melamine in dairy products with molecularly imprinted polymers: matrix challenges. Sensors 19. https://doi.org/10.3390/s19102366
243. Cakir O, Bakhshpour M, Yilmaz F, Baysal Z (2019) Novel QCM and SPR sensors based on molecular imprinting for highly sensitive and selective detection of 2,4-dichlorophenoxyacetic acid in apple samples. Mater Sci Eng C 102:483–491. https://doi.org/10.1016/j.msec.2019.04.056
244. Garabrant DH, Philbert MA (2002) Review of 2,4-dichlorophenoxyacetic acid (2,4-D) epidemiology and toxicology. Crit Rev Toxicol 32:233–257. https://doi.org/10.1080/20024091064237
245. Dayal H, Ng WY, Lin XH, Li SFY (2019) Development of a hydrophilic molecularly imprinted polymer for the detection of hydrophilic targets using quartz crystal microbalance. Sens Actuators B 300:127044. https://doi.org/10.1016/j.snb.2019.127044
246. Fang G, Yang Y, Zhu H et al (2017) Development and application of molecularly imprinted quartz crystal microbalance sensor for rapid detection of metolcarb in foods. Sens Actuators B 251:720–728. https://doi.org/10.1016/j.snb.2017.05.094
247. Wang Y, Zhang C, Wang J, Knopp D (2022) Recent progress in rapid determination of mycotoxins based on emerging biorecognition molecules: a review. Toxins (Basel) 14. https://doi.org/10.3390/toxins14020073
248. Fang G, Wang H, Yang Y et al (2016) Development and application of a quartz crystal microbalance sensor based on molecularly imprinted sol-gel polymer for rapid detection of patulin in foods. Sens Actuators B 237:239–246. https://doi.org/10.1016/j.snb.2016.06.099
249. Fang G, Liu G, Yang Y, Wang S (2016) Quartz crystal microbalance sensor based on molecularly imprinted polymer membrane and three-dimensional Au nanoparticles@mesoporous carbon CMK-3 functional composite for ultrasensitive and specific determination of citrinin. Sens Actuators B 230:272–280. https://doi.org/10.1016/j.snb.2016.02.053
250. Gu Y, Wang Y, Wu X et al (2019) Quartz crystal microbalance sensor based on covalent organic framework composite and molecularly imprinted polymer of poly(o-aminothiophenol)

with gold nanoparticles for the determination of aflatoxin B1. Sens Actuators B 291:293–297. https://doi.org/10.1016/j.snb.2019.04.092
251. Bräuer B, Unger C, Werner M, Lieberzeit PA (2021) Biomimetic sensors to detect bioanalytes in real-life samples using molecularly imprinted polymers: a review. Sensors 21. https://doi.org/10.3390/s21165550
252. Karaseva N, Ermolaeva T, Mizaikoff B (2016) Piezoelectric sensors using molecularly imprinted nanospheres for the detection of antibiotics. Sens Actuators B 225:199–208. https://doi.org/10.1016/j.snb.2015.11.045
253. Pan M, Li R, Xu L et al (2018) Reproducible molecularly imprinted piezoelectric sensor for accurate and sensitive detection of ractopamine in swine and feed products. Sensors 18. https://doi.org/10.3390/s18061870
254. Neethirajan S, Ahmed SR, Chand R et al (2017) Recent advances in biosensor development for foodborne virus detection. Nanotheranostics 1:272–295. https://doi.org/10.7150/ntno.20301
255. Babaei A, Rafiee N, Taheri B et al (2022) Recent advances in early diagnosis of viruses associated with gastroenteritis by biosensors. Biosensors 12. https://doi.org/10.3390/bios12070499
256. Luo L, Zhang F, Chen C, Cai C (2019) Visual simultaneous detection of hepatitis A and B viruses based on a multifunctional molecularly imprinted fluorescence sensor. Anal Chem 91:15748–15756. https://doi.org/10.1021/acs.analchem.9b04001
257. Devane ML, Moriarty E, Weaver L et al (2020) Fecal indicator bacteria from environmental sources; strategies for identification to improve water quality monitoring. Water Res 185:116204. https://doi.org/10.1016/j.watres.2020.116204
258. Sadiq SM, Hazen TH, Rasko DA, Eppinger M (2014) EHEC genomics: past, present, and future. Microbiol Spectr 2:55–71. https://doi.org/10.1128/microbiolspec.ehec-0020-2013
259. Spagnolo S, De La Franier B, Davoudian K et al (2022) Detection of E. Coli bacteria in Milk by an acoustic wave aptasensor with an anti-fouling coating. Sensors 22. https://doi.org/10.3390/s22051853
260. De La Franier B, Jankowski A, Thompson M (2017) Functionalizable self-assembled trichlorosilyl-based monolayer for application in biosensor technology. Appl Surf Sci 414:435–441. https://doi.org/10.1016/j.apsusc.2017.04.111
261. Yadav AK, Verma D, Dalal N et al (2022) Molecularly imprinted polymer-based nanodiagnostics for clinically pertinent bacteria and virus detection for future pandemics. Biosens Bioelectron X 12:100257. https://doi.org/10.1016/j.biosx.2022.100257
262. Mujahid A, Mustafa G, Dickert FL (2018) Label-free bioanalyte detection from nanometer to micrometer dimensions-molecular imprinting and QCMs. Biosensors 8:1–21. https://doi.org/10.3390/bios8020052
263. Yilmaz E, Majidi D, Ozgur E, Denizli A (2015) Whole cell imprinting based Escherichia coli sensors: a study for SPR and QCM. Sens Actuators B 209:714–721. https://doi.org/10.1016/j.snb.2014.12.032
264. Yu X, Chen F, Wang R, Li Y (2018) Whole-bacterium SELEX of DNA aptamers for rapid detection of E. coli O157:H7 using a QCM sensor. J Biotechnol 266:39–49. https://doi.org/10.1016/j.jbiotec.2017.12.011
265. Ali AA, Altemimi AB, Alhelfi N, Ibrahim SA (2020) Application of biosensors for detection of pathogenic food bacteria: a review. Biosensors 10
266. Karadurmus L, Bilge S, Sınağ A, Ozkan SA (2022) Molecularly imprinted polymer (MIP)-based sensing for detection of explosives: current perspectives and future applications. Trends Anal Chem 155. https://doi.org/10.1016/j.trac.2022.116694
267. Tomita Y, Ho MH, Guilbault GG (1979) Detection of explosives with a coated piezoelectric quartz crystal. Anal Chem 51:1475–1478. https://doi.org/10.1021/ac50045a027
268. Bunte G, Hürttlen J, Pontius H et al (2007) Gas phase detection of explosives such as 2,4,6-trinitrotoluene by molecularly imprinted polymers. Anal Chim Acta 591:49–56. https://doi.org/10.1016/j.aca.2007.02.014

269. Huynh TP, Sosnowska M, Sobczak JW et al (2013) Simultaneous chronoamperometry and piezoelectric microgravimetry determination of nitroaromatic explosives using molecularly imprinted thiophene polymers. Anal Chem 85:8361–8368. https://doi.org/10.1021/ac4017677
270. United Nations office on Drugs and Crime (2022) World Drug Report 2022. United Nations
271. Ballantyne SM, Thompson M (2004) Superior analytical sensitivity of electromagnetic excitation compared to contact electrode instigation of transverse acoustic waves. Analyst 129: 219–224. https://doi.org/10.1039/b313314c
272. Neves MAD, Blaszykowski C, Thompson M (2016) Utilizing a key aptamer structure-switching mechanism for the ultrahigh frequency detection of cocaine. Anal Chem 88:3098–3106. https://doi.org/10.1021/acs.analchem.5b04010
273. Xiao D, Jiang Y, Bi Y (2018) Molecularly imprinted polymers for the detection of illegal drugs and additives: a review. Microchim Acta 185. https://doi.org/10.1007/s00604-018-2735-4
274. Romero Guerra M, Chianella I, Piletska EV et al (2009) Development of a piezoelectric sensor for the detection of methamphetamine. Analyst 134:1565–1570. https://doi.org/10.1039/b819351g

Applications and Recent Trends in Surface Acoustic Wave Biosensors

Najla Fourati, Ghada Attia, Sohayb Khaoulani, and Chouki Zerrouki

Contents

Abstract This chapter presents the most relevant applications of surface acoustic wave (SAW) biosensors published between 2019 and the beginning of 2023. These recent studies showed that besides quantifying several types of proteins and detecting bacteria and viruses, SAW biosensors can access cells' viscous/elastic properties and their adhesion/growth/detachment processes. Numerous functionalization methods are presented, from the most common ones, such as self-assembled layers and molecularly imprinted polymers, to sophisticated ones, such as sandwich structures incorporating doped nanoparticles (NP) or NP-decorated graphene tubes. In this chapter, we also present new trends in SAW biosensors. Two routes can be used separately or simultaneously: using new multi-layered piezoelectric materials with high coupling coefficients and/or high acoustic wave velocities and new geometries of interdigital transducers (IDTs). This chapter finally puts forward the interest of multi-transduction to access multiparametric response accurately and fully characterize analytes in complex media. It highlights

N. Fourati (✉), G. Attia, S. Khaoulani, and C. Zerrouki
Cnam, SATIE Laboratory, UMR CNRS 8029, Paris, France
e-mail: fourati@cnam.fr; ghada.attia@lecnam.net; sohayb.khaoulani@lecnam.net; zerrouki@cnam.fr

P. Lieberzeit (ed.), *Piezoelectric Sensors*, Springer Series on Chemical Sensors and Biosensors (2024) 18: 225–252, https://doi.org/10.1007/5346_2023_31,

Published online: 11 November 2023

the potential of biosensors to address different public health and to accompany the current trends toward detecting increasingly small biological entities.

Keywords SAW sensors, New piezoelectric materials, New geometries of IDTs, Surface functionalization, Proteins detection, cancer biomarkers monitoring, Neurodegenerative diseases detection, Cell-based SAW biosensors, Cell viscoelastic properties monitoring, Gravimetric–electrochemical coupling, Gravimetric–optical coupling

1 Introduction

Surface acoustic wave (SAW) devices are widely used in several applications, such as mobile and wireless communications [1], signal processing [2], and band-pass filtering [3]. The principle of SAW sensors relies on generating surface acoustic waves by metallic interdigital transducers (IDTs) patterned in thin metal films (Al, Ti/Au, or Cr/Au) on the surface of a piezoelectric material. An alternating voltage applied to the input IDT generates an electric field, leading the substrate to vibrate mechanically near its eigenfrequency due to inverse piezoelectricity. This results in a mechanical wave that propagates along (or through) the surface of the piezoelectric substrate up to the output transducers. These latter convert the mechanical signal into a measurable electrical one due to direct piezoelectricity (Fig. 1).

Due to their high sensitivity, robustness, reliability, and ability to follow up all phenomena that occur on their surfaces in real time, SAW devices have become increasingly used for biological sensing. Biosensors are investigated in several domains: medicine, healthcare, clinical services, and diagnosis of urinary tract infections (UTI), along with identifying pathogens and susceptibility to antimicrobials. The recent COVID-19 pandemic highlighted the urgent demand for analytical devices to detect the outbreak of viruses and/or diseases in real time. Nowadays,

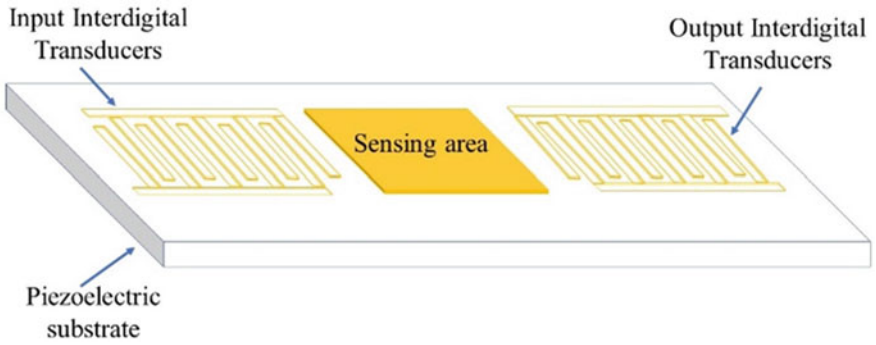

Fig. 1 Schematic representation of a SAW transducer in delay line configuration

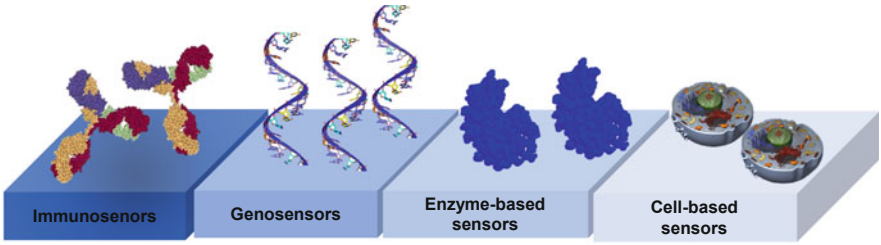

Fig. 2 Schematic representation of biological sensors

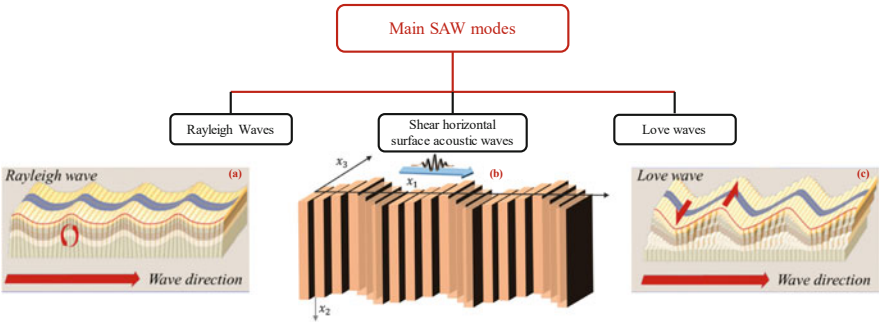

Fig. 3 Schematic representation of (**a**) Rayleigh [5], (**b**) shear horizontal [6], and (**c**) Love-mode [5] waves

medical specialists and scientists are increasingly interested in diagnosing and understanding diseases. In this context, highly sensitive and accurate SAW biosensors were designed to detect different biological entities such as proteins, cells, and nucleic acids.

In biological applications, the sensing area of the SAW devices (the zone separating the interdigital transducers) is functionalized with a selective coating (bioreceptor) that specifically (or selectively) interacts with the target of interest. Depending on the type of bioreceptor, one can distinguish four types of SAW biosensors (Fig. 2): (1) immunosensors, in which antibodies grafted on the sensing area recognize their target antigen, (2) genosensors which permit to follow up the hybridization of single DNA strands by their complementary probes anchored to the sensing area, (3) enzyme-based sensors in which the enzyme recognizes only a specific substrate and catalyzes a specific chemical reaction, and (4) cell-based sensors which permit to follow either cell's adhesion growth or viscous and elastic properties or bacteria and viruses detection [4].

Several modes of surface acoustic waves can be investigated in the design of biosensors. In this chapter, we have focused on the most commonly cited in the literature: the Rayleigh (Fig. 3a), shear horizontal SAW (Fig. 3b), and Love-mode waves (Fig. 3c).

SAW devices based on Rayleigh waves are rare despite their high sensitivity to surface perturbations. This mode generates compressional waves with a surface-normal displacement component, making them unsuitable for applications in liquid media due to their high insertion loss [7]. Shear horizontal SAW (SH-SAW)-based sensors have thus been developed to overcome this limitation. In SH-SAW mode, particle displacements take place predominantly parallel to the surface and normal to the direction of propagation. The absence of a normal displacement component allows for wave propagation in liquids without excessive loss of acoustic energy. SH-SAW sensors are thus sensitive only to events in close-surface layers with a given penetration depth δ, a factor which depends on the sensor's operating angular frequency ω, fluid viscosity η, and density ρ according to (Eq. 1):

$$\delta = \sqrt{\frac{2\,\eta}{\rho\,\omega}} \tag{1}$$

Mass sensitivity S of SAW sensors can be calculated using Eq. (2):

$$S = \lim_{\Delta m \to 0} \frac{1}{\Delta m} \times \frac{\Delta \mathrm{f}}{f_0} \tag{2}$$

where Δm is the change in mass on the SAW surface, f_0 is the operating frequency, and Δf is the frequency shifts after molecules' immobilization on the sensing area.

The perpetual quest for increasing the sensors' sensitivity has led researchers to take two routes: increasing the operating frequencies of their devices and/or designing Love-wave sensors which comprise depositing a thin layer of a dielectric material on the piezoelectric substrate. This layer acts as a wave guide and confines the acoustic energy at the sensor's surface, rendering it more sensitive to any surface perturbations.

2 Recent Applications of SAW Biosensors

This section exclusively focuses on recent and relevant applications published from 2019 to the beginning of 2023 concerning protein and cell detection.

2.1 SAW Sensors for Protein Detection

Accurate, selective, and sensitive detection of proteins has broad applicability in medical diagnosis and therapeutic monitoring. Notably, the ability of SAW-based sensors to identify biomarkers at very low concentrations paves the way for

advances in predicting, diagnosing, and prognosing severe diseases, such as cancers and cardiovascular and neurodegenerative diseases.

2.1.1 Detection of Cancer Biomarkers

Designing biosensors for monitoring the variations of cancer biomarkers in body fluids, mainly at very low levels, has an enormous promise not only for an early diagnosis (before tumor growth) but also for following up the prognosis and monitoring of responses to treatment [8, 9]. Several SAW-based sensors were thus designed to detect cancer biomarkers selectively. The most recent applications concern the detection of:

(i) Carcinoembryonic antigen (CEA), a non-specific serum biomarker whose concentration is elevated in various malignancies such as breast, lung, liver, pancreatic, and stomach cancer [10]
(ii) Cancer antigen 125 (CA125) to target ovarian cancer [14]
(iii) Alpha-fetoprotein (AFP) towards hepatocellular carcinoma [13]
(iv) Epidermal growth factor (EGF) a biomarker for head, neck, and lung cancer diagnosis, prognosis, and prediction of treatment response to platinum-based chemotherapy [16]
(v) The matrix metalloproteinase-8 (MMP-8) detected in various cancers [11]
(vi) Antigen transferrin receptor (CD71) highly expressed in nearly all tumor types including metastatic ones [19].

Many studies have reported the design and use of SAW sensors for CEA detection. Li et al. [12] designed a 196 MHz Love-mode sensor in which a 1 μm SiO_2 wave-guiding layer was deposited on an ST-cut quartz substrate. CEA antibodies were first incubated on the sensing area for 12 h, prior to immersion in a solution of bovine serum albumin (BSA)/0.1% PBS for 90 min. Gold nanoparticles–antibody conjugates containing the anti-CEA antibodies were then added. The designed immunosensor showed a logarithmic sensor characteristic with CEA concentration in the range of 0.2–5 ng/mL; the limit of detection (LOD) was equal to 0.2 ng/mL.

Jandas et al. [13] designed a 120 MHz SAW sensor on ST-cut quartz which was functionalized by incubating first the device in 5 mM thioglycolic acid for 12 h, and then by activating the acid groups with the couple N-ethyl-N-(3-dimethylamino) propyl carbodiimide/N-hydroxysuccinimide (EDC/NHS, 1:1 in volume ratio) during 3 h. 100 g/mL anti-CEA was then incubated at 4°C for 12 h and CEA detection was investigated in the concentration range of 0.1–30 ng/mL. The LOD of the sensor was equal to 0.31 ng/mL. In this study, the bioreceptor was regenerated by running a buffer of 0.8 M HCl, 0.06 M KCl, and 0.06 M glycine for half an hour over its surface. The designed biosensor was tested for real-time detection of CEA in 12 human sera. The obtained results were in good agreement with those obtained from ELISA tests. The same team investigated two other functionalization strategies to detect CEA. One relied on the use of AuNP–MoS_2-rGO nano-cluster doped

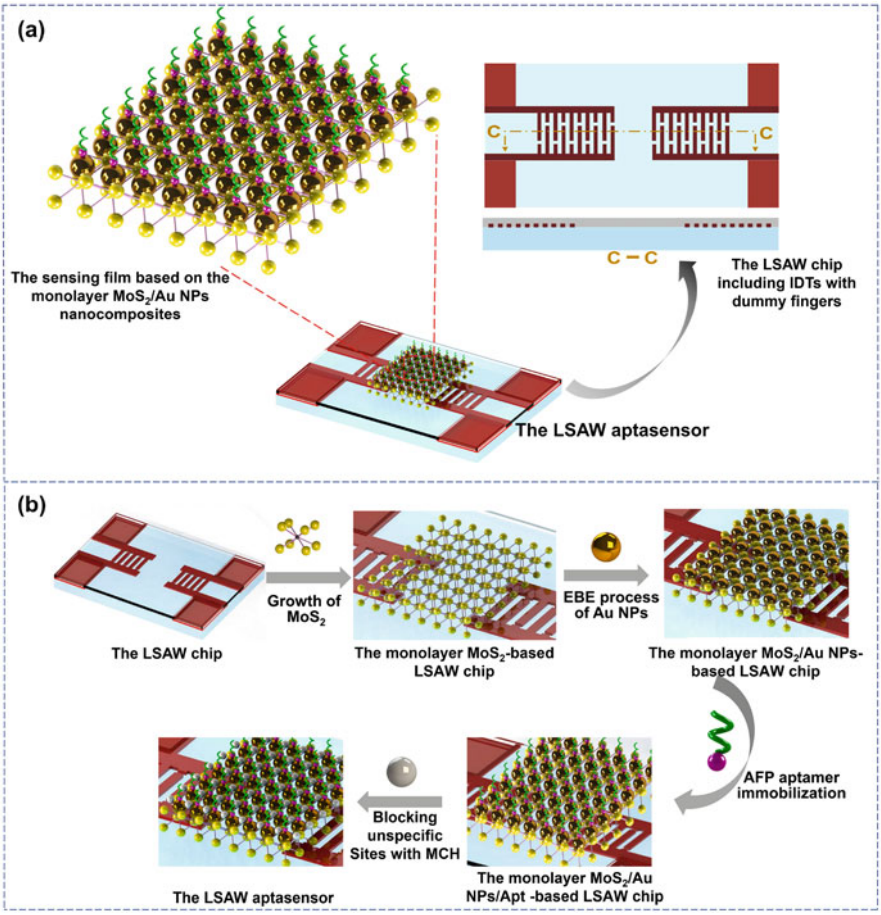

Fig. 4 Schematic illustration of (**a**) the Love-mode (LSAW) apta-sensor. (**b**) The functionalization steps [16]

polyimide [14], while the second investigated Ti_3C_2Tx MXene-Au nanoparticles doped polyimide [15]. The corresponding LODs of the designed sensors were of order 0.084 ng/mL and 0.001 ng/mL, respectively. Both sensors were tested in real samples, and the results were in good agreement with those issued by ELISA.

The detection of alpha-fetoprotein (AFP) with classical immunosensors encountered several difficulties because of low sensitivity, time-consuming operation, and instability of antibodies [16]. Wang et al. [16] designed a 237.5 MHz Love-mode apta-sensor (ST-90° X cut quartz piezoelectric substrate coated with 1.5 μm thick SiO_2 guiding layer) with dummy MoS2/Au NPs fingers for AFP detection in the serum. A schematic representation of the SAW and the functionalization strategy is depicted in Fig. 4. The proposed apta-sensor detected AFP in serum in the

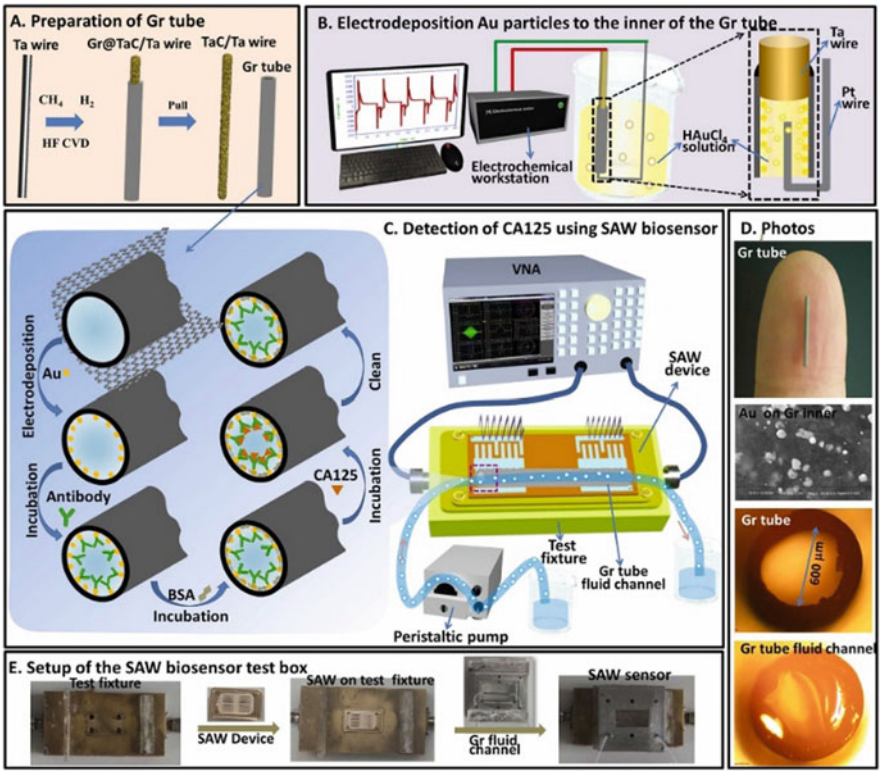

Fig. 5 (**a**) Schematic illustration of the preparation for the graphene tubes; (**b**) schematic illustration of the electrodeposition of AuNPs in the inner Gr tube's wall; (**c**) schematic illustration of CA125 detection with the SAW sensor; (**d**) photos of the Gr tubes; and E. SAW sensor setup [17]

concentration range 0.01 ng/mL–100 ng/mL. The LOD of the designed sensors was equal to 4.79 pg/mL.

Zhao et al. [17] proposed a 203.5 MHz Rayleigh SAW immunosensor functionalized with gold-nanoparticles-decorated graphene (AuNPs-Gr) for CA125 detection. The authors used tiny volumes for the Gr tubes (4.8 μL) and positioned the AuNPs-Gr tubes on the bus bar, which is slightly off the middle of the waves propagation path, and not on the delay region to reduce energy damping (Fig. 5). In this study, the anti-CA125 (antibody, Ab) solution was filled into the AuNPs-Gr tubes and incubated at 37°C to bind the Ab to the AuNPs on the inner wall of the tubes. A BSA solution (0.1 wt%), prepared in PBS (0.1 M), was then introduced and incubated at the same temperature for 10 min to block the non-specific adsorption sites. The SAW immunosensor showed a wide linear response range from 0.01 to 300 mU/mL, a sensitivity of 8.57 Hz/log(mU/mL), and a calculated LOD of 0.00371 mU/mL.

Lo et al. [18] designed a 122 MHz Love-mode sensor fabricated on a 36° Y-X $LiTaO_3$ piezoelectric substrate coated with a 2 μm thick SiO_2 wave-guiding layer to

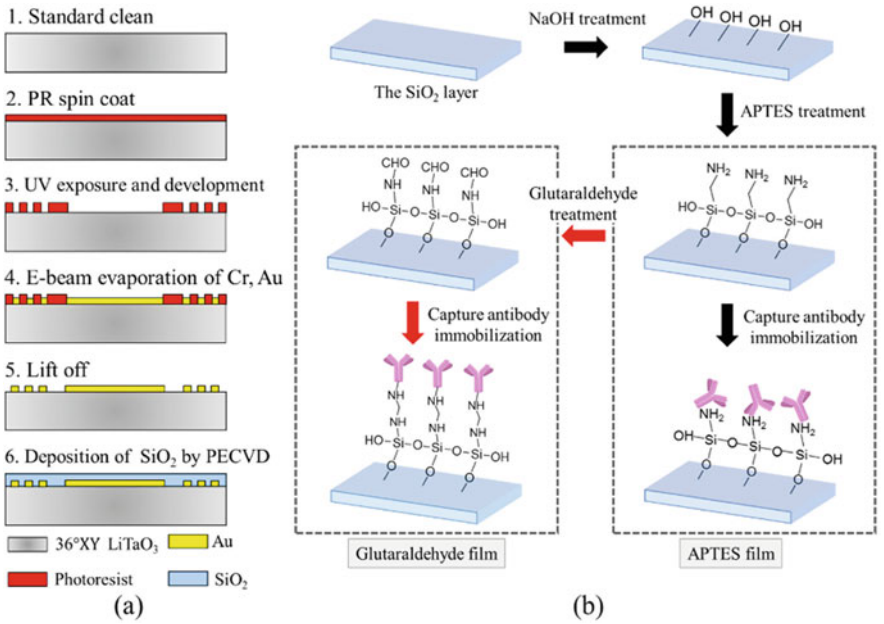

Fig. 6 (**a**) Process flow of Love-mode sensor fabrication. (**b**) Functionalization strategies involving APTES and glutaraldehyde films [18]

detect epidermal growth factor (EGF). The authors functionalized the sensing area of the devices with two types of sensing films: 3-aminopropyltriethoxysilane (APTES) and glutaraldehyde (Fig. 6). The concentration of EGF was varied from 0.2 to 5 ng/mL. Results indicated that the sensitivity of the glutaraldehyde film, 1.709 kHz/(ng/mL), is higher than that of the APTES film (0.641 kHz/(ng/mL)). This difference may be attributed to the nature of the binding between the receptor and EGF: mainly electrostatic and hydrophobic interactions in the case of APTES and covalent for the glutaraldehyde film.

A SAW biosensor to assess salivary matrix metalloproteinase-8 (MMP-8) was developed by Taylor et al. [19]. The SAW surfaces were functionalized by incubating anti-MMP-8 antibody (100 µg/mL) in PBS and blocking non-specific bindings with bovine serum albumin (BSA). MMP-8 biomarker was then detected in the 0–1,000 ng/mL range. The SAW sensor's detection limit was estimated at 62.5 ng/mL. The device was tested to detect MMP-8 in human saliva samples; the obtained results were comparable to those of an ELISA assay. The designed biosensor has two main advantages compared to ELISA: the possibility of real-time measurements and more straightforward preparation protocols. This results in reducing the analysis time from 20 to 15 min.

Lo et al. [20] designed a Love-mode biosensor (a 36°Y-X piezoelectric $LiTaO_3$ substrate coated with a 0.5 µm SiO_2 thick wave-guiding layer) to detect CD71. A

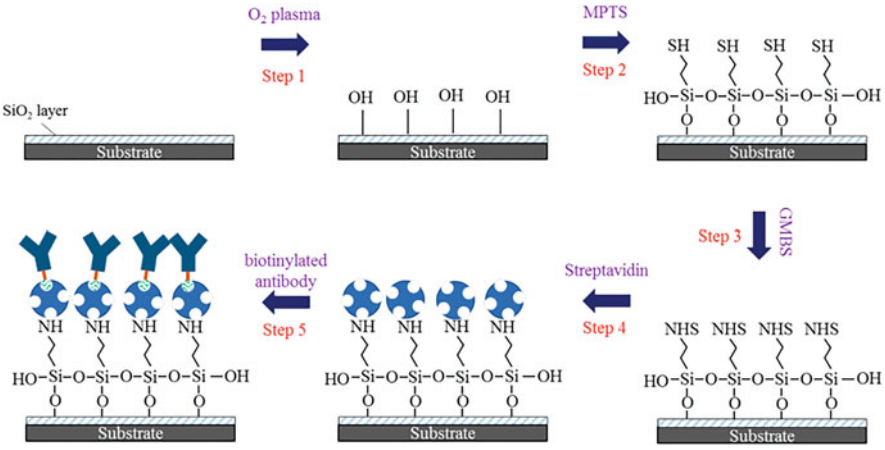

Fig. 7 Steps for the surface modification of the SiO_2 guiding layer; MPTS is 3-mercaptopropyl trimethoxysilane and GMBS is 4-maleimidobutyric acid N-hydroxysuccinimide ester [20]

schematic representation of the functionalization process is depicted in Fig. 7. The concentrations of CD71 antigen were varied from 0.66 to 4.16 μg/mL.

The sensitivity of the designed sensor was equal to 974 Hz/(μg/mL) for a biomarker concentration below 1.66 μg/mL. The authors simulated the frequency shifts with COMSOL Multiphysics® and proposed a semi-empirical model based on their experimental and numerical results, which can analyze the frequency shifts resulting from concentration of the respective sensed molecules.

2.1.2 Detection of Biomarkers of Neurodegenerative Diseases and Traumatic Brain Injury

Due to their high sensitivity, selectivity, and very low LOD values, SAW biosensors could be valuable tools for detecting and diagnosing neurodegenerative diseases at a very early stage [21] and traumatic brain injuries [22].

Kidakova et al. [23] used a pair of 147–150 MHz Love-wave sensors (ST-cut quartz substrates and a SiO_2 guiding layer) for cerebral dopamine neurotrophic factor (CDNF) protein detection. The authors immobilized the CDNF target on the SAW sensing area pre-functionalized with 4-ATP/DTSSP linker before electropolymerizing m-phenylenediamine (mPD) at a constant potential of 0.6 V (versus Ag/AgCl). To form the molecular imprints, the PmPD polymer was treated in 0.1 M ethanolic solution of 2-mercaptoethanol and then in an aqueous solution of 3 M NaCl and DMSO (Fig. 8). The MIP-based sensor shows a linear response for CDNF concentrations ranging from 5 to 50 ng/mL. The detection and quantitation limits were equal to 4.2 ng/mL and 14 ng/mL, respectively.

Agostini et al. [24] designed a ≈ 1 GHz ultra-high-frequency surface acoustic wave (UHF-SAW) for glial-fibrillary-acidic-protein (GFAP) detection in a bovine

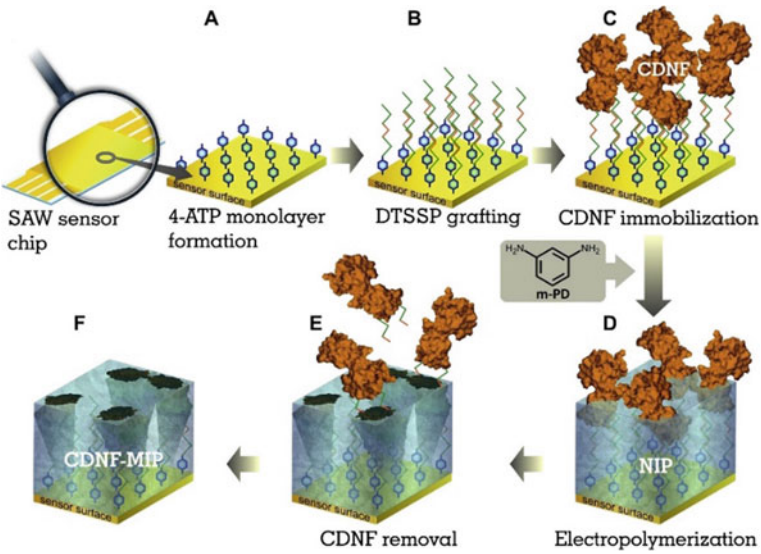

Fig. 8 The surface imprinting strategy for CDNF-MIP layer synthesis on the gold sensing area of the SAW chip [23]

serum albumin matrix. Three functionalization protocols were first tested with quartz crystal microbalance: in the first one, an antifouling polyethylene glycol (PEG) layer was exploited; protein G for antibody orientation was used in the second one; the third protocol relies on antibody-splitting to enhance surface coverage. Results indicate that the most performing route is the first one. GFAP was then detected at clinically relevant concentrations in clean buffers (superior to 23 pM) and sera matrix (35 pM).

2.1.3 Monitoring of SARS-Cov-2 Proteins

A great need for early and sensitive diagnosis analytical devices has arisen due to the COVID-19 pandemic. Despite the availability of vaccines, there is a constant requirement for sensitive and selective biosensors to detect SARS-Cov-2 through its corresponding antibodies.

Peng et al. [25] designed a 250 MHz two-channel SH-SAW biosensor on a 36°Y-cut 90°X quartz piezoelectric substrate for SARS-CoV-2 nucleocapsid antibody detection. The sensing channel was coated with 2% BSA (in double distilled water) before adding SARS-CoV-2 nucleocapsid protein (1.6 mg/mL or 0 8 mg/mL in 50 mM Tris buffer, 400 mM NaCl, and 500 mM imidazole). 2% gelatin (in PBS) or 2% casein (in PBS) was then added at pH 7.4 to reduce the non-specific adsorption of the proteins followed by a stabilizer and blowing dry the chips. Spike-in antibody samples at different concentrations (34.375 to 1,100 ng/mL) and blanks (rabbit serum) were monitored; the sensitivity of the SH-SAW biosensor was

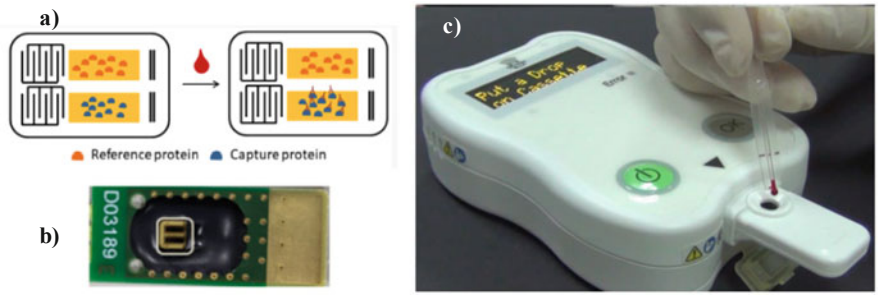

Fig. 9 (**a**) Schematic and (**b**) photograph of the dual-channel SH-SAW sensor; (**c**) photograph of the iProtin immunoassay and the SH-SAW sensor [26]

compared to that of the ELISA platform. The authors concluded that an SH-SAW sensor is more advantageous than ELISA as it (i) permits real-time measurements (about 10 min per measurement compared to at least 6 h by ELISA), (ii) is portable, which favors in situ measurements, (iii) can be used for semi-continuous measurements, and (iv) needs only small samples volumes. In addition, measurements of anti-N-specific antibodies produced by rabbit sera indicated that the SH-SAW device has better sensitivity than ELISA. Moreover, detection with significant output signal change was recorded on day 6 with the SH-SAW biosensor and on day 9 with ELISA.

Cheng et al. [26] designed a dual-channel SH-SAW biosensor coated with SARS-CoV-2 spike protein to quantify the amount of anti-SARS-CoV-2S antibodies produced after vaccination (Fig. 9). Twenty-five persons participated in the follow-up of total anti-SARS-CoV-2S protein antibodies after vaccination. Only 5 µL of finger blood and 40 s were needed to achieve the analysis. Results indicate that total anti-SARS-CoV-2S antibody concentrations spiked 10–14 days after the first vaccination and 7–9 days after the second. SH-SAW biosensors are thus powerful tools that can investigate the local prevalence of COVID-19.

2.1.4 Detection of Other Types of Proteins

Toma et al. [27] fabricated a 250 MHz SAW immunosensor on a 36Y-90X quartz substrate to detect anti-mouse (a-mIgG) antibodies. The sensitive area was modified with dithiobis(succinimidyl propionate) (DSP) to immobilize mIgG and create a sandwich assay in the presence of a-mIgG. Figure 10 depicts the functionalization, detection, and regeneration strategies.

Various concentrations (from 10 ng/mL to 10 µg/m) of a-mIgG were measured to evaluate sensitivity of the SAW immunosensor and to compare outputs to those obtained from ELISA. Results indicate that the LOD of ELISA (1.30 ng/mL) is lower by almost one order of magnitude to the SAW immunosensor (13.6 ng/mL), but the SAW measurement time (≈15 min) is substantially shorter than that of

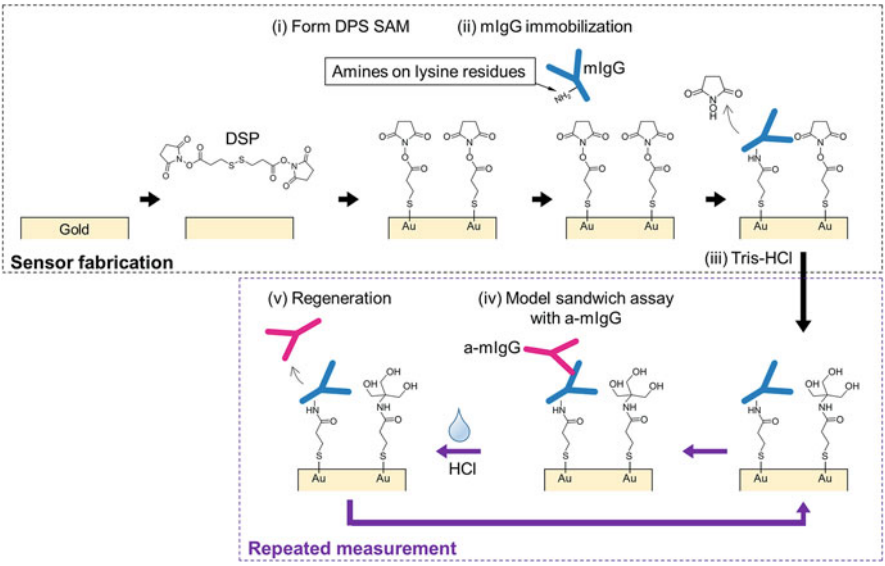

Fig. 10 (i)–(iii) Processes of SAW immunosensor design and (iv–vi) repeated immunoassays [27]

ELISA (at least 2 h). This feature of rapid measurement allows for realistically considering SAW sensors for semi-continuous measurements of a-mIgG.

High levels of C-reactive protein (CRP) inflammatory biomarker in the blood can be related to predicting adverse cardiovascular events or to the presence of cancer. Jeng et al. [28] fabricated, on a 64° Y-cut $LiNbO_3$, a SAW sensor with microfluidic channels to detect the CRP protein. The sensing area was functionalized with 2-methacryloyloxyethyl phosphorylcholine polymers. CRP was detected by the sensor in the concentration range of 10 ng/mL to 0.1 mg/mL. The LOD was equal to 4 ng/mL, and a linear relationship was recorded between SAW output signals and CRP concentrations.

2.2 Cell-Based SAW Sensors

Cell-based biosensors are generally investigated in monitoring drug–ligand interactions and in studying the effects of bioactive agents and environmental toxins. Nowadays, they are also used for in situ (or ex vivo in some cases) monitoring with living cells in their native environments [29]. The research field using SAW devices can be divided into three main categories: cell adhesion and growth, viscous and elastic properties of cells, and detection of bacteria and viruses [4].

2.2.1 Bacteria Identification

The standard way of detecting and identifying bacteria requires culturing, enumerating, and isolating presumptive colonies for further identification. Nucleic acid amplification methods [30], immunological methods [31], and flow cytometry [32] are the most common techniques for detecting and identifying bacteria. The most recent ones rely on using biosensors in general and SAW-based ones in particular.

Agostini et al. [33] investigated a SAW-based Lab-on-chip (LOC) for detecting measles virions (MV) in human saliva. The SAW-LOC comprised a lithium niobate substrate onto which a coplanar wave guide was patterned: seven 1-port SAW 740 MHz resonators (among them, one was isolated and used as reference) and one central interdigital transducer operating at 100 MHz (which serves as the fluid actuator). The originality of this study relies on using the SAW device for both sensing and sample circulation. The authors highlight the critical importance of liquid mixing during the incubation step: the LOD decreased from 741 U mL^{-1} in the absence of mixing to 209 U mL^{-1} with SAW mixing. The LOC was validated with whole human saliva for an MV concentration of 2,400 U mL^{-1}.

Gagliardi et al. [34] designed SAW immuno-biosensors to detect *Legionella pneumophila* in water. The biosensor was fabricated on a 128° Y-X lithium niobate (LN) substrate, generating an ultra-high-operating frequency of order of 740 MHz (Fig. 11). The sensors' surfaces were functionalized as follows: (1) formation of an antifouling adlayer layer (obtained from the incubation during 90 min of a solution of heterobifunctional thiol-polyethyleneglycol-streptavidin) which serves as probe linker, (2) conjugation of biotinylated anti-Legionella Pneumophila antibodies onto the adlayer (PBS, 90 min), and (3) blockage of the non-specific binding sites with BSA (1 mg/mL in PBS, 15 min). *L. pneumophila* was detected in the range·10^6 to 10^8 CFU/mL; the limit of detection of the designed sensor reached 2.01·10^6 CFU/mL.

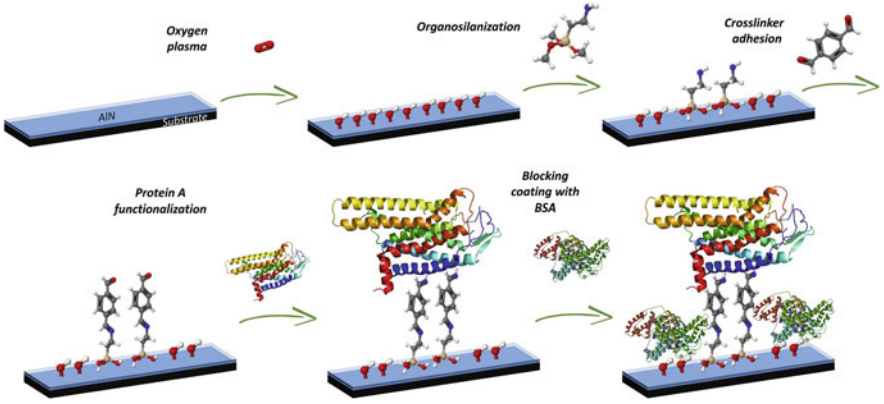

Fig. 11 Functionalization strategy of the piezoelectric substrate [35]

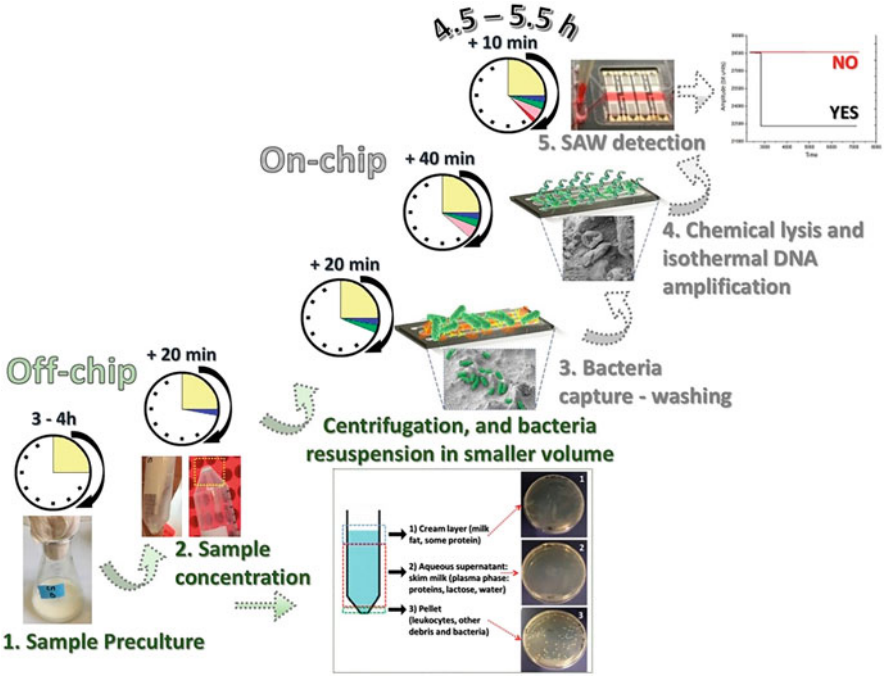

Fig. 12 Schematic representation of the chip operation protocol [37]

Lamanna et al. [35] built a flexible immunosensor (aluminum nitride SAW fabricated on recyclable polyethylene naphthalate) to detect *Escherichia coli*. Figure 11 depicts the functionalization strategy.

Results indicate that the sensitivity of the Lamb waves traveling on the polymeric device (LSAW) is superior to that of SAWs traveling on AlN on a silicon substrate (RSAW). The LOD of the designed LSAW and RSAW devices was equal to 6.54×10^5 CFU/mL and 1.04×10^6 CFU/mL, respectively. The authors estimated the single *E. coli* mass at approximately 9×10^{-13} g from a finite element method.

In 2019, Ji et al. [36] constructed a 210 MHz delay line SH-SAW biosensor on a 36° Y-X $LiTaO_3$ substrate to detect *Pseudomonas aeruginosa*, a bacterium responsible for many infections. The authors grafted ss-DNA probes on the sensing area and then detected different complementary sequence concentrations. The biosensor showed a linear response in the range 0.1 nmol/L to 1,000 nmol/L. Its LOD was 0.28 nmol/L.

Tsougeni et al. [37] designed a Lab-on-Chip integrating a 155 MHz SAW array with four acoustic channels to rapidly detect *Bacillus cereus, Salmonella, E. coli,* and *Listeria* bacteria in food samples. The chip operation protocol is presented in Fig. 12. Results showed a signal increase with increasing number of cells up to 10^3 CFUs. Saturation was reached after 30 min of incubation. This work attempts to meet the requirement of the ISO protocol to achieve the detection limit of 1 bacterium using smaller sample volumes and less preculture time.

Yao et al. [38] realized a SAW biosensor for quantifying *Escherichia coli L-asparaginase (E. coli l-ASNase)*. The authors investigated polyclonal antibody (pAb) as an interaction partner and tested several pAb immobilization strategies. The most suitable one was that with bis [sulfosuccinimidyl] suberate activated amide coupling via protein G. This study indicated the suitability of the designed SAW biosensor to quantify E. coli L-ASNase.

2.2.2 Monitoring of Cell Viscous and Viscoelastic Properties

The viscoelastic characteristics of cells have gained significant attention as valuable indicators of several disease states, such as cancer and neurodegenerative disorders, and their progression [39, 40]. Analyzing cells' mechanical properties, such as elasticity and viscosity, provides a deeper understanding of diseases' mechanisms [41, 42] and cell's biological functions [41]. Several techniques, such as atomic force microscopy (AFM) [43], microrheology [44], microfluidic method [45], optical laser tweezers [46], and hydrodynamic stretching [47], were used to monitor cells' viscoelastic properties. Five studies, published between 2019 and the beginning of 2023, reported the use of SAW sensors.

Chávez et al. [48] designed a 30 MHz Love-mode biosensor (fabricated on 36Y-X $LiNbO_3$ substrate and coated with an 8-μm thick SU-8 polymeric guiding layer) to study the viscosity changes in cell monolayers beyond the zone where focused adhesion with the sensor occurs. Brugger et al. [49] designed a 207 MHz SAW sensor to analyze wound-healing assay using the epithelial cell as a cell line model. The device was fabricated on a 36° XY-cut $LiTaO_3$ piezoelectric substrate with a thin SiO_2 layer. Results indicated that the biosensor can quantify the cell lysis ability, healing process, and growth, like cytoskeletal activity.

We et al. [50] designed a 12.8 MHz SAW device to measure cell compressibility and differentiate the cell's size. The authors investigated epithelial cells (A549), human airway smooth muscle (HASM), and MCF-7 breast cancer cells. Results indicated that the more compressible cells are A549. Link et al. [51] investigated the mechanical properties of erythrocytes with 162.2 MHz sensors fabricated on $LiNbO_3$ substrate. The authors used traveling surface acoustic waves (T-SAW) to generate a tunable standing acoustic wave field, in which red blood cells (RBCs) are captured and deformed. This technique can be used for high-throughput screening of blood samples to monitor diseases in their early stages. Zhang et al. [52] designed a 160 MHz Love-wave biosensor (an ST-cut quartz piezoelectric substrate coated with SiO_2 film) for the monitoring of the viscoelastic variations of HL-1 cardiomyocytes in the presence of an anticancer drug, hydrochloride (ADM). The results showed that the viscoelasticity decreased with increasing doses of ADM in the concentration range of 0.1–10 μM. The authors proved that the proposed Love-wave biosensor is a potentially valuable tool for early medication cardiotoxicity assessment.

3 Current Trends on SAW Biosensors

These various applications highlight the potential of SAW-based sensors to address different public health. However, the current trends toward detecting increasingly small molecules and epitopes instead of antibodies require a significant increase in sensitivity and efficient manipulation, mixing, or controlled displacement of low analyte volume. Several of the above solutions can be separately or jointly implemented:

3.1 The Use of New Piezoelectric Materials

Choosing "the" piezoelectric substrate is critical in the design of a given biosensor. It relies on a judicious compromise between a high value of the electromechanical coupling coefficient (K^2), which is related to the efficiency of the piezoelectric material in converting a mechanical signal to an electric one and vice versa, and a low-temperature coefficient of frequency (TCF), which is related to the thermal stability of the devices. Crystals like quartz (SiO_2), lithium tantalate ($LiTaO_3$), and lithium niobate ($LiNbO_3$) are the most investigated substrates. The literature also reports the use of polymers, like polyvinylidene fluoride (PVDF), ceramics, such as lead zirconium titanate (PZT), and thin films of aluminum nitride (AlN) or zinc oxide (ZnO) deposited on silicon substrates.

The current trend is to use new multi-layered piezoelectric materials to operate in the Gigahertz range with high K^2 values. Even if most studies presented in the following paragraphs are theoretical, there is no doubt that these piezoelectric materials will play a crucial role in the next generation of SAW biosensors.

The most promising materials consist of multilayer films deposited on diamond or sapphire. Jinbo et al. [53] designed SH-SAW resonators fabricated on 42°Y-X-$LiTaO_3$/SiO_2/sapphire substrate. The device, operating at 1.76 GHz, exhibits an effective electromechanical coupling coefficient of 13.34% and a well-compensated temperature coefficient of frequency of – 9.1 ppm/°C. These performance parameters are highly superior to conventional substrates. Han et al. [54] investigated ZnO/ZnO/diamond and AlN/AlN/diamond structures. They showed that it was possible to increase the electromechanical coupling coefficient to 8.26% for the former ($K^2_{ZnO} \approx 1.5$) and 4.64% for the latter ($K^2_{AlN} \approx 0.31$). The corresponding operating frequencies could reach 2 GHz and 3.76 GHz, respectively. Another theoretical study realized by Wang et al. [55] showed that the K^2 maximum value of a Mn-doped $Pb(In_{1/2}Nb_{1/2})O_3$-$Pb(Mg_{1/3}Nb_{2/3})O_3$-$PbTiO_3$ thin film/diamond layered structure could attain 79.5% for the main SH-SAW. Zhang and Wang [56] conducted a theoretical study concerning the realization of a layered SiO_2 /IDT/128° Y-X-LiNbO3/diamond/Si structure. Compared to the conventional $LiNbO_3$ single crystal, the novel multi-layered material's phase velocity and electromechanical

Table 1 Intrinsic properties of common and new piezoelectric materials

Piezoelectric material	Wave velocity (m/s)	Coupling coefficient K^2 (%)	Temperature coefficient of frequency (TCF) (ppm/°C)	Reference
ST-X quartz	3,159	0,1 - 0,2	0	[60]
64Y-X $LiNbO_3$	4,450	10.2	79	
128Y-X $LiNbO_3$	3,680–3,980	5–7	75	
36°Y-X $LiTaO_3$	4,160	5–6.6	30	
42°Y-X $LiTaO_3$	4,022	7.6	40	[61]
112°X $LiTaO_3$	3,300	0.75	18	
26.6°Y-X $La_3Ga_5SiO_{14}$	2,742	0.32	0.078	
Lead zirconium titanate (PZT)	3,900	20–35	–	[60]
AlN	5,607	0.31	25	[62, 63]
ZnO	2,645	1.5–1.7	−15 to −60	[60]
Polyfluorure de vinylidène (PVDF)	2,600	2.9	–	
Mn-doped $Pb(In_{1/2}Nb_{1/2})O_3$-$Pb(Mg_{1/3}Nb_{2/3})O_3$-$PbTiO_3$/diamond	1,646	79.5	–	[55]
$Sc_{0.43}Al_{0.57}N$/diamond	–	3.2–3.7	–	[64]
ZnO/ZnO/diamond	–	8.26	–	[54]
AlN/AlN/diamond	–	4.64	–	[54]
Diamond/AlN/IDT/AlN/diamond/Si	12,470	5.53	6.3	[65]
42_YX-$LiTaO_3$/SiO_2/sapphire	–	13.34	9.1–11.3	[53]
Y42-cut-$LiTaO_3$/sapphire	–	5.14–7.6	–	[66]
TeO_3/BeO/128° YX $LiNbO_3$	4,476	~9.66	60	[59]

coupling coefficient were increased by 144% and 17.7%, respectively. In addition, the layered structure is highly stable at high temperatures.

Shen et al. [57] studied the basic properties of ZnO and GaN multilayers SAW devices. They demonstrated that ZnO and GaN multilayers permit to increase the electromechanical coupling coefficient from about 0 to 7% and that the c-ZnO/c-GaN/c-sapphire structure can be used for high-frequency and large bandwidth SAW devices.

N.F. Naumenko [58] carried out numerical calculations of a structure combining lithium niobate thin plates with a langasite substrate. Results show that with increasing $LiNBO_3$ thickness, the K^2 value increased from 5.5% to 14.5%. Besides, low shear bulk wave velocities in langasite substrate provide a wide spurious-free frequency range. Soni and Bhola [59] showed that coating a 128 Y-X $LiNbO_3$ single crystal with thin films of BeO overlaid with TeO_3 permits to increase the theoretical K^2 value to 9.66%, a value superior by one and a half to that of 128 Y-X $LiNbO_3$.

Table 1 collects all the details concerning common and novel piezoelectric substrates.

3.2 New Generation of IDTs

Depending on the desired applications, several geometries of interdigital transducers (IDTs) have been adopted. Thanks to the current Multiphysics simulation tools, one can expect a substantial gain in time and cost when optimizing the IDTs structures (geometry, thickness, and nature) before actually manufacturing them [67–71]. Figure 13 gathers the main geometries of IDTs used in biosensors [6, 72, 73]. Other specific configurations exist, such as structures in which additional floating electrodes are added to improve the sensor's performance (high-quality factor and low insertion loss) or apodized IDTs, in which the bus bars overlap varies according to the length of the transducers. Nevertheless, the latter is used more in the electronic field to achieve the impulse response of the generated signal.

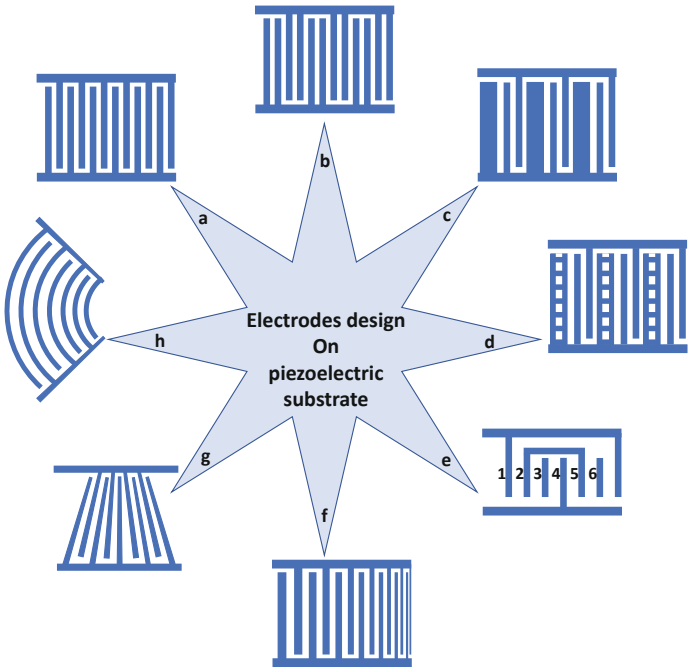

Fig. 13 Schematic representation of electrodes configuration in primary SAW transducers: (**a**) Bidirectional single electrode; (**b**) split electrodes; (**c**) single-phase unidirectional transducers; (**d**) Distributed reflective acoustic transducer; (**e**) Floating electrode unidirectional transducers; (**f**) Dispersive delay line; (**g**) Tapered (slanted) interdigitated electrodes; and (**h**) Focusing IDTs

In addition to their use as sensors, SAW devices are increasingly used to move, mix, or sort particles/material, thanks to mechanical waves generated on the surface [74].

3.2.1 Bidirectional IDTs

The bidirectional single-electrode IDT (Fig. 13. a) is widely used because of its relative simplicity since the widths and spacings of all electrodes are equal to one-quarter of the acoustic wavelength ($\lambda/4$). Nevertheless, the main drawback of this configuration comes from reflections on the edges of the electrodes. This problem is often overcome by extending the number of electrodes to increase the transmitted energy, but this solution can lead to distortion of the frequency response. Dual electrode type (or split electrodes) are generally considered to overcome these limitations (Fig. 13b). This configuration is similar to that of single-electrode IDT, with one difference: the electrodes are split to have a characteristic distance of ($\lambda/8$) for both width and electrodes' spacing. These structures allow reducing reflections and triple transit and operation at the third harmonic and thus at higher frequencies [6]. Despite their widespread use, research was directed to improve these configurations, mainly to reduce electrodes' reflections.

3.2.2 Unidirectional IDTs

Several configurations have been considered as an alternative to dual-electrode IDTs to design devices having lower insertion losses and permitting higher acoustic energy transfer in the forward direction. The basic principle relates to generating phase shifts between the multiple reflections on the different electrodes of suitable widths and spacing, eventually canceling each other by destructive interference. The first one is the single-phase unidirectional transducer (SPUDT), which is more efficient for removing triple transit and decreasing insertion loss, thanks to the specific configuration (Fig. 13c) with alternating large ($\lambda/4$) and thin ($\lambda/8$) electrodes and comprising two different spacings of ($\lambda/8$) and ($3\lambda/16$). Another close configuration, the distributed reflective acoustic transducer (DART), can be used for the same purposes (Fig. 13d). Here, the electrodes' width and spacing are adjusted to achieve optimized performance in applications such as biosensors or microfluidic systems. Floating electrode unidirectional transducers (FEUDTs) constitute another configuration where some electrodes are patterned without connection and seem to float on the piezoelectric substrate (Fig. 13e). These unidirectional IDTs introduced first by Yamanouchi [75] are widely used thanks to their improved sensitivity compared to bidirectional IDTs. Unidirectional transducers are based on creating a shift between the transduction and reflection centers. The FEUDTS have six electrodes per cell, unlike the conventional 2-electrodes IDTs structure. Electrodes 1 and 4 are connected to the power supply, while electrodes 2, 3, 5, and 6 are floating (Fig. 13e). The excitation center, related to electrodes 1, 2, 4, and 5, is, in this case,

separated from the reflection one (located between electrodes 3 and 6). This results in a phase shift between reflections from the floating electrodes' free and connected metal strips. Therefore, the generated surface acoustic waves mainly propagate forward with a very low loss, giving access to several harmonic frequencies that enable the high-frequency operation of FDEUT-based SAW sensors [67].

3.2.3 Variable Frequency IDTs

The configuration of the dispersive delay line (Fig. 13f) exhibits the particularity of comprising variable width and spacing of the electrodes in the propagation direction, resulting in variable frequencies and large bandwidth. With a similar concept of gradually changing the electrode's periodicity, tapered (slanted) interdigitated electrodes (Fig. 13g) are designed to progressively change the electrode's width and spacing in the direction perpendicular to the propagation path. Both configurations are progressively integrated into biosensing systems, thanks to the possibility of varying the operating frequency in the bandwidth, where increased sensitivity is required to fulfill growing needs for diagnosis and environment. Besides sensing, the main interest of these two structures is the integration in microfluidic systems to manipulate droplets or perform particle and cell separation. It has also been reported that these structures could contribute to partially focusing the acoustic energy [6].

3.2.4 Focusing IDTs

The focusing IDT corresponds to a structure in which the interdigitated electrodes are designed in arcs of concentric circles to focus the generated waves in a localized zone (Fig. 13h). It is thus easy to understand that the energy density in this area is very high. This focusing property permits efficient pumping and mixing of fluids on one side and ultrasensitive detection on the other. It takes advantage of the tiny size of the detection area and the high signal-to-noise ratio due to this high energy density [6, 73].

3.3 Multi-Transductions

The combination of two types of transduction modes quickly attracted researchers, as it gives access to multiparametric response providing valuable complementary information on the investigated medium. Dual sensing permits the benefit of each mode's advantages and reduces influence parameters, which act differently depending on the considered technique. It thus allows for accurate and complete characterization of the analytes of interest in complex media. Here, we focus on the most investigated and used combinations: gravimetry/electrochemistry and gravimetry /optical transduction.

3.3.1 Gravimetric/Electrochemical Coupling

Gravimetric–electrochemical coupling is the most developed and used combined mode. In delay line configuration, the gold sensitive area of the SAW sensors also acts as a working electrode (WE). A reference (Ref) and a counter-electrode (CE) complete the 3-electrode setup system (Fig. 14).

Lattach et al. [66] pointed out the interest in such dual transduction about 10 years ago. The authors designed an original electrochemical-surface acoustic wave (ESAW) sensor to detect atrazine in liquid media. The same principle presented in Fig. 14 was considered, except that the reference and counter-electrodes were part of an external circuit instead of being integrated into a 2D configuration.

Note that other configurations, such as resonators, were also used, as K. Kustanovich et al. reported in recent work [76]. They developed a dual sensor integrating two different modes in one device: SAW resonance and electrochemical impedance spectroscopy (EIS). They showed that, even embedded in the same substrate, no noticeable interference occurred between both measurements (crosstalk lower than 60 dB), thanks to separate electrical ports and the difference of frequency domains for each mode (up to 1 MHz for EIS and around 185 MHz for SAW resonance). The dual sensor was used for lipid deposition sensing and investigating interactions between liposomes and calcium ions. This combination permitted to obtain multiparametric responses providing rich information on physicochemical interactions and surface phenomena.

3.3.2 Gravimetric/Optical Coupling

Gravimetric/optical coupling recently has attracted increasing interest, mainly due to the absence of crosstalk between the two modes and the possibility of obtaining complementary parameters.

The most studied and investigated gravimetric/optical coupling involves surface plasmon resonance (SPR), mainly for its relatively simple implementation. In this case, the translucent SAW sensor substrate is placed on a prism, and a close link is ensured with an index-matching gel (Fig.15).

Based on this principle, E. Gizeli et al. [77] developed dual surface plasmon resonance (SPR) and Love-wave surface acoustic wave (LW-SAW) sensors platform on ST-quartz (Y-cut 42°45′) for real-time monitoring of biomolecular interactions. By studying the adsorption of proteins on gold, they highlight the complementary information brought by dual transduction. The energy dissipated

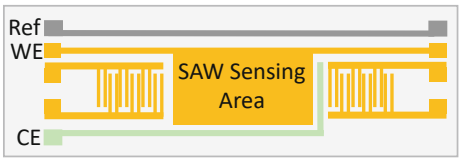

Fig. 14 Schematic diagram of a SAW sensor designed in delay line configuration incorporating electrodes for electrochemical transduction

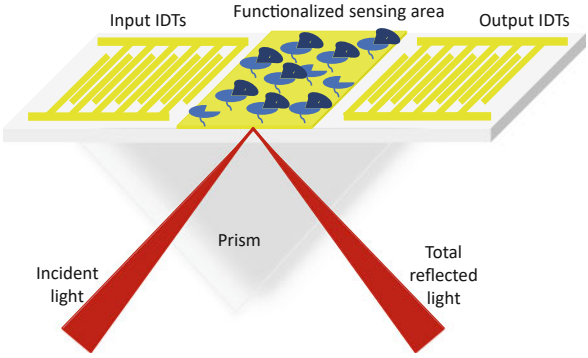

Fig. 15 Schematic diagram of a SAW/SPR sensor coupled via a prism

during the adsorption process and mass and rigidity of the growth film are estimated by gravimetry, while optical measurements simultaneously give access to the hydration amount of adsorbed layer. One can imagine the promising path traced by such combined systems in investigating biomolecular interactions in various interfaces: liquid/solid, protein/protein, liposomes/ions, etc.

Recently, in a different way, Wang and co-authors engineered a highly sensitive photoacoustic (PA)-surface acoustic wave (SAW) for malaria parasite detection in blood [78]. This biosensor had significant advantages as it combines the SAW detection sensitivity and the PA's high optical selectivity. The surface of the device was fabricated using a 128° YX lithium niobate ($LiNbO_3$) substrate with an operating frequency of 10 MHz. Hence, the PA signals elicited by blood plasma and red blood cells isolated from uninfected and infected whole blood have been quantified and characterized by the variation in feature frequencies. The PA-SAW sensing and detecting system showed a rapid single-run test, taking less than 2 min.

As mentioned before, the advantage of using double transduction is not limited to multiparametric detection but can find many other advantageous applications. J. Liu et al. proposed coupling of metal-enhanced fluorescence and SAW for the quantification of carcinoembryonic antigens (CEA) [79] to reach high sensitivity and a low limit of detection. The contribution of the SAW, in this case, was not in detection but in effectively mixing the solution and efficiently removing all non-specifically bound proteins.

4 Conclusion

This chapter presents an overview of recent applications of surface acoustic wave biosensors that fulfill the perpetual quest for increasing the sensitivity and decreasing the limit of detection. Each of the presented biosensors is designed and functionalized with the aim of specific detection of the analyte of interest with the highest sensitivity and the lowest limit of detection.

Improvements in SAW biosensors can be made in two complementary directions. The first one is related to synthesis and use of new multi-layered piezoelectric materials with high K^2 values, such as lead composites/diamond multilayers (K^2 of 79.5), or allowing easy operation in the high-frequency domain such as diamond/AlN/Si-based structures (acoustic wave velocity of 12,470 m/s). The second concerns the optimization of the interdigital transducers (IDTs) design. Several geometries have been optimized according to the aimed application, thanks to the current Multiphysics simulation tools, to reach high-quality factors and low insertion loss for enhanced sensing (unidirectional IDTs) or to focus the acoustic energy (variable and/or focusing IDTs) for efficient pumping and mixing of fluids.

These various applications highlight the potential of SAW-based sensors to address different public health concerns and to accompany the current trends toward the detection of increasingly small molecules, which require high sensitivity and efficient manipulation, mixing, or controlled displacement of low analyte volume. Besides, the trend is also a combination of SAW with other modes of transduction to access multiparametric response that provides a promising route for accurate and full characterization of analytes of interest in complex media.

References

1. Campbell C (1998) Surface acoustic wave devices for mobile and wireless communications, four-volume set. Academic press
2. Campbell C (1989) 2 – Basics of acoustic waves and piezoelectricity. In: Campbell C (ed) Surface acoustic wave devices and their signal processing applications. Academic Press, pp 9–30
3. Skowronek V, Rambach RW, Franke T (2015) Surface acoustic wave controlled integrated band-pass filter. Microfluid Nanofluid 19(2):335–341. https://doi.org/10.1007/s10404-015-1559-3
4. Baumgartner K, Westerhausen C (2023) Recent advances of surface acoustic wave-based sensors for noninvasive cell analysis. Curr Opin Biotechnol 79:102879. https://doi.org/10.1016/j.copbio.2022.102879
5. Xu Z, Yuan YJ (2018) Implementation of guiding layers of surface acoustic wave devices: a review. Biosens Bioelectron 99:500–512. https://doi.org/10.1016/j.bios.2017.07.060
6. Mandal D, Banerjee S (2022) Surface acoustic wave (SAW) sensors: physics. Mater Appl 22(3):820
7. Ballantine Jr D, White RM, Martin SJ, Ricco AJ, Zellers E, Frye G et al (1996) Acoustic wave sensors: theory, design and physico-chemical applications. Elsevier
8. Iqbal MJ, Javed Z, Herrera-Bravo J, Sadia H, Anum F, Raza S et al (2022) Biosensing chips for cancer diagnosis and treatment: a new wave towards clinical innovation. Cancer Cell Int 22(1): 354. https://doi.org/10.1186/s12935-022-02777-7
9. Roberts A, Gandhi S (2022) A concise review on potential cancer biomarkers and advanced manufacturing of smart platform-based biosensors for early-stage cancer diagnostics. Biosens Bioelectron X 11:100178. https://doi.org/10.1016/j.biosx.2022.100178
10. (NHS), E. N. H. S. Carcinoembryonic antigen (CEA) test. https://www.nhs.uk/conditions/cea-test/. Accessed 8 Apr 2023
11. Juurikka K, Butler GS, Salo T, Nyberg P, Åström P (2019) The role of MMP8 in cancer: a systematic review. Int J Mol Sci 20(18). https://doi.org/10.3390/ijms20184506

12. Li C, Zhang J, Xie H, Luo J, Fu C, Tao R et al (2022) Highly sensitive love mode acoustic wave platform with SiO(2) wave-guiding layer and gold nanoparticles for detection of carcinoembryonic antigens. Biosensors (Basel) 12(7). https://doi.org/10.3390/bios12070536
13. Jandas PJ, Luo J, Quan A, Qiu C, Cao W, Fu C et al (2020) Highly selective and label-free love-mode surface acoustic wave biosensor for carcinoembryonic antigen detection using a self-assembled monolayer bioreceptor. Appl Surf Sci 518:146061. https://doi.org/10.1016/j.apsusc.2020.146061
14. Jandas PJ, Luo J, Prabakaran K, Chen F, Fu YQ (2020) Highly stable, love-mode surface acoustic wave biosensor using Au nanoparticle-MoS2-rGO nano-cluster doped polyimide nanocomposite for the selective detection of carcinoembryonic antigen. Mater Chem Phys 246:122800. https://doi.org/10.1016/j.matchemphys.2020.122800
15. Jandas PJ, Prabakaran K, Luo J, Fu C, Fu YQ, Holaday MGD (2021) Ti3C2Tx MXene-Au nanoparticles doped polyimide thin film as a transducing bioreceptor for real-time acoustic detection of carcinoembryonic antigen. Sens Actuators A Phys 331:112998. https://doi.org/10.1016/j.sna.2021.112998
16. Wang X, Ji J, Yang P, Li X, Pang Y, Lu P (2022) A love-mode surface acoustic wave aptasensor with dummy fingers based on monolayer MoS2/Au NPs nanocomposites for alpha-fetoprotein detection. Talanta 243:123328. https://doi.org/10.1016/j.talanta.2022.123328
17. Zhao C, Li C, Li M, Qian L, Wang L, Li H (2022) Surface acoustic wave immunosensor based on Au-nanoparticles-decorated graphene fluidic channel for CA125 detection. Sens Actuators B Chem 367:132063. https://doi.org/10.1016/j.snb.2022.132063
18. Lo X-C, Li J-Y, Lee M-T, Yao D-J (2020) Frequency shift of a SH-SAW biosensor with glutaraldehyde and 3-Aminopropyltriethoxysilane functionalized films for detection of epidermal growth factor. Biosensors (Basel) 10(8). https://doi.org/10.3390/bios10080092
19. Taylor JJ, Jaedicke KM, van de Merwe RC, Bissett SM, Landsdowne N, Whall KM et al (2019) A prototype antibody-based biosensor for measurement of salivary MMP-8 in periodontitis using surface acoustic wave technology. Sci Rep 9(1):11034. https://doi.org/10.1038/s41598-019-47513-w
20. Lo XC, Lee MT, Yao DJ (2021) Detection of transferrin receptor CD71 on a shear horizontal surface acoustic wave biosensor. IEEE Open J Nanotechnol 2:1–7. https://doi.org/10.1109/OJNANO.2020.3044352
21. Karaboğa MNS, Sezgintürk MK (2022) Biosensor approaches on the diagnosis of neurodegenerative diseases: sensing the past to the future. J Pharm Biomed Anal 209:114479. https://doi.org/10.1016/j.jpba.2021.114479
22. Krausz AD, Korley FK, Burns MA (2021) The current state of traumatic brain injury biomarker measurement methods. Biosensors 11(9):319. https://doi.org/10.3390/bios11090319
23. Kidakova A, Boroznjak R, Reut J, Öpik A, Saarma M, Syritski V (2020) Molecularly imprinted polymer-based SAW sensor for label-free detection of cerebral dopamine neurotrophic factor protein. Sens Actuators B 308:127708. https://doi.org/10.1016/j.snb.2020.127708
24. Agostini M, Amato F, Vieri ML, Greco G, Tonazzini I, Baroncelli L et al (2021) Glial-fibrillary-acidic-protein (GFAP) biomarker detection in serum-matrix: functionalization strategies and detection by an ultra-high-frequency surface-acoustic-wave (UHF-SAW) lab-on-chip. Biosens Bioelectron 172:112774. https://doi.org/10.1016/j.bios.2020.112774
25. Peng Y-C, Cheng C-H, Yatsuda H, Liu S-H, Liu S-J, Kogai T et al (2021) A novel rapid test to detect anti-SARS-CoV-2 N protein IgG based on shear horizontal surface acoustic wave (SH-SAW). Diagnostics 11(10):1838. https://doi.org/10.3390/diagnostics11101838
26. Cheng C-H, Peng Y-C, Lin S-M, Yatsuda H, Liu S-H, Liu S-J et al (2022) Measurements of anti-SARS-CoV-2 antibody levels after vaccination using a SH-SAW biosensor. Biosensors (Basel) 12(8):599. https://doi.org/10.3390/bios12080599
27. Toma K, Oishi K, Yoshimura N, Arakawa T, Yatsuda H, Mitsubayashi K (2019) Repeated immunosensing by a dithiobis(succinimidyl propionate)-modified SAW device. Talanta 203: 274–279. https://doi.org/10.1016/j.talanta.2019.05.080

28. Jeng M-J, Li Y-C, Sharma M, Chen C-W, Tsai C-L, Lin Y-H et al (2021) A surface acoustic wave sensor with a microfluidic channel for detecting C-reactive protein. Chemosensors 9(5): 106. https://doi.org/10.3390/chemosensors9050106
29. Gupta N, Renugopalakrishnan V, Liepmann D, Paulmurugan R, Malhotra BD (2019) Cell-based biosensors: recent trends, challenges and future perspectives. Biosens Bioelectron 141: 111435. https://doi.org/10.1016/j.bios.2019.111435
30. Jensen MA, Webster JA, Straus N (1993) Rapid identification of bacteria on the basis of polymerase chain reaction-amplified ribosomal DNA spacer polymorphisms. ASM J 59(4): 945–952. https://doi.org/10.1128/aem.59.4.945-952.1993
31. Schloter M, Aßmus B, Hartmann A (1995) The use of immunological methods to detect and identify bacteria in the environment. Biotechnol Adv 13(1):75–90. https://doi.org/10.1016/0734-9750(94)00023-6
32. Kennedy D, Wilkinson MG (2017) Application of flow cytometry to the detection of pathogenic bacteria. Curr Issues Mol Biol 23:21–38. https://doi.org/10.21775/cimb.023.021
33. Agostini M, Lunardelli F, Gagliardi M, Miranda A, Lamanna L, Luminare AG et al (2022) Surface-acoustic-wave (SAW) induced mixing enhances the detection of viruses: application to measles sensing in whole human saliva with a SAW lab-on-a-Chip. Adv Funct Mater 32(44): 2201958. https://doi.org/10.1002/adfm.202201958
34. Gagliardi M, Agostini M, Lunardelli F, Lamanna L, Miranda A, Bazzichi A et al (2023) Surface acoustic wave-based lab-on-a-chip for the fast detection of legionella pneumophila in water. Sens Actuators B 379:133299. https://doi.org/10.1016/j.snb.2023.133299
35. Lamanna L, Rizzi F, Bhethanabotla VR, De Vittorio M (2020) Conformable surface acoustic wave biosensor for E-coli fabricated on PEN plastic film. Biosens Bioelectron 163:112164. https://doi.org/10.1016/j.bios.2020.112164
36. Ji J, Yang C, Zhang F, Shang Z, Xu Y, Chen Y et al (2019) A high sensitive SH-SAW biosensor based 36° Y-X black LiTaO3 for label-free detection of pseudomonas aeruginosa. Sens Actuators B 281:757–764. https://doi.org/10.1016/j.snb.2018.10.128
37. Tsougeni K, Kaprou G, Loukas CM, Papadakis G, Hamiot A, Eck M et al (2020) Lab-on-chip platform and protocol for rapid foodborne pathogen detection comprising on-chip cell capture, lysis, DNA amplification and surface-acoustic-wave detection. Sens Actuators B 320:128345. https://doi.org/10.1016/j.snb.2020.128345
38. Yao H, Fernández CS, Xu X, Wynendaele E, De Spiegeleer B (2019) A surface acoustic wave (SAW) biosensor method for functional quantification of E. coli l-asparaginase. Talanta 203:9–15. https://doi.org/10.1016/j.talanta.2019.05.046
39. Bao G, Suresh S (2003) Cell and molecular mechanics of biological materials. Nat Mater 2(11): 715–725. https://doi.org/10.1038/nmat1001
40. Moeendarbary E, Harris AR (2014) Cell mechanics: principles, practices, and prospects. WIREs Syst Biol Med 6(5):371–388. https://doi.org/10.1002/wsbm.1275
41. Nguyen TL, Polanco ER, Patananan AN, Zangle TA, Teitell MA (2020) Cell viscoelasticity is linked to fluctuations in cell biomass distributions. Sci Rep 10(1):7403. https://doi.org/10.1038/s41598-020-64259-y
42. Barriga EH, Franze K, Charras G, Mayor R (2018) Tissue stiffening coordinates morphogenesis by triggering collective cell migration in vivo. Nature 554(7693):523–527. https://doi.org/10.1038/nature25742
43. Haase K, Pelling AE (2015) Investigating cell mechanics with atomic force microscopy. J R Soc Interface 12(104):20140970. https://doi.org/10.1098/rsif.2014.0970
44. Crocker JC, Hoffman BD (2007) Multiple-particle tracking and two-point microrheology in cells. In: Methods in cell biology, vol 83. Academic Press, pp 141–178
45. Gerum R, Mirzahossein E, Eroles M, Elsterer J, Mainka A, Bauer A et al (2022) Viscoelastic properties of suspended cells measured with shear flow deformation cytometry. Elife 11: e78823. https://doi.org/10.7554/eLife.78823

46. Arbore C, Perego L, Sergides M, Capitanio M (2019) Probing force in living cells with optical tweezers: from single-molecule mechanics to cell mechanotransduction. Biophys Rev 11(5): 765–782. https://doi.org/10.1007/s12551-019-00599-y
47. Li F, Cima I, Vo JH, Tan M-H, Ohl CD (2020) Single cell hydrodynamic stretching and microsieve filtration reveal genetic, phenotypic and treatment-related links to cellular deformability. Micromachines 11(5). https://doi.org/10.3390/mi11050486
48. Segura Chávez PA, Bonhomme J, Bellaredj MLF, Olive L, Beyssen D, Oudich M et al (2022) Love wave sensor with high penetration depth for potential application in cell monitoring. Biosensors 12(2):61. https://doi.org/10.3390/bios12020061
49. Brugger MS, Schnitzler LG, Nieberle T, Wixforth A, Westerhausen C (2021) Shear-horizontal surface acoustic wave sensor for non-invasive monitoring of dynamic cell spreading and attachment in wound healing assays. Biosens Bioelectron 173:112807. https://doi.org/10.1016/j.bios.2020.112807
50. Wu Y, Stewart AG, Lee PVS (2019) On-chip cell mechanophenotyping using phase modulated surface acoustic wave. Biomicrofluidics 13(2):024107. https://doi.org/10.1063/1.5084297
51. Link A, Franke T (2020) Acoustic erythrocytometer for mechanically probing cell viscoelasticity. [10.1039/C9LC00999J]. Lab Chip 20(11):1991–1998. https://doi.org/10.1039/C9LC00999J
52. Zhang J, Wei X, Qiu Y, Yu W, Xue Y, Xiong Y et al (2021) Real-time monitoring of HL-1 cell viscoelasticity for drug cardiotoxicity assessment using a love wave biosensor. J Electrochem Soc 168(10):107504. https://doi.org/10.1149/1945-7111/ac29de
53. Wu J, Zhang S, Chen Y, Zheng P, Zhang L, Yao H et al (2022) Advanced surface acoustic wave resonators on $LiTaO_3/SiO_2$/sapphire substrate. IEEE Electron Device Lett 43(10):1748–1751. https://doi.org/10.1109/LED.2022.3200418
54. Han X, Wang F, Zhang K, Kong D, Hu K, Qian L et al (2022) Effect on coupling coefficient of diamond-based surface acoustic wave devices using two layers of piezoelectric materials of different widths. Diamond Relat Mater 125:109041. https://doi.org/10.1016/j.diamond.2022.109041
55. Wang J, Zhang Q, Zhao X, Liu H, Zhang S, Gu YJD et al (2022) Ultra-wide band and improved quality factor SH-type SAW devices by employing Mn-doped Pb (In1/2Nb1/2) O3–Pb (Mg1/3Nb2/3) O3–PbTiO3 thin film/diamond layered structure. Diamond Relat Mater 130: 109478. https://doi.org/10.1016/j.diamond.2022.109478
56. Zhang H, Wang HJM (2021) Investigation of surface acoustic wave propagation characteristics in new multilayer structure: SiO2/IDT/LiNbO3/diamond/Si. Micromachines 12(11):1286. https://doi.org/10.3390/mi12111286
57. Shen J, Fu S, Su R, Xu H, Zeng F, Song C et al (2021) Systematical study of the basic properties of surface acoustic wave devices based on ZnO and GaN multilayers. Electronics 10(1):23. https://doi.org/10.3390/electronics10010023
58. Naumenko NF (2020) Advanced substrate material for SAW devices combining $LiNbO_3$ and langasite. IEEE Trans Ultrason Ferroelectr Freq Control 67(9):1909–1915. https://doi.org/10.1109/tuffc.2020.2985744
59. Soni ND, Bhola J (2021) Enhanced properties of SAW device based on beryllium oxide thin films. Crystals 11(4):332. https://doi.org/10.3390/cryst11040332
60. Fu YQ, Luo J, Nguyen N-T, Walton A, Flewitt AJ, Zu X-T et al (2017) Advances in piezoelectric thin films for acoustic biosensors, acoustofluidics and lab-on-chip applications. Prog Mater Sci 89:31–91. https://doi.org/10.1016/j.pmatsci.2017.04.006
61. T. R. I. C. Ltd. http://www.roditi.com/. Accessed 8 Apr 2023
62. Fei S, Ren H (2020) A contour mode AIN piezoelectric resonator based on SOI substrate. In: 2020 IEEE 15th international conference on nano/micro engineered and molecular system (NEMS), IEEE, pp 180–183. https://doi.org/10.1109/NEMS50311.2020.9265593
63. Fei S, Ren H (2021) Temperature characteristics of a contour mode MEMS AlN piezoelectric ring resonator on SOI substrate. Micromachines 12(2). https://doi.org/10.3390/mi12020143

64. Sinusia Lozano M, Fernández-García L, López-Romero D, Williams OA, Iriarte GFJM (2022) SAW resonators and filters based on Sc0. 43Al0. 57N on single crystal and polycrystalline diamond. Micromachines 13(7):1061. https://doi.org/10.3390/mi13071061
65. Lei L, Dong B, Hu Y, Lei Y, Wang Z, Ruan SJS (2022) High-frequency surface acoustic wave resonator with diamond/AlN/IDT/AlN/diamond multilayer structure. Sensors 22(17):6479. https://doi.org/10.3390/s22176479
66. Wu J, Zhang S, Zhang L, Zhou H, Zheng P, Yao H et al (2022) Exploring low-loss surface acoustic wave devices on heterogeneous substrates. IEEE Trans Ultrason Ferroelectr Freq Control 69(8):2579–2584. https://doi.org/10.1109/TUFFC.2022.3179699
67. Bin S, Yang H, Jiang L, Liu X (2022) Simulation study of FEUDT structure optimization and sensitive film loading of SAW devices. Micromachines 13(10):1643. https://doi.org/10.3390/mi13101643
68. Shevchenko SY, Mikhailenko DA (2022) Topological optimization of circular SAW resonators: overcoming the discreteness effects. Sensors 22(3):1172. https://doi.org/10.3390/s22031172
69. Xie B, Ding F, Dong Z, Shang H, Huang D, Gu H (2020) FEM analysis of piezoelectric film as IDT on the diamond substrate to enhance the quality factor of SAW devices. Diamond Relat Mater 102:107659. https://doi.org/10.1016/j.diamond.2019.107659
70. Nagmani AK, Turuk BK, Behera B (2021) Simulation and optimization of geometrical structure of one-port SAW resonator using FEM. In: AIP conference proceedings. AIP Publishing LLC, vol 2341(1), p 020043. https://doi.org/10.1063/5.0049919
71. Achour B, Attia G, Zerrouki C, Fourati N, Raoof K, Yaakoubi N (2020) Simulation/experiment confrontation, an efficient approach for sensitive SAW sensors design. Sensors 20(17):4994. https://doi.org/10.3390/s20174994
72. Hashimoto K-Y, Hashimoto K-Y (2000) Surface acoustic wave devices in telecommunications, vol Vol. 116. Springer
73. Mazalan MB, Noor AM, Wahab Y, Yahud S, Zaman WSWK (2022) Current development in interdigital transducer (IDT) surface acoustic wave devices for live cell in vitro studies: a review. Micromachines 13(1):30. https://doi.org/10.3390/mi13010030
74. Agostini M, Cecchini M (2021) Ultra-high-frequency (UHF) surface-acoustic-wave (SAW) microfluidics and biosensors. Nanotechnology 32(31):312001. https://doi.org/10.1088/1361-6528/abfaba
75. Yamanouchi K, Furuyashiki H (1984) New low-loss SAW filter using internal floating electrode reflection types of single-phase unidirectional transducer. Electron Lett 24(20):989–990. https://doi.org/10.1049/el:19840672
76. Kustanovich K, Yantchev V, Doosti BA, Gözen I, Jesorka A (2019) A microfluidics-integrated impedance/surface acoustic resonance tandem sensor. Sens Bio-Sens Res 25:100291. https://doi.org/10.1016/j.sbsr.2019.100291
77. Samarentsis AG, Pantazis AK, Tsortos A, Friedt J-M, Gizeli E (2020) Hybrid sensor device for simultaneous surface Plasmon resonance and surface acoustic wave measurements. Sensors 20(21):6177. https://doi.org/10.3390/s20216177
78. Wang W, Zheng Z, Yang C, Fang Z, Wang S, Yuen C et al (2022) Laser-induced surface acoustic wave sensing-based malaria parasite detection and analysis. IEEE Trans Instrum Meas 71:1–9. https://doi.org/10.1109/TIM.2021.3124841
79. Liu J, Li S, Bhethanabotla VR (2018) Integrating metal-enhanced fluorescence and surface acoustic waves for sensitive and rapid quantification of cancer biomarkers from real matrices. ACS Sens 3(1):222–229. https://doi.org/10.1021/acssensors.7b00876

FBAR Gas Sensors

Zilun Wang, Xueyou Sun, Ye Chang, Xuexin Duan, and Wei Pang

Contents

Abstract Small-sized, high-sensitivity, and low-cost sensors are required for gas-sensing applications because of their critical role in environmental monitoring, clinic diagnosis, process control, and anti-terrorism. Given the rapid developments in micro-fabrication and microelectromechanical system (MEMS) technologies, film bulk acoustic resonator (FBAR) gas sensors have received increased research attention because of their improved working frequency and reliability. This chapter discusses the state-of-the-art and recent developments in FBAR gas sensors. The sensing mechanism and limitations of these sensors are summarized. Recent progress in the development of four major aspects of FBAR gas sensors, namely, FBAR gas sensors using different sensing materials, FBAR gas sensors used in electronic noses, system integration of FBAR gas sensors, and FBAR gas sensors used as micro-GC detectors, is reviewed. The potential future of FBAR sensors used in flexible electronics is also discussed.

Z. Wang, X. Sun, Y. Chang, X. Duan, and W. Pang (✉)
State Key Laboratory of Precision Measuring Technology and Instruments, Tianjin University, Tianjin, China
e-mail: zilun_wang_94@tju.edu.cn; xueyousun@tju.edu.cn; cy0803@tju.edu.cn; xduan@tju.edu.cn; weipang@tju.edu.cn

P. Lieberzeit (ed.), *Piezoelectric Sensors*, Springer Series on Chemical Sensors and Biosensors (2024) 18: 253–290, https://doi.org/10.1007/5346_2023_32,

Published online: 1 November 2023

Keywords Electronic noses, FBAR, Gas sensors, GC detectors, Sensitive membranes

1 Introduction

Film bulk acoustic resonator (FBAR) has been considered a small-sized high-Q resonator in the radio-frequency (RF) field [1]. Over the last decade, FBAR also plays an essential role as actuators and sensors (Fig. 1). Advances in acoustic streaming have allowed the application of FBAR actuators to a wider range of scenarios, such as particle manipulation [2–7], biomolecular enrichment [8–10], exosome screening [11], and drug delivery [12–14]. In the sensing area, FBAR has received increased attention with regard to its high sensitivity, low cost, and small size. Several attempts for sensing applications using FBARs, particularly pressure sensing, temperature sensing, and humidity sensing, have been made with remarkable results.

In recent years, gas detection has been of great interest for widespread applications such as environmental monitoring, clinic diagnosis, process control, and anti-terrorism. To satisfy the needs of these applications, gas sensors are required not only to be affordable for on-site analysis but also suitable for complex analytes discrimination. With rapid progress in micro-fabrication and microelectromechanical system (MEMS) technologies, FBAR gas sensors have received increased attention because of their GHz-level resonant frequency and high-quality factor. The selectivity and sensitivity of an FBAR gas sensor can be tuned by materials modification. The mass-based sensing mechanism of FBAR allows its response to represent information with regard to the sorption process of analytes. And due to its compatibility with semiconductor processes, FBAR is well suited for wafer-scaled production, demonstrating its feasibility for large-scale industrial production.

Thus far, FBAR has worked as gas sensors for volatile organic compound (VOC) analysis [15–22] which is indispensable for respiratory metabolomics. For neurotoxic gas sensing [16, 23] and other inorganic gases [24], FBAR also demonstrates its great potential and advanced performance. In this chapter, we discuss the state-of-the-art and recent developments in such FBAR gas sensors. First, an overview of the sensing mechanism and limitations of FBAR sensors is summarized. Next, we present recent advancements in the development of four major aspects of FBAR gas sensors, namely, FBAR gas sensors using different sensing materials, FBAR gas sensors used in electronic noses, system integration of FBAR gas sensors, and FBAR gas sensors used as micro-GC detectors. Finally, we conclude this chapter and outline perspectives on the potential future of FBAR sensors used in flexible electronics.

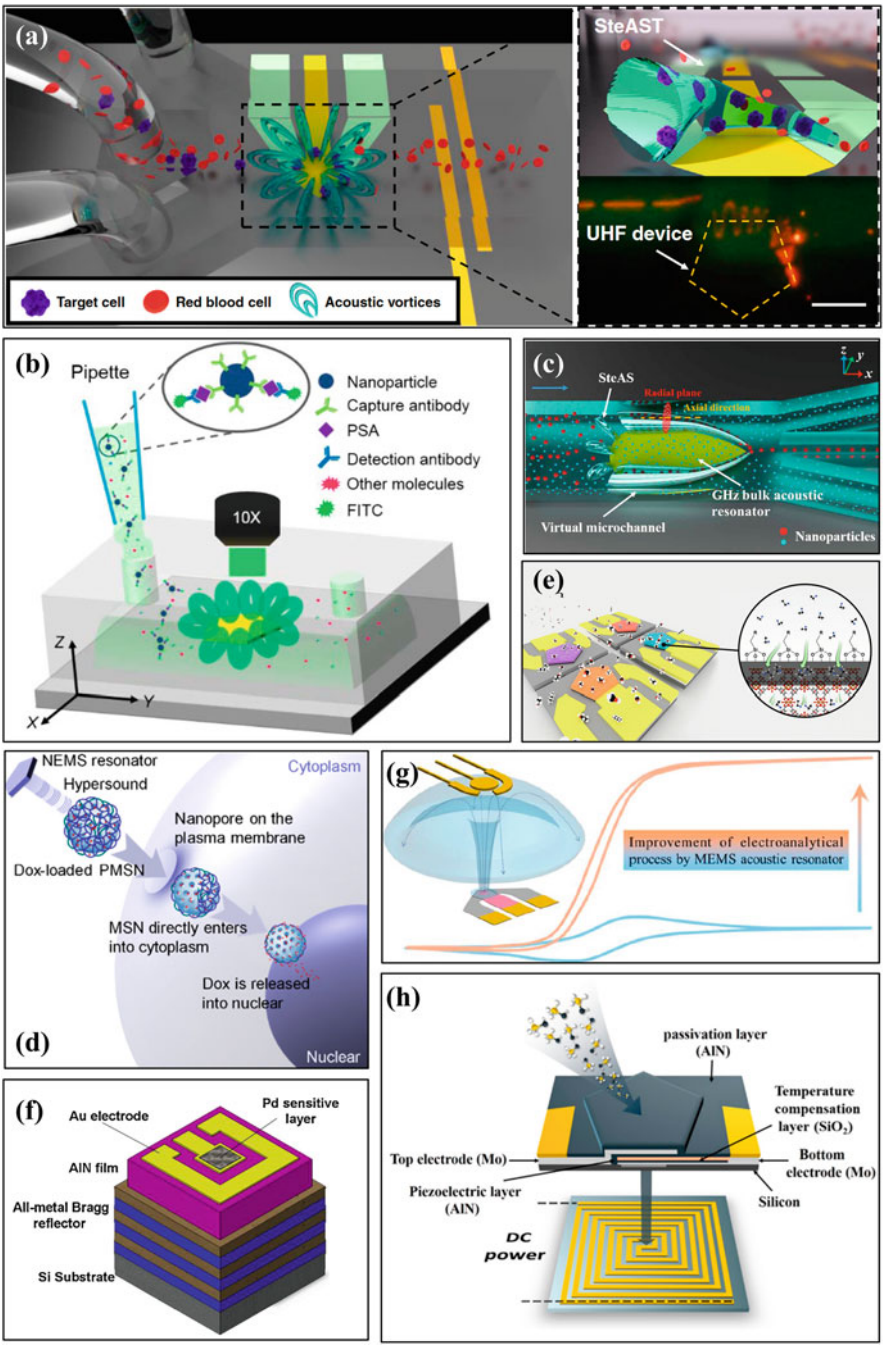

Fig. 1 FBAR used as actuators and sensors. (**a**) Illustration of the particle manipulation platform [6] (reprinted with permission from Springer Nature). (**b**) Illustration of the biomolecular enrichment platform. © [2019] IEEE. Reprinted, with permission, from [8]. (**c**) Schematic of exosome separation based on the virtual microchannel. Reprinted with permission from [11]. (**d**) Schematic

2 Fundamentals of FBAR Gas Sensors

2.1 Sensing Mechanism of FBAR Devices

In 1959, Sauerbrey conducted a pioneering study demonstrating the potential of bulk acoustic wave (BAW) resonators as mass sensors. He developed an equation that allows the measurement of the characteristic frequency and its variations by utilizing the resonator as the frequency-determining component within an oscillator circuit [25]. The Sauerbrey equation can be defined as follows:

$$\Delta f = -\frac{2{f_0}^2}{A\sqrt{\rho_q \mu_q}}\Delta m \tag{1}$$

Sauerbrey's equation is applicable to systems only if the following three conditions are met:

1. Rigidity of the deposited mass
2. Even distribution of the deposited mass
3. Limit on frequency change. $\Delta f/f$ is less than 2%

The equation illustrates a linear correlation between the mass applied to the surface of the resonator and the shift in resonant frequency. This relationship can be comprehended by considering that the additional mass loading layer increases the path length of the acoustic wave, thereby extending its half wavelength and reducing the resonant frequency [25].

The equation could estimate the natural resonant frequency of an acoustic resonator:

$$f_0 = \frac{1}{2d}\sqrt{\frac{c}{\rho}} \tag{2}$$

By using Eqs. (1) and (2), the approximate equation for nearly all resonant-based mass sensor types becomes:

Fig. 1 (continued) representation of hypersound-triggered intracellular delivery of Dox-loaded PMSNs into cells. Reprinted with permission from [14]. Copyright (2019) American Chemical Society. (**e**) Illustration of the FBAR VOC sensing. Reprinted with permission from [20]. Copyright (2020) American Chemical Society. (**f**) Description of the FBAR hydrogen sensing device. Reprinted from [24], Copyright (2011), with permission from Elsevier. (**g**) Description of the sensing enhanced FBAR-electrochemical sensing system. Reprinted with permission from [10]. Copyright (2019) American Chemical Society. (**h**) Temperature modulation a multiparameter FBAR sensor array for VOCs sensing. Reprinted with permission from [19]. Copyright (2019) American Chemical Society

$$\frac{\Delta f}{f_0} \approx -\frac{\rho_m d_m}{\rho_0 d_0} \tag{3}$$

The equation defines the relationship between the resonant frequency (f_0), the frequency shift (Δf), the density (ρ_m) and thickness (d_m) of the added layer, and the density (ρ_0) and thickness (d_0) of the resonator. This equation demonstrates that the resonant frequency of an acoustic resonator is directly proportional to the mass of a material absorbed by the resonator. The negative sign in the equation indicates that as the mass loading increases, the resonant frequency of a resonant sensor decreases.

In the gas-sensing area, FBAR works as a mass-based sensor. The most crucial factors of FBAR gas sensors are mass sensitivity, the limit of detection, and mass detection resolution.

Sensor sensitivity is commonly defined as the change in the output signal obtained with an incremental change in the input signal being detected. In the case of an acoustic wave mass sensor, the mass sensitivity refers to the characterization of the frequency change per unit mass accumulation on the sensor. It is typically expressed in units of [frequency]/[mass].

It is important to note that there are various definitions of mass sensitivity, leading to the use of different units in the literature. Some alternative units used to describe mass sensitivity include [frequency]/[mass per unit area], [ppm]/[mass per unit area], and [ppm]/[ppm]. For a piezoelectric mass sensor, the mass sensitivity (S_m) can be defined as follows:

$$S_m = \lim_{\Delta m \to 0} \left(\frac{\Delta f}{f_0}\right) \cdot \left(\frac{1}{\Delta m}\right) \tag{4}$$

Let Δm represent the mass added to the sensor per unit area. f_0 denotes the resonant frequency, while Δf represents the absolute frequency shift before and after the mass addition [25].

A mass sensor outputs a response within a range known as the dynamic range. The lower end of the dynamic range is determined by the sensor's mass detection resolution. Before delving into the resolution of mass detection, it is essential to introduce the concept of the minimum detectable relative resonant frequency change, denoted as L:

$$L = \frac{\Delta f_{\min}}{f_0} \tag{5}$$

where $\Delta f_{\min}$ is the minimum detectable resonant frequency change.

L can be affected by the quality factor of the resonator, the properties and thickness of the sensitive material, interactions between the material and gas molecule, ambient environmental conditions, and system noise in measurement

equipment or circuits [25]. And the mass detection resolution R is determined by both mass sensitivity S and the minimum detectable relative frequency change L:

$$R = \frac{L}{S} \tag{6}$$

2.2 Limitations of FBAR Gas Sensors

Although FBAR has shown great potential to work as a gas sensor, many factors (noise, temperature, humidity, etc.) still limit its performance.

Noise

Micromachined BAW resonators [26], which can be designed in either a suspended configuration, i.e., FBAR, or in alternative configurations, e.g., solidly mounted resonator (SMR), have become indispensable components in the seamless integration of high Q filters and oscillators (Fig. 2).

Typically, the phase noise present in microwave oscillators stems from active devices, whereas the resonator itself is purely passive, contributing solely a white noise component associated with thermal effects. This holds true for LC resonators or dielectric resonators, where only thermal noise or the introduction of external deterministic factors, known as microphonic noise, may be observed (effective mitigation of microphonic noise can be achieved through the utilization of suitable mechanical shielding techniques).

Contrarily, it is known that BAW resonators produce 1/f noise, at least for those operating in the Megahertz region, which has been extensively researched. The source of this noise is still a matter of debate, but it is linked to the vibrations of crystal phonons. When exposed to a strong microwave signal, these phonons alter the parameters of ultrasound propagation, causing fluctuations in the resonant frequency. Consequently, this phenomenon adversely affects the performance of gas-sensing applications by degrading their functionality.

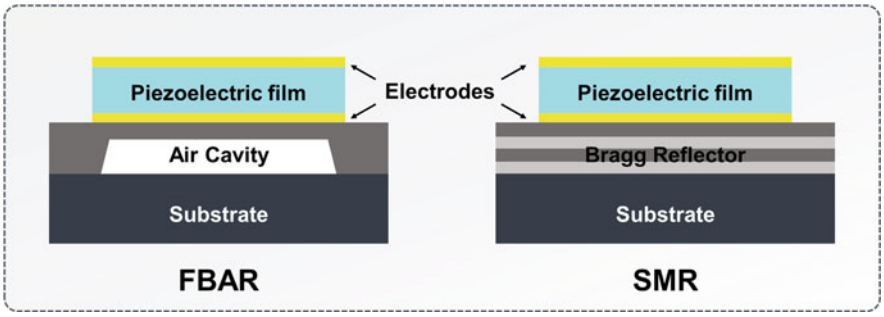

Fig. 2 Schematic of an air-cavity type FBAR and a solidly mounted resonator (SMR)

Temperature

In certain applications, where the resonant frequency is influenced by temperature variations, it becomes necessary to employ a temperature-compensating technique. Passive temperature compensation utilizing SiO_2 has been proven effective in addressing the negative temperature coefficient of frequency typically exhibited by conventional FBARs. Unlike other materials, SiO_2 displays a distinctly positive temperature coefficient of frequency. This compensation method aims to minimize frequency drift or fluctuation in relation to temperature variations. A study demonstrated that an FBAR integrated with SiO_2 compensation exhibited less than 80 parts per million (ppm) frequency drift over a temperature range of 120°C [27].

The impact of the SiO_2 layer on mode separation (TE and TS modes), effective electromechanical coefficient, and temperature compensation has been simulated for both the first and second harmonics of TE mode and TS mode. Opting for second harmonic operation involves balancing trade-offs between temperature compensation and electromechanical coupling, as well as between operating frequency and quality factor [25].

The voltage-controlled oscillator (VCO) utilizing FBAR technology exhibits a high tunability of $-4{,}305$ ppm V^{-1}. To maintain precise frequency stability within 1 ppm K^{-1} across a temperature range of 5°C, a control voltage is applied to the VCO [28]. A temperature-compensated 1.5 GHz FBAR is achieved using digitally switched capacitors, ensuring a frequency drift of only ±10 ppm over a temperature range of 0–100°C (Fig. 3) [29].

A lateral-field-excited shear mode FBAR has been reported to exhibit a positive thermal coefficient of resonant frequency [30]. This could be due to the fact that the lateral thermal expansion of ZnO is significantly greater than its thickness-directed thermal expansion, leading to an increase in shear wave velocity with temperature. Consequently, the apparent stiffness tensor related to shear coupling (c_{44}) may increase with temperature [25].

Temperature can have an indirect influence on sensor performance due to its effect on fluid properties, including viscosity. However, the specific impact of

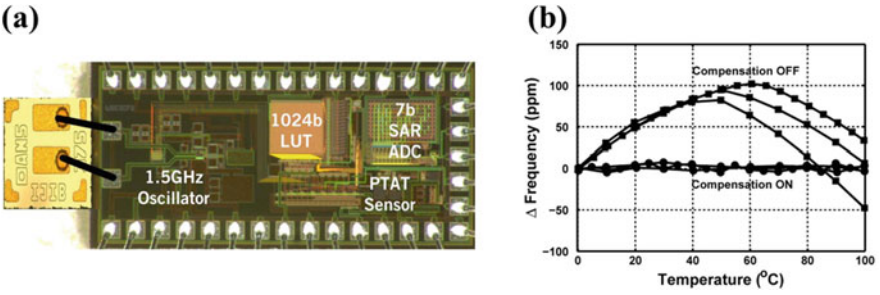

Fig. 3 (**a**) Chip micrograph of FBAR/CMOS frequency reference. (**b**) Frequency drift over temperature for three samples with compensation. © [2010] IEEE. Reprinted, with permission, from [29]

temperature on the FBAR can be measured and accounted for separately from the effects caused by the fluid being studied [25].

3 Recent Advances in FBAR Gas Sensors

FBAR has been widely used in the gas sensor field as a quality sensor. In the following, we will discuss the development status of FBAR in the field of gas sensing, from sensitive membranes, electronic noses, integrated sensors, system integration, and micro-chromatographic detectors.

3.1 FBAR Gas Sensors Using Different Sensing Materials

While the Sauerbrey equation indicates that any mass loaded onto the resonator will cause a shift in the resonant frequency, sensors are typically only designed to detect one material. A detection material can be added to the surface for selective or more sensitive detection of gas analytes. It is common to combine multiple types of sensitizers into a single sensitization layer. Common sensitive membranes include polymers, monolayers, metal-organic frameworks (MOFs), graphene, carbon nanotubes, etc.

3.1.1 Polymer-Based Sensors

Polymers are long-chain or large molecules built by linking repeated chemical units. Each polymer molecule may consist of hundreds, thousands, or even millions of repeating units. Due to their wide range of properties, synthetic and natural polymers play an essential role in daily life. Polymer is the most widely used sensitive film in the gas sensor due to its excellent adsorption performance. Since the mid-1990s, surface acoustic wave (SAW) resonator and quartz crystal microbalance (QCM) have been coated with polymers for VOC sensing [31, 32]. Pure or functional polymers are widely used because they are cheap and easy to synthesize, buy, and use. Of course, due to the volume adsorption characteristics of the polymer itself, its sensitivity is low, and the response time is long. The most used polymers are PDMS, PIB, PI, PEI, PMMA, etc.

Ruby et al. first reported the viability of FBARs coated with polymer for gas sensing [33]. Polyimide was coated on the surface of FBAR by spin coating to form a thick film with a controllable thickness of 50–650 nm. Here the resonance frequency shift is caused by an increase in the polymers' effective mass by absorbing water molecules. A nearly linear decrease in frequency with increasing humidity is observed. A sensitivity of 6.8 kHz/% RH has been extracted. Also, based on polyimide films for humidity measurement, Liu et al. proposed a novel FBAR design

based on polyimide film [34]. The PI film was employed to simultaneously provide multifunction for the structural supporting and humidity sensing, first used in the back-trench FBAR. It is proved that the sensitivity reaches +67.3 kHz/% RH (about 64 ppm/%) between 15% RH and 85% RH, which is 39 times higher than the sample without PI film.

Multiple polymers are applied to the sensor array, which will adjust the sensitivity of each sensor in the array, selectively absorbing different types of gas vapors to identify the unique chemical composition of their odors. Lee et al. coated the FBAR array with six different polymers: PVP, PIB, PVP40, PVPy, SAA, and PVA [35]. The results show that toluene has an excellent affinity for PIB, a polymer with nonpolar and high dispersive force. Ethanol has a significant response to polar proton/alkaline polymer PVPy. Similarly, polar aprotic ethyl acetate interacts well with acidic SAA polymers. In addition, acetone vapors with polar and acidic polymers such as PVP and SAA show very selective patterns. This characteristic gas–polymer interaction pattern confirms the polymer-coated sensor's high selectivity to these solvents, which form the basis of many odors.

Polymer suspension coating has disadvantages, such as poor uniformity and challenges in controlling film thickness. To solve these problems, Liu et al. proposed a novel method to adjust FBAR resonant frequency using a layer-by-layer (LBL) self-assembly method [36]. By simply controlling the concentration of the polymer and the number of deposition layers, precise adjustment of FBAR resonance frequency can be achieved in Fig. 4. Five layers of PAA/PVP bilayer assembled were modified onto the surface of FBAR. It was found that the signal enhancement of LBL coating may be due to the porous structure of the multi-layer coating that can absorb more n-propanol vapor. This demonstrates the ability of FBAR's LBL polymer coating to functionalize sensor surfaces for chemical sensing applications. Twenty layers of self-assembled poly (sodium 4-styrene sulfonate)/poly (diallyldimethyl ammonium chloride) film were coated on the surface of temperature-compensating FBAR by LBL method for the detection and identification of six VOCs (methanol, ethanol, acetone, isopropanol, cyclohexane, and toluene) [19].

Some research groups use finite element analysis (FEA) to simulate the response of FBAR in a gas environment and have achieved some results. The development of powerful FEA solvers that can handle millions of elements has opened up new opportunities to advance the use of resonators. Their performance for sensing application can be improved by optimizing parameters such as acoustic impedance characteristics [37]. Johar et al. analyzed and summarized the effects of the thickness and area of two polymers (PIB and polyethylene) on resonance characteristics using finite element simulation [38]. The simulation results of toluene gas showed that the sensitivity of the PIB sensor is twice that of polyethylene because the distribution coefficient of PIB/toluene is twice that of polyethylene. The author also optimized the response of the flexible FBAR with surface-modified PDMS to toluene gas by using finite element simulation [39]. The sensor was exposed to toluene gas at concentrations ranging from 0 to 500 ppm, and the resonant frequency decreased, achieving a sensitivity of 12 kHz/ppm. Guo et al. proposed a model for the

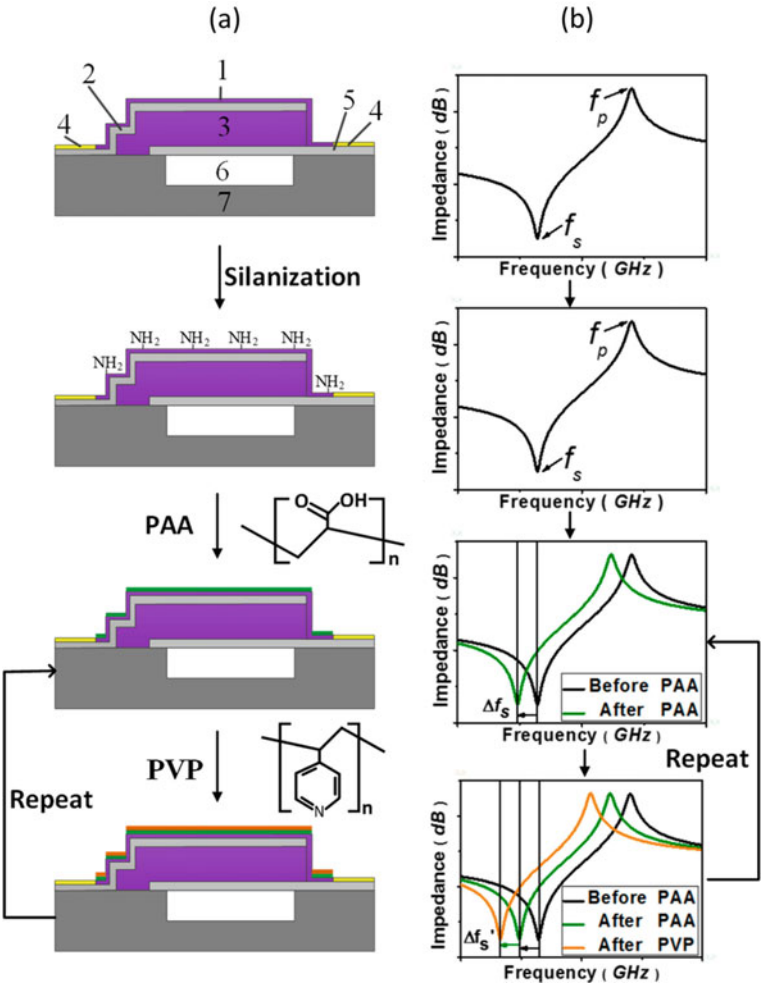

Fig. 4 (**a**) Cartoon showing the growth of PAA/PVP bilayers on FBAR surface through molecular LBL self-assembly approach and (**b**) the series resonant frequency shift of FBAR according to the impedance characteristic. Reprinted with permission from [36]. Copyright (2015) American Chemical Society

interaction between the diaphragm embedded with FBAR and the sensing layer [40]. This model uses finite element analysis based on the equivalent principle of polymer swelling. Simulation results show that the resonant frequency shift of the output of the steam sensor changes linearly with the concentration of steam, and the sensitivity of the sensor to chloroform is about 2.5 Hz/ppm.

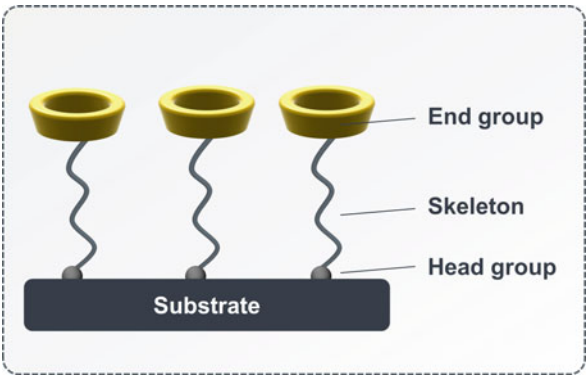

Fig. 5 Structure of a self-assembled monolayer

3.1.2 Monolayer-Based Sensors

Monolayers, sometimes referred to as self-assembled monolayers (SAMs), are highly ordered 2D arrays of molecules that spontaneously grow on various substrate surfaces (see Fig. 5) [41]. The head groups of SAMs bind to the surface, while the skeleton, composed of aromatic oligomers or aliphatic chains, is responsible for molecular ordering. End groups define the surface morphology and functionality of SAMs and can be further modified for specific purposes, such as immobilizing target molecules.

In 2013, Kim et al. demonstrated that antibody-SAM-modified FBARs can be used to detect target antigens [42]. Using Langmuir Blodgett technology, Lu et al. coated four 4.4 GHz FBAR resonators with different supramolecular SAMs: calix[8] arene, porphyrin, β-CD, and CB [8] as shown in Fig. 6 [15]. Supramolecular monolayers are used as advanced sensing interfaces for improving sensing selectivity and recognizing different VOCs, which makes FBAR suitable for analyzing adsorption isotherms and kinetics of VOCs.

Then, Chang et al. applied nine different SAMs as gas-sensitive materials to coat the FBAR sensor and discussed the effect of functional group properties, in terms of their hydrophilicities, length, and functional group densities, on gas surface interaction [43]. Chen et al. first used a transfer method to apply a single layer of graphene onto the surface of SMR and seamlessly integrate the graphene field-effect transistor (FET) with the resonator. This integration resulted in the formation of a dual-mode gas sensor capable of detecting gas molecules through two independent physical processes: mass attachment and charge transfer (Fig. 7). These dual signals generated by graphene allow for the identification and quantification of target gases, reflecting their inherent properties [44].

On this basis, Zhao et al. introduced a surface modification strategy to enhance the sensitivity of FBAR gas sensors exposed to ammonia vapor. They achieved this enhancement through the functionalization of graphene oxide (GO) using oxygen plasma treatment [45]. The oxygen plasma treatment of the GO-coated sensor significantly improved its sensitivity compared to a freshly prepared GO-coated

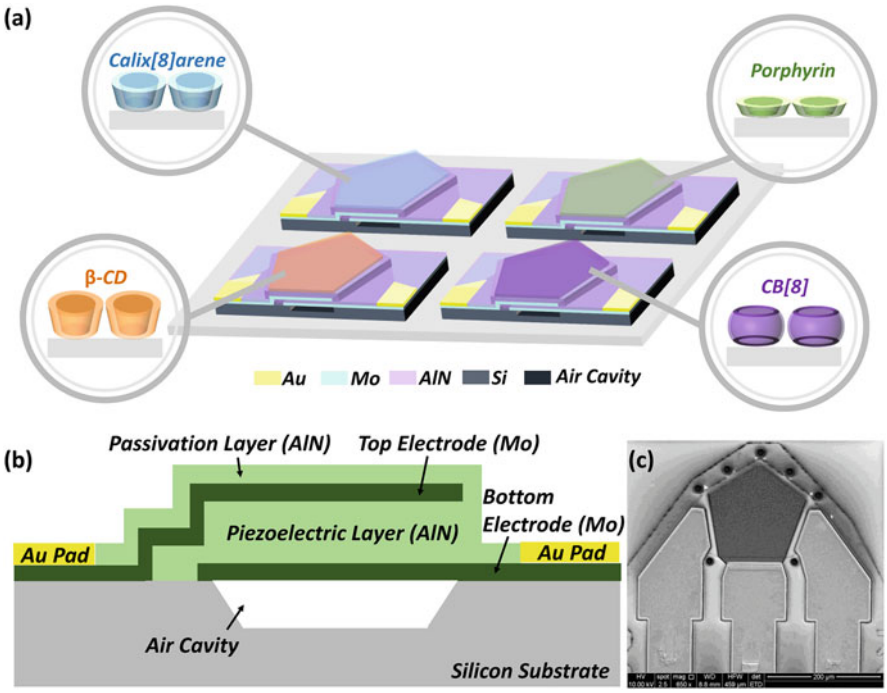

Fig. 6 (**a**) Schematic of an FBAR sensor array functionalized with four supramolecular monolayers, (**b**) sectional view of the FBAR structure, and (**c**) top view of scanning electron micrograph image of an FBAR. Reprinted with permission from [15]. Copyright (2015) American Chemical Society

sensor (Fig. 8). The treatment induced numerous defects uniformly distributed across the GO surface, creating additional binding sites for gas molecules.

3.1.3 MOF-Based Sensors

MOFs are a class of compounds consisting of metal ions or clusters coordinated to organic ligands to form 1D, 2D, or 3D structures. They are a subclass of coordination polymers, with the unique feature that they are often porous. Since their discovery, MOFs have attracted much attention and become a rapidly growing material category. Due to its unique structure (topologically diverse MOFs can be synthesized with different metal nodes and different coordination number organic linkers), individual characteristics (ultra-high porosity (up to 90% free volume), and large specific surface area (BET specific surface area up to 7,000 $m^2\ g^{-1}$). With pore volumes up to 4.4 $cm^3\ g^{-1}$) [46], adjustable pore sizes/shapes, and adjustable inner surfaces, functional MOFs have great potential for application in many fields such as

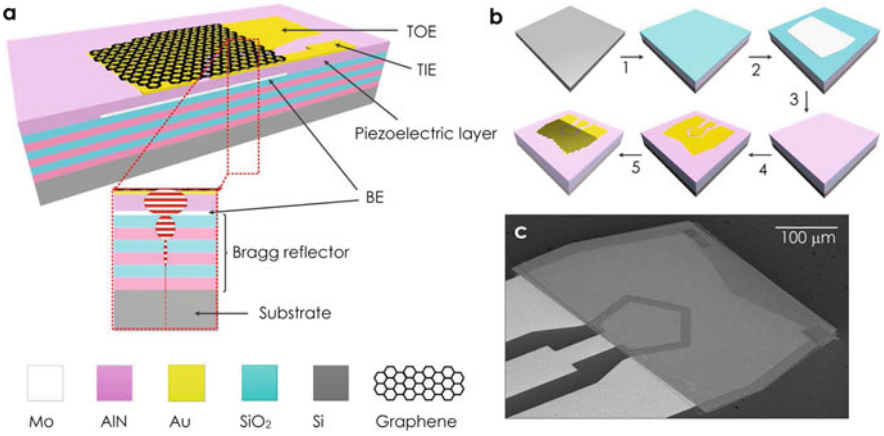

Fig. 7 (**a**) Cross-sectional illustration of the dual-mode gas sensor. From bottom to top are high-resistivity silicon substrate, Bragg reflector (containing 6 AlN and SiO_2 layers to attenuate acoustic waves leaking to the Si substrate (inset)), bottom electrode (BE), piezoelectric layer, top electrodes (TIE and TOE), and monolayer graphene film. (**b**) The entire process flow includes Bragg reflector deposition (1), BE deposition and patterning (2), piezoelectric layer deposition (3), TIE/TOE deposition and wet etch (4), and graphene transfer and patterning (5). (**c**) SEM image of a completed device. Scale bar is 100 μm. Reprinted with permission from [44]. Copyright (2016) American Chemical Society

gas adsorption [47, 48], catalysis [49–52], optoelectronics [53], bioimaging, and energy storage and conversion [54–56].

Wang et al. disclosed a simple coating process of MOFs on FBARs, as shown in Fig. 9. A MOF film (ZIF-8) can be formed on AlN by soaking FBAR in a mixture of freshly prepared $Zn(NO_3)^2$ (25 mM, 10 mL) solution and 2-methylimidazole (mIm) (50 mM, 10 mL) solution [57]. After washing with water and methanol, the resulting film was dried under nitrogen flow. By repeating this process many times, the thickness of the film can be increased. The frequency shift produced by the MOF coating is about 1 MHz. The MOF-coated FBAR with ethanol vapor gets to equilibrium in seconds and can be recovered entirely in seconds by nitrogen, indicating rapid adsorption and desorption. The sensitivity of FBAR gas sensor is increased by 10–20 times after MOF coating.

Based on the above work, Yan et al. found that the surface hydrophilicity and hydrophobicity of MOFs can be regulated by PDMS coating and subsequent monolayer self-assembly. HKUST-1 grows on the FBAR surface by a layer-by-layer path, and then the PDMS layer is coated on HKUST-1 by chemical vapor deposition. Finally, a self-assembly layer can be further introduced on the PDMS surface

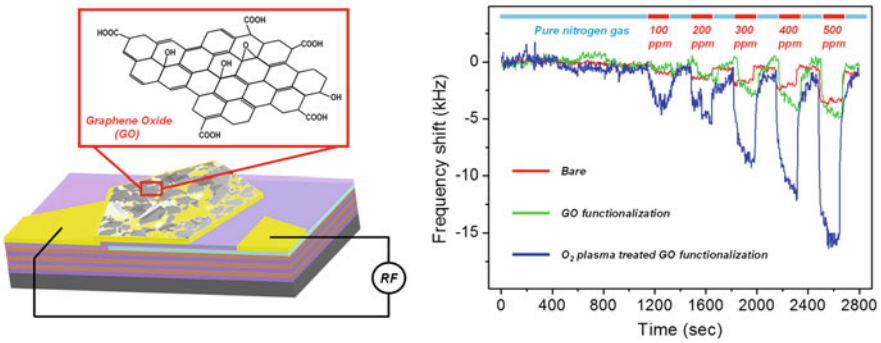

Fig. 8 Schematics of the SMR modified with base-rich GO sheets to enhance surface gas adsorption. Reprinted with permission from [45]. Copyright (2017) American Chemical Society

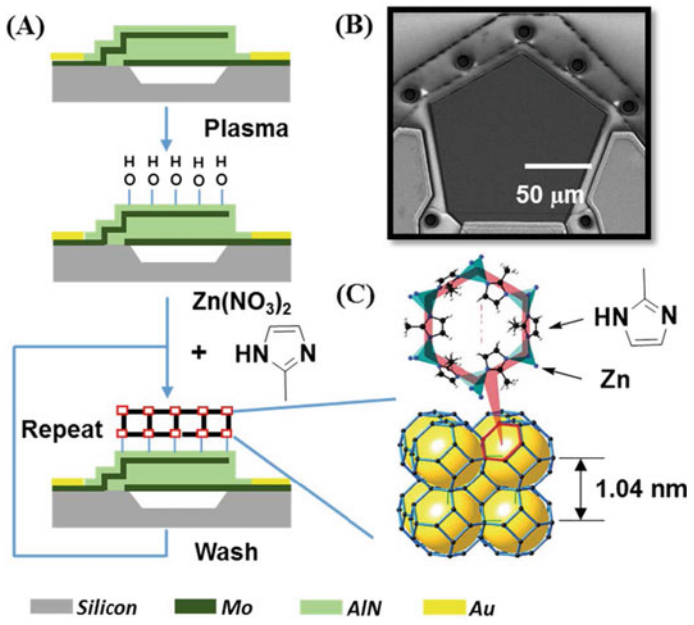

Fig. 9 (**a**) Process showing that FBAR was modified with ZIF-8; (**b**) top SEM view of FBAR; (**c**) structure of ZIF-8. © [2017] IEEE. Reprinted, with permission, from [57]

[20]. The experimental process is shown in Fig. 10. The preparation process is simple and can be applied to other sensors and MOFs. It is demonstrated that this kind of surface treatment significantly improves the water stability of MOFs from less than 1 h to more than 4 h.

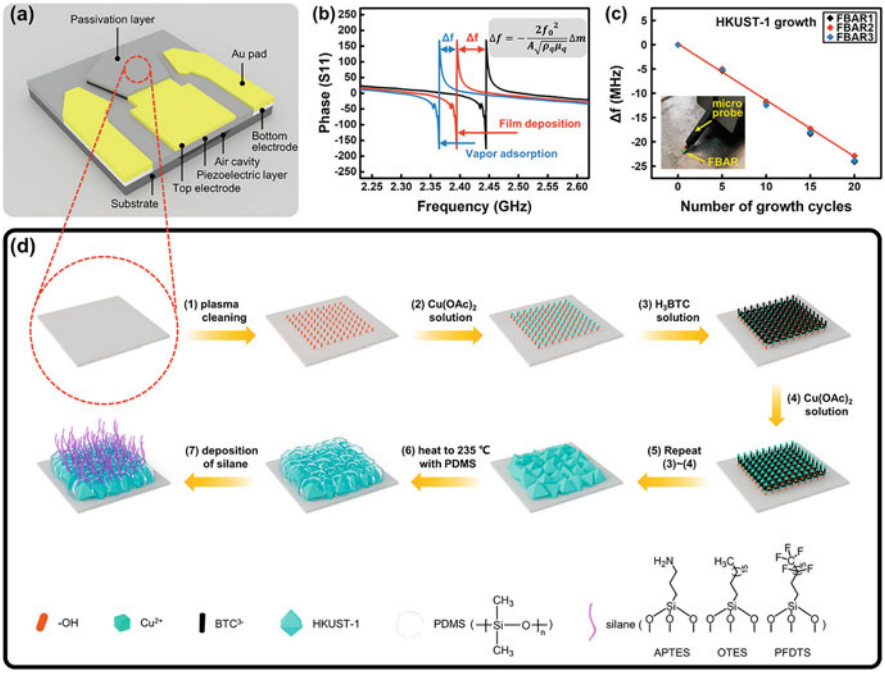

Fig. 10 (**a**) Illustration of the FBAR device. (**b**) Working principle of FBAR as a gravimetric sensor. (**c**) The plot of frequency shift (Δf) with growth cycles (the fitting line indicates a linear relation between Δf and deposition cycle). (**d**) Absorption layer fabrication and surface modification process. Reprinted with permission from [20]. Copyright (2020) American Chemical Society

3.1.4 Other Film-Based Sensors

Many other materials also play an important role in FBAR gas sensing, such as carbon nanotubes, thin metal film materials, and composite film materials, which tend to be more sensitive, selective, and stable than single materials. Therefore, composite materials are more and more favored by researchers. Wang et al. assembled layer-by-layer carbon nanotubes/polyethylene imine multilayers on the surfaces of FBAR resonator as a sensitive coating to detect trace formaldehyde vapor in Fig. 11 [58]. The multilayer films have a random porous structure and provide a larger specific surface area for gas adsorption and diffusion. Because the amine group in the polyethylene imine has a strong affinity for formaldehyde, when exposed to gaseous formaldehyde, the attachment of gaseous molecules leads to a slight decrease in the resonance frequency, making it easy for the sensor to detect formaldehyde at the ppb level within the response time of 1 min.

Benetti et al. deposited two kinds of thin films (Pd and Co-TPP(Co-tetra-phenyl porphyrin)) on the reverse side of FBAR using thermal evaporation with a thickness of 15 and 36 nm for Pd and Co-TPP, respectively [59]. The results showed the ability

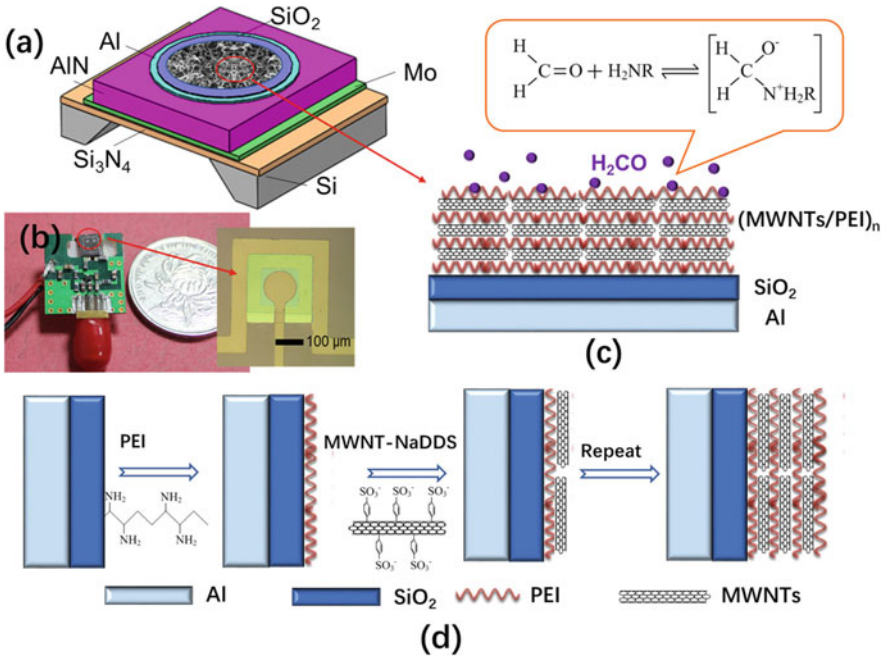

Fig. 11 (**a**) Schematic structure of the FBAR sensor, (**b**) photographs of the fabricated device on a PCB, (**c**) $(MWNTs/PEI)_n$ multilayer assembled on the top of FBAR, (**d**) LBL assembly process of the $(MWNTs/PEI)_n$ multilayer [58]. © IOP Publishing. Reproduced with permission. All rights reserved

of the device to detect concentrations of H_2, CO, and ethanol as low as about 2, 40, and 500 ppm, respectively. Similarly, Chen et al. developed a Pd-functionalized FBAR for hydrogen detection [24]. A Pd film with a thickness of 50 nm was coated on the electrode surface as a unique layer to capture hydrogen. Hydrogen absorption will cause a change in the elastic properties of the Pd layer, which will affect the resonance frequency of the resonator. The Pd-functionalized film cavity has a rapid, sensitive, reversible, and repeatable response to 0.3–2% hydrogen. They also modified the gold electrode with a self-assembled Cu^{2+}/11-mercaptodecanoic acid composite layer as a special coating for trapping organophosphorus compounds [60]. The chemically modified FBAR has a rapid, sensitive, reversible, and repeatable reaction to the vapor of dimethylphosphonate (a nerve agent irritant) at concentrations as low as 100 ppb. Penza et al. prepared an AlN/Si_3N_4-based FBAR on a silicon substrate with a resonance frequency of 1.045 GHz. The surface was decorated with a nanocomposite material composed of single-walled carbon nanotubes and cadmium arachidate [61]. The sensing device has high sensitivity (e.g., acetone: 12 kHz/ppm; ethyl acetate: 17.3 kHz/ppm), fast response (within 2–3 min), and slow reversibility (within 1 h).

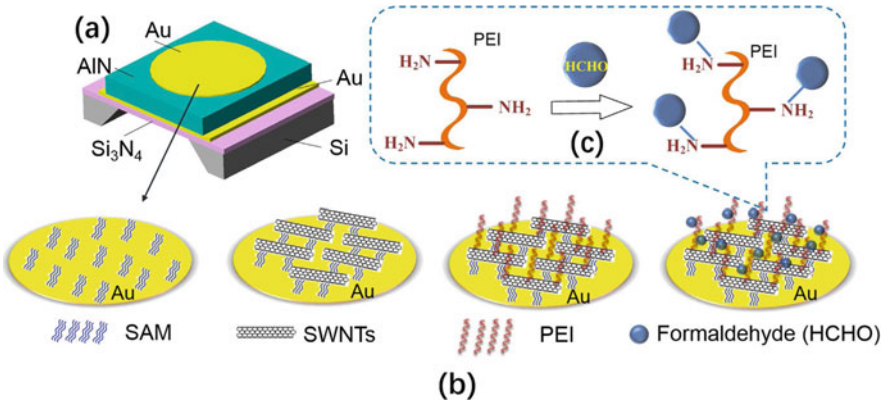

Fig. 12 Schematic structure (**a**), surface functionalization of Au electrode (**b**), and sensing mechanism (**c**) of the FBAR sensor assembled with PEI-modified SWNTs for formaldehyde detection. Reprinted from [63], Copyright (2018), with permission from Elsevier

Amino-polysiloxane was used as CO_2 and humidity-sensitive material, and ethyl cellulose was used as humidity-sensitive material. Hoffmann et al. used two FBARs coated with two materials to detect CO_2 and water vapor molecules [62].

Song et al. used self-assembled polyethylene imine-modified single-walled carbon nanotubes as sensitive coatings for FBAR formaldehyde sensors shown in Fig. 12 [63]. The PEI-modified single-wall nanotubes (SWNTs) on the FBAR surface showed excellent selectivity toward formaldehyde over those interfering organic vapors. The sensor has a reversible linear response to formaldehyde in the range of 50–400 ppb with a detection limit of 24 ppb. The response time and recovery time are less than 1 min.

3.2 FBAR Gas Sensors Used in Electronic Noses

3.2.1 Sensor Array-Based Electronic Noses

In 1961, Moncrieff proposed that coating multiple devices with multiple sensitive materials can provide complementary data, thus realizing the identification of multiple gases [64]. In the 1980s, with the development of computer technology and sensor technology, Persaud and Dodd of Warwick University and Ikegami and Kaneyasu of Hitachi Research Institute successively proposed the concept of an electronic nose [65]: the use of intelligent chemical array sensing systems to mimic the mammalian olfactory system for gas analysis (Fig. 13). Eventually, Gardner and Bartlett of the University of Warwick coined the term "electronic nose" in 1988. They defined it as "an electronic nose is an instrument, which comprises an array of electronic chemical sensors with partial specificity and an appropriate pattern-recognition system, capable of recognizing simple or complex odors" [66].

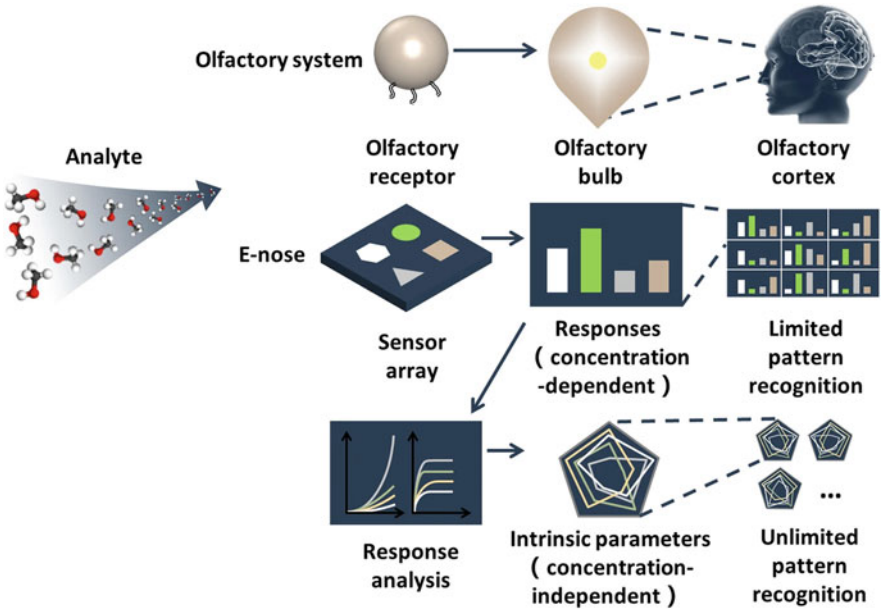

Fig. 13 Schematic illustration of the mechanism of olfactory system and electronic nose (e-nose) system (both concentration-dependent and concentration-independent) [43] (reprinted with permission from Springer Nature)

Lee et al. used FBAR array to form an electronic nose platform for indoor air monitoring and successfully identified and classified four gases, including ethanol, toluene, ethyl acetate, and acetone. Lu et al. reported a single molecular membrane-modified FBAR electronic nose system to detect VOCs [15]. By coating each resonator with a different supramolecular monomer layer, the selectivity of the sensor is improved. Each VOC has an independent sensor matrix (matrix parameters are calculated from the response curve), which is used for the fingerprint analysis of the electronic nose system, facilitating the identification and classification of VOCs. Zhao et al. demonstrated a novel e-nose system for VOCs detections composed of three high-Q piezotransduced single-crystal silicon bulk acoustic resonators (PSBARs) and functionalized with different SAMs. The different sensitivities of the PSBARs to VOCs are utilized to constitute unique identification codes for IPA, ethanol, hexane, and heptane detections and successfully realize discriminations of different VOCs [67]. The limit of detection for ethanol vapor is demonstrated to be as low as 25 ppm with a sensitivity of about 1.5 Hz/ppm (Fig. 14) [68].

For further data mining, we achieved multiple chemical functionalizations on FBAR array surfaces using SAM [43]. Adsorption isotherms of five vapors (methanol, ethanol, NPA, IPA, and acetone) on nine functional groups were successfully obtained. Accordingly, the adsorption energy constant and monolayer adsorption capacity were determined by fitting the adsorption isotherms to a BET equation. The desorption rate was determined by fitting a Johnson–Mehl–Avrami (JMA) equation

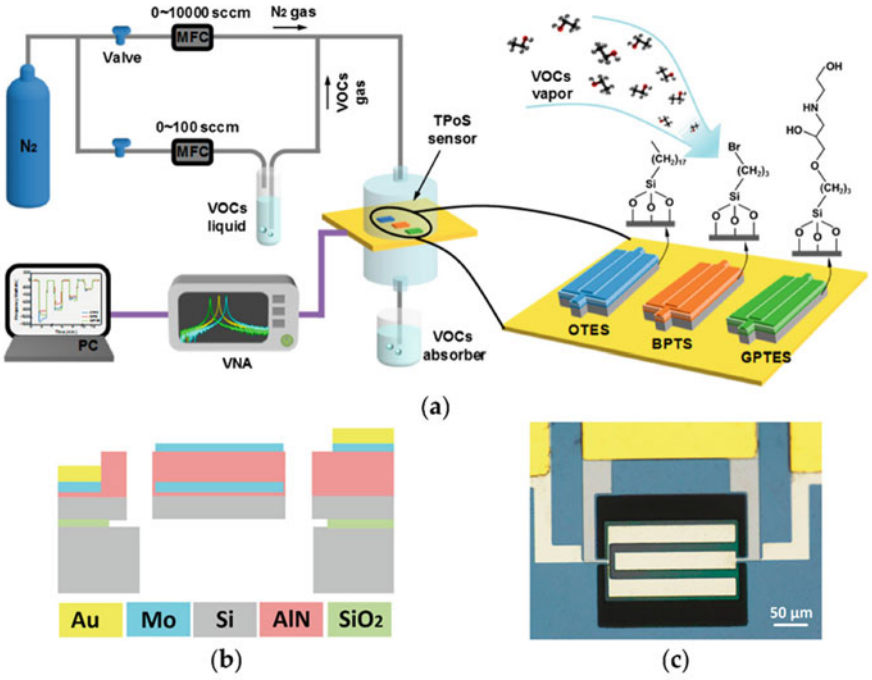

Fig. 14 (**a**) Schematic of the gas sensing setup and a piezotransduced silicon bulk acoustic resonator (PSBAR) sensor array; (**b**) schematic of the PSBAR structure; (**c**) an optical microscope graph of a PSBAR 120 μm in width and 200 μm in length [68] (reprinted with permission from MDPI)

[69]. Relying on the three parameters, concentration-independent fingerprints were well established (Fig. 15). Such a concentration-independent fingerprint library facilitates the discrimination of target VOCs using the sensor array, leading to a more reliable method for VOCs detections.

In the hybrid array gas sensing system, it was found that qualitative identification can be achieved through polarity analysis of Si-NW FET, quantitative concentration information can be obtained through polymer-coated FBAR, and detection is limited to ppm level [72]. A schematic illustration of the mechanism of the olfactory system and electronic nose system is shown in Fig. 16. The complementary properties of sensing elements provide higher analysis efficiency. The system can recognize a dual mixture of two types of CFC-113 and HCFC-141B.

Electronic nose arrays will inevitably increase in size due to the need to arrange multiple sensors. To ensure the output of multiple signals and achieve miniaturization simultaneously, a virtual sensor array (VSA) has been proposed recently. It is based on the principle that one individual sensor produces multidimensional output vectors like those generated from an electronic nose [73–75]. Pattern recognition algorithms are then adopted to process the output vectors for accurate identifications

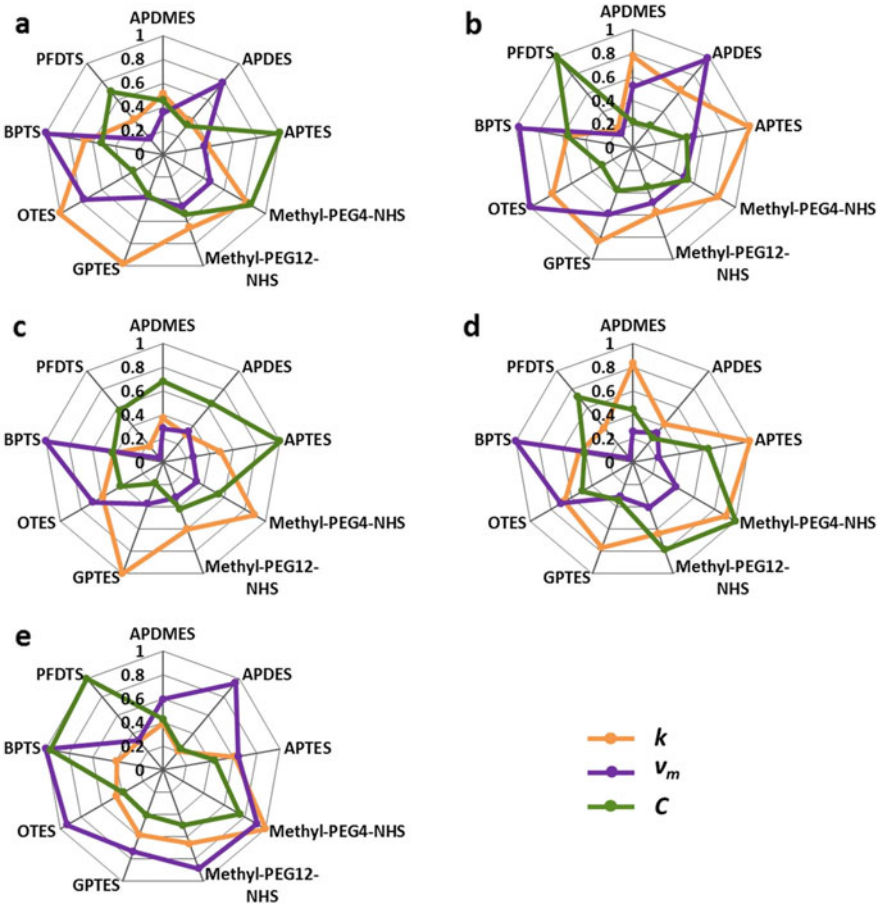

Fig. 15 Concentration-independent fingerprints of five VOCs: (**a**) methanol, (**b**) ethanol, (**c**) NPA, (**d**) IPA, and (**e**) acetone [43] (reprinted with permission from Springer Nature).While most electronic noses, either reported in the literature or available in the market, utilize a sensors array comprising of identical transducers, it is potentially possible to further optimize electronic noses with a sensors array operating on different transduction principles, usually known as "hybrid array" [70]. The hybrid array can increase the amount of chemically "orthogonal" information deduced from the independent response characters of each sensor. Chang et al. subsequently designed a novel multi-mode electronic nose that incorporates a mass-sensitive sensor and an electrosensitive sensor to detect VOCs [71]. In this system, the FBAR is used to obtain the qualitative information, and the silicon nanowire field-effect transistor (Si-NW FET) is used to collect the electrical information of the analyte. The hybrid array was applied to the identification of the ethanol-n-hexane mixture

of different VOCs. Recently multiple resonant modes of a single piezoelectric resonator have also been explored to develop VSA [17, 76]. Zeng et al. reported a

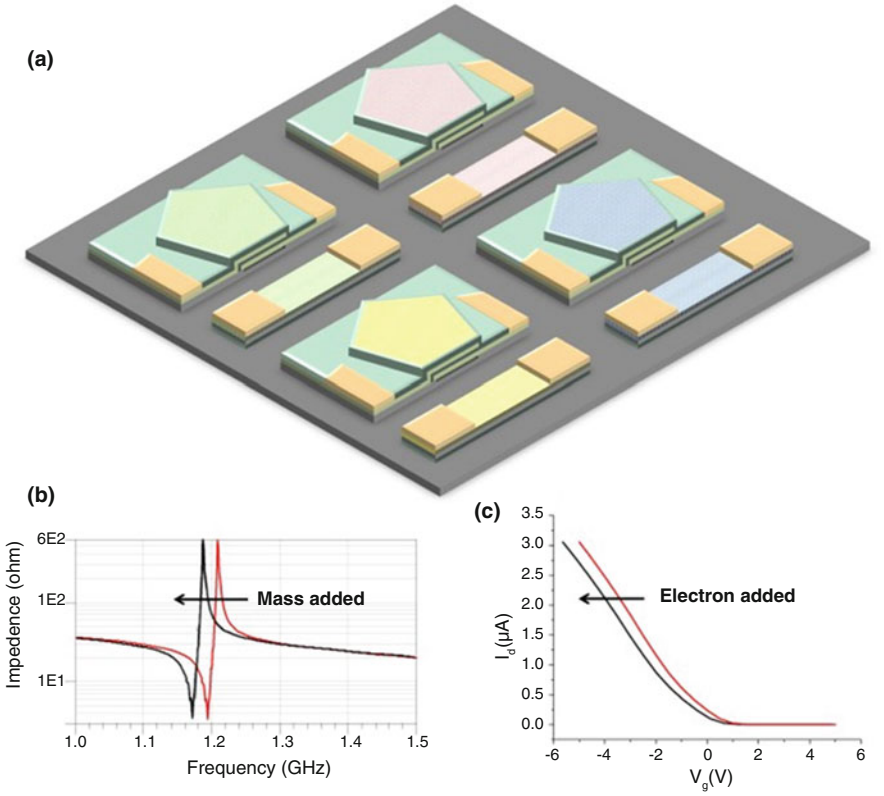

Fig. 16 (**a**) Schematic of the multimode e-nose based on FBAR and Si-NW FET array. Each sensor is modified by one kind of gas-sensitive material. (**b**) Sensing mechanism of FBAR. (**c**) Sensing mechanism of Si-NW FET. © [2016] IEEE. Reprinted, with permission, from [71]

multi-parameter VSA-based electronic nose system (Fig. 17) consisting of polymer-modified single-chip temperature-compensated FBAR (TC-FBAR), which can realize high-frequency scale FBAR multi-parameter virtual array system through temperature modulation for the detection and identification of VOCs (acetone, ethanol, cyclohexane, isopropanol, methanol, and toluene) [19]. The frequency shifts and impedance responses generated at different temperatures were measured and evaluated using principal component analysis (PCA) and linear discriminant analysis. Results showed that all analytes could be distinguished and classified with more than 97% accuracy.

Zhao et al. realized a VSA by seven different resonant modes of a PSBAR which can significantly reduce the complexity of a conventional e-nose system (Fig. 18) [17]. The single-chip VSA represents a novel generation of an e-nose system for VOC detection and identification. It gives a perspective to realize the gas discrimination by the single multi-mode sensor instead of the conventional e-nose based on the sensor array with various surface modifications.

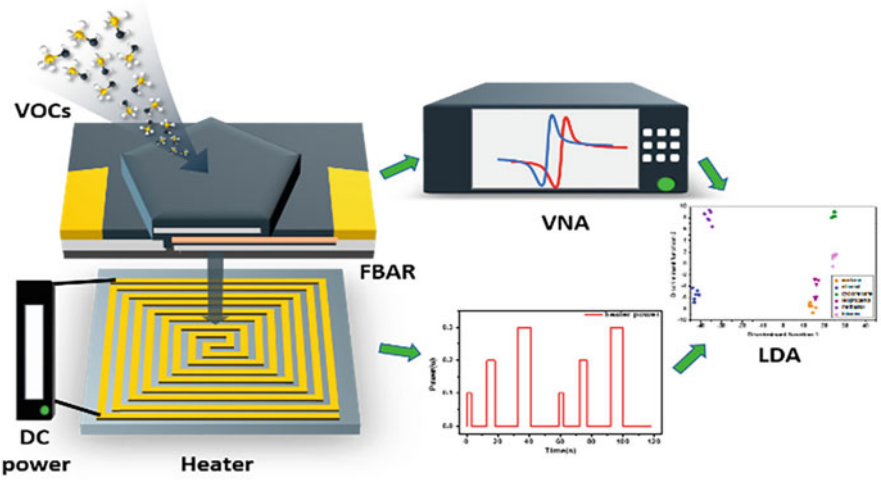

Fig. 17 Scheme of the temperature-modulated FBAR gas sensor with its surface chemically functionalized with PSS and PDDA. The heater between the FBAR and evaluation boards heats the FBAR through the programmable DC power supply module, changing the temperature of the FBAR. Reprinted with permission from [19]. Copyright (2019) American Chemical Society

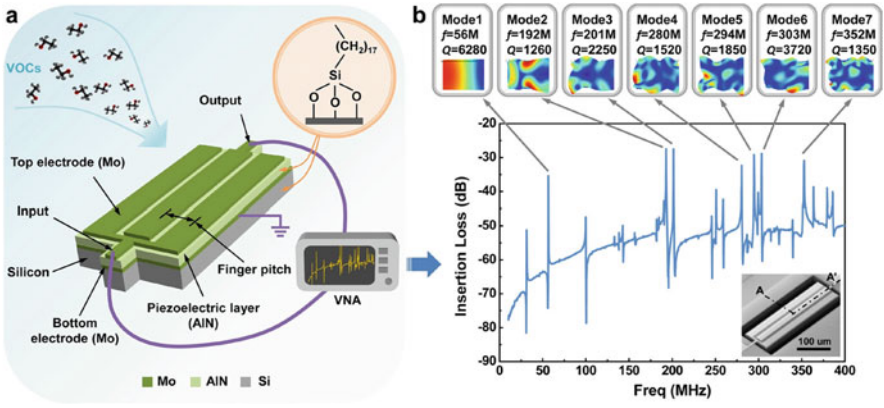

Fig. 18 Schematic illustration of PSBAR sensors and corresponding multi-mode resonances. (**a**) Scheme of the two-port PSBAR gas sensor with surface chemically functionalized trimethoxy (octadecyl) silane (OTES). (**b**) Large-span frequency responses of a PSBAR, where multi-mode resonances can be identified, and seven high-Q resonant modes were selected. The corresponding mode shapes are numerically calculated and displayed in sectional views. Colors represent the deformation of the mechanical mode. Reprinted from [17], Copyright (2018), with permission from Elsevier

3.2.2 Multimode Sensor-Based Electronic Noses

A sensor array is usually a collection of sensors using the same sensing mechanism. Although they are coated with different sensitive films, their differences are limited, and the output signals are of a single type. Such a single type of signal is often detrimental to subsequent data analysis and gas composition classification. Currently, a single-chip sensor array with multiple sensor mechanisms is proposed; multiple sensor modes are integrated into one chip to output multiple sensor signals. Increasing the difference of signal is conducive to analysis.

A dual-mode gas sensor based on FBAR and graphene FET was developed by Chen et al. to simultaneously measure the mass adsorption and charge transfer occurring at the sensing interface shown in Fig. 19 [44]. Four target gases, including NO_2, NH_3, C_2H_5OH, and $C_6H_{14,}$ were used to evaluate the function and performance of the device. The dual-mode gas sensor precisely measures the amount of gas molecules adsorbed on the graphene surface. The ability of simultaneous measurements of mass adsorption and charge transfer guides us to a more precise understanding of the interactions between graphene and various gas molecules.

Gao et al. designed a novel dual transduction gas sensor by integrating an FBAR and interdigitated electrodes (Fig. 20) [77]. Mass changes are detected by the shift of FBAR's resonant frequency, while resistance changes are detected by FBAR's integrated cross-interdigitated electrodes. The sensor material is formed by dripping a thin PEDOT: PSS conductive film onto the device. A configurable dual-mode oscillator circuit is also proposed to simultaneously read the sensor's frequency and resistance responses. The sensor is tested with five gases: methanol, ethanol-amyl alcohol, acetone, and tetrahydrofuran. The method of single chip integrated multi-

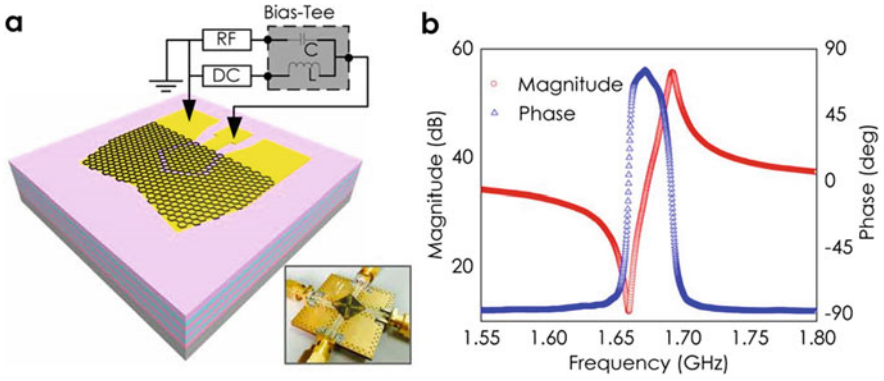

Fig. 19 (**a**) Test configuration and picture of the evaluation board (inset). The bias tee separates RF and DC signals from the same port and feeds them to the network analyzer and semiconductor parameter analyzer, respectively. (**b**) RF output of the device. Red and blue curves are the magnitude and phase of electrical impedance at various frequencies, exhibiting sharp transitions at series (1.660 GHz) and parallel (1.693 GHz) resonance frequencies. Reprinted with permission from [44]. Copyright (2016) American Chemical Society

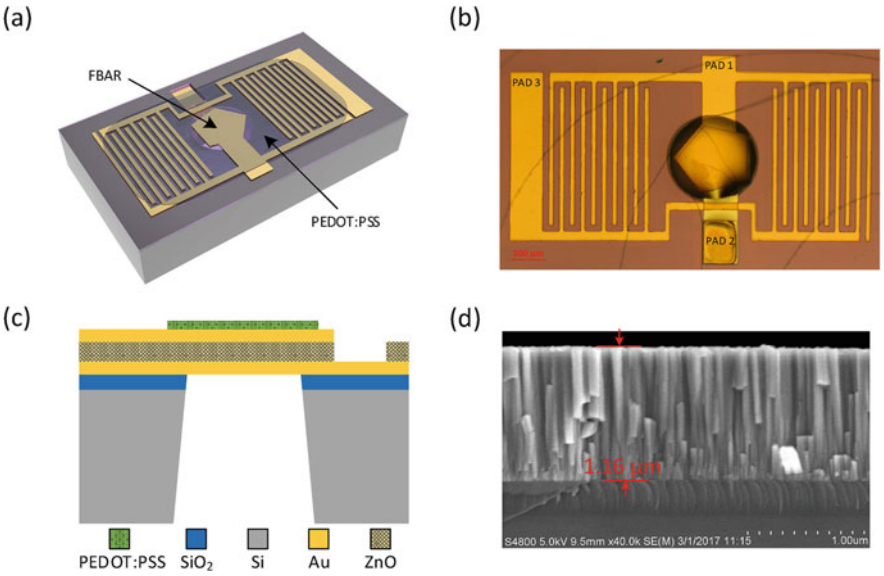

Fig. 20 (**a**) Diagram of the dual transduction gas sensor, which includes an FBAR in the center and interdigitated electrodes on the two sides. (**b**) Photo of the fabricated sensor. The dark circular area corresponds to the film structure of FBAR. (**c**) Cross-sectional diagram of FBAR. The acoustic waves are generated by the piezoelectric zinc oxide layer sandwiched between two gold electrodes. (**d**). Cross-sectional SEM image of the 1.16 μm ZnO layer grown on the substrate. Reprinted from [77], Copyright (2019), with permission from Elsevier

sensor is helpful to reduce the size of the gas sensor array, expand the sensing range of a single sensor, and reduce the false alarm rate of the gas sensor array.

Inspired by a previous article, Sun et al. developed a single-chip dual-transduction gas sensor for BTX detection, shown in Fig. 21 [22]. The sensor integrates an SMR and an interdigitated electrode in the resonant region to detect the shift of resonant frequency and the change in the resistance of the sensing material. Multiwalled carbon nanotubes (MWNTS) were used as sensing films and sprayed onto the surface of composite materials by inkjet printing. Since the carbon nanotubes are adsorbed to the gas analyte, their status can be recorded by the frequency signal and resistance signal of the sensor. This dual transduction mechanism makes it possible to improve the linear range and detection range of gas sensing.

3.3 System Integration of FBAR Gas Sensors

A system integration approach is adopted to build high-quality acoustic passive circuits together with CMOS circuits to miniaturize wireless hardware. It is possible to form close on-chip integration between acoustic devices and high-performance

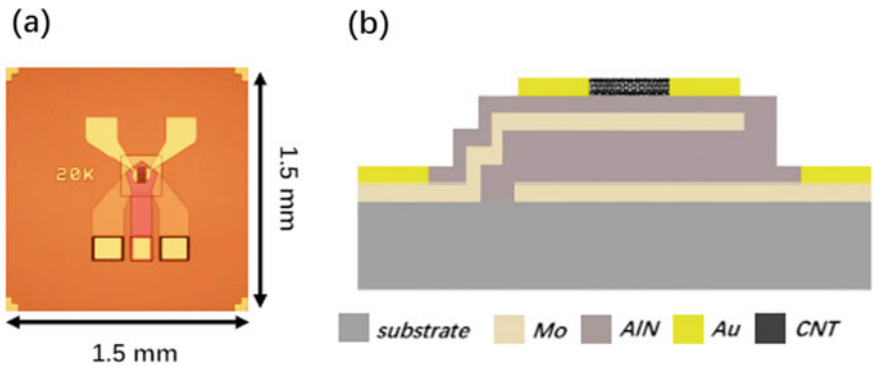

Fig. 21 (**a**) Photo of the dual-transduction sensor. (**b**) Cross-sectional of the sensor. © [2021] IEEE. Reprinted, with permission, from [22]

CMOS transistors. This allows for increased levels of integration. More importantly, the close interaction between CMOS and acoustic devices provided by integration can allow for new circuit design paradigms that simultaneously leverage the strengths of both components to get the best of both worlds. The current trend of FBAR test system integration includes a board-level circuit, CMOS integration, wireless, etc.

Lee et al. designed and manufactured an integrated multi-array FBAR-CMOS integrated system [35]. The size of the circuit system is 180 mm × 100 mm. Traditional gas sensors work at different operating temperatures and are difficult to integrate. The CMOS-compatible FBAR architecture will significantly reduce the electronic nose's form factor, a feature that is difficult to achieve with traditional MOS sensor platforms. The system has successfully monitored ethanol, toluene, ethyl acetate, and acetone gases. FBAR-CMOS sensor array can become an essential platform for small indoor air quality monitoring devices.

A monolithic FBAR mass sensor array on CMOS was demonstrated by Johnston et al. for the first time [78]. They have a mass sensitivity of 3.28×10^{11} Hz × cm^2/g and an oscillation frequency of about 870 MHz. This implementation overcomes the spatial and parasitic limitations of package-level FBAR integration and traditional QCM to achieve a dense sensor array, realizing a truly multiplexed, label-free biomolecular detection platform unhindered by complex and expensive external measurement hardware. The combined sensor platform uses a thin polymer layer as a single FBAR functionalized gas absorber and measures the response of frequency changes to VOC concentration on the chip. The integration of sensor, driver, and readout functions on a single CMOS chip enables a robust multi-sensor platform and avoids external measurement devices [79]. Edrees et al. demonstrated an SMR-CMOS oscillator integrated on 65 nm CMOS [80]. Fully supported SMR is built directly on CMOS transistor circuits using custom-developed mold-level post-processing to ensure low surface roughness by using BEOL characteristics to overcome the roughness normally associated with proportional copper low-K

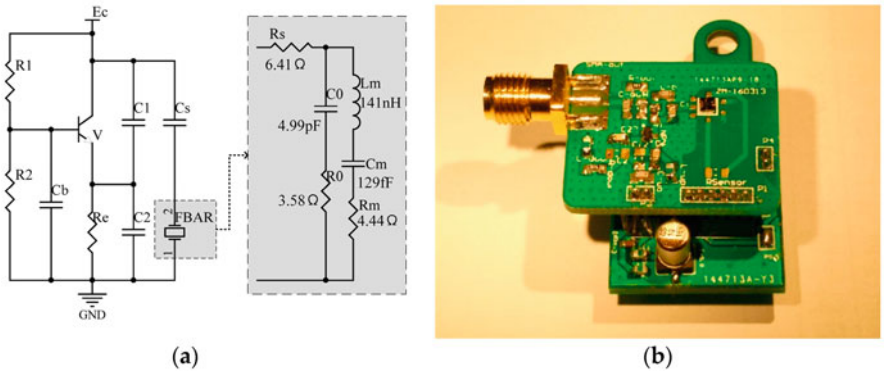

Fig. 22 (**a**) Schematic diagram of the oscillator circuit and (**b**) the photo of a sensor sample [81] (reprinted with permission from MDPI)

processes. This marks the first demonstration of a monolithic integrated piezoelectric resonator on a 65-nm CMOS. In addition, the process was demonstrated as a 2 mm by 1.7 mm CMOS mold, which is more than four times smaller than the previous mold-level CMOS resonator integration demonstration.

Zhang et al. designed and manufactured a gas-sensing system consisting of an FBAR sensor and an oscillator circuit [81]. The schematic diagram and the photo of the oscillator circuit are shown in Fig. 22. The sensor was driven by a Colpitts oscillator circuit, and the output signal characteristic power was 2.6 dBm@3 V, and the phase noise was 90 dBc/Hz@100 kHz. When the relative humidity is in the range of 25–88%, the frequency shift of the sensor is 733 kHz, and the measurement error is within 0.8% RH. When the ethanol concentration is 0–0.2355 g/L, the frequency shift of the sensor is 365 kHz.

In a conventional sensing situation, sensors require a wired connection to the readout system. However, conventional sensing methods are not useful in experiments that require medical sensing inside living beings or under harsh environmental conditions, such as corrosive media. The piezoelectric resonant sensors are powered and detected without connecting wire and the embedded power source but are achieved by resonant inductive coupling. Duan et al. developed a wireless passive piezoelectric resonance sensor to continuously detect VOCs [82]. The schematic of the Lamb wave resonator (LWR) array is integrated with a single coil, as shown in Fig. 23. An equivalent circuit is proposed to simulate the sensor system, and an LWR is used to demonstrate the wireless inquiry via near-field inductive coupling. Compared with wired sensors, the sensitivity of wireless sensors has almost no decrease in monitoring ethanol vapor concentration.

Gao et al. reported a monolithic oscillator chip integrated by an FBAR and CMOS chip using FleMEMS technology [83, 84]. In the 3D-stacked integrated chip, the thin-film FBAR sits directly over the CMOS chip, between which a 4 μm-thick SU-8 layer provides a robust adhesion and acoustic reflection cavity

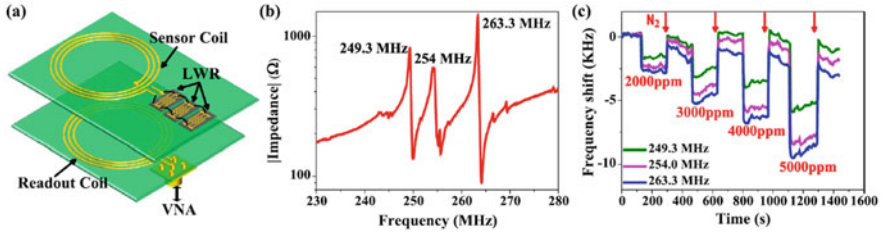

Fig. 23 (**a**) Schematic of the LWR array integrated with a single coil. (**b**) The measured frequency response for the LWR sensor array. (**c**) Simultaneously and continuously tracked parallel resonance frequency shifts of the three sensors in response to different gas concentrations. Reprinted from [82], with the permission of AIP Publishing

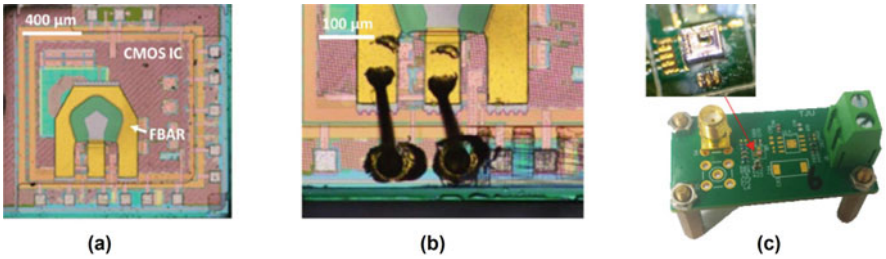

Fig. 24 (**a**) Transferred FBAR film above the CMOS chip. (**b**) Short Au wire bonding for electrical connection. (**c**) Under-test system with the oscillator chip on PCB. Reprinted from [83], with the permission of Tianjin University

(Fig. 24). FlexMEMS technology guarantees compact and accurate assembly, process compatibility, and high performance, thereby demonstrating its great potential in SoC hetero-integration applications.

Yan et al. developed a portable chemical warfare agent (CWA) gas sensor, which consists of a MEMS micropreconcentrator (μPC) and an FBAR gas sensor shown in Fig. 25 [9]. μPC is coated with nanoporous metal-organic skeleton material to enrich the target material, while FBAR does not require additional carrier gas to achieve rapid detection. The experimental results show that μPC can provide effective sample pretreatment, and the FBAR gas sensor has good sensitivity to DMMP vapor. The combination of μPC and FBAR in one instrument gives full play to their respective advantages and reduces the detection limit of analytes. In addition, both μPC and FBAR are fabricated by CMOS compatible method. The prototype is small and easy to carry, which has the potential to be used in CWAs field detection.

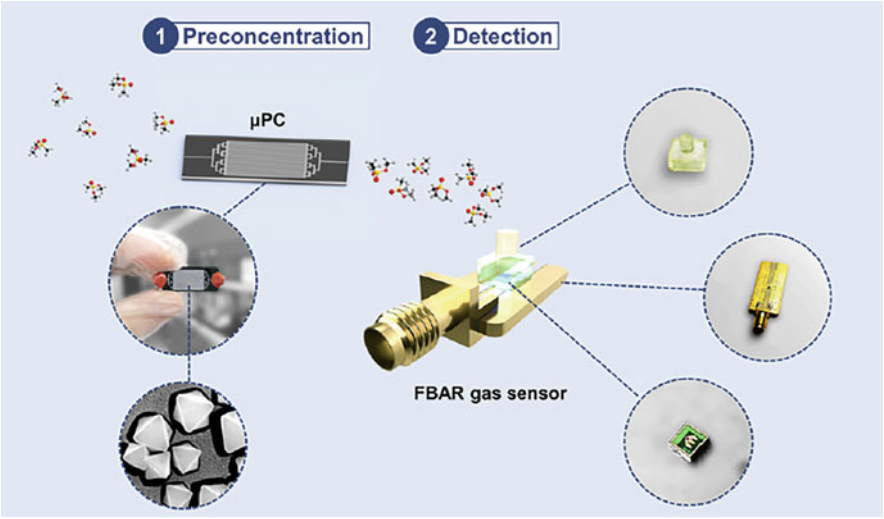

Fig. 25 Schematic of the mechanism of the prototype instrument for CWA detection. The insets show photographs of the μPC, the test chamber, the test circuit board, and the FBAR. Reprinted from [9], with the permission of Tianjin University

3.4 FBAR Gas Sensors Used as Micro GC Detectors

Piezoelectric resonator microsensors, such as SAW, BAW, and cantilevers, are emerging sensing techniques in gas chromatography (GC) applications due to their excellent mass resolution. In 1996, Sandia National Laboratories conducted a study on SAW for μGC, which was named the MicroChemLab System [85]. The prototype utilized a polymer-coated SAW detector array which can generate response patterns with algorithms to analyze the subject matter eluded from the separation column.

Similarly, FBAR sensors can accurately identify and quantify GC eluates. The compact size makes FBARs highly compatible with integration into microsystems, while the high resonating frequency offers improved sensitivity when employed as GC detectors. Wang et al. first reported a miniaturized, highly sensitive GC detector based on FBAR [57]. They achieved a 10–20 times enhancement in sensitivity by coating the FBAR surface with MOFs. The study also presented a novel coating process of MOFs on FBARs (Fig. 9). Additionally, FBAR was successfully utilized as a detector in a prototype GC for the first time. As shown in Fig. 26, the peak for FBAR gas sensors appears after 3.8 min, while the peak for FID measurement appears after 3.4 min. The width of the peak is nearly identical between FBAR sensors and FID. This comparison indicated the promising application potential of FBAR sensors as detectors in GC.

Later, Hu et al. conducted a study in which they demonstrated that polymer-coated FBARs can offer quantitative detection and orthogonal selectivity between overlapping dual mixtures using algorithms in GC [16]. To further reduce the dead

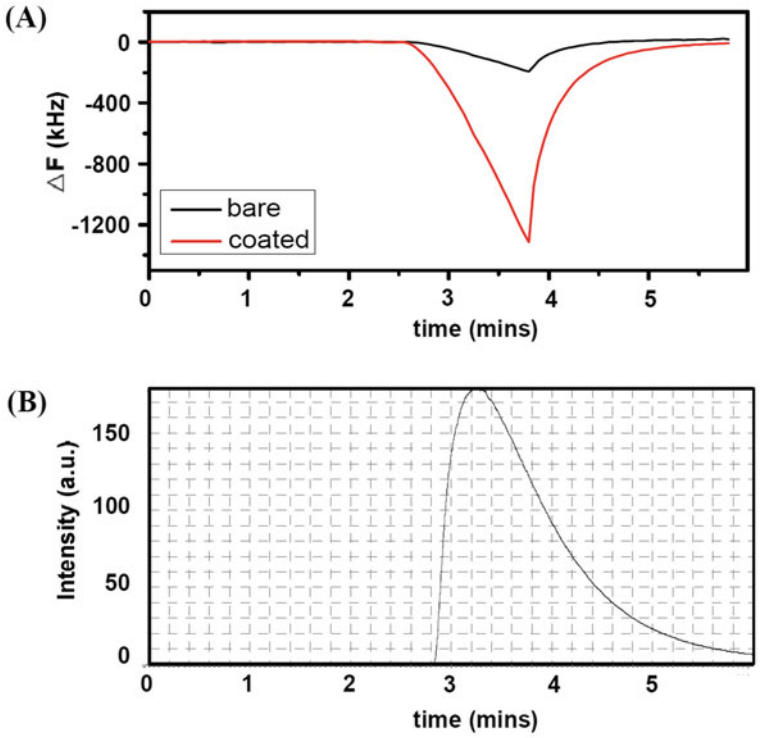

Fig. 26 Gas chromatographic detection by (**a**) FBAR gas sensors (bare and coated), and (**b**) flame ionization detector (FID). © [2017] IEEE. Reprinted, with permission, from [57]

volume of the detector and improve the detection limit, an FBAR based on microfluidic control was designed [86]. FBAR is packaged on a 15 mm × 15 mm × 1 mm microfluidic chip with a dead volume of only 0.2 μL shown in Fig. 27. The detector has a very low detection limit (parts per billion) for mimics of the chemical warfare agent dimethylphosphonate and a relatively short response time (about 15 s).

In a separate work, Sun et al. presented a novel on-chip monolithic integrated CNT sensor. This sensor design incorporated a BAW resonator beneath a CNT chemiresistor, as illustrated in Fig. 28. The researchers discovered that acoustic stimulation could enhance the gas desorption rate from the surface of the CNT, thereby addressing the slow desorption issue typically encountered in GC conditions. The multimode CNT sensor exhibited improved sensitivity and dynamic range compared to a single-mode detector due to the different sensing mechanisms involved. Consequently, it provided complementary responses to various target analytes. To validate the capabilities of the multimode CNT sensor, the researchers analyzed a gas mixture comprising methanol, n-heptane, toluene, ethylbenzene, o-xylene, and DMMP under different chromatographic conditions. The results

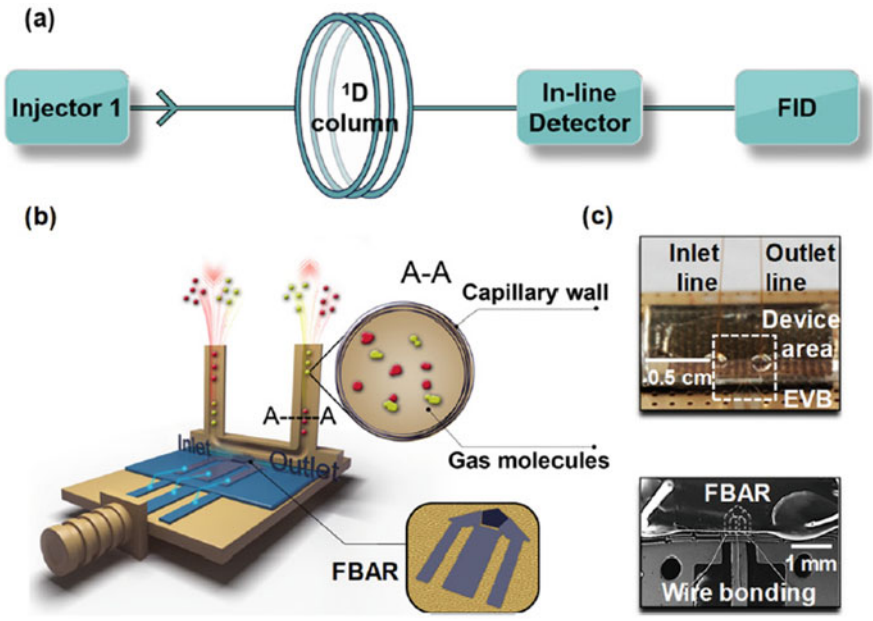

Fig. 27 Simplified instrument configuration diagram showing the facilely hyphenated GC (**a**). (**b**) Cartoon showing the prototype microfluidic FBAR detector in a gas chromatography system. (**c**) The digital photo and SEM picture show the microfluidic FBAR detector [86] (reprinted with permission from MDPI)

confirmed that the multimode CNT sensor functioned as a reliable microdetector for quantitative chromatographic analysis [87].

4 Outlook and Perspective

The explosive growth of wireless communications and the rapidly increasing demand for higher data rates and greater communication bandwidth have led to the emergence of many wireless communication standards, each with its dedicated frequency band. At the current state of the art, acoustic BAW/SAW filters are used for each frequency band [88]. FBAR is the main filter in BAW; its operating frequency range is about 1.5–6 GHz, up to 10 GHz. At the same time, it has the advantages of minor temperature sensitivity, small insertion loss, and large out-of-band attenuation [89]. Modern communication mobile phones can have up to 10 filters in the front end. It is worth mentioning that size decreases with the increase in frequency for the BAW filter, which is suitable for the application of 5G.

The MEMs-based FBAR manufacturing process is compatible with the CMOS process, so a monolithic integration approach can be adopted to build high-quality acoustic passivity directly on top of CMOS circuits, enabling tight integration

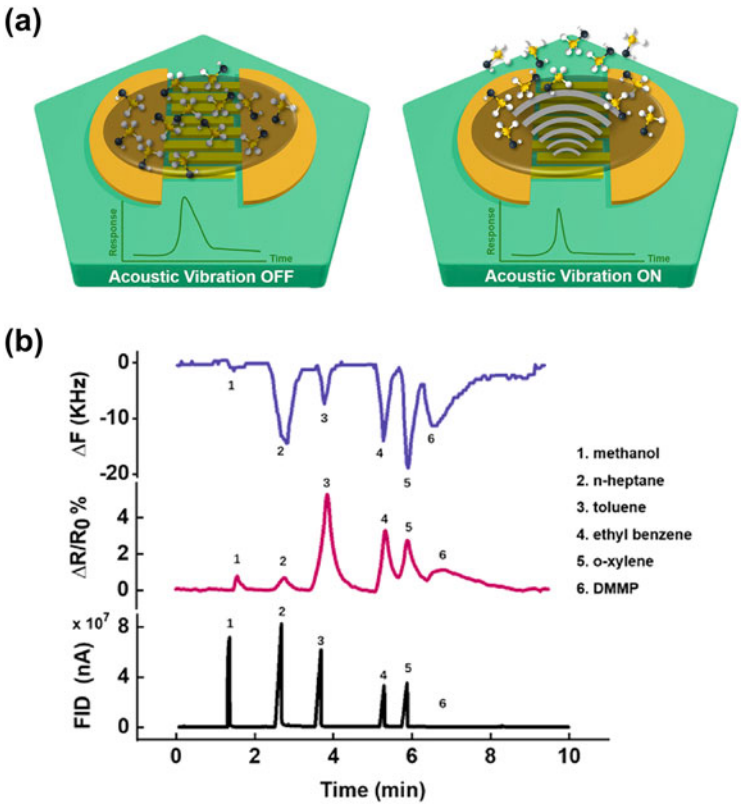

Fig. 28 (**a**) Schematic diagram of the desorption action of the multimode CNT sensor in a gas molecule without and with acoustic simulation. (**b**) Real-time sensing characteristics (frequency mode and resistance mode) of the multimode CNT sensor and FID signal coupled with GC for mixture gases. Reprinted with permission from [87]. Copyright (2022) American Chemical Society

between acoustic devices and high-performance CMOS transistors. This allows for increased integration levels and further miniaturization of wireless hardware. More importantly, the close interaction between CMOS and hearing devices, as provided by integration, can allow new circuit design paradigms, thereby simultaneously leveraging the advantages of both components to get the best of both worlds [80]. To date, there have been some very promising demonstrations of monolithic integration of piezoelectric acoustic resonators on CMOS for applications in RF receiver circuits [90, 91] and biological sensing [78, 79, 92, 93].

When FBARs work as filters or sensors, they are usually connected to CMOS circuits. However, this degrades the sensitivity for sensing applications and prevents the integration of dense sensor arrays in a system. Miniaturization attempts, including monolithic integration of the sensor and the circuitry, have been shown to substantially increase the development cost [78]. Therefore, a commercially viable highly integrated wireless sensor has been developed, which includes a mass sensor,

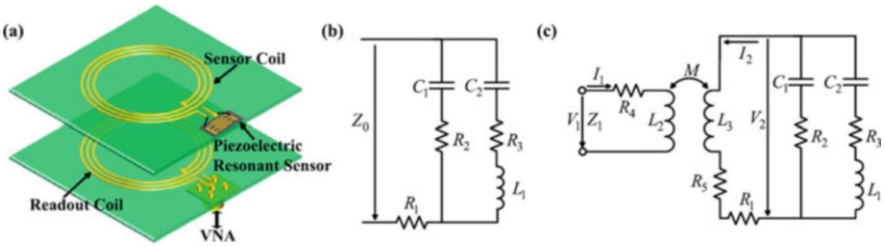

Fig. 29 (**a**) Schematic diagram of the wireless and passive piezoelectric resonant sensor. (**b**) The modified Butterworth–Van Dyke (mBVD) equivalent circuit of piezoelectric resonant sensors. (**c**) The equivalent circuit model of the wireless and passive piezoelectric resonant sensors. Reprinted from [82], with the permission of AIP Publishing

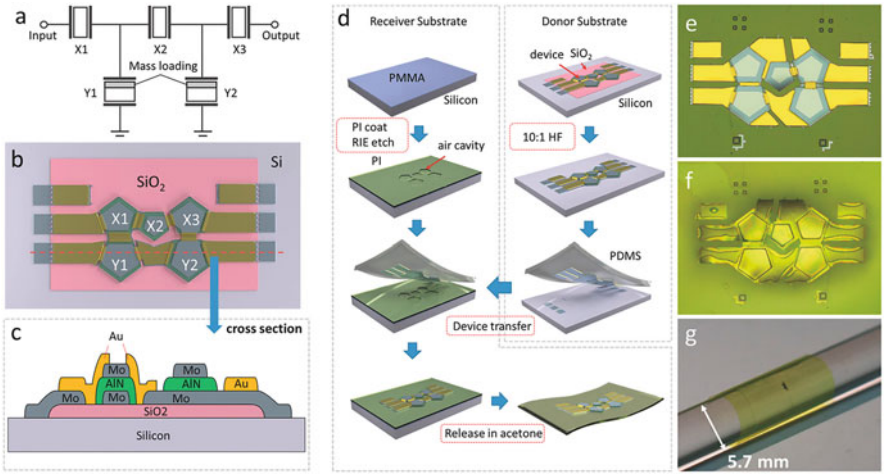

Fig. 30 (**a**) The circuit topology diagram of the flexible FBAR filter with three series and two shunt resonators. (**b**) Top and (**c**) cross-sectional schematic illustration of the donor device. (**d**) Schematic illustration of the main steps of receiver substrate preparation and final assembly. (**e**) Front and (**f**) backside microscopic images of the flexible filter. (**g**) Photograph of the flexible filter bent on a glass stirring rod [95] (Reprinted with permission of Wiley)

a sealed reference sensor, an interface circuit, and a wireless connection [94]. A method based on the near-field inductive coupling is proposed for wirelessly actuating and reading piezoelectric resonant sensors (Fig. 29) [82]. The wireless piezoelectric resonator sensor performs as well as the wired one in temperature sensing and VOC detection. This will open up opportunities for monitoring the physiological and pathological information in biochemical research and clinical practice.

The fabrication of universal MEMS devices on flexible polymer substrates has been reported, which is of great significance for building future fully integrated and multi-functional wireless flexible electronic systems (Fig. 30) [95]. A viable

approach for the fabrication of flexible FBAR with superior mechanical flexibility and electrical performance provides opportunities for the next generation of flexible electronic systems that require various sensing and actuation abilities [83, 96]. Among different realization technologies, FBARs, traditionally used as basic building blocks of modern RF filters, are natural candidates for flexible wireless electronics. Moreover, as MEMS devices bridge the mechanical and electrical domains, FBARs demonstrated significant sensing [43, 97, 98] and actuating [99, 100] potentials. Transplanting this technology into the flexible electronic realm will enrich the functionalities of future flexible electronic systems.

References

1. Liang J, Zhang H, Zhang D et al (2015) Design and fabrication of aluminum nitride Lamb wave resonators towards high figure of merit for intermediate frequency filter applications. J Micromech Microeng 25:035016. https://doi.org/10.1088/0960-1317/25/3/035016
2. Liu W, Sun C, Liang J et al (2016) Directly trapping of nanoscale biomolecules using bulk acoustic wave resonators. In: 2016 IEEE sensors. IEEE, Orlando, pp 1–3
3. He M, Cui W, Zhang H et al (2017) In-line trapping and rotation of bio-particles via 3-D micro-vortices generated by localized ultrahigh frequency acoustic resonators. In: 2017 19th international conference on solid-state sensors, actuators and microsystems (TRANSDUCERS). IEEE, Kaohsiung, pp 1789–1792
4. Liu W, Pan S, Zhang H et al (2018) A universal biomolecular concentrator to enhance biomolecular surface binding based on acoustic NEMS resonator. ACS Cent Sci 4:899–908. https://doi.org/10.1021/acscentsci.8b00301
5. Chen X, Ning Y, Pan S et al (2021) Mixing during trapping enabled a continuous-flow microfluidic smartphone immunoassay using acoustic streaming. ACS Sens 6:2386–2394. https://doi.org/10.1021/acssensors.1c00602
6. Yang Y, Pang W, Zhang H et al (2022) Manipulation of single cells via a stereo acoustic streaming tunnel (SteAST). Microsyst Nanoeng 8:88. https://doi.org/10.1038/s41378-022-00424-9
7. Zhao L, Niu P, Casals E et al (2021) Phase separation of a nonionic surfactant aqueous solution in a standing surface acoustic wave for submicron particle manipulation. Lab Chip 21:660–667. https://doi.org/10.1039/D0LC00986E
8. Cui W, Mu L, Pang W et al (2019) Rapid purification, enrichment, and detection of biomolecules using bulk acoustic wave resonators. In: 2019 20th international conference on solid-state sensors, actuators and microsystems & Eurosensors XXXIII (TRANSDUCERS & EUROSENSORS XXXIII). IEEE, Berlin, pp 621–624
9. Yan X, Qu H, Chang Y et al (2022) A prototype portable instrument employing micro-preconcentrator and FBAR sensor for the detection of chemical warfare agents. Nanotechnol Precision Eng 5:013005. https://doi.org/10.1063/10.0009664
10. Zheng Z, Niu P, Wang X et al (2019) Miniature gigahertz acoustic resonator and on-chip electrochemical sensor: an emerging combination for electroanalytical microsystems. Anal Chem 91:15959–15966. https://doi.org/10.1021/acs.analchem.9b04508
11. Yang Y, Zhang L, Jin K et al (2022) Self-adaptive virtual microchannel for continuous enrichment and separation of nanoparticles. Sci Adv 8:eabn8440. https://doi.org/10.1126/sciadv.abn8440
12. Zhang Z, Tang Z, Liu W et al (2016) Acoustically triggered disassembly of multilayered polyelectrolyte thin films through gigahertz resonators for controlled drug release applications. Micromachines 7:194. https://doi.org/10.3390/mi7110194

13. Zhang Z, Wang Y, Zhang H et al (2017) Hypersonic poration: a new versatile cell poration method to enhance cellular uptake using a piezoelectric nano-electromechanical device. Small 13:1602962. https://doi.org/10.1002/smll.201602962
14. Lu Y, Palanikumar L, Choi ES et al (2019) Hypersound-enhanced intracellular delivery of drug-loaded mesoporous silica nanoparticles in a non-endosomal pathway. ACS Appl Mater Interfaces 11:19734–19742. https://doi.org/10.1021/acsami.9b02447
15. Lu Y, Chang Y, Tang N et al (2015) Detection of volatile organic compounds using microfabricated resonator array functionalized with supramolecular monolayers. ACS Appl Mater Interfaces 7:17893–17903. https://doi.org/10.1021/acsami.5b04385
16. Hu J, Qu H, Chang Y et al (2018) Miniaturized polymer coated film bulk acoustic wave resonator sensor array for quantitative gas chromatographic analysis. Sens Actuators B 274: 419–426. https://doi.org/10.1016/j.snb.2018.07.162
17. Zhao Y, Yang Q, Chang Y et al (2018) Detection and discrimination of volatile organic compounds using a single multi-resonance mode piezotransduced silicon bulk acoustic wave resonator (PSBAR) as virtual sensor array. Sens Actuators B 254:1191–1199. https://doi.org/10.1016/j.snb.2017.07.206
18. Tao J, Chang Y, Liang J et al (2019) Hydrophobin-functionalized film bulk acoustic wave resonators for sensitive and polarity-sensitive sensing of volatile organic compounds. Appl Phys Lett 115:163502. https://doi.org/10.1063/1.5124525
19. Zeng G, Wu C, Chang Y et al (2019) Detection and discrimination of volatile organic compounds using a single film bulk acoustic wave resonator with temperature modulation as a multiparameter virtual sensor array. ACS Sens 4:1524–1533. https://doi.org/10.1021/acssensors.8b01678
20. Yan X, Qu H, Chang Y et al (2020) Surface engineering of metal–organic framework prepared on film bulk acoustic resonator for vapor detection. ACS Appl Mater Interfaces 12:10009–10017. https://doi.org/10.1021/acsami.9b22407
21. Lu Y, Chang Y, Tang N et al (2015) Concentration-independent fingerprint library of volatile organic compounds based on gas-surface interactions by self-assembled monolayer functionalized film bulk acoustic resonator arrays. In: 2015 IEEE sensors. IEEE, Busan, pp 1–4
22. Sun X, Chang Y, Qu H et al (2021) A single-chip dual-transduction gas sensor for BTX detection. In: 2021 IEEE sensors. IEEE, Sydney, pp 1–4
23. Hu J, Qu H, Guo W et al (2019) Film bulk acoustic wave resonator for trace chemical warfare agents simulants detection in micro chromatography. In: 2019 20th international conference on solid-state sensors, actuators and microsystems & Eurosensors XXXIII (TRANSDUCERS & EUROSENSORS XXXIII). IEEE, Berlin, pp 45–48
24. Chen D, Wang JJ, Li DH, Xu Y (2011) Hydrogen sensor based on Pd-functionalized film bulk acoustic resonator. Sens Actuators B Chem 159:234–237. https://doi.org/10.1016/j.snb.2011.06.078
25. Pang W, Zhao H, Kim ES et al (2012) Piezoelectric microelectromechanical resonant sensors for chemical and biological detection. Lab Chip 12:29–44. https://doi.org/10.1039/C1LC20492K
26. Dubois M-A, Muller C (2013) Thin-film bulk acoustic wave resonators. In: Enz CC, Kaiser A (eds) MEMS-based circuits and systems for wireless communication. Springer US, Boston, pp 3–28
27. Pang W, Ruby RC, Parker R et al (2008) A temperature-stable film bulk acoustic wave oscillator. IEEE Electron Device Lett 29:315–318. https://doi.org/10.1109/LED.2008.917116
28. Zhang X, Xu W, Abbaspour-Tamijani A, Chae J (2009) Thermal analysis and characterization of a high Q film bulk acoustic resonator (FBAR) as biosensers in liquids. In: 2009 IEEE 22nd international conference on micro electro mechanical systems. IEEE, Sorrento, pp 939–942
29. Rai S, Su Y, Pang W et al (2010) A digitally compensated 1.5 GHz CMOS/FBAR frequency reference. IEEE Trans Ultrason Ferroelect Freq Contr 57:552–561. https://doi.org/10.1109/TUFFC.2010.1447

30. Dickherber A, Corso CD, Hunt WD (2008) Optimization and characterization of a ZnO biosensor array. Sens Actuators A Phys 144:7–12. https://doi.org/10.1016/j.sna.2008.01.007
31. Grate JW, Patrash SJ, Abraham MH, Du CM (1996) Selective vapor sorption by polymers and cavitands on acoustic wave sensors: is this molecular recognition? Anal Chem 68:913–917. https://doi.org/10.1021/ac950518z
32. Penza M, Milella E, Anisimkin VI (1998) Monitoring of NH3 gas by LB polypyrrole-based SAW sensor. Sens Actuators B Chem 47:218–224. https://doi.org/10.1016/S0925-4005(98)00026-4
33. Gabl R, Green E, Schreiter M et al (2003) Novel integrated FBAR sensors: a universal technology platform for bio- and gas-detection. In: Proceedings of IEEE sensors 2003 (IEEE cat. No.03CH37498). IEEE, Toronto, ON, Canada, pp 1184–1188
34. Liu J, Zhao Z, Fang Z et al (2020) High-performance FBAR humidity sensor based on the PI film as the multifunctional layer. Sens Actuators B Chem 308:127694. https://doi.org/10.1016/j.snb.2020.127694
35. Lee SH, Jung Y, Kim T et al (2015) Polymer coated film bulk acoustic resonator (FBAR) arrays for indoor air quality (IAQ) monitoring. In: 2015 IEEE sensors. IEEE, Busan, pp 1–4
36. Liu W, Wang J, Yu Y et al (2015) Tuning the resonant frequency of resonators using molecular surface self-assembly approach. ACS Appl Mater Interfaces 7:950–958. https://doi.org/10.1021/am507640g
37. Ning Y, Zhang M, Lang Y et al (2022) Electronic stethoscope based on triangular cantilever piezoelectric bimorph MEMS transducers. J Microelectromech Syst 31:450–456. https://doi.org/10.1109/JMEMS.2022.3160761
38. Johar AK, Varma T, Periasamy C et al (2020) Design, analysis and finite element modeling of solidly mounted film bulk acoustic resonator for gas sensing applications. J Electronic Mater 49:1503–1511. https://doi.org/10.1007/s11664-019-07843-x
39. Johar AK, Sharma GK, Kumar TB et al (2021) Optimization of a flexible film bulk acoustic resonator-based toluene gas sensor. J Electronic Mater 50:5387–5395. https://doi.org/10.1007/s11664-021-09059-4
40. Guo H, Gao Y, Liu T (2018) A theoretical study of the VOC sensor based on polymer-coated diaphragm embedded with FBAR. Measurement 129:206–210. https://doi.org/10.1016/j.measurement.2018.07.021
41. Blodgett KB (1935) Films built by depositing successive monomolecular layers on a solid surface. J Am Chem Soc 57:1007–1022. https://doi.org/10.1021/ja01309a011
42. Kim E, Choi Y-K, Song J, Lee J (2013) Detection of various self-assembled monolayers by AlN-based film bulk acoustic resonator. Mater Res Bull 48:5076–5079. https://doi.org/10.1016/j.materresbull.2013.05.096
43. Chang Y, Tang N, Qu H et al (2016) Detection of volatile organic compounds by self-assembled monolayer coated sensor array with concentration-independent fingerprints. Sci Rep 6:23970. https://doi.org/10.1038/srep23970
44. Chen Y, Zhang H, Feng Z et al (2016) Chemiresistive and gravimetric dual-mode gas sensor toward target recognition and differentiation. ACS Appl Mater Interfaces 8:21742–21749. https://doi.org/10.1021/acsami.6b02682
45. Zhao H, Fan S, Chen Y et al (2017) Oxygen plasma-treated graphene oxide surface functionalization for sensitivity enhancement of thin-film piezoelectric acoustic gas sensors. ACS Appl Mater Interfaces 9:40774–40781. https://doi.org/10.1021/acsami.7b09547
46. Das S, Kim H, Kim K (2009) Metathesis in single crystal: complete and reversible exchange of metal ions constituting the frameworks of metal−organic frameworks. J Am Chem Soc 131:3814–3815. https://doi.org/10.1021/ja808995d
47. Li T, Kozlowski MT, Doud EA et al (2013) Stepwise ligand exchange for the preparation of a family of mesoporous MOFs. J Am Chem Soc 135:11688–11691. https://doi.org/10.1021/ja403810k

48. Sun D, Liu W, Qiu M et al (2015) Introduction of a mediator for enhancing photocatalytic performance via post-synthetic metal exchange in metal–organic frameworks (MOFs). Chem Commun 51:2056–2059. https://doi.org/10.1039/C4CC09407G
49. Liu C, Rosi NL (2017) Ternary gradient metal–organic frameworks. Faraday Discuss 201: 163–174. https://doi.org/10.1039/C7FD00045F
50. Liu C, Zeng C, Luo T-Y et al (2016) Establishing porosity gradients within metal–organic frameworks using partial postsynthetic ligand exchange. J Am Chem Soc 138:12045–12048. https://doi.org/10.1021/jacs.6b07445
51. Yuan S, Chen Y-P, Qin J-S et al (2016) Linker installation: engineering pore environment with precisely placed functionalities in zirconium MOFs. J Am Chem Soc 138:8912–8919. https://doi.org/10.1021/jacs.6b04501
52. Yuan S, Lu W, Chen Y-P et al (2015) Sequential linker installation: precise placement of functional groups in multivariate metal–organic frameworks. J Am Chem Soc 137:3177–3180. https://doi.org/10.1021/ja512762r
53. Dolgopolova EA, Shustova NB (2016) Metal–organic framework photophysics: optoelectronic devices, photoswitches, sensors, and photocatalysts. MRS Bull 41:890–896. https://doi.org/10.1557/mrs.2016.246
54. Niknam E, Panahi F, Daneshgar F et al (2018) Metal–organic framework MIL-101(Cr) as an efficient heterogeneous catalyst for clean synthesis of benzoazoles. ACS Omega 3:17135–17144. https://doi.org/10.1021/acsomega.8b02309
55. Chávez AM, Rey A, López J et al (2021) Critical aspects of the stability and catalytic activity of MIL-100(Fe) in different advanced oxidation processes. Sep Purif Technol 255:117660. https://doi.org/10.1016/j.seppur.2020.117660
56. López J, Chávez AM, Rey A, Álvarez PM (2021) Insights into the stability and activity of MIL-53(Fe) in solar photocatalytic oxidation processes in water. Catalysts 11:448. https://doi.org/10.3390/catal11040448
57. Wang YW, Ao CY, Hui ZP et al (2017) Film bulk acoustic resonator based gas sensor: a sensitive detector for gas chromatography. In: 2017 19th international conference on solid-state sensors, actuators and microsystems (TRANSDUCERS). IEEE, Kaohsiung, pp 1471–1474
58. Wang W, Chen D, Wang H et al (2018) Film bulk acoustic formaldehyde sensor with layer-by-layer assembled carbon nanotubes/polyethyleneimine multilayers. J Phys D Appl Phys 51: 055104. https://doi.org/10.1088/1361-6463/aaa2af
59. Benetti M, Cannatà D, Di Pietrantonio F et al (2005) Microbalance chemical sensor based on thin-film bulk acoustic wave resonators. Appl Phys Lett 87:173504. https://doi.org/10.1063/1.2112187
60. Chen D, Xu Y, Wang J, Zhang L (2010) Nerve gas sensor using film bulk acoustic resonator modified with a self-assembled Cu2+/11-mercaptoundecanoic acid bilayer. Sens Actuators B Chem 150:483–486. https://doi.org/10.1016/j.snb.2010.07.047
61. Penza M, Aversa P, Cassano G et al (2008) Thin-film bulk-acoustic-resonator gas sensor functionalized with a nanocomposite Langmuir–Blodgett layer of carbon nanotubes. IEEE Trans Electron Devices 55:1237–1243. https://doi.org/10.1109/TED.2008.919283
62. Hoffmann R, Schreiter M, Heitmann J (2017) The concept of thin film bulk acoustic resonators as selective CO_2 gas sensors. J Sens Sens Syst 6:87–96. https://doi.org/10.5194/jsss-6-87-2017
63. Song S, Chen D, Wang H et al (2018) Film bulk acoustic formaldehyde sensor with polyethyleneimine-modified single-wall carbon nanotubes as sensitive layer. Sens Actuators B Chem 266:204–212. https://doi.org/10.1016/j.snb.2018.03.129
64. Moncrieff RW (1961) An instrument for measuring and classifying odors. J Appl Physiol 16: 742–749. https://doi.org/10.1152/jappl.1961.16.4.742
65. Persaud K, Dodd G (1982) Analysis of discrimination mechanisms in the mammalian olfactory system using a model nose. Nature 299:352–355. https://doi.org/10.1038/299352a0

66. Gardner JW, Bartlett PN (1994) A brief history of electronic noses. Sens Actuators B Chem 18:210–211. https://doi.org/10.1016/0925-4005(94)87085-3
67. Zhao Y, Yang Q, Chang Y et al (2016) Detection of volatile organic compounds by high-Q piezotransduced single-crystal silicon bulk acoustic resonator arrays. In: 2016 IEEE sensors. IEEE, Orlando, pp 1–3
68. Zhao Y, Yang Q, Chang Y et al (2017) Novel gas sensor arrays based on high-Q SAM-modified piezotransduced single-crystal silicon bulk acoustic resonators. Sensors 17: 1507. https://doi.org/10.3390/s17071507
69. Rudman PS (1983) Hydriding and dehydriding kinetics. J Less Common Metals 89:93–110. https://doi.org/10.1016/0022-5088(83)90253-9
70. Li C-L, Chen Y-F, Liu M-H, Lu C-J (2012) Utilizing diversified properties of monolayer protected gold nano-clusters to construct a hybrid sensor array for organic vapor detection. Sens Actuators B Chem 169:349–359. https://doi.org/10.1016/j.snb.2012.05.009
71. Chang Y, Qu H, Duan X et al (2016) VOC detection using multimode E-nose composed of bulk acoustic wave resonator and silicon nanowire field effect transistor array. In: 2016 IEEE sensors. IEEE, Orlando, pp 1–3
72. Chang Y, Hui Z, Wang X et al (2018) Dual-mode gas sensor composed of a silicon nanoribbon field effect transistor and a bulk acoustic wave resonator: a case study in Freons. Sensors 18: 343. https://doi.org/10.3390/s18020343
73. Potyrailo RA, Bonam RK, Hartley JG et al (2015) Towards outperforming conventional sensor arrays with fabricated individual photonic vapour sensors inspired by Morpho butterflies. Nat Commun 6:7959. https://doi.org/10.1038/ncomms8959
74. Speller NC, Siraj N, McCarter KS et al (2017) QCM virtual sensor array: vapor identification and molecular weight approximation. Sens Actuators B Chem 246:952–960. https://doi.org/10.1016/j.snb.2017.02.042
75. Li D, Xie Z, Qu M et al (2021) Virtual sensor array based on Butterworth–Van Dyke equivalent model of QCM for selective detection of volatile organic compounds. ACS Appl Mater Interfaces 13:47043–47051. https://doi.org/10.1021/acsami.1c13046
76. Speller NC, Siraj N, Regmi BP et al (2015) Rational design of QCM-D virtual sensor arrays based on film thickness, viscoelasticity, and harmonics for vapor discrimination. Anal Chem 87:5156–5166. https://doi.org/10.1021/ac5046824
77. Gao F, Xuan W, Bermak A et al (2019) Dual transduction on a single sensor for gas identification. Sens Actuators B Chem 278:21–27. https://doi.org/10.1016/j.snb.2018.09.029
78. Johnston ML, Kymissis I, Shepard KL (2010) FBAR-CMOS oscillator array for mass-sensing applications. IEEE Sens J 10:1042–1047. https://doi.org/10.1109/JSEN.2010.2042711
79. Johnston ML, Edrees H, Kymissis I, Shepard KL (2012) Integrated VOC vapor sensing on FBAR-CMOS array. In: 2012 IEEE 25th international conference on micro electro mechanical systems (MEMS). IEEE, Paris, pp 846–849
80. Edrees HM, Colon-Berrios AR, de Godoy PD et al (2017) Monolithically integrated CMOS-SMR oscillator in 65 nm CMOS using custom MPW die-level fabrication process. J Microelectromech Syst 26:846–858. https://doi.org/10.1109/JMEMS.2017.2691585
81. Zhang M, Du L, Fang Z, Zhao Z (2017) A sensitivity-enhanced film bulk acoustic resonator gas sensor with an oscillator circuit and its detection application. Micromachines 8:25. https://doi.org/10.3390/mi8010025
82. Duan Y, Chang Y, Liang J et al (2016) Wireless gas sensing based on a passive piezoelectric resonant sensor array through near-field induction. Appl Phys Lett 109:263503. https://doi.org/10.1063/1.4973280
83. Gao C, Zhang M, Jiang Y (2019) FlexMEMS-enabled hetero-integration for monolithic FBAR-above-IC oscillators. Nanotechnol Precision Eng 2:105–109. https://doi.org/10.1016/j.npe.2019.08.002
84. Gao C, Zhang M, Jiang Y et al (2019) A monolithic FBAR oscillator based on heterogeneous system-on-chip integration. In: 2019 IEEE 32nd international conference on micro electro mechanical systems (MEMS). IEEE, Seoul, pp 895–898

85. Thomas RC, Ricco AJ, Yang HC et al (1996) Chemical class specificity using self-assembled monolayers on SAW devices. Sandia National Lab. (SNL-NM), Albuquerque, NM (United States)
86. Hu J, Qu H, Pang W, Duan X (2021) In-line detection with microfluidic bulk acoustic wave resonator gas sensor for gas chromatography. Sensors 21:6800. https://doi.org/10.3390/s21206800
87. Sun X, Hu J, Yan X et al (2022) On-chip monolithic integrated multimode carbon nanotube sensor for a gas chromatography detector. ACS Sens 7:3049–3056. https://doi.org/10.1021/acssensors.2c01359
88. Hashimoto K, Tanaka S, Esashi M (2011) Tunable RF SAW/BAW filters: dream or reality? In: 2011 joint conference of the IEEE international frequency control and the European frequency and time forum (FCS) proceedings. IEEE, San Francisco, pp 1–8
89. Campanella H, Qian Y, Romero CO et al (2021) Monolithic multiband MEMS RF front-end module for 5G mobile. J Microelectromech Syst 30:72–80. https://doi.org/10.1109/JMEMS.2020.3036379
90. Aigner R (2005) MEMS in RF-filter applications: thin film bulk-acoustic-wave technology. In: The 13th international conference on solid-state sensors, actuators and microsystems, 2005. Digest of technical papers. TRANSDUCERS '05. IEEE, Seoul, Korea, pp 5–8
91. Fang C-M, Pao S-Y, Lee C-Y et al (2009) Development of 2.4-GHz film bulk acoustic wave filter for wireless communication. JM31 8:021121. https://doi.org/10.1117/1.3094749
92. Johnston ML, Kymissis I, Shepard KL (2009) An array of monolithic FBAR-CMOS oscillators for mass-sensing applications. In: TRANSDUCERS 2009–2009 international solid-state sensors, actuators and microsystems conference. IEEE, Denver, pp 1626–1629
93. Nirschl M, Rantala A, Tukkiniemi K et al (2010) CMOS-integrated film bulk acoustic resonators for label-free biosensing. Sensors 10:4180–4193. https://doi.org/10.3390/s100504180
94. Nagaraju M, Gu J, Lingley A et al (2014) A fully integrated wafer-scale sub-mm^3 FBAR-based wireless mass sensor. In: 2014 IEEE international frequency control symposium (FCS). IEEE, Taipei, pp 1–5
95. Jiang Y, Zhao Y, Zhang L et al (2018) Flexible film bulk acoustic wave filters toward radiofrequency wireless communication. Small 14:1703644. https://doi.org/10.1002/smll.201703644
96. Zhang L, Jiang Y, Liu B et al (2018) Highly flexible piezoelectric MEMS resonators encapsulated in polymer thin films. In: 2018 IEEE micro electro mechanical systems (MEMS). IEEE, Belfast, pp 170–173
97. Voiculescu I, Nordin AN (2012) Acoustic wave based MEMS devices for biosensing applications. Biosens Bioelectron 33:1–9. https://doi.org/10.1016/j.bios.2011.12.041
98. Wingqvist G, Bjurström J, Liljeholm L et al (2007) Shear mode AlN thin film electro-acoustic resonant sensor operation in viscous media. Sens Actuators B Chem 123:466–473. https://doi.org/10.1016/j.snb.2006.09.028
99. Friend J, Yeo LY (2011) Microscale acoustofluidics: microfluidics driven via acoustics and ultrasonics. Rev Mod Phys 83:647–704. https://doi.org/10.1103/RevModPhys.83.647
100. Qu H, Yang Y, Chang Y et al (2017) On-chip integrated multiple microelectromechanical resonators to enable the local heating, mixing and viscosity sensing for chemical reactions in a droplet. Sens Actuators B Chem 248:280–287. https://doi.org/10.1016/j.snb.2017.03.173

Resonant Silicon Microcantilevers for Particle and Gas Sensing

Jiushuai Xu and Erwin Peiner

Contents

Abstract Resonant Silicon Microcantilevers (RSMCs) serve as highly suitable Mass-Sensitive Transducers (MSTs) for effective miniaturization, owing to their uncomplicated cantilever device structure and the inherent architectural adaptability of silicon. In comparison with conventional technologies, resonant microcantilevers offer several promising advantages: exceptional sensitivity, cost-effectiveness, robustness, scalability, minimal sample requirements, low energy consumption,

J. Xu
Institute of Semiconductor Technology (IHT), Technische Universität Braunschweig, Braunschweig, Germany
e-mail: jiushuai.xu@tu-braunschweig.de

E. Peiner (✉)
Laboratory for Emerging Nanometrology (LENA), Technische Universität Braunschweig, Braunschweig, Germany
e-mail: e.peiner@tu-braunschweig.de

P. Lieberzeit (ed.), *Piezoelectric Sensors*, Springer Series on Chemical Sensors and Biosensors (2024) 18: 291–338, https://doi.org/10.1007/5346_2023_33,

Published online: 22 November 2023

rapid response times, and a label-free process devoid of hazards. The extensive research conducted on microcantilever sensors has underscored their versatile analytical capabilities, encompassing the detection of particulate matter in both air and liquids, humidity measurement, and gas sensing applications. This comprehensive chapter presents a thorough exploration of the cutting-edge advancements in microcantilever-based particle and gas sensors. It delves into their underlying working principles, design considerations, the functionalization and packaging of microcantilevers, and the manifold applications they serve, while also shedding light on the future potential in this domain.

Keywords Gas sensor, Mass-sensitive transducers, MEMS, Microcantilever, Particulate matter, Resonator

Abbreviations

AFM	Atomic force microscopy
ALD	Atomic-layer deposition
APTES	(3-Aminopropyl)-trimethoxysilane
BAW	Bulk acoustic wave
CFD	Computational fluid dynamics
CMOS	Complementary metal oxide semiconductor
C-MSN	Carboxyl-group-functionalized mesoporous-silica nanoparticle
CPC	Condensation particle counter
cryo-DRIE	Deep reactive ion etching at cryogenic temperature
CSD	Chemical-solution deposition
CSE	Chemical-solution etching
CVD	Chemical vapor deposition
CWA	Chemical warfare agents
DFP	Di-isopropyl fluorophosphate
DI	De-ionized
DMA	Differential mobility analyzer
DMMP	Dimethyl methyl phosphonate
DPMS	Differential mobility particle sizer
EAM	Electromechanical amplitude modulation
FBAR	Film bulk acoustic resonator
FMPS	Fast mobility particle sizer
GND	Ground
HEPA	High-efficiency particulate air filter
HR	Heating resistor
IDLH	Immediately dangerous for life or health
LOD	Limit of detection
LPCVD	Low pressure chemical vapor deposition
MBE	Molecular-beam epitaxy

MEMS	Micro electro mechanical system
MOF	Metal-organic framework
MOS	Metal oxide semiconducting
MOX	Metal oxide
MST	Mass-sensitive transducer
MTF	Mesoporous thin film
NF	Nanofin
NPC	Nanoporous carbon
NPL	Nanopillar
NR	Nanorod
OP	Organophosphorus
OPC	Optical particle counter
PAAM	Poly-acryl amide
PCB	Printed circuit board
PECH	Polyepichlorohydrin
PECVD	Plasma enhanced chemical vapor deposition
PEI	Poly-ethylene imine
PETN	Pentaerythritol tetranitrate
PLL	Phase-locked loop
PM	Particulate matter
PMMA	Polymethyl methacrylate
PVA	Poly-vinyl alcohol
PμC	Piezoresistive microcantilever
μFC	Microfluidic channel
PVC	Poly-vinyl chloride
PVD	Physical vapor deposition
PVP	Poly-vinyl pyrrolidone
QCM	Quartz crystal microbalance
RDX	Hexahydro-1,3,5-triazine
RIE	Reactive ion etching
RSMC	Resonant silicon microcantilever
SAM	Self-assembled monolayer
SAW	Surface acoustic wave
SEM	Scanning electron microscopy
TAE	Tris(hydroxymethyl)aminomethane acetate ethylenediaminetetraacetic acid
TEACl	Triethylamine hydrochloride
TEOM	Tapered element oscillating microbalance
TL-FM AFM	Tipless force modulation atomic force microscopy
TMAH	Tetramethylammonium hydroxide
TPO	Thermal-piezoresistive oscillator
TPoS	Thin-film piezoelectric-on-silicon
TSMR	Thickness shear mode resonator
TTIP	Titanium tetraisopropoxide

UFP	Ultrafine particle
UV	Ultraviolet
4-MBA	4-Mercaptobenzoic acid
VOC	Volatile organic compound
WB	Wheatstone bridge
WHO	World Health Organization
ZIF	Zeolitic-imidazolate-framework

1 Introduction

Micro electro mechanical system (MEMS) is a broad domain, as sensors and actuators cover almost all aspects of our present life. MEMS exhibits excellent feasibilities toward miniaturized sensors due to its small dimensions, superior performance, low power consumption, as well as cost-effective manufacturing using batch-fabrication. A sensing system detects and responds to multiple physical, chemical, or biological inputs and converts them into analog or digital signals. MEMS technology has deliberated the combination of microelectronics with micromachining technique on a standard silicon wafer into metal oxide semiconducting (MOS) devices.

Proper understanding of the actuation and sensing mechanisms of microcantilever-based devices plays a vital role in effective selection for novel and complex application design. As all sensors, microcantilever-based sensing platforms are typically consisting of three parts: sensing elements to detect physical quantities or recognize bio-/chemical/physicochemical targets, transducers to convert the detected parameters to electrical signals, and a readout to read and interpret electrical signals to visualized information. Typical dimensions of microcantilevers are generally measured in tens to hundreds of micrometers.

Cantilever-based sensors allow for two operation modes: static bending/deflection and resonant vibration. Cantilevers working in their static mode (Fig. 1a) are generally considered as force/stress transducers, and they can be of any elastic materials. Different, resonant cantilevers (Fig. 1b) belong to the class of *M*ass-*S*ensitive *T*ransducers (MSTs), which can sample analytes from the environment and detect them by their mass [2–6]. *R*esonant *S*ilicon *M*icro*c*antilevers (RSMCs) are MSTs best suited for miniaturization, due to the simple device structure of cantilevers and the architecting feasibility and flexibility of silicon. The cantilever mass is increased by the attached particle or gas species, which is indicated by a decrease of resonance frequency. For particle detection they are transported in a fluid to the cantilever, where they are captured within an effective cross section around the cantilever defined by external forces (impaction, electro-, dielectro-, thermophoresis...) and can reside for a long time. As a consequence, particle sampling is limited by mass transport in a fluidic channel, i.e., a constant concentration of particles in the fluid sample induces a constant rate of deposited mass on

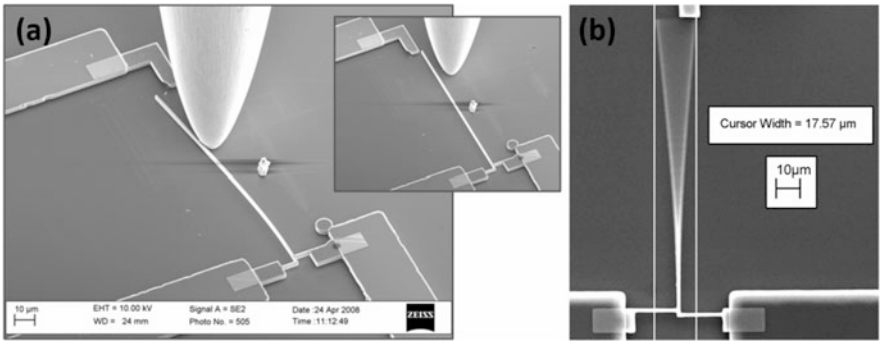

Fig. 1 (**a**) Tungsten needle statically deflecting a microcantilever in a scanning electron microscope (SEM), before deflection (inset) and after deflection, (**b**) SEM micrograph of a microcantilever in resonance [1]

the cantilever. Thus, particle concentration in the fluid sample is indicated by the rate of cantilever-mass change corresponding to a measured resonance-frequency shift rate $\Delta f/\Delta t$.

On the contrary, gas molecules with their much smaller hydrodynamic radius can move easier over large distances than airborne particles. For adsorption of molecules on a cantilever, physical-adhesion- or chemical-reaction-based capture sites are required, which are provided by a specific functionalization layer. In RSMCs as MSTs for gas sensing, a certain (or the full) region of its beam is directly coated/doped with a sensing layer for reception. Despite numerous kinds of receptors and various types of bio/chemical/physical reaction mechanisms involved in interactions between sensing layer and target analyte, in the case of MSTs, the receptor–analyte interaction mechanism is not directly used for detection, e. g., via a change in resistivity or dielectric constant. Instead, the mass change induced by analytes reception modulates the transducer output and is interpreted as response. Sensitive layers offering high sensitivity and selectivity to target analytes have to be considered.

Gas molecules injected into a chamber spread out quickly into a constant concentration around the functionalized cantilever, on which an equilibrium state between adsorption and desorption is attained within a certain response time. The number of gas molecules bound to reaction sites on the cantilever is determined by the law of mass action between the target species and the capture sites on the cantilever's functionalization layer. Thus, sampling of gas molecules on the cantilever is limited by reaction between the gas molecule and the capture sites, unlike particle sampling, which is limited by mass transport. Consequently, the concentration of gas molecules in the analyzed air-sample volume is indicated by a cantilever-mass change corresponding to a frequency shift Δf (instead of a frequency-shift rate $\Delta f/\Delta t$ in the case of particle mass-concentration measurement). Mass concentration c_m (in µg/m^3) and volume concentration c_v (in part per million/billion by volume

(ppmv/ppbv)) are typical metrics for describing the content of particulate matter (PM) and gas, respectively, in a fluid.

The limit of detection (LOD) is an important parameter for sensing applications, e. g., monitoring of toxic or hazardous substances in the environment, domestic or occupational sites. It is determined by the noise and the sensitivity of the sensor. In RSMCs, noise is characterized by a minimum detectable frequency shift, as the mean square deviation of a series of frequency measurements, while the cantilever is protected from being exposed to a measurand (either particles or gas) [7]. As an important factor of noise, the resonator's quality factor (Q) has to be maximized by an appropriate geometrical-design of low damping in air and even more in liquid.

Sensitivity of a mass-sensitive sensor depends reciprocally on the resonator mass, which should thus be as small as possible [7]. Additionally, it can be enhanced via the analyte-sampling process, which should be as efficient as possible. In the case of PM, a particle-laden fluid is directed toward the cantilever. Depending on the selected method, either particles are accelerated to large velocity and impacted onto the cantilever, herein, particle-sampling efficiency can be enhanced by the cross-sectional area of the resonator, or particles flown at small velocity around the cantilever are attracted to it by an electrical field or a temperature gradient. Particle loss from a sample taken from the ambient should be minimized, which is promoted by a monolithic integration of the cantilever within a microfluidic channel in single chip [3]. Its design should enable separation of an initially polydisperse aerosol into distinct size bins.

Gravimetric loading of gas sensors is limited by the number of reaction sites offered at the resonator's surface, which is determined by the selected functionalization material. This number can be enhanced by increasing the internal surface area, e.g., 3D convex or concave structures of nanometer-sized dimensions. Nanopores and nanowires, preferentially combined into a hierarchical architecture, can increase the area of a bare surface by orders of magnitude. For fast response and recovery all reaction sites have to be easily accessible, while an activation of adsorption or desorption reactions by illumination may be required at room temperature. Furthermore, gravimetric gas sensors based on RSMCs should be selective to a specific gas species, which is established by the selected functional receptors.

In addition to mass, a cantilever's resonance frequency is determined by its spring constant or stiffness, which can also be used as an intermediate mechanical parameter for sensing. Magnetic particles polarized perpendicular to the cantilever's top surface and brought into a parallel magnetic force gradient field reduce the cantilever stiffness, leading to a negative frequency shift [10]. The magnetic particles can be deposited on the cantilever via a liquid droplet, which evaporates afterwards. The frequency shift due to the residual particle mass is a measure for the number of deposited particles. Thus, the average magnetic moment of single micro- and nanoparticles can be determined using RSMCs. Cantilever stiffness is also changed, when it is brought into contact with a body, e.g., via a tip at beam's free-end [11]. The generated contact stiffness, which depends on the body's elasticity, increases the cantilever stiffness resulting in an increased resonance frequency. By scanning across the body's surface an elasticity map can be acquired superimposed

Table 1 Features of RSMCs for various applications

Measurand	Interaction with cantilever	Measured parameter	Response function	Application	Reference
Ultrafine particle (UFP) concentration, c_m	Electrostatic field	Mass-change rate, $\Delta m/\Delta t$	$c_m \frac{\Delta f}{\Delta t}$	Size classifying of UFPs	[8]
Gas (NO_2, ...) concentration, c_m	Physical/chemical reaction	Mass change, Δm	$c_m \Delta f$	ppb-range gas detection at room temperature	[9]
Magnetic moment, μ	Droplet dispensing	Stiffness change, Δk & mass change, Δm	$\frac{\mu}{N} \frac{\Delta f(\Delta k)}{\Delta f(\Delta m)}$	Magnetic moment per particle	[10]
Elasticity, E	Tip in contact to sample	Contact stiffness, Δk_c	$E = f(\Delta f_c)$	Elasticity/topography imaging	[11]

to the surface topography. The features of some applications of RSMCs are summarized in Table 1. According to the topic of this book chapter, we focus on gravimetric sensing applications of RSMCs in particulate-matter- and gas-molecules-containing environments.

2 Resonant Silicon Microcantilevers-Based Mass-Sensitive Sensors

2.1 Resonance Frequency

In the dynamic mode of operation, achieving optimal performance for a cantilever-mass sensor necessitates the stimulation of a mechanical resonant frequency. Various principles and methodologies of actuation can be employed to induce different resonant modes in MEMS devices, encompassing in-plane modes, out-of-plane modes, and torsional modes. Among the foremost actuation techniques are electrostatic, electrothermal, electromagnetic, and piezoelectric actuation. Detailed explanations and comparisons of these actuation techniques and resonant modes are available in existing literature [9, 12–15]. The dynamic behavior of a microcantilever is characterized by an array of harmonic flexural modes, each typically associated with amplitude maxima in the spectrum at the corresponding resonance frequencies (f_n). To capture the output signal of an RSMC, diverse mechanisms such as piezoresistive, capacitive, and optical methods can be employed for sensing. However, these distinct sensing mechanisms entail their own set of advantages and disadvantages, and an evaluation of their properties and comparisons was reported [9, 12–15]. The resonance frequency of a vibrating system is primarily

determined by two key parameters: the spring constant (k_0) of the cantilever beam and its effective mass (m_0). Generally, it is assumed that the Young's modulus of the cantilever material remains frequency-independent, and any potential effect of a coating (assuming a thin sensitive layer of uniform density ρ_s and thickness t_s) on elasticity around the relevant resonance peak can be disregarded. The resonance frequency f_0 of a coated microcantilever depends on its m_0 and k_0 according to:

$$f_0 \propto \sqrt{\frac{k_0}{m_0}} \tag{1}$$

A change of cantilever mass (Δm) and stiffness (Δk) due to uniform attachment/detachment of analytes on the sensing layer then leads to corresponding resonance-frequency shift:

$$\Delta f = \frac{1}{2} f_0 \left(\frac{\Delta k}{k_0} - \frac{\Delta m}{m_0} \right) \tag{2}$$

In case of dominant mass-change effect the stiffness term can be neglected leading to a mass sensitivity of:

$$\frac{\Delta f}{\Delta m} \approx -\frac{1}{2} \frac{f_0}{m_0} \tag{3}$$

2.2 Quality Factor

RSMCs utilized as MSTs typically function in a resonant mode, wherein the oscillation amplitude experiences attenuation over time without recurring energy input [16]. The quality factor (Q factor), a standard measure of energy dissipation in mechanical systems, is often employed to quantify this phenomenon. It is defined as 2π multiplied by the ratio of the maximum energy stored in a resonating system to the energy dissipated within one period [17]. In practical environmental applications, the operational efficiency of RSMCs can be compromised by a significant reduction in their Q factor due to damping effects. When evaluating the cantilever's amplitude spectrum, the Q factor is frequently derived from the 3-dB bandwidth $\Delta f_{3\mathrm{dB}}$ of the cantilever and is expressed as [18, 19]:

$$Q = \frac{f_0}{\Delta f_{3dB}} \tag{4}$$

The Q factor serves as a measure of the sharpness of the resonant peak and is subject to modulation due to damping effects attributed to coatings and the

viscoelastic properties of the surrounding medium. In the context of gaseous analytes, the influence of ambient damping is generally outweighed by that emanating from a sensing layer or the viscoelastic nature of a liquid-phase environment. Inadequately low Q factors can have a detrimental impact on the precision of resonance-frequency measurements, thereby diminishing the efficacy of RSMCs. To illustrate, the fundamental out-of-plane mode of a cantilever typically exhibits Q values around 20, and when immersed in water, it falls short of the requisite Q range of 25–35 necessary for maintaining stable closed-loop operation [20]. Consequently, the minimal detectable mass attainable through MSTs is inversely proportional to the Q factor ([21]; Shengle [22]).

$$\Delta m_{\min} \propto \frac{m_0}{\mathrm{Q}} \tag{5}$$

In RSMCs, the Q factor therefore contributes strongly to the figure of merit of a gravimetric sensor, i.e., for high resolution and efficient transduction, high Q factors are required [23, 24]. Thus, the LOD is lowered by improving the microcantilever's Q factor, such as choosing a higher-order resonance mode, using in-plane and torsional modes instead of out-of-plane flexural modes [17], miniaturized cantilever dimensions [25], or special device geometries such as triangular [23], disk [26], and hammerhead shapes [27].

2.3 Sensitivity

Sensitivity is a primary property to evaluate the performance of a particle or gas sensor. Exceptional mass-sensitivity values of RSMCs have been reported, without relating mass sensitivity of microcantilever platform to its sensitivity as a gas sensor, which relies on the analyte's adsorption:

$$S = \frac{\partial f}{\partial c_a}. \tag{6}$$

In this context, our consideration is centered on the assumption that the change in mass of the responsive layer, brought about by the adsorption of the specific target species, is the sole factor contributing to the shift in resonance frequency. It is imperative to acknowledge that a heightened mass sensitivity does not necessarily correlate to an equivalent increase in gas-sensor sensitivity, as the area covered by the coated layer can be notably limited. Moreover, to ensure a fair comparison of the performance of MSTs operating at distinct fundamental frequencies (f_0), it becomes requisite to employ the relative sensitivity (S_r) rather than the absolute sensitivity (S). This relative sensitivity signifies the proportional frequency alteration ($\Delta f/f_0$) of a resonant transducer concerning the concentration variation (Δc_a) of the analyte under consideration. As elaborated in a previous study [9], for instance, within the

context of utilizing mass-sensitive chemical gas sensors such as RSMCs, having uniformly coated responsive layers and vibrating in either lateral (in-plane) or transverse (out-of-plane) flexural modes, the resultant relative sensitivity S_r remains unaffected by the dimensions (length and width) of the microcantilever as well as the specific flexural eigenmode employed. Rather, it is contingent upon the thickness and density of both the microcantilever and the sensing film and further influenced by the adsorption/desorption characteristics of the sensing film [9, 17].

Alternatively, S can be expressed as the product of relative gravimetric sensitivity S_g [17] (that is, Δf due to a change in the density ρ_s of the sensing layer, cf. Eq. (3)) and S_a (i.e., the ability of this layer to adsorb/desorb the target gas given by the density change of the sensitive layer $\Delta\rho_s$ related to Δc_a). With $m_0 = \rho t + \rho_s t_s$, where ρ, ρ_s, t, and t_s are density and thickness of the microcantilever and the sensing layer, respectively, we obtain:

$$S = S_g S_a \tag{7}$$

with:

$$S_g = \frac{\partial f}{\partial \rho_c} = \frac{-1}{2} f_0 \frac{t_s}{(\rho t + \rho_s t_s)} \tag{8}$$

and:

$$S_a = \frac{\partial \rho_c}{\partial c_a}. \tag{9}$$

Evidently, the gas sensitivity (S_g) of a gas sensor cannot be enhanced through the diminution of the microcantilever's in-plane dimensions, namely its width and length. This stands in contrast to the mass sensitivity of an RSMC utilized for particle sensing, where augmenting the mass sensitivity is feasible through a reduction in the resonator's mass (effective mass), which is achieved by decreasing any of its dimensions. Additionally, it is evident that the sensitivity pertaining to adsorption and desorption (S_a) within a resonant sensor will not be enhanced through the reduction in its physical dimensions.

2.4 Limit of Detection

The pinnacle performance of a gas or particle sensor is encapsulated within its limit of detection (LOD), which designates the most minimal detectable concentration of targeted analytes. Within the context of an MST, the LOD is demarcated as thrice the noise-equivalent concentration of the analyte [17]. This can be approximated by the ratio of the minimal detectable frequency change (Δf_{min}) to the sensor's sensitivity.

$$\mathrm{LOD} = 3\frac{\Delta f_{\min}}{S} \tag{10}$$

Hence, a reduced LOD can be accomplished through the synergy of elevated sensitivity and minimal measurement noise, the latter is contingent upon the Q factor.

2.5 *Selectivity*

Selectivity embodies the capability of gas and particle sensors to distinguish a specific target gas amid a multitude of chemical molecules within an environment and to discern a particular size range of particles from a polydisperse aerosol. In the context of RSMCs, achieving selective sensing involves the strategic application of a suitable coating, acting as receptors on the cantilever surface, that can interact exclusively with the intended target gas. If the coated layer exhibits sensitivity to specific groups of gases, it often necessitates the separation of these gases before reaching the sensing layer, typically facilitated by a gas chromatography column or other pre-conditioning methodologies. This need for separation can be circumvented by utilizing arrays of RSMCs (as depicted in Fig. 2a), where individual cantilever beams are, respectively, coated with distinct materials sensitive to different gases (as illustrated in Fig. 2b). Consequently, such RSMC arrays function as a cohesive system for detecting individual species from a gas mixture, serving applications like environmental air-quality monitoring. Moreover, RSMC arrays can be employed for size-selective particle detection. In this context, their integration with microfluidic channels becomes essential, wherein specific size fractions of a polydisperse aerosol are segregated from an airflow and directed toward the corresponding RSMC for analysis.

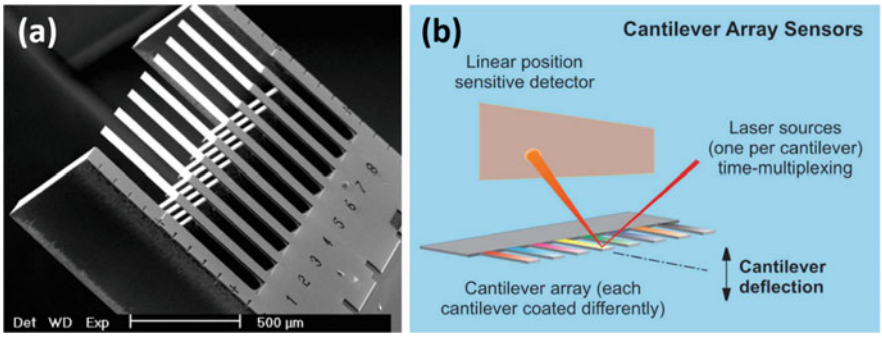

Fig. 2 (**a**) Scanning electron micrograph of a cantilever sensor array, (**b**) schematic of the cantilever-array sensor readout. Different sensing layers are shown in different colors (Courtesy of Viola Barwich, University of Basel, Switzerland) [28]

3 Methods for Fabricating Sensitive Layers

The fabrication of a sensitive layer holds paramount importance for the gas sensing performance of RSMCs. An optimal receptor material should exhibit strong, selective, and reversible interactions with analytes, while also demonstrating attributes such as rapid response and recovery times, long-term stability, reproducibility, and resistance to corrosive environments. Notably, unlike resistive or capacitive sensors, the concerns regarding changes in resistivity or dielectric constant can be mitigated when selecting receptors for RSMCs. Furthermore, since the sensitive layer is devoid of applied voltage or current, which can be particularly destructive for nanostructures, an extended operational lifespan for the devices is anticipated. In principle, any material capable of capturing specific amounts of analyte molecules either on its surface (adsorption) or within its volume (absorption), thereby inducing a mass alteration, can serve as a suitable sensitive layer on an RSMC. A miniaturized cantilever beam, characterized by a high surface-to-volume ratio, substantially enhances sensing performance. Nevertheless, the diminutive dimensions pose challenges in the fabrication of sensitive layers. Additionally, there are supplementary attributes that are favored in receptors: (a) The ability to interact with the cantilever beam without imposing stress, as such stress could trigger nongravimetric stiffness-related changes in resonance frequency. (Only a limited number of RSMCs exhibiting nongravimetric effects display responses proportionate to changes in analyte concentration.) [16] (b) The capability to avoid excessive damping of the RSMC's free oscillation, as excessive damping leads to a substantial reduction in the quality factor (Q factor), thereby impeding the limit of detection (LOD).

A large variety of sensing materials have been investigated for volume absorption and surface adsorption of gases. Bulk sorption receptors have been mostly investigated and well established as sensitive layers, they are typically polymer films or soft organic materials. The absorption mechanism of gaseous analytes to the bulk volume of a sensing layer to its saturated status is not a simple condensation, diffusion, and replacement process. Their volatility and thermodynamic potentials have to be considered, which has been discussed thoroughly in literature [16]. In general, mass change is directly proportional to the analyte concentration in the gas phase, if there are no stressing effects generated, resulting linear responses of the RSMCs. Mostly, when the thickness of a sensitive layer is comparable to the beam thickness of the cantilever, the influence of nongravimetric responses caused by viscoelasticity and stiffness change have to be deliberated, since they may lead to resonance-frequency and oscillation-phase change. Viscoelastic effects between before and after gaseous-analyte absorption should not be a concern for sensor design, since the detected concentrations of target gases are in the range of hundreds ppm level or lower. Humidity is the exception to be noted, because the usual environmental humidity level (50%) at 25°C corresponds to absolute volume concentration of about 15,600 ppm, which is huge compared to the threshold limit values of other target gases.

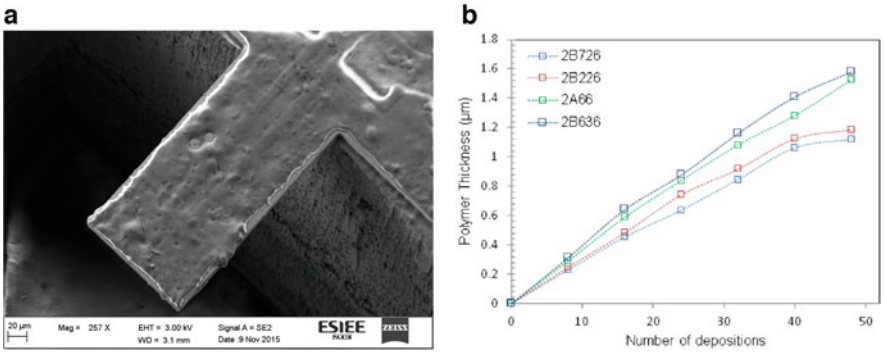

Fig. 3 (**a**) Silicon microcantilever coated with a film of polyepichlorohydrin (PECH) polymer by spray coating, (**b**) Polymer film thickness as a function of the number of depositions for four microcantilevers of width = 140 µm and length = 260 µm [32]

Dip coating (also as dip casting, drop coating/casting) is the easiest and most commonly used method to immobilize molecular recognition agents on microcantilevers. The cantilever beam is simply dipped in a (water-based) droplet, and the physically adsorbed liquid is subsequently evaporated by annealing at a certain temperature, after which the contained sensing material stays on the cantilever surface. Dip coating is especially preferred for thiol and amino self-assembled monolayers (SAMs) and organosilane modification. For example, when using thiol SAMs to attach receptors, metal layers of chromium/gold are previously deposited using e-beam evaporation, where chromium of few to tens nanometers acts as an adhesion layer for gold and the gold layer is used to attach the thiol groups. Similarly, a silicon-oxide layer on a microcantilever is effective for immobilizing organosilane included chemical compounds. After dipping the pre-modified microcantilevers in prepared solutions, either single or multifunctional SAMs are coated on the microcantilevers. Various biomolecules and gases have been detected using cantilever platforms with dip-coated and self-assembled sensitive layers [15, 29–31].

Spray coating can be thought as improved dip coating technique, which enables the coating of materials solubilized or suspended as particles in carrier solvents as aerosol flow. As for coating on cantilever beams, shadow masks can be used to achieve the area-selective deposition (Fig. 3a). In an airbrush spray-coating process, the distance between sample and nozzle together with pressure has to be optimized to allow for reproducible layer deposition, where the layer thickness can be controlled by varying the concentration of polymer solution and the deposition cycles (Fig. 3b) [32, 33]. In addition, a post annealing process is generally required for solidifying and homogenizing the coated film. As reported by E. Lange et al. [33], for a polymer-coated RSMC (thickness of ~6 µm), a linear model for the decrease of the resonance frequency with increasing polymer thickness is valid for thicknesses less than 1 µm, with increasing thickness of the polymeric layer, the decrease of the cantilever resonance frequency is less than proportional. In fact, for thicknesses

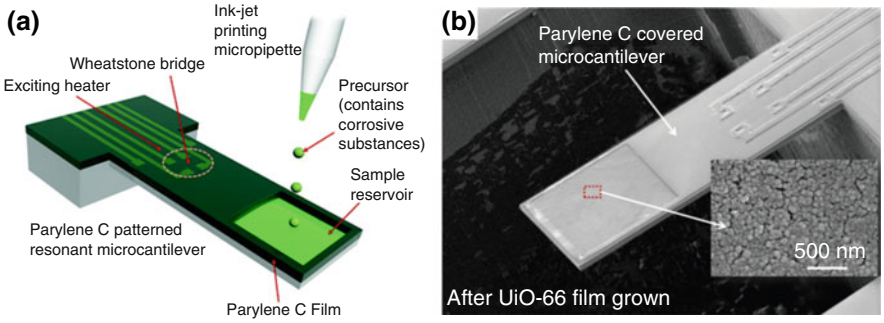

Fig. 4 (**a**) Schematic showing the structure of the Parylene-C patterned RSMC, where a sample reservoir is formed at the free-end of the beam. (**b**) scanning electron micrograph showing that the precursor is precisely loaded onto the reservoir [35]

above 30 μm, the resonance frequency would increase again, since the system has now changed from a polymer-loaded silicon cantilever to a silicon-loaded polymeric cantilever with the consequence that the resonance frequency increases linearly with increasing polymer thickness. Not only is the resonance frequency affected by the polymer thickness but the vibration amplitude and the Q factor are also affected. This is partially due to the fact that Q factor and vibrational amplitude depend to a critical extent on the plastic or viscous properties of the thin polymer films (homogeneity and morphology), thus, on the quality of the deposited layer and the reproducibility of the deposition process. Researches of polymer-induced nongravimetric response of cantilever beams have been seldom reported, while the frequency dependence of viscoelastic receptors on other types of MSTs can be found [16].

Inkjet printing of functional materials is a digital structuring process inspired by paper printing technology [34]. Metals, polymers, or ceramics transferred into low viscous inks can be applied selectively and contactless. The inkjet-printing process takes place mostly at room atmosphere and low temperature. It allows for good control of deposition area and layer thickness, and is, therefore, suitable for precisely printing sensing materials on a microcantilever surface (Fig. 4). Liposomes with specific membrane proteins [13], carboxyl-group-functionalized mesoporous-silica nanoparticles (C-MSNs) [36], and a metal-organic framework (MOF) of a UiO-66 film [35] have been inkjet-printed on microcantilever for phages and gases detection.

Chemo-physical deposition encompasses the process of depositing thin inorganic films and extremely thin layers. Within the realm of semiconductor technology, a plethora of methodologies have been developed to facilitate this, including but not limited to chemical vapor deposition (CVD), sputtering (in its various iterations such as direct-current, radio-frequency, reactive, and magnetron sputtering), atomic-layer deposition (ALD), and molecular-beam epitaxy (MBE). Commonly referred to as “bottom-up” techniques, these methods involve the gradual deposition of materials, layer by layer. Consequently, the utilization of shadow masks facilitates the achievement of area-selective deposition.

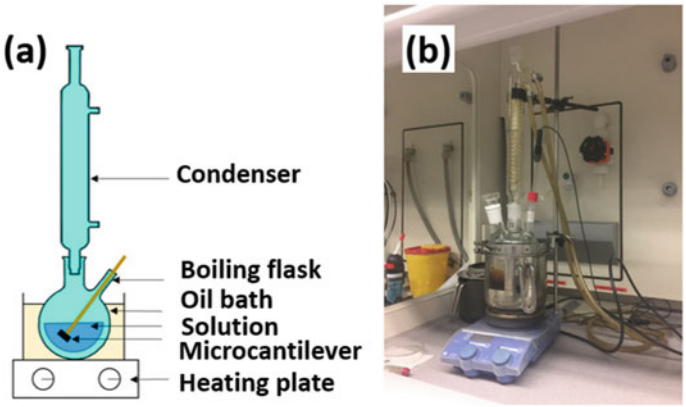

Fig. 5 Schematic (**a**) and photo (**b**) of setups of ZnO NRs array synthesis using CSD method on the surface of the microcantilever

Chemical-solution deposition has been developed to synthesize composite nanomaterials. The internal surface area of the microcantilevers can be enhanced by depositing nanostructures on its surface, therefore its sensitivity can be notably improved. Nanostructures, especially of MOS, such as titanium dioxide (TiO_2), thin dioxide (SnO_2), and zinc oxide (ZnO), have attracted great research interests for gas sensing. Chemical-solution deposition of MOS nanostructures is considered as a "bottom-up" method. To deposit nanostructures on microcantilevers, prior to the CSD process, a pre-surface-modification is required, for example by sputtering or self-assembling. Recently, J. Xu et al. reported a two-step ZnO nanorod (NR) deposition method. A zinc nanofilm has been sputtered using a direct-current sputtering technique, and the sputtered zinc was further oxidized at a certain temperature to transform into a ZnO nanofilm. The obtained ZnO nanofilm worked then as a seed-layer for a subsequent growth of ZnO NRs using a CSD method (Fig. 5). Area-selective deposition was realized on either the top or bottom surfaces of the microcantilever, depending on the cantilever-release order, with the help of photolithography or a shadow mask [15, 37]. Similarly, vertical ZnO NRs, ZnO nanotubes (NTs) [38], CuO NRs [39], and TiO_2 NRs [40–42] have been fabricated on the whole backside surface of commercial Tipless Force Modulation atomic force microscopy cantilevers (TL-FM AFM cantilevers) by CSD method.

Rather, for high-sensitive RSMCs-based sensors, assembling of a sensitive organic-polymer nanofilm onto a high-dimensional nanomaterial matrix is beneficial to enlarge the resonator's specific surface area for increasing the amount of active reaction sites to the gaseous analytes [15, 43]. To build these three-dimensional (3D) sensing nanostructures on a microcantilever, a combination of several of the aforementioned methods is necessary. -NH_2-functionalized mesoporous thin films (MTFs) have been fabricated on the cantilever free-end by premodification, dip coating, self-assembling, chemical-solution etching (CSE), and annealing [44]. Furthermore, due to the special properties of Si, a microcantilever can also be

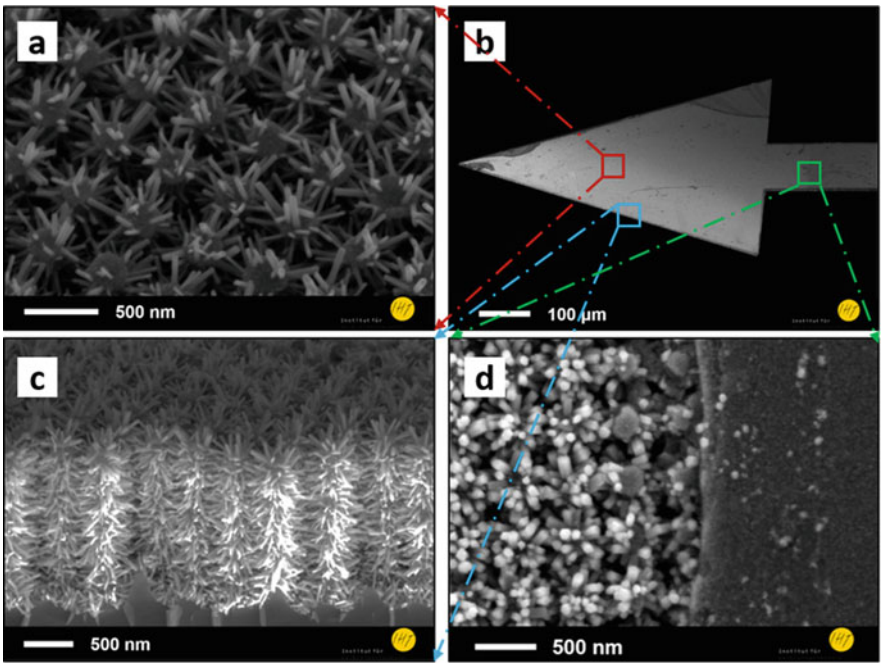

Fig. 6 Scanning electron micrograph (SEM) of a 3D ZnO-NRs@Si-NPLs-patterned RSMC (3-PμC): (**b**) inclined view (30°C) of RSMC with triangular-shape free end and 3D ZnO-NRs@Si-NPLs; (**a**), (**c**), partial enlargement views of 3D nanostructures, (**d**) top view of the boundary between 3D ZnO-NRs@Si-NPLs-patterned and bare silicon [30, 31]

micromachined by etching to form nanostructures using a top-down reducing process. Si nanopillars (NPLs) have been top-down etched on microcantilevers and used as sensing platform as reported [30, 31, 45, 46]. ZnO nanofilms and NRs have been deposited on Si-NPLs leading to 3D frameworks (Fig. 6). With specific functional groups, selective reactions can be defined within mixtures of different target molecules.

4 Particulate Matter

4.1 Particle Sensing

Particulate matter (PM) is among the biggest hazards worldwide for quality of air and water. A prominent example is micro- or nanometer-sized plastics, generated by wear or abrasion from tires, textiles, or disposables. A wasted coffee cup lid of polystyrene exposed to ultraviolet (UV) light over a period of 8 weeks, e. g., can release more than 10^8 particles with an average diameter of 224 nm per mL in water

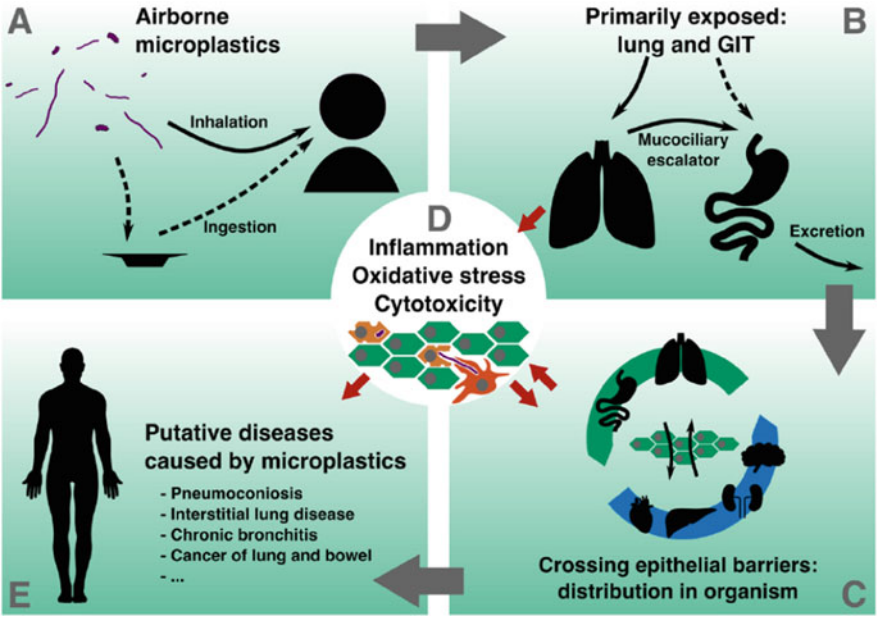

Fig. 7 Micro-/nanoparticles' toxicity pathways: (**a**) Inhalation or ingestion facilitates the entry of airborne microparticles into the human body, predominantly affecting the lungs and gastrointestinal tract (GIT). (**b**) Microparticles residing in the upper airways can be cleared through the mucociliary escalator, leading to their migration into the GIT. While some particles are expelled through excretion, others penetrate deeper into lung and GIT tissues. (**c**) Microparticles have the potential to breach epithelial barriers, accessing the lymphatic system and bloodstream. This enables their systemic dissemination, ultimately reaching various secondary organs. (**d**) Interaction with exposed tissues can incite inflammation and oxidative stress, potentially culminating in cytotoxicity. These outcomes compromise epithelial barrier integrity, elevate microparticle mobility within the organism, and can lead to additional adverse health effects. (**e**) Conditions such as pneumoconiosis, interstitial lung disease, chronic bronchitis, and lung and bowel cancer may be linked to microparticle exposure [48]

[47]. Such submicron plastics can also be generated by degradation of microplastics, entering the environment via wastewater, it may be consumed by aquatic organisms and thus contaminate seafood [48], then released in the air (Fig. 7a). PM can cause long-term exposure of breathing air becoming a life-expectancy hazard similar to inhaling tobacco smoke [49]. Airborne PM can be inhaled into the lung and deposited in the respiratory tract (Fig. 7b), where pulmonary alveoli and human cells have diameters of 200 μm and 8 μm, respectively. Deep-penetrated nanometer-sized particles (ultrafine particles, UFPs) can be left unrecognized from alveolar macrophages for more than 100 days [50]. During this long residence time, they may cross the air–blood barrier, move to the organs via the bloodstream, and translocate through the blood–brain barrier to the brain (Fig. 7c, d). Pollutants transported with the particles can accumulate in its functional tissues to develop toxic effects there (Fig. 7e) [50]. In this context, PM as possible carriers of viruses were related to the

severity of COVID-19 as well as the emergence SARS-CoV-2 variants [51–53]. A correlation was supposed between the worldwide deaths from the early corona pandemic to long-lasting exposure to air polluted by anthropogenic sources, e.g., PM generated by combustion [54]. Since SARS-CoV-2 is believed to spread mainly by aerosols, their detection in exhaled air sampled using inertial impaction in a micromachined silicon chip can give more comprehensive and faster testing results than conventional nasopharyngeal swab tests [55]. However, the portable device for sampling exhaled air is still labor-intensive, requires 1 h for the testing, and is limited to particles of size larger than 300 nm.

Lightweight and battery-powered personal concentration and size monitors are needed to protect people from exposure to PM in harmful concentrations. Low-cost detectors of PM concentration are available based on optical scattering and in use for outdoor PM monitoring. However, the minimum detectable particle size is limited by the detectable light scattering intensity, which is inversely proportional to the sixth power of the particle diameter. Recently, methods relying on a laser source and an image sensor are reported, which can detect particles less than 100 nm in diameter [56], but commercial low-cost optical particle counters (OPCs) are typically limited to the size range above 300 nm [57]. However, environmental airborne PMs, which are emitted by diesel and gasoline engine vehicles, have diameters in the ranges of 20–130 nm and 40–80 nm, respectively [50]. Despite that, among the studies on toxicological effects of PMs, only few consider such UFPs, which was attributed to the technically challenging measurement of UFP concentrations [50]. To be detectable by optical scattering, UFPs can be increased in size by a liquid sheath in a condensation particle counter (CPC), i.e., system complexity is higher compared to OPCs. For UFP size classification, CPCs can be combined with impactor stages.

Charging of UFPs is used in several commercial handheld monitors, using diffusion classifiers with sensitive electrometers for detection [58]. Size distributions of charged UFPs can be measured by separating polydisperse-UFPs into several size bins in the electrostatic field of a miniature differential mobility analyzer (DMA) channel [58]. By combining the DMA with a two-stage inertial classifier, a UFP dosimeter is obtained for monitoring particle density and size distributions [59, 60]. Nevertheless, printed-circuit-board-(PCB)-based DMA channels are still rather bulky with millimeter-scale electrode distance and several tens of millimeter length [58, 60]. Correspondingly, the reported designs require supply voltages in the kV range for operating the DMA and a unipolar charger [58]. A diaphragm pump of several Watts of power consumption is necessary to provide the necessary pressure drop across the fluidic channel for maintaining required flow rates in the range of hundreds mL/min [59, 61].

Optical detectors and electrometers indicate number concentrations of PM, while air-pollution limits by the World Health Organization (WHO) and national authorities are given as mass concentrations (in $\mu g/m^3$). They can be directly determined by weighing of particulates sampled on a filter (so-called gold standard). For real-time monitoring of mass concentrations of environmental air pollution and occupational exposures, tapered element oscillating microbalance (TEOM) devices have been

approved by the U.S. National Agencies, e.g., for personal dust monitoring in coal mines. Unfortunately, TEOMs give only concentrations, not sizes of PMs.

Real-time monitoring of in-situ levels of air pollutants for healthcare demands more compact, integrated and personalized devices, for which chip-based MEMS have been considered [61]. Low limits of detection are possible with respect to both particle size and mass concentration using MEMS devices which have typically much smaller dimensions than those basing on optical scattering, complementary metal oxide semiconductor (CMOS) imaging, quartz crystal microbalance (QCM), surface acoustic wave (SAW), and bulk acoustic wave/film bulk acoustic resonator (BAW/FBAR) [5]. MEMS resonators, to which NPs are attached, deliver mass concentrations (in $\mu g/m^3$) according to the regulatory air-pollution limits.

Particles can be separated into size classes (PM_x), passively, by aerodynamic filtering or impacting them on plates and, actively, by differential analyzing of the particles' mobility in an electrostatic field [3]. MEMS devices more frequently use passive technologies for separating airborne PM, like virtual and cascade impactors, due to their simplicity. Furthermore, particle-deposition probability in impactors has a size-dependence, which is similar to that of the different sections of the respiratory system [3]. Extensional-mode resonators like the thermal-piezoresistive oscillator (MEMS-TPO) or the thin-film piezoelectric-on-silicon (TPoS) oscillator can be assembled together on a PCB with a separate millimeter-sized impactor. A TPR with a single-stage impactor offer an LOD of 50 $\mu g/m^3$ for cigarette smoke in the size class of $PM_{2.5}$ [62] and a TPoS with a dual-stage cascade impactor made of aluminum can detect 10 $\mu g/m^3$ of an aerosol nebulized from a sugar solution in a size-bin range of 1.03–2.54 μm [63].

The necessity of aligning a nozzle or an air-microfluidic channel for manipulating the aerosol jet toward the microscale surface of a resonator is challenging and a source of uncertainty. Alternatively, a resonant mass balance can be integrated on a single chip aerosol impactor, e.g., an AlN thin-film piezoelectric resonant mass balance, an impactor nozzle, and an impaction microchamber are fabricated on the same silicon substrate [64]. It can measure very low concentrations (2.5 ng/m^3) of residual particles of 80 nm to several μm size in a laboratory environment, whose particle concentration is controlled by a high-efficiency particulate air filter (HEPA). A cascade assembly of two separate sets of thermal-piezoresistive resonators (MEMS-TPRs), each combined with impactor nozzle and impactation chamber, can detect UFPs in a defined size bin of 40 to 141 nm [65]. A drawback of impactors is that their operation requires an external pump to maintain a certain pressure drop across the channel for a sufficient flow rate and velocity of the particles. Thus, on the one hand, large flow rate (0.25 mL/min) and particle velocity (276 m/s) are necessary for enhancing probability of particle landing on the desired location [64], while, on the other hand, measures may be required for minimizing particle loss by impacting on the fluidic-channel wall and bouncing from the collection area.

Alternatively, the natural charge of aerosol nanoparticles can be used for sampling them on an RSMC particle detector. The portable (0.4 kg) and battery-powered (3.5 W) standalone particle monitor Cantor (*Can*tilever-based nanoparticle moni*tor*) [62] (Fig. 8, left) is a direct-reading/real-time gravimetric monitor for UFPs, which

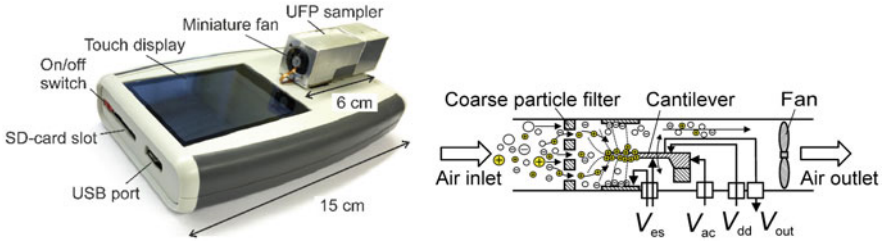

Fig. 8 Pocket-size, battery-powered NP monitor "Cantor" with a weight of 0.4 kg and a power consumption of 3.5 W (V_{es}: cantilever bias voltage for particle sampling, V_{ac}: voltage for electro-thermal actuation of cantilever in-plane oscillation, V_{dd}: supply voltage of piezoresistive full Wheatstone bridge (WB), V_{out}: bridge output voltage) [66]

are sampled by an electrostatic field. Particle velocity can be much lower than in an impactor sampler, i.e., instead of an external pump, an integrated low-power and noiseless miniature fan (MF_10A03A, SEPAEUROPE GmbH, Germany, 10 mm × 10 mm × 2.2 mm, 0.17 W, 1.6 dB noise) is used to generate a continuous flow of particle-laden air [66]. The miniature sampling head (60 mm × 20 mm × 23 mm, 52.3 g, 0.41 W) with plug connectors comprises a micro filter (μF) and an impactor filter (IF) at its inlet for separating coarse particles of >2.5 μm and >1 μm in diameter, respectively, from the air flow (Fig. 8, right).

The positively charged fraction from the size-filtered particle stream is moved to a negatively biased (V_{es}), in-plane resonant-operated (V_{ac}) piezoresistive microcantilever (PμC), where the particles are captured. Owing to the mass increase by the attached particles on cantilever surface, the resonance frequency f_0 of the MEMS-PμC decreases at a rate given by the particle mass concentration c_m, i.e. c_m is indicated by the resonance-frequency shift rate $\Delta f/\Delta t$ according to:

$$c_m = \frac{2m_0}{\xi \dot{Q} f_0} \frac{\Delta f}{\Delta t} \tag{11}$$

with the cantilever mass m_0, the air-flow rate $\dot{Q}$, and the particle-sampling efficiency ξ. Cantor was tested in a sealed chamber containing carbon aerosols, whose polydisperse size distribution in nano range (Fig. 9a) was controlled using a fast mobility particle sizer (FMPS, 5.6–560 nm, 32 size bins, TSI Inc., Model 3091, Shoreview, MN, USA). Cantor's resonance frequency and the mass concentrations calculated from $\Delta f/\Delta t$ using Eq. (1) are depicted as Fig. 9b. A high correlation of $R^2 = 0.995$ (Pearson's $R = 0.997$) is observed between the Cantor's output and the FMPS (Fig. 9c). In addition to carbon, polydisperse titanium, silica and silver aerosols of different average diameters were measured in the same camber showing correlations between 0.945 and 0.996 (Pearson's $R = 0.973$ to 0.998). The sampling efficiency of the Cantor increases with decreasing particle diameter (Fig. 9d), which is expected if the PμC in the particle flow channel is described as an electrostatic precipitator in a coaxial tube-wire configuration [67].

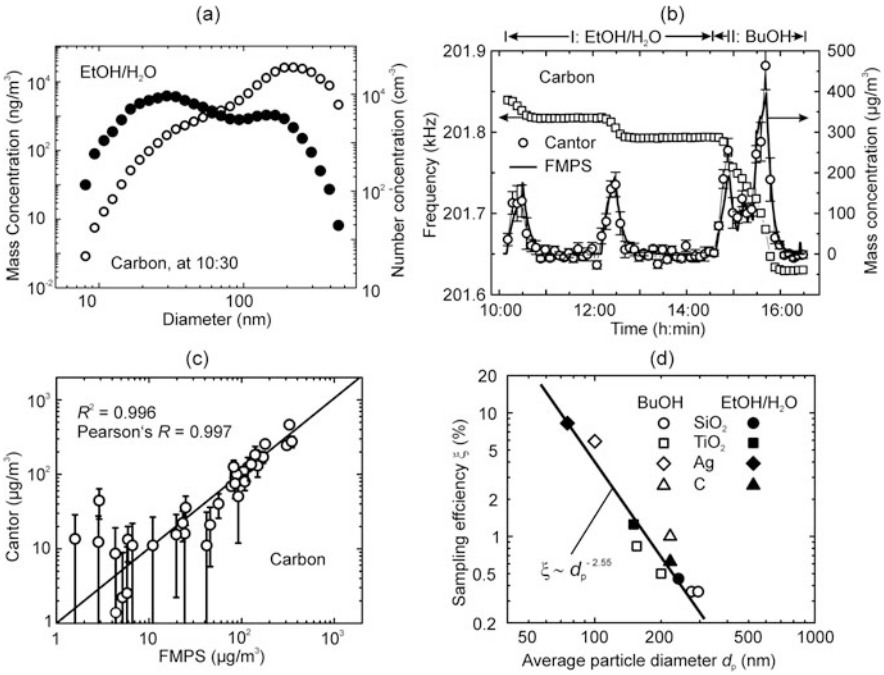

Fig. 9 Size distribution of carbon nanoparticles (**a**), temporal change of mass concentration (**b**), correlation of Cantor vs. reference (FMPS) of $R^2 = 0.996$ and Pearson's $R = 0.997$ (**c**) and sampling efficiency of four different nano aerosols (**d**) [66]

The Cantor's LOD $= 3 \times \delta f/S = 15$ µg/m^3 (with the minimum detectable frequency-shift rate $\delta f/\delta t$ and the mass-concentration sensitivity $S = \delta f/c_m$ [7]) was further improved to 1.4 µg/m^3 by reducing an adverse effect by the parasitic feedthrough between the electrothermal actuator and the piezoresistive Wheatstone bridge (WB), which are both integrated on the cantilever [68]. Furthermore, sensitivity depends inversely on cantilever mass ($S \propto 1/m_0$), i.e., can be enhanced using a tiny commercial atomic-force-microscopy PµC with thermal bimorph out-of-plane actuator (SCL Sensor Tech., PRSA 300 × 100 µm TL Probes) with a mass of $m_0 \approx 0.31$ µg. This is by a factor of ~20 lower than the Cantor's cantilever mass (7.5 µg) and leads to a correspondingly increased sensitivity and a reduction of the LOD of carbon nanoparticles to 0.7 µg/m^3 [68] and cigarette smoke to 1.3 µg/m^3 [69].

Further improvement of the LOD as well as size selectivity will be needed for meeting the requirement of monitoring health hazards, beyond those imposed by inorganic PM from artificial sources (industry, traffic, domestic). Bioaerosols (viruses, bacteria, fungal spores, plant pollen, …) are excessively generated and emitted into the atmosphere caused, e. g., by the dramatically increasing demand of food, and may act as possible spreaders of various deadly infections. Onsite bioaerosol sampling and detection devices are required for real-time and continuous

monitoring of bioaerosols in the field, enabling quick response to sudden risks [61]. They should be able to separate airborne particles in microsamples taken from the environment in bins of defined target sizes. To minimize sample loss, such miniaturized air collectors should be coupled with microfluidic devices in a microfluidic chip-based integrated platform.

In Table 2, chip-size sensors for gravimetric detection and sizing of PM are listed. A single-chip MEMS thin-film piezoelectric-on-silicon (TPoS) oscillator in a microchamber can be impacted by particles injected via a micro nozzle [65]. The AlN resonant mass balance has a very low LOD in the range of ng/m^3, for which 1 h of sampling is necessary. For particle size only a lower limit of 80 nm is defined. A piezoresistive microcantilever (PμC) with an integrated microfluidic channel (μFC) can measure particles in the size range between 1 and 4 μm, which is defined by micro-pillar filters at the inlet and the outlet of the μFC [70]. Here, an LOD of 2 μg/m^3 within 41 min is obtained. The PμC with the filter-containing microchannel for collecting the particles >1 μm is fabricated using low-cost non-SOI Si (111) substrate requiring a combination of anisotropic wet etching (tetramethylammonium hydroxide, TMAH), low pressure chemical vapor deposition (LPCVD), and reactive ion etching (RIE). A virtual impactor of two vertically stacked μFC chips with at 50% cut point at 2.5 μm can separate $PM_{2.5}$ from coarse particles and sample them by thermophoresis on a bonded film bulk acoustic resonator (FBAR) [71]. Although such gravimetric sensors can detect UFPs (unlike optical sensors), separation in size bins has not demonstrated so far. Using microfilters, separation of a defined size bin of 1–4 μm from an incoming polydisperse aerosol was reported, which is not in the UFP range [70]. Classification of UFPs in the size range between 40 and 250 nm by their electrical mobility into several bins, however, is possible using a chip-size differential mobility particle sizer (DMPS), represented by a μFC integrated with a PμC [8, 25, 72].

Figure 10, left shows a DMPS chip based on a PμC ($171 \pm 1 \times 10.5 \pm 0.4 \times 3.0 \pm 0.5$ μm^3), which is integrated in a microfluidic channel (μFC) with a small volume of ($270 \pm 15 \times 191 \pm 1 \times 72.4 \pm 0.5$ μm^3). Four arrays of eight sets of these μFC/PμC microsamplers are designed on an MEMS die of 8×8 mm^2 (Fig. 10, right). A combined anisotropic–isotropic process with standard *n*-type (1–10 Ω cm), 275 ± 15 μm-thick (100) silicon was used for releasing a PμC above a μFC from its front side [25]. Deep reactive ion etching at cryogenic temperature (cryo-DRIE) was employed using photoresist (AZ 5214) as mask material. First, the μFC's cross-sectional area with the cantilever inside was anisotropically etched using SF_6/O_2 (−95°C, O_2: 9 sccm, 1 min) to a depth slightly exceeding the cantilever's desired height (3 μm). The inherent passivation of the sidewalls with silicon oxyfluoride (SiO_xF_y) deposits from the etching reaction is stable at cryogenic temperatures, i.e., unlike the Bosch process, a separate deposition step is not needed. By lowering the O_2 content to 4.5 sccm in the process gas mixture, etching is then switched to combined vertical and lateral etching from both sides below the cantilever until it is completely released. The PμC's and μFC's sidewalls are protected by the SiO_xF_y passivation, if the O_2 content is carefully set. At too-high values (5 sccm) lateral under etching is not efficient enough to

Table 2 Gravimetric chip-sized aerosol particle detectors for personal air-quality monitoring. Abbreviations are given below[a]

Detection method	Air-flow generator	Sampling/separating			LOD (μg/m^3)	Sample mass (pg)	d_P size bin (nm)	Reference
		Method	Rate (mL/min)	Time (min)				
MEMS-TPoS	Pump	Impactor	250	60	2.5×10^{-3}	37.5	> 80	[64]
MEMS-PμC	Pump	Dual-stage microfilter	0.11	41.6	2	9.2	1,000 – 4,000	[70]
FBAR (ext.)	Fan	Thermophoresis	9.5	7	1	66.5	$PM_{2.5}$	[71]
MEMS-PμC	Fan	DMA	0.3	9.5	0.73	2.1	43.2, 77.3, 138.0, 245.9	[8]

[a] Limit of detection (LOD), particulate matter of aerodynamic diameter of less than 2.5 μm $PM_{2.5}$, micro-electro mechanical system (MEMS), piezoresistive microcantilever (PμC), film bulk acoustic resonator (FBAR), thin-film piezoelectric-on-silicon (TPoS) oscillator, differential mobility analyzer (DMA)

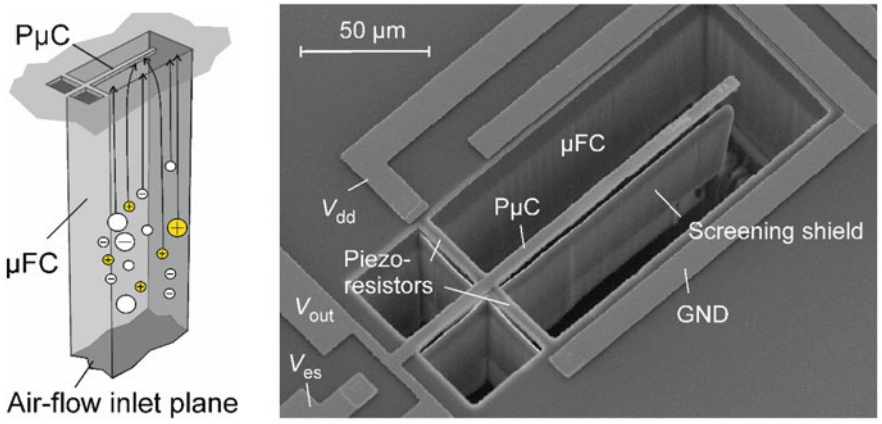

Fig. 10 Schematic of a microfluidic channel (μFC) guiding airborne particles to a piezoresistive micro cantilever (PμC) (left) and scanning electron microscopy (SEM) photograph of a fabricated device (right) [25]

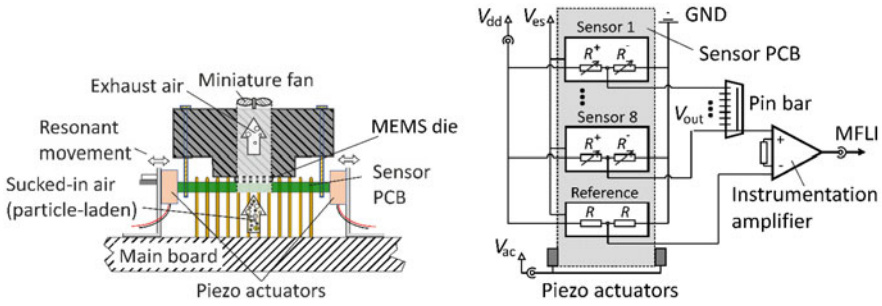

Fig. 11 Schematic of a differential mobility particle sizer (DMPS) (left) and electric circuit diagram of the system (right) [8]

completely release the cantilever, at too-small O_2 content (3.5 sccm) the SiO_xF_y passivation starts to be attacked. Furthermore, the highly *p*-doped contact areas (e. g., to the piezoresistors) need to be protected from preferential etching compared to low-doped silicon using a Au/Cr metallization. Finally, a second anisotropic etching (−80°C, 7 sccm O_2, 72 min) is done from the backside through the entire wafer, while the front side is covered by photoresist (AZ 5214) as an etch stop. After removing the resist, the PμC-in-μFC structure is completed (Fig. 10, right). Due to the slender shape of the cantilever, piezoresistors for oscillation detection are not integrated on it but are realized as suspended struts between the cantilever and the μFC's sidewalls. Similar design is reported with nanowire-based piezoresistive elements [73].

The completed MEMS die is connected via soldered copper wires of the Au/Cr thin-film metallization to a printed circuit board (PCB, 40 mm × 40 mm), which is screwed to a 3D-printed air-intake socket (Fig. 11, left). For excitation of the PμC in

in-plane resonant oscillation mode, the PCB is pressed between two miniature piezo actuators (PL055.3, PI Ceramic GmbH, Lederhose, Germany). The electric circuit diagram in Fig. 11, right shows the pins to the excitation voltage (V_{ac}), the supply voltage of the piezoresistive half bridges (V_{dd}), the bias voltage for particle sampling (V_{es}), and ground (GND). The output of the piezoresistive half bridges (V_{out}) is connected via a pinbar to an instrumentation amplifier (INA217, Texas Instruments) followed by a Lock-in amplifier (MFLI, Zurich Instruments). Laminar air flow (10^{-2} m/s) is generated by a low-noise, low-power miniature fan (HY10A03A, SEPA Europe, Germany max. Flow rate: 0.8 L/min, max. Pressure difference: 7.0 Pa). The naturally positive-charged fraction of the sucked-in aerosol is directed to the negatively biased PμC, where they are deposited and detected continuously by the resonance-frequency shift acquired within a sampling time of 9.5 min. Resonance frequencies are obtained from repeated frequency sweeps. Owing to the small dimensions of the μFC, sampling of UFPs is possible at low voltages (< 30 V) and a low flow rate of ~300 μL/min per μFC. Large sensitivity and thus low LOD can be obtained for the PμC with a very small mass $m_0 \approx 16$ ng and $Q \approx 700$ in normal room atmosphere and 15,500 in vacuum.

Separation of an aerosol of defined size in a DMA requires knowledge of the percentage of the charged fraction and the particles charging state in dependence on particle size. A determined charge distribution can be adjusted using a unipolar diffusion charging unit. Furthermore, large supply voltages in the kV range are required. However, multiple charging may occur and different size bins may thus overlap in mobility. Instead, the naturally positive-charged fraction of the aerosol can be used, whose charge distribution was determined beforehand. Instead, the size and charge distributions of an NaCl aerosol measured in the range of $d_p = 20$ nm to 400 nm [74] could be used as a model system for other aerosols. The percentage of positive-charged fraction of the particles in the air stream varies between ~10% to ~40% in the size range between 20 and 400 nm, with the maximum values between 100 and 200 nm [8]. Their average charging state (in units of elementary charges) increases from ~1 to ~3 between 20 and 400 nm.

Computational fluid dynamics (CFD) modelling with air-fluidic components for separation of particles in flow channels is employed, i.e., the electrostatic and laminar flow modules of COMSOL Multiphysics 4.4b for electrical-field and air-flow modelling, and is "particle tracing for fluid flow module" for computing particle motion. Electrical, drag, gravity, and Brownian forces are taken into account in the electrical and air-flow fields. Smooth spherical particles are considered without collisions and with a uniform lateral distribution across the inlet plane of the μFC. Wall loss of particles can be expected to be lower than ±5% in case of small length-to-width ratio (3.73) of the μFC. The electrical field is realized by the negative potential V_{es} applied to the PμC and keeping the wall of the μFC at ground potential.

CFD modelling shows that positive-charged particles are directed to the PμC and deposited there depending on their velocity (at a pressure drop across the μFC of 1 Pa) and charging state. Based on the model assumptions, the number of collected particles in separate size classes was determined at distinct bias potentials in the range of −5 V and −160 V, yielding collection efficiencies for each size bin and

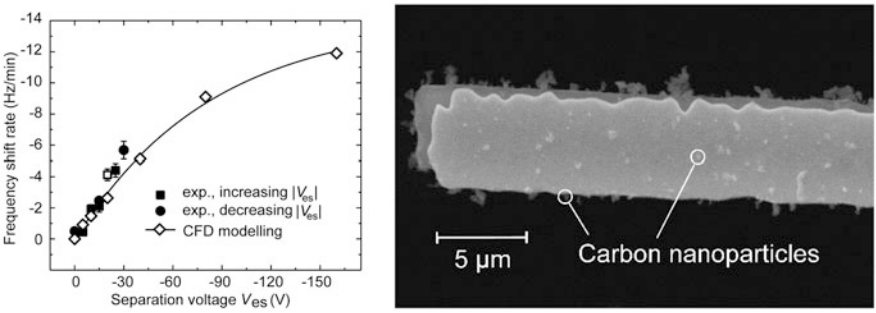

Fig. 12 Frequency-shift rate determined by computational fluid dynamics (CFD) modelling and measured with a MEMS-DMPS operated in a carbon nano aerosol ($c_m = 10$ µg/m^3) vs. sampling voltage (left) and PµC with attached carbon nanoparticles (right) [8, 25]

collection voltage. The mass of the deposited particles in each size class can be calculated assuming the model particles have spherical shape and a uniform density (i.e., carbon, 2.26 g/cm^3). By adding the sampled particle mass in the selected size bins (in the range of 20–400 nm), the total deposited mass Δm is obtained for each bias voltage setting. From Δm, a frequency-shift rate of the PµC can be calculated according to $\Delta f/\Delta t = f_0/(2\, m_0 \times \Delta t) \times \Delta m$. With the sampling time Δt, an analytical dependence can then be fitted through the data points by CFD modelling. Alternatively, this dependence can be described by a voltage-resolved frequency-shift vector, which is related to a size-separated mass-concentration vector according to:

$$\begin{pmatrix} [\Delta f/\Delta t]_1 \\ \vdots \\ [\Delta f/\Delta t]_v \end{pmatrix} = \frac{f_0}{2m_0} \dot{Q} \begin{pmatrix} \xi_{11} & \cdots & \xi_{1u} \\ \vdots & \ddots & \vdots \\ \xi_{v1} & \cdots & \xi_{vu} \end{pmatrix} \begin{pmatrix} c_{m,1} \\ \vdots \\ c_{m,u} \end{pmatrix} \tag{12}$$

The $v \times u$ particle-collection efficiency matrix at $v = u$ is obtained from CFD modelling using the charge distribution data from the model system. Solving the system of eight equations represented by Eq. (12) mass concentrations in separate size bins is obtained. Taken the LOD of 0.73 µg/m^3 into account, 4 bins could be realized [8].

For proving CFD modelling, carbon NPs (Ø ≈ 40–250 nm, 10 µg/cm^3) nebulized in a sealed chamber are investigated using FMPS (5.6–560 nm, 32 size bins, TSI Inc., Model 3,091, Shoreview, MN, USA) as reference particle sizer. On active PµCs, which are connected to a µFC (Fig. 10, left), carbon NPs are deposited at $V_{es} = -30$ V as revealed by scanning electron microscopy (SEM, Fig. 12, right), while the passive reference cantilever without connection to a µFC remains clean. For repeated use, particle-loaded PµCs can be cleaned in acetone steam. For this, the sensor PCB has to be detached from the main board and plugged onto a box containing a petri dish with acetone. The cleaning process can be controlled after reconnecting the sensor PCB to the main board and restarting the fan. A positive resonance-frequency shift indicates loss of material from the PµC. After 90 min a

saturation is visible at a mass of 200 ng of dissolved carbon particles, which was collected before within 110 min from the aerosol of $c_m = 10\ \mu g/m^3$.

As predicted by modelling, the experimental resonance-frequency shift rate increases with $|V_{es}|$ (Fig. 12, left). However, larger values than expected by CFD are found in the experiment above $|V_{es}| = 20$ V. One reason for this deviation can be a material dependence of charge distribution, leading to a deviation of charge distribution in the carbon aerosol from the model system (NaCl). Furthermore, a non-zero distance, within which propagating particles will be captured on the PμC, is not considered by CFD modelling. More deposited particles and larger frequency shift have to be expected with increasing electrical field, which is confirmed in the experiment. Finally, direct particle impinging on the cantilever may lead to unspecific particle deposition and thus increased frequency shifts, independent of the electrical field.

According to CFD modelling, a shield below the cantilever will screen it from direct-impinging particles and improve size separation [72]. It can be realized by an additional anisotropic etching step at −95°C, 9 sccm O_2, 15 min before front-side release. A copy of the cantilever structure is generated below the PμC as shown in Fig. 12, right. The backside etching duration is then reduced to 55 min.

The number of particles, which can be sampled in a μFC is rather small. This may cause large statistical error and uncertainty of measured concentration values. Model calculations show that the uncertainty obtained with a sampled PM_1 mass of 30 pg amounts to ±10% [75]. Correspondingly, a mass of 30 pg is deposited on the PμC from 10 $\mu g/m^3$ carbon nanoparticles in the sample volume of 0.3 mL of the MEMS-DMPS at a flow rate of 0.3 mL/min over 9.5 min. To improve uncertainty, either particle concentration or air-flow rate has to be increased. Furthermore, sampling efficiency should be as high as possible. For the latter, the particle-capture cross section has to be maximized. Correspondingly, a single-chip impactor is operated at a large flow rate of 250 mL/min and a TPoS detector with a large sampling area of $150 \times 450\ \mu m^2$ [64]. Alternatively, particle-capture cross section can be increased using an attractive force acting on the particles toward the resonator. In case of thermophoresis rather large temperature gradients have to be generated by a heater (130–150°C) above an FBAR [71]. A sampling efficiency of 12.6 ± 4.2% is found with a DMPS chip at −30 V, whose PμC resonator has a small capture cross section of $171 \times 10.5\ \mu m^2$. In this case, the vertical design of the device has the inherent advantage that μFCs can be arranged in an array and operated simultaneously. Thus, the total volume of sampled particles will be largely enhanced. For sizing, according to the described procedure different constant sampling voltages may be used for each channel. For readout of the different channels a multiplexer may be used, as included in a small-area low-power interface circuit reported for MEMS gas sensors [22]. Table 3 shows the main features of different solutions of gravimetric chip-sized aerosol particle detectors.

Table 3 Features of gravimetric chip-sized aerosol particle detectors

	Impactor & TPoS [64]	Filter & PμC [70]	Thermoph. & FBAR [71]	DMA & PμC [8]
Integration	One chip	One chip	Three chips	One chip
μFC orientation	Vertical	Lateral	Lateral	Vertical
Sizing ability	Lower limit	One bin	One bin	Four bins
Particle class	UFP	PM2.5	PM2.5	UFP

4.2 Particles in Liquids via Microfluidic Channel

PμCs have unveiled the potential for remarkably sensitive label-free detection by transforming target mass alterations into shifts in resonant frequency. While a majority of such assessments have been conducted in air or vacuum conditions due to the detrimental effects of liquid immersion on mechanical responsiveness, in-plane oscillation modes have emerged as the preferred choice compared to the first out-of-plane modes. This preference arises from their reduced damping and susceptibility to mass loading from the surrounding liquid. Even though Q factors reaching up to 1,500 have been documented for the first out-of-plane bending mode in air [76], liquid operation presents challenges due to the substantial viscous damping introduced by the fluid. Additionally, operating in liquid, particularly water, is accompanied by considerably lower Q factors, typically remaining within the range of 10–20 [77]. This milieu also leads to a significant reduction in the out-of-plane resonance frequency, typically by about 30–50%, owing to the substantial effective mass introduced by the fluid. Furthermore, RSMCs interacting with the fluid experience heightened sensitivity to changes in viscosity and density within the liquid medium, which could hinder accurate identification of frequency shifts originating from the attachments of analyte molecules or particles from the liquid.

L.A. Beardslee et al. [79] have meticulously investigated 60 distinct combinations of cantilever length, width, and thickness in water to assess their resonant attributes in relation to the first in-plane flexural mode, with an eye toward their viability for liquid-phase biochemical sensing applications. Their findings indicate that shorter, wider, and thinner cantilevers exhibit the most favorable sensing characteristics. The enhancement of Q factors through geometric optimization of RSMCs has also been explored by Y. Tao et al. [78] (Fig. 13a). In their study, they successfully detected dyna-beads within de-ionized (DI) water by attaching them to a thiolated biotin-modified gold layer on a hammer-structured cantilever (Fig. 13b). Operating the cantilever in its in-plane mode, they achieved a mass sensitivity of − 8.8 Hz/pg. Further functionalization of this cantilever involved immobilizing anti-*E. coli* polyclonal antibodies (pAb) on its Au-pads, enabling the capture and monitoring of *E. coli* in a phosphate-buffered saline (PBS) solution.

Parasitic feedthrough between the actuating and sensing parts on a PμC can affect the spectral shape of amplitude and phase at resonance, which is a severe challenge for (electro-)thermal-piezoresistive resonators and oscillators [80]. Differential-mode

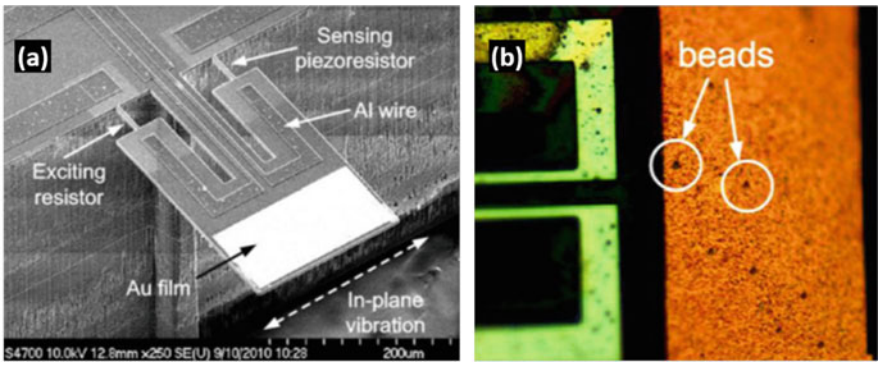

Fig. 13 (**a**) SEM image of the fabricated hammer-structure cantilever-based resonator, (**b**) the adsorbed 10 beads that can be observed in the microscopic image [78]

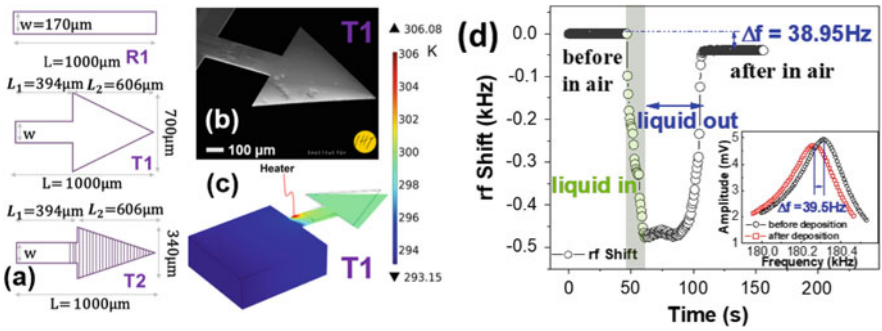

Fig. 14 (**a**) various cantilever configurations, (**b**) SEM graph of cantilever T1, (**c**) finite-element model result: temperature profile along the heating resistor of cantilever T1 and (**d**) continuous resonance frequency monitoring and spectral comparison (inset) of liquid-transported dye particles in microfluidics, depicting adsorption of liquid-borne dye particles from staining microfluidics onto T1 [82]

detection and common-mode drive of active and inactive resonators were proposed for eliminating the feedthrough signal from the resonance response. Alternatively, a reference-signal subtraction method, implemented in a phase-locked loop (PLL) LabVIEW-based user interface with embedded reference parameters, can keep an optimized phase-locking state during resonance tracking [80]. Rectangular and triangular-shaped in-plane oscillating RSMCs (Fig. 14, left) immersed to defined depths into a chamber of 2 mm in diameter and 6.6 mm in height show reasonable Q factors of ~100–670. But non-Lorentzian amplitude shape and reversing-phase characteristic by parasitic feedthrough between the on-cantilever electrothermal actuator and piezoresistive strain gauge hinder an unambiguous resonance-phase tracking using a phase-locked loop (PLL)-based circuit. Electromechanical amplitude modulation (EAM) of the supply voltage of the piezoresistive strain is effective for separating and removing the parasitic actuator-detector feedthrough

from amplitude and phase characteristics, enabling tracking and recording cantilever response in real-time. Resonance-frequency shift measured (Fig. 14, right) in the case of immersing and removing a cantilever into a solution dye particles reveal a deposited mass of ~5.6 ng. The LOD is ~1.0 ng for a totally immersed triangular-tip cantilever. Furthermore, the small density difference of 21 μg/mL between DI water (1.004 g/mL) and tris(hydroxymethyl)aminomethane acetate ethylenediaminetetraacetic acid (TAE) buffer (1.006 g/mL) was clearly resolved by real-time measurements at the same immersed depth of $h = 90$ μm.

5 Gas

The detection of various gases, including hazardous inorganic gases (NO_2, CO, CO_2, SO_2, NH_3, H_2S, etc.), chemical warfare agents (CWA, such as Dimethyl methyl phosphonate (DMMP) and di-isopropyl fluorophosphate (DFP)), and volatile organic compounds (VOCs), has significant implications for assessing potential harm to individuals, animals, and the environment. This concern has prompted global legal regulations. Some of these gases exhibit adverse biological effects, such as toxicity, irritant properties, carcinogenicity, mutagenicity, and reproductive toxicity, while others possess flammable or explosive characteristics. Many other gases, though chemically harmless, can have significant implications for industries, agriculture, and various human activities when present in the atmosphere or enclosed spaces.

The physiological and clinical implications of exposure to harmful gases and vapors extend from cutaneous contact to inhalation, influencing the entire metabolic process. For instance, nitrogen dioxide (NO_2) ranks among the key air pollutants, capable of initiating photochemical reactions that result in photochemical smog, acid rain formation, and increased tropospheric (O_3) concentrations upon light exposure [83, 84]. Even at low concentrations, such as 1 ppmv, NO_2 proves toxic and irritating to the human respiratory system, leading to various respiratory ailments [85–88]. Higher concentrations (3 ppmv) can result in lung lesions, pulmonary edema, or even fatality [84, 89, 90]. To safeguard public health and the environment, the World Health Organization (WHO) recommends air-quality guideline values of 82 ppbv in an hour and 410 ppbv in a year as thresholds beyond which health concerns arise [91, 92]. Similarly, the U.S. Environmental Protection Agency (EPA) has set a maximum exposure level of 100 ppbv for NO_2 in ambient air [86, 87, 93–95]. These guidelines underscore the criticality of monitoring and managing harmful gas exposure.

Although commercial sensors have already been developed for various applications, such as capacitive transducers for humidity detection and chemoresistive sensors for detecting reducing gases, semiconductor-based chemoresistive sensors have garnered substantial attention. These sensors function by altering the resistance of inorganic active materials as gas molecules adsorb or desorb, subsequently inducing space-charge effects. Due to their comparable sensitivity to electrochemical

sensors, extended lifespan, cost-effectiveness, and ease of miniaturized production, they have emerged as a prominent sensor type in the market. Solid-state sensing processes are primarily governed by surface reactions, making nanostructured semiconductors appealing candidates for sensing materials due to their elevated surface-to-volume ratios. However, semiconductor oxides generally possess a limited number of active surface sites for the adsorption of target gas molecules at room temperature. To address this limitation, recent efforts have concentrated on modifying the morphology and doping of nanostructures or creating composite nanostructures to enhance sensitivity, while simultaneously reducing the operating temperature and lowering the LOD to ppbv levels.

Recent advancements include gas sensors achieving LODs of ppbv-level based on various nanostructured materials. For example, ZnO nanostructures operating at temperatures of 150°C [96] and 200°C [97], WO_3 at 140°C [84], In_2O_3 nanobricks at 50°C [89], Fe doped WO_3 nanostructures at 120°C and 150°C [98, 99], 3DOM (three-dimensional ordered macrostructures) WO_3/Li [98] and Pd-doped 3DOM In_2O_3 [100] at room temperature among others have demonstrated enhanced sensing performance. Additionally, UV activation has exhibited improved trace NO_2 gas detection capabilities [92, 101–104], as energetic light illumination can activate sorption sites similarly to high-temperature operation. Ppbv-range sensing behavior of materials has been investigated and reported such as SnO_2-nanosheet composites with ZnO quantum dots [105], MoS_2-nanosheet/ZnO-nanowire heterojunctions [92], and 2D MoS_2 under UV activation at room temperature. All these attempts of nanostructured inorganic metal-oxide sensors that were used for providing a good sensitivity to different gases so far have been based on their high surface–to-volume ratio [106]. Various nanostructured inorganic metal-oxide sensors have been developed to achieve superior sensitivity to diverse gases, primarily owing to their high surface-to-volume ratio. However, the sensing mechanisms often rely on oxygen–vacancy–gas interactions, which lack selectivity for specific gas species.

Over the past few decades, extensive research efforts have been devoted to the exploration of micro- and nano-cantilevers as sensors for particulates, humidity, chemicals, and biological entities. This interest stems from their remarkable capability to detect minute mass changes, rendering them a significant subject of investigation [13, 37, 107–110]. By applying thin polymer films, porous inorganic films, metal oxide (MOX) nanostructures, and MOX nanostructure/polymer hybrids as coatings, PμCs can be effectively transformed into sensors for physical, chemical, or biological interactions. In comparison with conventional technologies, RSMCs present several promising attributes. Notably, they exhibit high sensitivity, affordability, robustness, high-throughput mass production capability, minimal sample volume requirements, low energy consumption, rapid response times, and a label-free operational approach. These advantages make RSMCs highly attractive for a wide range of applications [111–113]. This work aims to address these challenges and offer insights into the development of highly selective RSMCs-based gas sensors.

5.1 Relative Humidity Sensing

The investigation of relative humidity sensing stands as a prominent application within the domain of microcantilever-based resonators. Currently, resistive humidity sensors and capacitive humidity sensors serve as the prevailing choices for commercial humidity sensing. This preference arises from their facile fabrication process, uncomplicated readout circuits (in the case of resistive humidity sensors), and their attributes of low power consumption, wide operational temperature range, and long-term stability (in the case of capacitive humidity sensors). However, inherent limitations still accompany these sensors, manifesting as prolonged recovery periods and diminished stability in the former case, and the need for intricate readout circuitry to achieve high-precision detection in the latter [67, 114–116]. Furthermore, the performance of both resistive and capacitive humidity sensors experiences direct influence from the electrical characteristics of their sensitive materials, resulting in non-linear sensing responses either at low relative humidity (RH) levels, as observed in resistive sensors, or at high RH levels, as in capacitive sensors [114, 117–119]. In the realm of gravimetric sensors, RSMCs endowed with micro/nano-patterns have exhibited remarkable efficacy as relative humidity sensors. Examples include SiO_2 microcantilevers bearing meticulously designed micro-patterns on their surfaces [120], as well as Si RSMCs enhanced with chitosan self-assembled monolayers (SAMs)-modified ZnO nanorods [15]. These nanostructured RSMCs demonstrate heightened sensitivity and rapid response/recovery times (~1 s) across a broad spectrum of relative humidity levels (0–97.3% RH). An instance of multifunctional relative humidity detection has been illustrated by a microcantilever-based sensor, meticulously micromachined with Si nanofins (NFs, Fig. 15a, c), subsequently coated with a ZnO nanofilm and chitosan-SAMs (Fig. 15b) to form the sensing component [121]. The fabricated RSMC (NFs-PMC-0.8) showcases enhanced surface area and improved wettability, resulting in swift response and recovery times when juxtaposed with a state-of-the-art capacitive RH sensor (Fig. 15d) under ambient conditions (26.4 ± 0.2%RH, 26.2 ± 0.1°C). This multifaceted functionality extends to noncontact finger moisture monitoring and respiration testing (Fig. 15e, underscoring the potential of utilizing these NF-patterned ZnO/chitosan-coated RSMCs for real-time multifunctional relative humidity detection.

5.2 Gas Sensing

Early utilization of RSMCs for gas sensing purposes centered around gold-coated commercial atomic force microscopy (AFM) cantilevers, primarily due to the gold-mercury affinity. Notably, commercially available delta-shaped Si nitride AFM cantilevers (Ultralevers, Park Scientific, Sunnyvale, CA) have been embraced for this purpose. These cantilevers, characterized by dimensions of approximately 180 μm in length, 0.6 μm in thickness, and a force constant of 0.06 N/m, underwent

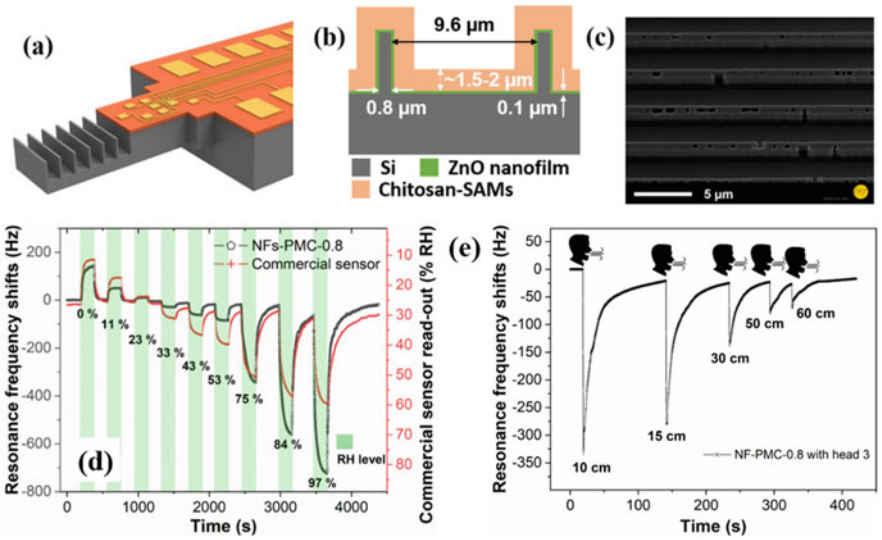

Fig. 15 (**a**) schematic graph of a PµC incorporating micromachined nanofins, (**b**) schematic of Si nanofins (NFs) coated by ZnO nanofilms and chitosan-SAMs, (**c**) 30° tilted SEM graph of a section of the micromachined Si nanofins on a PµC, and (**d**) comparative measurements conducted with the sensor (NFs-PMC-0.8) and a C.A 1246 Logger Thermo-Hygrometer in room atmosphere [121]

complete one-sided gold coating with a 50 nm layer through the process of physical vapor deposition [122]. Similarly, platinum oxide film has been deposited onto commercial AFM cantilevers to enable the detection of 4% hydrogen in argon gas. This mechanism is rooted in the exposure-induced reduction of alpha platinum oxide by hydrogen, leading to an irreversible mass reduction and an increase in resonance frequency [123].

Among the reported and researched sensitive layers on microcantilevers, soft organic films hold a prominent position. These layers are favored due to their ease of fabrication via techniques such as sol-gel dip coating, spray coating, and inkjet printing, among others. The reversible noncovalent interactions existing between organic polymers and gas molecules endow organic materials with an advantage over inorganic counterparts when it comes to the selective detection of toxic gases like nitrogen dioxide (NO_2), sulfur dioxide (SO_2), and ammonia (NH_3) at room temperature [43, 124, 125]. This capability is of significant relevance for operations in intricate and potentially hazardous gaseous environments.

In the year 2000, the initial endeavor in the realm of Si-based PµCs entailed the coating of a 10 µm-thick layer of photoresist polymer onto a Si PMC, which was subsequently exposed to vapors of diverse alcohols. This pioneering study, conducted by Jensenius et al. [126], successfully determined a detection limit below 10 ppm. In a subsequent development, D. Lange and colleagues introduced a compact PµC-based gas sensing system that encompassed integrated resistors for both resonant excitation and detection, as well as driving circuitry and

signal-processing circuitry on a single chip [33]. Utilizing this thermal-excited PμC configuration, the group managed to detect single-ppm gas-phase concentrations of *n*-octane or toluene. Following this, L.A. Pinnaduwage et al. [127] demonstrated the potential of achieving a remarkably low LOD for pentaerythritol tetranitrate (PETN) and hexahydro-1,3,5-triazine (RDX) vapors in the low parts-per-trillion range by depositing 4-mercaptobenzoic acid (4-MBA) self-assembled monolayers (SAMs) on a gold-coated PμC. This achievement was marked by rapid response times in mere seconds, and through the integration of a microcantilever into a non-optical handheld device, a practical handheld gas detection device was realized.

The year 2009 witnessed the fabrication of similar PμC arrays, which were coated on one side with various polymers including poly-vinyl alcohol (PVA), poly-ethylene imine (PEI), poly-acryl amide (PAAM), and poly-vinyl pyrrolidone (PVP). Utilizing piezoresistive Wheatstone bridge (WB) technology to monitor the output signal resulting from the bending of these polymer-coated cantilevers, the selective differentiation of individual alkanes within a homologous series was achieved. A sub-ppm LOD was attained in these endeavors [128]. However, the preference for thick organic layers, stemming from their low surface area, inadvertently led to sluggish response-recovery behavior, causing organic-based semiconductor sensors to exhibit recovery times of approximately 1 h, rendering them unsuitable for many practical applications [43, 129, 130].

In a pursuit to enhance sensor performance, arrays of RSMC were inkjet-printed with diverse polymers, including poly-vinyl alcohol (PVA), poly-ethylene imine (PEI), poly-acryl amide (PAAM), and poly-vinyl pyrrolidone (PVP), which were employed as receptors for gas molecules. Uncoated cantilevers served as reference points. Optically gauging the deflection of cantilever beams allowed the array sensors to discern individual alkanes within a homologous series with sensitivity operating at sub-ppm levels (Fig. 16) [128]. It is pertinent to note that the long-term repeatability and longevity of these RSMCs coated with soft organic films have not yet been formally investigated, thus potential aging of materials might impact receptors and the stiffness of sensitive layers, subsequently influencing sensor responses. Table 4 summarizes other state-of-the-art coated RSMCs, indicating that the LODs of RSMCs to VOCs at room temperature predominantly reside at the ppm level. The trajectory of future efforts is aimed at elevating these LODs to the sub-ppm level.

As expounded upon within the realm of sensitive layer fabrication, the intrinsic long-term reproducibility and reliability of nanostructures of metal oxide semiconductors (MOS) have ignited substantial research interest in the domain of chemoresistive gas sensors. Endeavors aimed at integrating RSMCs and MOS technology have been documented. Various MOS nanostructures, encompassing vertical ZnO NRs [15, 37], ZnO nanotubes [38], CuO NRs and $Cu(OH)_2$ NRs [39], as well as TiO_2 NRs [40, 41] and TiO_2 nanotubes [41], have been meticulously fabricated. These nanostructures have been situated on either commercial AFM cantilevers or on silicon beams during the cantilever fabrication process. The comprehensive overview of these nanofabrication techniques can be found in the

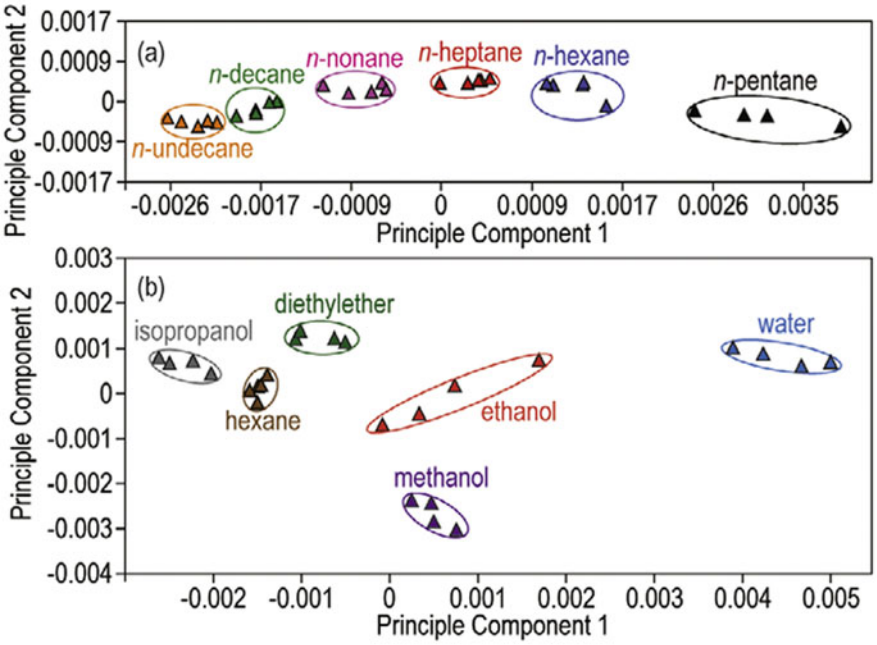

Fig. 16 Principal component analysis case scores of (**a**) alkane molecules with different chain length and (**b**) various solvent vapors with different kinds of substituent [128]

study by Xu and Peiner [9], therefore, we shall refrain from reiterating them within this particular chapter.

In contrast to MOS-based chemoresistive sensors that mandate high operating temperatures, the integration of MOS nanostructures onto RSMCs has enabled the detection of NO_2, VOCs, CWAs at ambient room temperature. The solvothermal synthesis of TiO_2 nanostructures onto silicon cantilevers (as depicted in Fig. 17a) has emerged as a notable endeavor. Various facets pertinent to nanostructure preparation, which significantly influence sensing performances, including the morphology and dimensions of TiO_2 nanorods, are amenable to precise control through the adjustment of diverse synthesis parameters. Among these parameters, the nature of the solvent (as depicted in Fig. 17b) and the volume of titanium tetraisopropoxide (TTIP) hold paramount importance [40]. Subsequently, grafting of oxime molecules (as depicted in Fig. 17c) onto the nanostructured cantilevers has been achieved. This achievement yields a theoretical detection threshold of 2.25 ppm for dimethyl methylphosphonate (DMMP) through utilization of this functionally enhanced and nanostructured RSMC (as depicted in Fig. 17d). It's worth noting, however, that this concentration still remains relatively high when juxtaposed with the Immediately Dangerous to Life or Health (IDLH) threshold.

To enhance the LOD, diverse strategies have been explored, encompassing improved control over resonant frequency tracking to enhance the signal-to-noise

Table 4 State-of-the-art coated RSMC gas sensors

Dimension $L \times W \times T$ µm	actuation	Resonating mode	Readout	Sensing layer	Fabrication of sensing layer	Target analytes	LOD/Q	Reference
150 × 150 × 6	Embedded thermal resistor	Out of plane	PLL	Polar poly(etherurethane) (PEUT) film (4 µm)	Spray coating	n-octane	2.5 ppm/ 1,000	[33]
8 arrays 500 × 100 × 8.6	External piezoelectric crystal	Out of plane	Optical	PVC, PMMA	Drop coating	VOCs, perfume oil		[131]
350 × 150 × 11	Al-bimorph heater	Out of plane	Vibration amplitude	CuO, $Cu(OH)_2$ NRs	PVD, CSD	NO_2/VOCs	3 ppm/> 2 ppm (acrolein)	[39]
Hammerhead T: 8 µm	Embedded thermal resistor	In-plane flexural	PLL	Peptide modified carbon nanotubes	PVD, CSE, PECVD	VOCs	11 ppm to ethanol	[27]
200 × 100 × 3	Embedded thermal resistor	Out of plane	PLL	-COOH and $-NH_2$ modified mesoporous-silica nanoparticles	CSD, inkjet printing	VOCs	~mg/L	[70]
260 × 140 × T (not given)				Poly(epichlorohydrin) (PECH) (2.42 µm)	Spray coating	VOCs	7.5 ppm	[32]
225 × 38 × 7	External piezoelectric crystal	Out of plane	Optical	TiO2 nanotubes	PVD, CSD and CSE	Organophosphorus compounds	2.8 ppm to DMMP	[41]
200 × 100 × 3	Embedded thermal resistor	Out of plane	PLL	Metal–organic framework (MOF) of UiO-66 film	CSD, inkjet printing	Organophosphorus compounds	5 ppb to DMMP	[35]
200 × 100 × 3	Embedded thermal resistor	Out of plane	PLL	$-NH_2$ functionalized mesoporous thin film	Dip coating, SAM, CSE	CO_2	30 ppm	[44]

Triangular length: 700, beam width: 170, beam length: 300, *T*: 12	Embedded thermal resistor	In-plane flexural	PLL	(3-aminopropyl)-trimethoxysilane functionalized ZnO NRs@Si Nanopillars	DRIE, sputtering, CSD SAM	NO_2	~2 ppb	[31]

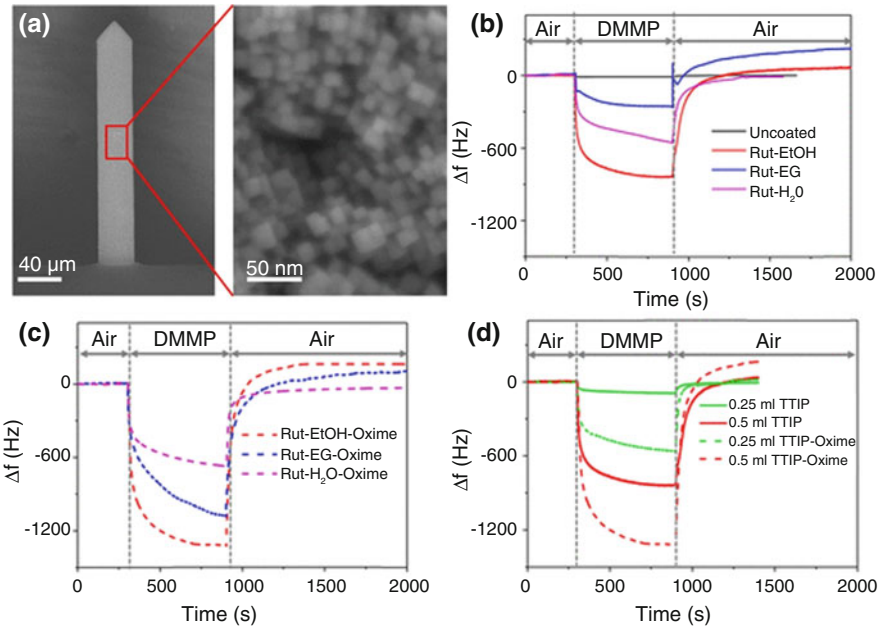

Fig. 17 (**a**) TiO_2 nanostructured cantilever, prepared in ethanol, hydrochloric acid, 0.5 mL of triethylamine hydrochloride (TEACl), and 0.5 mL of titanium tetraisopropoxide (TTIP) at 150°C for 8 h, and measured resonant frequency responses for exposition to 500 ppm of DMMP vapor for (**b**) cantilevers prepared in 0.5 mL of TTIP and a solvent (ethanol, ethylene glycol, or water) and pristine microcantilever and (**c**) oxime-functionalized cantilevers. (**d**) cantilevers prepared in 0.25 and 0.5 mL of TTIP [40]

ratio, utilization of elongated nanorods, and innovative three-dimensional nanomaterials capable of offering an augmented surface area. Noteworthy contributions have emerged, such as the work by S. Cai et al., who established a uniform UiO-66 film in situ upon an RSMC for detecting trace organophosphorus (OP) compounds [35]. Employing a specialized solvothermal-like treatment, the UiO-66 film is meticulously fashioned in situ onto the sensing region defined by the Parylene-C pattern at the unbound end of the microcantilevers. The experimental detection limit achieved by this sensor is superior to 5 ppbv, thereby showcasing a commendable sensing performance with respect to DMMP molecules. In a similar vein, L. Tang et al. proposed an integrated dual-PμC-based gas sensor tailored for the detection of hydrogen sulfide (H_2S) [132]. This sensor integrates an inkjet-deposited layer of basic copper carbonate and nitrogen-doped nanoporous carbon (NPC) derived from zeolitic-imidazolate-framework (ZIF). The combined sensor achieves an impressive LOD of 1 ppbv for H_2S, a feat attributed to the exceptional specific surface area of the ZIF-derived NPC. These approaches have effectively disentangled the synthesis of sensing nanomaterials from their incorporation onto the microcantilever, thereby mitigating compatibility issues and culminating in limit of detection levels in the parts per billion by volume range (as tabulated in Table 4).

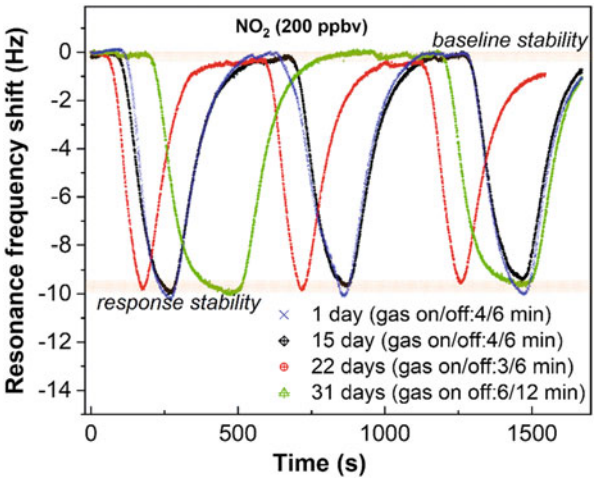

Fig. 18 Dynamic resonance-frequency variation of an S3-PμC in response to exposure to 200 ppbv NO_2 gas, recorded in a dry air environment across various time intervals (1, 15, 22, and 31 days after the sensor was fabricated) [31]

The inkjet-printed coating procedure offers simplicity and reproducibility. However, it's important to note that nanomaterials are deposited in a physically adhered manner, rendering them susceptible to environmental humidity fluctuations, which in turn could undermine their long-term stability. Furthermore, the deployment of nanoporous structures leads to extended response and recovery times.

An alternative method to enhance the surface area of a cantilever beam for sensing involves micromachining the beam prior to its release. This approach has been explored by J. Xu et al., who detailed the fabrication of Si nanopillars on cantilevers' upper side [31, 46] or backside [45]. In addition, ZnO NRs were grown on the etched-Si nanopillars through chemical-solution deposition, thus creating intricate 3D nano frameworks on the cantilever beam. This augmentation resulted in an enlargement of the surface area by two orders of magnitude. The functionalization of these 3D nanostructures with a thin organic self-assembled monolayer (SAM) – specifically (3-aminopropyl)-trimethoxysilane (APTES) – facilitated selective interactions with NO_2. This modification yielded a notable limit of detection (LOD) for NO_2 detection at approximately 2 ppbv. Furthermore, the reliability and stability of the RSMC under both short-term and extended (31 days) exposure to NO_2 were investigated. Remarkably, negligible resonance-frequency shift deviations of at most ±5% and ±9% were observed, respectively (as depicted in Fig. 18). This finding holds potential for the development of highly responsive sensors designed to exhibit robust molecular recognition capabilities, not only for inorganic gases but also for other compounds, by altering the chemical composition of the grafted molecule.

It is preferable to assess directly the gas sensing properties of RSMCs to the other mass-sensitive transducers (MSTs), in spite of the fact that researches comparing RSMCs to other MSTs using identical or approximative sensitive layers are lacking, several reports showed that they have comparable performance to VOCs [33] and DMMP [42]. Although the fundamental resonance frequency of RSMCs is more

than two orders of magnitude lower than that of the other MSTs, the large fractional resonance frequency ($\Delta f_0/f_0$) upon gas exposure contributes to their good gas sensing performance. Besides, some general differences of RSMCs to thickness shear mode resonators (TSMRs) and surface acoustic waves (SAWs) are also helpful for evaluating their properties: (a) different to the TSMRs whose resonance frequency can be geometrically tuned only in thickness, the RSMCs have more geometrical flexibility and feasibility in optimizing their sensitivity, for example, a higher resonance frequency can be obtained by shortening its length, at the same time, its mass sensitivity can be increased by reducing cantilever thickness. (b) Resonant cantilever sensors operate at comparably low frequency, and therefore, the circuitry requirements are less stringent than the high-frequency requirements of SAW devices. In comparison with TSMRs, the RSMCs offer the advantage of co-integration of signal conditioning and processing circuitry which enables the development of very compact array.

6 Conclusions

Resonant silicon microcantilevers (RSMCs) offer simple structure and transduction mechanism, which is applicable to identifying and monitoring a multitude of particle and gas species by changes in mass. They are operated at room temperature and thus have been and remain an attractive platform for various sensing applications. Geometrical consideration for designing of cantilevers, methods for actuating the cantilever beams in resonance as mass sensors and electrical and optical techniques for reading and visualizing their output signals have been well established and developed. Many attempts have been made to improve the sampling efficiency (sensitivity of particle capture or of adsorbing/desorbing a target gas) of RSMCs to target analytes, such as electrophoretic sampling of particles and size-selecting, as well as exploring methods for sensitive coatings on nanostructured 3D hierarchical architectures of large internal surface area. Diverse techniques compatible to fabricate desired structures and materials on the miniature beams have been reported, ranging from simple (such as dip coating, spray coating, sputtering, etc.) to complicated (like chemical-solution deposition/etching, self-assembling, molecular tailoring, biosynthetic methods, etc.), or requiring of special instrumentation (for example, atomic-layer deposition, physical/chemical vapor deposition. . .). Various RSMCs-based devices have been presented, which are designed for the detection of different particles/gases/vapors, such as aerosols, particular matters, inorganic oxides, volatile organic compounds, chemical warfare agents, humidity, etc.). However, the expected breakthrough in RSMCs has occurred to a very limited extent in application areas and is barely visible in the market. Even with the considerable effort spent to develop numerous techniques for coating various sensitive layers, the market situation has not improved. There are still challenges and issues to be faced in the future: (a) Lifetime of sensors is not sufficiently addressed: In most reports, characterization of proposed devices is straightforward to highlight a single

improved property without systematical evaluation of all relevant parameters, i.e., experimental data are often not comprehensively described. Among them, mostly long-time repeatability and lifetime are not announced or tested, especially for devices, which are coated with dip-coated/printing-coated soft organic films. However, aging of materials may lead to a change of receptor performance, e.g., the stiffness of the sensitive layers, which alter the response of the sensor. (b) Most of the sensor prototypes have been characterized in moderate conditions, i.e., their sensing selectivity is not sufficiently proven. However, the working condition of sensors following the market requests is harsher and cross-sensitivity from the environment may be severe. (c) Readout and visualization of the RSMCs' signal is still complex, which make RSMC-based instruments bulkier and more expensive than low-cost optical particle sensors and MOS chemoresistive gas sensors.

Even so, as we can see from these summaries in this chapter, research on mass-sensitive and gravimetric gas sensors based on RSMCs continues to grow in importance, quantity, and geographic scope. The great interest in this scientific and applied topic, witnessed by the increasing number of published reports, publications and patents, reflects a growing market demand to high-performance particle and gas sensors at room temperature, but shows also the free space for future research approaches in this field. The combination of microcantilever and semiconductor nanotechnology offers a variety of innovative methods for the further progress of gravimetric sensing of particles and gases.

Acknowledgment This project has received funding from the EMPIR program co-financed by the Participating States and from the European Union's Horizon 2020 research and innovation program under No. 19ENG05 Nanowires.

References

1. Fletcher PC, Xu Y, Gopinath P et al (2008) Piezoresistive geometry for maximizing microcantilever array sensitivity. Proceedings IEEE Sensors. pp 1580–1583.
2. Daryani MM, Manzaneque T, Wei J, Ghatkesar MK (2022) Measuring nanoparticles in liquid with attogram resolution using a microfabricated glass suspended microchannel resonator. Microsyst Nanoeng 8. https://doi.org/10.1038/s41378-022-00425-8
3. Ezrre S, Reyna MA, Anguiano C et al (2022) Lab-on-a-chip platforms for airborne particulate matter applications: a review of current perspectives. Biosensors 12. https://doi.org/10.3390/bios12040191
4. Muñoz-Galán H, Alemán C, Pérez-Madrigal MM (2023) Beyond biology: alternative uses of cantilever-based technologies. Lab Chip. https://doi.org/10.1039/d2lc00873d
5. Pachkawade V, Tse Z (2022) MEMS sensor for detection and measurement of ultra-fine particles. Eng Res Express 4. https://doi.org/10.1088/2631-8695/ac743a
6. Vasagiri S, Burra RK, Vankara J, Kumar Patnaik MSP (2022) A survey of MEMS cantilever applications in determining volatile organic compounds. AIP Adv 12. https://doi.org/10.1063/5.0075034
7. Mouro J, Pinto R, Paoletti P, Tiribilli B (2021) Microcantilever: dynamical response for mass sensing and fluid characterization. Sensors 21:1–35. https://doi.org/10.3390/s21010115

8. Bertke M, Kirsch I, Uhde E, Peiner E (2021) Ultrafine aerosol particle sizer based on piezoresistive microcantilever resonators with integrated air-flow channel. Sensors 21:3731. https://doi.org/10.3390/s21113731
9. Xu J, Peiner E (2022) Dimensional-nanopatterned piezoresistive silicon microcantilever for environmental sensing. In: Yang Z (ed) Advanced MEMS/NEMS fabrication and sensors1st edn. Springer, Cham, pp 19–47
10. Nyang'au WO, Kahmann T, Viereck T, Peiner E (2021) MEMS-based cantilever sensor for simultaneous measurement of mass and magnetic moment of magnetic particles. Chemosensors 9. https://doi.org/10.3390/chemosensors9080207
11. Fahrbach M, Friedrich S, Behle H et al (2021) Customized piezoresistive microprobes for combined imaging of topography and mechanical properties. Meas Sens 15:100042. https://doi.org/10.1016/j.measen.2021.100042
12. Algamili AS, Khir MHM, Dennis JO et al (2021) A review of actuation and sensing mechanisms in MEMS-based sensor devices. Nanoscale Res Lett 16. https://doi.org/10.1186/s11671-021-03481-7
13. Boisen A, Dohn S, Keller SS et al (2011) Cantilever-like micromechanical sensors. Rep Prog Phys 74:036101. https://doi.org/10.1088/0034-4885/74/3/036101
14. Schmid S, Kurek M, Adolphsen JQ, Boisen A (2013) detection with nanomechanical resonant, pp 3–7. https://doi.org/10.1038/srep01288
15. Xu J, Bertke M, Wasisto HSHS, Peiner E (2019) Piezoresistive microcantilevers for humidity sensing. J Micromech Microeng 29:053003. https://doi.org/10.1088/1361-6439/ab0cf5
16. Oprea A, Weimar U (2019) Gas sensors based on mass-sensitive transducers part 1: transducers and receptors – basic understanding. Anal Bioanal Chem:1761–1787. https://doi.org/10.1007/s00216-019-01630-7
17. Brand O, Dufour I, Stephen Heinrich FJ (2015) Resonant MEMS-fundamentals, implementation and application. Wiley-VCH
18. Bargatin I, Kozinsky I, Roukes ML (2007) Efficient electrothermal actuation of multiple modes of high-frequency nanoelectromechanical resonators. Appl Phys Lett 90:88–91. https://doi.org/10.1063/1.2709620
19. Dufour I, Lochon F, Josse F (2007) Effect of coating viscoelasticity on quality factor and limit of detection of microcantilever chemical sensors. IEEE Sens J 7:230–236. https://doi.org/10.1109/JSEN.2006.888600
20. Schultz JA, Heinrich SM, Josse F et al (2015) Lateral-mode vibration of microcantilever-based sensors in viscous fluids using Timoshenko beam theory. J Microelectromech Syst 24:848–860. https://doi.org/10.1109/JMEMS.2014.2354596
21. Johnson BN, Mutharasan R (2012) Biosensing using dynamic-mode cantilever sensors: a review. Biosens Bioelectron 32:1–18. https://doi.org/10.1016/j.bios.2011.10.054
22. Ren S, Ren M, Xu H (2023) A readout circuit for MEMS gas sensor. Micromachines 14:150. https://doi.org/10.3390/mi14010150
23. Bertke M, Hamdana G, Wu W et al (2017) Analysis of asymmetric resonance response of thermally excited silicon micro-cantilevers for mass-sensitive nanoparticle detection. J Micromech Microeng 27:064001. https://doi.org/10.1088/1361-6439/aa6b0d
24. Lavrik NV, Sepaniak MJ, Datskos PG, Lavrik NV (2004) Cantilever transducers as a platform for chemical and biological sensors. Rev Sci Instrum 2229:2229–2253. https://doi.org/10.1063/1.1763252
25. Bertke M, Xu J, Setiono A et al (2020) Fabrication of a microcantilever-based aerosol detector with integrated electrostatic on-chip ultrafine particle separation and collection. J Micromech Microeng 30:014001. https://doi.org/10.1088/1361-6439/ab4e56
26. Seo JH, Brand O (2008) High Q-factor in-plane-mode resonant microsensor platform for gaseous/ liquid environment. J Microelectromech Syst 17:483–493. https://doi.org/10.1109/JMEMS.2008.916328
27. Beardslee LA, Truax S, Lee JH et al (2011) Selectivity enhancement strategy for cantilever-based gas-phase VOC sensors through use of peptide-functionalized carbon nanotubes. In:

Proceedings of the IEEE international conference on micro electro mechanical systems (MEMS). IEEE, pp 964–967
28. Lang HP, Hegner M, Gerber C (2005) Cantilever array sensors. Mater Today 8:30–36. https://doi.org/10.1016/S1369-7021(05)00792-3
29. Boisen A, Thundat T (2009) Design & fabrication of cantilever array biosensors surface immobilization of functional receptors on microfabricated. Mater Today 12:32–38. https://doi.org/10.1016/S1369-7021(09)70249-4
30. Xu J (2020) Three-dimensional-nanopatterned resonant silicon microcantilevers for gas detection. Technische Universität, Braunschweig
31. Xu J, Setiono A, Peiner E (2020) Piezoresistive microcantilever with SAM-modified ZnO-Nanorods@Silicon-nanopillars for room-temperature parts-per-billion NO2 detection. ACS Appl Nano Mater 3:6609–6620. https://doi.org/10.1021/acsanm.0c01055
32. Possas-Abreu M, Ghassemi F, Rousseau L et al (2017) Development of diamond and silicon MEMS sensor arrays with integrated readout for vapor detection. Sensors 17:1–15. https://doi.org/10.3390/s17061163
33. Lange D, Hagleitner C, Hierlemann A et al (2002) Complementary metal oxide semiconductor cantilever arrays on a single chip: mass-sensitive detection of volatile organic compounds. Anal Chem 74:3084–3095. https://doi.org/10.1021/ac011269j
34. Gates BD, Xu Q, Stewart M et al (2005) New approaches to nanofabrication: molding, printing, and other techniques. Chem Rev 105:1171–1196. https://doi.org/10.1021/cr030076o
35. Cai S, Li W, Xu P et al (2019) In situ construction of metal-organic framework (MOF) UiO-66 film on parylene-patterned resonant microcantilever for trace organophosphorus molecules detection. Analyst 144:3729–3735. https://doi.org/10.1039/c8an02508h
36. Liu M, Guo S, Xu P et al (2018) Revealing humidity-enhanced NH3 sensing effect by using resonant microcantilever. Sens Actuators B Chem 257:488–495. https://doi.org/10.1016/j.snb.2017.10.179
37. Xu J, Bertke M, Li X et al (2018) Fabrication of ZnO nanorods and Chitosan@ZnO nanorods on MEMS piezoresistive self-actuating silicon microcantilever for humidity sensing. Sens Actuators B Chem 273:276–287. https://doi.org/10.1016/j.snb.2018.06.017
38. Bogue R (2014) Nanomaterials for gas sensing: a review of recent research. Sens Rev 34:1–8. https://doi.org/10.1108/SR-03-2013-637
39. Schlur L, Hofer M, Ahmad A et al (2018) Cu(OH)2 and CuO nanorod synthesis on piezoresistive cantilevers for the selective detection of nitrogen dioxide. Sensors 18:1108. https://doi.org/10.3390/s18041108
40. Biapo U, Ghisolfi A, Gerer G et al (2019) Functionalized TiO2 nanorods on a microcantilever for the detection of organophosphorus chemical agents in air. ACS Appl Mater Interfaces 11:35122–35131. https://doi.org/10.1021/acsami.9b11504
41. Thomas G, Gerer G, Schlur L et al (2020) Double side nanostructuring of microcantilever sensors with TiO2-NTs as a route to enhance their sensitivity. Nanoscale 12:13338–13345. https://doi.org/10.1039/d0nr01596b
42. Thomas G, Spitzer D (2021) 3D core-shell TiO2@MnO2 nanorod arrays on microcantilevers for enhancing the detection sensitivity of chemical warfare agents. ACS Appl Mater Interfaces 13:47185–47197. https://doi.org/10.1021/acsami.1c07994
43. Jalil AR, Chang H, Bandari VK et al (2016) Fully integrated organic nanocrystal diode as high performance room temperature NO2 sensor. Adv Mater 28:2971–2977. https://doi.org/10.1002/adma.201506293
44. Yu H, Xu P, Xia X et al (2012) Micro-/nanocombined gas sensors with functionalized mesoporous thin film self-assembled in batches onto resonant cantilevers. IEEE Trans Ind Electron 59:4881–4887. https://doi.org/10.1109/TIE.2011.2173094
45. Xu J, Bertke M, Bornemann S et al (2019) Silicon nanopillars with ZnO nanorods by nanosphere lithography on a piezoresistive microcantilever. 2019 20th international conference solid-state sensors, actuators microsystems Eurosensors XXXIII (TRANSDUCERS

EUROSENSORS XXXIII), pp 2420–2423. https://doi.org/10.1109/TRANSDUCERS.2019.8808435
46. Xu J, Setiono A, Bertke M et al (2019) Piezoresistive microcantilevers 3D-patterned using ZnO-Nanorods@Silicon-nanopillars for room-temperature ethanol detection. 2019 20th International conference solid-state sensors, actuators microsystems Eurosensors XXXIII (TRANSDUCERS EUROSENSORS XXXIII), pp 1211–1214. https://doi.org/10.1109/TRANSDUCERS.2019.8808821
47. Lambert S, Wagner M (2016) Characterisation of nanoplastics during the degradation of polystyrene. Chemosphere 145:265–268. https://doi.org/10.1016/j.chemosphere.2015.11.078
48. Wieland S, Balmes A, Bender J et al (2022) From properties to toxicity: comparing microplastics to other airborne microparticles. J Hazard Mater 428:128151. https://doi.org/10.1016/j.jhazmat.2021.128151
49. Lelieveld J, Klingmüller K, Pozzer A et al (2019) Cardiovascular disease burden from ambient air pollution in Europe reassessed using novel hazard ratio functions. Eur Heart J 40:1590–1596. https://doi.org/10.1093/eurheartj/ehz135
50. Moreno-Ríos AL, Tejeda-Benítez LP, Bustillo-Lecompte CF (2022) Sources, characteristics, toxicity, and control of ultrafine particles: an overview. Geosci Front 13. https://doi.org/10.1016/j.gsf.2021.101147
51. Baron YM (2022) Are there medium to short-term multifaceted effects of the airborne pollutant PM2.5 determining the emergence of SARS-CoV-2 variants? Med Hypotheses 158:110718. https://doi.org/10.1016/j.mehy.2021.110718
52. Marquès M, Domingo JL (2022) Positive association between outdoor air pollution and the incidence and severity of COVID-19. A review of the recent scientific evidences. Environ Res 203. https://doi.org/10.1016/j.envres.2021.111930
53. Nor NSM, Yip CW, Ibrahim N et al (2021) Particulate matter (PM2.5) as a potential SARS-CoV-2 carrier. Sci Rep 11:1–6. https://doi.org/10.1038/s41598-021-81935-9
54. Pozzer A, Dominici F, Haines A et al (2020) Regional and global contributions of air pollution to risk of death from COVID-19. Cardiovasc Res 116:2247–2253. https://doi.org/10.1093/cvr/cvaa288
55. Stakenborg T, Raymenants J, Taher A et al (2022) Molecular detection of SARS-COV-2 in exhaled breath at the point-of-need. Biosens Bioelectron 217:114663. Contents. https://doi.org/10.1016/j.bios.2022.114663
56. Ye YY, Ou Q, Chen W et al (2022) Detection of airborne nanoparticles through enhanced light scattering images. Sensors 22:1–11. https://doi.org/10.3390/s22052038
57. Schilt U, Barahona B, Buck R et al (2023) Low-cost sensor node for air quality monitoring: field tests and validation of particulate matter measurements. Sensors 23:794. https://doi.org/10.3390/s23020794
58. Lee SM, Kim HL, Kwon HB et al (2019) MEMS based particle size analyzer using electrostatic measuring techniques. 2019 20th international conference solid-state sensors, actuators microsystems Eurosensors XXXIII, TRANSDUCERS 2019 EUROSENSORS XXXIII, pp1289–1292. https://doi.org/10.1109/TRANSDUCERS.2019.8808773
59. Kwon HB, Song WY, Lee TH et al (2021) Monitoring the effective density of airborne nanoparticles in real time using a microfluidic nanoparticle analysis chip. ACS Sens 6:137–147. https://doi.org/10.1021/acssensors.0c01986
60. Lee TH, Kwon HB, Song WY et al (2021) Microfluidic ultrafine particle dosimeter using an electrical detection method with a machine-learning-aided algorithm for real-time monitoring of particle density and size distribution. Lab Chip 21:1503–1516. https://doi.org/10.1039/d0lc01240h
61. Lee I, Jeon E, Lee J (2023) On-site bioaerosol sampling and detection in microfluidic platforms. Trends Anal Chem 158:116880. https://doi.org/10.1016/j.trac.2022.116880
62. Liu TY, Sung CA, Weng CH et al (2018) Gated CMOS-MEMS thermal-piezoresistive oscillator-based PM2.5 sensor with enhanced particle. In: 2018 IEEE micro electro mechanical systems (MEMS). IEEE, Belfast, UK, pp 75–78.

63. Weng CH, Pillai G, Li SS (2020) A PM2.5 sensor module based on a TPoS MEMS oscillator and an aerosol impactor. IEEE Sens J 20:14722–14731. https://doi.org/10.1109/JSEN.2020.3010283
64. Maldonado-Garcia M, Mahdavi M, Pourkamali S, Wilson JC (2016) Miniaturized aerosol impactor with integrated piezoelectric thin film resonant mass balance. 2016 IEEE International Frequency Control Symposium IFCS 2016 – Proceedings, pp 22–25. https://doi.org/10.1109/FCS.2016.7563575
65. Maldonado-Garcia M, Kumar V, Wilson JC, Pourkamali S (2017) Chip-scale implementation and cascade assembly of particulate matter collectors with embedded resonant mass balances. IEEE Sens J 17:1617–1625. https://doi.org/10.1109/JSEN.2016.2638964
66. Bertke M, Wu W, Wasisto HS et al (2017) Size-selective electrostatic sampling and removal of nanoparticles on silicon cantilever sensors for air-quality monitoring. TRANSDUCERS 2017 – 19th international conference solid-state sensors, actuators microsystems, vol 1, pp 1493–1496. https://doi.org/10.1109/TRANSDUCERS.2017.7994342
67. Chen Z, Lu C (2005) Humidity sensors: a review of materials and mechanisms. Sens Lett 3:274–295. https://doi.org/10.1166/sl.2005.045
68. Setiono A, Bertke M, Nyang'au WO et al (2020) In-plane and out-of-plane MEMS piezoresistive cantilever sensors for nanoparticle mass detection. Sensors 20:618. https://doi.org/10.3390/s20030618
69. Setiono A, Fahrbach M, Deutschinger A et al (2021) Performance of an electrothermal mems cantilever resonator with fano-resonance annoyance under cigarette smoke exposure. Sensors 21. https://doi.org/10.3390/s21124088
70. Bao Y, Cai S, Yu H et al (2018) A resonant cantilever based particle sensor with particle-size selection function. J Micromech Microeng 28:085019. https://doi.org/10.1088/1361-6439/aabdac
71. Fahimi D, Mahdavipour O, Sabino J et al (2019) Vertically-stacked MEMS PM2.5 sensor for wearable applications. Sens Actuators A Phys 299:111569. https://doi.org/10.1016/j.sna.2019.111569
72. Bertke M, Xu J, Fahrbach M et al (2019) Strategy toward miniaturized, self-out-readable resonant cantilever and integrated electrostatic microchannel separator for highly sensitive airborne nanoparticle detection. Sensors 19:901. https://doi.org/10.3390/s19040901
73. Yadav S, Tripathy S, Sarkar D (2022) NEMS sensors based on novel nanomaterials. In: Yang Z (ed) Advanced MEMS/NEMS fabrication and sensors1st edn. Springer, Cham, pp 133–185
74. Simones MP, Loyalka SK, Duffy C et al (2014) Measurement of the size and charge distribution of sodium chloride particles generated by an Aeroneb Pro® pharmaceutical nebulizer. Eur J Nanomed 6:29–36. https://doi.org/10.1515/ejnm-2013-0018
75. Maierhofer P, Röhrer G, Bainschab M, Bergmann A (2020) On the inherent variability of particulate matter concentrations on small scales and the consequences for miniaturized particle sensors. Aerosol Air Qual Res 20:271–280. https://doi.org/10.4209/aaqr.2019.01.0048
76. Naeli K, Brand O (2009) Dimensional considerations in achieving large quality factors for resonant silicon cantilevers in air. J Appl Phys 105. https://doi.org/10.1063/1.3062204
77. Vančura C, Li Y, Lichtenberg J et al (2007) Liquid-phase chemical and biochemical detection using fully integrated magnetically actuated complementary metal oxide semiconductor resonant cantilever sensor systems. Anal Chem 79:1646–1654. https://doi.org/10.1021/ac061795g
78. Tao Y, Li X, Xu T et al (2011) Resonant cantilever sensors operated in a high-Q in-plane mode for real-time bio/chemical detection in liquids. Sens Actuators B Chem 157:606–614. https://doi.org/10.1016/j.snb.2011.05.030
79. Beardslee LA, Josse F, Heinrich SM et al (2012) Geometrical considerations for the design of liquid-phase biochemical sensors using a cantilever's fundamental in-plane mode. Sens Actuators B Chem 164:7–14. https://doi.org/10.1016/j.snb.2012.01.035

80. Wei L, You Z, Kuai X et al (2022) MEMS thermal-piezoresistive resonators, thermal-piezoresistive oscillators, and sensors. Microsyst Technol 29:1–17. https://doi.org/10.1007/s00542-022-05391-9
81. Setiono A, Fahrbach M, Bertke M et al (2020) Phase characteristic optimization of resonant MEMS environmental sensors. In: Sensoren und Messsysteme – Beitrage der 19. ITG/GMA-Fachtagung
82. Xu J, Cao E, Fahrbach M et al (2023) Real-time operation of microcantilever-based in-plane resonators partially immersed in a microfluidic sampler. In: Proceedings of the IEEE international conference on micro electro mechanical systems (MEMS). IEEE, pp 1037–1040
83. Kirby C, Fox M, Drye T (2001) Influence of environmental parameters on the accuracy of nitrogen dioxide passive diffusion tubes for ambient measurement. Environ Sci Process Impacts:150–158. https://doi.org/10.1039/b007839p
84. Xiao B, Wang D, Wang F et al (2017) Preparation of hierarchical WO3 dendrites and their applications in NO2 sensing. Ceram Int 43:8183–8189. https://doi.org/10.1016/j.ceramint.2017.03.144
85. Atkinson R (2000) Atmospheric chemistry of VOCs and NOx. Atmos Environ 34:2063–2101. https://doi.org/10.1016/S1352-2310(99)00460-4
86. Guarnieri M, Balmes JR (2014) Outdoor air pollution and asthma. Lancet 383:1581–1592. https://doi.org/10.1016/S0140-6736(14)60617-6
87. Huang Y, Jiao W, Chu Z et al (2019) Gas sensors based on SnS2/rGO nanohybrids with P–N transition and optoelectronic visible light enhancement performance. J Mater Chem C 7:8616–8625. https://doi.org/10.1039/c9tc02436k
88. Vineis P, Forastiere F, Hoek G, Lipsett M (2004) Outdoor air pollution and lung cancer: recent epidemiologic evidence. Int J Cancer 111:647–652. https://doi.org/10.1002/ijc.20292
89. Han D, Zhai L, Gu F, Wang Z (2018) Sensors and actuators B: chemical highly sensitive NO 2 gas sensor of ppb-level detection based on In 2 O 3 nanobricks at low temperature. Sens Actuators B Chem 262:655–663. https://doi.org/10.1016/j.snb.2018.02.052
90. Tamaekong N, Liewhiran C, Wisitsoraat A et al (2014) NO2 sensing properties of flame-made MnOx-loaded ZnO-nanoparticle thick film. Sens Actuators B Chem 204:239–249. https://doi.org/10.1016/j.snb.2014.07.089
91. World Health Organization (2006) WHO air quality guidelines-global update 2005. Copenhagen
92. Zhou YCG, Guo Y (2018) UV assisted ultrasensitive trace NO2 gas sensing based on few-layer MoS2 nanosheet–ZnO nanowire heterojunctions at room temperature. J Mater Chem A 6:10286–10296. https://doi.org/10.1039/c8ta02679c
93. Andringa AM, Meijboom JR, Smits ECP et al (2011) Gate-bias controlled charge trapping as a mechanism for NO2 detection with field-effect transistors. Adv Funct Mater 21:100–107. https://doi.org/10.1002/adfm.201001560
94. Hu J, Liang Y, Sun Y et al (2017) Highly sensitive NO 2 detection on ppb level by devices based on Pd-loaded In 2 O 3 hierarchical microstructures. Sens Actuators B Chem. https://doi.org/10.1016/j.snb.2017.05.113
95. Wang Z, Zhang T, Han T et al (2018) Oxygen vacancy engineering for enhanced sensing performances: a case of SnO2 nanoparticles-reduced graphene oxide hybrids for ultrasensitive ppb-level room-temperature NO2 sensing. Sens Actuators B Chem 266:812–822. https://doi.org/10.1016/j.snb.2018.03.169
96. Patil VL, Vanalakar SA, Patil PS, Kim JH (2017) Chemical fabrication of nanostructured ZnO thin films based NO 2 gas sensor via SILAR technique. Sens Actuators B Chem 239:1185–1193. https://doi.org/10.1016/j.snb.2016.08.130
97. Öztürk S, Kılınç N, Ta N, Öztürk ZZ (2011) A comparative study on the NO2 gas sensing properties of ZnO thin films, nanowires and nanorods. Thin Solid Films 520:932–938. https://doi.org/10.1016/j.tsf.2011.04.177

98. Wang Z, Fan X, Han D, Gu F (2016) Structural and electronic engineering of 3DOM WO3 by alkali metal doping for improved NO2 sensing performance. Nanoscale 8:10622–10631. https://doi.org/10.1039/c6nr00858e
99. Zhang Z, Wen Z, Ye Z, Zhu L (2018) Applied surface science ultrasensitive ppb-level NO 2 gas sensor based on WO 3 hollow nanospheres doped with Fe. Appl Surf Sci 434:891–897. https://doi.org/10.1016/j.apsusc.2017.10.074
100. Wang Z, Men G, Zhang R et al (2018) Pd loading induced excellent NO2 gas sensing of 3DOM In2O3 at room temperature. Sens Actuators B Chem 263:218–228. https://doi.org/10.1016/j.snb.2018.02.105
101. Ilin A, Martyshov M, Forsh E et al (2016) UV effect on NO 2 sensing properties of nanocrystalline In 2 O 3. Sens Actuators B Chem 231:491–496. https://doi.org/10.1016/j.snb.2016.03.051
102. Park S, An S, Mun Y, Lee C (2013) UV-enhanced NO2 gas sensing properties of SnO2 -Core/ZnO-shell nanowires at room temperature. ACS Appl Mater Interfaces 5:4285–4292. https://doi.org/10.1021/am400500a
103. Saboor FH, Ueda T, Kamada K et al (2016) Enhanced NO2 gas sensing performance of bare and Pd-loaded SnO2 thick film sensors under UV-light irradiation at room temperature. Sens Actuators B Chem 223:429–439. https://doi.org/10.1016/j.snb.2015.09.075
104. Wei Y, Chen C, Yuan G, Gao S (2016) SnO2 nanocrystals with abundant oxygen vacancies: preparation and room temperature NO2 sensing. J Alloys Compd 681:43–49. https://doi.org/10.1016/j.jallcom.2016.04.220
105. Wu T, Wang Z, Tian M et al (2018) UV excitation NO2 gas sensor Sensitized by ZnO quantum dots at room temperature. Sens Actuators B Chem 259:526–531. https://doi.org/10.1016/j.snb.2017.12.101
106. Hoffmann MWG, Prades JD, Mayrhofer L et al (2014) Highly selective SAM-nanowire hybrid NO2sensor: insight into charge transfer dynamics and alignment of frontier molecular orbitals. Adv Funct Mater 24:595–602. https://doi.org/10.1002/adfm.201301478
107. Kilinc N, Cakmak O, Kosemen A et al (2014) Fabrication of 1D ZnO nanostructures on MEMS cantilever for VOC sensor application. Sens Actuators B Chem 202:357–364. https://doi.org/10.1016/j.snb.2014.05.078
108. Wasisto HS, Merzsch S, Stranz A et al (2013) Femtogram aerosol nanoparticle mass sensing utilising vertical silicon nanowire resonators. Micro Nano Lett 8:554–558. https://doi.org/10.1049/mnl.2013.0208
109. Wasisto HS, Merzsch S, Uhde E et al (2015) Handheld personal airborne nanoparticle detector based on microelectromechanical silicon resonant cantilever. Microelectron Eng 145:96–103. https://doi.org/10.1016/j.mee.2015.03.037
110. Ziegler C (2004) Cantilever-based biosensors. Anal Bioanal Chem 379:946–959. https://doi.org/10.1007/s00216-004-2694-y
111. Goeders KM, Colton JS, Bottomley LA (2008) Microcantilevers: sensing chemical interactions via mechanical motion. Chem Rev 108:522–542. https://doi.org/10.1021/cr0681041
112. Vashist SK (2007) A review of microcantilevers for sensing applications. J Nanotechnol 3:1–18. https://doi.org/10.2240/azojono0115
113. Vashist SK, Holthöfer H (2010) Microcantilevers for sensing applications. Meas Control 43:84–88. https://doi.org/10.1177/002029401004300305
114. Farahani H, Wagiran R, Hamidon MN (2014) Humidity sensors principle, mechanism, and fabrication technologies: a comprehensive review. Sensors 14:7881–7939. https://doi.org/10.3390/s140507881
115. Fenner R, Zdankiewicz E (2001) Micromachined water vapor sensors: a review of sensing technologies. IEEE Sens J 1:309–317. https://doi.org/10.1109/7361.983470
116. Lee C-Y, Lee G-B (2005) Humidity sensors: a review. Sens Lett 3:1–15. https://doi.org/10.1166/sl.2005.001
117. Huang JQ, Li F, Zhao M, Wang K (2015) A surface micromachined CMOS MEMS humidity sensor. Micromachines 6:1569–1576. https://doi.org/10.3390/mi6101440

118. Kim JH, Hong SM, Moon BM, Kim K (2010) High-performance capacitive humidity sensor with novel electrode and polyimide layer based on MEMS technology. Microsyst Technol 16:2017–2021. https://doi.org/10.1007/s00542-010-1139-0
119. Wang Y, Park S, Yeow JTWW et al (2010) A capacitive humidity sensor based on ordered macroporous silicon with thin film surface coating. Sens Actuators B Chem 149:136–142. https://doi.org/10.1016/j.snb.2010.06.010
120. Balasubramanian S, Polaki SR, Prabakar K (2020) Ultrahigh sensitive and ultrafast relative humidity sensing using surface enhanced microcantilevers. Smart Mater Struct 29:095006. 13 p. https://doi.org/10.1088/1361-665x/ab9f1a
121. Xu J, Peiner E (2021) Micromachined silicon cantilever resonator-based humidity sensors for multifunctional applications. Proceedings IEEE international conference micro electro mechanical systems, pp 326–329. https://doi.org/10.1109/MEMS51782.2021.9375323
122. Thundat T, Wachter EA, Sharp SL, Warmack RJ (1995) Detection of mercury vapor using resonating microcantilevers. Appl Phys Lett 1695:1695. https://doi.org/10.1063/1.113896
123. Thundat T, Maya L (1999) Monitoring chemical and physical changes on sub-nanogram quantities of platinum dioxide. Surf Sci 430. https://doi.org/10.1016/S0039-6028(99)00422-7
124. Di CA, Zhang F, Zhu D (2013) Multi-functional integration of organic field-effect transistors (OFETs): advances and perspectives. Adv Mater 25:313–330. https://doi.org/10.1002/adma.201201502
125. Zhang C, Chen P, Hu W (2015) Organic field-effect transistor-based gas sensors. Chem Soc Rev 44:2087–2107. https://doi.org/10.1039/c4cs00326h
126. Jensenius H, Thaysen J, Rasmussen AA et al (2000) A microcantilever-based alcohol vapor sensor-application and response model. Appl Phys Lett 76:2615–2617. https://doi.org/10.1063/1.126426
127. Pinnaduwage LA, Hedden DL, Gehl A et al (2004) A sensitive, handheld vapor sensor based on microcantilevers. Rev Sci Instrum 75:4554–4557. https://doi.org/10.1063/1.1804998
128. Yoshikawa G, Lang H-P, Akiyama T et al (2009) Sub-ppm detection of vapors using piezoresistive microcantilever array sensors. Nanotechnology 20:015501. https://doi.org/10.1088/0957-4484/20/1/015501
129. Ji S, Wang H, Wang T, Yan D (2013) A high-performance room-temperature NO2 sensor based on an ultrathin heterojunction film. Adv Mater 25:1755–1760. https://doi.org/10.1002/adma.201204134
130. Ji S, Wang X, Liu C et al (2013) Controllable organic nanofiber network crystal room temperature NO 2 sensor. Org Electron Phys Mater Appl 14:821–826. https://doi.org/10.1016/j.orgel.2013.01.006
131. Battiston FM, Ramseyer J, Lang HP et al (2001) A chemical sensor based on a microfabricated cantilever array with simultaneous resonance-frequency and bending readout. Sens Actuators B 77:122–131
132. Tang L, Xu P, Li M et al (2020) H2S gas sensor based on integrated resonant dual-microcantilevers with high sensitivity and identification capability. Chin Chem Lett 31:2155–2158. https://doi.org/10.1016/j.cclet.2020.01.018